Springer Series in Biomaterials Science and Engineering 3

Mitsuo Niinomi
Takayuki Narushima
Masaaki Nakai *Editors*

Advances in Metallic Biomaterials

Tissues, Materials and Biological Reactions

Springer

Springer Series in Biomaterials Science and Engineering

Volume 3

Series editor
Prof. Min Wang
Department of Mechanical Engineering
The University of Hong Kong
Pokfulam Road, Hong Kong
e-mail: memwang@hku.hk

Aims and scope

The Springer Series in Biomaterials Science and Engineering addresses the manufacture, structure and properties, and applications of materials that are in contact with biological systems, temporarily or permanently. It deals with many aspects of modern biomaterials, from basic science to clinical applications, as well as host responses. It covers the whole spectrum of biomaterials – polymers, metals, glasses and ceramics, and composites/hybrids – and includes both biological materials (collagen, polysaccharides, biological apatites, etc.) and synthetic materials. The materials can be in different forms: single crystals, polycrystalline materials, particles, fibers/wires, coatings, non-porous materials, porous scaffolds, etc. New and developing areas of biomaterials, such as nano-biomaterials and diagnostic and therapeutic nanodevices, are also focuses in this series. Advanced analytical techniques that are applicable in R & D and theoretical methods and analyses for biomaterials are also important topics. Frontiers in nanomedicine, regenerative medicine and other rapidly advancing areas calling for great explorations are highly relevant.

The Springer Series in Biomaterials Science and Engineering aims to provide critical reviews of important subjects in the field, publish new discoveries and significant progresses that have been made in both biomaterials development and the advancement of principles, theories and designs, and report cutting-edge research and relevant technologies. The individual volumes in the series are thematic. The goal of each volume is to give readers a comprehensive overview of an area where new knowledge has been gained and insights made. Significant topics in the area are dealt with in good depth and future directions are predicted on the basis of current developments. As a collection, the series provides authoritative works to a wide audience in academia, the research community, and industry.

More information about this series at http://www.springer.com/series/10955

Mitsuo Niinomi • Takayuki Narushima
Masaaki Nakai
Editors

Advances in Metallic Biomaterials

Tissues, Materials and Biological Reactions

Springer

Editors
Mitsuo Niinomi
Institute for Materials Research
Tohoku University
Sendai, Japan

Takayuki Narushima
Department of Materials Processing
Tohoku University
Sendai, Japan

Masaaki Nakai
Institute for Materials Research
Tohoku University
Sendai, Japan

ISSN 2195-0644 ISSN 2195-0652 (electronic)
Springer Series in Biomaterials Science and Engineering
ISBN 978-3-662-46835-7 ISBN 978-3-662-46836-4 (eBook)
DOI 10.1007/978-3-662-46836-4

Library of Congress Control Number: 2015941728

Springer Heidelberg New York Dordrecht London

Printed on acid-free paper

Springer-Verlag GmbH Berlin Heidelberg is part of Springer Science+Business Media (www.springer.com)

Preface

Metallic biomaterials are of great importance in the development of implant devices. They are usually used in load-bearing implants, such as artificial joints (for instance, a hip joint), spinal fixation devices, nails, bone plates and screws, and dental implants, which are designed for reconstruction of failed hard tissue. Metallic biomaterials may be employed not just as a replacement for failed hard tissue but also in the reconstruction of soft tissues such as blood vessels. Some of the representative metallic biomaterials include stainless steels, Co–Cr alloys, and titanium and its alloys. Other examples of metallic biomaterials are magnesium-based alloys, tantalum-based alloys, niobium-based alloys, and precious alloys such as gold-based alloys and silver-based alloys containing a large amount of platinum and gold. Metallic biomaterials are also employed in the fabrication of dental prostheses including crowns, dentures, inlays, and bridges.

The research and developments in metallic biomaterials are energetically being carried out, and significant new results have been achieved or currently are being achieved. According to the developments in metallic biomaterials, the latest advances in the construction of implant devices using metallic biomaterials are remarkable.

Understanding the properties of biological tissues and organs is important for the development of bio-functional metallic biomaterials, and understanding their fundamental behavior is also important. The ways in which biomaterials react with the body should also be well understood for further development of metallic biomaterials that are safe to use within the human body.

Even the safest metallic biomaterials exhibit no bio-functionality. Therefore, bioactive or bio-functional surface modifications must be performed on metallic biomaterials in order to achieve the required biological properties, for example, bone conductivity or blood compatibility.

A review of the latest advances and current fundamental knowledge concerning tissues, materials, biological reactions, and the processing and applications of metallic biomaterials is given in two volumes of books entitled *Advances in*

Metallic Biomaterials: Tissues, Materials, and Biological Reactions and *Advances in Metallic Biomaterials: Processing and Applications*.

The volume *Advances in Metallic Biomaterials: Tissues, Materials, and Biological Reactions* has the following structure: Part I Biological Tissues and Organs, Part II Metallic Biomaterials, and Part III Reaction of Metals in Human Body. Part I consists of five chapters, each focusing on one of the following: bone tissue and biomaterials design based on the anisotropic microstructure, joint and articular cartilage, metallurgy of spinal instrumentation, biomechanics of blood vessels, and tooth and tooth-supporting structures. Part II consists of six chapters, each describing one of the following: nickel-free high-nitrogen stainless steel, Co–Cr alloys as effective metallic biomaterials, titanium alloys for biomedical applications, zirconium alloys for biomedical applications, porous tantalum for applications in orthopedic surgery, and niobium-based biomaterials. Part III consists of three chapters, with each describing one of the following: corrosion of metallic biomaterials, metal allergy to metallic biomaterials, and cytotoxicity of metallic biomaterials, respectively.

The volume *Advances in Metallic Biomaterials: Processing and Applications* has the following structure: Part I Processing Techniques, Part II Surface Modification, and Part III Applications. Part I consists of four chapters, each focusing on one of the following techniques: additive manufacturing technology for orthopedic implants, metal injection molding (MIM) processing, smart hot forging technique in producing biomedical Co–Cr–Mo artificial implants, and electroforming as a new method for the fabrication of degradable pure iron stent. Part II consists of five chapters, each describing one of the following: bioactive ceramic coatings, biofunctionalization of metals with polymers, adhesive strength of bioactive surface layer, surface improvement for biocompatibility of biomedical titanium alloys by dealloying in metallic melt, and functionally graded metallic biomaterials. Part III consists of three chapters, with each describing one of the following applications: metallic biomaterials in orthopedic surgery; stents – functions, characteristics, and materials; and dental metallic materials, respectively.

It is our hope that these books will be useful to readers working in a wide variety of fields that take scientific and practical interests in current and future developments in metallic biomaterials. Each chapter has been written by an international expert who works in relevant fields. We wish to express our sincere thanks to the authors named on a separate page for their excellent contributions. We also wish to express our thanks to Professor Ming Wang at the Department of Mechanical Engineering, University of Hong Kong, who is the Series Editor of Springer's books series; Springer Series in Biomaterials Science and Engineering for giving us a chance to edit these books; and Springer Beijing office for their support, especially to Ms. June Tang and Ms. Heather Feng in publishing these volumes.

Sendai, Japan — Mitsuo Niinomi
Sendai, Japan — Takayuki Narushima
Sendai, Japan — Masaaki Nakai

Contents

Contributors

Alfirano Metallurgy Engineering Department, Sultan Ageng Tirtayasa University, Cilegon, Indonesia

Reed A. Ayers Department of Orthopaedics, University of Colorado SOM, Aurora, CO, USA

Carl J. Boehlert Department of Chemical Engineering and Materials Science, Michigan State University, East Lansing, MI, USA

Evalina Levina Burger Department of Orthopaedics, University of Colorado SOM, Aurora, CO, USA

Burak Dikici Department of Mechanical Engineering, Yuzuncu Yil University, Van, Turkey

Ozgur Duygulu Materials Institute, TUBITAK Marmara Research Center, Gebze-Kocaeli, Turkey

Ziya Esen Department of Materials Science and Engineering, Cankaya University, Ankara, Turkey

Stuart B. Goodman Department of Orthopaedic Surgery, Stanford Medical Center, Stanford University, Redwood City, CA, USA

Serap Gungor Department of Mechanical Engineering, Yuzuncu Yil University, Van, Turkey

Shinji Kamakura Bone Regenerative Engineering Laboratory, Graduate School of Biomedical Engineering, Tohoku University, Aoba-Ku, Sendai, Japan

Toshihiro Kasuga Graduate School of Engineering, Nagoya Institute of Technology, Showa-ku, Nagoya, Japan

Yasuyuki Katada Academic Collaboration Office, National Institute for Materials Science, Tsukuba, Ibaraki, Japan

Mitsuko Kawano Department of Immunobiology, Institute of Development, Aging and Cancer, Tohoku University, Aoba-ku, Sendai, Miyagi, Japan

Christopher J. Kleck Department of Orthopaedics, University of Colorado SOM, Aurora, CO, USA

Takeo Matsumoto Department of Mechanical Engineering, Nagoya Institute of Technology, Showa-ku, Nagoya, Japan

Takayoshi Nakano Biomaterials & Structural Materials Design Area, Course of Materials Science & Engineering, Division of Materials & Manufacturing Science, Graduate School of Engineering, Osaka University, Suita, Osaka, Japan

Takayuki Narushima Department of Materials Processing, Tohoku University, Aoba-ku, Sendai, Japan

Mitsuo Niinomi Institute for Materials Research, Tohoku University, Aoba-ku, Sendai, Japan

Naoyuki Nomura Department of Materials Processing, Graduate School of Engineering, Tohoku University, Aoba-ku, Sendai, Japan

Barry O'Brien Biomedical Engineering, School of Engineering and Informatics, National University of Ireland Galway, Galway, Ireland

Akiko Obata Graduate School of Engineering, Nagoya Institute of Technology, Showa-ku, Nagoya, Japan

Kouetsu Ogasawara Department of Immunobiology, Institute of Development, Aging and Cancer, Tohoku University, Aoba-ku, Sendai, Miyagi, Japan

Vikas Patel Department of Orthopaedics, University of Colorado SOM, Aurora, CO, USA

Nilesh Patil Department of Orthopedics, Millinocket Regional Hospital, Millinocket, ME, USA

Takashi Sakai Department of Orthopaedic Surgery, Osaka University Graduate School of Medicine, Suita, Japan

Shukei Sugita Department of Mechanical Engineering, Nagoya Institute of Technology, Showa-ku, Nagoya, Japan

Tetsushi Taguchi Biomaterials Unit, MANA, National Institute for Materials Science, Tsukuba, Ibaraki, Japan

Yuri Takeda Department of Immunobiology, Institute of Development, Aging and Cancer, Tohoku University, Aoba-ku, Sendai, Miyagi, Japan

Kyosuke Ueda Department of Materials Processing, Tohoku University, Aoba-ku, Sendai, Japan

Toshiyuki Yaguchi Department of Mechanical Engineering, Nagoya Institute of Technology, Showa-ku, Nagoya, Japan

Part I
Biological Tissues and Organs

Chapter 1
Bone Tissue and Biomaterial Design Based on the Anisotropic Microstructure

Takayoshi Nakano

Abstract Bone possesses many functions because of its well-organized hierarchical structure at various levels. Original intact bone exhibits specific anisotropic biological apatite (BAp) crystallite orientation that is closely related to the arrangement of collagen fibrils. Preferential alignment of anisotropic BAp crystallites/collagen fibrils in typical cortical and spongy bones, for example, changes depending on the bone shape, in vivo stress distribution, and bone turnover. The preferential alignment of the BAp *c*-axis, in particular, tends to orient along the stress distribution in the original bones, indicating bone mechanical anisotropy.

Recovery of anisotropic BAp alignment strongly depends on the regenerated portion and regeneration period, which is insufficient to reach the original level, while bone mineral density (BMD) is almost improved to its original value. This finding suggests that BMD recovers prior to the improvement of BAp alignment and the related mechanical function of the regenerated tissue. Remarkable changes in degree of anisotropic BAp orientation are also found in some pathological hard tissues including gene-defected animals developing osteoporosis, osteopetrosis, and osteoarthritis.

The bone tissue from the macro- to nano- scale level, including BAp/collagen orientation, exhibits anisotropic integrity that is closely related to mechanical adaptation. In fact, BAp/collagen alignment is among the most important bone quality indices that can be used to evaluate in vivo stress distribution, nanoscale microstructure, and the related mechanical function in various bones. Optimal design of biomaterials for bone replacement can be provided from the viewpoint of bone tissue anisotropy.

Keywords Bone tissue • Hierarchical structure • Bone quality • Bone cell • Biological apatite (BAp) • Bone anisotropy • Stress distribution • Implant design

T. Nakano (✉)
Biomaterials & Structural Materials Design Area, Course of Materials Science & Engineering, Division of Materials & Manufacturing Science, Graduate School of Engineering, Osaka University, 2-1, Yamada-Oka, Suita, Osaka 565-0871, Japan
e-mail: nakano@mat.eng.osaka-u.ac.jp

M. Niinomi et al. (eds.), *Advances in Metallic Biomaterials*, Springer Series in Biomaterials Science and Engineering 3, DOI 10.1007/978-3-662-46836-4_1

1.1 Introduction

Bone plays many roles such as supporting body weight, protecting the organs, assisting with movement, promoting mineral homeostasis, creating the blood supply, and storing triglycerides [1]. The various functions of bone tissue are strongly related to its hierarchical and anisotropic structure [1]. Bone is often lost due to disease and trauma. Therefore, substitution with artificial medical devices and regenerative medicine is developing and becoming more common in clinical settings, but it is difficult to fully realize the complex role of complicated bony structure. The first step toward this goal is developing a deep understanding of bone structure and function. Thus, this chapter focuses on the anisotropy of bone tissue in terms of its complicated structure and mechanical function.

1.2 Bone Tissue

1.2.1 Bone Structure

Bone has various forms, such as long, flat, short, and irregular, and the sizes and shapes vary among individuals [2]. The adult human skeletal system basically contains approximately 206 bony pieces [2]. Due to its various roles ranging from load support to the regulation of minerals such as calcium or phosphorus, bone is organized hierarchically and anisotropically at various levels (Fig. 1.1) [3]. This composition contributes to essential functions of bone in terms of optimal

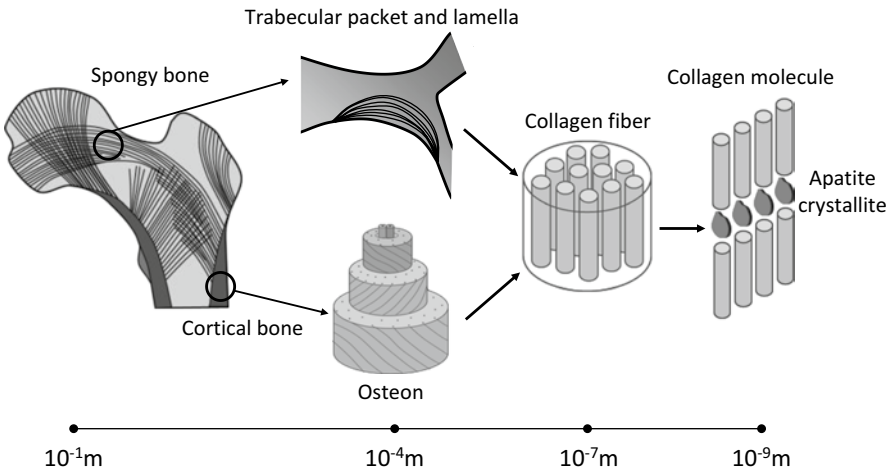

Fig. 1.1 Schematic illustration of hierarchical structure of bone ranging from the atomic to organ level

mechanical properties and homeostasis while cooperating with other important organs. Therefore, in terms of differences in macroshape, various size scales and hierarchical structures, especially an anisotropic organization, are recognized. Bone is controlled from the organ and tissue level down to the micro- and nano-structural levels (Fig. 1.1). At the nanostructural level, cross-linked type I collagen and the mineralized constituent BAp give bone its strength and flexibility, respectively [4]. The BAp is based on hydroxyapatite expressed as the chemical formula $Ca_{10}(PO_4)_6(OH)_2$, but the ionic sites are replaced by large amounts of CO_3^{2-} ion and small amounts of other ionic elements. Thus, BAp is described as (Ca, Na, Mg, K, etc.)$_{10}$(PO_4, CO_3, HPO_4)$_6$(OH, Cl, F)$_2$ [5]. Furthermore, bone cells play important roles and contain very small amounts of protein, cytokines, and hormones. Calcification begins around a collagen hall zone of 27 nm, and the collagen molecule and overlap zones are approximately 300 and 40 nm long, respectively [6].

Bones are classified into cortical and spongy types, which are responsible mainly for load support and turnover, respectively. The relative ratio of spongy bone surface area to volume is greater than that of cortical bone since it contributes to essential mineral homeostasis through the bone marrow.

Figure 1.2 shows the anatomical median section of the human proximal femoral bone. The trabeculae in the maximum principal stress vector are preferentially aligned in abundant spongy bone at the end of cortical bone according to Wolff's law [7, 8]. From the viewpoint of trabecular direction, the areas of spongy bone within bony trabeculae of the proximal femur are classified into the following groups based on the dominant principal stress direction: greater trochanter group; secondary compressive group; secondary tensile group; principal tensile group; principal compressive group; and Ward's triangle, a radiolucent area between the principal compressive, secondary compressive, and principal tensile trabeculae near the neck of the femur that features low-density trabeculae [9].

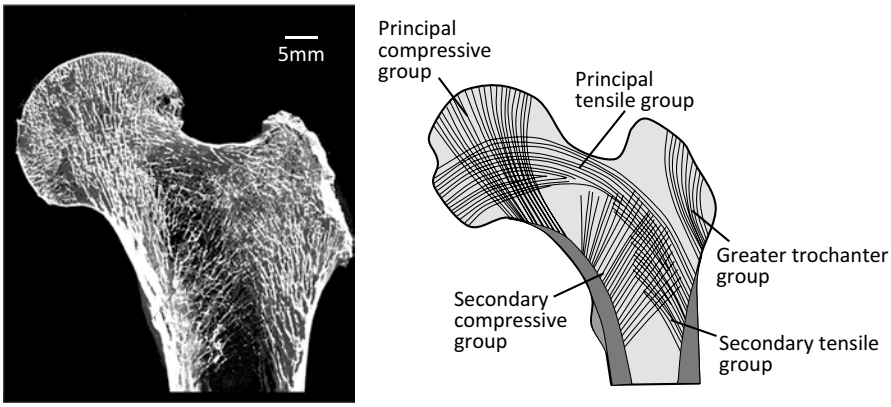

Fig. 1.2 Schematic illustration of typical trabecular pattern in the proximal portion of a human femur. The directions of the trabecular extension are well correlated with the in vivo stress pattern

Bone dynamics are regulated by bone cell function and the related abundant blood vessels and nerves. A cylindrical unit called the osteon forms multiple concentric circles in the Haversian canal through which a blood vessel traverses longitudinally in a long bone (Fig. 1.3) [10]. The internal system remains among the newly formed osteons in the osteal remodeling process.

Furthermore, the diaphysis is surrounded by the outer circumferential lamellae just below the periosteum, while inner circumferential lamellae are located just below the endosteum. The nucleation site of calcification for each osteon is heterogeneous. The Haversian canal runs almost parallel to the bone longitudinal axis and connects with Volkmann's canal and then produces the extensive blood vessel network within the cortical bone [11].

Bone is an internal organ with a very complicated structure that is difficult to mimic artificially. Therefore, bone replacement materials or an artificial joint including metal is used to support functional degradation of bone or bony joints. However, there is a significant difference in microstructure and related function between artificial materials and bone. Therefore, bone repair and artificial joint replacement must place great importance on mechanical safety and joint mobility but may result in only partial bone function recovery. In addition, a bone regenerative technique is also being developed that can reconstruct original bone tissue [12].

Diagnosis and treatment in orthopedic surgery are mainly performed according to bone mineral density (BMD) and bone mass. Therefore, new biomaterials and biodevices for bone development or bone joint replacement should consider the hierarchical and complicated organization of bone tissue containing anisotropic microstructure.

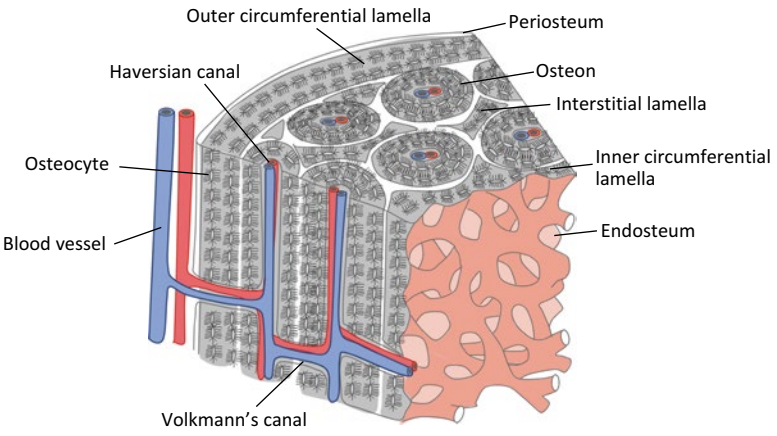

Fig. 1.3 Schematic illustration of the basic microstructure of a cortical bone

1.2.2 Bone Cells

The three dominant bone cell types, namely, osteoblasts, osteoclasts, and osteocytes, interact with other bone-related cells such as mesenchymal stem cells (Fig. 1.4) [13].

Osteoblasts are primarily arranged in a single layer on the surface of both cortical and spongy bones and exhibit an oval-like morphology that covers the bone surface like epithelial cells. Known as active as opposed to quiescent osteoblasts, they preferentially exist on the bone surface for active bone formation and possess cytoplasm, a localized cell nucleus, and a Golgi body near the cell nucleus. Active osteoblasts secrete non-collagen proteins such as osteocalcin and osteopontin and cytokines such as transforming growth factor-β (TGF-β) and bone morphogenetic protein (BMP). Furthermore, matrix vesicles are secreted that calcify the collagen fibril. Calcification of the bone tissue proceeds through the matrix vesicle-mediated process and mineralization along collagen fibers, both of which are preceded by active osteoblast [14].

As bone formation activity weakens, osteoblasts flatten and change into quiescent osteoblasts (bone-lining cells). Quiescent osteoblasts communicate with osteocytes through gap junctions and form well-developed networks. In such networks, osteoblasts become involved in the acceptance of various signal transduction pathways induced by the stimuli including mechanical stress, hormones, and

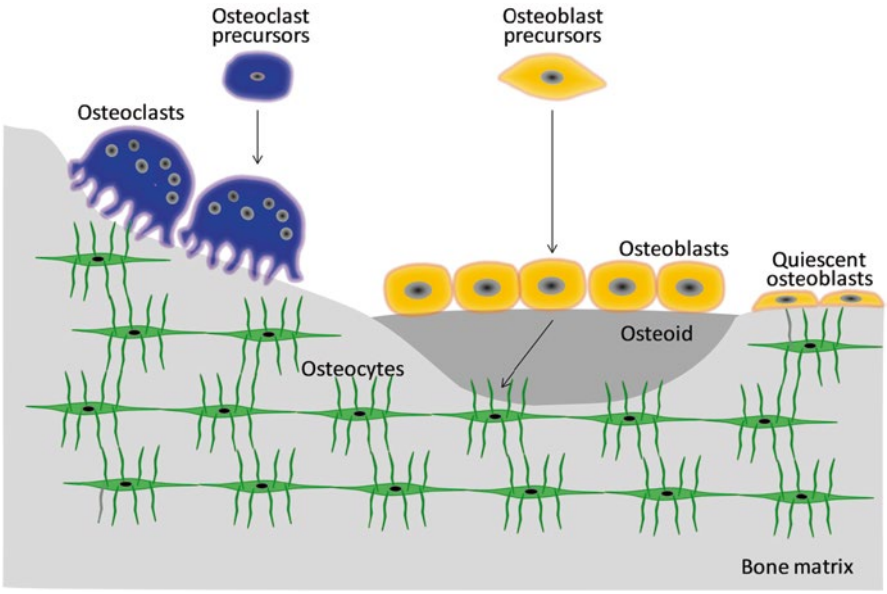

Fig. 1.4 Bone cells involved in bone modeling/remodeling

cytokines and play a role in the regulation of mineral metabolism in collaboration with osteocytes. Runx2 (runt-related transcription factor 2) and Osterix are transcription factors that promote osteoblast differentiation through a BMP cascade [15].

Osteoblasts buried within the newly formed bone matrix subsequently change into osteocytes due to calcification of the surrounding pericellular matrix. Bone canaliculi connect the adjacent osteocyte lacunae. Osteocytes have anisotropic morphology and are surrounded by an anisotropically developed network. The bone canaliculi network is saturated by an interstitial fluid and is very important for the transport of solutes such as cytokines and metabolic products [16]. Osteocytes are the main receptor cells that detect mechanical stimuli and quickly transmit information to osteoblasts and osteoclasts through canaliculi. Sclerostin, a protein encoded by the SOST gene in osteocytes, suppresses bone formation by inhibiting Wnt signaling pathway [17]. Furthermore, fibroblast growth factor 23 (FGF-23) is produced in relation to sclerostin and suppresses phosphorous reabsorption by the kidney [18].

Osteoclasts, which have 5–10 nuclei and are 20–100 μm in diameter, control bone dissolution and absorption. The ruffled border, a deeply indented cell membrane, develops on the surface and dissolves bone mineral and organic bone constituents using acid and hydrolase, respectively, which are secreted by osteoclasts.

Osteoblasts, osteocytes, and osteoclasts work together to achieve bone homeostasis [19]. Bone tissue exhibits complicated functions derived from its hierarchical anisotropic microstructure. The intercellular communication between bone cells is extremely important for functional expression, as is parathyroid hormone and the nervous system, which are closely related to bone metabolic turnover [20]. Clarifying the mutual interaction based on the molecular biology of the cell–cell coupling is necessary to understand both bone formation and the promotion of bone repair when a bone defect is introduced.

1.2.3 Bone Fracture and Natural Healing

When a bone fracture occurs, small defects can be cured spontaneously. Figure 1.5 demonstrates the repair process of general bone fractures in terms of the macroscopic changes. The bone fracture healing process is classified into three phases: inflammatory, reparative, and remodeling [21].

In the inflammatory phase, in addition to the bone damage of the periosteum and bone marrow, the fractured space is occupied by a hematoma, and osteonecrosis occurs due to osteocyte necrosis and extinction near the broken end of the bone. An inflammatory reaction occurs in which the hematoma is removed, inflammatory granulation tissue forms, and osteoclasts remove necrotic bone (Fig. 1.5a).

The reparative phase consists of the soft callus phase and subsequent hard callus phase [22]. In the soft callus phase, capillary blood vessels invade and cells infiltrate

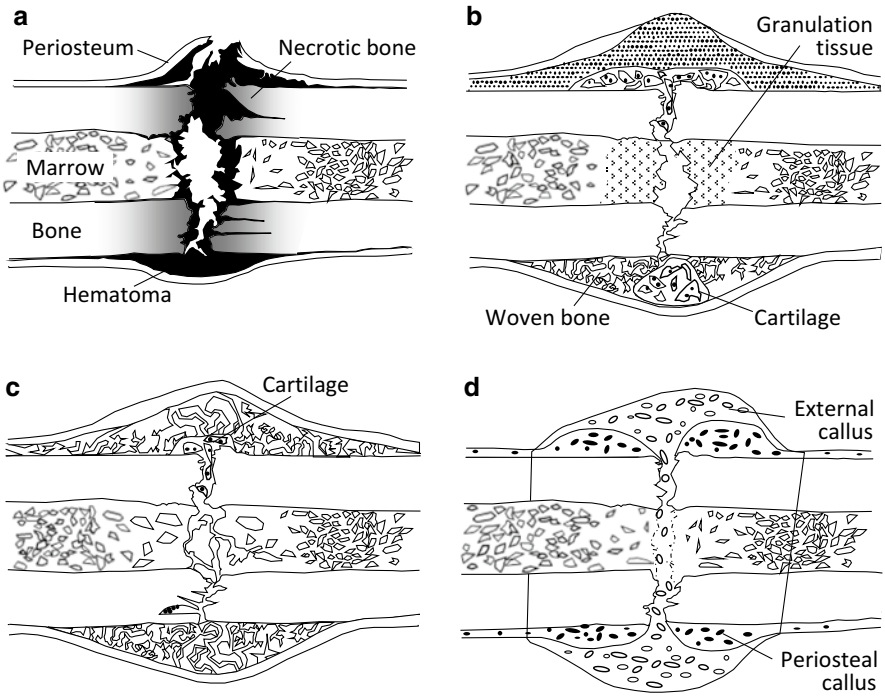

Fig. 1.5 Typical fracture healing process: (**a**) inflammatory phase, (**b**) reparative phase, (**c**) remodeling phase, and (**d**) bone union by external callus formation

the hematoma, the hematoma is removed, and granulation tissue is substituted. The hard callus phase is classified into endochondral and intramembranous ossification according to whether it occurs through cartilage [23]. Intramembranous ossification induces mineral deposition into a callus just under the periosteum without the appearance of chondrocytes when fixation is strong enough in the bone fracture region depending on mechanical stability [24]. In contrast, endochondral ossification proceeds via chondrocytes during calcification. In the remodeling phase, immature bone is substituted for lamellar bone due to remodeling, and the bone shape is gradually corrected to the original shape accompanied by marrow cavity formation (Fig. 1.5c). Bone union is finally achieved and the healing process is complete (Fig. 1.5d).

The bone reconstruction process proceeds when accompanied by the release of functional proteins such as BMP [25]. This process is characterized by simultaneous changes in macroshape and microstructure. Thus, changes of bone tissue from the macroscopic shape to the nanostructure level should be hierarchically understood during the process of bone fracture/repair or bone disease from the viewpoint of materials and structural parameters.

1.3 Bone Anisotropy

1.3.1 Anisotropy of Bone Mechanical Properties

Natural creatures under a gravitational environment have anisotropic and multiscale structures that exert efficient and anisotropic functions in the required direction. In other words, living beings can demonstrate the absolutely imperative ability to the fullest in a certain direction [26]. Bone is a typical anisotropic product.

In the human femoral shaft, bone strength strongly depends on the angle from the longitudinal bone axis in tension (Fig. 1.6) [27]. The anisotropy is clear in the stress–strain curves in Fig. 1.6, and the highest ultimate strength is seen parallel to the longitudinal bone axis but rapidly decreases as it approaches the vertical direction. A similar tendency is conspicuously seen in Young's modulus and yield stress, and it is clear that a mechanical function adapts itself to the bone direction and is correlated to the applied in vivo stress. The anisotropy of a bone, represented by mechanical anisotropy in particular, is concerned with the anisotropic structure at the various size levels as mentioned in Sect. 1.2. Therefore, this section focuses upon microstructural anisotropy as it correlates with the mechanical, biological, and chemical functions of bone.

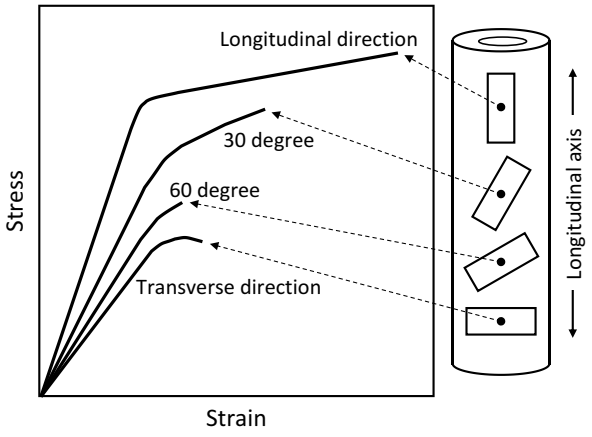

Fig. 1.6 Anisotropic biomechanical property of a long bone. Bone specimens taken in different orientations within the human cortical femur show different stress–strain behaviors (Redrawn from Frankel and Nordin [27])

1.3.2 Bone Anisotropic Structure in Intact Bones

1.3.2.1 Bone Microstructure Based on Apatite/Collagen Orientation

The development of biomaterials and medical devices depends on a clear understanding of the mechanical functions, related microstructure, and microenvironment of bone. Since the consensus statement by the US National Institutes of Health in 2000, bone quality has received attention as a factor determining bone strength as opposed to the traditional indicators of BMD and bone mass [28]. In 2000, proposed bone quality candidates included bone microstructure formation and restoration—typically, the trabecular network structure—and microcracks, collagen status, bone turnover, and cell viability. However, other essential controlling factors for bone quality focus on bone anisotropic microstructure [29, 30].

BAp crystallizes in an anisotropic hexagonal crystal system as an ionic crystal as shown in Fig. 1.7, and its base unit resembles a hexagonal pencil. The arrangement of ions is quite different along the *a*- and *c*-axes in the BAp crystallite, as the *c*-axis is parallel to the hexagonal pencil tip (Fig. 1.7) [5]. As a result, various bone functions are expected depending on the crystallographic direction such as the *a*- and *c*-axes [31]. Moreover, BAp crystallite is roughly distributed along the extending collagen fibril in bone, resulting in enhanced bone anisotropy [32]. Formation of the BAp/collagen complex with an anisotropic arrangement must be closely related to bone function. However, in terms of the present bone diagnosis, BMD and bone mass are generally analyzed by X-ray radiography and X-ray computed tomography (CT) method from the principle of X-ray absorption. In this case, the bone tissue anisotropy based on the BAp/collagen complex is undetectable.

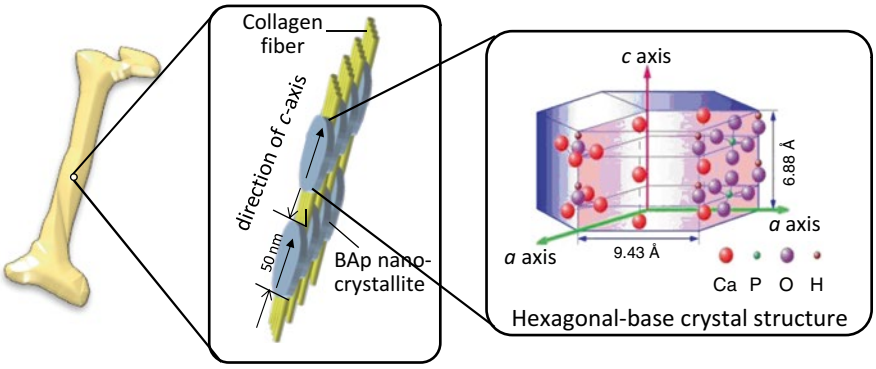

Fig. 1.7 Preferential orientation of biological apatite (BAp) nanocrystallite and collagen fiber in a long bone. The BAp that shows an anisotropic hexagonal crystal structure crystallizes epitaxially on the collagen fiber, where its *c*-axis is almost parallel to the collagen fiber direction

If there is no preferential three-dimensional arrangement of the BAp/collagen complex, the orientation of bone does not depend on its direction and does not influence the bone characteristics. However, because of the strong hierarchical anisotropy of bone, the preferred orientation degree and directional characteristics as a bone quality indicator should be considered in addition to BMD and bone mass as quantitative indices of BAp.

1.3.2.2 Analysis of Anisotropic Biological Apatite (BAp) Crystallite Using Microbeam X-Ray Diffraction (μXRD)

The preferential orientation of the BAp *c*-axis is roughly related to the direction of extended collagen and can be evaluated by various μXRD systems with collimators that are several dozen or hundreds of micrometers in diameter. Such systems are equipped with two-dimensional (2D) detectors (Fig. 1.8) [33]. One-dimensional (1D) or 2D detectors are generally used because the diffracted beam from the small volume of bone specimen is very weak, while the detected diffracted X-ray beam does not come from the symmetrical condition against the specimen surface. In addition, the preferential orientation of the collagen fibrils can be determined using micro-Raman spectroscopy by rotating the specimens with respect to polarization

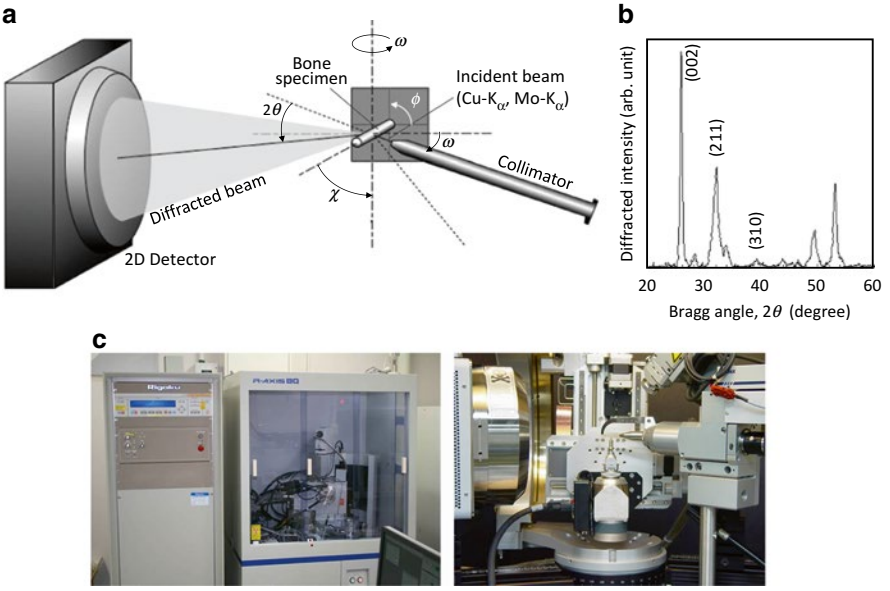

Fig. 1.8 Microbeam X-ray diffraction (μXRD) system for analyzing the biological apatite (BAp) orientation within bones: (**a**) schematic drawing of the transmission optical system, (**b**) X-ray diffraction peak profile taken from a long bone specimen along the long axis, and (**c**) pictures of the μXRD system developed by Rigaku (*right*) and Bruker AXS (*left*)

of the incident laser beam. Collagen molecules exhibit characteristic optical features that can aid in the identification of collagen fiber orientation by referring to the intensity between certain Raman bands, e.g., the amide I (~1,664 cm^{-1}) and C–H bending (~1,451 cm^{-1}) bands [34].

Figure 1.8 shows a schematic illustration of the transmission optics in the Bruker D8 with GADDS system. In this case, diffracted beams were simultaneously detected by a 2D position-sensitive proportional counter (2D PSPC) in which the intensity of the diffracted beam could be detected along the χ and 2θ axes. Distances between the specimen and collimator and between the specimen and detector are very important to the detectable resolution of diffracted beams within the detector. The focused incident beam with characteristic X-ray is used with wavelength of 0.15418 or 0.07107 nm for a Kα ray of copper or molybdenum, respectively. The balance between specimen width and penetration ability is very important, and the latter increases as wavelength decreases.

The specimens are fixed on an Eulerian goniometer with an *X*-*Y*-*Z* stage. The ϕ axis was closest to the specimen and provided complete specimen rotation around that axis. The χ-axis, the next closest to the specimen, was used to tilt the specimen. The specimens were moved to their desired positions by the *X*-*Y*-*Z* stage. The distribution of the X-ray absorption of the bone specimens was measured by an X-ray scintillation counter operating in the integrating mode [35].

Two diffraction peaks of hexagonal-based BAp, (002) and (310), are typically used to analyze BAp *c*-axis orientation [30]. The (002) and (310) diffraction peaks appear via a Cu-Kα incident beam around Bragg angles of 25.9° and 39.8°, respectively (Fig. 1.8b), when the cortical long bone is applied along the bone longitudinal axis. The peak positions of the (002) and (310) diffractions are changed depending on the wavelength of the incident beam into 11.9° and 18.1°, respectively, by the Mo-Kα beam. The degree of BAp *c*-axis orientation is defined to be an integrated intensity ratio of the (002) diffraction to the (310) diffraction.

1.3.2.3 Cortical Bone

The degree of BAp orientation in the bone structure corresponding to the intensity ratio of (002) to (310) changes substantially depending on the bone position and condition, even in the case of normal bones [30]. Figure 1.9 shows the degree of BAp *c*-axis orientation depending on the bone axis and position in various mature cortical bones analyzed using μXRD [30]. In the case of non-orientation, the relative XRD intensity ratio of (002)/(310) is approximately 2, indicating that in cases with higher diffraction intensity, it shows a preferential orientation of the BAp *c*-axis. In mature cortical bone structures, BMD does not change significantly, but BAp shows 1D preferential alignment with the *c*-axis arranged with the priority along the bone longitudinal, mesiodistal, and craniocaudal directions in the long bone of the rabbit ulna, monkey mandible, and monkey lumbar vertebra, respectively, within the cortical bone portions. On the other hand, a flat bone of the rabbit cranial bone shows a 2D orientation along the bone surface. The characteristic orientation distribution is

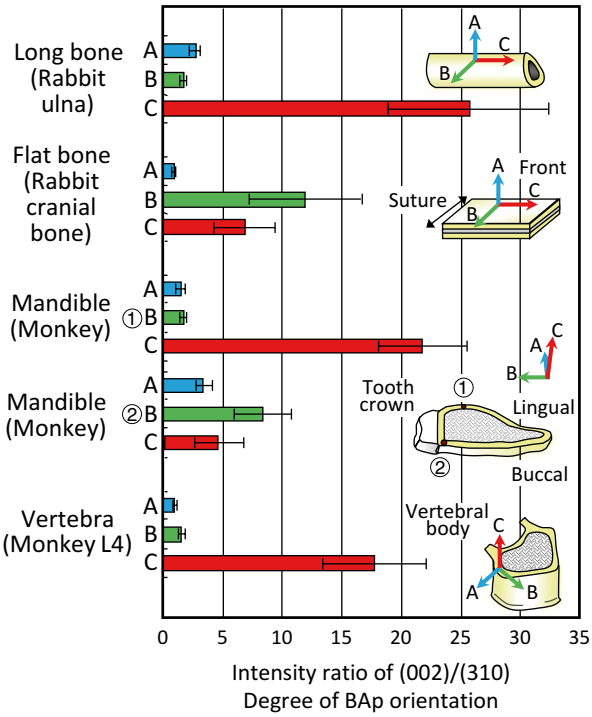

Fig. 1.9 The biological apatite (BAp) orientation distribution assessed as the relative intensity ratio of (002)/(310) in the long bone of a rabbit ulna, flat bone of a rabbit cranial bone, monkey mandible, and monkey vertebra. The BAp orientation largely varies depending on the bone type and direction despite similar bone mineral density (Reprinted from Ref. [30], Copyright 2002, with permission from Elsevier)

closely related to the in vivo stress condition and bone growth process during normal bone turnover. In particular, the direction with the highest degree of BAp *c*-axis orientation is associated with the maximum principal stress direction in bones [30].

The monkey mandible essentially shows the BAp orientation along the mesiodistal direction (the C orientation), but just below the crown of the tooth, the preferential orientation of the BAp *c*-axis changes to the mastication direction (the B orientation) due to the biting direction [30]. This tendency is more remarkable on the buccal side than on the lingual side, which is easily exposed to mastication stress, and it controls the BAp orientation by handling the complex local changes in the in vivo stress distribution due to mastication [30, 36].

1.3.2.4 Spongy Bone

Preferential alignment of BAp *c*-axes is observed even inside each trabecula of spongy bone despite high turnover rate [37, 38].

Figure 1.10 shows preferential distribution of BAp orientation for a trabecula in a human lumbar vertebra analyzed detected using 2D PSPC as shown in Fig. 1.8a [37]. Bright circles or arcs correspond to the diffraction peak, and the (002) diffraction peak that shows the *c*-axis (*c*-plane) of BAp crystallite shows bright arcing along the

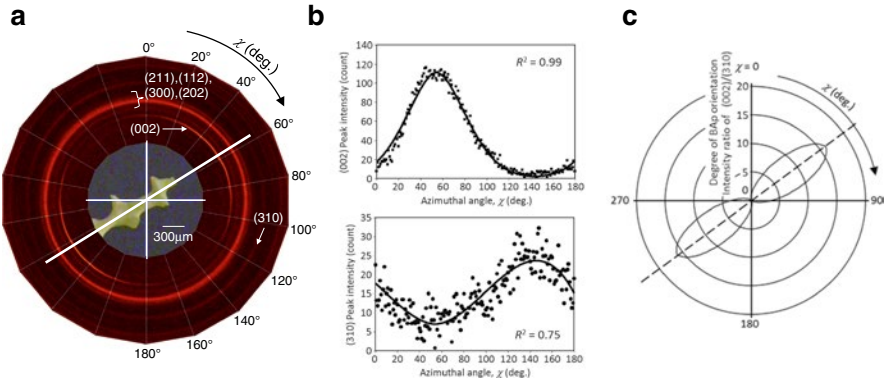

Fig. 1.10 Two-dimensional (2D) analysis of the biological apatite (BAp) *c*-axis for isolated trabecula from human vertebra: (**a**) typical microbeam X-ray diffraction pattern taken from the rod-shaped trabecula, (**b**) variation in diffraction intensity of (002) and (310) planes as a function of azimuthal angle χ, and (**c**) two-dimensional diagrams of BAp orientation distribution along the plane including the trabecular longitudinal axis defined by the intensity ratio of (002)/(310) (Reprinted from Ref. [37], Copyright 2007, with permission from The Japan Institute of Metals and Materials)

extended direction of the trabecula. At the same time, the (310) diffraction intensity increases perpendicularly to the trabecular direction. This means that the trabeculae have a 1D orientation relationship of the preferred BAp *c*-axis along the extended direction similar to the cortical portion of long bone with a 1D orientation. This finding suggests that the trabecular bone is strengthened by the combination of the BAp preferential orientation and extending trabecular morphology along the maximum principal stress direction in vivo as mentioned in Fig. 1.2.

Such a 2D distribution of BAp orientation degree is expressed after background removal for peaks of (002) and (310), and the peak intensity (I) is determined to be a modified elliptic function with the rotation angle χ in the following equation [39]:

$$I(\chi) = \left\{ \frac{\cos^2(\chi - \mu)}{a^2} - \frac{\sin^2(\chi - \mu)}{b^2} \right\}^{-\frac{1}{2}} - c \tag{1.1}$$

This equation can be quantitatively determined by least squares fitting where a, b, c, and μ are the constants that approximate the equation, and μ corresponds to the angle at the intensity peak of the equation. Furthermore, the degree of BAp orientation and preferred direction of BAp alignment are quantitatively enabled by calculation of the intensity ratio I(002)/I(310) after fitting parameter determination. The preferential orientation of BAp crystallites is visualized 2D in the radar diagram, e.g., preferred orientation along the dashed line direction (Fig. 1.10c). The degree of orientation changes in the presence of bone diseases such as osteoporosis [40].

1.3.3 *Effects of Bone Growth and Turnover on Bone Tissue Anisotropy*

The preferential orientation of collagen/BAp is also closely related with bone growth and turnover.

Figure 1.11 shows the relationship between the BAp orientation degree and mineral apposition rate (MAR) around the periosteum in the rat femur [41]. The degree of BAp orientation decreases with increasing MAR independent of alendronate treatment. This finding suggests that the rapid progression rate of calcification induces a decrease in BAp *c*-axis orientation.

Figure 1.12 shows a three-dimensional μCT image reconstructed from the cortical bone with the medullary bone (spongy bone) in a male quail after the injection of adequate doses of estrogen for 90 days as well as the degree of BAp orientation at the distance from the periosteum into the bone marrow site along longitudinal (L) and tangential (T) directions [42]. In the female quail during the egg-laying season, the medullary bone (which acts as a calcium storage site) is quickly absorbed and reformed repeatedly with high turnover to create the egg shells [43]. In contrast, most of the medullary bone is not absorbed when estrogen is administered to a male quail because the medullary bone is not hypermetabolized for producing egg shells [44]. Therefore, the medullary bone which starts to form at the final stage is subjected to the in vivo stress field for a shorter period than the medullary bone which is maintained for 90 days. Because the medullary bone begins to form near the cortical bone, the medullary bone at approximately 0.4 mm from the cortical bone has highly dense trabeculae and preferential alignment of the BAp *c*-axis along the longitudinal bone axis along the applied load. Thus, there is a significant difference in the degree of BAp orientation along the L and T directions in portions of highly dense medullary bone due to the different periods of load application.

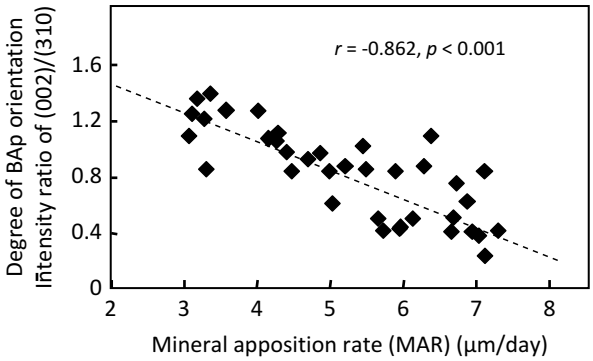

Fig. 1.11 Correlation between the mineral apposition rate (MAR) estimated by calcein double labeling and the degree of the biological apatite (BAp) orientation. The significant negative correlation indicates that slowly produced bone tissue exhibits a high degree of BAp orientation (Reprinted from Ref. [41], with kind permission from Springer Science + Business Media)

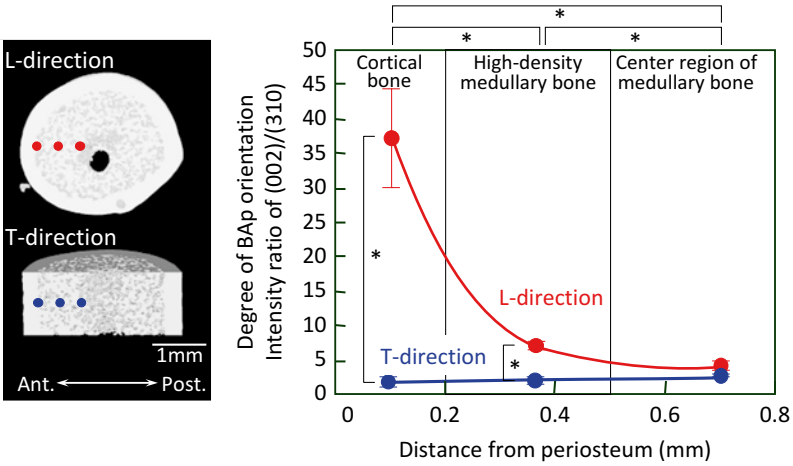

Fig. 1.12 Variation in the degree of biological apatite (BAp) orientation in the femoral midshaft of an estrogen-administered mail quail as a function of distance from the periosteum. The medullary bone induced by estrogen is not used for eggshell formation; hence, the enhancement of the BAp orientation along the bone long axis shown at the high-density region is due to in vivo stress application (Redrawn from Nakano and Yamamoto [42])

On the other hand, the difference in the degree of BAp orientation disappears in the center region of the medullary bone because the load is only applied for a short period. This suggests that the load with extremely low turnover induces an increase in BAp orientation along the loading direction even in the medullary bone.

When both cortical and spongy bones show low bone growth rates and hypometabolism, the degree of BAp orientation tends to increase. As a result, medullary bone with hypometabolism enables load supporting. In other words, bone metabolic turnover affects BAp orientation similar to the significant effect of in vivo stress on bone anisotropy.

1.4 Bone Tissue Microstructure of Regenerated and Pathological Bone

1.4.1 Anisotropic Microstructure Based on BAp Orientation

1.4.1.1 Regenerative Bone

A solid understanding of the microstructure healing process is needed prior to the development of bony biomaterials and medical devices for bone or cartilage defects. Thus, this section focuses on the relationship between bone mechanical function and bone tissue parameters such as BMD and BAp orientation as anisotropic parameters.

Recovered BAp *c*-axis orientation and local BMD are summarized, and the radiographic visualization of repairs is shown in Fig. 1.13 [45, 46]. A 20-mm-long defect, which cannot recover spontaneously, was introduced into a rabbit ulna and regenerated by the controlled release of recombinant BMP-2 (rBMP-2) from gelatin hydrogel [47]. During the early phase of regeneration (2–4 weeks postoperatively), the degree of BAp orientation in the regenerated bone tissue is much lower than that in the non-defected portion. Significant increases are observed from 2 to 4 weeks, 6 to 12 weeks, and 12 to 24 weeks in local BMD and from 4 to 6 weeks and 12 to 24 weeks in the degree of BAp orientation. There are no significant differences from baseline (intact bone) at 24 weeks in either local BMD or degree of BAp orientation [45]. Thus, in the regeneration of rabbit ulnae with controlled release of rBMP-2, recovery of the preferential BAp *c*-axis orientation tends to follow that of BMD.

As an index of bone mechanical function, Young's modulus was measured by the nanoindentation technique in the regenerated and intact bone specimens accompanied by changes in BMD and the BAp orientation (Fig. 1.14) [45]. Because there was little new bone formation, nanoindentation measurements [48] could not be performed at 2 weeks. Due to the recoveries in BMD and preferential BAp *c*-axis orientation, Young's modulus increases monotonically as a function of the regeneration period; the values for regenerated bones are collected at 4, 6, 12, and 24 weeks postoperatively. Twelve weeks postoperatively, the regenerated bone tissue has a much lower Young's modulus than the intact baseline despite high BMD restoration.

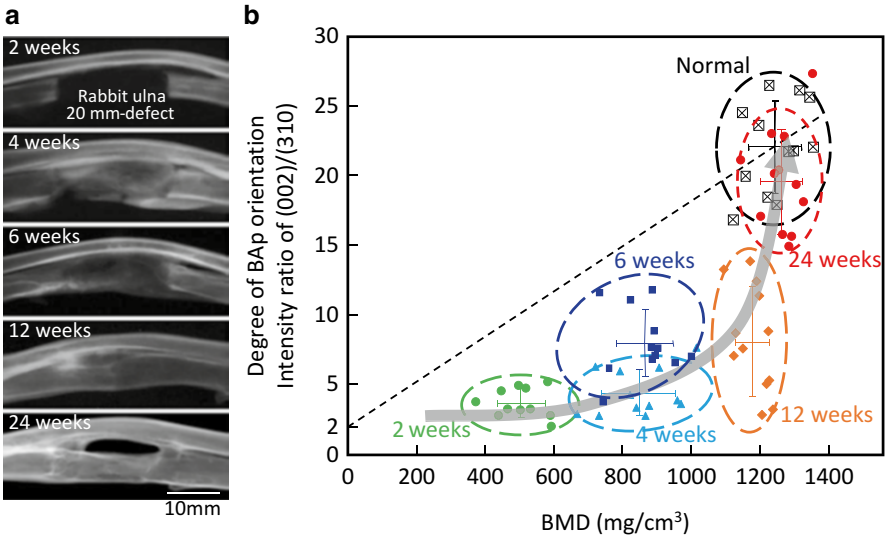

Fig. 1.13 Recovery process of (**a**) bone shape and (**b**) bone mineral density (BMD) and the BAp *c*-axis orientation in the regenerated ulna under the sustained release of recombinant bone morphogenetic protein-2 (rBMP-2). Biological apatite (BAp) (Reproduced from Ref. [45] by permission of John Wiley & Sons Ltd)

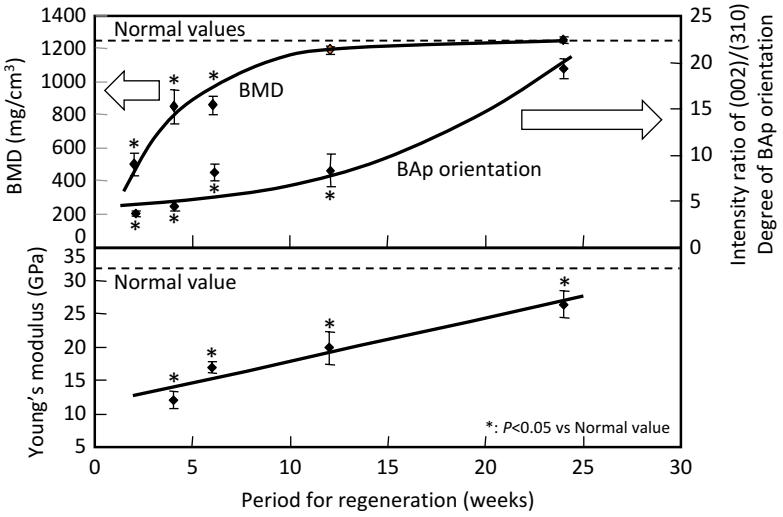

Fig. 1.14 Changes in the biological apatite (BAp) orientation, bone mineral density (BMD), and Young's modulus along with bone healing. Young's modulus value at 12 weeks does not reach the normal value, although the BMD does, indicating that the BMD is not an accurate index for the mechanical function of the bone (Reproduced from Ref. [45] by permission of John Wiley & Sons Ltd)

Figure 1.15 shows correlations between Young's modulus and local BMD or BAp *c*-axis orientation at 4, 6, 12, and 24 weeks postoperatively [45]. In this figure, a significant correlation is represented by a straight line. Young's modulus value is significantly correlated with BMD at 4 weeks only. In contrast, at 6, 12, and 24 weeks postoperatively, Young's modulus value is significantly correlated with the intensity ratio of (002)/(310).

Based on multiple linear regression analysis, Young's modulus can be expressed as a function of BMD and BAp *c*-axis orientation (intensity ratio of (002)/(310)) as follows [45]:

$$\begin{aligned}\text{Young's modulus [GPa]} &= 7.3 + 3.5\times10^{-6}\ (\text{BMD [mg/cm}^3\text{]}) \\ &+ 0.74(\text{intensity ratio of (002)/(310)})\end{aligned} \tag{1.2}$$

The adjusted R^2 for this regression is 0.83, indicating that Young's modulus is largely explained using BMD and BAp *c*-axis orientation as explanatory variables. Thus, BAp *c*-axis orientation is the dominant contributing factor (approximately 70 %) to Young's modulus value of the regenerated bone.

Moreover, new bone formation depends strongly on the strain amplitude on the long bone as shown in Fig. 1.16 [49]. The peak load is strongly influenced by bone

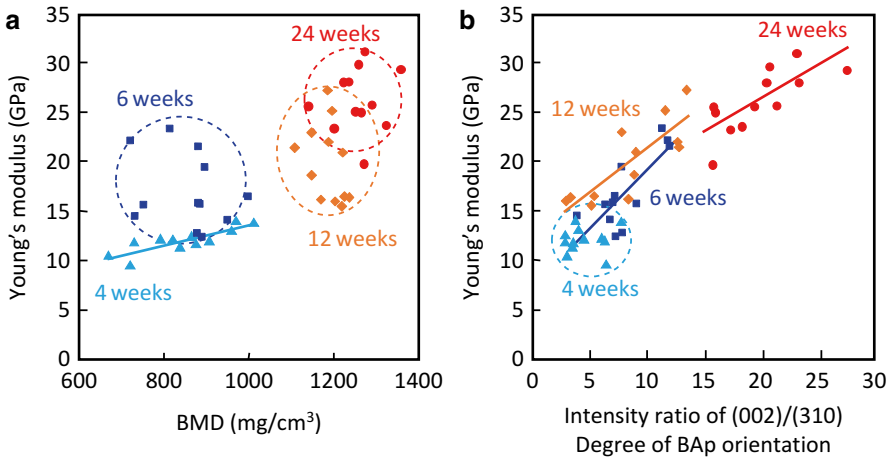

Fig. 1.15 Correlations between Young's modulus and (**a**) bone mineral density (BMD) and (**b**) the biological apatite (BAp) *c*-axis orientation at 4, 6, 12, and 24 weeks. The straight lines represent significant correlations between the parameters. The degree of BAp orientation is the important controlling factor of Young's modulus, especially in the later phase of bone healing (Reproduced from Ref. [45] by permission of John Wiley & Sons Ltd)

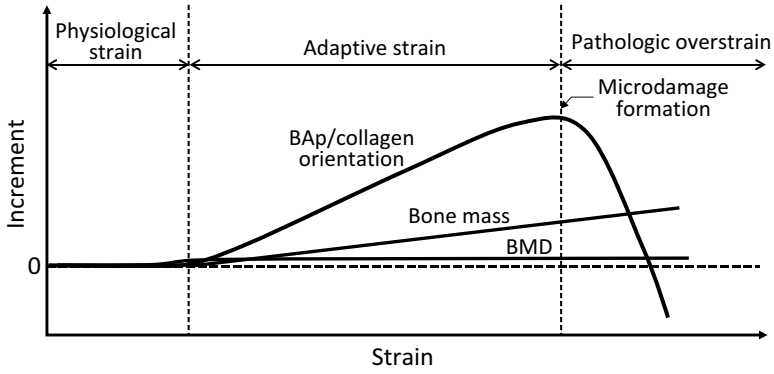

Fig. 1.16 Relative increase in bone mass, bone mineral density, and biological apatite (BAp)/collagen orientation in response to exposure to an artificially applied load. The orientation is the most sensitive in the mechanical adaptation (Redrawn from Wang [49])

mass, BMD, and BAp/collagen orientation, while the anisotropy as the degree of BAp/collagen orientation more strongly influences the adaptive load region over the region for normal walking. In the stage of overload, microcracks are often produced and the degree of BAp/collagen orientation abruptly decreases.

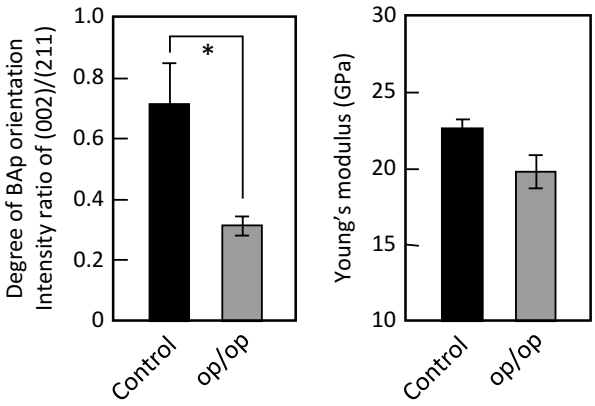

Fig. 1.17 The biological apatite (BAp) orientation and Young's modulus value measured along the femur long axis of osteopetrotic (op/op) and control mice

1.4.1.2 Diseased Bone

In the presence of osteoporosis, osteoarthritis, and osteopetrosis with or without gene defects, the BAp orientation is quite different from that in the normal condition.

Figure 1.17 shows BAp orientation and related mechanical properties as well as Young's modulus in osteopetrotic mice (op/op) lacking macrophage colony-stimulating factor (M-CSF) and control mice. In the op/op mice, osteoclasts hardly appear at 5 weeks [50]. The degree of BAp orientation in op/op mice is much lower than that in the control group, resulting in a decreased Young's modulus value. Thus, the decrease in the degree of anisotropic BAp orientation induces the lack of the optimal mechanical properties corresponding to the bone portion.

In the case of primary osteoporosis rats (OVX), the degree of BAp orientation increases due to mechanical adaptation of the cranial body. This is closely related to the increased in vivo stress load on the cortical portion due to the bone loss [40]. The 3D optimal distribution of the degree of BAp orientation corresponds to the in vivo stress distribution; thus, the increase in the BAp/collagen arrangement is not appropriate because the bone microstructure cannot appropriately support the body weight under unexpected load. The degree of BAp orientation along the craniocaudal direction of preferential direction of the BAp *c*-axis is higher than that of the original bone, indicating an abnormal state.

1.4.2 Parameters Dominating Bone Anisotropy

The controlling factors acting on the degree of BAp orientation are numerous as summarized in Fig. 1.18 [30, 35, 36, 39–41, 45, 46, 51–53]. The BAp orientation is controlled through in vivo mechanical stress information, mechanosensitivity of

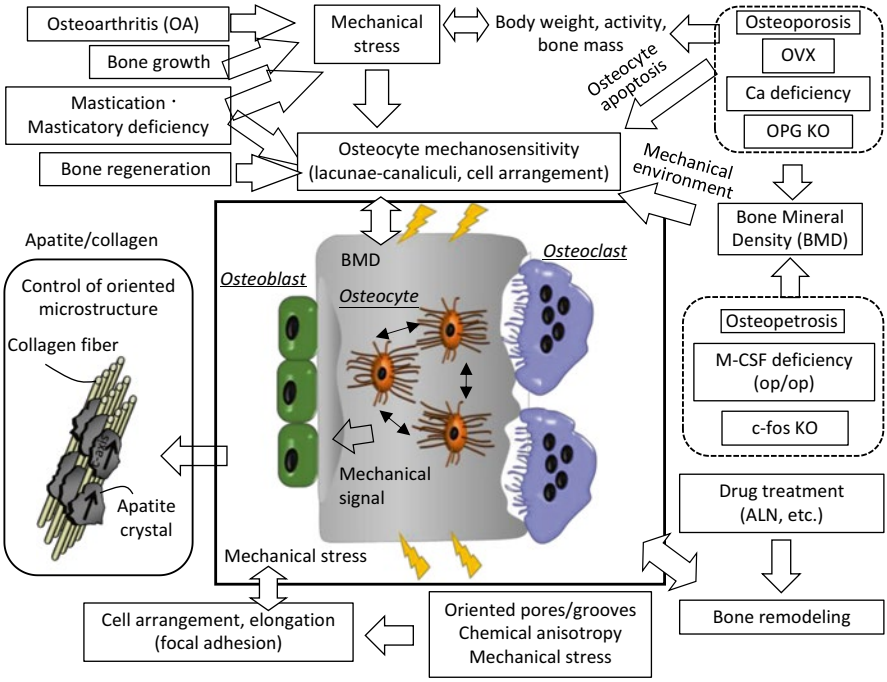

Fig. 1.18 Controlling factors of bone tissue anisotropy based on the biological apatite (BAp)/collagen orientation

osteocytes, and bone metabolic turnover in various processes such as osteoarthritis (OA), bone growth, mastication, bone regeneration, osteoporosis, osteopetrosis, gene defects, drug treatment, cellular arrangement, and other anisotropic conditions. The degree of BAp orientation is a vector quantity, whereas bone density is in scalar field; therefore, bone microstructure information increases markedly.

The BAp/collagen formation and reconstruction mechanism is gradually elucidated at the macro- to microscales, and such anisotropic tissue will finally be artificially controlled in the near future. Of course, the BAp orientation is related to the external environment, including the stress distribution and in vivo environment through molecules and other messengers, and there is no doubt of the roles of osteoclast, osteoblast, and osteocyte coupling.

1.5 Biomaterial Design Concepts for Bone Replacement

The μXRD method is a powerful tool for analyzing the atomic arrangement in the BAp crystallites of bones under various conditions [30]. Moreover, many scientific techniques in addition to traditional methods such as radiography can be applied to

clarify the bone functions [54–57]. This section discusses the development and design of bone implants based on bony structural anisotropy, which is optimally designed for providing suitable BAp orientation that is closely related to mechanical and other functions.

1.5.1 Novel Implant Design

Principal stress promotes alignment of the BAp/collagen preferential orientation [30], in which a novel surface design for an artificial hip joint, tooth implant, etc., can be established toward the formation of the preferred alignment of BAp/collagen (Fig. 1.19a) [39].

In the stem of an artificial hip joint, the groove angle is optimized based on the principal stress inside the grooves through finite element analysis (FEA) (Fig. 1.19b). Only the groove oriented proximally by 60° from the normal direction of the stem surface induces a healthy maximum principal stress along the groove. An in vivo implantation of the artificial hip joint exhibits that the aligned groove is effective in inducing new bone with preferential BAp/collagen alignment along the groove wall that responds to the direction of maximum principal stress inside the groove (Fig. 1.19c).

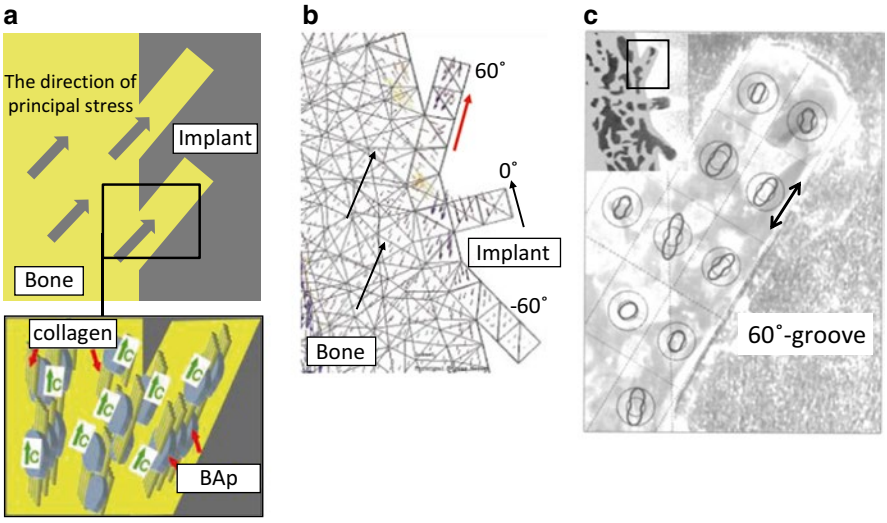

Fig. 1.19 Novel design of implant surface morphology. The oriented grooves are introduced on the metallic stem surface of an artificial hip joint to control stress conditions within the grooves. As a result, new bone with anisotropic biological apatite (BAp)/collagen micro-arrangement forms in the grooves (Redrawn from Noyama et al. [39])

The anisotropic principal stress distribution and oriented microstructure tissue inside the groove are similar to those found in the femoral trabeculae. This suggests that the creation of the oriented groove is a potent surface modification for optimizing implant design for long-term fixation [39].

1.5.2 Control of Bone Cells and Related Extracellular Matrix

Bone tissue provides the appropriate anisotropic structure for exerting its proper function, which is controlled by surface morphology and the chemical and/or physical environment surrounding the constituent cells.

Control of cell alignment is one of the methodologies for arranging the anisotropic extracellular matrix of tissue [58–61]. Figure 1.20 shows the degree of osteoblast arrangement along the slip traces caused by dislocation gliding [62]. Dislocations are introduced into α-titanium single crystals by plastic deformation of the prism slip system, which induces a step-like structure with acute angles between the normal surface and the slip plane. The topographical properties of step patterning, including step interval and height, could be controlled by variation of the compressive plastic strain (Fig. 1.20). The step geometry introduced by plastic deformation strongly influences osteoblast elongation along the slip traces. Cell morphology and preferred alignment are very important because anisotropic control of bone structural formation in vitro is established by organizing cell alignment and the following BAp/collagen preferential orientation.

Bone tissues are derived from the collagen fiber scaffold and the related osteoblast alignment [63]. The oriented collagen substrates were fabricated by a hydrodynamic method, resulting in string-type (strongly oriented) and sheet-type (weakly oriented) scaffolds. Osteoblast orientation is regulated by the degree of the substratum collagen orientation, with preferential alignment along the collagen molecular orientation (Fig. 1.21) [64]. The directional secretion and fibrogenesis of collagen matrix and BAp crystallite formation, which has preferential *c*-axis orientation along the cell direction, are shown in Fig. 1.21. The degree of BAp orientation deposited by osteoblasts depends on the directional distribution of osteoblasts cultured on the oriented collagen substrates (Fig. 1.22).

1.6 Summary

In this chapter, bone structure was described as hierarchical, and anisotropic tissues were shown to be composed primarily of BAp/collagen. Load support, one of the important functions of bone, is regulated by microstructural anisotropy, including prior orientation of the BAp/collagen. Therefore, the development of a biomaterial considering only BMD and bone mass is insufficient. Bone tissue homeostasis is generally maintained, and bone remodeling progresses due to osteoblasts that form

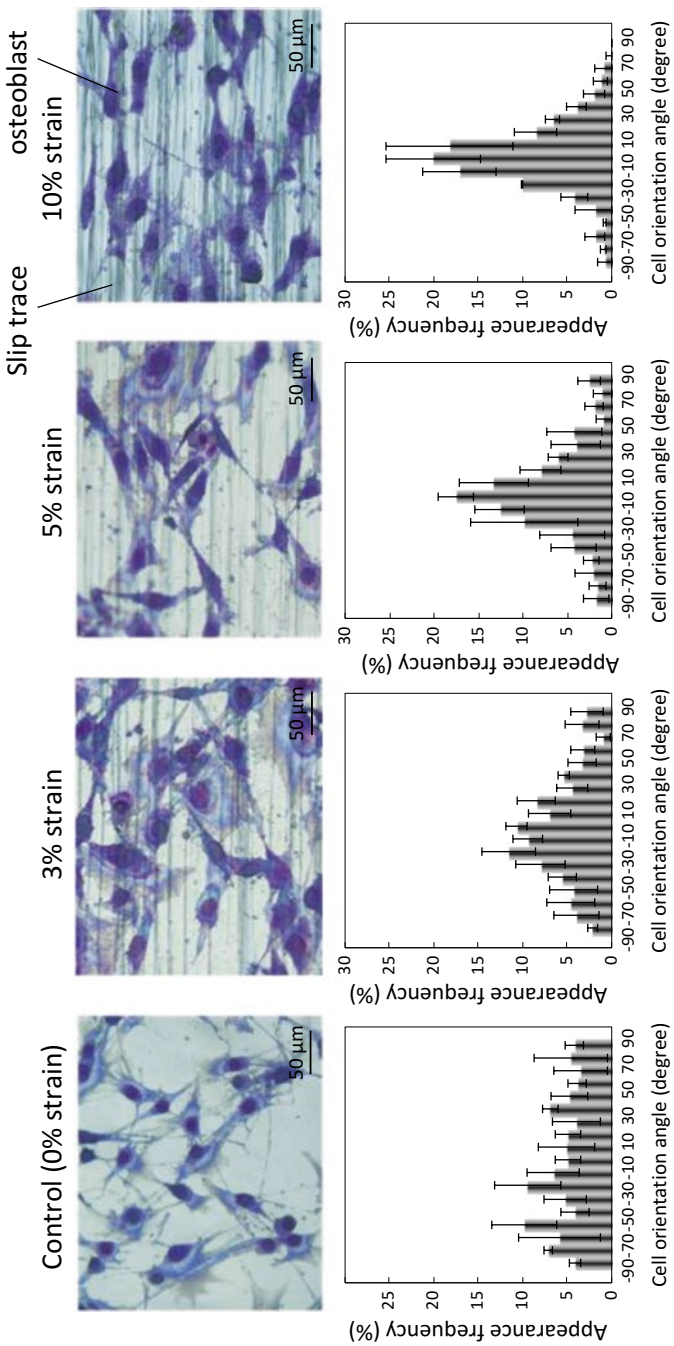

Fig. 1.20 Osteoblast alignment along slip traces. The degree of cell orientation is effectively controlled by the topographical feature of step patterning introduced strongly depending on the compressive strain (Reprinted from Ref. [62], Copyright 2012, with permission from Elsevier)

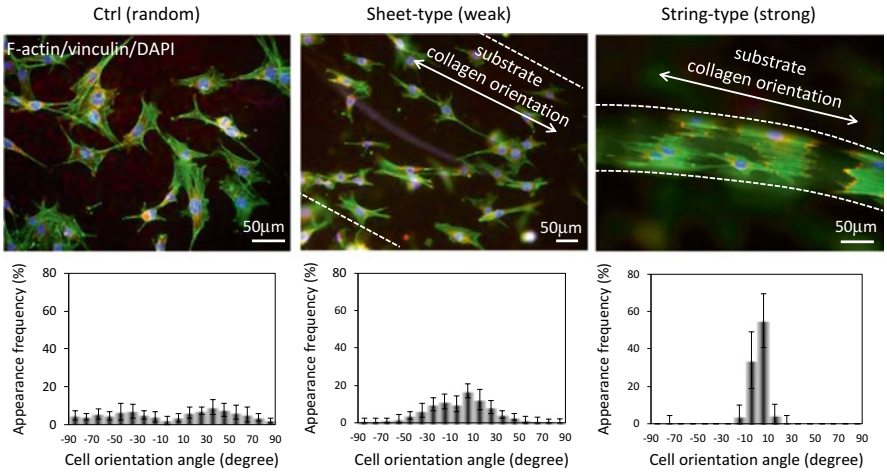

Fig. 1.21 Osteoblast alignment along the substrate collagen molecular orientation. Actin stress fibers elongate along the substrate collagen orientation, while the degree of cell alignment is controlled by the level of substrate collagen anisotropy (Reproduced from Ref. [64] by permission of John Wiley & Sons Ltd)

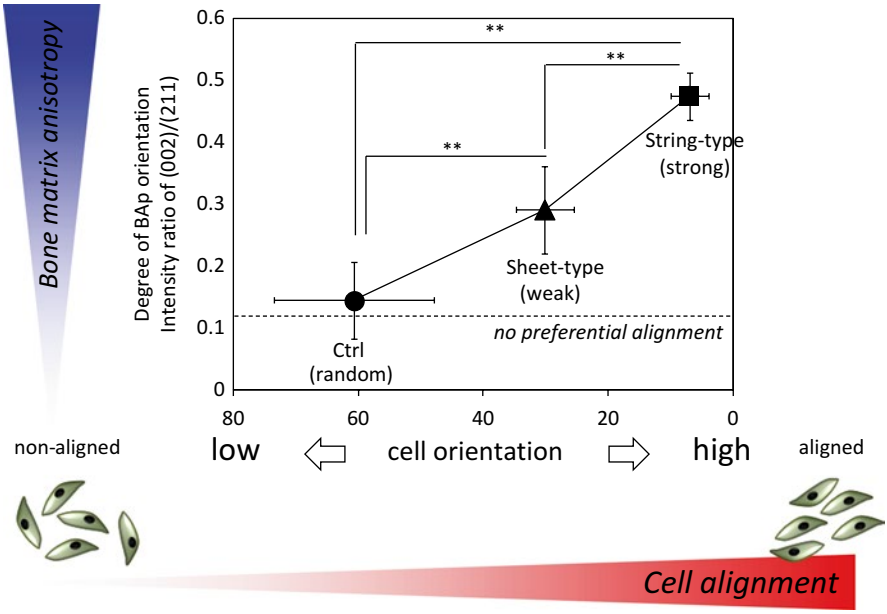

Fig. 1.22 Quantitative regulation of bone matrix anisotropy by osteoblast alignment. The degree of collagen/biological apatite (BAp) alignment produced by osteoblasts is determined by the cell orientation, which was induced by the substrate collagen molecular anisotropy (Reproduced from Ref. [64] by permission of John Wiley & Sons Ltd)

the bone, osteoclasts that resorb the bone, and osteocytes that sense the stress within the bones. Matching the direction of the grooves and pores to the principal stress direction provides an optimal environment for the bone cells, and alignment in particular direction enables stress sensing by the osteocytes to approach a more normal state.

Prior to the development of new biomaterials and medical devices for bone replacement, bone tissues at various scale levels as well as their functions should be precisely understood. Regenerative medicine and curing of bone diseases should be performed based on the anisotropic bone microstructure. Because the molecular mechanism of bone formation has been becoming clear, the novel artificial methodologies for giving bone biomimicking functions may be constructed. Taken together, anisotropic-complicated microstructures of bone tissue should always be considered in the development of bone-related biomaterials and medical devices.

Acknowledgments This work was supported by Grants-in-Aid for Scientific Research (S) from the Japan Society for Promotion of Science (JSPS).

References

1. Burr DB, Allen MR (eds) (2014) Basic and applied bone biology. Academic, New York
2. Standring S (ed) (2004) Gray's anatomy, 39th edn. Elsevier, New York
3. Rho JY, Kuhn-Spearing L, Ziouposc P (1998) Mechanical properties and the hierarchical structure of bone. Med Eng Phys 20:92–102
4. Nakano T, Tabata Y, Umakoshi Y (2005) Texture and Bone Reinforcement. In: Encyclopedia of materials science and technology updates. Elsevier, Oxford, pp 1–8 (Ms: 2061)
5. Elliot JC (1994) Structure and chemistry of the apatites and other calcium phosphates. Elsevier, Amsterdam
6. Hodge AJ, Petruska JA (1963) Recent studies with the electron microscope on ordered aggregates of the tropocollagen molecule. In: Ramachandran GN (ed) Aspects of protein structure. Academic Press, New York, pp 289–300
7. Wolff J (1892) Das Gesetz der Transformation der Knochen. August Hirschwald, Berlin
8. Boyle C, Kim IY (2011) Three-dimensional micro-level computational study of Wolff's law via trabecular bone remodeling in the human proximal femur using design space topology optimization. J Biomech 44:935–942
9. Srinivasan S, Peh WGC (2013) Radiography in osteoporosis. In: Guglielmi G (ed) Osteoporosis and bone densitometry measurements. Springer, Berlin, pp 15–30
10. Applegate E (ed) (2010) The anatomy and physiology learning system, 4th edn. Elsevier Health Sciences, Philadelphia
11. Keaveny TM, Morgan EF, Yeh OC (2003) Bone mechanics. In: Kutz M (ed) Standard handbook of biomedical engineering & design. McGraw-Hill Professional, New York
12. Gurtner GC, Callaghan MJ, Longaker MT (2007) Progress and potential for regenerative medicine. Ann Rev Med 58:299–312
13. Berridge MJ (2012) Cellular processes. In: Cell signalling biology. Portland Press, Cambridge, pp 7-1–7-136
14. Anderson HC, Reynolds JJ (1973) Pyrophosphate stimulation of calcium uptake into cultured embryonic bones. Fine structure of matrix vesicles and their role in calcification. Dev Biol 34:211–227

15. Matsubara T, Kida K, Yamaguchi A, Hata K, Ichida F, Meguro H, Aburatani H, Nishimura R, Yoneda T (2008) BMP2 regulates Osterix through Msx2 and Runx2 during osteoblast differentiation. J Biol Chem 283:29119–29125
16. Piekarski K, Munro M (1977) Transport mechanism operating between blood supply and osteocytes in long bones. Nature 269:80–82
17. van Bezooijen RL, Roelen BA, Visser A, van der Wee-Pals L, de Wilt E, Karperien M, Hamersma H, Papapoulos SE, ten Dijke P, Löwik CW (2004) Sclerostin is an osteocyte-expressed negative regulator of bone formation, but not a classical BMP antagonist. J Exp Med 199:805–814
18. Liu S, Quarles LD (2007) How fibroblast growth factor 23 works. J Am Soc Nephrol 18:1637–1647
19. Nakashima T, Hayashi M, Fukunaga T, Kurata K, Oh-Hora M, Feng JQ, Bonewald LF, Kodama T, Wutz A, Wagner EF, Penninger JM, Takayanagi H (2011) Evidence for osteocyte regulation of bone homeostasis through RANKL expression. Nat Med 17:1231–1234
20. Potts JT (2005) Parathyroid hormone: past and present. J Endocrinol 187:311–325
21. Cruess RL, Dumont J (1975) Fracture healing. Can J Surg 18:403–413
22. Bolander ME (1992) Regulation of fracture repair by growth factors. Proc Soc Exp Biol Med 200:165–170
23. Bastian O, Pillay J, Alblas J, Leenen L, Koenderman L, Blokhuis T (2011) Systemic inflammation and fracture healing. J Leukoc Biol 89:669–673
24. Rahn BA, Gallinaro P, Baltensperger A, Perren SM (1971) Primary bone healing. An experimental study in the rabbit. J Bone Joint Surg Am 53:783–786
25. Deschaseaux F, Sensébé L, Heymann D (2009) Mechanisms of bone repair and regeneration. Trends Mol Med 15:417–429
26. Fratzl P, Weinkamer R (2007) Nature's hierarchical materials. Prog Mater Sci 8:1263–1334
27. Frankel VH, Nordin M (1980) Basic biomechanics of the skeletal system. Lea & Febiger, Philadelphia, p 22
28. NIH Consensus Development Panel on Osteoporosis Prevention, Diagnosis, and Therapy (2001) Osteoporosis prevention, diagnosis, and therapy. JAMA 285:785–795
29. Souzanchi MF, Palacio-Mancheno P, Borisov YA, Cardoso L, Cowin SC (2012) Microarchitecture and bone quality in the human calcaneus: local variations of fabric anisotropy. J Bone Miner Res 27:2562–2572
30. Nakano T, Kaibara K, Tabata Y, Nagata N, Enomoto S, Marukawa E, Umakoshi Y (2002) Unique alignment and texture of biological apatite crystallites in typical calcified tissues analyzed by microbeam X-ray diffractometer system. Bone 31:479–487
31. Viswanath B, Raghavan R, Ramamurty U, Ravishankar N (2007) Mechanical properties and anisotropy in hydroxyapatite single crystals. Scripta Mater 57:361–364
32. Sasaki N, Sudoh Y (1997) X-ray pole figure analysis of apatite crystals and collagen molecules in bone. Calcif Tissue Int 60:361–367
33. He BB, Preckwinkel U (2001) X-ray optics for two-dimensional diffraction. Adv X-ray Anal 45:332–337
34. Timlin JA, Carden A, Morris MD (1999) Chemical microstructure of cortical bone probed by Raman transects. Appl Spectrosc 53:1429–1435
35. Nakano T, Ishimoto T, Ikeo N, Matsugaki A (2012) Advanced analysis and control of bone microstructure based on a materials scientific study including microbeam X-ray diffraction. In: Kakeshita T (ed) Progress in advanced structural and functional materials design. Springer, Tokyo, pp 155–167
36. Nagisa N, Nakano T, Hashiguchi N, Fujitani W, Umakoshi Y, Shimahara M (2010) Analysis of biological apatite orientation in rat mandibles. Oral Sci Int 7:19–25
37. Miyabe S, Nakano T, Ishimoto T, Takano N, Adachi T, Iwaki H, Kobayashi A, Takaoka K, Umakoshi Y (2007) Two-dimensional quantitative analysis of preferential alignment of BAp c-axis for isolated human trabecular bone using microbeam X-ray diffractometer with a transmission optical system. Mater Trans 48:343–347

38. Rokita E, Chevallier P, Mutsaers PHA, Tabor Z, Wróbel A (2005) Studies of crystal orientation and calcium distribution in trabecular bone. Nucl Instrum Methods Phys Res B 240:69–74
39. Noyama Y, Nakano T, Ishimoto T, Sakai T, Yoshikawa H (2013) Design and optimization of the oriented groove on the hip implant surface to promote bone microstructure integrity. Bone 52:659–667
40. Shiraishi A, Miyabe S, Nakano T, Umakoshi Y, Ito M, Mihara M (2009) The combination therapy with alfacalcidol and risedronate improves the mechanical property in lumbar spine by affecting the material properties in an ovariectomized rat model of osteoporosis. BMC Musculoskelet Disord 10:paper #66
41. Kashii M, Hashimoto J, Nakano T, Umakoshi Y, Yoshikawa H (2008) Alendronate treatment promotes bone formation with a less anisotropic microstructure during intramembranous ossification in rats. J Bone Miner Metab 26:24–33
42. Nakano T, Yamamoto T, unpublished data
43. Dacke CG, Arkle S, Cook DJ, Wormstone IM, Jones S, Zaidi M, Bascal ZA (1993) Medullary bone and avian calcium regulation. J Exp Biol 184:63–88
44. Yamamoto T, Nakamura H, Tsuji T, Hirata A (2001) Ultracytochemical study of medullary bone calcification in estrogen injected male Japanese quail. Anat Rec 264:25–31
45. Ishimoto T, Nakano T, Umakoshi Y, Yamamoto M, Tabata Y (2013) Degree of biological apatite c-axis orientation rather than bone mineral density controls mechanical function in bone regenerated using rBMP-2. J Bone Miner Res 28:1170–1179
46. Nakano T, Kaibara K, Ishimoto T, Tabata Y, Umakoshi Y (2012) BAp crystallographic orientation and texture as a new index for assessing the microstructure and function of bone regenerated by tissue engineering. Bone 51:741–747
47. Yamamoto M, Takahashi Y, Tabata Y (2006) Enhanced bone regeneration at a segmental bone defect by controlled release of bone morphogenetic protein-2 from a biodegradable hydrogel. Tissue Eng 12:1305–1311
48. Ishimoto T, Nakano T, Yamamoto M, Tabata Y (2011) Biomechanical evaluation of regenerated long bone by nanoindentation. J Mater Sci Mater Med 22:969–976
49. Wang J (2014) Regulation of anisotropic bone nano-organization by artificial stress field. Doctoral Dissertation, Osaka University
50. Takatsuka H, Umezu H, Hasegawa G, Usuda H, Ebe Y, Naito M, Shultz LD (1998) Bone remodeling and macrophage differentiation in osteopetrosis (op) mutant mice defective in the production of macrophage colony-stimulating factor. J Submicrosc Cytol Pathol 30:239–247
51. Shimomura A, Matsui I, Hamano T, Ishimoto T, Katou Y, Takehana K, Inoue K, Kusunoki Y, Mori D, Nakano C, Obi Y, Fujii N, Takabatake Y, Nakano T, Tsubakihara Y, Isaka Y, Rakugi H (2014) Dietary L-lysine prevents arterial calcification in adenine-induced uremic rats. J Am Soc Nephrol 25:1954–1965
52. Wang J, Ishimoto T, Nakano T (2013) Preferential orientation of collagen/biological apatite in growing rat ulna under an artificial loading condition. Mater Trans 54:1257–1261
53. Lee JW, Nakano T, Toyosawa S, Tabata Y, Umakoshi Y (2007) Areal distribution of preferential alignment of BAp crystallite on cross-section of center of femoral diaphysis in osteopetrotic (op/op) mouse. Mater Trans 48:337–342
54. Gourion-Arsiquaud S, Faibish D, Myers E, Spevak L, Compston J, Hodsman A, Shane E, Recker RR, Boskey ER, Boskey AL (2009) Use of FTIR spectroscopic imaging to identify parameters associated with fragility fracture. J Bone Miner Res 24:1565–1571
55. Yerramshetty JS, Akkus O (2008) The associations between mineral crystallinity and the mechanical properties of human cortical bone. Bone 42:476–482
56. Hansma PK, Turner PJ, Fantner GE (2006) Bone diagnostic instrument. Rev Sci Instrum 77:075105
57. Barak MM, Currey JD, Weiner S, Shahar R (2009) Are tensile and compressive Young's moduli of compact bone different? J Mech Behav Biomed Mater 2:51–60
58. Wang JH, Jia F, Gilbert TW, Woo SL (2003) Cell orientation determines the alignment of cell-produced collagenous matrix. J Biomech 36:97–102

59. Wu L, Lee LA, Niu Z, Ghoshroy S, Wang Q (2011) Visualizing cell extracellular matrix (ECM) deposited by cells cultured on aligned bacteriophage M13 thin films. Langmuir 27:9490–9496
60. Matsugaki A, Fujiwara N, Nakano T (2013) Continuous cyclic stretch induces osteoblast alignment and formation of anisotropic collagen fiber matrix. Acta Biomater 9:7227–7235
61. Matsugaki A, Aramoto G, Ninomiya T, Sawada H, Hata S, Nakano T (2015) Abnormal arrangement of a collagen/apatite extracellular matrix orthogonal to osteoblast alignment is constructed by a nanoscale periodic surface structure. Biomaterials 37:134–143
62. Matsugaki A, Aramoto G, Nakano T (2012) The alignment of MC3T3-E1 osteoblasts on steps of slip traces introduced by dislocation motion. Biomaterials 33:7327–7335
63. Jones SJ, Boyde A, Pawley JB (1975) Osteoblasts and collagen orientation. Cell Tissue Res 159:73–80
64. Matsugaki A, Isobe Y, Saku T, Nakano T (2015) Quantitative regulation of bone-mimetic, oriented collagen/apatite matrix structure depends on the degree of osteoblast alignment on oriented collagen substrates. J Biomed Mater Res 103:489–499

Chapter 2
Joint: Normal Anatomy, Function, and Pathological Condition

Takashi Sakai

Abstract Various motions of the body trunk and extremities are performed through the joint. The interdependent aspects of joint function are stability, motion, and load distribution. Joint structure is related with the joint function. The range of joint motion depends on the joint structure, articular cartilage, and soft tissue around the joint including the ligament, tendon, and muscle. Generally, the range of motion of the body trunk is much smaller than that of the extremities. Articular cartilage is evaluated using various modalities. Especially, cartilage degeneration has been studied by magnetic resonance imaging including dGEMRIC, T2 mapping, and T1rho mapping. Pathological condition is derived from the biological abnormalities such as cartilage degeneration and synovial inflammation and from the mechanical abnormalities such as ligament rupture and meniscal injury. Joint diseases are monitored using various biochemical markers. Recently, joint instability or translation, which is thought to be causative factor of osteoarthritis, has been evaluated using several modern methods.

Keywords Joint • Function • Structure • Articular cartilage • Pathological condition

2.1 Joint Structure

2.1.1 Anatomical Classification

The junction between adjacent bones is a joint. Gross type of joint is classified into three types: immovable joint, amphiarthrodial joint, and diarthrodial joint.

T. Sakai (✉)
Department of Orthopaedic Surgery, Osaka University Graduate School of Medicine, 2-2 Yamadaoka, Suita 565-0871, Japan
e-mail: tsakai-osk@umin.ac.jp

M. Niinomi et al. (eds.), *Advances in Metallic Biomaterials*, Springer Series in Biomaterials Science and Engineering 3, DOI 10.1007/978-3-662-46836-4_2

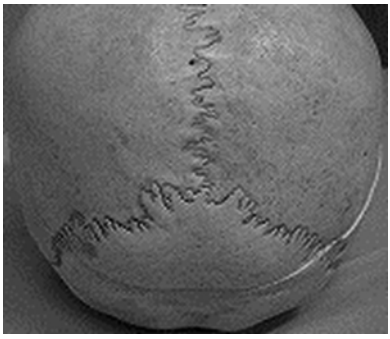

Fig. 2.1 Immovable joint (skull structures)

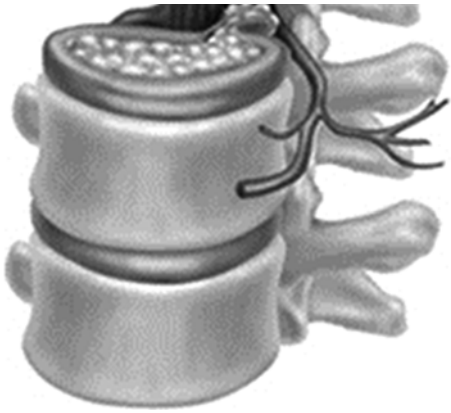

Fig. 2.2 Amphiarthrodial joint (intervertebral disc)

2.1.1.1 Immovable Joint

Immovable joint is the fibrous synarthrosis which is filled with dense collagenized fibrous tissue, such as the skull structures (Fig. 2.1). There is no mobility in this joint. The epiphyseal plate which includes the cartilage plate is also classified into the immovable joint.

2.1.1.2 Amphiarthrodial Joint

Amphiarthrodial joint is the symphysis which is characterized by limited mobility, such as the intervertebral disc and the symphysis pubis (Fig. 2.2). The amphiarthrodial joint where the bone is connected with the ligament is syndesmosis, such as the distal tibiofibular joint and the interosseous membrane of the forearm. On the other hand, the amphiarthrodial joint where the bone is connected with the fibrocartilage is symphysis, such as symphysis pubis. The intervertebral disc is a fibrocartilaginous

complex that forms the articulation between the vertebral bodies. The intervertebral disc can be divided into two components: an outermost fibrous ring, annulus fibrosus, and within a gelatinous core, nucleus pulposus.

2.1.1.3 Diarthrodial Joint/Synovial Joint

The diarthrodial joint is the most common joint which is cavitated to form a freely movable connecting unit between two bones. The diarthrodial joint has the articular cavity between the bones, and the synovial fluid exists in the cavity. Hyaline cartilage covers the articulating surfaces of the diarthrodial joins; the exceptions are the sternoclavicular and temporomandibular joints, which are covered by fibrocartilage.

The diarthrodial joint generally consists of concave side and convex side. Motion type of the joint depends on the joint structure, for example, gliding, angular motion, rotation, uniaxial motion, biaxial motion, triaxial motion, and multiaxial motion. Combined motion such as ellipsoidal movement is performed by biaxial or triaxial (multiaxial) motion.

The diarthrodial joint is supported by ligaments to stabilize the joint and to prevent from dislocation. Ligaments are classified into three types: capsular ligament, intra-articular ligament, and extra-articular ligament.

Blood vessels are supplied by artery, vein, and lymph flow around the joint. Nerves in the joint are classified into two types: sensory nerve fibers with abundant mechanoreceptors and free nerve ending that exists at the capsule and ligament. According to Hilton's law [1], the innervation of the joint is subjected by the same nerve as is in charge of muscles that function the joint itself.

The functions of the diarthrodial joint are the following: (1) the freedom of the articulating surfaces to move over each other, (2) the ability to maintain stability during motion, and (3) a proper distribution of stress through the tissues that comprise the joint so that they are not damaged. The diarthrodial joints are classified into four functional categories: hinge joint, pivot joint, ball-and-socket joint, and saddle joint.

Hinge Joint

Hinge motion shows angular motion on one plane, namely, flexion and extension, for example, knee joint and humeroulnar joint.

Knee joint functions not only angular motion on one plane as hinge joint, but also sliding motion on the contact surface because the medial femoral condyle and lateral femoral condyle have different shapes (Fig. 2.3). Knee joint includes femorotibial joint and patellofemoral joint. As specific characteristics of the knee joint, medial and lateral meniscus exist between the femorotibial joint. Femorotibial joint is supported by many ligaments including patellar ligament, medial and lateral

Fig. 2.3 Hinge joint (knee joint)

Fig. 2.4 Pivot joint (proximal radioulnar joint)

collateral ligament, popliteal ligament, and anterior and posterior cruciate ligament.

Pivot Joint

Pivot joint shows only uniaxial rolling motion, such as proximal radioulnar joint surrounded by the annular ligament (Fig. 2.4).

Fig. 2.5 Ball-and-socket joint (hip joint)

Ball-and-Socket Joint

Ball-and-socket joint consists of the hemispherical bony head and the concave bony fossa such as hip joint (femoral head and acetabulum) and shoulder joint (humeral head and glenoid cavity). This joint shows a large range of motion because of triaxial motion.

Hip joint is anatomically ball-and-socket joint and has a large range of motion, including flexion, extension, abduction, adduction, internal rotation, and external rotation (Fig. 2.5). Hip joint has also an important role as a weight-bearing site. The femoral head and the acetabulum have thick articular cartilage. Hip joint is stabilized by many ligaments, such as iliofemoral ligament, pubofemoral ligament, ischiofemoral ligament, transverse ligament, and ligamentum teres, and muscles. The joint cavity is so small that synovial inflammation leads to the increase of the joint pressure due to increased synovial fluid.

Saddle Joint

Saddle joint shows large angular motion, not rolling motion, such as the carpometacarpal joint (Fig. 2.6).

2.1.2 Function and Anatomy

2.1.2.1 Gross Articulation

Generally, one joint surface is convex, whereas the other is concave. The convex side of the joint usually has a larger articular surface than the concave side. The concave side of the joint is often augmented by a pliable dense fibrous component,

Fig. 2.6 Saddle joint (carpometacarpal joint)

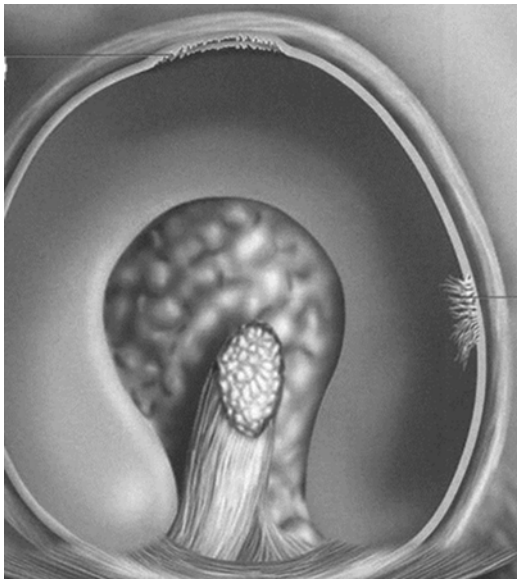

Fig. 2.7 The labrum of the hip

for example, the labrum of the hip (Fig. 2.7) or the meniscus of the knee, that has an important role in normal function. The complementary shapes of the surfaces are necessary to permit the normal range of motion for that particular joint as well as to provide stability and ensure the most equitable loading during use.

In some ball-and-socket joints, for example, the hip and the ankle joint, the articular surfaces appear to fit exactly, while in other joints, for example, the knee and

finger joints, it is readily apparent that the surfaces are incongruent. In many joints, of which the knee is a notable example, the gross incongruence of the opposed surfaces is partially compensated for by the interposed, pliable intra-articular fibrocartilaginous menisci.

Because the tissues of a joint undergo elastic deformation under load, as the load increases, the surfaces of the joint come into increasing contact, thereby distributing the load more equitably. Both the incongruence and the deformation of the joint space under loading conditions provide for the circulation of the synovial fluid essential to the metabolism of the chondrocytes.

2.1.2.2 Mechanical Properties of Extracellular Matrices

The mechanism of the joint includes the articular cartilage, the bone beneath the cartilage, the ligaments that conjoin the articular bone ends, and other structures. Alterations in the mechanical properties of bone or disruption of the ligaments may have equally disastrous effects on the joint function as alterations in cartilage properties.

The physical properties of connective tissues are determined by their extracellular matrices. In each connective tissue, the matrices have a unique composition and organization that provide for mechanical function at that locus. The connective tissue matrices are both synthesized and broken down by their intrinsic cells including osteoblast, osteocytes, osteoclast, and chondrocytes. In maintaining the physicochemical and mechanical properties of tissues, the function of these cells must be subjected to highly sensitive feedback systems involving both local and systemic factors.

2.1.2.3 Supporting Joints and Neuromuscular Controls

Sensory feedback monitors the movements through the perception of touch, temperature, pain, and position. Correct joint function is dependent on intact ligaments and neuromuscular coordination. A breakdown of neuromuscular coordination can lead to profound arthritis, Charcot's joint (Fig. 2.8).

2.1.2.4 Normal Joint Physiology

According to Wolff's law, bone density and bone architecture correlate with the magnitude and direction of applied load [2]. In the articular end of a bone, this implies that subchondral bone trabeculae must also undergo a self-regulated modeling that maintains a joint shape capable of optimal load distribution. The shape of the articular end reflects a dynamic state that also incorporates a feedback dependent on mechanical stress. Endochondral ossification is exemplified in the epiphyseal growth plate, where calcified cartilage is invaded by blood vessels from the

Fig. 2.8 Charcot joint (hip joint)

metaphyseal bone and replaced by bone tissue synthesized by osteoblasts lying close to the invading blood vessels.

Blood vessels from the subchondral bone penetrate the calcified zone of the articular cartilage. The calcified cartilage is slowly replaced by new subchondral bone. The thickness of the calcified zone of articular cartilage remains much the same throughout life because the tidemark continues to advance into the noncalcified cartilage at a slow rate that is in equilibrium with the rate of replacement from the subchondral bone. The extracellular matrix and the chondrocytes are replaced throughout life, and the joint undergoes continuous remodeling.

2.2 Articular Cartilage

The articular ends of the bones are covered by hyaline cartilage, which is a bloodless and firm tissue. Hyaline cartilage deforms under pressure but slowly recovers its original shape on removal of pressure. In young individuals, articular cartilage is translucent and bluish white while in older individuals, it is opaque and slightly yellowish probably related to a number of factors, including dehydration of the tissues, increased numbers of cross-linkages in the collagen, and the accumulation of lipofuscin pigment in the tissues.

2.2.1 Histology of Hyaline Cartilage

On microscopic examination, articular cartilage is characterized by its abundant glassy extracellular matrix with isolated, relatively sparse cells located in well-defined spaces. It consists of four layers or zones: (1) the superficial zone, (2) intermediate zone, (3) deep zone, and (4) calcified zone (Fig. 2.9).

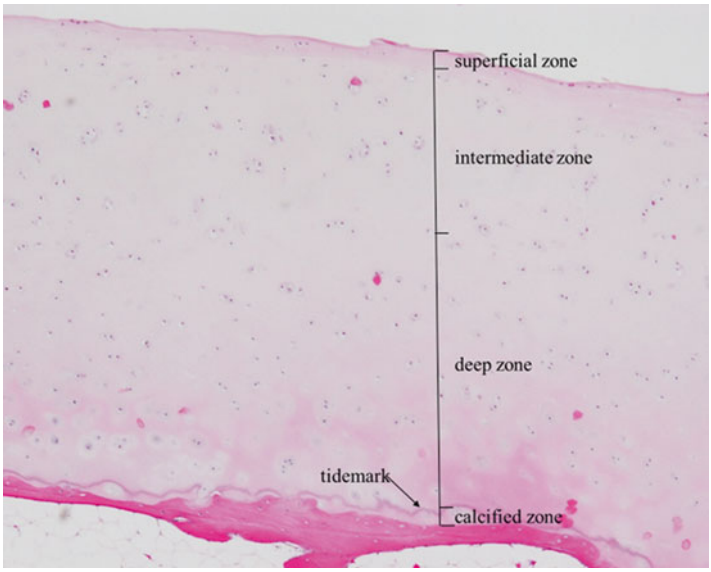

Fig. 2.9 Histology of hyaline cartilage with four layers: (1) the superficial zone, (2) intermediate zone, (3) deep zone, and (4) calcified zone (hematoxylin–eosin ×40)

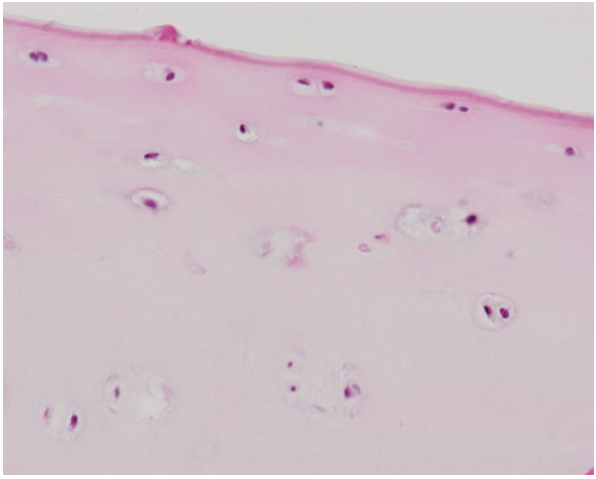

Fig. 2.10 Superficial/tangential zone (hematoxylin–eosin ×200)

2.2.1.1 Superficial/Tangential Zone (Fig. 2.10)

In the superficial layer, the cells are relatively small and flat, oriented with their long axis parallel to the surface. In the surface layer of articular cartilage, the collagen fibers are closely packed and oriented parallel to the joint surface. The collagen content of cartilage progressively diminishes from the superficial to the deep layer,

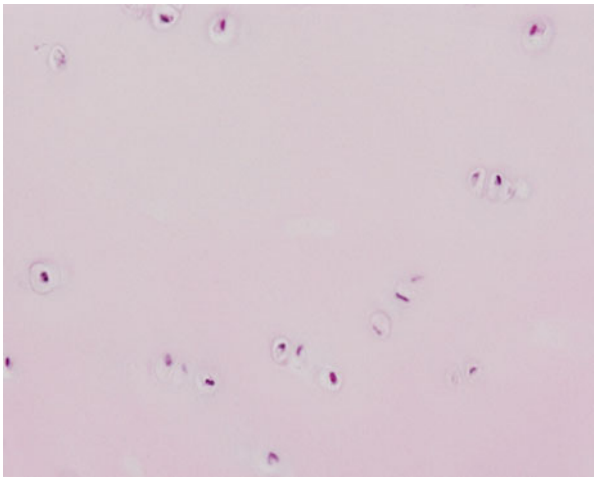

Fig. 2.11 Intermediate/transitional zone (hematoxylin–eosin ×200)

and in deeper layers the collagen fibers are more widely separated, thicker in diameter, and vertically aligned in such a fashion as to form a web of arch-shaped structures. The superficial layers of the cartilage contain much less proteoglycan than the deeper layers. In the deeper layers, there is a higher concentration of staining of the proteoglycans with safranin O and methylene blue around the cells, the pericellular matrix, than between the cells, the intercellular matrix.

2.2.1.2 Intermediate/Transitional Zone (Fig. 2.11)

In the intermediate zone, the cells are larger and rounder, but also sparse and randomly distributed. The collagen fibers are continuous with those in the tidemark and the calcified layer of cartilage but not with those of the underlying subchondral bone.

2.2.1.3 Tidemark (Fig. 2.12)

The cells are even larger and have a tendency to form radial groups that apparently follow the pattern of collagen disposition in the extracellular matrix. In histologic sections stained with hematoxylin–eosin, the junction between the calcified cartilage and the noncalcified cartilage is marked by a basophilic line known as the tidemark or calcification front. This basophilic line clearly visible in the adult is not seen during development. The tidemark is sometimes damaged by trauma because of the physical differences between the calcified cartilage and the noncalcified cartilage.

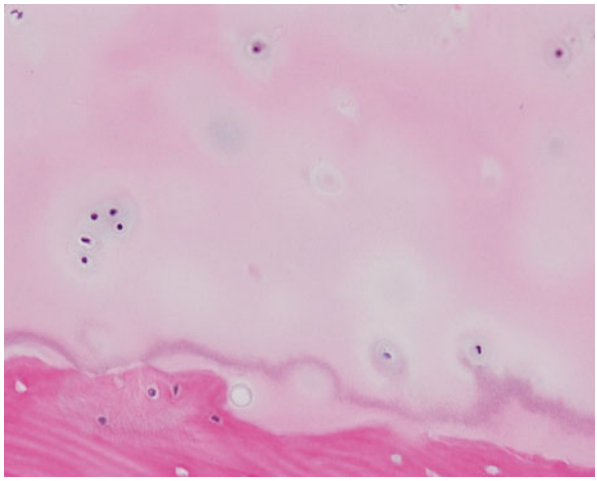

Fig. 2.12 Tidemark (hematoxylin–eosin ×200)

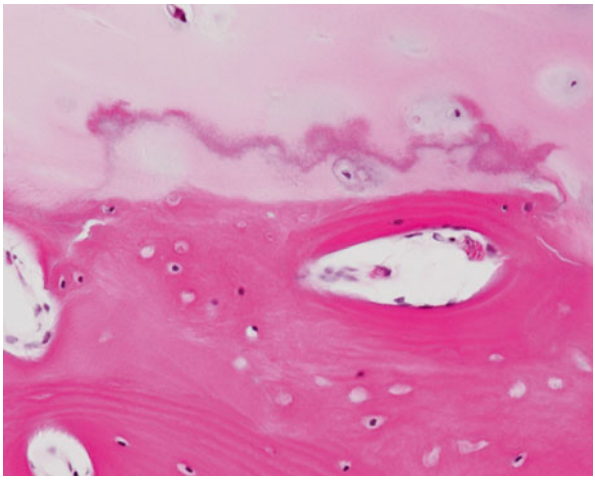

Fig. 2.13 Calcified zone (hematoxylin–eosin ×200)

2.2.1.4 Calcified Zone (Fig. 2.13)

The calcified zone is adjacent to the bone, and the cells are mostly nonviable and the matrix heavily calcified. Blood vessels flow into this zone form the adjacent bone tissue and bone remodeling always occurs in this zone. The thickness of the calcified zone decreases in the older individuals. The boundary between the calcified zone and the subchondral bone is the bone/cartilage transitional area.

2.2.2 Non-hyaline Cartilage

Fibrocartilage is a tissue in which is rounded with a halo of proteoglycan around them. It is found at the insertions of ligaments and tendons into the bone and on the inner side of tendons as they angle around pulleys. The second type of non-hyaline cartilage, elastic cartilage, contains a high proportion of elastic fibers in the matrix. It is present in the ligamentum flavum, external ear, and epiglottis, where some element of stretch is necessary in the tissue.

2.2.3 Cartilage Components

2.2.3.1 Cartilage Matrix

Chondrocytes occupy only 2–3 % in volume in the articular cartilage. Chondrocytes exist in the cartilage matrix which consists of collagen and proteoglycan they produce. Cartilage components include water in about 80 % of wet weight, collagen in 20 %, and proteoglycan in 5 % [3]. The two main components of the extracellular matrix of articular cartilage are type II collagen and aggrecan, both of which are almost specific to this tissue. Collagen acts to maintain structure, to absorb impact, and to keep proteoglycan. Proteoglycan has a negative charge and draws water into the cartilage matrix. Thus, cartilage possesses adequate viscosity and resistance to pressure.

2.2.3.2 Collagen

Type II collagen is predominant and occupies 15–22 % of wet weight. Type II collagen is present with type IX and XI collagen. Type IX collagen contributes only 1 % of the total collagen in mature articular cartilage. Type IX collagen exists on the surface of type II collagen fibrils in an antiparallel manner and appears to have an important role in stabilizing the three-dimensional organization of the collagen network, and its reduced functioning can contribute to degeneration of articular cartilage [4].

Type II collagen is degraded by proteolytic enzymes secreted by the chondrocytes and synoviocytes, including matrix metalloproteinases (MMPs) such as MMP-1, MMP-3, MMP-8, MMP-13, membrane-type MMP, and gelatinases. MMP-3 could contribute indirectly to collagen breakdown by activating the other MMPs. MMP-13, whose expression is increased in osteoarthritis, could be one of the major enzymes involved in the increased type II collagen degradation [5–7].

2.2.3.3 Proteoglycan

Proteoglycans composed of core protein and glycosaminoglycan (GAG) chains that are covalently attached to the core protein. Aggrecan is predominant in cartilage, and various types of proteoglycan exist including hyaluronic acid, link protein [8], small leucine-rich proteins and proteoglycans (SLRPs) [9–11], and perlcan [12].

2.2.4 Cartilage Evaluation

2.2.4.1 Quality (Degeneration)

Magnetic resonance imaging (MRI) is an effective diagnosing tool for articular cartilage degeneration. Generally, fat suppression proton-weighted images/T2-weighted images using 2D fast spin echo (FSE) and fat suppression T1-weighted images using 3D gradient echo (GRE) have been performed for examination of articular surface degeneration. Recently, to detect early findings of the articular cartilage in osteoarthritis patients, delayed gadolinium-enhanced magnetic resonance imaging of cartilage (dGEMRIC) [13], T2 mapping [14], and spin–lattice relaxation in the rotating frame (T1rho) mapping [15] have been applied for in vivo cartilage condition evaluation. 3 T MRI imaging is more useful for cartilage degeneration detection than 1.5 T MRI because theoretical signal-to-noise (S/N) ratio of 3 T MRI is twice and because 3 T MRI has higher spatial resolution and shorter imaging time than 1.5 T MRI [16]. In vivo cartilage condition in the knee joint under loading is also able to be evaluated using three-dimensional reconstruction T2 mapping method before and after meniscectomy [17].

2.2.4.2 Quantity (Thickness)

Cartilage thickness has been measured using various methods including ultrasound [18–20], magnetic resonance imaging (MRI) [21], computed tomography (CT) arthrography [22], and three-dimensional digitizer [23]. Three-dimensional distribution of the articular surface thickness is able to be evaluated using reconstructed three-dimensional CT images and three-dimensional digitizer in the cadaveric study [24, 25] (Fig. 2.14) and contrast-enhanced CT [26].

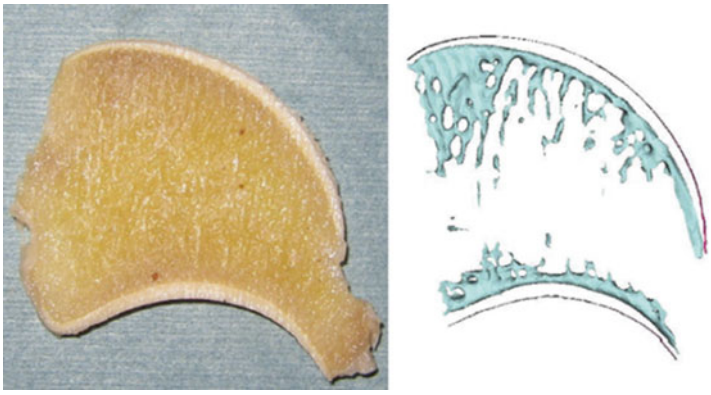

Fig. 2.14 Cartilage thickness analysis using reconstructed three-dimensional CT images and three-dimensional digitizer. *Left*: gross section of the bone and cartilage thickness. *Right*: reconstructed image using three-dimensional CT image and three-dimensional digitizer

2.3 Synovium

Normal synovial fluid supplies nutrition into the hyaline cartilage and shows yellowish, transparent, and hyperviscosity due to hyaluronic acid, which is related with lubrication of the articular surface. When the weight-bearing is loaded on the articular cartilage, the fluid is discharged from the cartilage and forms the articular surface with the synovial fluid. When the weight-bearing is halted, the fluid is drawn into the cartilage. Thus, the fluid flow is thought to be related with the cartilage nutrition supply. Normal synovial fluid contains <200/mm^3 cells that include leukocyte and monocyte, is alkaline, and does not coagulate because of no fibrinogen. The characteristics changes in septic arthritis.

The synovial membrane lines the inner surface of the joint capsule and all other intra-articular structures, with the exception of articular cartilage and the meniscus; it consists of two components. The first is the synovial lining or intimal layer bounding the joint space; this is predominantly cellular. The second component is a supportive or backing layer, formed of fibrous and adipose tissues in variable proportions.

The surface of the synovial lining is smooth, moist, and glistening, with a few small villi and fringe-like folds. The cellular elements of the joint lining consist of a single row or sometimes multiple rows of closely packed intimal cells with large elliptical nuclei; in the subintima are other connective tissue cells.

Electron microscopic studies have revealed two principal types of synovial lining cells. Normal synovial intima contains 25 % of type A and 75 % of type B cells. The less common cell (type A) has many of the features of a macrophage and phagocytic functions. The more common type B cells are richly endowed with rough endoplasmic reticulum, contain Golgi systems, and often show pinocytotic vesicles [27].

The synovial membrane has three principal functions: (1) secretion of synovial fluid hyaluronate (B cells), (2) phagocytosis of waste material derived from the various components of the joint (A cells), and (3) regulation of the movement of solutes, electrolytes, and proteins from the capillaries into the synovial fluid. Thus, the synovial membrane provides the metabolic requirement of the joint chondrocytes and a regulatory mechanism for maintenance of the matrix.

2.4 Pathological Condition

2.4.1 Pathophysiology of a Dysfunctional Joint

The dysfunctions of joint include loss of capacity for the articulating surfaces to move over one another easily, loss of joint stability, and cause pain. The loss of freedom of motion is usually associated with a change in joint shape and alterations in the tissue matrices themselves or affects their mechanical properties. Instability

is caused due to alterations in ligamentous support and neuromuscular control. As causes of pain, the bone as a result of maldistribution of load and the muscles as a reflex spasm can be suggested.

Several forms of arthritis have been well delineated, including infectious arthritides, both granulomatous and pyogenic; metabolic arthritides and the various rheumatic syndromes; and osteoarthritis.

2.4.2 Inflammation

When inflammation occurs in the joint (synovitis), various cells increase in the synovial membrane. Cells derived from bone marrow, monocyte, macrophage, T lymphocytes, and B lymphocytes infiltrate in the synovial membrane, and synovial membrane increases. Increased synovial membrane destroys articular cartilage and bone tissue in the joint. Activated synovium produces cytokine and growth factors including MMPs, cysteine proteinase, serine proteinase, and disintegrin and metalloprotease with thrombospondin motifs (ADAMTS) continuously, and inflammation is maintained.

2.4.3 Osteoarthritis

Osteoarthritis is a functional disorder of joints characterized by altered joint anatomy, especially by the loss of articular cartilage and the formation of osteophytes. Essentially it is noninflammatory. Four patterns of disease are generally recognized [28]:

1. Osteoarthritis presenting as disease limited to a single large joint, usually the knee or the hip, sometimes with bilateral involvement (Fig. 2.15).
2. A generalized process involving the distal and proximal interphalangeal joints of the hand, the first carpometacarpal joints, and metatarsophalangeal joints (Fig. 2.16).
3. Extreme cases of osteoarthritis known as Charcot's joints generally seen in association with a neurologic deficit (Fig. 2.8). In these patients, a characteristic rapidly destructive osteoarthritis is observed, complicated by the production of multiple loose bodies, severe subluxation, and even dislocation of the joints. The underlying neurologic disorder associated with Charcot's joint may be a peripheral neuropathy associated with pernicious anemia, diabetes mellitus, or spinal cord degeneration in tabes dorsalis or syringomyelia.
4. Rapidly destructive joint disease is rare condition (Fig. 2.17). IL-8 concentration significantly increases in rapid destructive coxopathy compared with osteoarthritis of the hip using homogeneous time-resolved fluorescence (HTRF) method [29].

Fig. 2.15 Osteoarthritis of the hip. *Left*: radiologic findings of bilateral terminal hip osteoarthritis. *Right*: gross image of osteoarthritis of the femoral head

Fig. 2.16 Osteoarthritis of the distal interphalangeal joints of the hand

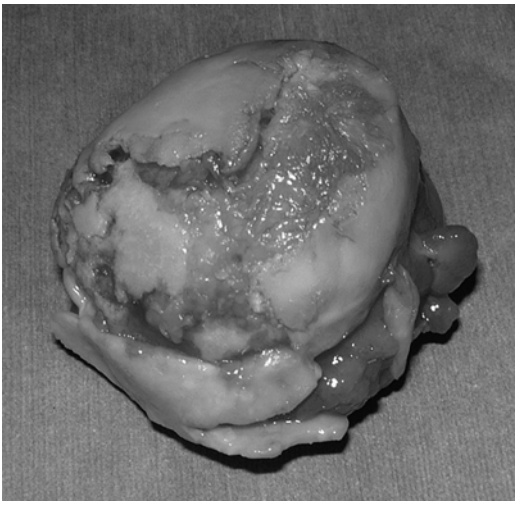

Fig. 2.17 Rapidly destructive joint disease. Rapidly destructive findings of the femoral head

Fig. 2.18 Radiologic finding of osteoarthritis: loss of the joint space, bony osteophyte formation

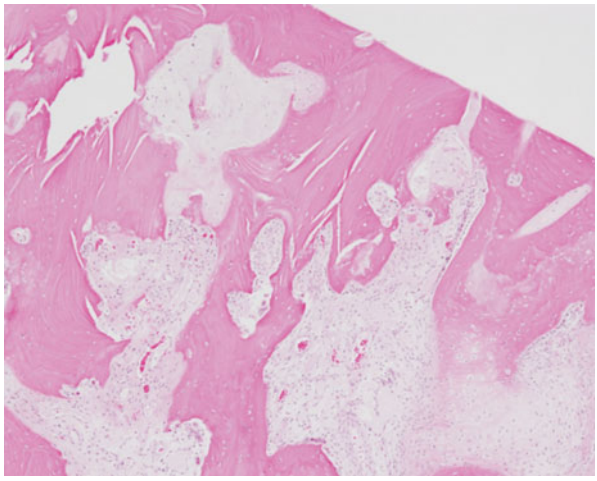

Fig. 2.19 Histological findings of osteoarthritis (hematoxylin–eosin ×40)

Typical osteoarthritis patients complain pain and stiffness of the joint. The range of the joint motion is usually limited. The most radiologic finding is loss of the joint space (Fig. 2.18). Bony osteophytes are seen around the periphery of the joint; the bone on both sides of the joint exhibits increased density, and cystic lesions can frequently be noted in the subchondral bone (Fig. 2.18). The autopsy of osteoarthritic joint reveals damaged cartilage, including eburnation and sclerotic subchondral bone, subarticular cysts, alterations in the shape of the articular surfaces and peripheral bone, and osteophytes (Fig. 2.19).

2.5 Biochemical Markers in Joint Diseases

2.5.1 Bone Turnover

As a synthesis marker in the serum, N- and C-procollagen propeptides (amino-terminal type I procollagen propeptide, PINP, and carboxy-terminal type I procollagen propeptide, PICP) are fractions of type I collagen. Bone-specific alkaline phosphatase (BAP) and osteocalcin are noncollagenous proteins.

As degradation marker (bone resorption marker), deoxypyridinoline, pyridinoline, and N- and C-telopeptides (NTX and CTX) are fractions from type I collagen, in the serum and urine. Plasma tartrate-resistant acid phosphatase 5b (TRACP 5b) and serum bone sialoprotein are noncollagenous proteins [3].

2.5.2 Cartilage Turnover

As a synthesis marker in the serum or synovial fluid, chondroitin sulfate is fraction of aggrecan. Type II procollagen propeptides (carboxy-terminal type II procollagen propeptide, PIICP, and amino-terminal type IIA procollagen propeptide, PIIANP) are fractions of type II collagen. YKL-40 is nonaggrecan and noncollagen protein.

As a degradation marker in the serum or synovial fluid, core protein fragments and keratin sulfate are fractions of aggrecan. Pyridinoline, type II collagen alpha chains, and type II collagen telopeptides are fractions of type II collagen. Cartilage oligomeric matrix protein (COMP) is noncollagenous protein [3].

2.5.3 Synovium Turnover

As synthesis marker in the serum and synovial fluid, type I and type III procollagen propeptides (amino-terminal type III procollagen propeptide, PIINP) are fractions of type I and type III collagens. YKL-40, COMP, MMP-1, MMP-3, and tissue inhibitor of metalloproteinase (TIMP) are noncollagen protein.

As a degradation marker in the serum and urine, pyridinoline and N- and C-telopeptides are fractions of type I and type III collagens [3].

2.6 Joint Instability/Translation

2.6.1 Native Joint

Recently, studies of in vivo kinematics and joint translation have been increasingly reported [30]. In the native hip joint, femoral head moves relatively compared with the acetabulum during hip motion using MRI [31] and triaxial accelerometry [32].

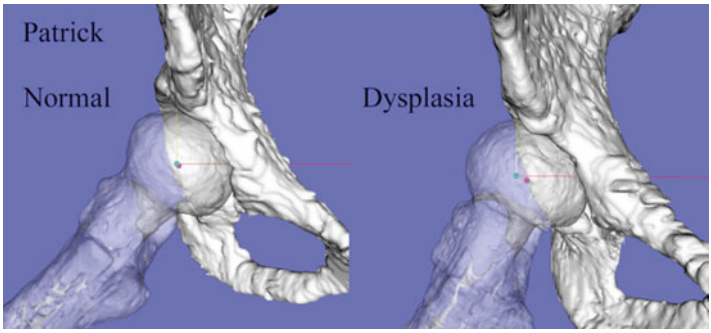

Fig. 2.20 Femoral head translation analysis using MRI and voxel-based registration

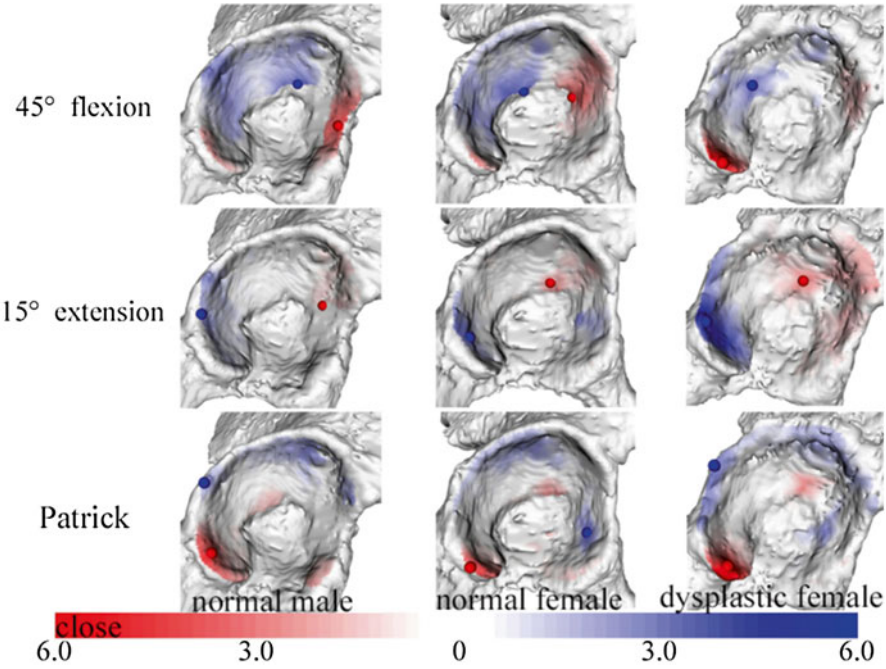

Fig. 2.21 Three-dimensional joint contact distribution of the acetabulum in the hip joint using MRI, voxel-based registration, and proximity mapping

Postoperative translation has been also evaluated in the patients who suffered pelvic osteotomy [33]. Femoral head moves anteriorly, medially, and proximally in Patrick position using MRI and voxel-based registration [34] (Fig. 2.20). Three-dimensional joint contact distribution has been also evaluated using MRI, voxel-based registration, and proximity mapping [35, 36] (Fig. 2.21).

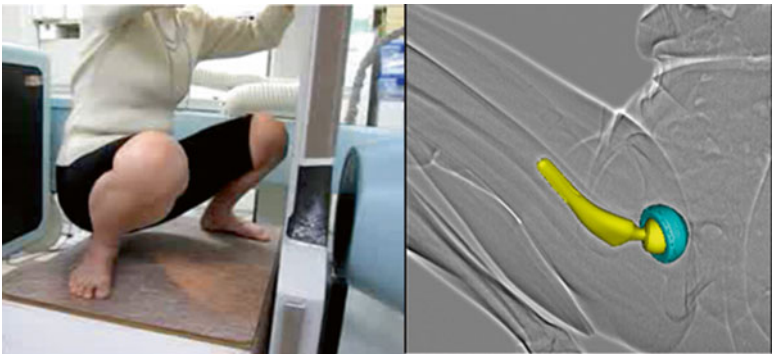

Fig. 2.22 In vivo kinematics of total hip arthroplasty evaluated using image-matching technique, two-dimensional/three-dimensional registration technique

2.6.2 Arthroplasty

Terminal stage of osteoarthritis is generally treated using arthroplasty. In vivo kinematics of total knee arthroplasty [37–41] and total hip arthroplasty have been reported [42, 43] using image-matching technique and two-dimensional/three-dimensional registration technique (Fig. 2.22).

References

1. Herbert-Blouin MN, Tubbs RS, Carmichael SW, Spinner RJ (2014) Hilton's law revisited. Clin Anat 27:548–555
2. Wolff J (1986) The law of bone remodeling (trans: Maquet P, Furlong R). Springer, New York
3. Garnero P, Rousseau JC, Delmas PD (2000) Molecular basis and clinical use of biochemical markers of bone, cartilage, and synovium in joint diseases. Review. Arthritis Rheum 43:953–968
4. Fassler R, Schnegelsberg PN, Dausman J, Shinya T, Muragaki Y, McCarthy MT et al (1994) Mice lacking alpha 1 (IX) collagen develop non-inflammatory degenerative joint disease. Proc Nat Acad Sci USA 91:4571–4576
5. Reboul P, Pelletier J-P, Tardif G, Cloutier J-M, Martel-Pelletier J (1996) The new collagenase, collagenase-3, is expressed and synthesized by human chondrocytes but not synoviocytes. J Clin Invest 97:2011–2019
6. Mitchell PG, Magna HA, Reeves LM, Lopresi-Morrow LL, Yocum SA, Rosner PJ et al (1996) Cloning, expression, and type II collagenolytic activity of matrix metalloproteinase-13 from human osteoarthritic cartilage. J Clin Invest 97:761–768
7. Billinghurst RC, Dahlberg L, Ionescu M, Reiner A, Bourne R, Rorabeck C et al (1997) Enhanced cleavage of type II collagen by collagenases in osteoarthritic articular cartilage. J Clin Invest 99:1534–1545
8. Watanabe H, Yamada Y (1999) Mice lacking link protein develop dwarfism and craniofacial abnormalities. Nat Genet 21:225–229

9. Ameye L, Aria D, Jepsen K, Oldberg A, Xu T, Young MF (2002) Abnormal collagen fibrils in tendons of biglycan/fibromodulin-deficient mice lead to gait impairment, ectopic ossification, and osteoarthritis. FASEB J 16:673–680
10. Kizawa H, Kou I, Iida A, Sudo A, Miyamoto Y, Fukuda A, Mabuchi A, Kotani A, Kawakami A et al (2005) An aspartic acid repeat polymorphism in aspirin inhibits chondrogenesis and increases susceptibility to osteoarthritis. Nat Genet 37:138–144
11. Roughley PJ (2006) The structure and function of cartilage proteoglycans. Eur Cell Mater 12:92–101
12. Arikawa-Hirasawa E, Watanabe H, Takami H, Hassell JR, Yamada Y (1999) Perlcan is essential for cartilage and cephalic development. Nat Genet 23:354–358
13. Bashir A, Gray ML, Hartke J, Burstein D (1999) Nondestructive imaging of human cartilage glycosaminoglycan concentration by MRI. Magn Reson Med 41:857–865
14. Nieminen MT, Rieppo J, Toyras J, Hakumaki JM, Silvennoinen J, Hyttinen MM, Helminen HJ, Jurvelin JS (2001) T2 relaxation reveals spatial collagen architecture in articular cartilage; a comparative quantitative MRI and polarized light microscopic study. Magn Resonan Med 46:487–493
15. Wheaton AJ, Casey FL, Gougoutas AJ, Dodge GR, Borthankur A, Lonner JH, Schumacher HR, Reddy R (2004) Correlation of T1rho with fixed charge density in cartilage. J Magn Reson Imaging 20:519–525
16. Collins CM, Smith MB (2001) Signal-to-noise ratio and absorbed power as functions of main magnetic field strength, and definition of `90 degrees' RF pulse for the head in the birdcage coil. Magn Reson Med 45:684–691
17. Shiomi T, Nishii T, Tamura S, Tanaka H, Murase K, Yoshikawa H, Sugano N (2012) Influence of medial meniscectomy on stress distribution of the femoral cartilage in porcine knees: a 3D reconstructed T2 mapping study. Osteoarthr Cartil 20:1383–1390
18. Eckstein F, von Eisenhart-Rothe R, Landgraf J, Adam C, Loehe F, Muller-Gerbl M et al (1997) Quantitative analysis of incongruity, contact areas and cartilage thickness in the human hip joint. Acta Anat 158:192–204
19. Adam C, Eckstein F, Milz S, Putz R (1998) The distribution of cartilage thickness within the joints of the lower limbs of elderly individuals. J Anat 193:203–214
20. von Eisenhart-Rothe R, Adam C, Steinlechner M, Muller-Gerbl M, Eckstein F (1999) Quantitative determination of joint incongruity and pressure distribution during simulated gait and cartilage thickness in the human hip joint. J Orthop Res 17:532–539
21. Nishii T, Sugano N, Sato Y, Tanaka H, Miki H, Yoshikawa H (2004) Three-dimensional distribution of acetabular cartilage thickness in patients with hip dysplasia: a fully automated computational analysis of MR imaging. Osteoarthr Cartil 12:650–657
22. Wylar A, Bousson V, Bergot C, Polivka M, Leveque E, Vicaut E et al (2007) Hyaline cartilage thickness in radiographically normal cadaveric hips: comparison of spiral CT arthrographic and macroscopic measurements. Rdiology 242:441–449
23. Gu D, Chen Y, Dai K, Zhang S, Yuan J (2008) The shape of the acetabular cartilage surface: a geometric morphometric study using three-dimensional scanning. Med Eng Phys 30:1024–1031
24. Akiyama K, Sakai T, Koyamagi J, Murase T, Yoshikawa H, Sugamoto K (2010) Three-dimensional distribution of articular cartilage thickness in the elderly cadaveric acetabulum: a new method using three-dimensional digitizer and CT. Osteoarthr Cartil 18:795–802
25. Akiyama K, Sakai T, Sugimoto N, Yoshikawa H, Sugamoto K (2012) Three-dimensional distribution of articular cartilage thickness in the elderly talus and calcaneus analyzing the subchondral bone plate density. Osteoarthr Cartil 20:296–304
26. Tamura S, Nishii T, Shiomi T, Yamazaki Y, Murase K, Yoshikawa H, Sugano N (2012) Three-dimensional patterns of early acetabular cartilage damage in hip dysplasia; a high-resolutional CT arthrography study. Osteoarthr Cartil 20:646–652
27. Simkin PA (2001) Synovial physiology. Arthritis & allied conditions. In: Koopman WJ (ed) A textbook of rheumatology, 14th edn. Lippincott Williams & Wilkins, Baltimore, pp 174–186

28. Bullough PG (2010) Orthopaedic pathology, 5th edn. Mosby, New York
29. Abe H, Sakai T, Ando W, Takao M, Nishii T, Nakamura N, Hamasaki T, Yoshikawa H, Sugano N (2014) Synovial joint fluid cytokine levels in hip disease. Rheumatology (Oxford) 53:165–172
30. Ito H, Song Y, Lindsey DP, Safran MR, Giori NJ (2009) The proximal hip joint capsule and the zona orbicularis contribute to hip joint stability in distraction. J Orthop Res 27:989–995
31. Gilles B, Christophe FK, Magnenat-Thalmann N, Becker CD, Duc SR, Menetrey J et al (2009) MRI-based assessment of hip joint translations. J Biomech 42:1201–1205
32. Maeyama A, Naito M, Moriyama S, Yoshimura I (2008) Evaluation of dynamic instability of the dysplastic hip with use of triaxial accelerometry. J Bone Joint Surg Am 90:85–92
33. Maeyama A, Naito M, Moriyama S, Yoshimura I (2009) Periacetabular osteotomy reduces the dynamic instability of dysplastic hips. J Bone Joint Surg (Br) 91:1438–1442
34. Akiyama K, Sakai T, Koyamagi J, Yoshikawa H, Sugamoto K (2011) Evaluation of translation in the normal and dysplastic hip using three-dimensional magnetic resonance imaging and voxel-based registration. Osteoarthr Cartil 19:700–710
35. Moritomo H, Goto A, Sato Y, Sugamoto K, Murase T, Yoshikawa H (2003) The triquetrum-hamate joint: an anatomic and in vivo three-dimensional kinematic study. J Hand Surg 28:797–805
36. Akiyama K, Sakai T, Koyanagi J, Yoshikawa H, Sugamoto K (2013) In vivo hip joint contact distribution and bony impingement in normal and dysplastic human hips. J Orthop Res 31:1611–1619
37. Banks SA, Hodge WA (1996) Accurate measurement of three-dimensional knee replacement kinematics using single-plane fluoroscopy. IEEE Trans Biomed Eng 43:638–649
38. Watanabe T, Yamazaki T, Sugamoto K, Tomita T, Hashimoto H, Maeda D et al (2004) In vivo kinematics of mobile-bearing knee arthroplasty in deep knee bending motion. J Orthop Res 22:1044–1049
39. Yamazaki T, Watanabe T, Nakajima N, Sugamoto K, Tomita T, Yoshikawa H et al (2005) Visualization of femorotibial contact in total knee arthroplasty using X-ray fluoroscopy. Eur J Radiol 53:84–89
40. Tamaki M, Toimita T, Yamazaki T, Hozack WJ, Yoshikawa H, Sugamoto K (2008) In vivo kinematic analysis of a high-flexion posterior stabilized fixed-bearing knee prosthesis in deep knee bending motion. J Arthroplasty 23:879–885
41. Tamaki M, Toimita T, Watanabe T, Yamazaki T, Yoshikawa H, Sugamoto K (2009) In vivo kinematic analysis of a high-flexion posterior stabilized mobile-bearing knee prosthesis in deep knee bending motion. J Arthroplasty 24:972–978
42. Komistek RD, Dennis DA, Mahfouz MR (2006) Kinematics of the hip. The adult hip, 2nd edn. Lippincott Williams & Wilkins, Philadelphia, pp 91–101
43. Koyanagi J, Sakai T, Yamazaki T, Watanabe T, Akiyama K, Sugano N, Yoshikawa H, Sugamoto K (2011) In vivo kinematic analysis of squatting after total hip arthroplasty. Clin Biomech 26:477–483

Chapter 3
Metallurgy of Spinal Instrumentation

Reed A. Ayers, Evalina Levina Burger, Christopher J. Kleck, and Vikas Patel

Abstract Examination of clinical literature tends to suggest a rather limited diversity of metals used in spinal instrumentation (Netter FH (ed) Atlas of human anatomy, 5th edn. Saunders Elsevier, Philadelphia, 2011; Yoshihara H, Spine J in press, 2013). The American Society of Materials (ASM) Materials and Processes for Medical Devices (MPMD) database shows approximately 33 different alloys used in medicine in the USA. Within this database, only about one-third are used in orthopedic applications, and in the clinical environment, these alloys are generally referred to in very general terms such as titanium, Ti6Al4V, stainless steel A316L, or cobalt-chrome, CoCrMoC. For the purpose of spinal applications, it may be convenient to consider the general alloy systems, ferrous stainless steel, titanium and its alloys, cobalt-chromium, and tantalum. From this standpoint, the characteristics along with their clinical advantages and disadvantages can be discussed. The reader is kindly guided to many excellent texts concerning specific aspects of metallurgy as well as other chapters in this book for details on specific alloy systems and their properties (Yu WD, Oper Tech Orthop 13(3):159–170, 2003; Black J, Biological performance of materials, 4th edn. Taylor and Francis, Boca Raton, 2006; Hosford WF, Physical metallurgy, 2nd edn. Taylor and Francis, Boca Raton, 2010; Narayan RJ (ed) ASM handbook: vol 23, Materials for medical devices. ASM International, Materials Park, 2012; Yahia L (ed) Shape memory implants. Springer, Berlin, 2000). It should be noted based on the following section that for all metals represented herein, in terms of clinical applications, many of the properties discussed have little effect on their selection during surgery as the medical priority is maintaining bony alignment and minimizing patient discomfort.

Keywords Spine anatomy • Spinal fusion • Spinal deformity • Spinal instrumentation • Titanium alloy • CoCr alloy • Shape-memory alloy • Stainless steel

R.A. Ayers (✉) • E.L. Burger • C.J. Kleck • V. Patel
Department of Orthopaedics, University of Colorado SOM, Aurora, CO 80045, USA
e-mail: reed.ayers@ucdenver.edu

M. Niinomi et al. (eds.), *Advances in Metallic Biomaterials*, Springer Series in Biomaterials Science and Engineering 3, DOI 10.1007/978-3-662-46836-4_3

3.1 Spine Anatomy

The spine is composed of five regions: cervical, thoracic, lumbar, sacrum, and the coccyx. Each region has a characteristic anatomic form with a few exceptions within zones of transition from one segment to the next. When viewed in a coronal plane, from front to back or vice versa, the spinal column forms a straight line. The side profile, or sagittal plane, is described by a series of curves that have several biomechanical advantages. These include a cervical lordosis (bend backward/posterior), a thoracic kyphosis (bend forward/anterior), a lumbar lordosis, and a sacral kyphosis. Combined together, the curves allow for upright posture and a dynamic biomechanical balance (Fig. 3.1).

The basic anatomic building blocks are the vertebrae, each numbered in a given region. Anteriorly, from the second cervical to the first sacral vertebrae, intervening disks act as a shock absorber and allow motion. A motion segment is therefore defined as the vertebral body above and below with the intervening disk (Fig. 3.2). The basic bone anatomy includes a large mass of bone, which makes up the anterior column support. Two bridges of bone protrude posteriorly to connect the anterior structures to the posterior structures. These are known as the pedicles. Posteriorly, two joints are formed from processes extending from the vertebrae above and the vertebrae below the disk. This articulation is known as the facet joint. The pedicles and articular processes are confluent with a sheet of bone that overlies the spinal cord/nerves called the lamina. Finally, the posteriormost portion of the bone is the spinous process, which serves as a point of attachment for muscle and ligaments.

The cervical spine is formed by seven vertebrae and includes the articulation of the skull with the spinal column. The first and second vertebrae (axis and atlas, respectively) have a unique structure that allows for articulation with the base of the skull with a smooth transition into the spinal column. These levels are also responsible for a large portion of the rotation and flexion/extension motions of the cervical spine. Their unique shape, location, and surrounding anatomy pose particular difficulties with surgical management; however, that is beyond the scope of this chapter. The lower portion of the cervical spine (subaxial region) consists of the C3–C7 vertebrae, which have a common structure similar to that described above. The thoracic spine is characterized by the addition of articulations for the ribs that are also attached to the sternum. This creates a significantly more rigid biologic construct with little motion through the thoracic region. The lumbar spine is again a mobile region of the spinal column and necessarily bears the brunt of the body load in an upright species such as humans. The sacrum then serves as the attachment point of the spinal column with the pelvis at the sacroiliac joints, and the coccyx is a vestigial tail remnant without structural implications. The sacrum and the coccyx are formed by the fusion of vertebrae, five in the sacrum and four in the coccyx.

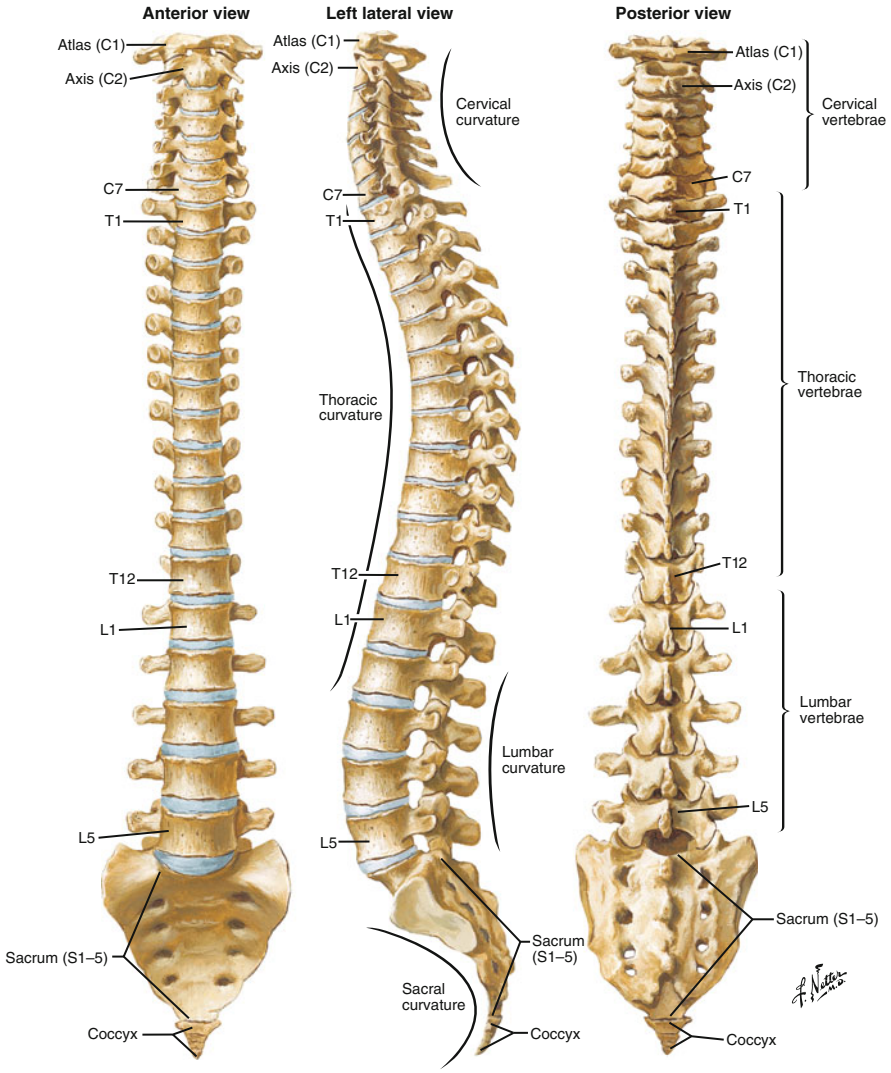

Fig. 3.1 Common spine anatomy. Note the anterior/posterior curvature typical of a normal, healthy spine (Reprinted from Ref. [1]. Copyright 2011 with permission from Suanders Elsevier)

3.2 Clinical Correlates

There are several clinical correlates with the use of metals in spinal surgery, but the most common is for the purposes of spinal fusion. With various disease processes including fracture, arthritis, and spinal deformity, the mainstay of treatment often involves fusion across several motion segments of the spine. The ultimate goal is to

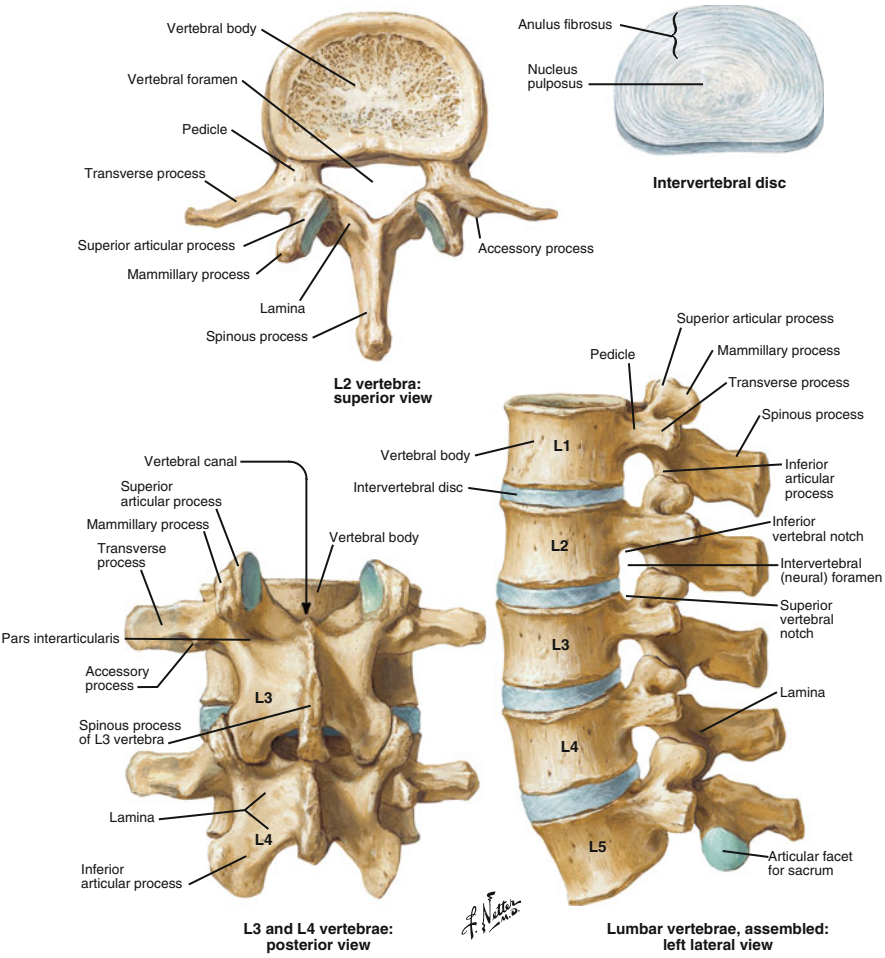

Fig. 3.2 Anatomy of the vertebra (Reprinted from Ref. [1] Copyright 2011 with permission from Suanders Elsevier)

create a biologic fusion with bone growth across the fused segments, but this is not easily accomplished in a mobile spine. Unlike a long bone fracture, the natural state of spine segments is motion rather than rigid fusion. General bone growth characteristics require a relatively stable environment to allow bone growth and maturation similar to casting a long bone fracture. Conversely, as is seen in long bone fractures, instability and motion lead to excess bone formation without bridging the fracture. This creates a need for relative stability during the initial attempt at fusion and has been one of the main focuses in the use of metals with spine surgery.

Initial fixations consisted of wiring of spinous processes. As previously discussed, a motion segment consists of two vertebral bodies and the intervertebral disk. Prior to many of the advances in spine instrumentation, fusions were attempted

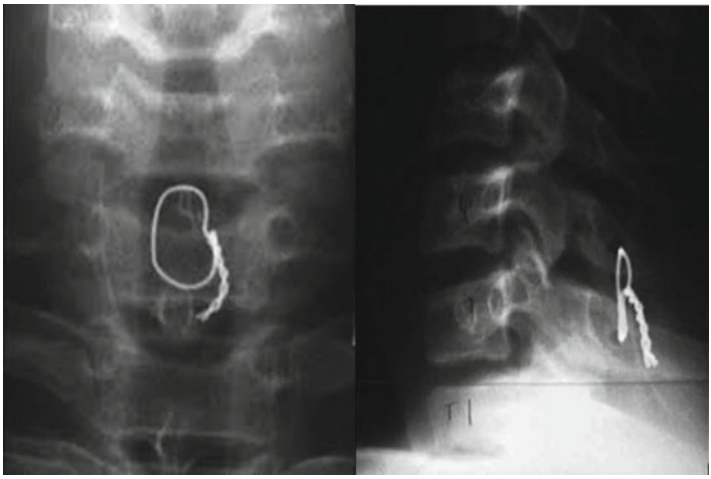

Fig. 3.3 Spinal fusion technique as described by Hadra http://www.wheelessonline.com/ortho/facet_joint_injuries

without internal stabilization. While there is still a debate in the literature as to the role of instrumentation in spine fusions for certain degenerative processes, stabilization of the spine in cases of fracture, infection, instability, and deformity is ultimately a necessary part of the surgical management. Early techniques, such as wiring of the spinous processes first described in the literature by Dr. Berthold Ernest Hadra in 1891, served as the introductions of metals in spine surgery (Fig. 3.3) [8]. Over time, techniques and implants were modified to include rod systems, metal hooks, variously placed screws, and eventually pedicle screws, which are now one of the most commonly used implants in spine surgery today. The combination of pedicle screws with rods allows the surgeon to create a fairly rigid construct for the maintenance of spinal stability. Further, this has allowed for the correction of spinal deformities to an even greater extent. However, it has also introduced issues for consideration based on an individual basis.

Several factors have influenced the metals used and the manner in which they have been implemented. Among these include the quality of the bone being manipulated, the intended use for the implants, and the patient-specific qualities such as age, surgical procedure, and outcome goals. While other surgical considerations are used to implement pedicle screw and rod constructs, such as anterior support with cages, we will focus on the specifics of metal implantation of screw and rod constructs.

Current techniques for spine fusion include the use of screws placed from the posterior through the pedicle (bridge of bone previously described) and into the vertebral body as shown in Fig. 3.4. Common metal alloys recognized by the governing agency for medical devices in the US Federal Drug Agency (FDA) for use in the production of pedicle screws include 316L stainless steel, 316LVM stainless steel, 22Cr-13Ni-5Mn stainless steel, Ti-6Al-4V, and unalloyed titanium (FDA final rule: Pedicle Screw Systems - 21 Code of Federal Regulations Part 888.3070).

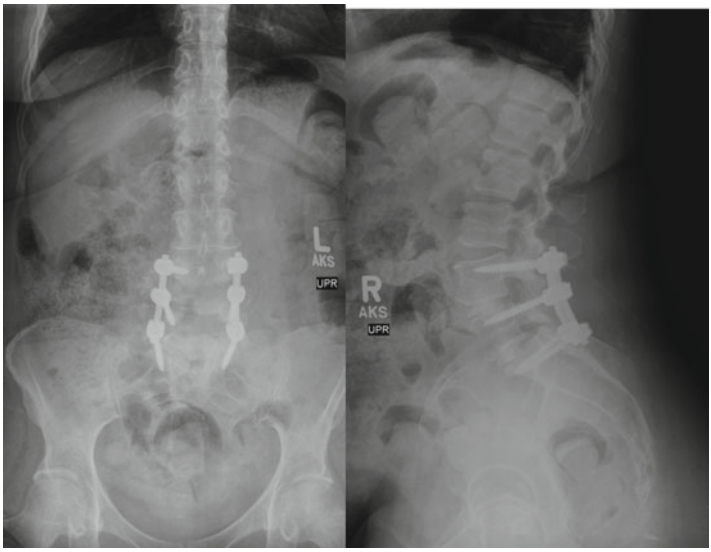

Fig. 3.4 Typical placement of spinal instrumentation including pedicle screws and rods

Nitinol, or NiTi, has also been evaluated for use more recently because its modulus of elasticity can be more closely matched to the bone and because of improved bone ingrowth when produced in a porous form [9, 10]. These advantages have not been fully parsed out in a clinical setting. Similar metals are often used to create the rods used in these systems with the inclusion of CoCr alloy (CoCr) as well. The ultimate goal for the pedicle screw is a metal or metal alloy that interfaces with the bone to allow ongrowth/ingrowth of the screw for improved screw purchase. This in turn reduces the incidence of screw loosening, screw pullout, or failure of the screw cyclic loading over time. Similarly, the rod is used in combination with screws to correct a deformity and/or stabilize a segment of the spine over time to allow a biologic bone fusion to occur. The current use of these metal implants is a time-sensitive process in which there is a race between ultimate implant failure and biologic healing. While this is ever improving, continued advances may help to mitigate failures of the bone and or the metal over time.

In situ, this race is partially dependent on the quality of the bone. In certain pediatric disease processes, as well as adults with osteopenia/osteoporosis, the loss of bone structure decreases the purchase of the screws and can lead to screw failure over time. This is seen clinically with screw pullout, fractures through instrumented segments, loss of deformity correction, and proximal fractures above a stiff construct. Currently, one of the most common practices is to augment the vertebral bone with a cement through which the screw may be inserted and provide improved purchase. Ultimately, the bone quality, in part, drives the surgical planning and choice of metal implants. The placement of a titanium alloy may be preferred to the stiffer metals/alloys to reduce the stress produced at the construct-bone interface.

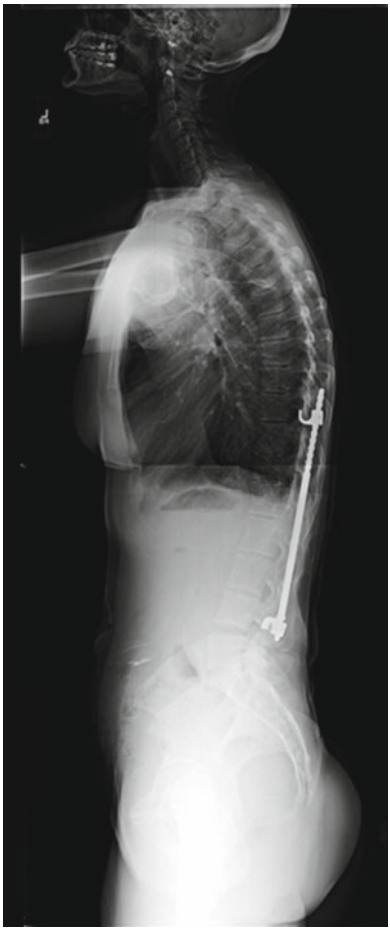

Fig. 3.5 Harrington rods in a patient with spinal fusion, one of the first devices to stabilize the spine and correct deformity based on distraction

Also, less correction may be expected with these deformities with the ultimate goal of a solid bony fusion in mind (Fig. 3.5).

When bone quality is less of an issue, such as younger patients, and the metal implants may be selected to allow for the greater correction of spine deformities, several issues still exist. One such issue inherent to the surgery is the inability to have a custom-contoured rod. Typically, a straight or pre-bent rod is contoured intraoperatively to fit the patient profile. This can cause several issues with the integrity of the metal as described in further detail later in the chapter. Also, over time, these rods have been shown to lose some of the contour in situ and, as a result, decrease the amount of surgical correction. Ultimately, the best scenario would involve the placement of a rod pre-contoured to the expected final position of the spine.

In the face of pedicle screw and rod instrumentation, advantages and disadvantages to the use of various metal/metal alloys have been studied and are further

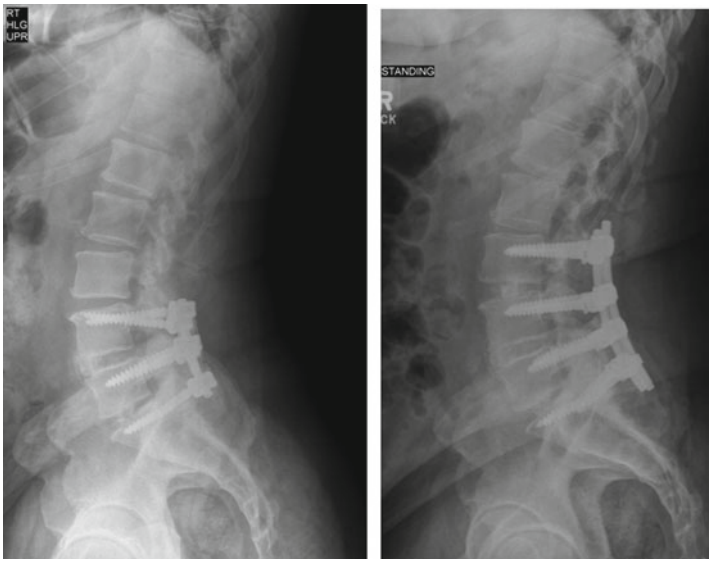

Fig. 3.6 Fractured pedicle screw in the S1 vertebra

described. Clinically, the ultimate goal of instrumentation is to provide fixation that allows stability over time and can withstand the body's environment in the face of cyclic loading. This has improved over time with changing surgical techniques and the improved understanding of metals and alloys. However, there is continued room for improvement. We will continue with a more in-depth discussion of the various metals and metal alloys commonly seen in spinal instrumentation with perceived advantages and disadvantages (Fig. 3.6).

3.3 Ferrous Alloys

Ferrous alloys encompass all metal alloys that use iron (Fe) as its predominant component. These are also commonly referred to as steels. The predominant orthopedic steel is termed A316L (AISI designation) stainless steel. However, there are other A316 alloys such as AISI A136Cb with compositions tailored to reduce grain boundary chromium carbide formation at elevated temperatures. These alloys retain the austenitic face-centered (FCC) unit cell structure, hence the "A" prefix in the designation. This structure enables ease of forming, high ductility (increased formability), and high impact strength while being nonmagnetic (allows for a patient to undergo magnetic resonance imaging, MRI). The FCC structure is retained at low temperatures (below the eutectoid) because the significant amount of nickel creates a substitutional solid solution at temperatures above the eutectoid. The 316 series stainless steel is a modified 304 stainless steel with increased Mo to reduce pitting

corrosion and reduced carbon to decrease the sensitivity of the alloy to forming undesired carbides in the grain boundaries, increasing its weldability. The additions of chromium (between 16 and 18 wt%) and molybdenum (2–3 wt%) enhance the corrosion resistance through the formation of oxides on the surface.

A316 alloys are also easily and economically processed. They are readily manufactured in existing basic oxygen furnaces in high volumes. Stainless steels, in general, lend themselves to forging processes, machining, and welding to create a specified device. They can be cold-worked, such as drawing and bending without necessary annealing, allowing for economic manufacture of spinal instrumentation.

3.4 Titanium Alloys

Titanium and its alloys offer unique advantages over steels in medicine, predominantly, low weight and high corrosion resistance. While there are 38 grades of titanium and its alloys, approximately five of those grades constitute almost 80 % of the production in the USA and a majority of that is Ti6Al4V (ASTM Grade 5; Type III) [11]. For the purposes of this chapter, it is easier to consider the available biomedical titanium not from their compositions, such as with steel, but by their microstructure.

First are the α-type titanium alloys. These are generally the commercially pure (CP Ti) forms but there are alloys as well. The α-phase in titanium is characterized by the hexagonal close-packed (HCP) unit cell. These alloys are characterized by good strength, toughness, creep resistance, and weldability. Common alloying elements are aluminum and tin. Other α-phase stabilizers are O and N. Strengthening is accomplished through increasing oxygen concentrations, from 0.18 wt% for ASTM Grade 1 CP Ti (240 MPa tensile strength) to 0.40 wt% for Grade 4 CP Ti (550 MPa tensile strength); however, this comes at a cost of decreasing formability.

Second are the (α + β)-type titanium alloys. The most common is Ti6Al4V. (α + β) describes the mixed microstructure where, in general, the "rigid" α-phase HCP unit cell is mixed with a more ductile β-phase, which has a BCC unit cell. In the case of Ti6AL4V, vanadium stabilizes the high-temperature β-phase to increase alloy ductility as well as to increase its strength well beyond the single-phase alloys. Additionally, these alloys can be strengthened via post-synthesis heat treatments rather than composition, reducing production costs and material complexity.

The β-phase enables super-plastic behavior of (α + β)-type titanium alloys. The mechanism of this comes from a combination of high diffusivity in the β-phase combined with grain coarsening in the α-phase [11]. The implications are that without any special processing Ti6Al4V can undergo an elongation of 750–1,100 % at elevated temperatures, further enhancing the formability of Ti6Al4V to generate medical devices. Additionally, these phenomena allow the surgeon to contour Ti6Al4V spinal instrumentation at room temperature to match

larger deformities in vivo. However, both springback and the Bauschinger effect cannot be neglected as that can lead to pedicle screw pullout and subsequent instrumentation failure.

β-type titanium alloys are becoming more popular in orthopedic applications as their lower modulus is believed to reduce the effect of stress-shielding on the bone as well as exhibit an increased fracture toughness as compared to an alpha-beta alloy of equivalent aging. Generally, β-type titanium alloys have good ductility, relatively low strength, low modulus, and excellent uniaxial formability. The ability to harden the alloy is easily controlled during the cooling process enabling the alloy to be better designed to the spinal biomechanical environment. These properties also suggest β-type titanium alloys as effective metals in spinal applications given the metal can be formed at room temperature without appreciable cold-work hardening. The more common biomedical alloy in this form is TNTZ (titanium-niobium-tantalum-zirconium) where each alloying element is both a beta-phase stabilizer and biocompatible.

3.5 Cobalt-Chromium Alloys

Originally, CoCrMoC alloys were used as cast dental alloys in the 1930s and then subsequently adapted to orthopedics. However, CoCr alloys are difficult to process due to the strong affinity of Cr to form carbides, reducing ductility and formability. CoCr alloys were adapted to medicine due to their excellent corrosion resistance as the result of dense chromium oxides present on metal surfaces. The common composition of CoCr-based alloys used in orthopedics is described by the ASTM standards F75, F90, F799, and F562. The base alloy standard is the ASTM F75 specification for cast CoCrMoC alloy. The specification outlines a composition range of 27–30 wt% Cr, 4–6 wt% Mo, and 0.5 wt% carbon (C) with the balance being cobalt. Small amounts of other trace metals such as nickel, iron, and silicon can be present in the alloy. The other standards cover reduced C (0.05–0.35 wt%) and Cr (18–22 wt%) content in order to enhance fabricability and cold-work strengthening by reducing the carbides formed in the grain boundaries.

The structure of CoCr alloys is a mixture of low-temperature ε-type Co (HCP) and high-temperature γ-type Co (FCC). The $\varepsilon-$phase is a very stiff phase, similar to the α-phase in Ti alloys, due to the limited number of slip systems. The inclusion of γ-phase stabilizers such as carbon and nitrogen yields increased ductility at the risk of increased carbide formation. However, facilitating the precipitation of carbides along the grain boundary of the low-temperature epsilon (ε)-phase can enhance strength. Carbides formed during cooling of CoCr cast alloys including Mo_2C, Cr_3C_2, and Co_2C. These are subsequently homogenized via a heat treatment and subsequent quenching. A typical post-casting heat treatment can involve hot isostatic pressing (HIP) at 1,200 °C under argon at positive pressure for 4 h followed by second homogenization cycle performed at 1,220 °C under argon for 4 h followed by a rapid quench to 760 °C to dissolve the carbides and improve the

isotropy of the microstructure. Subsequently, processing of CoCr alloys is difficult and time-consuming in order to attain the desired properties. However, newer methods of CoCr alloy synthesis such as powder metallurgy and combustion synthesis are providing economic alternatives to the current methods.

3.6 Shape-Memory Alloys

The most prominent shape-memory alloy (SMA) in spinal applications is nickel titanium (NiTi or Nitinol). While generally considered to be equiatomic, NiTi has a range of Ni and Ti ratios from 49 to 51 %. Slight changes in this ratio, primarily through the addition of nickel, can result in significant changes in the material properties. While there is a concern about the sensitivity to Ni in vivo, numerous studies suggest that NiTi is well tolerated in the bone and the spine [6, 12, 13].

A key tenet to shape-memory properties is a reversible martensitic (non-diffusion) phase transformation. In the case of NiTi, the parent phase, austenite, is a simple cubic structure (B2) that transforms to a monoclinic structure (B19) during heating or application of load. This austenite/martensite transformation axis is dependent on the temperature, following the Clausius-Clapeyron relationship, and as such the mechanical, acoustic, and conductive properties of NiTi can be changed or tailored to a given application, e.g., fusion or deformity correction. Pure titanium has some shape-memory properties through the martensitic transformation from the austenite to martensite phases; however, it does not result in significant property changes in bulk materials application – as it is not fully reversible below the transus temperature – and as such it is not considered a SMA. The same can be considered for pure cobalt in its transformation from the γ to ε phases, but again this does not result in significant property changes as previously stated.

NiTi is difficult to process and as such is relatively more expensive than the common metals presented. Because of Ti reactivity with oxygen, all processing must be done in a vacuum or inert atmosphere using plasma arc, electron beam, or induction melting. New, more economical methods for synthesis are being developed and researched such as the self-propagating high-temperature synthesis (SHS) mode of combustion synthesis or spark plasma sintering (SPS) [14, 15]. Once formed, NiTi ingots can be hot-worked to form the final parts. Cold-working is difficult as NiTi work hardens quickly; thus, frequent annealing must be done.

3.7 Challenges of Using Metals in Spinal Procedures

Spinal instrumentation is dependent on multiple material properties over both spatial and temporal frames. For the initial stabilization of the spine, yield and ultimate strength and ductility are prominent. Excellent fatigue properties, low modulus, corrosion resistance, and biocompatibility become increasingly important as the

Table 3.1 General metal alloy material mechanical properties

	ASTM F138 annealed stainless steel	ASTM F138 cold-worked stainless steel	Wrought CoCrMo	Ti6Al4V annealed	Ti annealed grade 4
Density (g/cm^3)	7.9	7.9	9.15	4.4	4.5
E (tensile)	200	200	230	127	127
Yield stress (MPa)	190	690	310	760–795	483
Ultimate stress (MPa)	490	860	860	825–860	550
Elongation (min %)	40	12	30	8	15

This table is in no means a definitive example of all alloys in use or the properties to be considered. This is provided to show the mechanical capacity differences in the general alloys

instrumentation remains in the patient (up to the lifetime of the patient). Overall, spinal instrumentation should be strong enough to protect and support spine stability and ductile enough to prevent stress-shielding, while not inducing any allergic or other deleterious condition in the patient.

Each metal listed is more than capable of supporting the loads imposed upon the spine during recovery as well as during a patient's daily activities. In procedures such as fusion, the ability of metal spinal instrumentation to accommodate all loads through the spine while maintaining sufficient stiffness of the spine until the bone is fused is unsurpassed. High strength also means the instrumentation can be undersized to further accommodate a patient's anatomy and comfort. To date no other class of materials is as capable as metals for functioning for extended periods by the stress environments generated in vivo.

The mechanical properties of these materials are different and determined not only by their chemical composition but also by their microstructure. In particular grain size as well as strengthening defects such as precipitates and secondary phases greatly affect the mechanical and corrsoison resistance properties of biomedical alloys. These physical structures are controlled during manufacturing by different methods which include but are not limited to heating, annealing, quenching, cold-working, casting, forging, and others. Table 3.1 presents some of the properties surgeons rely upon to effectively treat the patient. This is noninclusive of all materials and processes used to manufacture spinal instrumentation materials, but one can see the range of properties and how one may select a metal over another to accomplish a given therapeutic procedure.

Fundamentally, these properties come about due to metallic bonding which allows the continuous breaking and reforming of bonds between atoms during deformations of the material under load without large fractures or damage. During the breaking and reforming of bonds, atomic defects are generated and subsequently larger-scale (nanoscale) dislocations come to existence. Accumulation of dislocations can be used to further strengthen a metal, albeit at a reduction of ductility (cold-work hardening). Dislocation formation also occurs at loads and strains well below the yield point. This is fatigue. This is significant in spinal applications as the metals are in almost continuous loading cycles from patient movement, including axial tension and compression and bending and torsion.

From a clinical perspective, titanium constructs in scoliosis have become very popular in the recent years and are advocated because they allow repeat magnetic resonance images (MRIs), enabling the visualization of soft tissues and neural elements after surgery. Other benefits include a lower modulus of elasticity and a greater resistance to fatigue than stainless steel. However, these necessitate bulkier implants, to compensate for reduced tensile strength [16]. Titanium's density, which is 57 % of stainless steel, allows for a weight reduction to compensate for the lower modulus of elasticity [17] adding to the patient's comfort. The lower modulus of elasticity also transfers more stress from the implant to the bone, reducing the effects of "stress-shielding," wherein undesirable osteoporosis may develop after an implant has been inserted. Conversely, this results in greater deformation, strain, in the implant. Stainless steel rods have stood the test of time in spinal procedures. They are very pliable and much easier to contour during surgery and allow the placement of sublaminar wires to enhance fixation, which is very cost-effective.

From the biologic perspective, bone ingrowth with titanium is 33 % more than with stainless steel [18]. Bone contact is also good, as high as 29.4 % [19]. The pullout strength of stainless steel screws is equal to that of titanium screws due to the same amount of peripheral bone ingrowth [19, 20]. In laboratory pullout tests, no differences were found between the stainless steel screws and titanium screws in relation to the maximum load, stiffness, and energy to failure [18]. However, screw pullout still occurs in the clinical application. This may be due to spine rod springback, an elastic response to the deformation in the spine rods used to lock together the instrumentation into a mechanically coherent structure. For the purposes of this chapter, springback can defined as the deviation of the rod from the intended contoured shape to its original shape after the bending load is removed. Springback has been studied extensively in material processing literature as innumerable parts and devices are made using bending techniques. It was shown experimentally that increased springback is proportional to higher bending radius, higher yield strength, and reduction in thickness and/or Young's modulus [21, 22]. Given that commercially pure titanium and titanium alloys have a higher modulus and yield strength, it implies that they should have higher springback than those manufactured from stainless steel or cobalt-chromium alloys (Table 3.1). All metals have a springback effect that occurs during bending or "contouring" which typically requires additional bending or other mechanisms to reach the necessary curvature.

The concern is that there is a clinical impression that proximal screw-rod construct failure may be more frequent in cases that have been instrumented with titanium rods. One potential explanation for this observation is the possible tendency of titanium rods to approximate their original shape (Fig. 3.7). It is also postulated that postoperative sagittal balance may be lost when using titanium rods as an implant for the same reason. No matter what the cause is, the result is a continuation of difficulty for the patient such as a progression of kyphosis upon loss of instrumentation integrity (Fig. 3.8).

Anelastic strain responses have been studied in titanium and it alloys. In 2000, J. D. Cotton described the anelastic deformation of Ti6Al4V when used as a structural component [24]. His conclusion is that the elastic and anelastic responses of

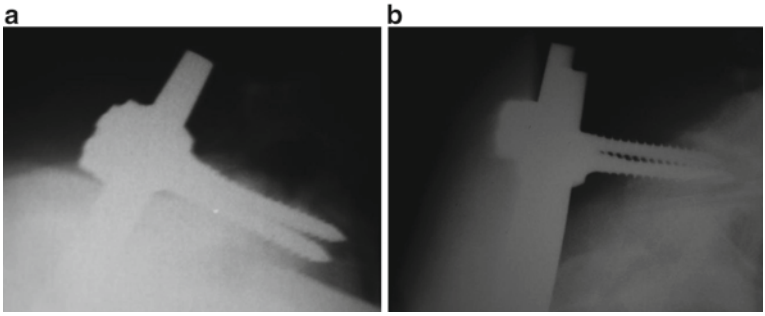

Fig. 3.7 (**a**) Postoperative close-up of proximal titanium rod construct. (**b**) The same construct after failure due to screw pullout (note the loss of rod curvature compared to part A)

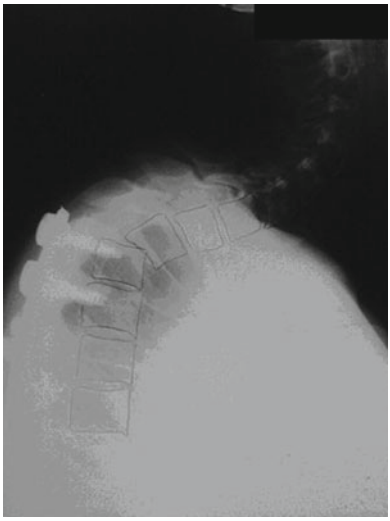

Fig. 3.8 "Over the top" principle is illustrated here. Kyphosis occurred proximal to the caudal-most screws

Ti6Al4V were roughly equivalent at -4με. The implication is that simply considering the elastic properties of titanium may underestimate the strain recovery response of the bulk material. Elmer et al. describe how the diffusion of vanadium causes lattice parameter changes and subsequent internal stresses even at temperatures around 400 °C [25]. When kept at that temperature for 2 h, there was a measureable effect showing that at least half of the measureable strain was an anelastic response. Pure titanium is highly susceptible to changes in loading and environment. Keeping temperature constant, increasing the pressure to 2 GPa will cause elemental Ti to transform to the β-phase from the hexagonal close-packed (HCP) α-phase [26].

Other work describes the anelastic effects of oxygen and hydrogen adsorption. Amadori et al. show the relaxation strength of α-α' titanium is very dependent on the amount of oxygen and hydrogen in both phases. Kaneko et al. showed that α-titanium, when placed in simulated saliva and cyclically loaded for 24 h, is

significantly embrittled as the result of the adsorption of hydrogen from the surrounding fluids even at room temperature [27]. Ti6Al4V used in hip replacements showed that while no changes to the crystal surface structure occurred, there were significant surface morphology changes, indicating that some form corrosion occurred when they were exposed to hydrogen peroxide [28]. Another work describes the microstructural relationship of the addition of hydrogen during hot rolling and its effect on the fracture properties of Ti6Al4V. While there was no specific effect on the orientation of the crystals, there were distinct changes to the microstructure and subsequent failure modes of the material [29]. As an example of how easy titanium alloys integrate oxygen and hydrogen, titanium alloys have been investigated for hydrogen storage. Titanium has octahedral interstices with suitable binding energies, allowing hydrogen adsorption near room temperature and atmospheric pressure [26]. Thermodynamically, the formation of titanium hydrides and oxides is very favorable at room temperature and pressure.

The evidence of springback in spine rods gives insight to issues with any metal used in spinal reconstruction: the surgeon fundamentally alters the strength and fatigue properties of the metals as the parts, such as rods and plates, are shaped to match the individual anatomy of the patient. Damage from the mechanical shaping where the surgeon uses mechanical methods, e.g., French bender, hammer, hand brakes, and benders, to fit and set implants in the bone can be significant, even if not obvious [30, 31]. Figure 3.9 shows multiple types of damage on a spine rod as the result of both its preparation for placement into the body (contouring) and its being locked into the spine to provide stabilization. The rod surface is damaged due to notching, at the same time countrouring creates significant residual stresses. The surface is damaged due to impingement caused by the bender or brake. Scratching and scrapes are evident due to the slipping of the rod in vivo against the locking caps in the pedicle screw tulip. In each case the properties of the rods change either mechanically or chemically. This type of damage is common in any operating room where the metal part must be shaped to accommodate the patient's disease or deformity.

In clinical practice very few spinal instrumentations fail catastrophically mechanically. Thus, the definition of "failure" must be revised to describe that the patient no longer tolerates the presence of the instrumentation, be it mechanically, biologically, or otherwise. The presence of the said instrumentation becomes detrimental to the patient's health. Thus, other forms of failure include mechanical damage or mechanically induced corrosion. Figure 3.10 shows a Ti6Al4V locking nut for a pedicle screw with the anodized titania coating removed due to being in continuous contact with the spine rod after locking the rod in place. The patient developed metal sensitivity post implantation as the result of continued exposure to the release of metal elements, thus leading to failure of the implant.

The ideal metal for spinal implantation should have a modulus of elasticity similar to the bone and should be lightweight, pliable, and MRI friendly with the ability to resist corrosion for decades in the body temperature and pH. With the changes in bone biology over the spectrum of an individual's life, we will potentially need different properties for metal depending on the aim of the surgery. Individualized instrumentation should be developed for use in the future as it is clear that one size does not fit all.

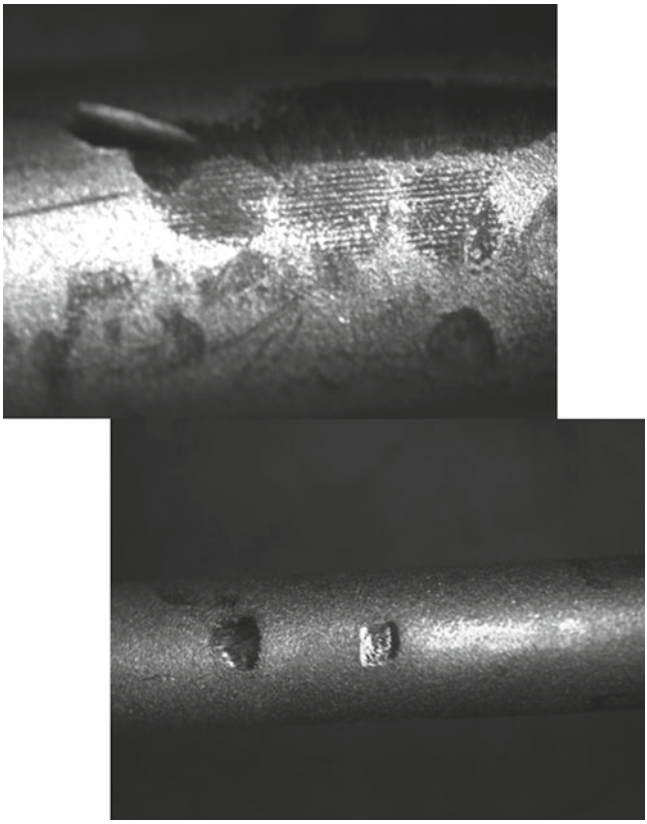

Fig. 3.9 *Left*: notching of a Ti6Al4V spine rod as the result of contouring prior to placement in the body. Other marks are due to the locking heads of the pedicle screws. Scratching as a result of fitting the rod in the pedicle screws is also evident. *Right*: wear damage from pedicle screws on a CoCrMoC (ASTM F75 wrought alloy) rod. Burnished mark above the wear is Ti6Al4V from the tulip heads smeared onto the rod

Fig. 3.10 Pedicle screw locking cap underside showing delamination of the titania coating, exposing the underlying Ti6Al4V alloy to the body environment

References

1. Netter FH (ed) (2011) Atlas of human anatomy, 5th edn. Saunders Elsevier, Philadelphia
2. Yoshihara H (2013) Review article: Rods in spinal surgery: a review of the literature. Spine J 13(10):1350–1358
3. Yu WD (2003) Advances in spinal instrumentation. Oper Tech Orthop 13(3):159–170
4. Black J (2006) Biological performance of materials, 4th edn. Taylor & Francis, Boca Raton
5. Hosford WF (2010) Physical metallurgy, 2nd edn. Taylor & Francis, Boca Raton
6. Narayan RJ (ed) (2012) ASM handbook: vol 23, Materials for medical devices. ASM International, Materials Park
7. Yahia L (ed) (2000) Shape memory implants. Springer, Berlin
8. Reed-Hill R, Abbaschian R (1994) Physical metallurgy principles, 3rd edn. PWS Publishing, Boston
9. Hadra BE (1891) Wiring of the vertebrae as a means of immobilization in fractures and Pott's disease. Med Times Reg 2:1–8
10. Simske SJ, Sachdeva R (1995) Cranial bone apposition and ingrowth in a porous nickel–titanium implant. J Biomed Mater Res 29:527–533
11. Ayers RA, Simske SJ, Bateman TA, Petkus A, Sachdeva RLC, Gyunter VE (1999) Effect of nitinol implant porosity on cranial bone ingrowth and apposition after 6 weeks. J Biomed Mater Res 45(1):42–47
12. Semiatin SL (ed) (2006) ASM handbook, vol 14B: Metalworking: sheet forming. ASM International, Materials Park, Ohio, USA, pp 656–669
13. Rhalmi S, Charette S, Assad M, Coillard C, Rivard CH (2007) The spinal cord dura mater reaction to nitinol and titanium alloy particles: a 1-year study in rabbits. Eur Spine J 16:1063–1072
14. Venugopalan R, Trepanier C (2000) Assessing the corrosion behaviour of Nitinol for minimally invasive device design. Minim Invasive Ther Allied Technol 9(2):67–74
15. Ayers R, Ferguson V, Belk D, Moore J (2007) Self-propagating high temperature synthesis of porous nickel-titanium. Mater Sci Forum 561–565:1643–1648
16. Majkic G, Chennoufi N, Chen YC, Salama K (2007) Synthesis of NiTi by low electrothermal loss spark plasma sintering. Metall Mater Trans A 38A:2523
17. Uhthof HK, Bardos DI, Liskova-Kiar M (1981) The advantages of titanium alloy over stainless steel plates for the internal fixation of fractures: an experimental study. J Bone Joint Surg Am 71A:1337–1342
18. Brown SA, Lemons JE (1994) Medical applications of titanium and its alloys: the material and biological issues. ASTM, West Conshohocken
19. Sun C, Huang G, Christensen FB et al (1999) Mechanical and histological analysis of bone-pedicle screw interface in vivo: titanium versus stainless steel. Chin Med J (Engl) 112:456–460
20. Hazan R, Brener R, Oron U (1993) Bone growth to metal implants is regulated by their surface chemical properties. Biomaterials 14:570–574
21. Christensen FB, Dalstra M, Sejling F et al (2000) Titanium-alloy enhances bone pedicle screw fixation: mechanical and histomorphometrical results of titanium- alloy versus stainless steel. Eur Spine J 9:97–103
22. Groche P, Beiter P, Henkelmann M (2008) Prediction and inline compensation of springback in roll forming of high and ultra-high strength steels. Prod Eng Res Dev 2:401–407
23. Garcia-Romeu M, Ciurana J, Ferrer I (2007) Springback determination of sheet metals in an air bending process based on an experimental work. J Mater Process Technol 191:174–177
24. Burger EL, Baratta RV, Andrew GS, King RE, Yun L, Solomonow M, Riemer BL (2005) The memory properties of cold-worked titanium rods in scoliosis constructs. Spine 30:375–379
25. Cotton JD (2000) Anelastic deformation measurements in structural engineering alloys. J Mater Eng Perform 9:463–466

26. Elmer JW, Palmer TA, Babu SS, Specht ED (2005) Low temperature relaxation of residual stress in Ti–6Al–4V. Scr Mater 52:1051–1056
27. Banerjee S, Mukhopadhyay P (2007) Phase transformations: examples from titanium and zirconium alloys, 1st edn. Elsevier, Oxford
28. Amadori S, Bonetti E, Pasquini L, Deodati P, Donnini R, Montanari R, Testani C (2009) Low temperature anelasticity in Ti6Al4V alloy and Ti6Al4V–SiCf composite. Mater Sci Eng A 521–522:340–342
29. Shigematsu M, Kitajima M, Ogawa K, Higo T, Hotokebuchi T (2005) Effects of hydrogen peroxide solutions on artificial hip joint implants. J Arthroplasty 20:639–646
30. Dunand DC, Zwigl P (2001) Hydrogen-induced internal-stress plasticity in titanium. Metall Mater Trans 32A:841–843
31. Lindsey C, Deviren V, Xu Z, Yeh RF, Puttlitz CM (2006) The effects of rod contouring on spinal construct fatigue strength. Spine (Phila Pa 1976) 31(15):1680–1687
32. Martola M, Lindqvist C, Hanninen H, Al-Sukhun J (2007) Fracture of titanium plates used for mandibular reconstruction following ablative tumor surgery. J Biomed Mater Res B Appl Biomater 80(2):345–352

Chapter 4
Biomechanics of Blood Vessels: Structure, Mechanics, and Adaptation

Takeo Matsumoto, Shukei Sugita, and Toshiyuki Yaguchi

Abstract Basics and recent advances in blood vessel wall biomechanics are overviewed. The structure of blood vessel walls is first introduced with special reference to heterogeneity in the mechanical properties of artery walls at a microscopic level. Then basic characteristics of the mechanical properties of blood vessel walls are explained from the viewpoints of mechanical parameters used in clinical investigations, elastic and viscoelastic analysis, and effects of smooth muscle contraction. As examples of mechanical analysis of blood vessel walls, stress and strain analyses of artery walls as thin- and thick-walled cylinders, analyses considering residual stress and microscopic heterogeneity, are introduced. One of the most important topics in the blood vessel mechanics, mechanical responses and adaptations of blood vessel walls, is then discussed from the viewpoints of long- and short-term responses of artery walls to increases in blood pressure or flow. And finally, the importance of studying microscopic mechanical environment to elucidate these mechanical adaptations is pointed out.

Keywords Artery • Vein • Biomechanics • Smooth muscle • Endothelium • Elastin • Collagen • Intima • Media • Adventitia

4.1 Structure and Function of Blood Vessel

The blood vessels are the network of tubing that transports blood throughout the body. Blood delivers substances necessary to the body such as oxygen and nutrients to the tissues and removes carbon dioxide and metabolic waste products from the tissues. There are three major types of blood vessels: the arteries carrying the blood away from the heart, the capillaries that enable the exchange of chemicals and water

T. Matsumoto (✉) • S. Sugita • T. Yaguchi
Department of Mechanical Engineering, Nagoya Institute of Technology,
Gokiso-cho, Showa-ku, Nagoya 466-8555, Japan
e-mail: takeo@nitech.ac.jp

M. Niinomi et al. (eds.), *Advances in Metallic Biomaterials*, Springer Series
in Biomaterials Science and Engineering 3, DOI 10.1007/978-3-662-46836-4_4

between the tissues and the blood, and the veins carrying blood from the capillaries back toward the heart. Among them, mechanical properties of arteries larger than a few millimeters in diameter have been studied extensively for their ease in handling and their importance in clinical medicine. In this chapter, we mainly focus on larger arteries.

The arteries and veins have three layers: tunica intima, tunica media, and tunica adventitia, or simply intima, media, and adventitia. The intima is the thinnest layer with the thickness around 10 μm. It is a single layer of endothelial cells aligning in the direction of blood flow on a thin layer of elastic tissue called the internal elastic lamina. It plays important roles relating to vascular diseases, especially to atherosclerosis, including prevention of thrombus formation, control of permeability to various substances, and blood flow sensing and control of vascular diameter (see Sects. 4.4.1 and 4.4.3 for details). The media is the thickest layer in the arteries and plays major roles in their mechanical properties. It consists of circularly arranged vascular smooth muscle cells, elastic fiber (elastin), connective tissue (mainly collagen), and polysaccharide substances. Smooth muscle cells are a type of muscle cells, and they contract and relax in response to chemical and mechanical stimuli to control the caliber of the vessel. Elastin is one of the most elastic materials in biological tissues. Collagen is the main structural protein of the connective tissues and is stiff compared to elastin as shown in the next paragraph. There are two types of arteries, elastic and muscular. The elastic arteries are large arteries close to the heart such as the aorta and the carotid arteries and are abundant in elastin. Their media is made of concentric layers whose unit is called a lamellar unit [1], a pair of elastic lamina mainly made of elastin and a smooth muscle-rich layer (Fig. 4.1). The muscular arteries are less abundant in elastin, and their media has a rather homogeneous structure (Fig. 4.2). The media and the adventitia are separated by another thin elastic tissue called external elastic lamina. The adventitia is the thickest layer in the veins. It is entirely made of collagen fibers and fibroblasts that synthesize collagen. Capillaries consist of little more than a layer of endothelium and occasional connective tissue.

From the viewpoint of biomaterials, blood vessel wall can be viewed as a composite material consisting of components with various mechanical properties such as elastin, collagen, and smooth muscle cells. Elastin is highly elastic material with Young's modulus of ~500 kPa [2–4]. It remains elastic at least until its length is doubled (Fig. 4.3). Compared to elastin, collagen is highly stiff material with Young's modulus of ~1 GPa (Fig. 4.4) [5, 6]. Although collagen fibers can bear high stress in the body, they are less deformable and become fractured at relatively low strain (less than 10 %). In case of artery wall, they align obliquely to stretch direction and are corrugated in a physiological state. Such oblique alignment and corrugation allow the artery walls large deformation (~100 %) in the physiological condition as well as their strain-hardening properties (see Sect. 4.2.1.1 for details). In contrast to elastin and collagen that behave mostly linearly elastic materials, smooth muscle cells are highly viscoelastic. Their mechanical properties change drastically depending on their contractile state. Their Young's modulus ranges from 10 kPa under relaxation to 100 kPa under contraction (Fig. 4.5) [7]. Smooth muscle cells

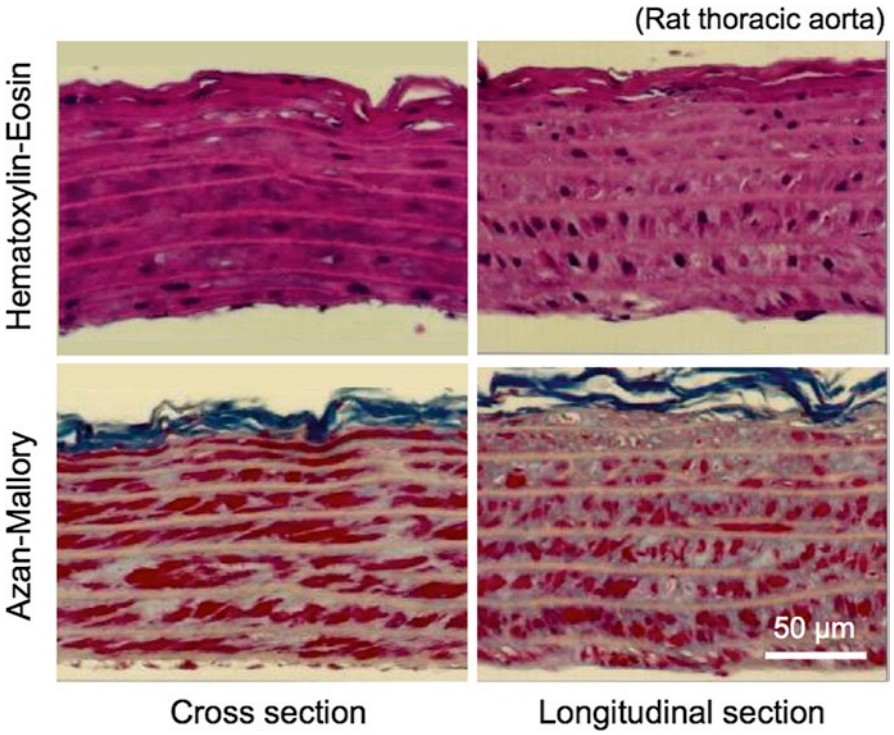

Fig. 4.1 Histological sections of an elastic artery fixed in a physiological condition, stained with hematoxylin-eosin (nucleus, *purple*) and Azan-Mallory (smooth muscle, *red*; collagen, *blue*; unstained, elastin)

also have a unique characteristic, *i.e.*, mechanical adaptation. They change their dimensions and mechanical properties in response to mechanical stimulation they receive to maintain homeostasis of intramural mechanical environment (see Sect. 4.4.2 for details).

The mechanical properties of the vascular wall are determined by relative amount of these components, their alignment, and their slackness, etc. The aorta, an elastic artery, is abundant in elastin and the largest artery. Due to its abundance in elastin and its large size, the aorta is the most compliant vessel in the vascular system. It expands in response to blood pressure increase in systole to store a part of the blood pumped out from the heart and thus helps to decrease the systolic pressure, *i.e.*, the load of the heart. In diastole, it shrinks in response to pressure decrease to maintain distal blood flow just like an air-pressurized reservoir in a water gun (Windkessel effect). As one goes from proximal to distal side, the diameter and wall thickness of the artery decrease monotonously, and the relative amount of smooth muscle cells and the ratio of collagen to elastin increase. Because collagen is much stiffer than elastin, distal arteries are generally stiffer than the proximal arteries. The collagen to elastin ratio continues to increase in the veins. The veins have larger diameter and

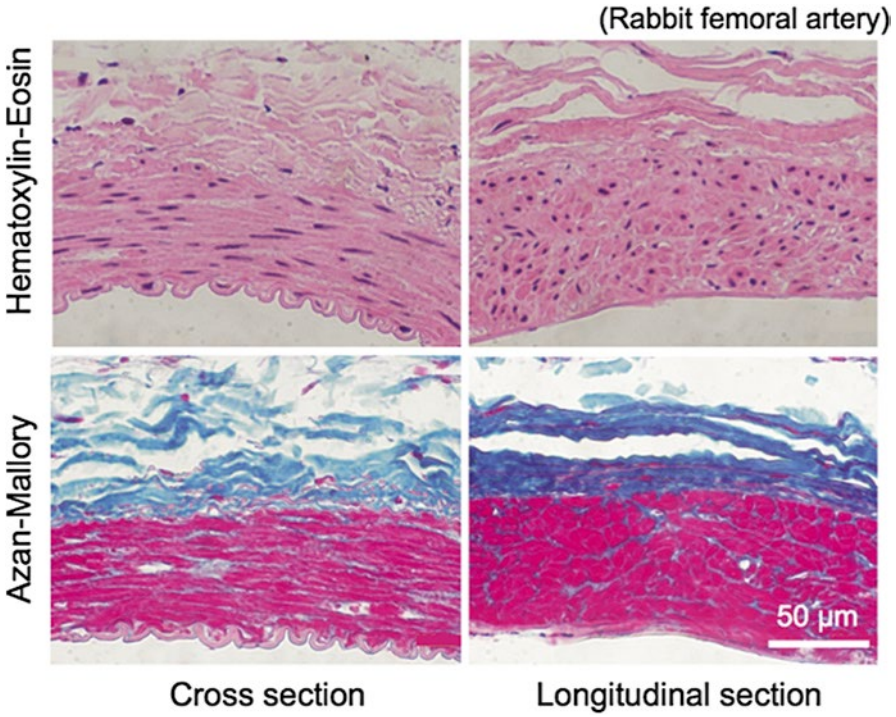

Fig. 4.2 Histological sections of a muscular artery fixed in a physiological condition, stained with hematoxylin-eosin (nucleus, *purple*) and Azan-Mallory (smooth muscle, *red*; collagen, *blue*; unstained, elastin)

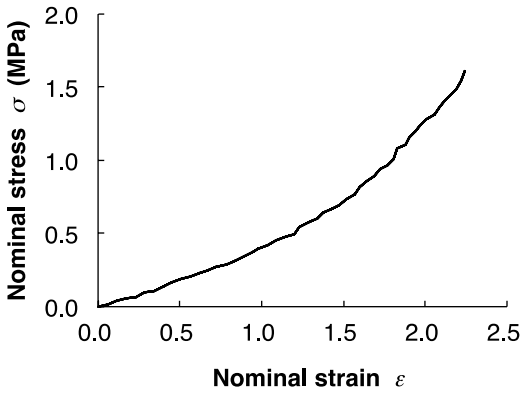

Fig. 4.3 Stress-strain relationship of an elastic lamina (porcine thoracic aorta). Nominal stress-strain curve is almost linear until nominal strain exceeds 1.0, *i.e.*, until the length is doubled

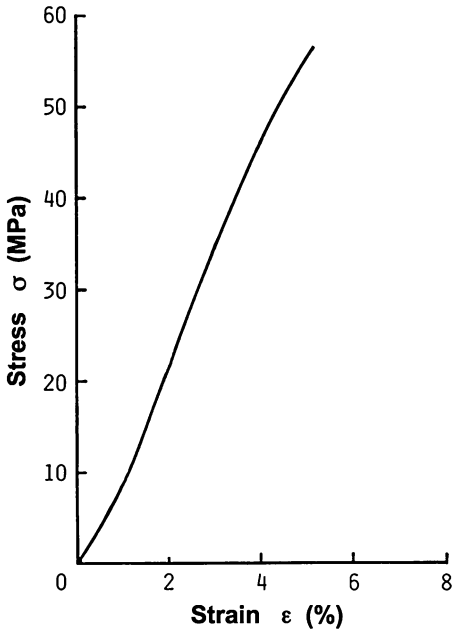

Fig. 4.4 Stress-strain relationship of a rabbit patellar tendon (Redrawn from [6])

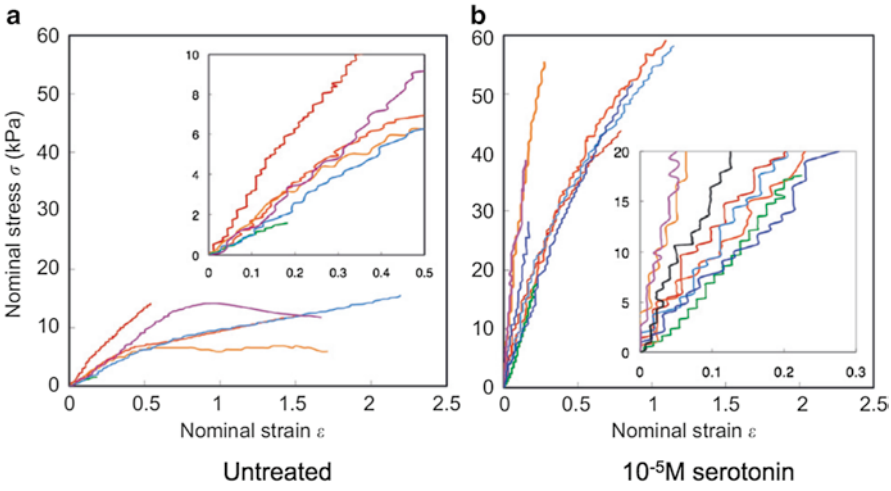

Fig. 4.5 Tension-elongation relationship of vascular smooth muscle cells obtained from rabbit thoracic aorta. Smooth muscle contraction was induced with serotonin (Reprinted from Ref. [7], Copyright 2012, with permission from Elsevier)

thinner wall compared to arteries at the same anatomical position. Because they occupy about 3/4 of the total vessel volume and show large deformation in the physiological condition, the veins serve as a reservoir of the blood that controls the circulating blood volume and called a capacitance vessel. Veins in the extremities have valves to prevent regurgitation. Blood vessel network from the arterioles to venules via capillaries is called a microcirculatory system. The microcirculatory system is called a resistance vessel for it is the major part of resistance in the circulatory system. The arterioles with abundant smooth muscle cells are responsible for the maintenance of the blood pressure by changing their diameter by smooth muscle contraction and relaxation.

4.2 Mechanics of Blood Vessel

4.2.1 Basic Characteristics

Blood vessel walls are exposed to various mechanical stresses in vivo. In case of artery wall, its intraluminal surface is subjected to mean pressure of ~13.3 kPa (100 mmHg) and pulse pressure of ~5.3 kPa (40 mmHg). Arterial walls are stretched by 30–50 % in the longitudinal direction, which can be confirmed by arterial contraction in the longitudinal direction after excision. Wall shear stress of a few Pa is applied to the intraluminal surface due to the blood flow, and wall shear stress oscillates during the cardiac cycle. Due to these mechanical stresses, the artery diameter changes by ~10 % and its length changes by a few % during the cardiac cycle. Twisting of the vessel is very small [8].

In case of the veins, quasistatic pressure of ~1.3 kPa is applied to the walls. The intraluminal pressure sometimes has a negative value due to the pressure difference between veins and the heart and/or due to other physical forces from the surrounding tissues. Under these circumstances, outer radius of the veins can change by several tens of percent.

From the mechanical point of view, keywords expressing basic characteristics of the blood vessel walls are as follows: (1) large deformation and nonlinear mechanical properties, (2) incompressibility, (3) viscoelasticity, and (4) anisotropy. Details of each characteristic are described in the following sections.

4.2.1.1 Large Deformation and Nonlinear Mechanical Properties

The vascular walls undergo large deformation, and its physiological strain ranges from several tens of percent to 100 %. Mechanical properties such as elasticity depend on the magnitude of pressure applied to the vessel walls significantly. Arterial wall shows remarkable strain-hardening properties. It is quite deformable in subphysiological pressure range, while in supraphysiological pressure range, it becomes less deformable sharply as pressure increases. This means that we need to

Table 4.1 Pressure dependence of incremental elastic modulus of the rabbit thoracic aortas

Pressure (mmHg)	Incremental elastic modulus (kPa)
20	200 ± 20
50	200 ± 10
100	430 ± 30
125	1,550 ± 150
150	4,480 ± 360
180	8,200 ± 720

Mean ± SEM, $n = 16$

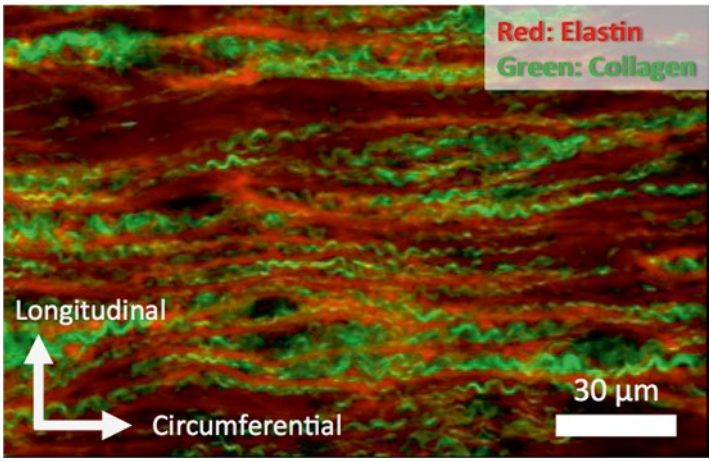

Fig. 4.6 Corrugation of collagen fibers in a rabbit thoracic aorta pressure-fixed at 80 mmHg

pay attention to strain or pressure levels when comparing elastic moduli between blood vessels. For example, in rabbit thoracic aortas, when pressure increases from 2.7 kPa (20 mmHg) to 23.9 kPa (180 mmHg), their circumferential stretch ratio increases from 1.1 to 2.0, and an incremental elastic modulus E_{inc} (see Sect. 4.2.2 for details) increases from 200 kPa to 8,200 kPa by 40 times (Table 4.1).

Nonlinearity of the stress-strain relationship of blood vessels can be explained by the degree of undulation and variation of alignment of collagen fibers in the vessel walls. Both elastic and collagen fibers in the fiber direction have linear mechanical properties. As described in Sect. 4.1, Young's modulus of elastin is ~0.5 MPa and that of collagen fibers is ~1 GPa. In low-pressure region, collagen fibers remain wavy (Fig. 4.6) and align obliquely to the circumferential direction [9], while elastic fibers are straight, and thus, the incremental elastic modulus is low (Table 4.1). In high-pressure region, stiff collagen fibers become straight and begin to be stretched [10], resulting in the strain hardening of the blood vessel wall. Since collagen fibers are not stretched in low-pressure region, breaking strain of the aorta (~100 %) is in

the range between breaking strain of elastin (~200 %) [2] and that of collagen (~10 %) [5]. The strain-hardening property of the blood vessel is very important for the arteries to prevent vessel rupture (see Sect. 4.3.1 for details).

4.2.1.2 Incompressibility

Generally speaking, soft biological tissues are mainly composed of water. For example, water content of canine arterial walls is around 70 % of total volume [11]. Because water is incompressible, *i.e.*, does not change its volume during deformation, the artery wall is also considered to be incompressible. Carew et al [12] measured the volumetric change of dog thoracic aortas during inflation-extension test. They found that volume strain was only 0.06 % when 40 and 70 % of strain were imposed in longitudinal and circumferential direction, respectively.

4.2.1.3 Viscoelasticity

Viscoelastic materials exhibit not only elastic characteristics but also viscous when undergoing deformation. Elastic materials deform when stretched and quickly return to their original state once the stress is removed. Viscous materials deform linearly with time when a stress is applied. Viscoelastic materials have elements of both of these properties and, as such, exhibit time-dependent strain. The effect of viscoelasticity on mechanical properties of large blood vessels is relatively small. Change in the stiffness due to change in strain rate could be several 10 % at most. Therefore, large vessels are often treated as elastic tubes. However, it should be noted that effects of viscoelasticity could be much larger and cannot be ignored in small arteries. For further discussion, see Sect. 4.2.3.

4.2.1.4 Anisotropy

Major constituents of blood vessels such as collagen, elastin, and smooth muscle cells predominantly orient in the circumferential-longitudinal plane. Since mechanical properties of arteries depend on the properties of the individual constituents and their orientations, mechanical properties in the radial direction are different from the circumferential and longitudinal directions. Even in the circumferential-longitudinal plane, anisotropy has been observed. Uniaxial tensile test has shown that the tensile strength of the aortas is larger in the circumferential direction than in the longitudinal direction [13]. In a bulge test, in which a platelike specimen is sandwiched with two plates having a hole at their center and pressurized from one side, porcine thoracic aortas initiated cracks in the circumferential direction [14]. Pressure-imposed tests for tubular specimens have indicated that the difference in an elastic modulus is at most twofolds for large arteries [15]. However, because

most of the blood vessels are tethered in the longitudinal direction and their compliance is mostly determined by the deformability in the circumferential direction, the mechanical properties in the circumferential direction, *i.e.*, pressure-diameter relationship, which is important from a practical standpoint.

4.2.2 *Parameters Expressing Mechanical Properties of Blood Vessel*

To obtain detailed mechanical properties of blood vessels, we excised them from bodies and loaded them with a wide range of pressure to obtain pressure-diameter relationship with an apparatus shown in Fig. 4.7, for example. A quasistatic and dynamic pressure-diameter curve of canine common carotid artery is shown in Fig. 4.8 [16]. The pressure-diameter curve shows characteristics of the nonlinear and downward-convex relationship as described in Sect. 4.2.1. These characteristics are seen in both arteries and veins. It also has a hysteresis as shown in the difference between the loading and unloading limbs. The hysteresis is derived mainly from viscoelasticity of smooth muscle cells. The area of the hysteresis loop depends on the relative volume and the activity of smooth muscle cells.

Stiffness of blood vessels can be measured from the pressure-diameter curve. It is affected by not only Young's modulus but also the geometry of the vessels such as radius and wall thickness. For example, for two cylindrical tubes made of the same material (*i.e.*, with the same Young's modulus) with the same outer radius, one

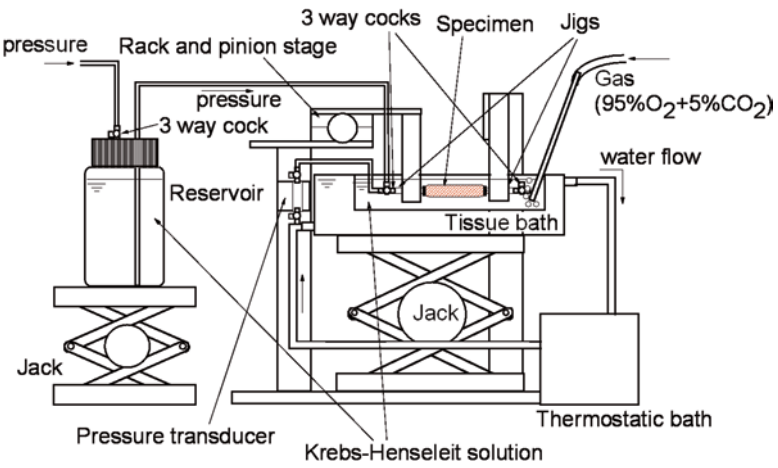

Fig. 4.7 An example of experimental setup for the measurement of pressure-diameter relationship of blood vessels. To mimic physiological condition, specimen was immersed in an aerated Krebs-Henseleit solution at 37 °C and pressurized pneumatically while measuring its outer diameter with a video camera and a video dimension analyzer (not shown)

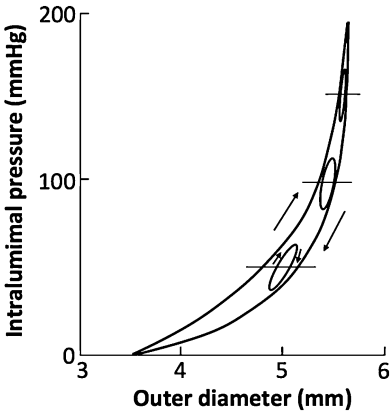

Fig. 4.8 Pressure-diameter relationship of a canine common carotid artery. The large nonlinear hysteresis loop is obtained in a quasistatic condition, *i.e.*, by changing the intraluminal pressure at the rate of ~1 mmHg/s. Small oval loops are obtained in a dynamic condition, *i.e.*, by changing intraluminal pressure sinusoidally at ~1 Hz (Reprinted from Ref. [16], with permission from JSME)

with thicker wall is stiffer. Similarly, two tubes made of the same material with the same wall thickness, one with smaller radius is stiffer. Thus, we need to evaluate stiffness and elastic modulus separately.

Although the pressure-diameter curves are highly nonlinear in a wide range of pressure, each of them can be regarded as linear if you divide them into small sections. Then elastic modulus can be defined using a linear equation. When pressure increases from P_i by ΔP_i and outer diameter from D_o by ΔD_o, elastic modulus and stiffness can be calculated from P_i, D_o, and $\Delta D_o/\Delta P_i$. In the following part of this section, some of the representative parameters expressing mechanical properties of the blood vessel are introduced.

4.2.2.1 Incremental Elastic Modulus E_{inc}

The incremental elastic modulus, E_{inc}, which corresponds to Young's modulus of blood vessel wall can be expressed by the following equation [17]:

$$E_{\mathrm{inc}} = 1.5 \frac{\Delta P_{\mathrm{i}}}{\Delta D_{\mathrm{o}}} \frac{D_{\mathrm{o}} \cdot D_{\mathrm{i}}^2}{D_{\mathrm{o}}^2 - D_{\mathrm{i}}^2} \tag{4.1}$$

To calculate the incremental elastic modulus, the inner diameter D_i or wall thickness, which is difficult to measure in clinical practices, is needed. This parameter is used mainly in experimental studies for excised specimens, but not for clinical medicine. Usually inner diameter D_i is calculated from inner and outer diameters d_i and d_o, respectively, at no-load state under the assumption of incompressibility of vessel wall as follows:

$$\pi\left(D_{\mathrm{o}}^2 - D_{\mathrm{i}}^2\right)\lambda_z / 4 = \pi\left(d_{\mathrm{o}}^2 - d_{\mathrm{i}}^2\right) / 4, \tag{4.2}$$

where λ_z is a longitudinal stretch ratio, which is defined as the ratio of the in vivo length of a vessel segment L to its length at no-load state l, *i.e.*, $\lambda_z = L/l$.

4.2.2.2 Pressure Strain Elastic Modulus E_p

The pressure strain elastic modulus, E_p, presenting stiffness of blood vessel can be expressed by the following equation [18]:

$$E_p = \Delta P_i / \left(\Delta D_o / D_o \right) \tag{4.3}$$

Since it can be easily calculated from obtained data in clinical practice, it has been used widely not only in experimental studies but also in clinical medicine.

4.2.2.3 Stiffness Parameter β

The stiffness parameter β can be expressed by the following equation:

$$\ln\left(P / P_s \right) = \beta \left(D_o / D_s - 1 \right) \tag{4.4}$$

where P_s and D_s are pressure and outer diameter, respectively, at a reference state in vivo [19]. Normally reference state is taken as $P_s = 100$ mmHg (13.3 kPa). It is well known that pressure-diameter curve of an artery is well fitted by an exponential function. This parameter is obtained based on this knowledge, and the nonlinearity of blood vessels can be eliminated at least partially in the physiological range, *i.e.*, it is relatively insensitive to the variation of blood pressure. And also, this parameter does not require blood vessel wall thickness that is difficult to measure in clinical practices. Thus, the stiffness parameter has been widely used in clinical medicine.

Typical values of these parameters are summarized in Table 4.2 for various species and anatomical sites.

4.2.3 Viscoelastic Properties

It is important to know dynamic mechanical properties of arteries because the arteries in vivo are cyclically stretched during the cardiac cycle. Parameters expressing dynamic mechanical properties can be obtained by measuring the amplitude of the dynamic change in the outer diameter ΔD_o and the amplitude of pressure waveform ΔP_i at various frequencies of the pressure waveform to calculate the parameters shown in Sect. 4.2.2. To investigate the viscoelasticity of arteries in detail, the

Table 4.2 Normal values for parameters expressing elastic properties of blood vessels of various species and anatomical sites [16]

Blood vessel	E_{inc}[a] (MPa)	E_p[b] (MPa)	β
Thoracic aorta	0.5 (D), 0.9 (R)	0.07 (H)	2.5 (R)
Abdominal aorta	1.0 (D), 2.0 (R)	0.10 (H)	5.6 (H)
Common carotid artery	0.9 (D), 1.5 (R)	0.08 (H)	5.3 (H)
Femoral artery	1.0 (D), 4.0 (R)	0.49 (H)	19.8 (H)
Pulmonary artery	0.6 (D)		
Coronary artery	1.7 (D)		29.8 (R)
Arteriole	0.12 (CM)		
Capillary	0.37 (CM)		
Venule	0.39 (CM)		
Saphenous vein	0.03 (D)		
Jugular vein	1.5 (D)		
Inferior vena cava	0.07 (D)		

D dog, *R* rabbit, *CM* cat mesentery, *H* human

[a]Incremental elastic modulus at intraluminal pressure of 100–125 mmHg (13.3–16.6 kPa, from thoracic aorta to capillary) or 10 cm H_2O (1 kPa, veins)

[b]At rest under normal blood pressure

dynamic elastic modulus E_{dyn} and the loss elastic modulus $\eta\omega$ need to be calculated considering phase lag $\Delta\phi$ between diameter and pressure waveform as follows:

$$E_{dyn} = E_{inc} \cdot \cos \Delta\phi \tag{4.5}$$

$$\eta\omega = E_{inc} \cdot \sin \Delta\phi, \tag{4.6}$$

where E_{inc} is the incremental elastic modulus (see Sect. 4.2.2) obtained from $\Delta D_o/\Delta P_i$, η viscosity modulus and ω angular velocity [20]. Figure 4.9 shows an example of dynamic elastic modulus calculated from Eq. 4.5 and normalized with the incremental elastic modulus obtained at static condition. In dynamic conditions, the elastic modulus increases generally by several 10 % from that in a static condition. However, frequency dependency is very low as shown in this figure.

4.2.4 Effects of Smooth Muscle Contraction

Mechanical properties of blood vessels change drastically in response to contractile state of the smooth muscle cells that reside in the media [21]. Smooth muscle cells are a type of muscle cells that exhibit contraction and relaxation in response to various chemical and mechanical stimuli to regulate the diameter of blood vessels. Figure 4.10 shows typical pressure-diameter curves of a canine common carotid artery in which smooth muscle contraction was induced with norepinephrine (NE)

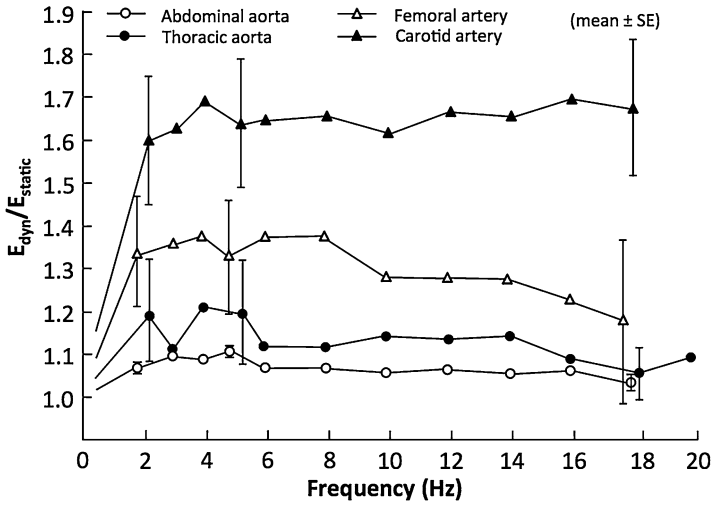

Fig. 4.9 Frequency dependency of dynamic elastic modulus of various arteries obtained from dogs (Redrawn from [20])

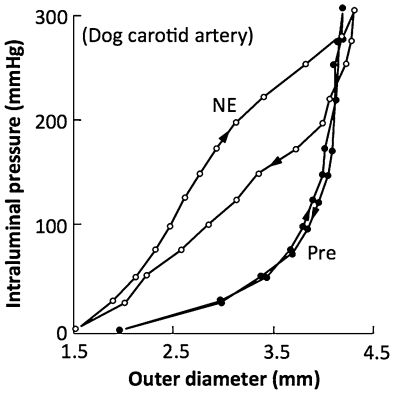

Fig. 4.10 Change in mechanical properties of an artery in response to smooth muscle contraction. Pre, before smooth muscle contraction; NE, contraction with 10^{-5} M norepinephrine (Redrawn from [22])

[22]. When norepinephrine is applied, the curve shifts to the left, its shape changes from downward-convex to upward-convex, and the hysteresis loop area increases significantly. External diameters, however, are equal for relaxed and contracted arteries at 300 mmHg. Effects of smooth muscle contraction on elastic properties are complex. Generally speaking, stiffness increases in the region with relatively smaller diameter while it decreases in the larger diameter region. And also, the magnitude of the effects of smooth muscle contraction depends on the relative amount of smooth muscle. The amount of contraction of the diameter in response to smooth muscle activation is 10 % at most for the aorta, while smooth muscle contraction almost occludes the lumen of muscular arteries such as digital arteries.

4.3 Mechanical Analysis of Blood Vessel Walls

Analysis of blood vessel deformation shown in the previous section is important to know the effects of the mechanical properties of the blood vessel wall on the intramural blood flow and pressure. However, we need to know intramural distributions of stress and strain to understand the blood vessel mechanics in detail and to study the mechanism of the mechanical adaptation in the blood vessel wall that will be shown in the next section. In this section, the outline of the various mechanical analyses [23, 24] is reviewed. For the ease of analysis, blood vessels are assumed to be a cylinder with a circular cross section, and the wall materials are assumed to be homogeneous and incompressible. Because most of the arteries are tethered by surrounding tissues in the longitudinal direction and their deformation in this direction is much smaller than the deformation in the circumferential direction, we concentrate on the mechanical analysis in the circumferential direction in this section.

4.3.1 Analysis of a Thin-Walled Cylinder

In reality, blood vessel has a finite wall thickness, and the stress and strain in the inner wall are different from that in the outer wall as shown in the next section. However, if the wall is very thin as in the case of the veins, the difference between the inner and outer walls may be negligible, and analysis on a representative or mean value will be enough. Assumption of thin-walled cylinder can be used not only in veins but also for the arteries with relatively thick wall as long as what you want to know is the mean values of stress and strain and not their radial distributions in the wall.

Mean value of the circumferential stress σ_θ is obtained precisely from the dimensions of blood vessel wall, inner radius R_i and wall thickness H, and intraluminal pressure P_i as follows (Law of Laplace):

$$\sigma_\theta = P_\mathrm{i} R_\mathrm{i} / H . \tag{4.7}$$

Mean value of circumferential strain can be expressed as extension ratio λ_θ:

$$\lambda_\theta = R_\mathrm{m} / r_\mathrm{m} = \left(R_\mathrm{o} + R_\mathrm{i}\right) / \left(r_\mathrm{o} + r_\mathrm{i}\right), \tag{4.8}$$

where subscript m indicates mean value, i inner wall, and o outer wall. Lowercase letters indicate reference state, *i.e.*, no-load state, and upper case letters physiological condition. If you assume that the blood vessel wall deforms maintaining its volume, *i.e.*, the wall is incompressible, then the following equation can be obtained:

$$2\pi r_\mathrm{m} h = 2\pi R_\mathrm{m} H \lambda_\mathrm{z} \tag{4.9}$$

and thus

$$\lambda_\theta = R_\mathrm{m}/r_\mathrm{m} = h/\left(H\lambda_\mathrm{z}\right). \tag{4.10}$$

As shown in Eq. 4.7, the circumferential stress is proportional not only to P_i but also R_i and inversely proportional to H. If the vessel is pressurized, the increase in σ_θ is much larger than that in P_i because of the increase in R_i and simultaneous decrease in H due to pressure increase. Thus, if the material properties of the wall are linear, the increase in P_i cannot be compensated by the increase in σ_θ over a certain vessel diameter. If this happens in an artery, it will be inflated until burst over a critical pressure. To prevent such a catastrophe, nonlinear (strain-hardening) mechanical properties of the artery are crucial.

4.3.2 Analysis of a Thick-Walled Cylinder

Generally speaking, wall thickness of an artery corresponds to 5–10 % of its radius, and the difference in the mechanical environment between the inner and outer walls cannot be neglected. In such cases, artery wall needs to be analyzed as a thick-walled cylinder to obtain stress and strain distribution in the direction of wall thickness, *i.e.*, radial direction. Strain distribution can be obtained by assuming that the artery wall is consisted of thin-walled cylinder. If it is assumed that a cylinder having the outer radius r_o, inner radius r_i, and length l deforms to a cylinder having the outer radius R_o, inner radius R_i, and length $L = l \cdot \lambda_\mathrm{z}$ and that the radius r of a thin-walled cylinder in the unloaded wall becomes R in the deformed state, R can be derived as follows assuming incompressibility:

$$R = \sqrt{R_\mathrm{o}^2 - \left(r_\mathrm{o}^2 - r^2\right)/\lambda_\mathrm{z}}. \tag{4.11}$$

Circumferential stretch ratio of this cylinder is thus defined as

$$\lambda_\theta(r) = \frac{2\pi R}{2\pi r} = \frac{R}{r} = \frac{\sqrt{R_\mathrm{o}^2 - \left(r_\mathrm{o}^2 - r^2\right)/\lambda_\mathrm{z}}}{r}. \tag{4.12}$$

Stress distribution can be obtained assuming that unloaded thick-walled cylinder is in a stress-free state. To obtain stress distribution, we need to know stress-strain relationship of each thin-walled cylinder. The stress-strain relationships can be obtained by assuming a strain energy density function [25]. Pressure-diameter relationship of the artery can be derived by integrating the stress-strain relationships of the thin-walled cylinders. Thus, the strain energy density function can be determined by fitting pressure-diameter curve derived from that function to actual pressure-diameter curve obtained in an experiment (see the literature [25] for details).

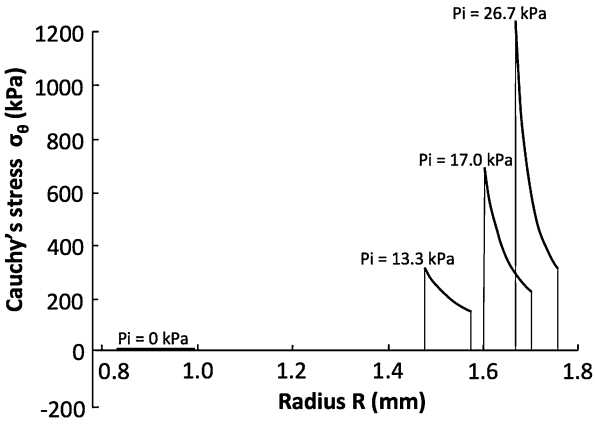

Fig. 4.11 Example of stress analysis of a rat thoracic aorta as a thick-walled cylinder (Reprinted from Ref. [25], with permission from ASME)

An example of such stress analysis is shown in Fig. 4.11. High stress concentration appeared in the inner wall with the increase in blood pressure. Generally speaking, when a thick-walled cylinder expands, an increase in the circumferential strain is larger in the inner wall than in the outer. Due to nonlinearity of the stress-strain relationship of the artery, stress increase is exaggerated in high strain region. Thus, sharp stress concentration occurs in the inner wall of the artery.

4.3.3 Consideration of Residual Stress

Does the sharp stress concentration shown in Fig. 4.11 really appear in the artery wall? It looks unnatural to have such stress concentration in a tissue if the rationality and optimality of biological system are considered. One of the reasons for such unnaturalness is that we assume that unloaded thick-walled cylinder is in a stress-free state. Actually, this assumption is not valid in many cases. Figure 4.12 shows an example of shape change of a ringlike specimen obtained from a porcine thoracic aorta upon cutting of the ring. The ringlike specimen sprang open to form an arc upon radial cutting, indicating that there existed compressive residual stress in the inner wall and tensile in the outer before radial cutting. Such residual stress attenuates stress concentration in the inner wall of a thick-walled cylinder (Fig. 4.13). Thus, we need to distinguish the no-load state and the stress-free state.

Figure 4.14 shows the configurations of a vascular wall in three states, stress-free, no-load, and loaded states. The vascular wall was assumed to be thick-walled cylinder in the loaded and no-load states. Inner and outer radii in the no-load state were measured in a ringlike specimen sliced out from a tubular

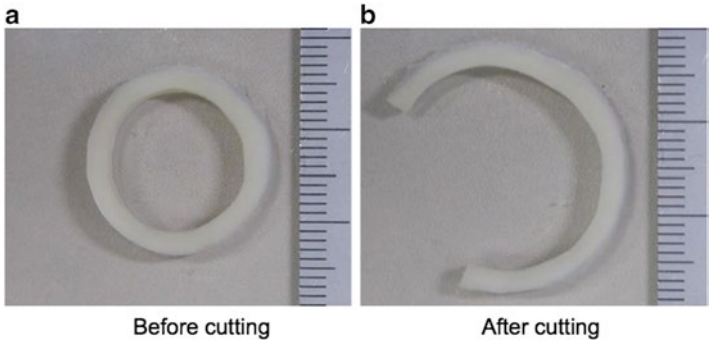

Fig. 4.12 Shape change of a porcine thoracic aorta following radial cutting

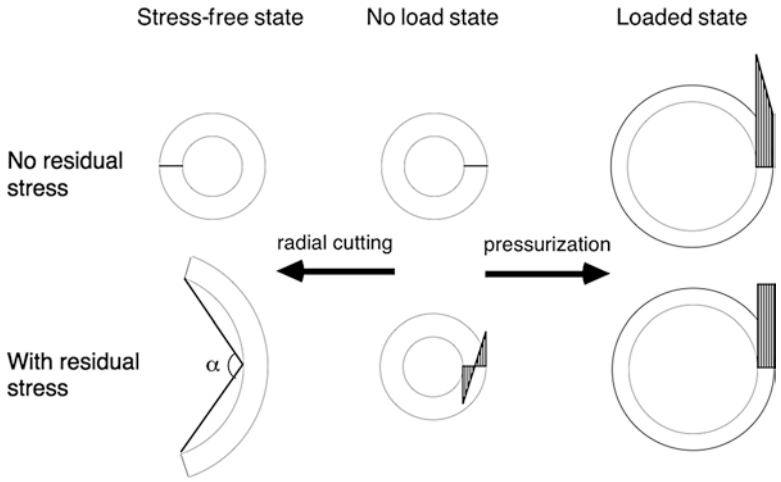

Fig. 4.13 Physiological significance of residual stress in the blood vessel wall. If there is no residual stress in the no-load state, high stress concentration will appear in the inner wall. If stress distribution is uniform in the radial direction, residual stress appears in the no-load state, and this causes opening of the ring following radial cutting

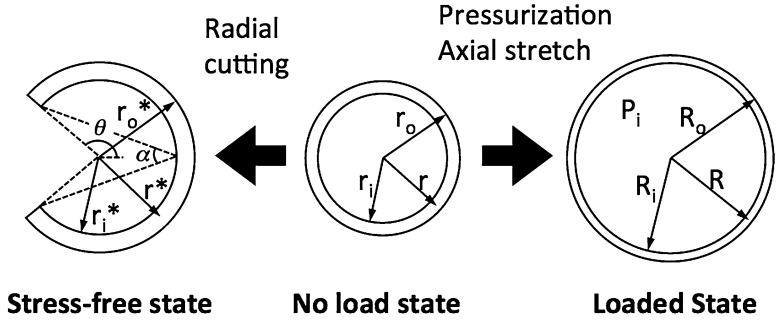

Fig. 4.14 Coordinate system used for strain analysis of a thick-walled cylinder

specimen that had been used to obtain pressure-diameter relationship of the blood vessel. The outer radius in the loaded state was obtained from the pressure-diameter curve, and the inner radius is obtained in Eq. 4.11 in Sect. 4.3.2. The ringlike specimen was then cut radially. If we assume that the aorta is a homogeneous and cylindrically orthotropic tube, the opened-up ring forms an arc of constant curvature and thickness. An opening angle, α, *i.e.*, the angle subtended by the two radii drawn from the midpoint of the arc of the inner wall of the vessel to the inner tips of the arc [26], was measured in the opened-up ring. The effective external radius of the opened-up ring specimen, r_o^*, was then calculated assuming that the mean circumference and the cross-sectional area of the specimen do not change by cutting as follows:

$$r_o^* = \frac{1}{2}\left\{\frac{\pi}{\theta}\left(r_o + r_i\right) + \left(r_o - r_i\right)\right\}, \tag{4.13}$$

where θ is one half of the central angle of the arc and is equal to the angle of circumference of the arc, *i.e.*, $\theta = \pi - \alpha$ [25].

Circumferential extension ratio at the radius R in a loaded wall is

$$\lambda_\theta(r) = \frac{\pi}{\theta}\frac{R}{r^*}, \tag{4.14}$$

where

$$r^* = \sqrt{r_o^{*2} - \frac{\pi\lambda_z}{\theta}\left(R_o^2 - R^2\right)} \quad (\theta > 0), \tag{4.15a}$$

$$= -\sqrt{r_o^{*2} - \frac{\pi\lambda_z}{\theta}\left(R_o^2 - R^2\right)} \quad (\theta < 0), \tag{4.15b}$$

or

$$\theta r^* = \frac{\pi}{2}\left(r_o + r_i\right) \quad (\theta = 0). \tag{4.15c}$$

An example of radial distributions of circumferential extension ratio is shown in Fig. 4.15. The distributions are obtained from pressure-diameter relationship and the opening angle of rat thoracic aortas in the literature [27]. High stretch ratio appeared in the inner wall as pressure increases when residual strain, *i.e.*, the opening angle, is not considered. Such intraluminal concentration of stretch ratio disappeared when the opening angle is considered. It has been suggested that distribution of circumferential stress is uniform in the radial direction [26–31].

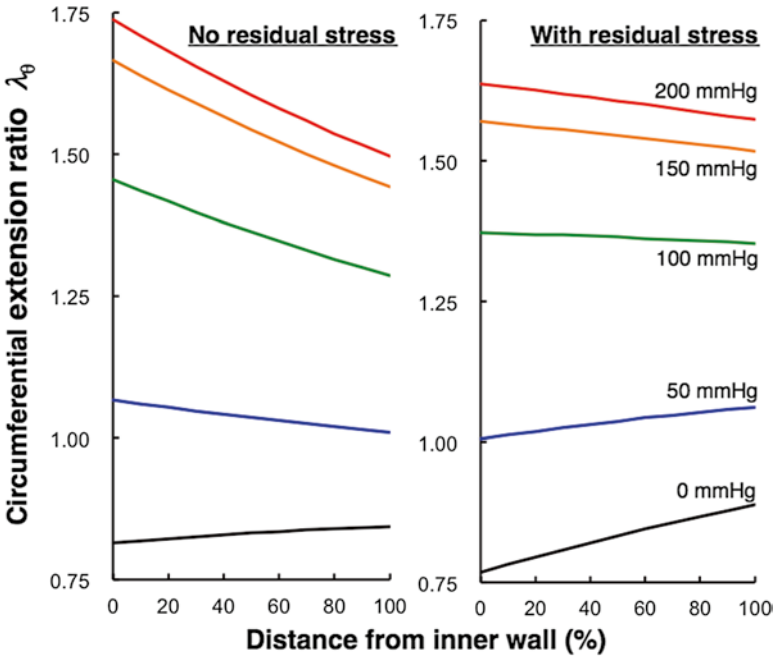

Fig. 4.15 Circumferential strain distribution in the wall of rat thoracic aorta

4.3.4 Consideration of Microscopic Heterogeneity

As stated in Sect. 4.1, blood vessel wall is heterogeneous at a microscopic level. It is composed of materials with various mechanical properties. Such heterogeneity may cause microscopic residual stress. For example, the wall of elastic arteries has layered structure composed of elastic lamina (EL) and a smooth muscle-rich layer (SML) as shown in Fig. 4.1. The EL is composed of elastin whose Young's modulus is ~500 kPa. The Young's modulus of the major components of the SML, smooth muscle cells, is 10–100 kPa. Thus, the EL is supposed to be much stiffer than the SML, and actually, it has been reported that the EL is 2.5 times stiffer than the SML [32]. If the stress-strain relationship is different between the EL and SML, residual stress of the two layers should be different (Fig. 4.16). If the circumferential stresses in the stiff and soft layers are the same in a physiological state, compressive residual stress should appear in the stiff layer and tensile in the soft in an unloaded wall. Such residual stress is not released by the radial cutting. It is well known that the elastic laminas are wavy in an unloaded wall (Fig. 4.17). In contrast, if you look at such a histological section carefully, you will notice that smooth muscle cells remain stretched. The ELs become straight when they are released from the surrounding tissues, indicating their corrugation is bucking caused by the compressive residual stress in the ELs. Stress analyses considering such microscopic residual stress are challenges for the future.

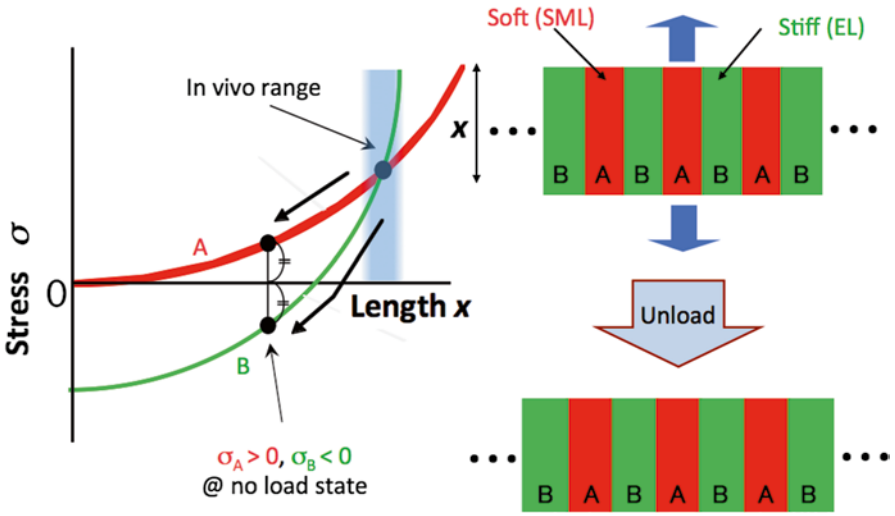

Fig. 4.16 Residual stress caused by mechanical heterogeneity

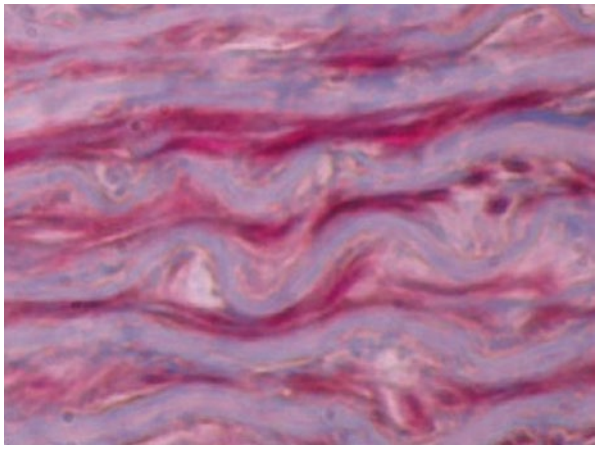

Fig. 4.17 Corrugated elastic lamina in the unloaded section of porcine thoracic aorta (Reprinted from Ref. [32], with permission from JSME)

4.4 Mechanical Response of Artery Walls

4.4.1 Long-Term Response to Flow Increase

Blood vessel dilates in response to increase in blood flow. This dilation has been reported to be an adaptive response of the blood vessel to maintain fluid shear stress applied to the intraluminal surface at a constant level [33, 34]. Kamiya and Togawa [33] studied the relationship between the blood flow and the radius of the

canine carotid arteries following an operation in which the carotid artery and the jugular vein were connected directly to increase the blood flow in the carotid arteries. Blood flow increased in 3 days after the operation, while the radius of the artery did not change. In contrast, arteries with higher blood flow had larger radius in 6–8 months after the operation. Interestingly, when blood flow in the arteries decreased for some reason, the radius of the artery also decreased. They then studied the relationship between the blood flow and wall shear rate. Wall shear rate was proportional to blood flow in 3 days after the operation because the radius did not change at this time point. In contrast, wall shear rate was maintained at the level before the operation in 6–8 months. This regulation was so powerful that the 3.5 times increase in flow could be compensated. This clearly indicates that the blood vessel wall maintains wall shear rate at a constant level. Wall shear stress is obtained by multiplying wall shear rate with viscosity. Since viscosity of the blood is almost the same among healthy subjects, it can be said that the diameter of blood vessel is regulated to maintain fluid shear stress at a constant level. This response does not occur when endothelial cells are removed from the lumen [35]. Detailed studies revealed that the dilation of the blood vessel in response to flow increase is driven by the endothelial cells. They sense fluid shear stress and secrete various substances causing blood vessel dilation and contraction to maintain the shear stress at a constant level [36].

4.4.2 Long-Term Response to Pressure Increase

Blood vessel wall thickens in response to hypertension. Figure 4.18 shows the relation between histology of blood vessel wall and systolic blood pressure in rats [25] in which Goldblatt hypertension was induced by placing a clip to the renal artery [37]. It is clear that the wall thickness increases markedly in response to blood pressure increase. This wall thickening is believed to be an adaptive response to maintain the circumferential wall stress at a constant level [37–40]. Relationships between the systolic blood pressure and circumferential stress at this pressure are shown in Fig. 4.19 for rats 2, 4, 8, and 16 weeks after the operation. There was no significant correlation between the blood pressure and the circumferential stress even at 2 weeks after the operation. Blood pressure of the rats continues to increase at 2 weeks after the operation and reaches a plateau at ~6 weeks, indicating that the wall thickening occurs very fast in response to blood pressure increase. In contrast, mechanical properties of the artery wall do not change as fast as the circumferential stress does. For example, incremental elastic modulus did not have a significant correlation with blood pressure at 16 weeks after the operation. However, the correlation was significant in 2, 4, and 8 weeks after the operation (Fig. 4.20). These results indicate that not only circumferential stress but also stiffness is restored [40, 41], but restoration of the elastic modulus takes longer time.

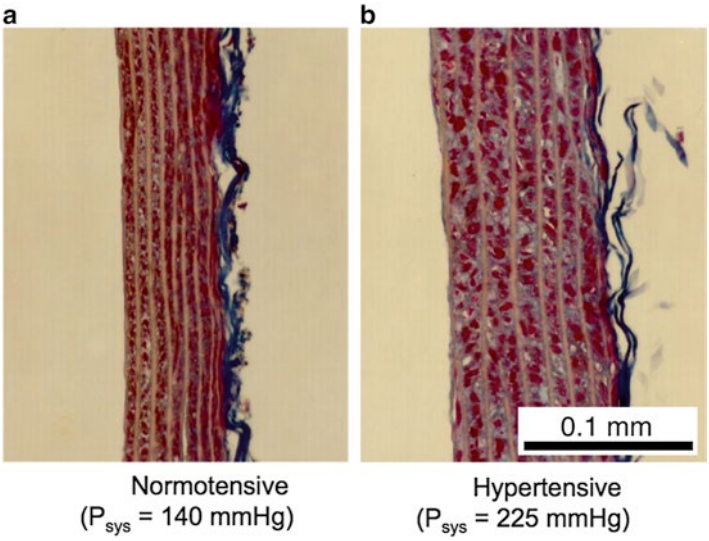

Fig. 4.18 Histological sections of normotensive (**a**) and hypertensive (**b**) rat thoracic aorta. Pressure-fixed in each in vivo condition and stained with Azan-Mallory. Psys, systolic blood pressure (Reprinted from Ref. [25], with permission from ASME)

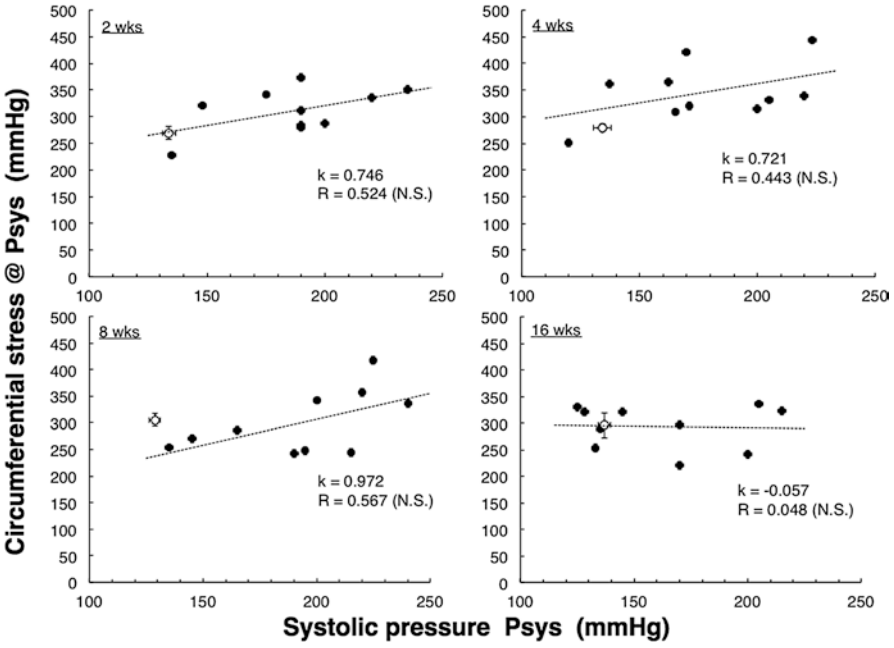

Fig. 4.19 Effect of hypertension on circumferential wall stress of rat thoracic aorta (Reprinted from Ref. [37], with permission from ASME)

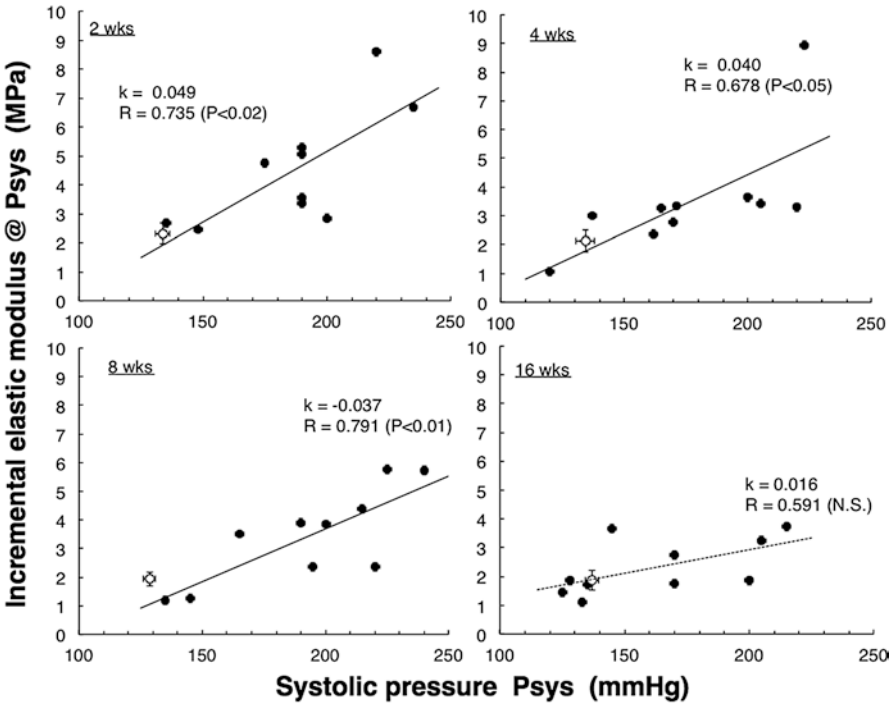

Fig. 4.20 Effect of hypertension on incremental elastic modulus of rat thoracic aorta (Reprinted from Ref. [37], with permission from ASME)

4.4.3 Short-Term Response to Flow Increase

Endothelial cells respond to change in blood flow immediately. For example, they increase the secretion of nitric oxide (NO) within seconds in response to flow increase [42]. NO diffuses into vascular wall and causes smooth muscle relaxation and thus vessel dilation. This dilation may reflect the ability of NO synthesis by the endothelial cells, and has been used to evaluate the endothelial cell function in clinical medicine and is called flow-mediated dilation (FMD) [43]. The brachial artery has been used widely [44, 45] for the FMD measurement. An increase in flow in the brachial artery is achieved by temporal occlusion of the forearm artery by the inflation of a pneumatic cuff placed on the forearm over systolic pressure for 5 min. Upon the release of the cuff, the blood flow in the brachial artery increased sharply, and this results in the increase in the shear stress which activates endothelial nitric oxide synthase to release NO. The NO causes the smooth muscle cells to relax resulting in vasodilatation. FMD is measured as the percentage change in brachial artery diameter from baseline in response to the increased flow. The diameter of the brachial artery is normally measured with an ultrasound probe. Typical example of brachial artery FMD is shown in Fig. 4.21. Dilation of the brachial artery caused by

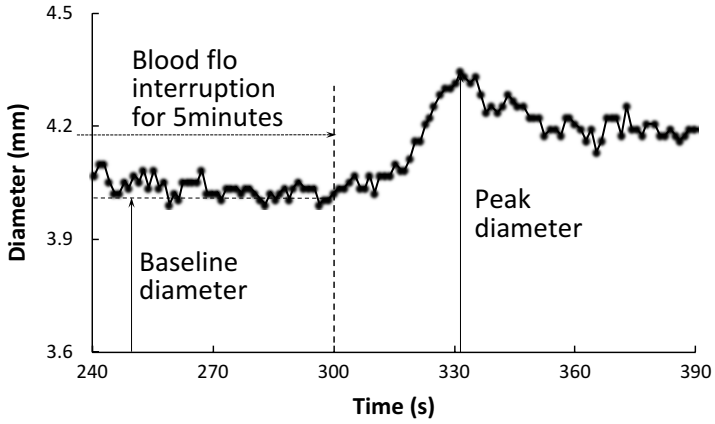

Fig. 4.21 Flow-mediated dilation measured in a human brachial artery

temporal increase in NO is within the range of 5–10 % of the vessel diameter for healthy subjects. FMD test is now one of the most important methods for the diagnosis of endothelial dysfunction and risk of coronary artery disease and other diseases caused by atherosclerosis and is used widely in clinical medicine [46].

4.4.4 Short-Term Response to Pressure Increase

It is well known that the smooth muscle cells show myogenic response, *i.e.*, smooth muscle cells actively contract after they are stretched. This response plays important roles in our body such as autoregulation of blood flow [47]. If the artery wall, especially at the arteriolar level, does not have myogenic response, *i.e.*, the resistance of a vascular bed does not change just like a rigid tube network, blood flow would change in response to change in the arterial pressure (Fig. 4.22a). In reality, blood flow in the vascular bed does not change much in a physiological pressure range (autoregulation, Fig. 4.22b), because slight stretch in the vascular bed due to increase in the arterial pressure causes active contraction of the arteriole and thus reduce the blood flow, and reverse phenomenon occurs when the arterial pressure dropped.

Myogenic response in the vasculature is called the Bayliss effect [48]. Typical example of the Bayliss effect in vascular smooth muscles cells is a response to stretch. When blood pressure is increased in the blood vessels and the blood vessels distend, they react with a constriction. Stretch of the cell membrane opens a stretch-activated ion channel. The cells then become depolarized, and this results in an increase in the intracellular Ca^{2+} ion and triggers muscle contraction. Recently, we have succeeded to observe the Bayliss effect in the brachial artery. We attached an airtight chamber to the upper arm and applied negative pressure in this chamber to

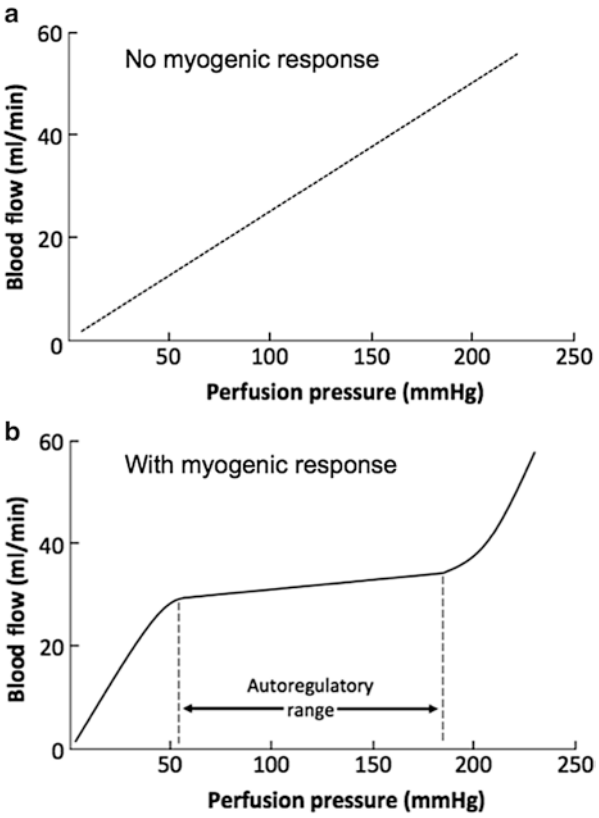

Fig. 4.22 Myogenic response of artery wall

dilate the brachial artery and observed temporal change in the brachial artery diameter with an ultrasound probe. As shown in Fig. 4.23, the artery diameter increased in a stepwise manner upon negative pressure application and then decreased gradually in two minutes. We have named this phenomenon a pressure-mediated contraction (PMC) and are now trying to use PMC as an index of smooth muscle cell function [49, 50].

4.5 Conclusions

Blood vessel is not a simple tube. It is an intelligent pipe which changes dimensions and mechanical properties adaptively in response to changes in blood flow and pressure. It can be said that vascular diseases such as hypertension, atherosclerosis, and aneurysms have a close correlation with the malfunctioning of the mechanical adaptation mechanism. Elucidation of the detailed mechanism of the mechanical

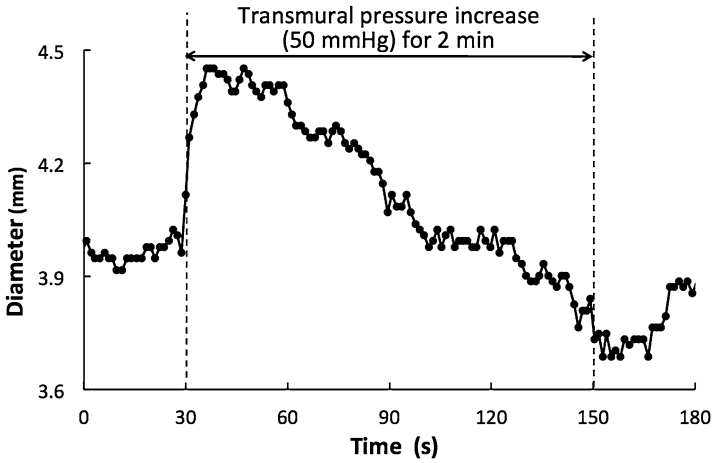

Fig. 4.23 Pressure-mediated contraction measured in a human brachial artery

adaptation of vascular walls may not only help our understanding of pathogenesis of various vascular diseases but also give us various hints in developing new intelligent materials for pipes that can adaptively change the diameter and wall thickness in response to intramural pressure and flow.

Such a mechanical adaptation is driven by the vascular smooth muscle cells in the media. To elucidate the mechanism of the mechanical adaptation, we need to know the mechanical environment of the cells in detail, *i.e.*, at a cellular level and in 3D. As stated in Sect. 4.1, artery wall has a highly complicated structure made of components with various mechanical properties. This indicates that the stress and strain distributions in the blood vessel wall are far from that shown in Figs. 4.11 and 4.15 and highly heterogeneous. Microscopic viewpoint is indispensable in elucidating the mechanism of mechanical adaptation.

Acknowledgements This work was supported in part by the "Knowledge Hub" of AICHI, The Priority Research Project and JSPS KAKENHIs (nos. 22240055 and 24650295 for T.M., 24650256 and 26709002 for S.S., and 24700495 for T.Y.).

References

1. Wolinsky H, Glagov S (1967) A lamellar unit of aortic medial structure and function in mammals. Circ Res 20:99–111
2. Urry DW, Okamoto K, Harris RD, Hendrix CF, Long MM (1976) Synthetic, cross-linked polypentapeptide of tropoelastin: an anisotropic, fibrillar elastomer. Biochemistry 15:4083–4089
3. Fung YC, Sobin SS (1981) The retained elasticity of elastin under fixation agents. J Biomech Eng 103:121–122

4. Matsumoto T, Fukunaga A, Narita K, Nagayama K (2008) Microscopic mechanical analysis of aortic wall: estimation of stress in the intramural elastic laminas and smooth muscle cells in a physiological state. In: Proceedings of the 2008 summer Bioengineering conference (CD-ROM), 192450.pdf
5. Svendsen KH, Thomson G (1984) A new clamping and stretching procedure for determination of collagen fiber stiffness and strength relations upon maturation. J Biomech 17:225–229
6. Yamamoto N, Ohno K, Hayashi K, Kuriyama K, Yasuda K, Kaneda K (1993) Effects of stress shielding on the mechanical properties of patellar tendon. ASME J Biomech Eng 115:23–28
7. Matsumoto T, Nagayama K (2012) Tensile properties of vascular smooth muscle cells: bridging vascular and cellular biomechanics (review). J Biomech 45:745–755
8. Patel DJ, Fry DL (1969) The elastic symmetry of arterial segments in dogs. Circ Res 24:1–8
9. Schriefl AJ, Zeindlinger G, Pierce DM, Regitnig P, Holzapfel GA (2012) Determination of the layer-specific distributed collagen fiber orientations in human thoracic and abdominal aortas and common iliac arteries. J R Soc Interface 9:1275–1286
10. Roy S, Boss C, Rezakhaniha R, Stergiopulos N (2010) Experimental characterization of the distribution of collagen fiber recruitment. J Biorheol 24:84–93
11. Fischer GM, Llaurado JG (1966) Collagen and elastin content in canine arteries selected from functionally different vascular beds. Circ Res 19:394–399
12. Carew TE, Vaishnav RN, Patel DJ (1968) Compressibility of the arterial wall. Circ Res 23:61–68
13. Ohashi T, Sugita S, Matsumoto T, Kumagai K, Akimoto H, Tabayashi K, Sato M (2003) Rupture properties of blood vessel walls measured by pressure-imposed test. JSME Int J Ser C 46:1290–1296
14. Sugita S, Matsumoto T, Ohashi T, Kumagai K, Akimoto H, Tabayashi K, Sato M (2012) Evaluation of rupture properties of thoracic aortic aneurysms in a pressure-imposed test for rupture risk estimation. Cardiovasc Eng Technol 3:41–51
15. Patel D, Janicki J, Carew T (1969) Static anisotropic elastic properties of the aorta in living dogs. Circ Res 25:765–779
16. Biomechanical engineering: a first course. Japan Society of Mechanical Engineers, Maruzen, Tokyo (1997)
17. Bergel DH (1961) The static elastic properties of the arterial wall. J Physiol 156:445–457
18. Peterson L, Jensen R, Parnell R (1960) Mechanical properties of arteries in vivo. Circ Res 8:622–639
19. Hayashi K, Handa H, Nagasawa S, Okumura A, Moritake K (1980) Stiffness and elastic behavior of human intracranial and extracranial arteries. J Biomech 13:175–184
20. Bergel DH (1961) The dynamic elastic properties of the arterial wall. J Physiol 156:458–469
21. Cox RH (1979) Contribution of smooth muscle to arterial wall mechanics. Basic Res Cardiol 74:1–9
22. Dobrin PB, Rovick AA (1969) Influence of vascular smooth muscle on contractile mechanics and elasticity of arteries. Am J Physiol 217:1644–1652
23. Fung YC (1993) Chapter 7: Bioviscoelastic solids, and Chapter 8: Mechanical properties and active remodeling of blood vessels. In: Biomechanics: mechanical properties of living tissues, 2nd edn. Springer, New York
24. Humphrey JD (2002) Cardiovascular solid mechanics: cells, tissues, and organs. Springer, New York
25. Matsumoto T, Hayashi K (1996) Stress and strain distributions in hypertensive and normotensive rat aorta considering residual strain. ASME J Biomech Eng 118:62–73
26. Fung YC, Liu SQ (1989) Change of residual strains in arteries due to hypertrophy caused by aortic constriction. Circ Res 65:1340–1349
27. Matsumoto T, Tsuchida M, Sato M (1996) Change in intramural strain distribution in rat aorta due to smooth muscle contraction and relaxation. Am J Physiol Heart Circ Physiol 271:H1711–H1716
28. Vaishnav RN, Vossoughi J (1983) Estimation of residual strains in aortic segments. In: Hall CW (ed) Biomedical engineering II, recent developments. Pergamon Press, New York

29. Fung YC (1984) Section 2.9: The need for a new hypothesis for residual stress distribution. In: Biodynamics: circulation. Springer, New York
30. Takamizawa K, Hayashi K (1987) Strain energy density function and uniform strain hypothesis for arterial mechanics. J Biomech 20:7–17
31. Fung YC (1990) Chapter 11: Stress, strain and stability of organs. In: Biomechanics: motion, flow, stress, and growth. Springer, New York
32. Matsumoto T, Goto T, Sato M (2004) Microscopic residual stress caused by the mechanical heterogeneity in the lamellar unit of the porcine thoracic aortic wall. JSME Int J Ser A 47:341–348
33. Kamiya A, Togawa T (1980) Adaptive regulation of wall shear stress to flow change in the canine carotid artery. Am J Physiol 239:H14–H21
34. Masuda H, Zhuang YJ, Singh TM, Kawamura K, Murakami M, Zarins CK, Glagov S (1999) Adaptive remodeling of internal elastic lamina and endothelial lining during flow-induced arterial enlargement. Arterioscler Thromb Vasc Biol 19:2298–2307
35. Sugiyama T, Kawamura K, Nanjo H, Sageshima M, Masuda H (1997) Loss of arterial dilation in the reendothelialized area of the flow-loaded rat common carotid artery. Arterioscler Thromb Vasc Biol 17:3083–3091
36. Koller A, Sun D, Kaley G (1993) Role of shear stress and endothelial prostaglandins in flow- and viscosity-induced dilation of arterioles in vitro. Circ Res 72:1276–1284
37. Matsumoto T, Hayashi K (1994) Mechanical and dimensional adaptation of rat aorta to hypertension. J Biomech Eng 116:278–283
38. Wolinsky H (1971) Effects of hypertension and its reversal on the thoracic aorta of male and female rats. Circ Res 28:622–637
39. Wolinsky H (1972) Long-term effects of hypertension on the rat aortic wall and their relation to concurrent aging changes. Circ Res 30:301–309
40. Vaishnav RN, Vossoughi J, Patel DJ, Cothran LN, Coleman BR, Ison-Franklin EL (1990) Effect of hypertension on elasticity and geometry of aortic tissue from dogs. ASME J Biomech Eng 112:70–74
41. Berry C, Greenwald S (1976) Effects of hypertension on the static mechanical properties and chemical composition of the rat aorta. Cardiovasc Res 10:437–451
42. Furchgott RF (1983) Role of endothelium in responses of vascular smooth muscle. Circ Res 53:557–573
43. Corretti MC, Anderson TJ, Benjamin EJ, Celermajer D, Charbonneau F, Creager MA, Deanfield J, Drexler H, Gerhard-Herman M, Herrington D, Vallance P, Vita J, Vogel R (2002) Guidelines for the ultrasound assessment of endothelial-dependent flow-mediated vasodilation of the brachial artery. J Am Coll Cardiol 39:257–265
44. Anderson EA, Mark AL (1989) Flow-mediated and reflex changes in large peripheral artery tone in humans. Circulation 79:93–100
45. Celermajer DS, Sorensen KE, Gooch VM, Spiegelhalter DJ, Miller OI, Sullivan ID, Lloyd JK, Deanfield JE (1992) Non-invasive detection of endothelial dysfunction in children and adults at risk of atherosclerosis. Lancet 340:1111–1115
46. Cox DA, Vita JA, Treasure CB, Fish RD, Alexander RW, Ganz P, Selwyn AP (1989) Atherosclerosis impairs flow-mediated dilation of coronary arteries in humans. Circulation 80:458–465
47. Fung YC (1997) Section 5.13: Local control of blood flow. In: Biomechanics: circulation, 2nd edn. Springer, New York
48. Bayliss WM (1902) On the local reactions of the arterial wall to changes of internal pressure. J Physiol 28:220–231
49. Matsumoto T, Nagayama K, Takezawa K, Masuda H (2008) US patent application no: 12/071873
50. Yaguchi T, Nagayama K, Tsukahara H, Masuda H, Matsumoto T (2013) Development of a non-invasive multifaceted evaluation system for arterial function under transmural pressure manipulation. International symposium on micro-nanomechatronics and human science (MHS2013). doi:10.1109/MHS.2013.6710460

Chapter 5
Tooth and Tooth-Supporting Structures

Shinji Kamakura

Abstract Tooth and tooth-supporting structures are involved in the function of mastication and articulation and are classified as enamel, dentin-pulp complex, and tooth-supporting structures. The dentin-pulp complex is sorted dentin and pulp, and the tooth-supporting structures are categorized as cementum, periodontal ligament, alveolar bone, and gingiva. Tooth consists of three different types of hard tissues, such as enamel, dentin, and cementum, and soft tissue of pulp and periodontal ligament. In clinical situation, a tooth is fundamentally made of the crown that is any part of the tooth visible in the mouth and the root that is any part of a tooth not visible in the mouth. Enamel covers the crown of a tooth and is the most highly mineralized substance in the human body, which includes the highest percentage of minerals. Cementum covers the root and is connected with alveolar bone, which surrounds and supports the tooth root by intervening with periodontal ligament. Dentin-pulp complex is surrounded by enamel and cementum. Dentin is the most voluminous mineralized tissue of the tooth and is formed by odontoblast that is part of the outer surface of the pulp. Pulp also includes vascular, lymphatic, and nervous elements.

Keywords Tooth • Enamel • Dentin • Cementum • Periodontal ligament • Alveolar bone

5.1 Introduction

Teeth are located in the oral cavity and help tear and grind food to swallow and digest (mastication). Also, the tooth is an essential organ for communication to be involved in pronunciation and facial expression.

S. Kamakura (✉)
Bone Regenerative Engineering Laboratory, Graduate School of Biomedical Engineering, Tohoku University, 2-1 Seiryo-Machi, Aoba-Ku, Sendai 980-8574, Japan
e-mail: kamakura@bme.tohoku.ac.jp

M. Niinomi et al. (eds.), *Advances in Metallic Biomaterials*, Springer Series in Biomaterials Science and Engineering 3, DOI 10.1007/978-3-662-46836-4_5

Teeth are located in jaws (maxilla and mandible), and a part of them (clinical crown) is erupted in the oral cavity. They stand in line and form arched structure in maxilla and mandible, respectively (dental arch). The relationship at rest between the maxillary (upper) and mandibular (lower) teeth is called occlusion [1].

Humans developed two sets of teeth, deciduous teeth and permanent teeth; the deciduous teeth are the first set of teeth and usually lost and replaced by the permanent teeth (diphyodontism) [1]. The eruption of the first set of teeth is called primary dentition (deciduous dentition), and the second set is called secondary dentition (permanent dentition). The same numbers of teeth are bilaterally erupted in the upper and lower sides. Deciduous dentition has the set of 20 teeth, and the permanent dentition has the set of 32 teeth. The first deciduous tooth erupts through the gum about 6 months after birth, and the deciduous dentition completes by around the age of two and half years old [1]. Around age 6, the replacement of deciduous teeth by permanent teeth begins and usually completes by the age of 12. Three most posterior teeth in permanent dentition are called molars and unchanged throughout life. Human teeth in the permanent dentition have distinct different morphological characteristics and are classified into four types, such as the incisor, the canine, the premolar, and the molar.

The incisors locate the front of the dental arch in both upper and lower jaws. Their function is cutting or slicing food into small pieces, and the generally flat and chisel-shape teeth meet in an edge-to-edge bite. Adult humans naturally have eight incisors and two of each type, named maxillary/mandibular central incisor and maxillary/mandibular lateral incisor. The central incisor is the closest tooth to the median line, and the lateral incisor is located distally (away from the median line) from central incisors (Fig. 5.1). The canine is placed distally from lateral incisors, projecting beyond the level of the other teeth. There is a pointed, tusk-shaped single cusp that is an eminence on an occlusal surface of canines and posterior teeth, and

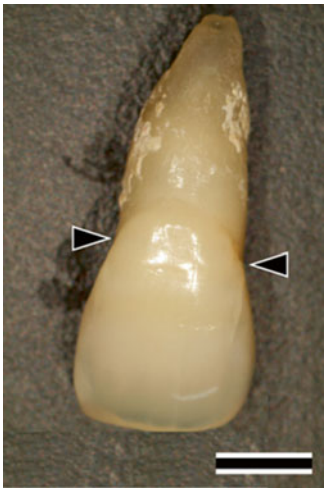

Fig. 5.1 Maxillary left central incisor, labial aspect. *Arrowheads*: cementoenamel junction; scale bar = 5 mm

Fig. 5.2 Mandibular right first molar, labial aspect. *Arrowheads*: cementoenamel junction; scale bar = 5 mm

their function is splitting of food. The premolar is placed distally from canine and has two cusps.

There are two premolars per quadrant and are identified as first and second premolars. The first premolar is located distally from canine, and the second premolar is positioned distally from the first premolar. Premolar can be considered as a transitional tooth during chewing, or mastication. It has the properties of both the anterior canines and molars, and so food can be transferred from the canines to the premolars and finally to the molars for grinding, instead of directly from the canines to the molars [1]. Clinical (tooth) crown of the premolars roughly indicates to the visible in the mouth exposed beyond the gingiva. And clinical crown of premolars has occlusal surface, which occludes with or contacts an opposing surface of a tooth in the opposing jaw. The molar is placed distally from second premolar and the most posterior teeth in permanent dentition. From the anterior to posterior, it consists of first, second, and third molars per quadrant (Fig. 5.2). The figure of clinical crown is different between maxillary and mandible molars. The molars have plural cusps and complex occlusal surface. The third molar is also called wisdom tooth. It usually appears after adolescence. Wisdom teeth occasionally tend to be impacted in maxilla and mandible throughout life. The primary dentition consists of central incisors, lateral incisors, canines, first molars, and secondary molars. All of these are gradually replaced by a permanent counterpart except for the primary first and second molars. First molars and secondary molars are replaced by first premolars and secondary premolars [1].

The appearance of human tooth consists of (tooth) crown and (tooth) root. The term crown can be used in two ways, namely, anatomical crown and clinical crown. The clinical crown means any part of the tooth visible in the mouth. Similarly, the term root can be used in two ways, namely, anatomical root and clinical root. The clinical root means any part of a tooth not visible in the mouth. Although the major tissues of tooth are enamel, dentin, cementum, and dental pulp, the surface of tooth

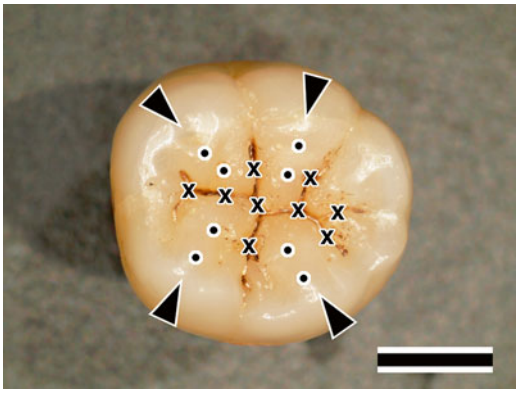

Fig. 5.3 Mandibular right first molar, occlusal aspect. *Arrowheads*: cusps, *Cross*: sulcus, *Dots*: ridges; scale bar = 5 mm

is generally covered with enamel and cementum. Crown is mainly covered with enamel, and root is mainly covered with cementum. The anatomical boundary between anatomical crown and anatomical root is identified with the cementoenamel junction (CEJ), that is, the line between the enamel and the cementum, and also known as the cervical line (Figs. 5.1 and 5.2). The types of teeth are mostly classified by the shape of tooth crown that is characterized by the appearance of enamel.

The surface area of the incisors used in eating is called an incisal edge, and the tip of crown of canine is called a cusp. Premolars and molars have occlusal surface, which comes in contact with those of the opposite jaw during occlusion. The occlusal surface is formed by cusps, ridges, and sulcus (Fig. 5.3). The cusp is an elevation on an occlusal surface, and the premolars and molars have more than two cusps. The ridge is linear, flat elevations on teeth [1]. The sulcus is a groove on the occlusal surface of a tooth. The roots of teeth are embedded in the maxilla or the mandible and are usually invisible in the mouth. Some teeth have one root, while others have multiple roots. Incisors, canines, and most premolars, except for maxillary first premolars, usually have one root. Maxillary first premolars and mandibular molars usually have two roots, and maxillary molars usually have three roots. The appearance of root is usually blunt and cone-shaped, and the tip of the root is called apex. Apical foramen is an opening at the apex of the root of a tooth, and the vascular, lymphatic, and neural structures are passed through this foramen between pulp and periodontal tissue.

In vertical section of a tooth, pulp cavity, which is the central cavity of a tooth containing the pulp, is observed (Fig. 5.4). The pulp cavity is surrounded by dentin, and the appearance of pulp cavity is not similar to that of tooth. The wide pulp cavity of the tooth crown is called pulp chamber, and the root canal is a narrow part of the pulp cavity extending from the pulp chamber to the apical foramen. The dental pulp in nature occupies the pulp chamber. And the pulp in pulp chamber is called coronal pulp and that in root canal is called radicular pulp [1]. Because dentin is covered by enamel in crown and cementum in root, it is hardly occurred that dentin is directly exposed to the outside alone.

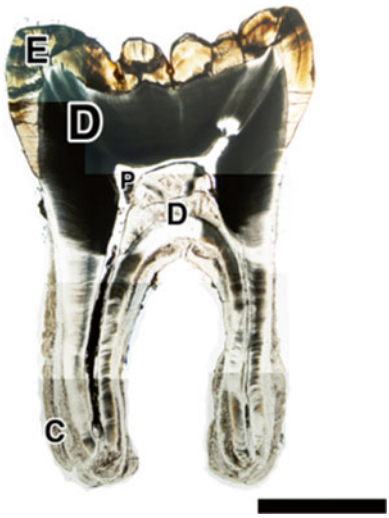

Fig. 5.4 Mesiodistal section of a mandibular first molar. *C* Cementum, *D* Dentin, *E* Enamel, *P* Pulp chamber, Bar = 5 mm

A tooth is embedded in (dental) alveolus, which is the sockets in the jaws, and the alveolar bone (alveolar process) is the thickened ridge of bone that contains the alveolus. Because a tooth root is not attached to an alveolus, there is a narrow space between them, which is called periodontal space. It contains a periodontal ligament, which is a fibrous connective tissue connecting the cementum on the root and alveolar bone. The periodontal ligament serves to hold the tooth in its socket and plays a role of periodontal mechanoreceptors. Gingiva consists of a mucosa (mucous membrane) that lies over the mandible and maxilla inside the mouth. It surrounds and supports the teeth and is tightly bound to the underlying alveolar bone, which helps resist the friction of food passing over them. Although the gingiva is penetrated by the tooth, the margin of the gingiva is attached to the surface of enamel (epithelial attachment) [2].

5.2 Enamel

5.2.1 Composition and Structure of Enamel

Tooth enamel is the only tissue of tooth, which is exposed to the oral cavity. It is the hardest substance in the human body, which covers a tooth crown and is formed by ameloblasts. It contains the highest percentage (>95 %) of minerals with very small amount of organic component (<1 %) and water [3]. Enamel has the semitransparent and milky-white appearance, and its color tends to vary from light yellow to grayish with aging. Because enamel is united to dentin by intervening with the dentinoenamel junction (DEJ), the appearance of a tooth is reflected by the color of dentin and any restorative dental material underneath the enamel. Within molars, the thickness of enamel is the largest near the cusps (up to approximately 2.5 mm) and then decreases to a minimum closest to the base of the crown [4]. The enamel

has some outstanding mechanical properties with brittleness. The Vickers hardness ranges of enamel are from approximately 3 GPa to 6 GPa, and the elastic modulus ranges from 70 GPa to nearly 120 GPa [4]. It is a poor conductor for heat and electric current, displaying birefringence [5].

The tooth enamel is occupied by more than 95 wt% of inorganic compound, which primarily consists of calcium phosphate. Because its crystal structure is the same as that of apatite stone, hydroxyapatite ($Ca_{10}(PO_4)_6(OH)_2$) serves as a prototype of the inorganic component of enamel. Although biologic apatites that are involved in teeth and bones are analogues of geologic hydroxyapatite, the physical and chemical properties of the crystals in teeth and bones are different from those of geologic hydroxyapatite. Because they have highly disordered, non-stoichiometric structures with numerous point deficiencies, and carbonate substitutions, these structures refer to "bioapatite" as distinct from stoichiometric hydroxyapatite [6]. The hydroxyapatite crystallizes in the hexagonal crystal system, and the unit cell of hydroxyapatite comprises three axes, 0.942 nm on a- and b-axis and 0.688 nm in c-axis. The hydroxyapatite lattice contains two kinds of calcium positions: columnar and screw axes. The columnar calcium forms a series of hexagons, and the screw axis calcium is arranged in triangles around the central axis c. Because the apatite structure permits substantial variation in its structure, other atoms can substitute each one of these atoms; Ca^{2+} can be replaced by Na^+ or Mg^{2+}, PO_4^{3-} can be replaced by CO_3^{2-}, and OH^- can be substituted by F^- or Cl^- [7].

The fundamental morphologic unit of enamel structure is enamel prism, and it is a structural unit approximately 4 μm in width and consists of numerous crystals of the hydroxyapatite (Fig. 5.5). The enamel prisms are arranged in a columnar fashion, extending from the dentinoenamel junction (DEJ), which is the interface between the dentin and enamel, to the enamel surface (Fig. 5.6). The enamel crystal composed of bundles of 40–60 nm wide apatite crystals with aspect ratios reaching up to 1:10,000 so demonstrates at least 100 μm long and is ~ 10× larger than those of bone or dentin [8]. The enamel prisms appear as a group of keyhole-shaped or tadpole-shaped structures, approximately 6–8 μm in diameter with the enlarged portion of the keyhole called the head and the narrow portion the tail [9]. The prisms

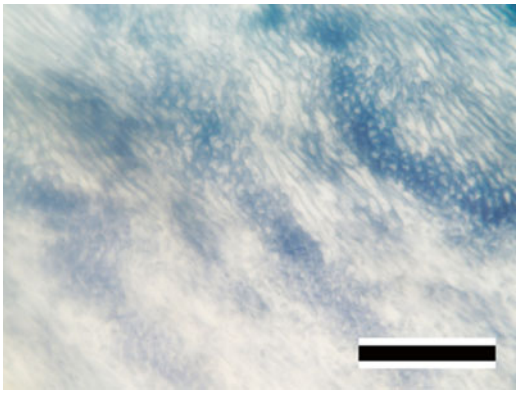

Fig. 5.5 Enamel prism. The enamel prisms are arranged in a columnar fashion and appear as a group of keyhole-shaped or ts structures. Villanueva bone stain; scale bar = 50 μm

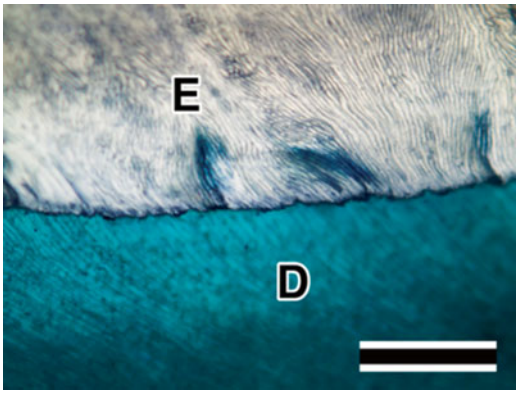

Fig. 5.6 Dentinoenamel junction (DEJ) is the plane of meeting between dentin (D) and enamel (E) on the crown of a tooth. Villanueva bone stain; scale bar = 100 μm

have cross-striations that are corresponding periodic features visible in the light microscope as slight striations perpendicular to the axis of the prism at regular intervals of approximately 3–4 μm (range 2–8 μm). They are the result of a circadian rhythm in the metabolic activity of ameloblasts. Also, the crystals' pattern of enamel is defined by both ameloblasts and Tomes' processes, which are distal cytoplasmic processes of ameloblasts. The outer surface of enamel frequently lacks the normal arrangement of prisms (prismless enamel) but is arranged either in continuous layers parallel to the surface.

5.2.2 Formation of Enamel

The tooth germ has the potential of developing into a tooth and is a mass of tissue, including the enamel organ, dentinal papilla, and dental sac (dental follicle). The enamel organ is a mass of ectodermal cells derived from the dental lamina and develops the ameloblast layer of cells. Amelogenesis is the formation and development of dental enamel and is considered to have two stages, unlike the formation of bone or dentin having one stage. The first stage is known as the secretory stage, and the second is the maturation stage [10]. During the secretory stage, secretory ameloblast is synthesized and secretes enamel proteins (e.g., mainly amelogenin and enamelin) and provides an organic template form in which the enamel crystals grow [10]. As soon as this organic matrix is secreted, it becomes partially mineralized, and the full volume of enamel tissue bundles into prisms in this stage. In the maturation stage, secretory ameloblast is transformed to maturation ameloblast, and the selective loss of enamel proteins (mostly amelogenin) and water as well as massive influx of calcium and phosphates, which provides for growth of hydroxyapatite crystals of the inorganic component, is occurred. During the process, mineralization of the enamel is completed.

The inner enamel epithelium is innermost layer of enamel organ, and the dental papilla contains cells that develop into odontoblasts, and the junction between the

dental papilla and inner enamel epithelium determines the crown shape of a tooth. The inner enamel epithelium, which is a layer of columnar cells located on the rim nearest the dental papilla of the enamel organ in a developing tooth, begins its differentiation first into differentiating ameloblast. Then, the differentiation of secretory ameloblast from differentiating ameloblast is completed by the formation of Tomes' processes. Enamel deposition starts at the dentinoenamel boundary, on top of mineralized mantle dentin, which is the peripheral portion of dentin adjacent to the enamel [11]. It has been stated that amorphous calcium phosphate (ACP) plays a special role as a precursor to bioapatite and as a transient phase in biomineralization [12]. ACP can transform to DCPD (dicalcium phosphate dihydrate) or OCP (octacalcium phosphate) [13]. Also, non-apatitic calcium phosphates (e.g., ACP, DCPD, OCP) can transform to apatites and substituted apatites or other calcium phosphates by dissolution-precipitation processes in biologic systems [14]. The early mineralized enamel crystals appear thin ribbonlike structure [15]. In the secretory stage, secretory ameloblasts are polarized columnar cells with abundant rough endoplasmic reticulum, secretary granules, and Golgi apparatus and form full volume of enamel tissue in immature enamel.

The organic component of immature enamel is mainly composed of enamel proteins, although that of bone and dentin is mainly composed of type I collagen. The enamel proteins contain amelogenin, enamelin, ameloblastin, enamel proteinase, and so on. And amelogenin is the major structural protein of the enamel organic matrix and constitutes more than 90 % of the enamel's protein content [16]. They are released into the surrounding area, and the ameloblast moves away from the interface with dentin during the synthesis of enamel. In secretory stage, Ca^{2+}-ATPase is presented in the entire plasma membrane of the secretory ameloblasts, and it is involved in the excretion of Ca^{2+} to the extracellular fluid [17].

Transitional stage is situated between the secretory stage and the maturation stage, and the morphology of the ameloblasts is changed from secretory ameloblasts into maturation ameloblasts. The height of ameloblast is decreased, and protein synthesis is considerably reduced. Also, this stage is featured by a reduction in the number of ameloblasts through apoptosis.

The maturation stage is featured by selective loss of enamel proteins and water as well as massive influx of calcium and phosphates, which provides for growth of hydroxyapatite crystals of the inorganic component. Maturation ameloblasts include two distinctly different types, ruffle-ended and smooth-ended, depending on the morphology of their distal ends [17]. Because the ruffle-ended ameloblasts were dominant and have a distinct distribution of Ca^{2+}-ATPase, they suppose to play an important role in enamel maturation [17]. During the maturation stage, rapid growth and thickening of the crystallites occur, which is associated with progressive degradation and eventual removal of the enamel extracellular matrix components mainly amelogenins [18]. Amelogenin is distributed in the sheath space, and enamelin mostly presents in the rod and inter-rod enamel. During the growth of the crystals, the sheath space decreases and removal of amelogenin has occurred, so a little amount of enamelin remains the crystal surface [18].

When the maturation stage is completed, the maturation ameloblasts lose their differentiation and become short cuboidal cells, namely, the reduced enamel epithe-

lium. It remains on the surface of fully formed enamel until the tooth erupts and protects enamel from being in contact with connective tissue cells in the dental sac. The reduced enamel epithelium and the oral epithelium cooperatively form the dentogingival junction of the erupting tooth. When a tooth erupts and in the oral cavity, the enamel has not yet received post-eruptive maturation. At this point, the enamel is more porous with larger carbonated apatite concentration, a greater percentage of impurities (sodium, magnesium, etc.) in its composition, and more sensitive to demineralization [19]. In this stage, an ionic exchange may occur between the enamel and outer environment (saliva, oral biofilm) [20]. Because the saliva contains sufficiently high concentrations of calcium and phosphate, it makes the enamel surface more resistant to demineralization [20]. Because the thickness of crystallites increases and crystallites are closely joined and fused, intercrystalline spaces are narrowed [21].

5.3 Dentin-Pulp Complex

5.3.1 Composition and Structure of Dentin

Dentin is a highly mineralized tissue containing large quantities of collagen fibers in the matrix and the most amount of constituent of a tooth. Because dentin is covered by enamel on tooth crown and cementum on tooth root, it is invisible in the mouth [1]. And it is formed by odontoblasts and includes inside pulp cavity that contains dental pulp (Fig. 5.4). The color of dentin reflects that of a tooth crown, and its original color is light yellow and light brown and becomes dark shade with aging. When the complete degeneration of pulp has happened, its color turns to brownish and dark grayish, because the pigments are derived from degradation products of pulp and blood deposit in dentin. Dentin is an opaque tissue due to the presence of numerous dentinal tubules, and the thickness of dentin is approximately 3.5 mm [22]. The microhardness ranges of dentin are from approximately 0.25–0.8 GPa [23], and the Young's moduli lie between 20 and 25 GP [24]. Dentin and enamel are bonded firmly, and it is considered that the elasticity of dentin protects the fracture of enamel. Dentin is composed of 70 % by weight mineral phase, 20 % by weight organic matrix, and 10 % by weight water [25]. It is less mineralized than enamel, but more than bone or cementum [25]. The thickness of these crystallites is approximately 5 nm [26]. The crystals in dentin are of similar size in bone, but enamel crystals are ~10 times larger in all dimensions [6]. The small crystal size, high degree of carbonate substitution, substantial OH deficiency, presence of lattice vacancies, and the resultant increased solubility make apatite in bone, dentin, cementum, and even enamel distinct from geologic hydroxyapatite [6].

The organic matrix is constituted by ~90 % of collagen, and the majority of it is type I, and about 3 % of the collagen fibrils are composed of type III and/or type V collagens. Collagen is an insoluble fibrous protein and is one of the most abundant proteins in the body [6]. And approximately 10 % of organic matrix is composed of

noncollagenous molecules, such as dentin sialophosphoprotein (DSPP), dentin matrix protein-1 (DMP-1), and proteoglycans (PGs) [25]. These noncollagenous proteins are important for the control of dentin and bone mineralization [6]. Also, dentin is a poor conductor for heat and electric current and displays weak birefringence.

Dentin is classified into two different types, mantle dentin and circumpulpal dentin. Mantle dentin, 15–30 μm thick, is the outer layer of dentin and is adjacent to the enamel or cementum. It corresponds to an initial stage of odontogenesis [25] and has mainly an atubular layer with few thin and curved tubules [25]. The circumpulpal dentin situates inside the mantle dentin and forms the largest part of the dentin layer, and it is subdivided into intertubular dentin and peritubular dentin. Hence, it is generally accepted that the structure of circumpulpal dentin represents that of dentin. Odontoblasts are large columnar cells, which produce dentin, are aligned at the surface of the dental pulp, and still remain lifetime. They demonstrate two distinct parts: a cell body and a process. The cell bodies are polarized outside the mineralized tissue, and a long process generally occupies the lumen of dentin tubule. As odontoblasts develop to polarize, they produce an orthodentin that is a tubular-shaped dentin. Although dentin is not vascularized, it is supposed that few free nerve endings extend more than 100 μm into dentinal tubules [22]. Dentinal tubules are small canals that extend across entire width of dentin, from DEJ (dentinoenamel junction) or DCJ (dentinocemental junction) to the pulp (Fig. 5.7). The number of dentine tubules is about 18,000 tubules per mm^2, and the diameter of tubules varies between 2.55 and 2.90 μm [27]. The diameters of dentinal tubules are different in location, and the diameter near the pulp is larger than that at the dentinoenamel junction. The most prominent part of the circumpulpal dentin is formed by intertubular dentin, and peritubular dentin is found around the lumen of the tubules [25]. Each tubule contains the cytoplasmic process of an odontoblast and is lined with a layer of peritubular dentin, which is more mineralized than surrounding intertubular dentin. Although the dentinal tubules run a straight course in the root, they run the S-shaped curvature in coronal dentine [28]. The approximately 250 μm-wide outer zones showed typical, terminal Y-branching of the dentinal tubules [28].

Fig. 5.7 Dentinal tubules. The dentinal tubules are small canals that extend across entire width of dentin, from dentinoenamel junction or dentinocemental junction to the pulp. Villanueva bone stain; scale bar = 50 μm

The formation of intertubular dentin provides three successive layers. The innermost layer is the cellular stratum that contains odontoblast cell bodies, the second one is the immature predentin layer, and the outermost one is the mineralized dentin [25]. And the interface between the immature predentin and the mineralized dentin is called mineralization front. Because the odontoblasts migrate toward the center of the tooth forming the odontoblast process, dentinogenesis (the formation of dentin) progresses toward the inside of the tooth. The immature predentin layer has a constant 15–20 μm thickness [25]. Radioautographic data and experiments using microtubule inhibitors suggest the occurrence of flux of forces in predentin and the active transport of collagen fibrils from the proximal to the distal predentin where the mineralization process occurs [25]. Dentin mineralization often initiates that the mineralized nodule is solely found in an immature noncalcified layer of predentin that is apart from the mineralization front. It means the mineralized nodule nucleates and develops the progress of calcification that is the deposit of calcium salts in a tissue. Consequently, the developed mineralized nodules are contacted with the mineralization front and fused with mineralized dentin.

As the formation of primary dentin that continues until the eruption of a tooth is completed, the tissue of dentin can restart or reconstitute its structure by several biological stimulations including addition of dentin or altered form of dentin. The former is secondary dentin and tertiary (restorative) dentin, and the latter is transparent (sclerotic) dentin. The secondary dentin begins to form by achieving the contacts between antagonistic cusps and continues throughout life [25]. However, there is not much difference between primary and secondary dentin [25]. The tertiary (restorative) dentin is a new dentin formed in response to stimuli associated with the normal aging process, such as tooth attrition, tooth abrasion, and pathological conditions including caries, injury, and cavity preparation [22]. Because the dentinal tubules in restorative dentin are highly curved and meander with short period, they are distinguished from those in primary dentin. The transparent dentin has some dentinal tubules becoming sclerotic or calcified with the appearance of translucency. However, these dentins are not remodeled as well as cementum, whereas the bone is remodeled [6].

The formation of dentin is initiated by differentiating from the neural crest cell-derived ectomesenchymal cells present in the dental papilla near inner enamel epithelium to odontoblast [29]. When odontoblasts are differentiated, they result in highly polarized cells with a columnar shape, about 50 μm in height [30]. They have all the organelles implicated in extracellular matrix synthesis, such as rough endoplasmic reticulum, Golgi apparatus, and immature and mature secretory vesicles, associated with lysosomal equipment. And they are connected by junctional complexes forming a densely packed palisade at the dentin-pulp interface, and each cell projects an odontoblastic process into the predentin/dentin matrix [30]. Odontoblasts are essentially dentin-secretory cells that produce predentin, an extracellular matrix formed by type I collagen as the major organic component (about 90 %), together with noncollagenous proteins including glycoproteins, proteoglycans, and dentin phosphoproteins [31]. Mature mineralized dentin is molded after the formation of predentin, and this process is involved in matrix vesicle-mediated mineral deposi-

tion [32]. Matrix vesicles are extracellular 100-nm-diameter membrane-invested particles selectively located within the matrix of bone, cartilage, and predentin and serve as the initial site of calcification in all skeletal tissues [32]. Alkaline phosphatase (ALP) is an enzyme known to be essential for mineralization. Because matrix vesicles are seeded in the selected areas, the subsequent mineralization is localized. In the initial stage, the generation of hydroxyapatite mineral crystals follows within the matrix vesicle membrane. This stage is controlled by phosphatases (including alkaline phosphatase) and Ca-binding molecules. In next stage, the breakdown of matrix vesicle membranes is occurred and exposed preformed hydroxyapatite to the extracellular fluid [32]. Consequently, numerous mineralized nodules derived from matrix vesicle-mediated mineral depositions are formed in the layer of predentin, and the mineralization progressed by fusion of these nodules with mineralized dentin. Primary dentin is formed at an appositional rate of about 4–8 μm per day, allowing the bulk of the tooth to be created within 2–3 years of continuous secretion [30]. After eruption of the tooth, the odontoblast phenotype is significantly changed to the mature odontoblast stage. Their secretory apparatus is reduced, and the autophagic vacuoles that are cytoplasmic degenerative debris engulfed by primary lysozymes are presented in cytoplasm. Also, the remaining cellular organelles are relocated to the base of the cell. In human teeth, this stage may persist for decades, but finally the odontoblast reduces cell size and flattens its shape [30].

5.3.2 Composition and Structure of Pulp

The dental pulp is a part of the dentin-pulp complex and is an unmineralized loose connective tissue forming the inner structure of a tooth and containing nerves and blood vessels [33]. It is located in the pulp chamber which is the natural cavity in the central portion of the tooth. The shape of the pulp in the pulp chamber corresponds to the overall shape of the tooth. The dental pulp is divided into coronal pulp that is the part contained in the tooth crown and radicular pulp (root pulp) that is the part contained within the tooth root [1]. The communication between the pulp and the periapical tissues is achieved via the apical foramen [34]. The dental pulp is derived from dental papilla that is a small mass of condensed ectomesenchymal cells in the enamel organ. Also, the dentin was formed by odontoblast that is differentiated from the outermost cells of dental papilla. The pulp contains abundant blood vessels and nerve trunks, although the dentin is devoid of blood vessels. The odontoblast needs nutrients from the blood, whereas the mineralized extracellular matrix of dentin itself does not need that. Therefore, the pulp supplies the nutrients to the dentin to keep the tooth alive and provides sensory and defensive functions to the tooth. Even though the dental pulp provides vitality to the tooth, the loss of the pulp does not mean that of the tooth. Except for odontoblasts, the pulp contains many cells that are responsible for the formation and turnover of a complex non-mineralized ECM. Most of the cells are fibroblasts, and they are sometimes called pulp cells. The pulp fibroblasts

are elongated, with a large nucleus and are functioned by well-developed rough endoplasmic reticulum. The Golgi apparatus is located near the nucleus, and the presence of secretory vesicles reflects the synthetic capacity of these cells, and lysosomes are also present. They do not exist in isolation but are connected by desmosome-like and gap junctions, which facilitate intercellular communication [34]. Defense cells also include mostly dendritic cells and histiocytes/macrophages, and a few lymphocytes and mast cells are also present. The large number of undifferentiated mesenchymal cells helps the recruitment of newly differentiating cells to replace other damaged cells. The endothelial cells, which produce type IV collagen, and Schwann cells that compose a continuous envelope around each nerve fiber of peripheral nerves are also included in the pulp. These various cells are especially abundant in the peripheral areas of the pulp, where they may participate in the immunosurveillance of this tissue and contribute to the pulp responses to dentinal caries [34]. Dental pulp stem cells (DPSCs) isolated from adult human dental pulp have the ability to form a dentin-pulp-like complex [35].

Pulp fibroblasts produce a complex extracellular matrix, which is considerably different from that of dentin. In the pulp, large intercellular spaces contain type I and type III collagen fibrils (56 and 41 %, respectively), in contrast to the predominant type I collagen of dentin [34]. Differences in the noncollagenous extracellular matrix components also exist between pulp and dentin. Fibronectin is prevalent in pulp, and chondroitin 4 and 6 sulfate (60 %), dermatan sulfate (34 %), and keratan sulfate (2 %) glycosaminoglycans (GAGs) are found as proteoglycans (PGs). The lack of mineralization in pulp might be explained by the absence of specific molecules that have been identified in dentin. DSP, DPP, DMP-1, and osteocalcin are predominantly expressed by odontoblasts. Osteonectin is found in the odontoblasts alone, and not in the pulp in adult teeth. Osteopontin and BSP are present in both dentin and pulp. These substantial differences in composition between dentin and pulp could partly explain why pulp is unable to mineralize under physiological conditions [34].

On the periphery of the pulp is specialized the following three zone. The odontoblastic layer is an outermost layer that contains odontoblasts and lies next to the predentin and dentin. Central to the odontoblastic layer is the cell-free zone of Weil. It is a layer that the plexuses of capillaries and small nerve fibers branch. Deep to the cell-free zone of Weil is the cell-rich zone, which contains fibroblasts and undifferentiated mesenchymal cells. These cells maintain the population of odontoblasts by proliferation and differentiation. The cell-free and cell-rich zones are usually indistinct or absent in the embryonic pulp and usually appear when dentin formation is active. The zones tend to become increasingly prominent as the pulp ages. Both of these zones are less constant and less prominent near the root apex. Cell-rich zones circumscribe the central pulp zone of pulpal core. It contains the principal support system for the peripheral pulp, which includes the large vessels and nerves from which branches extend to supply the critical outer pulp layers. The principal cells are fibroblasts, and the principal extracellular components are ground substance and collagen [36].

Aging of the pulp induces these specific changes in the pulp. The most significant change is a reduction in the size of the pulp by forming additional calcified tissues on the walls due to the continuous formation of dentin. There is an agreement that the number of cells decreases and the fibrous component increases with aging of the pulp. The increased fibrosis is not from continued formation of collagen but rather may be attributable to a persistence of connective tissue sheaths in an increasingly narrowed pulp space. Also, the remaining cells are likely to appear relatively inactive, and the decrease in the number of blood vessels and nerves with arteriosclerotic changes is observed [36]. Pulpal calcifications also known as pulp stones (denticles) become more prominent in older teeth. Pulp stones are small-calcified bodies that seem to be found predominantly in the coronal pulp. They are formed from clearly concentric or diffuse layers of calcified tissue on a matrix that seems to consist primarily of collagen. They may occur in the sheaths associated with blood vessels and nerves or thrombi in vessels or calcification of clumps of necrotic cells [36].

5.4 Tooth-Supporting Structures

Tooth-supporting structures are the periodontium, defined as those tissues supporting and investing the tooth, comprises root cementum, periodontal ligament, bone lining the tooth socket (alveolar bone), and that part of the gingiva facing the tooth (dentogingival junction) [2]. Cementum is the bonelike connective tissue that covers the teeth roots and helps to support them by providing a place of attachment for the periodontal ligament fibers and overlying dentin. Periodontal ligament is the fibrous connective tissue that surrounds the tooth root and attaches cementum with the alveolar bone. It permits to withstand the forces of mastication and has a sensory receptor of the jaws during mastication. Alveolar bone is the thin layer of bone containing the sockets (alveoli) for the teeth. Gingiva consists of a mucous membrane with supporting fibrous tissue that overlies the crowns of unerupted teeth and encircles the necks of teeth that have erupted. After the completion of crown formation, root development has begun in which the dental papilla, dental sac (dental follicle), and Hertwig's epithelial root sheath (HERS) are involved. The dental papilla is a small mass of condensed mesenchyme in the enamel organ and differentiates into the dentin and dental pulp. The dental sac differentiates into cementoblasts, osteoblasts, and fibroblasts, and these cells form cementum, periodontal ligament, and alveolar bone. HERS is a proliferation of epithelial cells located at the cervical loop of the enamel organ in a developing tooth. At the beginning of root development, HERS initiates the formation of predentin in the root by causing the differentiation of odontoblasts from the dental papilla. After that, HERS becomes fragmented, and ectomesenchymal cells from the inner portion of the dental sac can come in contact with the predentin. Then cementoblasts will differentiate and deposit cementum matrix onto the forming radicular dentin [2]. Some

cells from the fragmented root sheath form isolated masses surrounded by a basement membrane, known as epithelial rests of Malassez that persist in the mature periodontal ligament.

5.4.1 Composition and Structure of Cementum

The composition of cementum resembles that of bone. It contains about 50 % mineral (substituted apatite) and 50 % organic matrix [2]. Although the mineral is an analogue of the mineral hydroxyapatite, the crystals exhibit a variety of substitutions and vacancies that make the Ca/P molar ratio distinct from the stoichiometric hydroxyapatite ratio of 1.67 [37]. The organic matrix of cementum is composed primarily of collagens. Type I collagen is the major organic component, which plays structural roles and provides scaffolding for mineral crystals, and it accounts for 90 % of all collagens. Also, type III collagen is associated with cementum that is a less cross-linked collagen. Cementum contains two major noncollagenous proteins, bone sialoprotein (BSP) and osteopontin (OPN). These proteins, which are prominent, remain bound to the collagen matrix, and they possess cell attachment properties through the arg-gly-asp (RGD) sequence [38]. Compared with dentin, cementum seems to have a lower stiffness or elastic modulus. The microhardness ranges of cementum are from approximately 0.18–0.25 GPa, and the Young's moduli lie between 2.4 and 4.4 GP [39]. Although cementum is histologically resembled with bone, it is an avascular tissue, and its nutrition is received from the surrounding vascular periodontal ligament [40]. Cementum formation takes place along the entire root and during the entire life of the tooth [2]. Cementoblast is the large cuboidal cells that are responsible for the formation of cementum on the root dentin of developing teeth.

Cementum is classified on the basis of the collagen fibers of the matrix or the presence or absence of cells within it. The matrix fiber in cementum has two different types: intrinsic fiber and extrinsic fiber (Sharpey's fiber). The intrinsic fibers are collagen fiber produced by cementoblasts and are orientated parallel to the cementum surface. The Sharpey's fiber is the extremities of collagen fiber bundles of periodontal ligament and is embedded in the cementum or bone [2] (Fig. 5.8). When cementoblasts become surrounded within the matrix, they become a different type of cell, called cementocytes [2]. Acellular cementum is a cementum that contains no cementocytes, and cellular cementum contains cementocytes embedded within lacunae [2]. The acellular cementum is classified into acellular afibrillar cementum and acellular extrinsic fiber cementum. Acellular afibrillar cementum contains neither cells nor fibers [41]. It covers minor areas of the enamel, particularly at and along the cementoenamel junction [37]. Acellular extrinsic fiber cementum (AEFC) is composed of densely packed collagen bundles of Sharpey's fibers in a noncellular ground substance. It covers the cervical 1/3 to 2/3 of the roots of human teeth [41]. The production of AEFC is produced by cementoblasts and commences shortly after crown formation and continues to grow. It develops very slowly and directs

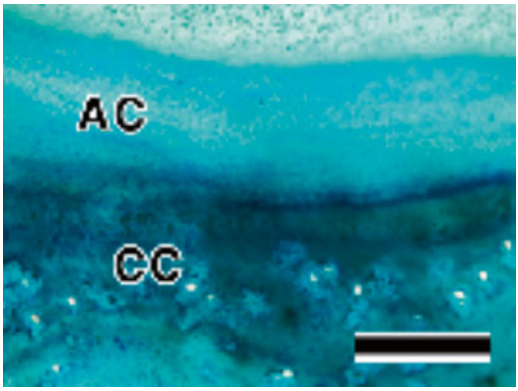

Fig. 5.8 Cementum. Cellular cementum (CC) covers the root surfaces of the teeth that contain cementocytes in lacuna, whereas acellular cementum (AC) contains no cementocytes. Villanueva bone stain; scale bar = 100 μm

perpendicular to the root surface [38]. The overall degree of mineralization of AEFC is about 45–60 %, but the innermost layer is less mineralized [2]. The high numerical density of fibers inserting into acellular extrinsic fiber cementum (approximately 30,000/mm^2) is a reflection for tooth anchorage to the surrounding bone [37].

The cellular cementum is divided into cellular intrinsic fiber cementum and cellular mixed stratified cementum. Cellular intrinsic fiber cementum contains cementocytes in a matrix composed almost exclusively of intrinsic fiber cementum. It may overgrow layers of acellular extrinsic fiber cementum and mainly participates in the repair process of previously resorbed roots [37]. It forms a less mineralized cementum and oriented mostly parallel to the root surface [2]. Cellular mixed stratified cementum is considered to have the matrix of acellular extrinsic fiber cementum with the intrinsic fibers. It generally has a lower mineral content than acellular extrinsic fiber cementum. It increases in thickness throughout life as pure acellular extrinsic fiber cementum does and may be up to 30-fold faster than the more regular acellular extrinsic fiber cementum deposition. As layers of acellular extrinsic fiber cementum and cellular and acellular intrinsic fiber cementum develop unpredictably in time, space, and thickness, particular root surface areas covered with cellular mixed stratified cementum may temporarily remain unsupported by periodontal fibers [37].

Reparative cementum is a new cementum deposited over the previously resorbed surface of the root. In physiological condition, it is deposited on the root surface in accordance with tooth movement. The resorption of cementum is initiated by fracture of root, tooth luxation, inflammation, and excessive orthodontic forces. If the cause of the resorption of cementum is eliminated, the affected cementum could be filled with reparative cementum. There is a controversy on the formation of reparative cementum. The cellular cementum is formed in the fast repair process, and the acellular cementum is filled in the slow one. The initial reparative cementum is often an acellular type, but the continued repair process of the resorption cavity occurs with rapid formed cellular cementum [42].

5.4.2 Composition and Structure of Periodontal Ligament

Periodontal ligament is the soft, specialized fibrous connective tissue located between the cementum and bone lining the alveolus in which the roots of the teeth are embedded. It extends from the base of the gingival mucosa to the bottom of the bony socket. It ranges in width from 0.15 to 0.38 mm, with its thinnest portion around the middle third of the root. Principal fibers that are the sizeable majority of collagen fibrils in the periodontal ligament bridged the periodontal space that lies between the tooth and its alveolar bone. The extremities of collagen fiber bundles are embedded in cementum or alveolar bone, and the embedded portion is referred to as Sharpey's fibers [2]. The periodontal ligament supports the teeth in their sockets and permits them to withstand the considerable forces of mastication. In addition, it is a cell reservoir for tissue homeostasis and regeneration. Mechanoreceptors situated in the periodontal ligament provide detailed information about intensive and spatial aspects of tooth loads, which support the neural control of masticatory forces [43].

The periodontal ligament is derived from the dental sac that is the dense fibrous layer of mesenchyme surrounding the enamel organ and dental papilla. At the beginning, the ligament space is occupied by an unorganized connective tissue. Then, the tissue is remodeled, and the transitional extracellular matrix is converted into a fiber system organized as bundles that extend between the bone and cementum surfaces. The reorganized tissue can now establish continuity across the ligament space and secure to attach between the tooth and bone. Eruptive tooth movement and the establishment of occlusion then further modify this initial attachment system [2].

The periodontal ligament consists of cells and an extracellular compartment comprising collagenous and noncollagenous matrix components. It has a high cellular component that consists of fibroblasts, epithelial cell rests of Malassez, undifferentiated mesenchymal cells, monocytes and macrophages, osteoblasts and osteoclasts, and cementoblasts [2]. Fibroblasts are the principal cells of the periodontal ligament and aligned along the general direction of the fiber bundles. Although all fibroblasts look alike microscopically, heterogeneous cell populations exist between different connective tissues and also within the same connective tissue. The fibroblasts of the periodontal ligament are featured by their rapid turnover of the extracellular compartment, such as collagen. The collagen fibrils of the bundles are continuously being remodeled by the fibroblasts, which are capable of simultaneously synthesizing and degrading collagen. The epithelial cell rests of Malassez are a part of the periodontal ligament cells, which are isolated clusters of residual cells from Hertwig's epithelial root sheath (HERS). The function of these rests is unclear, but they could be involved in periodontal repair/regeneration. Undifferentiated mesenchymal cells or progenitor cells are important cells that produce new cells for the periodontal ligament, whereas the cells of the ligament in a steady state balance the proliferation by apoptotic cell death [44]. Also, the cells with stem cell characteristics have been isolated from the human periodontal ligament [45].

The extracellular matrix of periodontal ligament is composed of fibrous component and amorphous ground substance. The former is mainly composed of collagen fibers and the rest are elastic fibers, such as oxytalan fibers [46]. The predominant collagens of the periodontal ligament are relatively smaller than average diameter of type I, III, and XII, and it is believed to reflect the relatively short half-life of ligament collagen. The principal fibers are arranged in distinct fiber bundles of great majority of collagen fibrils in the periodontal ligament. Because each bundle resembles a spliced rope, individual strands can be continually remodeled even as the overall fiber maintains its architecture and function. Thus, the fiber bundles are able to adapt to the continual stresses placed on them. The extremities of the collagen fiber bundles are embedded in cementum or bone, and the embedded portion is referred to as Sharpey's fibers. Sharpey's fibers in primary acellular cementum are fully mineralized, whereas those in cellular cementum and bone are generally only partially mineralized at their periphery. Other fiber bundles (gingival ligament fibers) are found extending from the cervical region of a tooth to that of the adjacent tooth (transseptal ligament fibers) and in the gingival connective tissue. These, together with the main alveolodental ligament fibers, constitute the periodontal ligament-fiber system [2]. The collagen fibers resist against tensile strength, and their arrangement is adapted to the loading environment. The high rate of remodeling and renewal of periodontal connective tissue requires the orderly and specific removal of nonfunctional, denatured collagen fibrils followed by replacement with newly synthesized collagen. Fibroblasts and cementoblasts in the periodontium are responsible for the secretion and resorption of collagen during remodeling and turnover. The phagocytosis of collagen by fibroblasts is regarded as an important pathway for the physiological degradation of collagen in the periodontium [47]. When the periodontal inflammation continues, matrix metalloproteinases (MMPs) that are capable of degrading all kinds of extracellular matrix proteins are progressively secreted by periodontal ligament fibroblasts and destroy the function of periodontal ligament [48].

The elastic fiber system of the periodontal ligament is mainly represented by oxytalan fibers rather than by more highly developed elastic fibers. Oxytalan fibers are composed of 10–12 nm wide microfibrils without any amorphous elastin substance. They are oriented in an occluso-apical direction and topographically related to the periodontal vascular system [49]. Elaunin fibers may also be found in association with fiber bundles in the gingival ligament. Although their function has not been fully determined, the elasticity is thought to regulate vascular flow in relation to tooth function [2]. Several noncollagenous matrix proteins produced locally by resident cells or brought in by the circulation are found in the periodontal ligament; these include alkaline phosphatase, proteoglycans, and glycoproteins such as undulin, tenascin, and fibronectin [50]. The periodontal ligament ground substance has been estimated to be 70 % water and is thought to have a significant effect on the tooth's ability to resist stress loads. There is an increase in tissue fluids within the amorphous matrix of the ground substance in areas of injury and inflammation [2]. The periodontal space is progressively decreased in thickness with age [2].

Because the cellular component in periodontal ligament decreases with time, fibrous component in that relatively increases. The periodontal ligament is able to maintain its width approximately over time, whereas it is squeezed in between cementum and alveolar bone. The cell populations within the periodontal ligament secrete molecules that can regulate the extent of mineralization and prevent the fusion of tooth root with surrounding bone. Among these molecules, bone sialoprotein and osteopontin may contribute to establishing and maintaining an unmineralized periodontal ligament region. Matrix Gla protein that is an inhibitor of mineralization may also act to preserve the periodontal ligament width [2]. The periodontal ligament has also the ability to adjust to functional changes. When the functional demand increases, the width of the periodontal ligament can increase markedly in thickness. Conversely, a reduction in function leads to narrowing of the ligament and a decrease in number and thickness of the fiber bundles [2].

5.4.3 Composition and Structure of Alveolar Bone

Alveolar bone (alveolar process) is the part of the bone in either the maxilla or mandible containing the sockets (alveoli) for the teeth. The free edge of alveolar bone is called alveolar crest. The alveolar bone is derived from the cells of dental follicle and is a membranous bone that forms directly in membranous connective tissue instead of developing from cartilage. It consists of outer cortical plates (buccal, lingual, and palatal), a central spongiosa, and bone lining the alveolus. The outer cortical plates are also called cortical bone (compact bone). The cortical bone consists of surface layers (lamellae) supported by osteon (Haversian systems) that is the fundamental functional unit of cortical bone. They are generally thinner in the maxilla and thickest on the buccal aspect of mandibular premolars and molars. The central spongiosa is also called cancellous bone that is the spongy substance of bone. Compared to cortical bone, the cancellous bone is less dense and has a higher surface area that makes suitable for metabolic activity, e.g., exchange of calcium ions [2]. It is highly vascular and frequently contains red bone marrow that produces blood cells (hematopoiesis). Also, it has many trabeculae that are the primary anatomical and functional unit of cancellous bone and anastomosing bony spicules that are filled with bone marrow. The cancellous bone is absent in the region of the anterior teeth, and, in this case, the cortical bone and the bone lining the alveolus are fused together. The bone lining the socket is also called bundle bone, because Sharpey's fiber that is a terminal portion of principal fibers of periodontal ligament is inserted in it. The bundle bone is thin and particularly compact and appears as a line on dental x-rays.

Because the presence of tooth is essential for alveolar bone, the loss of tooth leads to the resorption of alveolar bone. Since the tooth is constantly making minor movements and alveolar bone must respond to the functional demand

placed on it by the forces of mastication, the bone of the socket wall is constantly remodeled, and its structural organization varies along the wall [51]. Thus, the local regulatory mechanisms are particularly important in the case of alveolar bone.

The alveolar bone consists of cells and an extracellular compartment comprising collagenous and noncollagenous matrix components. The cellular component consists of osteoblast, osteocyte, bone-lining cell, osteoclast, and so on [52]. Osteoblast is a cuboidal-shaped bone-forming cell that arranges the bone surface in a single layer. Osteocyte is an osteoblast that has embedded within the bone matrix. It occupies a bone lacuna and delivers slender cytoplasmic processes that make contact with processes of other osteocytes through the canaliculi. Bone-lining cells cover most quiescent bone surfaces in the adult skeleton [52]. It is transformed from osteoblasts, which may represent the final phenotype of the osteoblast lineage. They show flattened shape and contain a few cell organelles, and their connecting cell processes form an extensive homeostatic network with osteoblasts or osteocytes. Osteoclast is a large multinucleate cell that is mainly responsible for bone resorption. Differentiation of osteoclasts is regulated by soluble or membrane-bound molecules expressed by osteoblasts and stromal cells in bone microenvironment [53]. The composition of the extracellular matrix of alveolar bone appears to be similar to other bone tissues.

The bone matrix consists of two-thirds of inorganic components and one-third of organic matrix. The inorganic components are deposited in small, uniform, plate-like crystals of carbonated hydroxyapatite ($Ca_{10}[PO4]_6[OH]_2$). At the element scale, bone apatite nanocrystals exhibit a variety of substitutions and vacancies that make the Ca/P molar ratio distinct from the stoichiometric hydroxyapatite ratio of 1.67. The crystals in bone have a plate-like habit and are nanosized, with a length of ~20–50 nm and a width of 12–20 nm, depending on age and species [6]. Collagen comprises the major (>80–90 %) organic component in mineralized bone tissues. Type I collagen (>95 %) is the principal collagen, and, together with type V (<5 %) collagen, the type I collagen forms heterotypic fiber bundles that provide the basic structural integrity of connective tissues [52]. Other proteins, including proteoglycans and acidic glycosylated and non-glycosylated proteins, associate with and regulate the formation of collagen fibrils and mineral crystals. Osteocalcin and bone sialoprotein are essentially unique to mineralized tissues. Bone modeling and bone remodeling are mechanisms that regulate the growth and development of skeletal tissue.

Bone modeling is the deposition of mineralized tissue at developmentally determined sites and change bone size and shape. Bone remodeling involves absorption of bone tissue and simultaneous deposition of new bone. It maintains the structural integrity of the skeleton and helps its metabolic functions as a store of calcium and phosphorus. The highly regulated steps of bone remodeling depend on the interactions of two cell lineages, the osteoblastic and the osteoclastic lineage [54]. The number of osteoblasts decreases as the bone surface area and volume decrease with aging.

5.4.4 Composition and Structure of Gingiva

Gingiva consists of a mucosa that overlies a part of the alveolar bone and the crowns of unerupted teeth and encircles the necks of teeth that have erupted. It provides a seal to protect the body from attack by foreign bodies and toxins including infections by oral bacteria. It is also a masticatory mucosa that protects the areas frequently utilized for the chewing of food and supports the tooth. Anatomically, the gingiva is divided into free gingiva and attached gingiva [55]. The free gingiva is the part of the gingiva that surrounds the tooth and is not directly attached to the tooth surface. The attached gingiva is the part that is firm, tough, and bound to the underlying cementum and alveolar bone.

Histologically, the gingiva is consisted of gingival epithelium and gingival connective tissue [2]. The gingival epithelium is a stratified squamous epithelium and is divided into external marginal epithelium (EE) and internal marginal epithelium (IE). The external marginal epithelium (EE) covers the gingiva facing the oral cavity, while the inner marginal epithelium (IE) covers the gingiva facing the tooth. It normally contains polymorphonuclear leukocytes and monocytes that pass from the connective tissue. The EE plays a role of masticatory mucosa. The IE is subdivided into sulcular epithelium and junctional epithelium. The sulcular epithelium lines the gingival sulcus that is an area of potential space between a tooth and the surrounding sulcular epithelium. It is apically bounded by the junctional epithelium and meets the epithelium of the oral cavity at the height of the free gingival margin and is nonkeratinized. The junctional epithelium (JE) that arises from the reduced enamel epithelium is a nonkeratinized stratified squamous epithelium with a very high rate of cell turnover. It lays the base of the gingival sulcus and attach to the enamel of the crown by means of a structural complex called the epithelial attachment. The junctional epithelium plays a crucial role since it essentially seals off periodontal tissues from the oral environment. Periodontal disease sets in when the structure of the junctional epithelium starts to fail [2].

The gingival connective tissue is composed of gingival fibers, ground substance, and cells, including neural and vascular elements. It is composed of a dense, predominantly collagenous matrix that contains collagen fibers. Most of the fibers are composed of collagen, with minor contributions from elastic fibers and oxytalan fibers. The ground substance occupies the space between cells, fibers, and neurovascular elements. Its major constituents are water, glycoproteins, and proteoglycans. The ground substance permits the diffusion of biological substances between various structural elements [2]. The number of leukocyte, lymphocyte, and plasma cell increases when inflammation of gingiva is present.

References

1. Ash MM, Nelson SJ (2010) Wheeler's dental anatomy, physiology, and occlusion, 9th edn. Saunders, St. Louis
2. Nanci A, Bosshardt DD (2006) Structure of periodontal tissues in health and disease. Periodontol 40:11–28

3. Baldassarri M, Margolis HC, Beniash E (2008) Compositional determinants of mechanical properties of enamel. J Dent Res 87:645–649
4. Park S, Wang DH, Zhang D, Romberg E, Arola D (2008) Mechanical properties of human enamel as a function of age and location in the tooth. J Mater Sci Mater Med 19:2317–2324
5. De Medeiros RC, Soares JD, De Sousa FB (2012) Natural enamel caries in polarized light microscopy: differences in histopathological features derived from a qualitative versus a quantitative approach to interpret enamel birefringence. J Microsc 246:177–189
6. Boskey AL (2007) Mineralization of bones and teeth. Elements 3:385–391
7. Nelson DG, Featherstone JD (1982) Preparation, analysis, and characterization of carbonated apatites. Calcif Tissue Int 34(Suppl 2):S69–S81
8. Uskokovic V, Khan F, Liu H, Witkowska HE, Zhu L, Li W, Habelitz S (2011) Hydrolysis of amelogenin by matrix metalloprotease-20 accelerates mineralization in vitro. Arch Oral Biol 56:1548–1559
9. Boyde A (1997) Microstructure of enamel. Ciba Found Symp 205:18–27; discussion -31
10. Lacruz RS, Smith CE, Kurtz I, Hubbard MJ, Paine ML (2013) New paradigms on the transport functions of maturation-stage ameloblasts. J Dent Res 92:122–129
11. Fang PA, Lam RS, Beniash E (2011) Relationships between dentin and enamel mineral at the dentino-enamel boundary: electron tomography and high-resolution transmission electron microscopy study. Eur J Oral Sci 119(Suppl 1):120–124
12. Zhao J, Liu Y, Sun WB, Zhang H (2011) Amorphous calcium phosphate and its application in dentistry. Chem Cent J 5:40
13. Wuthier RE, Rice GS, Wallace JE Jr, Weaver RL, LeGeros RZ, Eanes ED (1985) In vitro precipitation of calcium phosphate under intracellular conditions: formation of brushite from an amorphous precursor in the absence of ATP. Calcif Tissue Int 37:401–410
14. Wang L, Nancollas GH (2008) Calcium orthophosphates: crystallization and dissolution. Chem Rev 108:4628–4669
15. Cuisinier FJ, Steuer P, Senger B, Voegel JC, Frank RM (1992) Human amelogenesis. I: High resolution electron microscopy study of ribbon-like crystals. Calcif Tissue Int 51:259–268
16. Moradian-Oldak J (2012) Protein-mediated enamel mineralization. Front Biosci 17:1996–2023
17. Salama AH, Zaki AE, Eisenmann DR (1987) Cytochemical localization of Ca2+-Mg2+ adenosine triphosphatase in rat incisor ameloblasts during enamel secretion and maturation. J Histochem Cytochem 35:471–482
18. Moradian-Oldak J (2001) Amelogenins: assembly, processing and control of crystal morphology. Matrix Biol 20:293–305
19. Driessens FC, Heijligers HJ, Borggreven JM, Woltgens JH (1985) Posteruptive maturation of tooth enamel studied with the electron microprobe. Caries Res 19:390–395
20. Sabel N (2012) Enamel of primary teeth – morphological and chemical aspects. Swed Dent J Suppl 222:1–77, 2p preceding i
21. Daculsi G, Kerebel B (1978) High-resolution electron microscope study of human enamel crystallites: size, shape, and growth. J Ultrastruct Res 65:163–172
22. Pashley DH (1996) Dynamics of the pulpo-dentin complex. Crit Rev Oral Biol Med 7:104–133
23. Marshall GW Jr, Marshall SJ, Kinney JH, Balooch M (1997) The dentin substrate: structure and properties related to bonding. J Dent 25:441–458
24. Kinney JH, Marshall SJ, Marshall GW (2003) The mechanical properties of human dentin: a critical review and re-evaluation of the dental literature. Crit Rev Oral Biol Med 14:13–29
25. Goldberg M, Kulkarni AB, Young M, Boskey A (2011) Dentin: structure, composition and mineralization. Front Biosci 3:711–735
26. Kinney JH, Pople JA, Marshall GW, Marshall SJ (2001) Collagen orientation and crystallite size in human dentin: a small angle X-ray scattering study. Calcif Tissue Int 69:31–37
27. Schilke R, Lisson JA, Bauss O, Geurtsen W (2000) Comparison of the number and diameter of dentinal tubules in human and bovine dentine by scanning electron microscopic investigation. Arch Oral Biol 45:355–361

28. Mjor IA, Nordahl I (1996) The density and branching of dentinal tubules in human teeth. Arch Oral Biol 41:401–412
29. Thesleff I, Keranen S, Jernvall J (2001) Enamel knots as signaling centers linking tooth morphogenesis and odontoblast differentiation. Adv Dent Res 15:14–18
30. Couve E, Osorio R, Schmachtenberg O (2013) The amazing odontoblast: activity, autophagy, and aging. J Dent Res 92:765–772
31. Kawasaki K, Weiss KM (2008) SCPP gene evolution and the dental mineralization continuum. J Dent Res 87:520–531
32. Anderson HC (1995) Molecular biology of matrix vesicles. Clin Orthop Relat Res 314:266–280
33. Linde A (1985) The extracellular matrix of the dental pulp and dentin. J Dent Res 64 Spec No, 523–529
34. Goldberg M, Smith AJ (2004) Cells and extracellular matrices of dentin and pulp: a biological basis for repair and tissue engineering. Crit Rev Oral Biol Med 15:13–27
35. Gronthos S, Mankani M, Brahim J, Robey PG, Shi S (2000) Postnatal human dental pulp stem cells (DPSCs) in vitro and in vivo. Proc Natl Acad Sci U S A 97:13625–13630
36. Ingle JI, Barkland LK (2002) Endodomtics. BC Decker, London
37. Bosshardt DD, Selvig KA (1997) Dental cementum: the dynamic tissue covering of the root. Periodontol 2000(13):41–75
38. Grzesik WJ, Narayanan AS (2002) Cementum and periodontal wound healing and regeneration. Crit Rev Oral Biol Med 13:474–484
39. Srivicharnkul P, Kharbanda OP, Swain MV, Petocz P, Darendeliler MA (2005) Physical properties of root cementum: Part 3. Hardness and elastic modulus after application of light and heavy forces. Am J Orthod Dentofac Orthop 127:168–176; quiz 260
40. Liu HW, Yacobi R, Savion N, Narayanan AS, Pitaru S (1997) A collagenous cementum-derived attachment protein is a marker for progenitors of the mineralized tissue-forming cell lineage of the periodontal ligament. J Bone Miner Res 12:1691–1699
41. Hammarstrom L (1997) Enamel matrix, cementum development and regeneration. J Clin Periodontol 24:658–668
42. Owman-Moll P, Kurol J (1998) The early reparative process of orthodontically induced root resorption in adolescents–location and type of tissue. Eur J Orthod 20:727–732
43. Johansson AS, Svensson KG, Trulsson M (2006) Impaired masticatory behavior in subjects with reduced periodontal tissue support. J Periodontol 77:1491–1497
44. Lekic P, McCulloch CA (1996) Periodontal ligament cell population: the central role of fibroblasts in creating a unique tissue. Anat Rec 245:327–341
45. Seo B-M, Miura M, Gronthos S, Mark Bartold P, Batouli S, Brahim J, Young M, Gehron Robey P, Wang CY, Shi S (2004) Investigation of multipotent postnatal stem cells from human periodontal ligament. Lancet 364:149–155
46. Montes GS (1996) Structural biology of the fibres of the collagenous and elastic systems. Cell Biol Int 20:15–27
47. Yajima T, Sakakura Y, Tsuruga E, Hirai T, Ikeda Y, Fujii S, Shide N (1999) Collagen-phagocytosing ability of periodontal osteoblasts at the bone surface. Arch Histol Cytol 62:17–25
48. Chang YC, Yang SF, Lai CC, Liu JY, Hsieh YS (2002) Regulation of matrix metalloproteinase production by cytokines, pharmacological agents and periodontal pathogens in human periodontal ligament fibroblast cultures. J Periodontal Res 37:196–203
49. Staszyk C, Gasse H (2004) Oxytalan fibres in the periodontal ligament of equine molar cheek teeth. Anat Histol Embryol 33:17–22
50. Zhang X, Schuppan D, Becker J, Reichart P, Gelderblom HR (1993) Distribution of undulin, tenascin, and fibronectin in the human periodontal ligament and cementum: comparative immunoelectron microscopy with ultra-thin cryosections. J Histochem Cytochem 41:245–251
51. Goldring SR (2003) Inflammatory mediators as essential elements in bone remodeling. Calcif Tissue Int 73:97–100

52. Sodek J, McKee MD (2000) Molecular and cellular biology of alveolar bone. Periodontology 2000(24):99–126
53. Suda T, Takahashi N, Udagawa N, Jimi E, Gillespie MT, Martin TJ (1999) Modulation of osteoclast differentiation and function by the new members of the tumor necrosis factor receptor and ligand families. Endocr Rev 20:345–357
54. Raisz LG (1999) Physiology and pathophysiology of bone remodeling. Clin Chem 45:1353–1358
55. Lang NP, Loe H (1972) The relationship between the width of keratinized gingiva and gingival health. J Periodontol 43:623–627

Part II
Metallic Biomaterials

Chapter 6
Nickel-Free High-Nitrogen Stainless Steel

Yasuyuki Katada and Tetsushi Taguchi

Abstract High-nitrogen austenitic stainless steel (HNS) developed in NIMS shows high strength, high corrosion resistance, and nonmagnetic properties. This material was originally developed as a resource-saving type of HNS available in the seawater. It is well known that the nickel content of HNS can be reduced with increasing nitrogen content. In addition, it was found, derivatively, that nickel-free HNS was successfully produced with further increasing the nitrogen content, which is applicable to the field of biomedical area as an anti-nickel allergy biomaterial.

In this chapter, the following items are described such as production of HNS, mechanical properties, formability of HNS, corrosion properties, and the mechanism of the improvement of corrosion properties by addition of nitrogen. Finally, as one of the applications of HNS, R&D of coronary stent is introduced in terms of biocompatibility of HNS as well as in vivo test using the stents deployed into pigs' coronary arteries. It is found that the stent made from nickel-free high-nitrogen stainless steel shows not only very excellent biocompatibility but also outstanding restenosis suppressant effect.

Keywords Crevice corrosion • Ni-free high-nitrogen steel • Biometals • Nickel allergy • Biocompatibility • DES • Restenosis • Coronary stent • Neointima

6.1 Introduction

Since nitrogen (N) in steel is an effective element to improve both strength and corrosion properties, a lot of research and development on nitrogen-bearing steels has been conducted so far. From a historical viewpoint, Mn-Cr series steels have been

Y. Katada (✉)
Academic Collaboration Office, National Institute for Materials Science,
1-2-1, Sengen, Tsukuba, Ibaraki 305-0047, Japan
e-mail: KATADA.Yasuyuki@nims.go.jp

T. Taguchi
Biomaterials Unit, MANA, National Institute for Materials Science,
1-1, Namiki, Tsukuba, Ibaraki 305-0044, Japan
e-mail: Taguchi.Tetsushi@nims.go.jp

M. Niinomi et al. (eds.), *Advances in Metallic Biomaterials*, Springer Series
in Biomaterials Science and Engineering 3, DOI 10.1007/978-3-662-46836-4_6

investigated for the development of high-nitrogen steel due to the high-nitrogen solubility of manganese.

A lot of high-nitrogen austenitic stainless steel of nonmagnetic property has been investigated aiming for practical realization such as retail ring for generator retaining rings, drill collar for oil digging rig, and so on [1–3]. Recently nitrogen content of high-nitrogen austenitic Mn-Cr stainless steel is coming up to 0.7 mass%.

In 1992, high-nitrogen stainless steel of implants for surgery was registered in ISO (ISO 5832–9:1992, Implants for surgery——Metallic materials——Part 9: Wrought high-nitrogen stainless steel), of which the main chemical compositions (mass%) were Ni, 9–11; Cr, 19.5–22; Mo, 2–3; Nb, 0.25–0.8; and N, 0.25–0.5 [4]. The maximum nitrogen content of this material is 0.5 mass%, and 11 mass% in maximum of Ni was contained. Judging from the chemical compositions, this material could be regarded as nitrogen-added conventional austenitic stainless steel.

Worldwide research on high-nitrogen steel has a long history and has been conducted very actively so far [5–11]. The past conferences held at Lille, France (1988); Aachen, Germany (1990); Kiev, Ukraine (1992); Kyoto, Japan (1995); Helsinki and Stockholm, Finland and Sweden (1998); Chennai, India (2002); Zurich, Switzerland (2003); Oostende, Belgium (2004); Jiuzhaigou Valley, China (2006); Moscow, Russia (2009); Chennai, India (2012); and Hamburg, Germany (2014), showed the extraordinary developments in the HNS materials and their wide applications in many industrial sectors. High-nitrogen steels have been proven today to possess excellent corrosion and mechanical properties combined with good wear and abrasion resistance. They are finding increasing applications in power plants, chemical process industries, transportation, oil, gas and fertilizer industries, pulp and paper, food processing, civil construction, etc. The growing demands for the successive conferences show the importance of this new class of materials emerging globally in the recent past for a variety of new applications. The present conference in this line also provides a forum for the engineers, metallurgists, and scientists in academic, industrial, and research institutions to exchange their latest findings and update their professional knowledge for further developments.

As a representative example of research on high-nitrogen steel in Japan, research and development of high-nitrogen steel for anti-corrosion material in seawater, which was conducted as one of the main themes of Ultra-Steel Project (1997–2006) in National Institute for Materials Science (NIMS) [5,6], can be raised. The concept of R&D of this highly corrosion-resistant material is to develop super-stainless class material without increasing alloying elements too much such as Cr, Ni, and Mo, and at the same time, purification of material was another important factor employed.

6.2 Production of HNS

6.2.1 Metallurgy of HNS

In this session, the basic concept of how to produce nitrogen-bearing steel under atmospheric condition will be described followed by a pressurized ESR method.

In the case of alloying nitrogen, of which the standard state is gas, to melted iron or steel, the following two factors should be taken into account.

a. The solubility of nitrogen in the liquid metal
b. Nitrogen behavior in the solidification process

As for the nitrogen solubility in the liquid metal, much research has been reported for over a half century so far. Table 6.1 shows the historical progress of high-nitrogen steel production technology. Table 6.2 shows a list of representative high-nitrogen steels developed in the world.

Since the nitrogen solubility of pure iron is basically very low under atmospheric condition, in order to raise the nitrogen solubility in Fe matrix, some specific elements, which increase the nitrogen solubility, should be alloyed. Figure 6.1 shows the effects of alloying elements on the nitrogen solubility; specific elements such as V, Nb, Cr, Ta, and Mn are effective elements to raise the nitrogen solubility in steels [7].

The nitrogen solubility of Fe-Cr alloy under atmospheric condition is widely used as described in the following equation.

$$\log[\%N] = -518/T - 1.063 + 0.046[\%Cr] - 0.00028[\%Cr]2 + 0.02[\%Mn] - 0.007[\%Ni] - 0.048[\%Si] + 0.12[\%O] - 0.13[\%C] + 0.011[\%Mo] - 0.059[\%P] - 0.007[\%S]$$

Figure 6.2 shows the relation between the nitrogen solubility of Fe-Cr alloy and temperature. From the liquid metal condition, primary ferrite is solidified with decreasing temperature, of which nitrogen solubility is very low, while in the austenitic phase at lower temperature, the nitrogen solubility is strikingly increasing with decreasing temperature. Therefore, austenitic phase is a very effective factor in order to produce high-nitrogen steel. It is also necessary to use pressurized electroslag remelting (ESR) method as described in the next section.

Table 6.1 The historical progress of high-nitrogen steels

Year	Fabrication technology/facilities
1950s	Pressurized melting technology
1960s	Pressurized ESR furnace (Lab-scale, Bohler)
	Pressurized plasma melting furnace (Patton Research Institute)
1970s	Pressurized ESR furnace (Bohler, 1–2 t)
1980s	First mass production by pressurized ESR furnace (INTECO/LEYBOLD, 10–20 t)
1990–2000s	PAR, ESPR, PESR etc (10–20 t)

Table 6.2 The list of representative HNS developed in the world (mass%)

Alloys	Standards UNS/EN	Cr	Ni	Mo	Mn	N	Others	Makers
P900		19	0.42	0.07	19.06	0.57		VSG, Essen
Nicrofer3033	R20033 2.4700(EN)	33	30	1.45	0.74	0.38		Krupp VDM
Nicrofer5921		20	58	20	0.16	0.09		Krupp VDM
Cronidur30		15.5	–	1.02	–	0.38	Si, C	VSG, Essen
Nitronic40	521600 N08926 1.3840(EN)	20	7	–	9	0.15		Arm co
Cronifer 1925		20	25	6.2	–	0.2		Krupp VDM
Cromanite		19	–		10	0.5		Columbus & Nitrifer AG
Nitrinox	–	24	–	0-4	20	<1.20	Nb, V, Ti	Nitrofer AG
Am agn it 3947	1.3947 (EN)	23	17	3	6	0.4	Nb	KTN Thyssen
934LN	–	20	15	4.5	10	0.4		Avesta
Safurex		29	6.6	2.2		0.4		Sandvik
AL-6XN	N08367	20	24	6.3		0.22		Allegheny Ludlum
DP3	S31260	25	7	3		0.15	W	Sumitomo
Ferralim 255	S32550	25	6	3		0.15	Cu	Langley
654SMO	S32654	24	22	7.3	3	0.5		Avesta

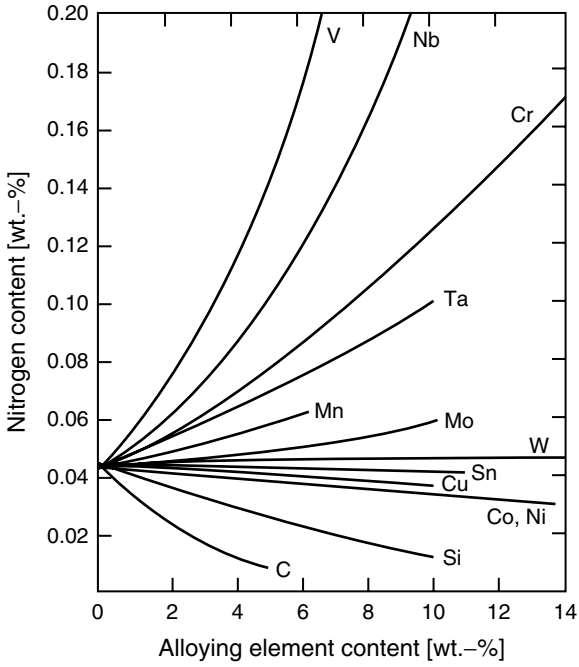

Fig. 6.1 Effects of alloying elements on the nitrogen solubility of iron-based alloy under 1 atm, 1,600°C (Reprinted from Ref. [7] Copyright 1968, AIME)

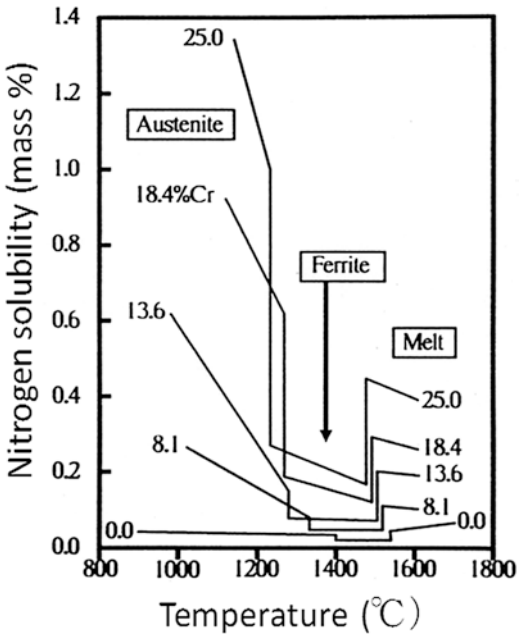

Fig. 6.2 Nitrogen solubility of Fe-Cr alloy under 1 atm, in the equilibrium state (Reprinted from Ref. [3]. Copyright 1990, Verlageisen)

6.2.2 Pressurized ESR Method

The technology and facility associated with pressurized electroslag remelting (ESR) were firstly invented in Austria and completed in Germany after long research [1–3]. The chemical compositions of the final ingot produced using a pressurized ESR method were determined by the combination of primary electrode and that of nitride or ferro-nitride under pressurized conditions.

A pressurized electroslag remelting furnace was developed for the first time in Japan, which is available for both the nitrogen alloying and purification of ingot, and successfully fabricated high-nitrogen steel without addition of manganese, which will cause impurity introduction to the ingot [5–7].

Basic specifications of the pressurized electroslag remelting furnace installed are as follows: ingot size, 20 kg (in case of steel); Cu crucible; AC current in max, 3,000A; and maximum nitrogen gas pressure, 5 MPa. Two types of basic alloys for high-nitrogen steels are Fe-23 %Cr-4 %Ni-2 %Mo and Fe-23 %Cr-2 %Mo. Phase diagram for these alloys calculated by a thermodynamic calculation is shown in Fig. 6.3. From this figure it is suggested that if even the nickel content is low, high-nitrogen steel with single austenitic phase would be available in the case of nitrogen content higher than 1 mass%. Furthermore, Nickel-free high-nitrogen steel would be available in the case of nitrogen content higher than 1.2 mass%.

Powder of Fe-Cr-N was used as nitrogen source for high-nitrogen steel. Furnace flux used in this process was the combination of CaF_2, CaO, and Al_2O_3. All necessary flux was installed in the furnace before starting to melt.

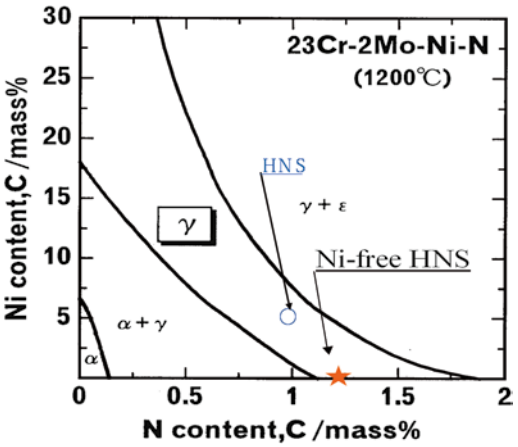

Fig. 6.3 Phase diagram of HNS calculated by thermodynamic method

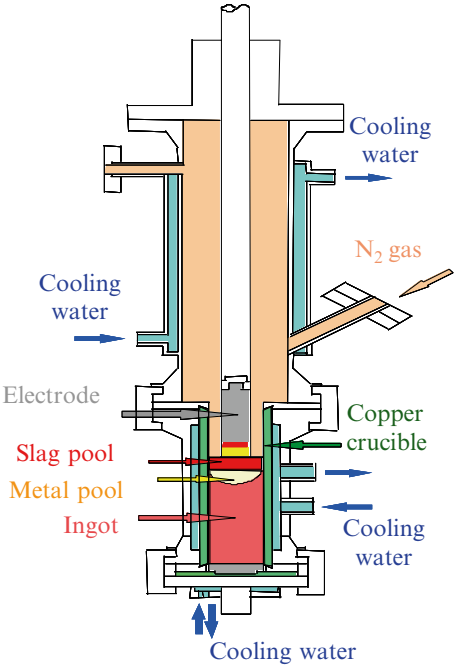

Fig. 6.4 Schematic diagram of pressurized electroslag remelting furnace

Figure 6.4 shows the schematic diagram of the pressurized ESR furnace developed in NIMS. The concept of how to fabricate high-nitrogen steel by pressurized ESR method is shown in Fig. 6.5. Primary electrode is energized by AC current through flux, which results in the flux being changed to the high-temperature liquid. Then primary electrode is melted in the high-temperature flux and goes down to Cu crucible below and is solidified to an ingot. Purified material is solidified into ingot through this process.

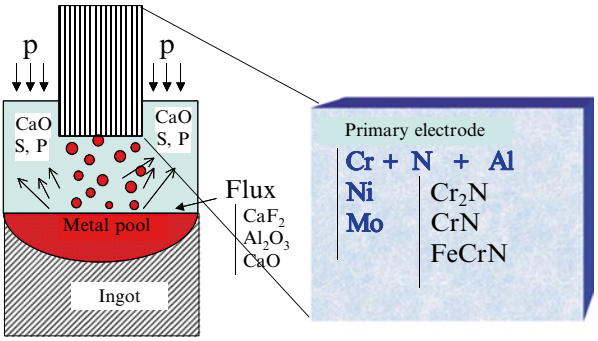

Fig. 6.5 Schematic principle of pressurized electroslag remelting furnace

6.2.3 Deoxidation Process

In general, if powder of ferro-chrome nitride was used as nitrogen source, the oxygen concentration of ingot is relatively high more than 100 ppm, since the oxygen pickup is inevitable to use powder ferro-chrome nitride.

In order to get an ingot with highly corrosion-resistant property, it is necessary to adopt deoxidation process. Aluminum or metallic calcium as deoxidation elements is effective.

6.3 Mechanical Properties of HNS

6.3.1 Material Strength of HNS

Figure 6.6 shows the comparison between elongation and tensile strength of the newly developed high-nitrogen steel (HNS) and those of commercial steels referred from the literature. These data of the 23 % Cr series of HNS were obtained after solution treatment. It is obvious from this figure that the elongation of the developed austenitic single phase HNS is almost equal to that of Type 304 stainless steel, while the tensile strength of HNS is located around 1,000–1,200 MPa.

Figure 6.7 shows the temperature dependence of the mechanical properties of HNS such as tensile stress, proof stress, elongation, and the reduction of area. The test material was 23 %Cr-4 %Ni-1 %N. After forging, hot working by caliber roll, tensile strengths of HNS were maintained as much as 1.5 times higher than those of Type 316 stainless steel in a wide range of temperature. The yield ratio (proof stress/tensile stress) of HNS varied from 0.5 to 0.6 for a wide range of temperatures.

It was interesting to note that the elongation and the reduction of area of HNS were almost equal to those of Type 316 stainless steel although HNS is a fairly high-strength material.

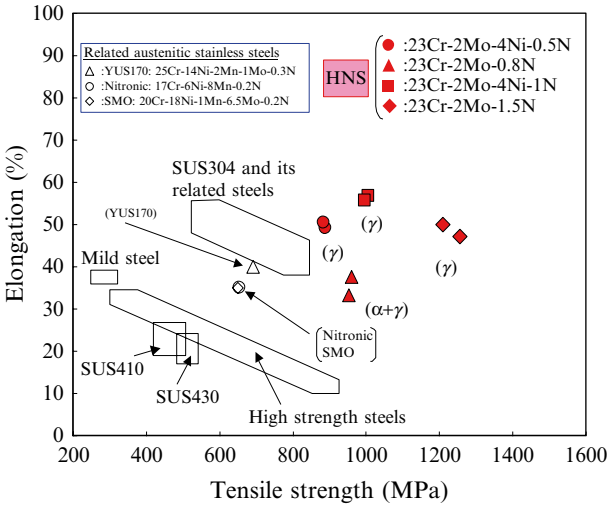

Fig. 6.6 Mechanical properties of HNS

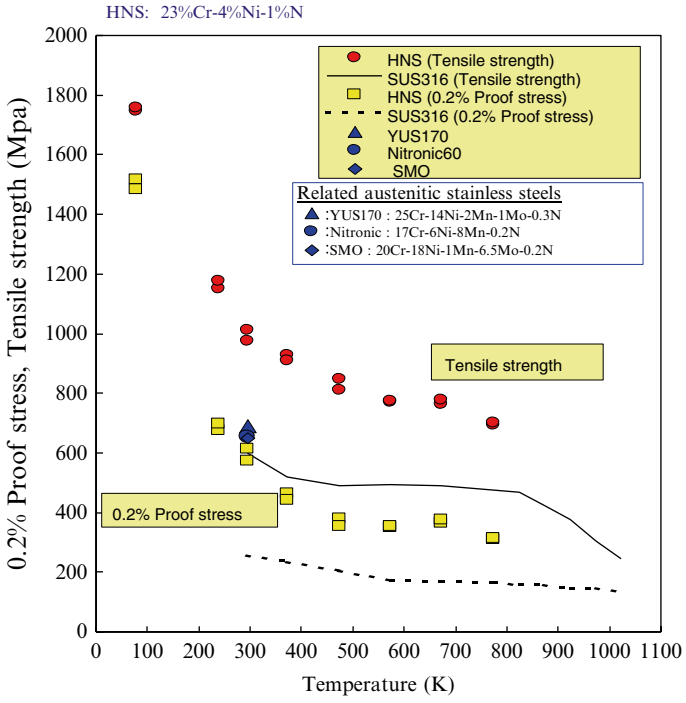

Fig. 6.7 Temperature dependence of mechanical properties of HNS

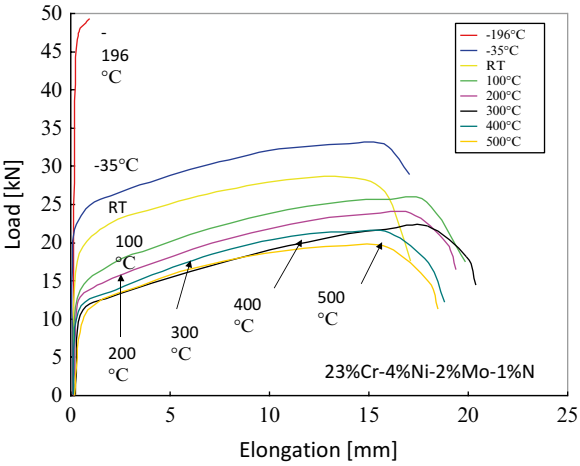

Fig. 6.8 Load-elongation curves of HNS in a wide range of wide temperature

Figure 6.8 shows tensile properties of HNS in a wide range of temperature. From this result, it is found that HNS shows remarkable work hardening behavior in a wide range of temperature from −35 to 500 °C, which means plastic forming of HNS is getting harder and harder with increasing deformation rate.

It is necessary to employ repeated processes of forming and tempering in order to remove the difficulty of plastic forming due to the work hardening property of HNS.

6.3.2 Formability of HNS

Figure 6.9 shows a typical microstructure of deformed HNS. Streaky patterns in the photo are actually pileup of dislocation along planes from 3-dimensional viewpoint, called planar dislocation. It seems that these planes are slipped easily corresponding to the outer deformation force.

Figure 6.10 shows an example of drawing wire made of HNS. The right-side photo indicates human hair of about 100 μm in diameter for comparison, while the left one indicates the HNS wire of about 50 μm in diameter. In order to form such thin tube and plate successfully, impurity such as oxides in the matrix should be removed well in advance, which might result in the origin of fracture in the middle of processing.

Figure 6.11 is an example of a thin plate of HNS (4 mass% Ni) of 100–120 mm in width and 0.08 mm in thickness. Although this plate was relatively hard and showed poor formability compared to those of conventional stainless steels, this thin plate was successfully fabricated by repeated processes between forming and tempering.

Figure 6.12 shows examples of thin-walled tubes (seamless pipe) made from Ni-free high-nitrogen stainless steel aiming for coronary stent. Bar samples of this

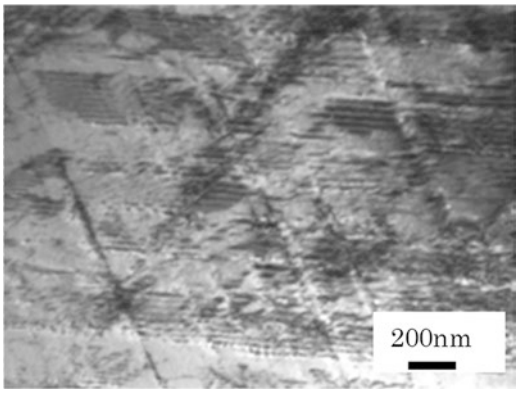

Fig. 6.9 Typical TEM micrograph of deformed HNS (after 20 % cold rolled)

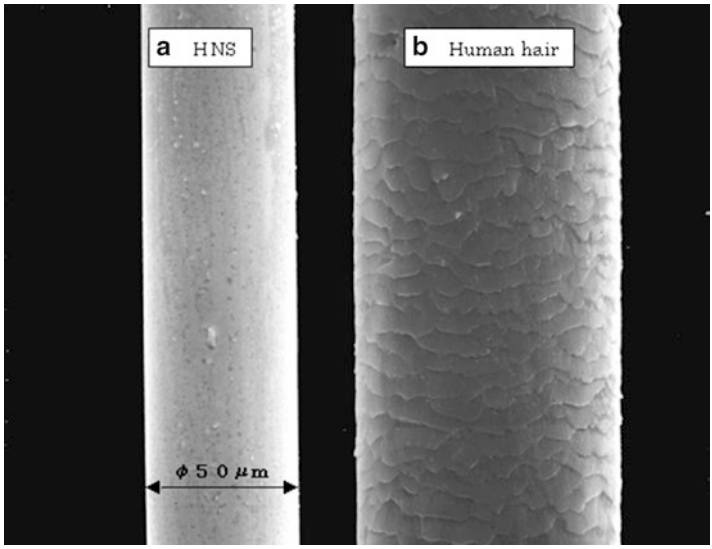

Fig. 6.10 HNS thin wire of 50 μm in diameter (**a**) HNS, (**b**) human hair of about 100 μm in diameter

material was machined to cylindrical pipes in the first step followed by drawing forming to thin-walled tubes down to 1.4 mm in outer diameter. As described in Sect. 6.5, biocompatible tests using the developed stent in vivo installed in pigs were successfully conducted.

Fig. 6.11 HNS thin plate of 80-100 μm in thickness

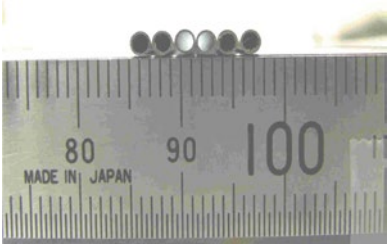

Fig. 6.12 Samples of HNS thin-walled tubes of 100 μm in thickness and 1,000-1,200 mm in length

6.3.3 Problems of HNS Produced by Future Pressurized ESR Method

As for the fabrication of austenitic high-nitrogen stainless steel by pressurized ESR method, the following two merits can be raised.

1. Since high-nitrogen solubility is also available under high-pressurized condition, it is not necessary to use specific element such as manganese to raise the nitrogen solubility, which causes the lowering corrosion property.
2. High-nitrogen stainless steel produced by pressurized ESR method possesses high-strength property, high corrosion resistant property, and nonmagnetic property, which are resulted from refining process by furnace flux and deoxidation process by Al or Ca.

Judging from the chemical compositions, high-nitrogen steel could be classified as austenitic stainless steel. Since high-nitrogen steel shows excellent properties, this material might be classified as a new material. There still exist issues to be solved in terms of application of high-nitrogen steel.

The most important issue to be solved from the viewpoint of practical application of high-nitrogen steel would be the establishment of formability technology to fabricate various products such as thin plates and small seamless pipes. In the case of high-nitrogen steel, of which nitrogen content is larger than 1 mass%, the Vickers hardness of HNS is around 300 even after solution treatment. Furthermore, this material shows remarkable work hardening behavior, which compels to repeat the forming and tempering treatment.

In addition, in order to solve the appropriate balance of strength and elongation of high-nitrogen steel, the establishment of microstructure control technology using a thermomechanical process and the refinement of grain size of materials are required.

6.4 Corrosion Properties

6.4.1 Pitting Corrosion and Crevice Corrosion

It is well known that the addition of nitrogen to steels or stainless steels results in the outstanding improvement of corrosion properties. The improvement of corrosion properties of steels and stainless steels by addition of nitrogen is especially striking in neutral chloride solution.

In recent research on pitting corrosion and crevice corrosion of high-nitrogen stainless steels, of which nitrogen concentrations are up to 0.3 mass% at most in austenitic stainless steels or dual-phase stainless steels.

6.4.2 Pitting Resistance Equivalent

For conventional ranking of stainless steels in terms of pitting resistance property, pitting resistance equivalent (PRE) or measure of alloying for resistance to corrosion (MARC) is widely used. It is well known that nitrogen is the element showing the maximum coefficient against PRE. PRE is a quite effective index from the viewpoint of engineering sense, while the physical and chemical meanings are not fully explicit yet.

The most popular description of PRE is probably described by the following Eq. (6.1) [12]:

$$\mathrm{PRE} = \mathrm{Cr}(\text{mass }\%) + 3.3\mathrm{Mo}(\text{mass }\%) + 16\mathrm{N}(\text{mass }\%) \tag{6.1}$$

In recent, for steels containing W [13]:

$$\mathrm{PRE} = \mathrm{Cr}(\text{mass }\%) + 3.3\left(\mathrm{Mo}(\text{mass }\%) + 0.5\mathrm{W}(\text{mass }\%)\right) + 16\mathrm{N}(\text{mass }\%) \tag{6.2}$$

The following Eq. (6.3) has been proposed by taking into account more sensitive effect of nitrogen [14]:

$$\mathrm{PRE} = \mathrm{Cr}(\text{mass }\%) + 3.3\left(\mathrm{Mo}(\text{mass }\%) + 0.5\mathrm{W}(\text{mass }\%)\right) + 30\mathrm{N}(\text{mass }\%) \tag{6.3}$$

Jargelius [15] proposed the following Eq. (6.4) taking into account of the synergistic effects of N and Mo, as well as the effect of minus ion of Mn:

$$\begin{aligned}\mathrm{PRE} = {} & \mathrm{Cr}(\text{mass }\%) + 3.3\mathrm{Mo}(\text{mass }\%) + 36\mathrm{N}(\text{mass }\%) + 7\mathrm{Mo}(\text{mass }\%) \\ & \times \mathrm{N}(\text{mass }\%) - 1.6\mathrm{Mn}(\text{mass }\%)\end{aligned} \tag{6.4}$$

Speidel et al. [16] have proposed MARC index described by the following Eq. (6.5) (Fig. 6.13):

$$\begin{aligned}\mathrm{MARC} = {} & \mathrm{Cr}(\text{mass }\%) + 3.3\mathrm{Mo}(\text{mass }\%) + 20\mathrm{N}(\text{mass }\%) + 20\mathrm{C}(\text{mass }\%) \\ & - 0.5\mathrm{Mn}(\text{mass }\%) - 0.25\mathrm{Ni}(\text{mass }\%)\end{aligned} \tag{6.5}$$

As shown in Fig. 6.12, MARC indicates good correlations with critical pitting corrosion temperature (CPT) and critical crevice corrosion temperature (CCT).

In addition, Gebeau and Brown [17] proposed 3.2 and 8 as the coefficients of N and Mo of high-nitrogen stainless steels of BioDur 108 and 734 for biomaterial use, respectively.

Although a variety of PRE indexes are widely used, they depend upon their chemical compositions and corrosive conditions, which means quite inconvenient to use widely.

It is well known that the addition of Mn to the steel results in the lowering corrosion resistant properties. Furthermore, positive effect of corrosion resistance by the addition of W and synergistic effects of N and Mo are also explicit by experimental background. An ideal PRE index should take into account of these factors moderately.

For example, a new index of ΣPRE has been newly proposed by the combination of Eqs (6.1) through (6.5), then the following Eq. (6.6) can be obtained,

$$\begin{aligned}S\mathrm{PRE} = {} & \mathrm{Cr}(\text{mass }\%) + 3.3\mathrm{Mo}(\text{mass }\%) + 0.5\mathrm{W}(\text{mass }\%)) + 7\mathrm{Mo}(\text{mass }\%) \times \mathrm{N}(\text{mass }\%) \\ & - 0.5\mathrm{Mn}(\text{mass }\%) + 20\mathrm{N}(\text{mass }\%) + 20\mathrm{C}(\text{mass }\%) - 0.25\mathrm{Ni}(\text{mass }\%)\end{aligned} \tag{6.6}$$

In general, stainless steels with PRE more than 40 are called super-stainless steels [18]. N might be an inevitable element to develop highly corrosion-resistant stainless steels.

Figure 6.14 shows a relationship between pitting resistance equivalent (PRE; Cr + 3Mo + 10 N) and pitting potential of nitrogen-bearing stainless steels in artificial seawater [19]. It was clearly seen that there was a positive correlation between PRE and pitting potential for all samples tested. Moreover, pitting potentials of stainless steels over 32 in PRE were not recognized below 0.9 V versus SCE.

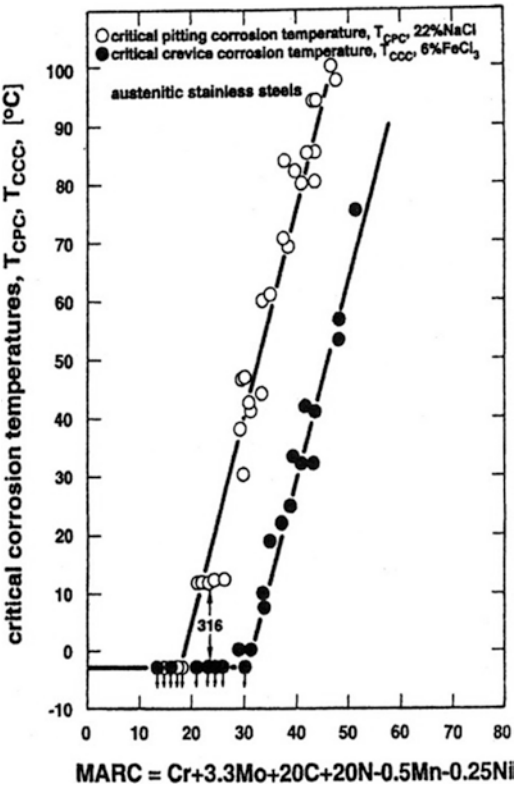

Fig. 6.13 Effect of composition on the critical temperatures for pitting corrosion and for crevice corrosion (Reprinted from Ref. [16], Copyright 2003, The Indian Institute of Metals)

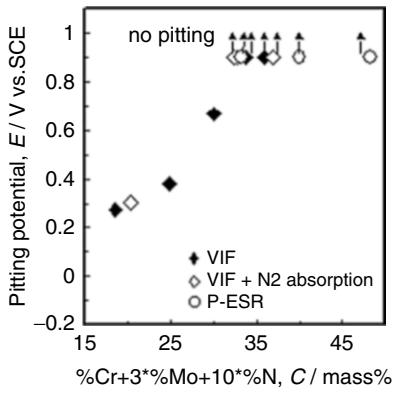

Fig. 6.14 Effect of composition on the critical temperatures for pitting corrosion and for crevice corrosion of nitrogen-bearing stainless steel in artificial seawater at the temperature of 45 °C

Figure 6.15 shows the effect of molybdenum content on pitting potential in artificial seawater. It was found that molybdenum was effective to improve pitting resistance. Then, ultrahigh-nitrogen-bearing steels showed good pitting resistance even molybdenum-free.

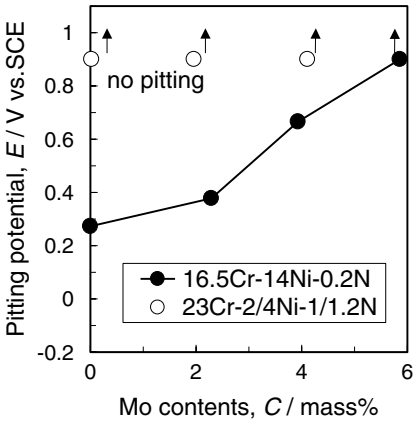

Fig. 6.15 Effect of molybdenum content on pitting potential of nitrogen-bearing stainless steel in artificial seawater at the temperature of 45 °C

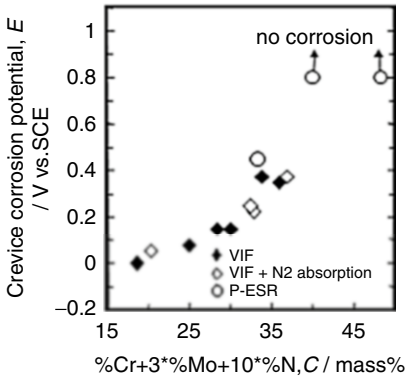

Fig. 6.16 Relationship between crevice corrosion resistance equivalent (%Cr + 3*%Mo + 10*%N in mass%) and crevice corrosion potential of nitrogen-bearing stainless steel in artificial seawater at the temperature of 35 °C

6.4.3 Crevice Corrosion Resistance of HNS

Crevice corrosion resistance of nitrogen-bearing stainless steels in artificial seawater was evaluated by electrochemical crevice corrosion tests. Figure 6.16 shows a relationship between crevice corrosion resistance equivalent (CRE; Cr +3Mo + 10 N, equal to PRE) and CCP in artificial seawater. It was seen that there was a positive correlation between CRE and CCP for all samples tested. Crevice corrosion of P2 (1 %N-2 %Mo steel in mass%) and P3 (1.2 %N-4 %Mo steel in mass%) was not recognized in any potential below 0.8 V versus SCE. It was also found that ultrahigh-nitrogen stainless steels containing molybdenum have superior crevice corrosion resistance.

Figure 6.17 shows the effect of molybdenum content on CCP of nitrogen-bearing stainless steel in artificial seawater at the temperature of 35 °C. Molybdenum improved crevice corrosion resistance for low nitrogen steels (16.5 %Cr-14 %Ni-

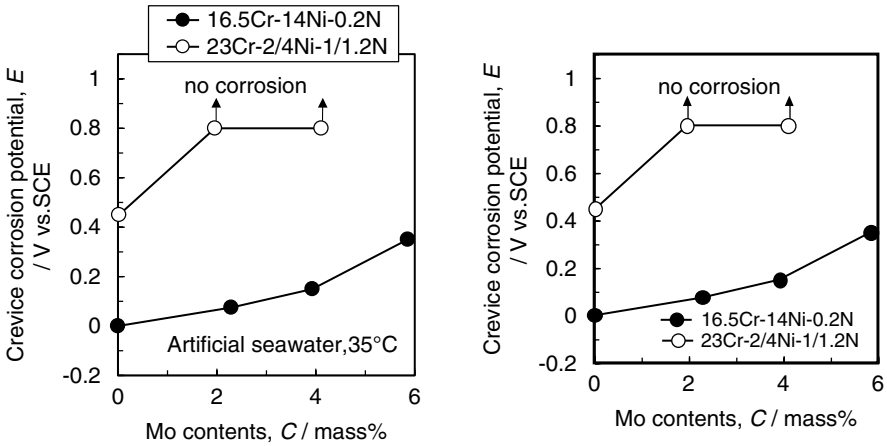

Fig. 6.17 Effect of molybdenum content on crevice corrosion potential of nitrogen-bearing stainless steel in artificial seawater at the temperature of 35 °C

0.2 %N) and ultrahigh-nitrogen steels (23 %Cr-2/4 %Ni-1/1.2 %N). Though ultrahigh-nitrogen-bearing steel of molybdenum-free showed good crevice corrosion resistance, that of molybdenum-bearing steels was better, indicating a synergistic effect between molybdenum and nitrogen.

6.4.4 Field Tests of High-Nitrogen Steel (HNS) in the Sea

Field tests of HNS were also carried out in the sea. The place of the field tests was located in a harbor in Chiba Prefecture, Japan, facing to the Pacific Ocean. Specimens used for the tests were multi-crevice specimens as shown in Fig. 6.18.

Field tests in the sea were carried out from February 2002 to March 2010 for up to 7 and half years. Field test samples were taken out after 0.5, 1, 2, 5, and 7.5 years. Seawater around the field tests was analyzed at each investigation in terms of temperature, pH, conductivity (Cond.), dissolved oxygen (DO), chlorine ion, and sulfate ion as shown in Table 6.3.

6.4.5 Results of Field Tests in the Sea

Figure 6.19 shows the appearance of a set of crevice specimen assembly in a rack. The specimen was a square with the side length of 50 mm and thickness of 5 mm. Figure 6.20 shows the appearance of the specimen assembly just after collecting from the sea for about 8 years. After removing the biofilm that covered the

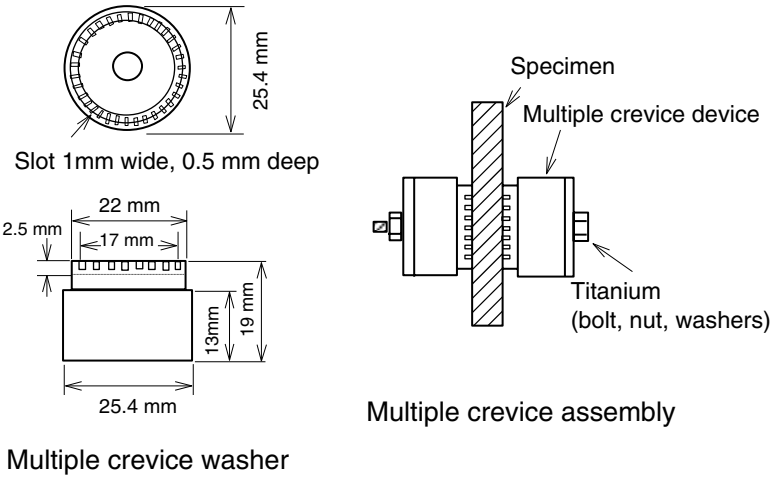

Fig. 6.18 Multi-crevice assembly of HNS

Table 6.3 Results of analysis of seawater components at the field tests in the seawater

Date of collection	Water temp. (Celsius)	pH	Cond. (micro--S/m)	DO (ppm)	Chlorine ion (ppm)	Sulfate ion (ppm)	Test duration (year)
February 7, 2002	13.5	8	48,300	9.2	19,800	2,780	0
July 31, 2002	27.0	8.0	43,900	8.8	19,200	2,800	0.5
February 7, 2003	11.3	8.2	43,900	8.6	19,500	2,280	1
February 5, 2004	10.5	8.1	38,600	9.6	19,800	1,880	2
March 1, 2007	12.0	8.1	37,000	9.7	20,030	2,610	5
March 8, 2010	12.3	8.0	47,800	10.9	22,200	3,310	8

specimens, no crevice corrosion on the specimen surface was observed at all. Titanium alloys were also tested under the same conditions for comparison with high-nitrogen stainless steel. As a result, both materials of high-nitrogen steel and titanium alloy showed high integrity in terms of corrosion resistance in the sea (Fig. 6.21).

6.4.6 Mechanism of the Improvement of Corrosion Properties by Addition of Nitrogen

Figure 6.22 shows ESCA (Electron Spectroscopy for Chemical Analysis) spectra before (as polished) and after crevice corrosion tests in corroded and noncorroded areas. Iron and chromium oxide formed at the as-polished surface. Since oxide films

Fig. 6.19 Specimen setup for the field test in the sea

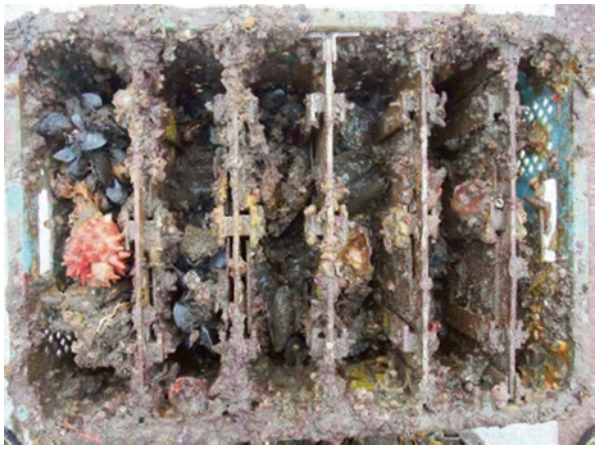

Fig. 6.20 The appearance of specimen setup collection after the period of 8 years

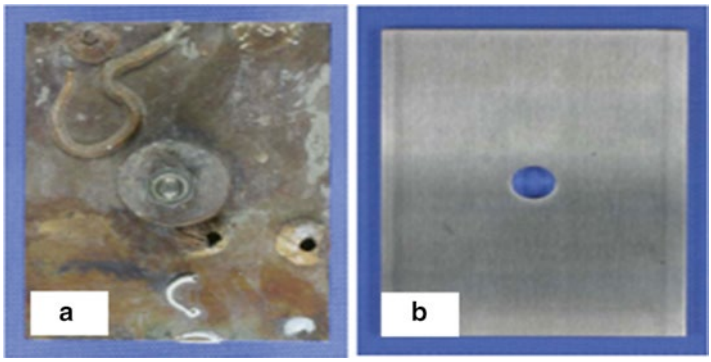

Fig. 6.21 The appearances of specimens tested for 8 years: (**a**) as collection, (**b**) after removing biofilm

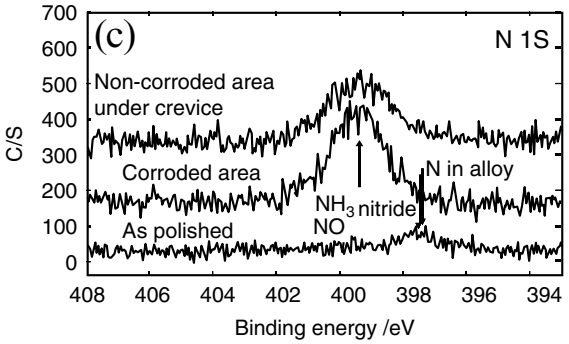

Fig. 6.22 ESCA spectra in terms of N1s recorded before (as polished) and after crevice corrosion test (corroded and noncorroded areas)

were very thin, the signal of the matrix metal was detected. At corroded areas, iron existed both as an oxide and as a metal, while chromium existed mainly as an oxide. On the other hand, iron and chromium formed an oxide at noncorroded areas. However, peak strength of metal was lower than that of as-polished areas. Considering the depth of X-ray irradiation, passive film forming at the surface was relatively thick. The peak at 397.5 eV indicates nitride or nitrogen elements in the alloy. Since 23 %Cr-4 %Ni-1 %N-0 %Mo steel has a single austenitic phase at 1,200 °C, nitrogen elements in the alloy are more likely. Signal around 400 eV is assumed to exist as N-O or NH_3 (NH_4^+) in both corroded and noncorroded areas.

As for the mechanism of the improvement of corrosion properties by addition of nitrogen, many theories *have been* proposed as follows:

1. Generation of ammonia by the dissolution of nitrogen suppresses the decrease of the pH value in the pit and facilitates repassivation of the surface of stainless steels [20]:

$$N + 3H_2O + 3e^- \rightarrow NH_3 + OH^- \tag{6.7}$$

   Baba et al. [21, 22]

$$M + N + 3H_2O + H^+ \rightarrow M(OH)_3 + NH_4^+ \tag{6.8}$$

   Yashiro et al. [23]
2. Stabilization of passivation film by the nitrogen enrichment at the interface between passivation film and metal substrate [24, 25]:

$$2CrN + 3H_2O_{ads} \rightarrow Cr_2O_3 + 2NH_3 \tag{6.9}$$

3. Suppression of corrosion by generation of nitrate ion caused by the dissolution of nitrogen [26, 27]:

$$NH_4^+ + 2H_2O \rightarrow HNO_2 + 7H^+ + 6e^- \tag{6.10}$$

$$HNO_2 + H_2O \rightarrow NO_3^- + 3H^+ + 2e^- \quad (6.11)$$

4. Preferred nitrogen enrichment after active pass reaction suppresses the movement of kink, resulting in the current rising in the pit [28].

According to many investigations of passivation film by XPS analyses, nitrogen is supposed to be enriched in the vicinity to the substrate at the interface of passivation film and metal substrate. As the existence form of nitrogen, NH_3^+, NH_4 [29, 31], or CrN [30, 31] has been reported so far. In addition, it has been also reported that the addition of nitrogen also resulted in the enrichment of Cr in the passivation film, which makes the passivation film more stable [32]. It is well known that there is a synergistic effect between N and Mo [33].

MoO_4^{2-} is firstly formed near the outside of the film, and it works as the electronic receptor to make hydroxide dehydrogenated. This leads to the enrichment of oxygen in the inside domain of the passivation film, resulting in the formation of stable CrO3/Cr2O3 protection oxide [34].

6.4.7 Stainless Steels as Biomaterials

6.4.7.1 Introduction

Metallic materials used for biomedical devices such as prosthesis or implants for bone fracture treatment require the characteristics of biocompatibility. Since the living organism recognizes the embedded metallic materials as foreign matters, metallic biomaterials should have the following properties: (1) biological reactions do not try to eliminate the embedded materials, (2) eluted substances from embedded materials should be small and harmless, and (3) wear particles generated between embedded materials themselves should be small.

In addition, since the bio-fluid is a quite serious corrosive environment, metallic biomaterials should have highly corrosion-resistant property. Biomaterials such as implant materials are sometime used under periodical stress; therefore, highly fatigue strength and fracture toughness are important factors to be provided.

Biomaterials or dental materials, metallic materials, ceramics, inorganic materials such as plastics, and inorganic materials are widely used. The merits of metallic materials are high strength, high stiffness, and high toughness.

As for implant materials used for orthopedics in terms of wire or plate, metallic materials are quite useful due to its high strength with moderate plastic deformation property. It is not an exaggeration to say that metallic materials are the most useful one and no alternatives are available. However, the toxicity of nickel ion in metallic materials such as stainless steels and Ni-Ti alloys is still an issue to be solved.

Metallic materials as biomaterials are getting more promising from the viewpoints of its high strength and high formability. The toxicity of these materials due

to the existence of nickel should be taken into account for material selection. In recent years, nickel-free materials such as titanium alloys, super-plastic shape memory alloys, Co-Cr alloys, and high-nitrogen steels have been intentionally investigated.

6.4.7.2 Metallic Allergy

Metallic materials used as implant devices have been recognized as basically harmless to the human body so far. For example, however, dental implant devices are usually placed in electrolytic solution at a temperature of 37°C such as saliva, where implants come into contact with some proteins that constructed tissue around as well as H_2S or acid produced by microbe reaction. In addition crevice corrosion at a limited area between the tooth and gingiva is easy to occur. Stress corrosion cracking due to the biting force and galvanic corrosion between different types of metallic materials is also taken into account. Therefore, the oral environment is a quite severe one from the viewpoint of corrosion conditions.

The symptom of the allergy to metal generally presents the flare with itch, swelling, and rash (dermatitis) including the blister formation, but it may sometimes cause a symptom such as asthma. The symptom of the metal allergy varies depending on the patient or contained allergen in the metal. In the case of dental metals implanted in the oral cavity even if the allergen is included, the symptoms sometimes appear rather far away or in systemic than in the oral cavity. Therefore, the patients often consult the dermatologist at first rather than the dentist. It is important for dermatologists to identify the cause of relevant symptoms appropriately.

Ni is a relatively cheap element and is widely used as a substrate of Au plating or Ni plating material. Although apparent corrosion behavior is not observed at the surface of alloys or the surface of Au plating, alloyed metallic ions are eluted in the solution. Especially the chlorine ions in the solution such as sweat or saliva facilitate the elution of Ni ions.

Therefore, allergic dermatitis is mainly observed in women, who are wearing metallic accessories such as pierce, earring, necklace, and so on.

6.4.7.3 Cause of Metal Allergy

The most reliable inspection for metal allergy is a patch test.

Patch test**ing** is a way of identifying whether a substance that comes into contact with the skin is causing inflammation of the skin or not. From literature survey, Ni, Cr, Co, and Hg show high positive rates, and Au and Pd show relatively high positive rates. Sn, Zn and Cu are prone to provocative reaction to the skin, there are needs to reduce the false positive rate caused by these metals. Local metal allergy is mainly caused by Ni, Cr, Co, and Au. In the case of dental metallic materials, Hg, Au, and Pd should be taken into account for inspection.

6.4.7.4 Evaluation Method (Dissolution Test)

An important property of metallic biomaterial to be provided is a superior corrosion resistance. In the case of severe environment such as bio-fluid of oral environment, metallic materials must exhibit high corrosion resistance. A well-known method for evaluating the corrosion property of the materials is dissolution test standardized in JIS T 0304 or ISO 10993.

6.4.7.5 The Role of High-Nitrogen Stainless Steel

It is important for high-nitrogen steels as biomaterial to appeal that Ni *does not alloy* in the material in order to get the reliability for medical doctors as well as patients.

Furthermore, it is also important that the corrosion resistance of high-nitrogen steel is much higher than those of SUS304 and SUS316L, which are conventional biomaterials.

In addition, the selection of biomaterials is directly depending upon the circumstances where they are used. Although the corrosion property of HNS is comparable to that of Ti alloy, the strength of HNS is much higher than that of Ti alloy. Therefore, devices made from Ti alloys could be replaced by HNS ones' in the case of the higher materials strength being required.

6.5 Applications of HNS for Coronary Stent

6.5.1 Requirements for Ni-Free Biometal Used as Coronary Stents

In-stent restenosis after the application of coronary stent is an important problem following the percutaneous coronary intervention (PCI) [35, 36]. Despite intensive efforts to improve the design and metal composition of stents, the rates of in-stent restenosis induced by bare metal stents are still ranging from 22 to 49 % [36, 37]. Drug-eluting stent (DES) has therefore been developed. DES is composed of three components including metallic stent, polymer matrix, and drug. The surface of the metallic stents is coated with non- or slow-biodegradable polymer, which works as reservoir of drug and as scaffolds for vascular endothelial cells [38, 39]. Also, some kinds of anticancer drugs and immune suppressants have been loaded on DES. Table 6.4 shows the classification of commercial DES [40]. DES has been reported to effectively reduce in-stent restenosis; its in-stent restenosis rates are from 0 to 31 % [37, 41]; however, they cause another problem, namely, "late thrombosis," after implantation of coronary stent for a long period [42]. Therefore, it would be highly

Table 6.4 Classification of commercial DES

Product name	Manufacturer	Drug	Polymer	Metal
Cypher	Cordis/J&J	Sirolimus	Acryl polymer	SUS316L
Taxus Liberte	Boston Scientific	Paclitaxel	Styrene-isobutylene-styrene triblock copolymer	SUS316L
Promus Element	Boston Scientific	Everolimus	Acryl polymer	Pt-Cr alloy
Endeavor	Medtronic	Zotarolimus	PC polymer	Co-Co alloy
Xience V	Abbott	Everolimus	Acryl/fluoropolymer	Co-Co alloy
Nobori	Terumo	Biolimus-A9	Poly(lactic acid)	SUS316L

Table 6.5 Composition of biometals (wt%)

Metal	Fe	Cr	Co	Ni	Mo	W	Pt	N	Other
SUS316L	64	18	–	14	3	–	–	–	–
Co-Cr alloy (L605)	3	20	52	10	–	15	–	–	–
Pt-Cr	37	18	–	9	3	–	33	–	–
HNS	74	23	–	<0.04	1	–	–	1	–

desirable to develop coronary stents that have better profiles with in-stent restenosis and vascular endothelial cell adhesion and proliferation.

For stent platforms of coronary stents, SUS316L, Co-Cr alloy and Pt-Cr alloy have been employed. More than 10 wt% of Ni element was added in these alloys. Detailed component of these alloys is shown in Table 6.5. The addition of Ni element plays an important role in improving workability, mechanical property, and corrosion resistance. However, it is known that Ni ion released from amorphous oxide layer of metal surface induces biological responses including Ni allergy and inflammation [43, 44]. It has also been reported that Ni allergy was associated with higher risks of restenosis after PCI [43]. Therefore, development of coronary stent made from Ni-free biometals has been highly required for cardiovascular application.

For development of Ni-free biometals, substitution of Ni element with nitrogen in stainless steel is one of the typical strategies. The adsorption of nitrogen into stainless steel has been reported. However, homogenous adsorption of nitrogen into stainless steel is quite difficult [45]. We therefore developed Ni-free austenitic stainless steel with high-nitrogen content (more than 0.8 wt%) using an electroslag remelting (P-ESR) method under a pressurized N_2 gas atmosphere [46]. This P-ESR method enables us to incorporate nitrogen homogenously into stainless steel, yielding Ni-free stainless steel with high corrosion resistance and fatigue.

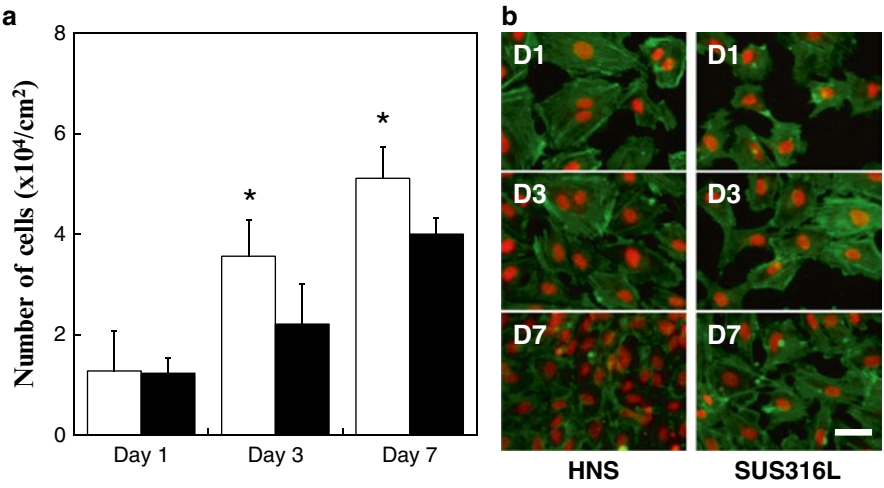

Fig. 6.23 HUVEC proliferation on HNS and SUS316L. (**a**) Number of HUVECs cultured on HNS (*white bar*) and SUS316L (*black bar*) for various periods. Data are the average ± standard deviations of five samples, with (*) indicating $p < 0.05$. (**b**) Morphology and distribution of HUVECs cultured on HNS and SUS316L for 1, 3, and 7 days. Actin filaments (*green*) and cell nuclei (*red*) of HUVECs were stained. Scale bar: 50 μm

6.5.2 Cell and Tissue Compatibility of HNS

Endothelial cell coverage on biometals is one of the important properties for coronary stent material. We therefore evaluated endothelial cell adhesion/proliferation on HNS by the cell culture in the presence of serum [47]. Human umbilical vein endothelial cells (HUVECs) were seeded on the surface of HNS. SUS316L whose Ni content was 12 wt% was also evaluated as a control material. Figure 6.23a shows the number of HUVECs cultured on HNS and SUS316L for 1, 3, and 7 days. No significant differences were observed in the number of HUVECs after the culture for 1 day when comparing HNS and SUS316L. However, the number of HUVECs on HNS was 1.6-fold higher than on SUS316L at 3 days. Further, the number of HUVECs on HNS was 2.8-fold higher at 3 days than at 1 day time point. After the culture for 7 days, the number of HUVECs was 1.3-fold higher on HNS than on SUS316L, and the number of HUVECs on HNS was 4-fold higher at 7 days than at 1 day time point. Figure 6.23b shows the distribution and morphology of HUVECs on HNS and SUS316L after culture for 1, 3, and 7 days. No noticeable differences were observed in HUVEC morphologies when comparing HNS or SUS316L, and cell distribution correlated with the number of HUVECs. The surfaces of HNS were covered with HUVECs after the culture for 3 and 7 days, while HUVEC distribution on SUS316L was in a quite low level compared with HNS, indicating that HNS had excellent cell compatibility and can work as a scaffold for the endothelial cells.

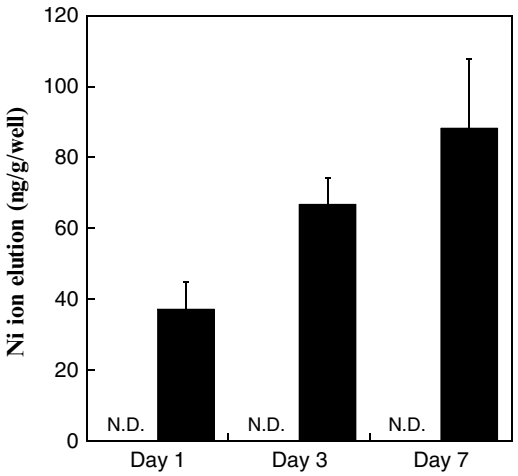

Fig. 6.24 Ni ion elution from HNS and SUS316L (*black bar*) after immersion in PBS at 37 °C for 1, 3, and 7 days. Data are the average ± SD of five samples. *N.D.* means not detected (Reproduced from Ref. [47] by permission of John Wiley & Sons Ltd)

Different proliferation behavior of HUVECs on HNS and SUS316L is thought to be caused by two factors: adsorption of cell adhesion protein such as fibronectin (FN) from serum and toxic ions release including Ni ion. In general, surface morphology of biomaterials also affects cell adhesion subsequent proliferation behavior. However, it is supposed that surface morphology of these metal surfaces did not affect cell adhesion/proliferation behavior, because these metal surfaces were mirror polished. The amount of adsorbed FN on HNS was 1.1-fold higher than that on SUS316L; however, statistical significance between them was not observed. This indicates that FN adsorption on metal surface is not the key factor for enhancement of HUVECs proliferation on HNS. Another factor influencing HUVECs proliferation is toxic ion release from metals. Focusing on the Ni ion, we assessed Ni ion release from each biometal. As can be seen from Figure 6.24, a total of 37.2 ± 7.7 ng/g/well of Ni ion was eluted from SUS316L after 1 day when SUS316L disk was immersed in phosphate buffer saline (PBS). The amount of Ni ion eluted from SUS316L gradually increased with time and reached 88.2 ± 19.7 ng/g/well after incubation for 7 days. On the other hand, the amount of Ni ions eluted from HNS was below the detection limit (limit of detection, 1.2 ppb) even after immersion in PBS for 7 days. These results suggested that enhanced proliferation of HUVECs on HNS surface was due to the Ni-free condition in the culture medium.

In order to evaluate/compare tissue compatibility of HNS and SUS316L, we focused on NF-κB expression after implantation in subcutaneous tissue. NF-κB is known as an inflammation transcriptional factor. And NF-κB-related gene expression is upregulated by Ni ions [48]. We therefore subcutaneously implanted these biometals in NF-κB/luciferase transgenic mice and evaluated NF-κB expression using a bio-imaging system. Figure 6.25 shows the intensity of the bioluminescent around the implant region. Bioluminescent became a maximum value after implantation of SUS316L for 3 weeks. On the other hand, the emission intensity of the HNS was nearly constant, even after implantation, indicating that the HNS does not

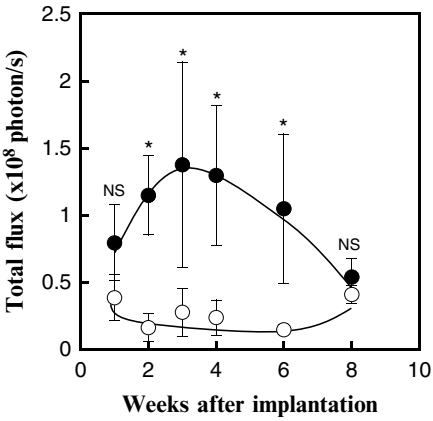

Fig. 6.25 Bioluminescence of NF-κB/luciferase transgenic mice after implantation of HNS (○) and SUS316L (●) for various periods of time. Data are the average ± SD of five samples, with (*) indicating $p < 0.05$. *N.S.* means no significant difference (Reproduced from Ref. [47] by permission of John Wiley & Sons Ltd)

elute Ni ions and does not cause any inflammation. After 3 weeks, the bioluminescent of the HNS (0.28 ± 0.18 ($\times 10^8$ photon/s)) was in a significantly lower level compared with SUS316L (1.37 ± 0.76 ($\times 10^8$ photon/s)) ($p < 0.05$), suggesting that inflammation may be induced by Ni ions derived from SUS316L. After 8 weeks, bioluminescent of SUS316L markedly decreased, and no significant differences were observed between them. This finding may reflect the encapsulation of SUS316L within the subcutaneous tissue at this time point. These results showed that HNS had excellent biocompatibility compared with SUS316L when used as a coronary artery stent material.

6.5.3 Implantation of HNS Stent in Pig Coronary

In order to evaluate biological reaction and in-stent stenosis ratio, coronary stents made from HNS and SUS316L were implanted in pig coronary for 28 days [49]. HNS coronary stents were associated with a significantly smaller percent in-stent stenosis (Fig. 6.26a). As can be seen from Fig. 6.26b, all stent struts were completely covered by the endothelium and vascular smooth muscle cells in both groups. Therefore, HNS coronary stents avoided neointima formation with no evidence of unfavorable healing delay (e.g., uncovered stent struts). A number of basophilic mononuclear cells were observed, mainly surrounding stent struts, in the SUS316L coronary stent-implanted arterial walls. On the contrary, HNS coronary stent-implanted arteries showed markedly fewer infiltrating cells, meaning that inflammation of HNS is quite low level compared with SUS316L. The SUS316L coronary stent sites also showed extensive proliferation of neointimal cells, and much less neointimal cell proliferation was seen following HNS coronary stent implantation. Moreover, histochemical characterization revealed that the deposition of extracellular matrix *was* greatly reduced in the walls of arteries implanted with HNS coronary stent compared with SUS316L coronary stent. Our results indicated that HNS can be useful for coronary stent material.

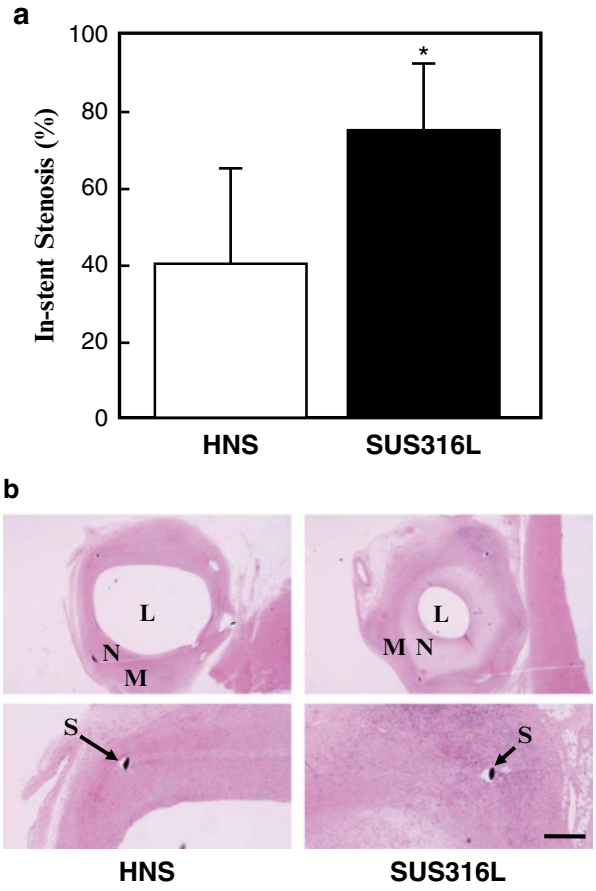

Fig. 6.26 Evaluation of in-stent stenosis and neointima formation following coronary stenting with HNS or SUS316L stainless steel stents. (**a**) Percentage of in-stent restenosis evaluated using angiography. (**b**) Representative sections of stented arteries stained with hematoxylin-eosin. *L* lumen, *N* neointima, *M* media, *S* stent, Scale bar: 200 μm (Reprinted with the permission from Ref. [49]. Copyright 2012 IOP Publishing)

6.5.4 Biofunctionalization of HNS and Immobilization of VEGF on HNS

Vascular endothelial growth factor (VEGF) is the most effective growth factor to promote endothelial cell growth. Recently, diverse strategies to immobilize VEGF or other biosignal molecules onto various metal surfaces have been investigated. Significantly, VEGF immobilized onto a substrate exhibited increasingly enhanced functions, because immobilized VEGF was not internalized into endothelial cells and continuously stimulated signal transduction for cell growth for a long time. There are various methods for the immobilization of biosignal molecules onto the

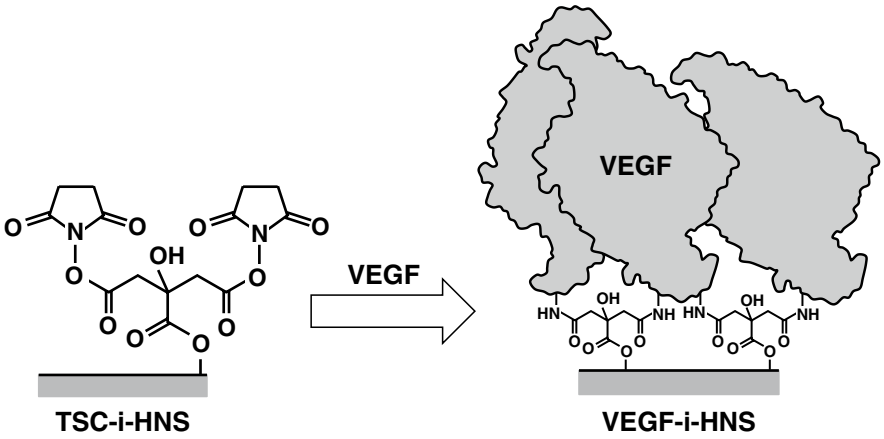

Fig. 6.27 Surface biofunctionalization of HNS for the enhancement of endothelial cell growth. VEGF is immobilized onto HNS surface via ester bond using trisuccinimidyl citrate (TSC)

surfaces of metallic biomaterials: using a silane coupling agent, polyacrylic acid, and polydopamine or utilizing electrodeposition, photoimmobilization, and plasma polymerization techniques. However, it is assumed that the inhibition of downregulation resulting from the long-term stability of immobilized growth factor results in over growth of cells during long-term implantation of the substrate in vivo or cell culture on the substrate. Therefore, we supposed that one of the most important aspects of biomaterial design is that the substrate promotes the growth of cells for a certain period of time but loses this function after moderate cell growth.

In order to achieve this hypothesis, we immobilized VEGF onto the surface of HNS via ester bonds [50]. Citric acid-based cross-linker, trisuccinimidyl citrate (TSC), with three active ester groups [51] was employed to link between the HNS surface and VEGF as shown in Figure 6.27. The biological activity of immobilized VEGF on HNS was then evaluated using HUVECs culture. Other substrates with different conditions were also prepared employing a commercial biometal, SUS316L, for the immobilization of VEGF. As shown in Figure 6.28, the number of HUVECs on VEGF-i-SUS316L was less than 10 % compared with the control, tissue culture polystyrene ($p<0.05$) at 1 day after seeding of HUVECs on each substrate. Further, the number of HUVEC on VEGF-s-HNS or Org-HNS was also significantly low compared with that on the control ($p<0.05$), while the number of HUVEC adhered on VEGF-i-HNS was similar to that on control. We cultured HUVECs on these substrates in medium without growth factors. Therefore, HUVEC adhesion onto VEGF-i-HNS is accomplished by the interaction between VEGF receptors and immobilized VEGF. After the culture for 3 days, the number of HUVEC on all substrates was approximately twice as much as that on day 1. Among them, the number of HUVECs on VEGF-i-HNS showed the significant increase compared with that on the other substrates ($p<0.05$). Over 7 days, VEGF-i-HNS continued to stimulate the proliferation of HUVECs. The number of HUVECs cultured on VEGF-i-HNS for 7 days *was* about four-fold higher than that

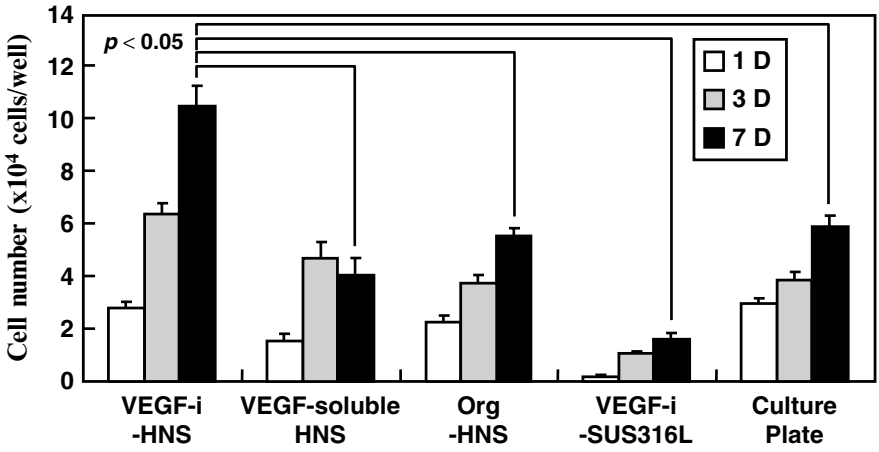

Fig. 6.28 Proliferation of HUVECs cultured on various substrates for various periods from 1 day (1D) to 7 days (7D). Data are the average ± S.D. of five samples, with (*) indicating $p < 0.05$. Abbreviations of substrates are as follows: *VEGF-i-HNS* VEGF-immobilized HNS, *VEGF-soluble HNS* the same amount of soluble VEGF added onto HNS, *Org-HNS* original HNS, *VEGF-i-SUS316L* VEGF-immobilized SUS316L, culture plate: tissue culture polystyrene

after 1 day, while VEGF-s-HNS stimulated the proliferation of HUVECs for 3 days; however, no significant increase of HUVECs was observed from 3 days to 7 days, indicating that downregulation of VEGF receptor occurred after the interaction with soluble VEGF, then the complex was endocytosed and degraded. On the contrary, immobilized VEGF continued to stimulate signal transduction to promote HUVEC growth because of the inhibition of endocytosis. We also evaluated the effect of immobilized VEGF on HUVEC growth using SUS316L as the substrate. As can be seen from Figure 6.28, VEGF immobilized on SUS316L (VEGF-i-SUS316L) did not stimulate the growth of HUVECs. From these results, VEGF-i-HNS effectively stimulated the proliferation of HUVECs compared with VEGF-i-SUS316L even though the density of immobilized VEGF was similar. We believe that one of the reasons of this phenomenon is nickel ions eluted from SUS316L because we detected nickel ions released only from SUS316L that was immersed in culture medium as shown above. Our results suggested that immobilization of VEGF on Ni-free biometals via TSC is an effective methodology for enhancing endothelialization.

6.5.5 *Future Perspectives of Ni-Free Biometals for Clinical Applications*

European regulations limit the amount of Ni ion that can be released from approved Ni-containing products and contact the skin to ≤ 0.5 μg/cm^2/week [52]. On the other hand, the use of coronary artery stents made of SUS316L is contraindicated in

patients with metal allergies in Japan [53]. As shown in this chapter, HNS shows the excellent cell and tissue compatibility. Thus, Ni-free biometals including HNS may be more useful than SUS316L for cardiovascular and orthopedic applications.

Acknowledgment Some parts of this chapter, especially Sects. 6.2 and 6.4, were created by partially referencing the final report titled "Advances in Steel Research on the Availability of Nitrogen," which was published by ISIJ as the final report of the research activities conducted by a research group of "the availability of nitrogen on the improvement in steel properties."

One of the authors (Y. Katada), as the chairperson of the research group, would like to express his sincere gratitude to the coauthors of the report.

The authors would also like to express their deepest appreciation to Dr. Motoki Inoue and Dr. Makoto Sasaki for their enthusiastic contributions to the research associated with Sect. 6.5. This research was partly supported by the Japan Society for the Promotion of Science (JSPS) through its Funding Program for World-Leading Innovation R&D on Science and Technology (FIRST Program).

References

1. Holzgruber W (1988) Process technology for high-nitrogen steels. In: Proceedings of the international conference on high-nitrogen steels, HNS88, pp 39–48
2. Stein G, Hucklenbroich I, Feichtinger HK (1998) Current and future applications of high-nitrogen steels. In: Proceedings of the HNS-conference 1988, Espoo/Stockholm, Finland/Sweden, 151–160
3. Feichtinger H (1990) Alternative routes to the production of high-nitrogen steels. In: Proceedings of the 2nd international conference on high-nitrogen steels, HNS 90, pp 298–302
4. ISO 5832-9 (1992) Implants for surgery——metallic materials——Part 9: Wrought high-nitrogen stainless steel
5. Katada Y, Sagara M, Kobayashi Y, Kodama T (2004) Fabrication of high strength high-nitrogen stainless steel with excellent corrosion resistance and its mechanical properties. Mater Manuf Process 19(1):19–22
6. Katada Y, Washizu N, Baba H (2004) Localized corrosion behavior of Mn-free high-nitrogen steel. In: Proceedings of the HNS 2004, GRIPS Media, Ostend, Belgium, pp 549–554
7. Small WM, Pehlke RD (1968) The effect of alloying elements on the solubility of nitrogen in liquid iron-chromium-nickel alloys. Trans Metall Soc AIME 242:2501–2505
8. Stein G, Menzel J, Dorr H (1988) Industrial manufacture of massively nitrogen-alloyed steels. In: Proceedings of the international conference on high-nitrogen steels, HNS88, pp 32–38
9. Holzgruber W (1974) Austrian patent no. 333.327, S12
10. Feichtinger HK, Stein G (1999) Melting of high-nitrogen steels. Mater Sci Forum 318–320:261–270
11. Kubich CH, Holzgruber W (1971) Proceedings of the 3rd international symposium on electroslag and other special meeting technology, Pittsburgh
12. Lorenz K., Medawar G (1969) Thyssen Forschung 1:97–108
13. Okamoto H (1992) The effect of tungsten and molybdenum on the performance of super duplex stainless steels. In: Proceedings of application of stainless steel '92, Stockholm, Sweden, Jernkontoret, p 360
14. Holmberg B (2002) Progress on welding of high nitrogen alloy austenitic stainless steels. Weld World 46(1–2):3–9
15. Jargelius-Petterson RFA (1998) Application of the pitting resistance equivalent to some highly alloyed stainless steels. Corrosion 54:162–168

16. Speidel Markus O, Zheng-Cui Ming-Ling, Kowanda Claudia, Speidel Hannes, Diener Markus (2003) High-nitrogen austenitic stainless steels – future materials for the chemical industries. Trans Indian Inst Met 56(3):281–286
17. Gebeau RC, Brown RS (2001) Biomedical implant alloy. Adv Mater Process 159(9):46–48
18. Hwang H-J, Park Y-S (2009) Effects of heat treatment on the phase ratio and corrosion resistance of duplex stainless steel. Mater Trans 50(6):1548–1552
19. Sagara M, Katada Y, Kodama T (2003) Localized corrosion behavior of high-nitrogen-bearing austenitic stainless steels in seawater environment. ISIJ Int 43(5):714–719
20. Osozawa K, Okato N (1976) Passivity and its breakdown on iron and steel based alloys (Stahle RW, Okada H, eds). NACE, Honolulu, p 135
21. Baba H, Katada Y (2008) Effect of nitrogen on crevice corrosion and repassivation behavior of austenitic stainless steel. Mater Trans 49(3):579–586
22. Baba H, Kodama T, Katada Y (2002) Role of nitrogen on the corrosion behavior of austenitic stainless steels. Corros Sci 44:2393–2407
23. Yashiro H, Hirayasu D, Kumagai N (2002) Effect of nitrogen alloying on the pitting of type 310 stainless steel. ISIJ Int 42(12):1477–1482
24. Lu YC, Bandy R, Clayton CR, Newman RC (1983) Surface enrichment of nitrogen during passivation of a highly resistant stainless-steel. J Electrochem Soc 130(8):1774–1776
25. Olsson C-OA (1995) The influence of nitrogen and molybdenum on passive films formed on the austenoferritic stainless steel-2205 studied by AES and XPS. Corros Sci 37:467–479
26. Komori T, Nakata M (1995) Effect of nitrogen on corrosion resistance of austenitic stainless steel. In: Proceedings of the 4th international congress on high-nitrogen steels, ISIJ, p 32
27. Baba H et al (2003) Proceedings of the 50th Japan conference on materials and environments, p 189
28. Newman RC, Shahrabi T (1987) The effect of alloyed nitrogen or dissolved nitrogen ions on the anodic behavior of austenitic stainless steel in hydrochloric-acid. Corros Sci 27(8):827–838
29. Huang CC, Tsai WT, Lee LT (1995) Electrochemical and surface studies on the passivity of nitrogen and molybdenum containing laser cladded alloys in 3.5 wt% NaCl solution. Corros Sci 37:769–780
30. Sagara M, Katada Y, Kodama T, Tsuru T (2003) Surface analysis of high nitrogen-bearing austenitic stainless steel using XPS. J Jpn Inst Metals 67:67–73
31. Katada Y, Sagara M, Kobayashi Y, Kodama T (2003) Fabrication of high strength high-nitrogen stainless steel with excellent corrosion resistance and its mechanical properties. In: Speidel MO (ed), Proceedings of HNS 2003, ETH Zurich, pp 189–198; Mudali UK (1994) Corrosion of high Nitrogen Steels – effects of nitrogen addition on passivation kinetics, composition of passivation films and pitting corrosion in Fe-N model alloys. Max-Planck Institute for Iron Research, Dusseldorf, Germany
32. Grabke HJ (1996) The role of nitrogen in the corrosion of iron and steels. ISIJ Int 36:777–786
33. Sagara M, Uno H, Katada Y, Kodama T (2002) Effect of alloy elements on localized corrosion characteristics of nitrogen-bearing stainless steels and evaluation of crevice corrosion in seawater environment. Tetsu-to-Hagane 88:86–91
34. Katada Y, Washizu N, Baba H (2005) Localized corrosion behavior of high-nitrogen steel. Mater Sci Forum 475–479:225–228; Wegrelius L, Falkenberg F, Olefjord I (1999) Passivation of stainless steels in hydrochloric acid. J Electrochem Soc 146:1397–1406
35. Dussaillant GR, Mintz GS, Pichard AD, Kent KM, Satler LF, Popma JJ, Wong SC, Leon MB (1995) Small stent size and intimal hyperplasia contribute to restenosis – a volumetric intravascular ultrasound analysis. J Am Coll Cardiol 26:720–724
36. Fischman DL, Leon MB, Baim DS, Schatz RA, Savavage MP, Penn I, Detre K, Veltri L, Ricci D, Nobuyoshi M, Cleman M, Heuser R, Almond D, Teirstein PS, Fish RD, Colombo A, Brinker J, Moses J, Shaknovich A, Hirshfeld J, Bailey S, Ellis S, Rake R, Goldberg S (1994) A randomized comparison of coronary-stent placement and balloon angioplasty in the treatment of coronary-artery disease. New Engl J Med 331:496–501

37. Stone GW, Ellis SG, Cannon L, Mann JT, Greenberg JD, Spriggs D, O'Shaughnessy CD, DeMaio S, Hall P, Popma JJ, Koglin J, Russell ME (2005) Comparison of a polymer-based paclitaxel-eluting stent with a bare metal stent in patients with complex coronary artery disease – a randomized controlled trial. J Am Med Assoc 294:1215–1223
38. Peng T, Gibula P, Yao K, Goosen M (1996) Role of polymers in improving in improving the results of stenting in coronary arteries. Biomaterials 17:685–694
39. Mani G, Feldman MD, Patel D, Agrawal CM (2007) Coronary stents: a materials perspective. Biomaterials 28:1689–1710
40. Daemen J, Serruys PW (2007) Drug-Eluting Stent Update 2007 – Part I (2007) A survey of current and future generation drug-eluting stents: meaningful advances or more of the same? Circulation 116:316–328
41. Stone GW, Teirstein PS, Meredith IT, Farah B, Dubois CL, Feldman RL, Dens J, Hagiwara N, Allocco DJ, Dawkins KD (2011) A prospective, randomized evaluation of a novel everolimus-eluting coronary stent. J Am Coll Cardiol 57:1700–1708
42. McFadden EP, Stabile E, Regar E, Cheneau E, Ong ATL, Kinnaird T, Suddath WO, Weissman NJ, Torguson R, Kent KM, Pichard AD, Satler LF, Waksman R, Serruys PW (2004) Late thrombosis in drug-eluting coronary stents after discontinuation of antiplatelet therapy. Lancet 364:1519–1521
43. Costa M, Yan Y, Zhao DJ, Salnikov K (2003) Molecular mechanisms of nickel carcinogenesis: gene silencing by nickel delivery to the nucleus and gene activation/inactivation by nickel-induced cell signaling. J Environ Monit 5:222–223
44. Thomas P, Braathen LR, Doerig M, Auboeck J, Nestle F, Werfel T, Willert HG (2009) Increased metal allergy in patients with failed metal-on-metal hip arthroplasty and peri-implant T-lymphocytic inflammation. Allergy 64:1157–1165
45. Kuroda D, Hanawa T, Hibaru T, Kuroda S, Kobayashi M, Kobayashi T (2003) New manufacturing process of nickel-free austenitic stainless steel with nitrogen absorption treatment. Mater Trans 44:414–420
46. Katada Y, Sagara M, Kobayashi Y, Kodama T (2004) Fabrication of high strength high-nitrogen stainless steel with excellent corrosion resistance and its mechanical properties. Mater Manuf Process 19:19–30
47. Inoue M, Sasaki M, Katada Y, Taguchi T (2014) Quantitative biocompatibility evaluation of nickel-free high-nitrogen stainless steel in vitro/in vivo. J Biomed Mater Res B 102:68–72
48. Viemann D, Schmidt M, Tenbrock K, Schmid S, Muller V, Klimmek K, Ludwig S, Roth J, Goebeler M (2007) The contact allergen nickel triggers a unique inflammatory and proangiogenic gene expression pattern via activation of NF-kappa B and hypoxia-inducible factor-1 alpha. J Immunol 178:3198–3207
49. Fujiul K, Manabe I, Sasaki M, Inoue M, Iwata H, Hasumil E, Komuro I, Katada Y, Taguchi T, Nagai R (2012) Nickel-free stainless steel avoids neointima formation following coronary stent implantation. Sci Technol Adv Mater 13:10pp
50. Sasaki M, Inoue M, Katada Y, Taguchi T (2012) The effect of VEGF-immobilized nickel-free high-nitrogen stainless steel on viability and proliferation of vascular endothelial cells. Colloids Surf B: Biointerfaces 92:1–8
51. Inoue M, Sasaki M, Nakasu A, Takayanagi M, Taguchi T (2012) An antithrombogenic citric acid-crosslinked gelatin with endothelialization activity. Adv Healthc Mater 1:573–581
52. http://www.teg.co.uk/nickel/94-27-EC.htm
53. http://www.info.pmda.go.jp/ygo/pack/21800BZY10216000_A_01_04/

Chapter 7
Co-Cr Alloys as Effective Metallic Biomaterials

Takayuki Narushima, Kyosuke Ueda, and Alfirano

Abstract Because of their excellent mechanical properties, high corrosion resistance, and high wear resistance, Co-Cr alloys have been recognized as effective metallic biomaterials and have been used as materials for dental and medical devices since a cast Co-Cr-Mo alloy, Vitallium, was developed in the 1930s. Further increases in the usage of Co-Cr alloys are still expected as well. In this chapter, first, the history and current status of biomedical Co-Cr alloys such as Co-28Cr-6Mo and Co-20Cr-15W-10Ni alloys are reviewed. Their microstructure, processing, and properties are then discussed. Control of the microstructure by optimization of chemical composition of the alloys and thermomechanical treatments is described, and newly developed processing techniques for grain refinement and newly found precipitates such as the π-phase and χ-phase are discussed. As a novel process for implant fabrication, an additive manufacturing technique using an electron beam and a laser beam is mentioned. Finally, the mechanical properties and corrosion and wear resistances of the alloys are presented, and the relationships between the microstructure and properties of the Co-Cr alloys are discussed.

Keywords Co-Cr-Mo alloy • Co-Cr-W-Ni alloy • Stacking fault energy • Microstructure • Precipitation • Additive manufacturing • Wear resistance

7.1 Introduction

Co-Cr alloys have been established as metallic biomaterials essential for orthopedic, cardiovascular, and dental fields because of their excellent mechanical properties, high corrosion resistance, and high wear resistance [1–3]. Their wear resistance

T. Narushima (✉) • K. Ueda
Department of Materials Processing, Tohoku University,
6-6-02 Aza Aoba, Aramaki, Aoba-ku, Sendai 980-8579, Japan
e-mail: narut@material.tohoku.ac.jp

Alfirano
Metallurgy Engineering Department, Sultan Ageng Tirtayasa University, Cilegon, Indonesia

M. Niinomi et al. (eds.), *Advances in Metallic Biomaterials*, Springer Series
in Biomaterials Science and Engineering 3, DOI 10.1007/978-3-662-46836-4_7

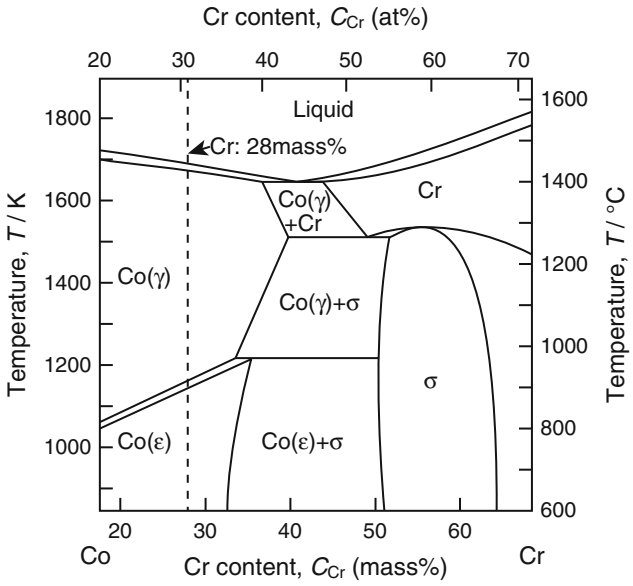

Fig. 7.1 Binary phase diagram of the Co-Cr system [6]

properties are particularly excellent as compared with those of other metallic biomaterials such as stainless steels and Ti alloys.

Pure Co undergoes an allotropic transformation at 690 K from the high-temperature γ-phase with the fcc (face-centered cubic) structure to the low-temperature ε-phase with the hcp (hexagonal close-packed) structure [4, 5]. This transformation is shear dominant with thermal hysteresis; therefore, it has been classified as martensitic [5]. The transformation temperature is changed by the addition of alloying elements to Co. In particular, biomedical Co-Cr alloys contain more than 20 mass% Cr, which improves the corrosion resistance by forming a passive layer consisting mainly of Cr oxide. The Co-Cr binary phase diagram is shown in Fig. 7.1 [6]. The addition of Cr increases the transformation temperature. The transformation temperatures in Co-20mass%Cr and Co-30mass%Cr alloys are around 1,100 and 1,200 K, respectively. Figure 7.2 summarizes the effects of alloying elements on the temperatures of the transformation from the hcp phase to the fcc phase of Co alloys [5]. The horizontal axis shows the change in the temperature of the hcp-to-fcc transformation from that for pure Co per 1at% of the alloying element, and the vertical axis shows the solubility of the alloying element in fcc Co. Alloying elements such as Fe, Mn, Ni, and carbon lower the hcp-to-fcc transformation temperature; they are fcc stabilizers. On the other hand, Mo, W, and Si increase the hcp-to-fcc transformation temperature and are hcp stabilizers, like Cr. This martensitic transformation is closely related to the microstructure and mechanical and chemical properties of the Co-Cr alloys.

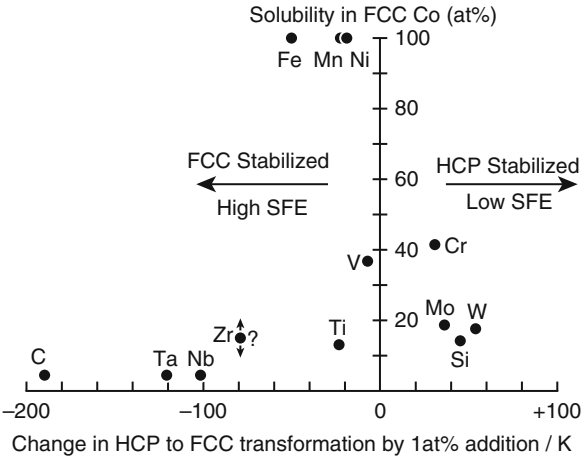

Fig. 7.2 Effects of alloying elements on the temperature of the transformation from hcp Co to fcc Co as a function of solubility of the elements in fcc Co [5]

In this chapter, first, the history and current status of biomedical Co-Cr alloys such as Co-28mass%Cr-6mass%Mo and Co-20mass%Cr-15mass%W-10mass%Ni alloys are briefly reviewed. Their microstructure, processing, and properties are then discussed. Control of the microstructure of Co-Cr alloys is essential for practical applications, as it is for other metallic materials. Therefore, the effects of different processing techniques and the alloy composition including minor alloying elements on the microstructure are described with a focus on grain refinement and precipitation. As a novel processing technique for implant fabrication, an additive manufacturing technique using an electron beam and a laser beam is mentioned. Finally, the mechanical properties and corrosion and wear resistances of the alloys are presented. Hereafter, the chemical composition of the alloys is reported in units of mass%, although the mass% notation is omitted.

7.2 Co-Cr Alloys as Metallic Biomaterials

7.2.1 History

Co-based alloys in the Co-Cr and Co-Cr-W systems have been established since the early 1900s, and the Stellite alloys manufactured by Haynes became important industrial materials for wear-resistant hardfacing applications [5]. In the 1930s, a cast Co-Cr-Mo alloy, Vitallium, was developed, a technique for the lost-wax (investment) casting of the alloy was established, and the alloy was commercialized for dental prosthetics [7, 8]. Venable and Stuck used Vitallium devices for internal fixation of fractures and showed in the late 1930s that the alloy can be used in medical implants [9–11]. Vitallium was also used for prosthetic acetabular cups by Smith-Petersen in the late 1930s [12, 13]. These cups were used in the standard

method for hip reconstruction until total hip replacement operations were introduced in the 1960s [12]. In the 1950s and early 1960s, metal-on-metal-type and metal-on-polymer-type artificial hip joints using Vitallium were developed. The former are represented by the McKee-Farrar joint, and the latter were pioneered by Charnley [14]. Other Co-Cr alloys such as Co-Cr-W-Ni (L-605, HS25, ASTM F 90) [15], Co-Ni-Cr-Mo (MP35N, ASTM F 562), and Co-Cr-Fe-Ni-Mo (Elgiloy, ASTM F 1058 grade 1) system alloys, which are still used in practical applications at the present time, had been developed in the early 1960s. Thus, the Co-Cr alloys have a long history consisting of more than 80 years of use as dental and medical materials.

Currently, cast and wrought Co-Cr alloys are widely used for implants such as artificial joints, denture wires, and stents. Metal-on-metal-type total hip replacements made of Co-Cr-Mo alloys were revived in the late 1980s [14] because the loosening of the metal-on-UHMWPE (ultrahigh molecular weight polyethylene)-type artificial hip joints was found to be related to osteolysis caused by the formation of UHMWPE wear debris [16]. Recently, however, a decrease in the number of stemmed metal-on-metal-type artificial hip joints made of Co-Cr-Mo alloys used for hip replacements in England and Wales was reported [17].

7.2.2 Types of Co-Cr Alloys

With their long history of practical applications, Co-Cr alloys have been listed in the ASTM standards for surgical implant applications [18]. Table 7.1 shows the chemical compositions from the standards. The contents of not only the main alloying elements such as Cr, W, and Mo but also minor alloying elements such as carbon and nitrogen are standardized. ASTM F 75 is for castings, and the others are for wrought products. The maximum carbon content in ASTM F 75 (Co-28Cr-6Mo) is 0.35 mass%. The low carbon content in ASTM F 75 alloy possibly causes the formation of the σ-phase (intermetallic compound, Co(CrMo)), which likely deteriorates the mechanical properties of the alloy. Carbon suppresses the formation of the σ-phase by forming carbides. The ASTM F 799 and F 1537 alloys, whose chemical compositions are registered as Co-28Cr-6Mo, have three types: Alloy 1 and Alloy 2 have low ($C \leq 0.14$mass%) and high ($0.15\text{mass}\% \leq C \leq 0.35\text{mass}\%$) carbon contents, respectively, and Alloy 3 contains Al and La, which form oxide particles that provide dispersion strengthening [19].

Another classification of the Co-Cr alloys focuses on Ni content. The Ni content in ASTM F 75 alloy is required to be less than 0.5 mass%, and the Ni contents in ASTM F 799 and F 1537 alloys are required to be less than 1.0mass%. Other Co-Cr alloys such as ASTM F 90 (Co-20Cr-15W-10Ni), ASTM F 562 (Co-35Ni-20Cr-10Mo), and ASTM F 1058 (40Co-20Cr-16Fe-15Ni-7Mo) are allowed to contain Ni as an alloying element.

Figure 7.3 shows the stacking fault energies (SFEs) of three types Co-Cr alloys compared with those of Fe-based alloys [20]. The ASTM F 75 alloy, which is represented as Co-29Cr-6Mo in the figure, has a low SFE, so the hcp ε-phase with poor

Table 7.1 Chemical compositions (mass%) of Co-Cr alloys registered in the ASTM standards for biomedical applications

ASTM	Conditions		Chemical composition (mass%)																
			Cr	Mo	Ni	Fe	C	Si	Mn	W	P	S	N	Al	Ti	B	La	Be	Co
F 75-12	Casting		27.00 −30.00	5.00 −7.00	<0.50	<0.75	<0.35	<1.00	<1.00	<0.20	<0.020	<0.010	<0.25	<0.10	<0.10	<0.010	–	–	Bal.
F 799-11	Forgings	Alloy1 (low carbon)	26.0 −30.0	5.0 −7.0	<1.0	<0.75	<0.14	<1.0	<1.0	–	–	–	<0.25	–	–	–	–	–	Bal.
F 1537-11	Wrought																		
		Alloy2 (high carbon)	26.0 −30.0	5.0 −7.0	<1.0	<0.75	0.15 −0.35	<1.0	<1.0	–	–	–	<0.25	–	–	–	–	–	Bal.
		Alloy3 (dispersion strengthened)	26.0 −30.0	5.0 −7.0	<1.0	<0.75	<0.14	<1.0	<1.0	–	–	–	<0.25	0.30 −1.00	–	–	0.03 −0.20	–	Bal.
F 90-09	Wrought		19.00 −21.00	–	9.00 −11.00	<3.00	0.05 −0.15	<0.40	1.00 −2.00	14.00 −16.00	<0.040	<0.030	–	–	–	–	–	–	Bal.
F 1091-12	Wrought (wire)																		
F 56-13	Wrought		19.0 −21.0	9.0 −10.5	33.0 −37.0	<1.0	<0.025	<0.15	<0.15	–	<0.015	<0.010	–	–	<1.0	<0.015	–	–	Bal.
F 68-10	Wrought (plate, sheet, and foil)																		
F 96-08	Forgings																		
F 1058-08	Wrought (wire and strip)	Grade 1	19.0 −21.0	6.0 −8.0	14.0 −16.0	Bal.	<0.15	<1.20	1.5–2.5	–	<0.015	<0.015	–	–	–	–	–	<0.10	39.0 −41.0
		Grade 2	18.5 −21.5	6.5 −7.5	15.0 −18.0	Bal.	<0.15	<1.20	1.0–2.0	–	<0.015	<0.015	–	–	–	–	–	<0.001	39.0 −42.0

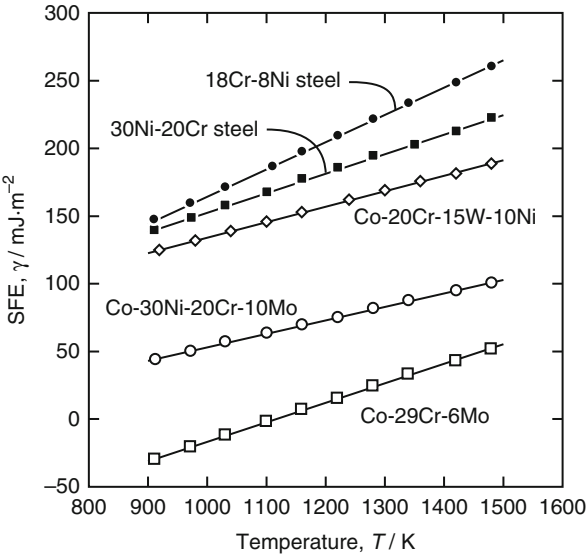

Fig. 7.3 Temperature dependence of the calculated SFEs of Co-Cr alloys and Fe-based alloys [20]

workability would form during the cooling process in a casting or heat treatment. In contrast, Co-30Ni-20Cr-10Mo (close composition to ASTM F 562) and Co-20Cr-15W-10Ni (ASTM F 90) alloys, which contain Ni as an alloying element, exhibit mid-level and high SFEs, respectively. Therefore, the formation of the hcp ε-phase is suppressed, and these alloys have excellent hot and cold workability. In this context, Co-28Cr-6Mo alloys are basically unsuitable for wrought applications, but the workability in the Co-28Cr-6Mo alloys can be improved by optimizing the amounts of minor alloying elements such as nitrogen and by thermomechanical treatments (see Sect. 7.4.1).

7.2.3 Applications

Table 7.2 summarizes the applications of Co-Cr alloys. Cast Co-28Cr-6Mo (ASTM F 75) alloy has been used in the stem, ball, and cup of artificial hip joints including both metal-on-UHMWPE and metal-on-metal joints as well as in the sliding components of artificial knee joints. Since artificial knee joints have complicated shapes, investment casting is essential for their production. Wrought Co-28Cr-6Mo Alloy 1 and Alloy 2 (ASTM F 799 and F 1537) have been used in the joint replacements for hips, knees, shoulders, and so on. The Co-Cr alloys in the Co-Cr-W-Ni (ASTM F 90/F 1091), Co-Ni-Cr-Mo (ASTM F 562), and Co-Cr-Fe-Ni-Mo (ASTM F 1058) systems are used for wrought products that require a large deformation to fabricate. Since they exhibit excellent hot and cold workability and can be

Table 7.2 Applications of Co-Cr alloys

ASTM	Alloys (mass%)	Trade name	Application
F 75-12	Co-28Cr-6Mo	Vitallium (Howmedica, Inc)	Stem, ball, and cup of artificial joints
		Haynes-Stellite 21(HS21) (Cabot Corp.)	Fixation screws
		Protasul-2 (Sulzer AG)	Bone plates
		Zimaloy (Zimmer Inc.)	
F 799-11		BioDur CCM Plus Alloy (Carpenter Technology Corp.)	Joint replacements (hip, knee, shoulder)
F 1537-11			Fixation devices
F 90-09	Co-20Cr-15W-10Ni	Haynes-Stellite 25 (HS25) (Cabot Corp.)	Fixation wires
F 1091-12		L-605 (Carpenter Technology Corp.)	Vascular stents
			Heart valves
F 562-13	Co-35Ni-20Cr-10Mo	MP35N (SPS Technologies, Inc.)	Lead conductor wires
F 688-10		Biophase (Richards Medical Co.)	Springs
F 961-08		Protasul-10 (Sulzer AG)	Stylets
			Catheters
			Orthopedic cables
			Cardiovascular stents
F 1058-08	40Co-20Cr-16Fe-15Ni-7Mo	Elgiloy (Elgiloy Ltd.)	Arch wires
		Phynox (ArcelorMittal Stainless & Nickel Alloys)	Springs
		Conichrome (Carpenter Technology Corp.)	Lead conductor wires
			Surgical clips
			Balloon-expandable stents (annealed)
			Self-expanding stents (aged)

strengthened by cold working, they have been used in fixation wires, vascular stents, springs, catheters, surgical clips, orthodontic dental archwires, and so on.

7.3 Microstructure and Processing in Co-Cr Alloys

7.3.1 Grain Refinement

Grain refinement can be used to strengthen metallic materials while maintaining their ductility. It is known that ultrafine grains smaller than 1 μm have been produced by severe plastic deformation; however, the severe plastic deformation techniques have not been applied to Co-Cr-Mo alloy parts because of their dual-phase microstructure and the strain-induced martensitic transformation during plastic deformation from the γ-phase to the ε-phase [21].

The grain refinement of Co-Cr-Mo alloys using conventional hot-compression deformation [21] and reverse transformation [22] has been reported. Yamanaka et al. [21] reported an ultrafine-grained microstructure with a grain size of around 0.6 μm obtained by the conventional hot-compression deformation of Co-29Cr-6Mo alloy with low carbon and low nitrogen contents. This microstructure was formed by dynamic recrystallization at 1,323 K under a strain rate of 0.1 s^{-1} from an initial average grain size of 40 μm. It was suggested that this fine microstructure was a product of the inhomogeneity in the local strain distribution induced by planar slips and deformation twins due to the lower SFE of this alloy at elevated temperatures [23]. A Co-29Cr-6Mo alloy with an average grain size of 0.8 μm produced by hot-compression deformation exhibited a significantly high 0.2 % proof strength of 1,330 MPa [24]. Kurosu et al. [22] developed a grain refinement process based on the reverse transformation from a lamellar (hcp ε-phase + Cr_2N) phase to an fcc γ-phase for the Co-27Cr-5Mo-0.16N alloy. Their process consisted of a two-step heat treatment without a hot or cold plastic transformation: solution-treated alloy was subjected to isothermal aging at 1,073 K for 90 ks to form a lamellar structure consisting of the hcp ε-phase + Cr_2N, and then the aged alloy with the complete lamellar microstructure was reverse-treated at a temperature of 1,273–1,473 K. The temperatures of 1,073 K and 1,273–1,473 K are in the stability regions for the ε -phase and γ-phase, respectively. The average grain size was reduced from 200 μm initially to 20–25 μm. Figure 7.4 shows the stress-strain curves of the Co-27Cr-5Mo-0.16N alloys after solution treatment (ST), aging treatment (AT), and reverse treatment (RT) at 1,273 K for 300 s [22]. The tensile strength was improved by the reverse transformation, while the ductility remained almost the same.

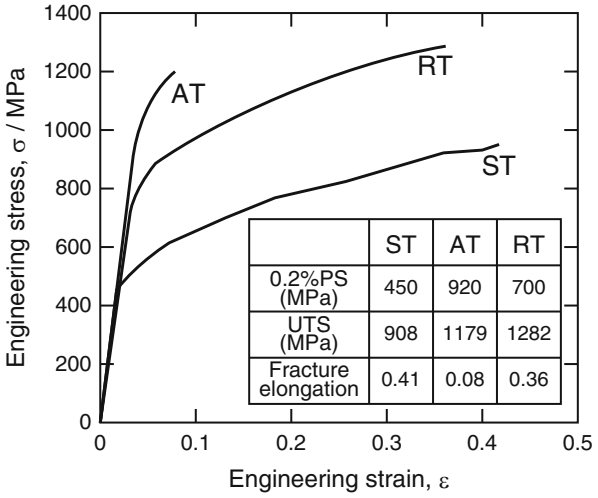

	ST	AT	RT
0.2%PS (MPa)	450	920	700
UTS (MPa)	908	1179	1282
Fracture elongation	0.41	0.08	0.36

Fig. 7.4 Stress-strain curves of the Co-27Cr-5Mo-0.16N alloys after solution treatment (ST), aging treatment (*AT*), and reverse transformation (*RT*) at 1,273 K for 300 s. A table of the mechanical properties for each specimen is shown as an inset in the figure (Reprinted from Ref. [22], Copyright 2010, with permission from Elsevier)

7.3.2 *Precipitation*

Precipitates in the Co-Cr alloys are known to affect the mechanical properties [25, 26] and corrosion [27–29] and wear [30–34] resistances of both cast and wrought products. Therefore, knowledge of the precipitates present in as-cast alloys and after heat treatment is essential for establishing reasonable production processes for biomedical Co-Cr alloy devices.

The precipitates in Co-Cr alloys are classified into intermetallic compounds and carbonitrides [1]. Therefore, the carbon and nitrogen contents in Co-Cr alloys significantly affect the phase and morphology of the precipitates. Figure 7.5 shows the microstructures of as-cast Co-28Cr-6Mo alloys with carbon contents of 0 to 0.41 mass% and nitrogen contents of 0 to 0.24 mass% [35, 36]. A dendrite matrix and interdendritic and grain boundary precipitates were observed in the alloys, except in Fig. 7.5e. The amount of precipitates increased with the carbon content in the alloys. As shown in Fig. 7.5e, no precipitates were detected in the as-cast Co-28Cr-6Mo-0.20N alloy. In addition, no precipitates were formed in Co-28Cr-6Mo-0.20N and Co-28Cr-6Mo-0.25N alloys even after heat treatment at temperatures of 1,473–1,573 K for up to 43.2 ks, and the microstructure consisted of a single fcc γ-phase [36]. Thus, the formation of the σ-phase and the martensitic transformation from the γ-phase to the ε-phase can be suppressed by the addition of nitrogen to Co-28Cr-6Mo alloys without added carbon. Up to 0.25 mass% nitrogen is allowed in the ASTM F 75, F 799, and F 1537 standards.

The morphologies of precipitates found in Co-Cr-Mo alloys are summarized in Fig. 7.6 [1]: blocky-dense morphologies (σ-phase, χ-phase, η-phase (M_6X-$M_{12}X$ type), and $M_{23}X_6$ type), starlike-dense morphologies (π-phase), starlike morphologies with striped patterns ($M_{23}X_6$ type), starlike morphologies with complicated microstructures (including M_7X_3 type), and lamellar cellular colony morphologies

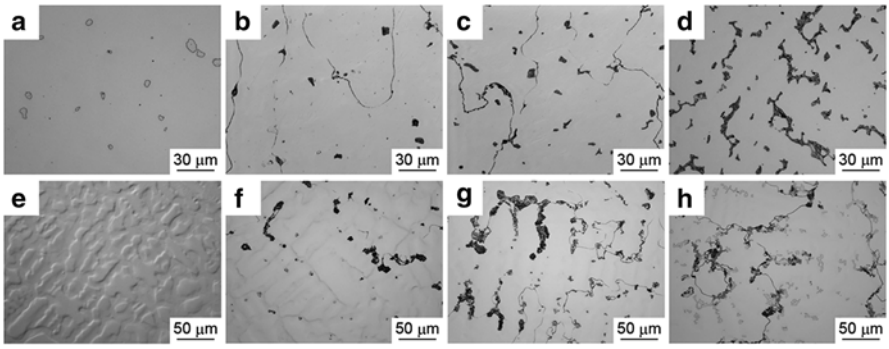

Fig. 7.5 Microstructures of as-cast Co-28Cr-6Mo alloys with various carbon and nitrogen contents: (**a**) 0C-0N, (**b**) 0.16C-0N, (**c**) 0.24C-0N, (**d**) 0.41C-0N, (**e**) 0C-0.2N, (**f**) 0.16C-0.2N, (**g**) 0.27C-0.24N, and (**h**) 0.34C-0.21N [35, 36]

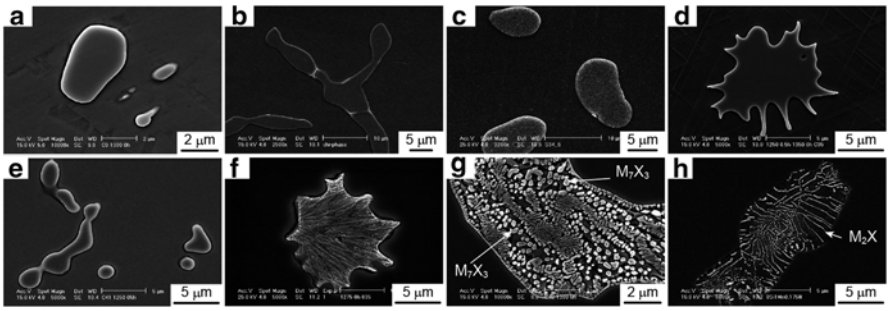

Fig. 7.6 Morphologies and phases of precipitates observed in biomedical Co-Cr-Mo alloys: (**a**) σ-phase (blocky dense), (**b**) χ-phase (blocky dense), (**c**) η-phase (blocky dense), (**d**) π-phase (starlike dense), (**e**) $M_{23}X_6$ type (blocky dense), (**f**) $M_{23}X_6$ type (starlike with stripe patterns), (**g**) M_7X_3 type (starlike with complicated microstructures), and (**h**) M_2X type (lamellar cellular colony) [1]

(M_2X type) have all been observed. In the notation for the precipitates, M refers to metallic elements such as Cr, and X refers to carbon and/or nitrogen. Clemow and Daniell [37] reported that the starlike shape was attributable to incipient melting around the edges of the carbide particles. The starlike shape of π-phase confirms that the π-phase forms under conditions where a liquid phase coexists. The $M_{23}X_6$-type precipitate contains little nitrogen, i.e., it is almost carbide [1], and it is coherent with the γ-phase because its lattice constant is around 3 times of that of the γ-phase. The M_2X-type precipitate is a nitrogen-rich carbonitride that forms in nitrogen-containing Co-Cr-Mo alloys [1, 36, 38]. The η-phase [38] and π-phase [39] are carbon-rich carbonitrides, while the σ-phase [1] and χ-phase [1, 40] are intermetallic compounds. The formation of M_7X_3-type precipitates in the Co-Cr-Mo alloys was suggested by Kilner et al. [41] and was confirmed by the present authors [39]. However, the chemical composition of the M_7X_3-type precipitate has not been clarified, because its size was too small to be analyzed (see Fig. 7.6g). The alloying elements affect the stabilization of the precipitates: carbon stabilizes the $M_{23}X_6$-type and M_7X_3-type precipitates [39], nitrogen stabilizes the M_2X-type and η-phase precipitates, and Si stabilizes the η-phase [42] and χ-phase [1] precipitates. The $M_{23}X_6$-type and η-phase precipitates were detected in Co-20Cr-15W-10Ni (ASTM F 90) alloy after heat treatment, although the as-forged alloy did not contain precipitates.

The presence of the π-phase [35, 39] and χ-phase [40, 43] was revealed by the present authors. Figure 7.7a shows the X-ray diffraction (XRD) pattern of precipitates electrolytically extracted from as-cast Co-28Cr-6Mo-0.16C-0.13N alloy [36]. The main reflections of the precipitate were in good agreement with the pattern of a $(Cr,Mo)_{12}(Fe,Ni)_{8-x}N_{4-z}$-type nitride (JCPDS card no. 26-0428) that was detected as a precipitate after aging of an Fe-25Cr-28Ni-2Mo-0.31N alloy [44]. This nitride phase is referred to as the π-phase [45] and exhibits a β-Mn structure. Its chemical composition can be ideally represented as M_2T_3X, where M and T are metallic elements with low and high affinities for X (carbon and/or nitrogen),

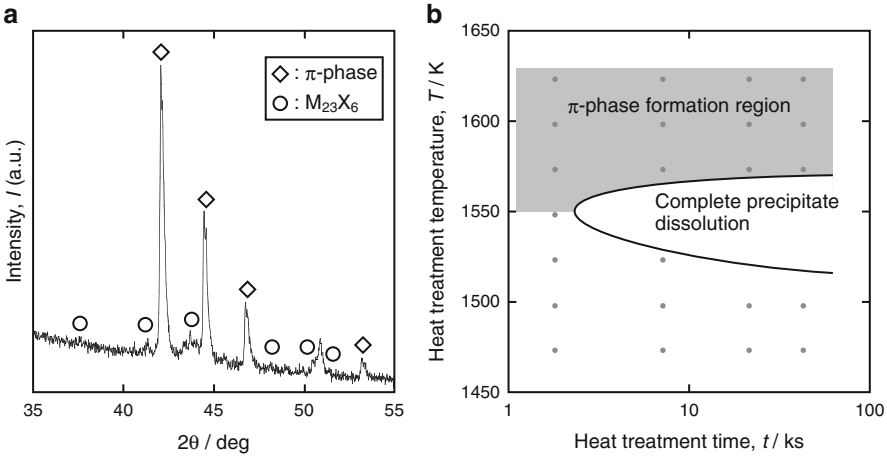

Fig. 7.7 (**a**) XRD pattern of precipitates electrolytically extracted from as-cast Co-28Cr-6Mo-0.16C-0.13N alloy and (**b**) schematic illustration of the formation region of the π-phase in Co-28Cr-6Mo alloys during heat treatment [36]

respectively. Figure 7.7b schematically shows the region where the π-phase was detected after heat treatment of the Co-28Cr-6Mo alloys. The formation of the π-phase is confirmed at temperatures of 1,548–1,623 K, where partial melting occurs in the alloys. The formation of the π-phase under the partial melting conditions was observed in the Co-28Cr-6Mo alloys from almost all of the carbon content region ($C \leq 0.35$ mass%) allowed by the ASTM F 75 standard. It was especially marked in the alloy with a carbon content of around 0.15mass%. Whether a π-phase precipitate is present in the alloys at room temperature depends on the cooling rate from the high temperatures at which the π-phase formed. Rapid cooling would be required to retain the π-phase precipitate in the alloys. A lower cooling rate seems to cause the π-phase to transform into other phases such as the $M_{23}X_6$-type + metallic fcc γ-phase.

The χ-phase has an α-Mn structure with 58 metallic atoms in the unit cell [46, 47]. The presence of the χ-phase as a precipitate in Fe-based alloys after isothermal heat treatment was reported previously [48, 49]. The χ-phase precipitate is considered to be harmful in Fe-based alloys because it is deleterious to their mechanical properties. As for Co-Cr-Mo alloys, the heat treatment periods and chemical compositions for which the χ-phase is formed are limited. Therefore, it is relatively easy to prevent the formation of the χ-phase during the fabrication of Co-Cr-Mo alloy devices.

7.3.3 Novel Processing for Implant Fabrication

Recently, additive manufacturing for metals has been paid much attention as a process for producing complex three-dimensional structures from precursor powders [50]. This technique can be used to make orthopedic implants optimized for each

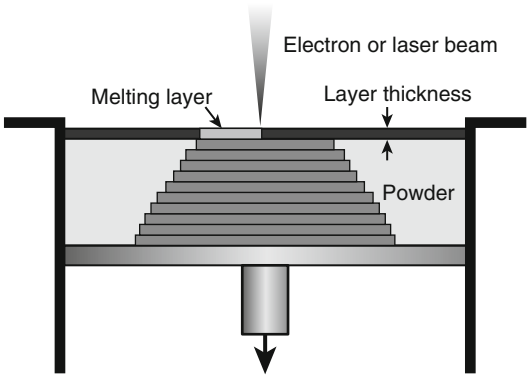

Fig. 7.8 Schematic diagram of additive manufacturing using electron beam melting and laser beam melting

patient's needs or skeletal structure. These custom-made implants are regarded as next-generation biomedical devices, and bone plates/screws, intramedullary nails, artificial joints, and so on are all expected to be fabricated using this technique [51]. Additive manufacturing using electron beam melting [52–54] and laser beam melting/sintering [55–58] has been performed to produce Co-Cr implants. In these techniques, CAD data for the implants are converted to data slices with heights of 20–100 μm. Using the slice data, an electron beam or a laser beam is irradiated onto a Co-Cr alloy powder with controlled particle size for melting and casting in a layer-by-layer manner (Fig. 7.8). Therefore, it is possible to precisely control the overall porosity and the size, shape, distribution, and direction of pores in the implants [59]. Electron beam melting is conducted under vacuum, while laser melting is operated under various atmospheres [60].

Gaytan et al. fabricated fully dense cylindrical and orthogonal structures and knee implant components by electron beam melting using Co-26Cr-6Mo-0.2C alloy powder [52, 53]. They observed $Cr_{23}C_6$ carbide arrays with dimensions of 2 μm in the building plane perpendicular to the building direction, which formed carbide columns in the vertical plane parallel to the building direction [52]. Hot isostatic pressing at 1,473 K produced an equiaxed fcc γ-phase grain structure with some grain boundary carbides. The anisotropy of the microstructures and mechanical properties of the as-cast Co-28Cr-6Mo-0.23C-0.17N alloy products fabricated by electron beam melting was also reported [54].

Selective laser melting has been applied to Co-Cr alloy implants in the dental [57, 58] and medical fields [55, 56]. Takaichi et al. [57] examined the microstructure, mechanical properties, and metal elution of the Co-29Cr-6Mo alloy products fabricated with different laser powers and scan spacings. Dense structures were obtained for input energies higher than 400 $J \cdot mm^{-3}$, whereas porous structures were formed for input energies lower than 150 $J \cdot mm^{-3}$. They observed a microstructure with fine cellular dendrites in elongated grains parallel to the building direction. Furthermore, the fcc γ-phase was dominant in the fabricated structures, and its preferential <001> orientation was found to be along the building direction. The

anisotropy of the mechanical properties due to the unique microstructure was also reported [57]. Finally, laser deposition of Co-Cr alloys was performed to add surface coatings for biomedical applications [61, 62].

7.4 Properties of Co-Cr Alloys

7.4.1 Mechanical Properties

Figure 7.9 summarizes the minimum requirements in the ASTM standards for the tensile strength and elongation of Co-Cr alloys. The mechanical strength and ductility of Co-Cr alloys can be changed over a wide range by controlling the microstructure using alloying and thermomechanical treatments, as is the case for other metallic materials.

The addition of small amount of alloying elements to cast Co-28Cr-6Mo (ASTM F 75) alloys is an effective way of controlling the microstructure. The addition of Zr [63] to ASTM F 75 alloys can yield a fine microstructure of the as-cast materials, resulting in increased tensile strength and elongation.

Nitrogen is an effective alloying element for improving the workability of wrought Co-28Cr-6Mo alloys [64], because it suppresses the σ-phase formation and γ-to-ε martensitic transformation, as described in Sect. 7.3.2. It has been reported that nitrogen stabilizes the γ-phase in the Co-29Cr-6Mo alloy by increasing the energy barrier for the γ-to-ε transformation and thus lowering the kinetic rate of the

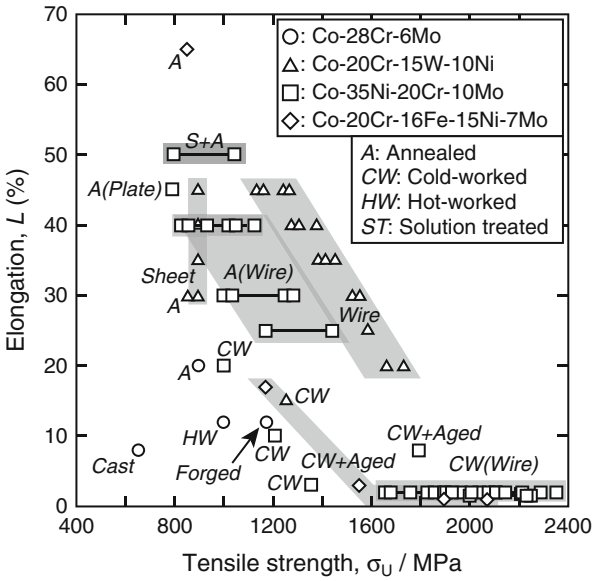

Fig. 7.9 Tensile strength and elongation required for biomedical Co-Cr alloys in ASTM standards

transformation by forming Cr-N short-range order [65] or nanoscale Cr_2N precipitates in the γ matrix [66]. In fact, it has been reported that the addition of nitrogen improves the hot-working properties of the Co-28Cr-6Mo-0.16N alloy in the temperature range between 1,273 and 1,473 K [67]. The addition of nitrogen to Co-Cr-Mo alloys also increases their mechanical strength [68, 69]. It was reported [69] that strengthening of Co-29Cr-6Mo alloys was caused by the nanosized Cr_2N precipitates in the γ matrix. Better elongation and workability were achieved in the alloy with a nitrogen content of 0.10 mass%, where the γ-to-ε martensitic transformation was completely suppressed. However, the further addition of nitrogen was reported to slightly decrease the elongation to failure because of the enhanced formation of annealing twins [69].

Carbide precipitation was reported to increase the tensile strength but decrease the elongation and workability of Co-Cr-Mo alloys, although these properties depend on the size and distribution of the precipitates.

Recently, an increase in the Cr content up to 34 mass%, which is above the ASTM F 75 composition range, was reported to increase the nitrogen solubility in Co-Cr alloys and improve the mechanical strength and ductility under as-cast condition [70]. Finally, a nitrogen-containing Co-33Cr-6Mo alloy with excellent ductility was reported to be promising for fabricating dentures with adjustable clasps using one-piece casting [71].

7.4.2 Corrosion Resistance

The excellent corrosion resistance of Co-Cr alloys is caused by the passive layer on their surface, which prevents further corrosion under biological conditions. The passive layer formed on Co-Cr-Mo alloy after polishing in pure water consisted of complex oxides of Cr and Co with a small amount of Mo oxides including hydroxyl groups, and its thickness was 2.5 nm [72, 73]. It is known that passive layers in contact with electrolytes undergo a continuous process of partial dissolution and reprecipitation from the microscopic viewpoint. Co was dissolved from the passive layer during immersion in Hanks' solution and a cell culture medium and during incubation in a cell culture. In this way, a passive layer consisting of mainly Cr oxide with small amount of Mo oxide was reconstructed [73]. Hodgson et al. [74] investigated the passive layer of a Co-28Cr-Mo alloy in simulated biological solutions using X-ray photoelectron spectroscopy (XPS). They discovered that the major component dissolving from the alloy was Co and that the passive layer was mainly Cr(III) oxide along with a smaller amount of Cr(III) hydroxide.

Figure 7.10 shows the anodic polarization curves of as-cast and heat-treated Co-28Cr-6Mo-0.24C alloys in Hanks' solution. The heat treatment was conducted at 1,523 and 1,623 K for 43.2 ks. The alloy heat-treated at 1,523 K had no precipitates, while the main precipitates in the as-cast alloy and the alloy heat-treated at 1,623 K were of $M_{23}X_6$ type and π-phase, respectively. The effect of the precipitates on the corrosion resistance of the alloys was not strong. However, Bettini et al. [29]

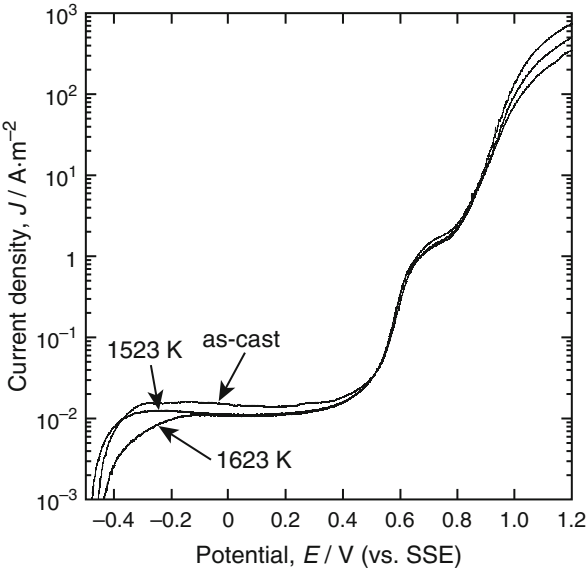

Fig. 7.10 Anodic polarization curves in Hanks' solution for as-cast Co-28Cr-6Mo-0.24C alloy and for alloys heat treated at 1,523 and 1,623 K

suggested that $M_{23}X_6$-type and M_6X-type precipitates affected the corrosion resistance of heat-treated Co-28Cr-6Mo-0.2C alloy on the basis of their microscopic surface observations after an electrochemical potential was applied. They observed that carbide boundaries were preferential sites for metal dissolution and that carbides with nonuniform compositions might exhibit different dissolution rates. Precise analyses of the microstructures of the precipitates and the chemical composition in the vicinity of the precipitates are required to understand the corrosion mechanisms of Co-Cr alloys under biological conditions.

7.4.3 Wear Resistance

Excellent wear resistance is one of the characteristics of Co-Cr alloys. Such wear resistance is required in the sliding parts of artificial joints, for which Co-28Cr-6Mo (ASTM F 75, F 799, and F 1537) alloys are generally used. Therefore, the wear properties of the Co-28Cr-6Mo alloys are examined in this section.

As stated in Sect. 7.2.1, a decrease in the number of operations using stemmed metal-on-metal-type artificial hip joints made of Co-Cr-Mo alloys has been reported [17]. The main concerns regarding the use of metal-on-metal-type hip replacements are the formation of wear debris [75] and ion elution [76], which seem to be closely related to the microstructure of the Co-Cr-Mo alloy implants, which is influenced by the γ-to-ε phase transformation and precipitation of intermetallic compounds and carbonitrides.

Some studies have reported the effects of precipitation on the metal-on-metal wear behavior of Co-Cr-Mo alloys [32, 34, 77, 78]. Chiba et al. reported that marked abrasive wear was caused by precipitates such as σ-phase precipitates and that the Co-Cr-Mo alloys with ε-phase formed by strain-induced martensitic transformation during wear tests exhibited excellent wear resistance because of the increased hardness [34, 78]. Some studies have suggested that a high carbon content in Co-Cr-Mo alloys improves the wear properties [32, 77].

The present authors reported the pin-on-disk wear behavior in Kokubo solution for Co-Cr-Mo alloy pins with different precipitates and an Al_2O_3 disk [33]. As-cast and solution-treated (ST) Co-28Cr-6Mo-0.3N (0Si0Mn0.3N), Co-28Cr-6Mo-1Si-1Mn-0.3N (1Si1Mn0.3N), Co-28Cr-6Mo-1Si-1Mn (1Si1Mn0N), and Co-28Cr-6Mo-1Si-1Mn-3Ni (1Si1Mn3Ni0N) alloys were used as materials for the pins. The ST alloys had no precipitates, while the as-cast alloys contained π-phase, $M_{23}X_6$-type, and M_2X-type precipitates, depending on the alloy composition. The mass loss of the pins after wear tests is shown in Fig. 7.11 [33]. The mass loss of the as-cast pins was higher than that of the ST pins. Figure 7.12 shows the surface morphologies of the as-cast and ST 1Si1Mn0.3N alloy pins after the wear tests [33]. The wear direction was from top to bottom in the figures. Continuous wear grooves were observed on the ST pin (Fig. 7.12b), while discontinuous deep wear grooves were detected in the as-cast pin after the wear tests (Fig. 7.12a). The formation of cavities and discontinuous deep grooves is likely to cause a higher mass loss for the as-cast pins than for the ST pins. Wear debris from both precipitates and the metallic matrix was found after wear tests of the as-cast pins. Some of the precipitates first detached from the metallic matrix, forming cavities during the wear tests, and then this debris caused discontinuous deep grooves through three-body abrasion.

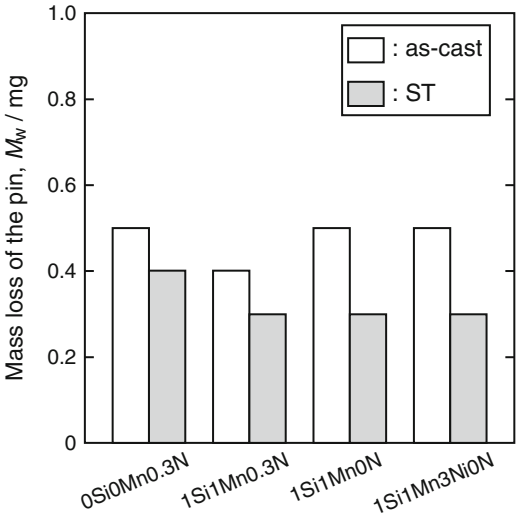

Fig. 7.11 Mass loss of the pins after a wear test in Kokubo solution (Reprinted from Ref. [33], Copyright 2013, with permission from The Japan Institute of Metals and Materials)

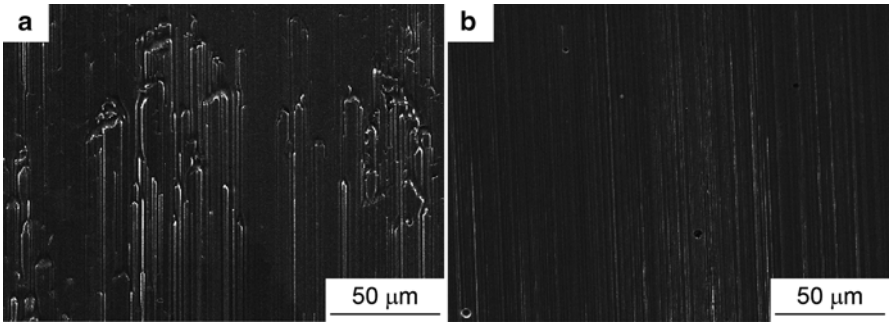

Fig. 7.12 SEM images of the surfaces of (**a**) as-cast and (**b**) ST pins of 1Si1Mn0.3N alloy after wear tests in Kokubo solution (Reprinted from Ref. [33], Copyright 2013, with permission from The Japan Institute of Metals and Materials)

The amounts of eluted ions of each metallic element (Co, Cr, Mo, Si, Mn, and Ni) after the wear tests are shown in Fig. 7.13 [33]. The Co/Cr and Co/Mn mass ratios for ions eluted from the 1Si1Mn3Ni0N alloy pin were calculated to be 53.1 and 225.0, which are much higher than the ratios of 2.1 and 49.3, respectively, calculated from the alloy composition. This means that the Cr and Mn ion contents are lower than expected based on the chemical composition of the alloy. EDX analysis suggested the formation of calcium phosphate on the wear tracks of the disks. The calcium phosphate included Cr and Mn, indicating that the Cr and Mn ions were preferentially incorporated into calcium phosphate [33].

Small amounts of Ni ions from Ni impurities in 0Si0Mn0.3N, 1Si1Mn0.3N, and 1Si1Mn0N alloy pins were detected after the wear tests. Decreasing the Ni content will be necessary to decrease Ni ion elution and thereby improve the safety of Co-Cr-Mo alloys.

7.5 Conclusions

The Co-Cr alloys have a long successful history of practical applications in the dental and medical fields since Vitallium was developed. It is impressive that Vitallium, or Co-Cr-Mo alloy, has been developed for dental applications and that the concept of Vitallium is still alive at the present time. The proportion of elderly people in the population is growing worldwide, and it is predicted that the number of patients suffering falls and deterioration of body functions will increase. Co-Cr alloys are seeing continued use in reconstruction devices for the human body, and the increases in their usage are expected. Co-Cr alloy has still much room for

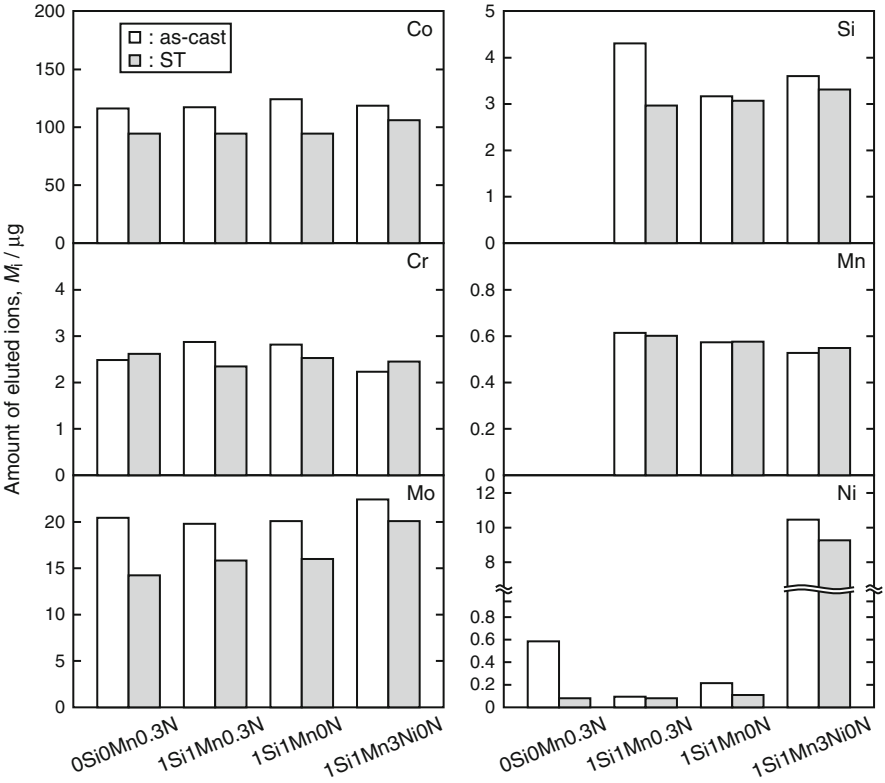

Fig. 7.13 Amounts of eluted Co, Cr, Mo, Si, Mn, and Ni ions after wear tests in Kokubo solution (Reprinted from Ref. [33], Copyright 2013, with permission from The Japan Institute of Metals and Materials)

improvement, and research into topics such as microstructure control using newly developed production processes and the optimization of alloy composition using metallic and light elements is required, especially for contents beyond the ASTM standards.

Acknowledgments This study was partially supported by a Grants-in-Aid for Scientific Research from the Ministry of Education, Culture, Sports, Science and Technology (MEXT), Japan.

References

1. Narushima T, Mineta S, Kurihara Y, Ueda K (2013) Precipitates in biomedical Co-Cr alloys. JOM 65:489–504
2. Narushima T (2010) New-generation metallic biomaterials. In: Niinoni M (ed) Metals for biomedical devices. Woodhead, Cambridge, pp 355–378

3. Niinomi M, Hanawa T, Narushima T (2005) Japanese research and development on metallic biomedical, dental, and healthcare materials. JOM 57(4):18–24
4. Davis JR (ed) (2000) ASM specialty handbook: nickel, cobalt, and their alloys. ASM International, Materials Park, p 356
5. Beltran AM (1987) Cobalt-base alloys. In: Sims CT, Stoloff NS, Hagel WC (eds) Superalloys II. Wiley, New York, pp 135–163
6. Baker H (ed) (1992) ASM handbook, vol 3, Alloy phase diagrams. ASM International, Materials Park, pp 2–140
7. Morral FR (1966) Cobalt alloys as implants in humans. J Mater 1:384–412
8. Morral FR (1968) The metallurgy of cobalt alloys – a 1968 review. J Met 20(7):52–59
9. Venable CS, Stuck WG, Beach A (1937) The effects on bone of the presence of metals; based upon electrolysis. Ann Surg 105:917–938
10. Venable CS, Stuck WG (1941) The use of Vitallium appliances in compound fractures. Am J Surg 51:757–778
11. Venable CS, Stuck WG (1943) Clinical uses of Vitallium. Ann Surg 117:772–782
12. http://www.sciencemuseum.org.uk/broughttolife/objects/display.aspx?id=4899
13. Smith-Petersen MN (1939) Arthroplasty of the hip: a new method. J Bone Joint Surg 21:269–288
14. Dowson D (2001) New joints for the millennium: wear control in total replacement hip joints. Proc Inst Mech Eng 215(Part H:JEIM):335–358
15. Wlodek ST (1963) Embrittlement of a Co-Cr-W (L-605) alloy. Trans ASM 56:287–303
16. Chan FW, Bobyn JD, Medley JB, Krygier JJ, Yue S, Tanzer M (1996) Engineering issues and wear performance of metal on metal hip implants. Clin Orthop Relat Res 333:96–107
17. Smith AJ, Dieppe P, Vernon K, Porter M, Blom AW (2012) Failure rates of stemmed metal-on-metal hip replacements: analysis of data from the National Joint Registry of England and Wales. Lancet 379:1199–1204
18. Mayer VA (ed) (2013) Annual book of ASTM standards, section thirteen, medical devices and services, vol 13.01. ASTM International, West Conshohocken
19. Wang KK, Berlin RM, Gustavson LJ (1999) A dispersion strengthened Co-Cr-Mo alloy for medical implants. In: Disegi JA, Kennedy RL, Pilliar R (eds) Cobalt-based alloys for biomedical applications, ASTM STP 1365. ASTM International, West Conshohocken, pp 89–97
20. Chiba A (2010) Co-Cr alloys. In: Hanawa T (ed) Metals for medicine. Japan Institute of Metals, Sendai, pp 84–92
21. Yamanaka K, Mori M, Kurosu S, Matsumoto H, Chiba A (2009) The grain refinement of biomedical Co-29Cr-6Mo alloy during conventional hot-compression deformation. Metall Mater Trans A 40A:1980–1994
22. Kurosu S, Matsumoto H, Chiba A (2010) Grain refinement of biomedical Co–27Cr–5Mo–0.16N alloy by reverse transformation. Mater Lett 64:49–52
23. Yamanaka K, Mori M, Chiba A (2012) Origin of significant grain refinement in Co-Cr-Mo alloys without severe plastic deformation. Metall Mater Trans A 43A:4875–4887
24. Yamanaka K, Mori M, Chiba A (2011) Mechanical properties of as-forged Ni-free Co–29Cr–6Mo alloys with ultrafine-grained microstructure. Mater Sci Eng A 528:5961–5966
25. Dobbs HS, Robertson JLM (1983) Heat treatment of cast Co–Cr–Mo for orthopaedic implant use. J Mater Sci 18:391–401
26. Gómez M, Mancha H, Salinas A, Rodríguez JL, Escobedo J, Castro M, Méndez M (1997) Relationship between microstructure and ductility of investment cast ASTM F-75 implant alloy. J Biomed Mater Res 34:157–163
27. Kuhn AT (1981) Corrosion of Co–Cr alloys in aqueous environments. Biomaterials 2:68–77
28. Yao MX, Wu JBC, Xu W, Liu R (2005) Metallographic study and wear resistance of a high-C wrought Co-based alloy Stellite 706K. Mater Sci Eng A 407:291–298
29. Bettini E, Eriksson T, Boström M, Leygraf C, Pan J (2011) Influence of metal carbides on dissolution behavior of biomedical CoCrMo alloy: SEM, TEM and AFM studies. Electrochim Acta 56:9413–9419

30. Wang A, Yue S, Bobyn JD, Chan FW, Medley JB (1999) Surface characterization of metal-on-metal hip implants tested in a hip simulator. Wear 225–229:708–715
31. Wimmer MA, Loos J, Nassutt R, Heitkemper M, Fischer A (2001) The acting wear mechanisms on metal-on-metal hip joint bearings: in vitro results. Wear 250:129–139
32. Varano R, Bobyn JD, Medley JB, Yue S (2006) The effect of microstructure on the wear of cobalt-based alloys used in metal-on-metal hip implant. Proc Inst Mech Eng 220(Part H: JEIM):145–159
33. Ueda K, Nakaie K, Namba S, Yoneda T, Ishimizu K, Narushima T (2013) Mass loss and ion elution of biomedical Co-Cr-Mo alloys during pin-on-disk wear tests. Mater Trans 54:1281–1287
34. Chen Y, Li Y, Kurosu S, Yamanaka K, Tang N, Koizumi Y, Chiba A (2014) Effects of sigma phase and carbide on the wear behavior of CoCrMo alloys in Hanks' solution. Wear 310:51–62
35. Mineta S, Namba S, Yoneda T, Ueda K, Narushima T (2010) Carbide formation and dissolution in biomedical Co-Cr-Mo alloys with different carbon contents during solution treatment. Metall Mater Trans A 41A:2129–2138
36. Mineta S, Alfirano Namba S, Yoneda T, Ueda K, Narushima T (2013) Phase and formation/dissolution of precipitates in biomedical Co-Cr-Mo alloys with nitrogen addition. Metall Mater Trans A 44A:494–503
37. Clemow AJT, Daniell BL (1979) Solution treatment behavior of Co–Cr–Mo alloy. J Biomed Mater Res 13:265–279
38. Alfirano Mineta S, Namba S, Yoneda T, Ueda K, Narushima T (2012) Precipitates in biomedical Co-Cr-Mo-C-N-Si-Mn alloys. Metall Mater Trans A 43A:2125–2132
39. Mineta S, Alfirano Namba S, Yoneda T, Ueda K, Narushima T (2012) Precipitates in biomedical Co-28Cr-6Mo-(0–0.41)C alloys heat-treated at 1473 K to 1623 K (1200 °C to 1350 °C). Metall Mater Trans A 43A:3351–3358
40. Narushima T, Mineta S, Alfirano Ueda K (2011) π-phase and χ-phase: new precipitates in biomedical Co–Cr–Mo alloys. In: Sasaki K (ed) Interface oral health science 2011. Springer, Berlin, pp 72–80
41. Kilner T, Pilliar RM, Weatherly GC, Allibert C (1982) Phase identification and incipient melting in a cast Co–Cr surgical implant alloy. J Biomed Mater Res 16:63–79
42. Alfirano Mineta S, Namba S, Yoneda T, Ueda K, Narushima T (2011) Precipitates in as-cast and heat-treated ASTM F75 Co-Cr-Mo-C alloys containing Si and/or Mn. Metall Mater Trans A 42A:1941–1949
43. Narushima T, Alfirano Mineta S, Namba S, Yoneda T, Ueda K (2011) Precipitates in biomedical Co-Cr-Mo-C-Si-Mn alloys. Adv Mater Res 277:51–58
44. Kikuchi M, Wakita S, Tanaka R (1973) β-manganese-type phase precipitated in high chromium-high nickel austenitic steels containing nitrogen. Trans ISIJ 13:226–228
45. Goldschmidt HJ (1957) Occurrence of the beta-manganese structure in transition metal alloys and some observations on chi-phase equilibria. Metallurgia 56:17–26
46. Kasper JS (1954) The ordering of atoms in the chi-phase of the iron-chromium-molybdenum system. Acta Metall 2:456–461
47. Joubert J-M, Phejar M (2009) Crystal chemistry and calphad modelling of the χ phase. Prog Mater Sci 54:945–980
48. Andrews KW (1949) A new intermetallic phase in alloy steels. Nature 164:1015
49. Redjaïmia A, Proult A, Donnadieu P, Morniroli JP (2004) Morphology, crystallography and defects of the intermetallic χ-phase precipitated in a duplex (δ + γ) stainless steel. J Mater Sci 39:2371–2386
50. Harris ID (2012) Additive manufacturing: a transformational advanced manufacturing technology. Adv Mater Process 170:25–29
51. Okazaki Y (2012) Development trends of custom-made orthopedic implants. J Artif Organ 15:20–25

52. Gaytan SM, Murr LE, Martinez E, Martinez JL, Machado BI, Ramirez DA, Medina F, Collins S, Wicker RB (2010) Comparison of microstructures and mechanical properties for solid and mesh cobalt-base alloy prototypes fabricated by electron beam melting. Metall Mater Trans A 41A:3216–3227
53. Gaytan SM, Murr LE, Ramirez DA, Machado BI, Martinez E, Hernandez DH, Martinez JL, Medina F, Wicker RB (2011) A TEM study of cobalt-base alloy prototypes fabricated by EBM. Mater Sci Appl 2:355–363
54. Sun S-H, Koizumi Y, Kurosu S, Li Y-P, Matsumoto H, Chiba A (2014) Build direction dependence of microstructure and high-temperature tensile property of Co–Cr–Mo alloy fabricated by electron beam melting. Acta Mater 64:154–168
55. Vandenbroucke B, Kruth J-P (2007) Selective laser melting of biocompatible metals for rapid manufacturing of medical parts. Rapid Prototype J 13:196–203
56. Hunt JA, Callaghan JT, Sutcliffe CJ, Morgan RH, Halford B, Black RA (2005) The design and production of Co–Cr alloy implants with controlled surface topography by CAD–CAM method and their effects on osseointegration. Biomaterials 26:5890–5897
57. Takaichi A, Suyalatu NT, Joko N, Nomura N, Tsutsumi Y, Migita S, Doi H, Kurosu S, Chiba A, Wakabayashi N, Igarashi Y, Hanawa T (2013) Microstructures and mechanical properties of Co–29Cr–6Mo alloy fabricated by selective laser melting process for dental applications. J Mech Behav Biomed Mater 21:67–76
58. Al Jabbari YS, Koutsoukis T, Barmpagadaki X, Zinelis S (2014) Metallurgical and interfacial characterization of PFM Co–Cr dental alloys fabricated via casting, milling or selective laser melting. Dent Mater 30:e79–e88
59. Ryan G, Pandit A, Apatsidis DP (2006) Fabrication methods of porous metals for use in orthopaedic applications. Biomaterials 27:2651–2670
60. Momose W (2013) Advantages of electron beam melting technology and application as real mass-production. Titan Jpn 61:198–199
61. Meacock CG, Vilar R (2009) Structure and properties of a biomedical Co-Cr-Mo alloy produced by laser powder microdeposition. J Laser Appl 21:88–95
62. Wilson JM, Jones N, Jin L, Shin YC (2013) Laser deposited coatings of Co-Cr-Mo onto Ti-6Al-4V and SS316L substrates for biomedical applications. J Biomed Mater Res B Appl Biomater 101B:1124–1132
63. Lee S-H, Uchikanezaki T, Nomura N, Nakamura M, Chiba A (2007) Effects of zirconium addition on microstructures and mechanical properties of Co-29Cr-6Mo Alloy. Mater Trans 48:1084–1088
64. Mori M, Yamanaka K, Matsumoto H, Chiba A (2010) Evolution of cold-rolled microstructures of biomedical Co–Cr–Mo alloys with and without N doping. Mater Sci Eng A 528:614–621
65. Li YP, Yu JS, Kurosu S, Koizumi Y, Matsumoto H, Chiba A (2012) Role of nitrogen addition in stabilizing the γ phase of biomedical Co–29Cr–6Mo alloy. Mater Chem Phys 133:29–32
66. Yamanaka K, Mori M, Chiba A (2013) Nanoarchitectured Co–Cr–Mo orthopedic implant alloys: nitrogen-enhanced nanostructural evolution and its effect on phase stability. Acta Biomater 9:6259–6267
67. Chiba A, Lee S-H, Matsumoto H, Nakamura M (2009) Construction of processing map for biomedical Co-28Cr-6Mo-0.16N alloy by studying its hot deformation behavior using compression tests. Mater Sci Eng A 513–514:286–293
68. Dempsey AJ, Pilliar RM, Weatherly GC, Kilner T (1987) The effects of nitrogen additions to a cobalt-chromium surgical implant alloy. Part 2 mechanical properties. J Mater Sci 22:575–581
69. Yamanaka K, Mori M, Chiba A (2014) Effects of nitrogen addition on microstructure and mechanical behavior of biomedical Co–Cr–Mo alloys. J Mech Behav Biomed Mater 29:417–426
70. Lee S-H, Nomura N, Chiba A (2008) Significant improvement in mechanical properties of biomedical Co-Cr-Mo alloys with combination of N addition and Cr-enrichment. Mater Trans 49:260–264

71. Yoda K, Suyalatu TA, Nomura N, Tsutsumi Y, Doi H, Kurosu S, Chiba A, Igarashi Y, Hanawa T (2012) Effects of chromium and nitrogen content on the microstructures and mechanical properties of as-cast Co–Cr–Mo alloys for dental applications. Acta Biomater 8:2856–2862
72. Smith DC, Pilliar RM, Metson JB, McIntyre NS (1991) Dental implant materials. II. preparative procedures and surface spectroscopic studies. J Biomed Mater Res 25:1069–1084
73. Hanawa T, Hiromoto S, Asami K (2001) Characterization of the surface oxide film of a Co–Cr–Mo alloy after being located in quasi-biological environments using XPS. Appl Surf Sci 183:68–75
74. Hodgson AWE, Kurz S, Virtanen S, Fervel V, Olsson C-OA, Mischler S (2004) Passive and transpassive behaviour of CoCrMo in simulated biological solutions. Electrochim Acta 49:2167–2178
75. Hallab NJ (2009) A review of the biologic effects of spine implant debris: fact from fiction. SAS J 3:143–160
76. Sargeant A, Goswami T (2007) Hip implants – Paper VI – ion concentrations. Mater Des 28:155–171
77. Tipper JL, Firkins PJ, Ingham E, Fisher J, Stone MH, Farrar R (1999) Quantitative analysis of the wear and wear debris from low and high carbon content cobalt chrome alloys used in metal on metal total hip replacements. J Mater Sci Mater Med 10:353–362
78. Chiba A, Kumagai K, Nomura N, Miyakawa S (2007) Pin-on-disk wear behavior in a like-on-like configuration in a biological environment of high carbon cast and low carbon forged Co–29Cr–6Mo alloys. Acta Mater 55:1309–1318

Chapter 8
Titanium Alloys for Biomedical Applications

Mitsuo Niinomi and Carl J. Boehlert

Abstract The low Young's modulus of β-type titanium alloys makes them advantageous for use in medical implant devices, as they are effective in both preventing bone resorption and promoting good bone remodeling. The development of low Young's modulus β-type titanium alloys for biomedical applications is described herein, along with a discussion of suitable methods for even greater modulus reductions. Since there is often occasion to remove implant devices, titanium alloys suitable for removable implants are also described. It has recently been noted that although patients require low Young's modulus titanium alloys, a high modulus is needed by surgeons. Consequently, β-type titanium alloys with a self-tunable Young's modulus are also explored. An evaluation of the effectiveness of low Young's modulus β-type titanium alloys in preventing stress shielding is provided, which is based on the results of animal testing. Means of enhancing the mechanical biocompatibilities of β-type titanium alloys for biomedical applications are also described along with the suitability of those β-type titanium alloys which exhibit super-elastic and shape-memory behavior. Finally, the unique behavior of some β-type titanium alloys for biomedical applications is discussed.

Keywords β-Type titanium alloys • TNTZ • Low Young's modulus • Self-tunable Young's modulus • Removable titanium alloys • Mechanical biocompatibility

M. Niinomi (✉)
Institute for Materials Research, Tohoku University,
2-1-1, Katahira, Aoba-ku, Sendai 980-8577, Japan
e-mail: niinomi@imr.tohoku.ac.jp

C.J. Boehlert
Department of Chemical Engineering and Materials Science, Michigan State University,
428 South Shaw Lane, 2527 Engineering Building, East Lansing, MI 48824, USA
e-mail: boehlert@egr.msu.edu

M. Niinomi et al. (eds.), *Advances in Metallic Biomaterials*, Springer Series
in Biomaterials Science and Engineering 3, DOI 10.1007/978-3-662-46836-4_8

8.1 Introduction

From the point of view of osteogenesis, the biocompatibility of titanium and its alloys is the greatest among all of the known metallic biomaterials [1]. Titanium alloys are also considered to be suitable alternatives to stainless steels and Co–Cr alloys, which are currently used commercially as biomaterials in implant devices. This is primarily attributable to the typically low Young's moduli of titanium alloys, which is effective in both inhibiting bone resorption and enhancing good remodeling as the load transfers through both the implant and bone when the Young's moduli of the two materials are closely matched [2–4]. Another advantage of titanium alloys is their relatively low density. The density of titanium alloys is approximately 4.5 g/cc, about half that of stainless steels and Co–Cr alloys [5]. There are other beneficial aspects of titanium alloys. Titanium alloys are resistant to in vivo corrosion, pitting attack, and crevice corrosion [6]. Since titanium does not enter the body chemistry as readily as other implant materials, healing is relatively unimpeded, and the life span of the implant is significantly extended [6, 7]. Titanium is the ninth most abundant element in the earth's crust and the fourth most abundant structural metal, and it is affordable, with the cost of titanium constantly dropping due to its demand in a large number of markets, including the aerospace and sports and recreational industries [8, 9]. Both Ti–6Al–4V (wt.%) ELI (henceforth all alloy compositions are given in weight percent unless noted otherwise), which is a widely used (α + β)-type titanium alloy in the aerospace field, and pure titanium have been previously used as biomaterials for constructing implant devices. However, problems still exist in that the strength of pure titanium is poor, whereas Ti–6Al–4V ELI contains elements that are harmful to the human body. Furthermore, the Young's moduli of pure titanium and Ti–6Al–4V ELI, at around 105 and 110 MPa, respectively, are much greater than the 10–30 GPa typical of bone [4]. This has therefore necessitated the developments of low Young's moduli titanium alloys composed of nontoxic and allergy-free elements.

Titanium alloys are generally grouped into α-type, (α + β)-, and β-type titanium alloys according to their primary constitutional phase(s). The α-type titanium alloys are composed of single-phase α-microstructures, and the β-type titanium alloys are composed of single-phase β-microstructures. The (α + β)-type titanium alloys are composed of two-phase α + β-microstructures. The α- and β-phases consist of the hexagonal closed-packed (HCP) and body-centered (BCC) structures, respectively, the latter possessing a lower atomic density. These characteristics are depicted in Fig. 8.1 [10]. The Young's modulus is typically smaller in β-type titanium alloys than in α- or (α + β)-type titanium alloys, and so β-type titanium alloys have been the focus of researchers aiming to produce titanium alloys with as low a Young's modulus as possible.

On the other hand, depending on the type of implant, a low Young's modulus can sometimes prove detrimental [11]. For example, when applying a β-type titanium alloy, with a low Young's modulus, to spinal fixation devices, the amount of

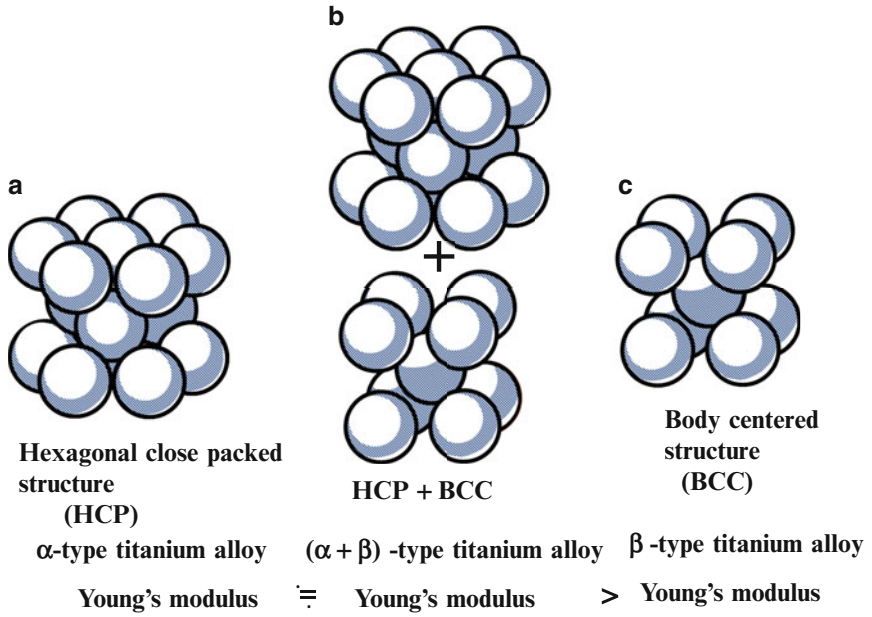

Fig. 8.1 Schematic explanation of α-, (α + β)-, and β-type titanium alloys based on crystal structure (Reprinted with permission from Ref. [10]. Copyright 2013, Jpn Soc For Bone Morphometry)

springback in the device should ideally be as small as possible in order to improve its handling ability during operations [11]. This degree of springback is considered to be related to the Young's modulus, with a lower Young's modulus correlating to a larger springback. To put it more simply, a higher Young's modulus is more desirable for surgeons, whereas a lower Young's modulus is more desirable for patients. Consequently, in developing spinal fixation devices, it is necessary to satisfy the competing requirements of both the surgeon and the patient [11]. In order to address this issue, β-type titanium alloys with a partially changeable Young's modulus have recently been developed. At the same time, removable β-type titanium alloys also have been developed [12], as removing implants is sometimes required, particularly in the case of younger people. As far as practical applications are concerned, the mechanical properties of biomaterials, such as fatigue properties, strength and elongation to fracture, fracture toughness, fretting fatigue properties, wear properties, and Young's modulus, are all important factors. Among these, the fatigue strength (i.e., endurance) is particularly important. However, a means of improving fatigue strength without significantly increasing the Young's modulus is desired.

In this chapter, the development of low Young's modulus titanium alloys, self-adjustable Young's modulus titanium alloys, and the enhancement of fatigue strength in titanium alloys with a low Young's modulus are all described.

8.2 Development of Low Young's Modulus Titanium Alloys

If the Young's modulus of an implant is higher than that of the cortical bone, then the load is preferentially transferred to the implant. This phenomenon is referred to as stress shielding, and it is especially true in the case of load-bearing implants, such as those used for replacing failed hard tissue (cortical bone). When stress shielding occurs, it results in bone resorption and poor bone remodeling, which are the leading causes of implant loosening and refracture of the bone after implant extraction. As previously mentioned, the Young's moduli of β-type titanium alloys are typically smaller than those of the other metallic biomaterials, such as stainless steels and Co–Cr alloys, as well as those of α- and (α + β)-type titanium alloys. For example, the Young's moduli of SUS316L stainless steel, Co–Cr alloy, α-type pure titanium, and (α + β)-type Ti–6Al–4V ELI are 180, 210, 105, and 110 GPa, respectively [4]. Various low-modulus β-type titanium alloys have been developed for biomedical applications as shown in Table 8.1 [13]. Those low-modulus β-type titanium alloys which contain the most biocompatible elements are Ti–35Nb–7Zr–5Ta (TNZT: TiOsteum) [14], Ti–29Nb–13Ta–4.6Zr (TNTZ) [15], and Ti–36Nb–2Ta–3Zr–O (gum metal) [16]. Nb, Ta, and Zr are relatively safe elements for the human body based on reported cytotoxicity [17] [18] and metal allergy [19] data. Ti–35Nb–7Zr–5Ta (TNZT: TiOsteum) and Ti–29Nb–13Ta–4.6Zr (TNTZ), developed using a d-electron alloy design method based on the DV-Xα theory, and Ti–36Nb–2Ta–3Zr–O (gum metal: single crystal) exhibit Young's modulus values of approximately 55, 60, and 70 GPa, respectively. Note, however, that these values are still much higher than that of cortical bone (10–30 GPa), and thus a means of lowering the Young's modulus of the Ti–Nb–Ta–Zr β-type titanium alloy system is desirable.

Owing to the high cost of rare metal elements, such as Nb, Ta, Mo, and Zr, low-modulus β-type titanium alloys have recently been proposed that are based on lower-cost elements such as Fe, Cr, Mn, Sn, and Al. Examples of such alloys include Ti–10Cr–Al [20], Ti–Mn [21], Ti–Mn–Fe [22], Ti–Mn–Al [23], Ti–Cr–Al [24], Ti–Sn–Cr [25], Ti–Cr–Sn–Zr [26], Ti–(Cr, Mn)–Sn [27], and Ti–12Cr [11].

8.3 Reducing Young's Modulus

The Young's moduli of several β-type titanium alloys used for biomedical applications are typically around 80 GPa. However, the Young's modulus of Ti–Nb–Ta–Zr alloys typically ranges between 55 and 70 GPa. Further reduction of the Young's moduli of β-type titanium alloys, such as TNTZ, can be achieved by severe cold rolling. As shown in Fig. 8.2 [28], the Young's modulus obtained with a high cold-working ratio is smaller than that without cold rolling. This decrease is attributable to the texture formation during cold rolling. A Young's modulus of around 40 GPa has been achieved in Ti–35Nb–4Sn using a 90 % reduction, as shown in Fig. 8.3

Table 8.1 Representative low-modulus β-type titanium alloys for biomedical applications.

β-type titanium alloys	ASTM standard	ISO standard	JIS standard
Ti-13Nb-13Zr	ASTM F 1713	–	–
Ti- 12Mo-6Zr-2Fe (TMZF)	ASTM F 1813	–	–
Ti-12Mo-5Zr-5Sn	–	–	–
Ti-15Mo	ASTM F 2066	–	–
Ti-16Nb-10Hf (Tiadyne 1610)	–	–	–
Ti-15Mo-2.8Nb-0.2Si	–	–	–
Ti-15Mo-5Zr-3Al			JIS T 7401-6
Ti-30Ta	–	–	–
Ti-45Nb	AMS 4982	–	–
Ti-35Zr-10Nb	–	–	–
Ti-35Nb-7Zr-5Ta (TNZT)	Task force F-04.12.23	–	–
Ti-29Nb- 13Ta-4.6Zr (TNTZ)	–	–	–
Ti-35Nb-4Sn	–	–	–
Ti-50Ta	–	–	–
Ti-8Fe-8Ta	–	–	–
Ti-8Fe-8Ta-4Zr	–	–	–
Ti-35Nb-2Ta-3Zr	–	–	–
Ti-22.5Nb-0.7Zr-2Ta	–	–	–
Ti-23Nb-0.7Ta-2.0Zr- 1.2O (Gum Metal)	–	–	–
Ti-28Nb-13Zr-0.5Fe (TNZF)	–	–	–
Ti-24Nb-4Zr-7.9Sn (Ti2448)	–	–	–
Ti-7.5Mo	–	–	–
Ti-12Mo-3Nb	–	–	–
Ti-12Mo-5Ta	–	–	–
Ti-12Cr	–	–	–
Ti-30Zr-7Mo	–	–	–
Ti-30Zr-3Mo-3Cr	–	–	–
Ti-5Fe-3Nb-3Zr	–	–	–

Reprinted with permission from Ref. [13]. Copyright 2006, Taylor & Francis Group

[29]. Severe plastic deformation (SPD) is also effective in reducing the Young's moduli of biomedical β-type titanium alloys. Figure 8.4 [30] shows the Young's moduli of TNTZ subjected to severe cold rolling ($TNTZ_{CR}$) and the SPD process of high-pressure torsion (HPT) after 5, 10, 40, and 60 rotations, N. The Young's modulus decreases as the texture increases, with an increase in N; a minimum Young's modulus of around 60 GPa can be achieved at $N = 60$.

Since texture affects the Young's moduli of polycrystalline β-type titanium alloys, a similar affect is expected for single crystals. The dependence of the Young's modulus on the crystal direction was therefore investigated in monocrystalline TNTZ, the results of which are shown in Fig. 8.5 [31]. A Young's modulus of around 35 GPa, which is comparable to the high-range Young's modulus values of cortical bone, was measured in the <100> direction.

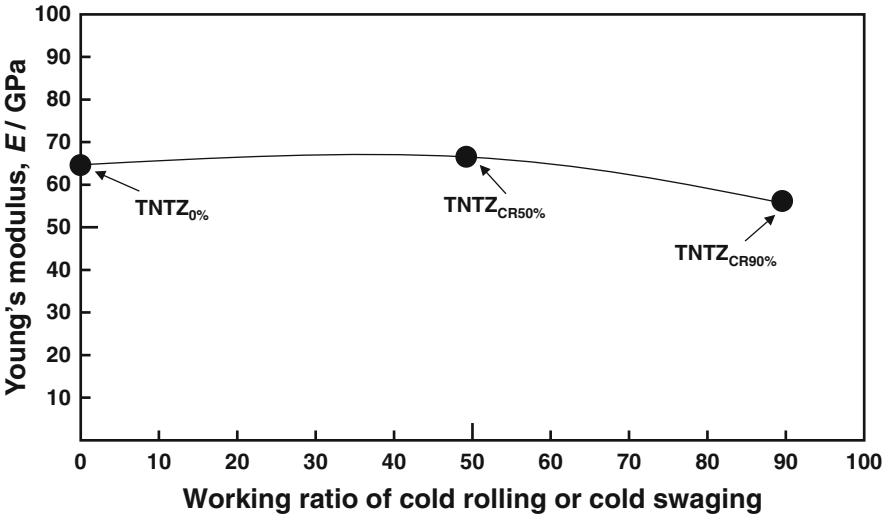

Fig. 8.2 Young's modulus of TNTZ subjected to cold rolling as a function of working ratio (Reprinted with permission from Ref. [28]. Copyright 2010, Iron and Steel Inst. Jpn)

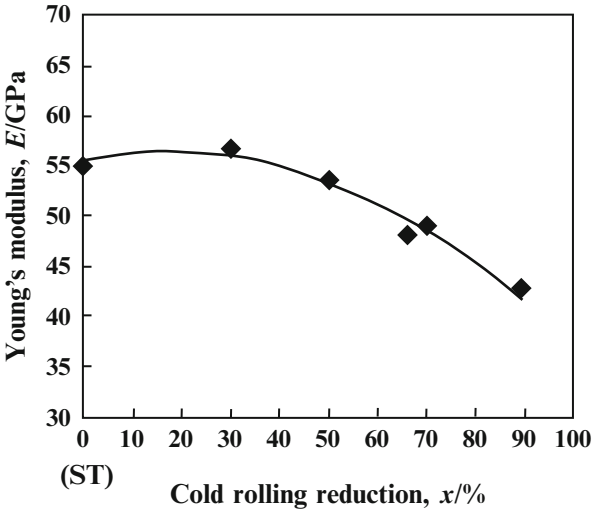

Fig. 8.3 Young's modulus of Ti–35Nb–4Sn as a function of reduction. *ST* stands for solution treatment (Reprinted with permission from Ref. [29]. Copyright 2006, ASM Int)

8.4 Titanium Alloys for Removable Implants

There are certain types of internal fixation devices that need to be removed after surgery in agreement with specific criteria. These include implants into the bone marrow, such as femoral, tibial, and humeral marrow, screws used for bone plate fixation [32], and some implants used for children, which would otherwise grow

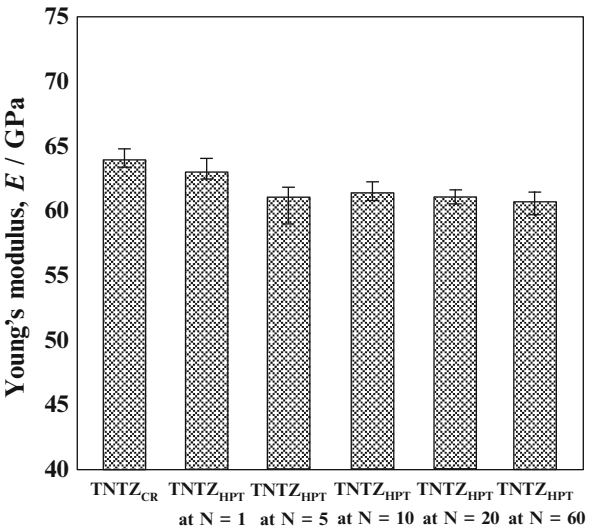

Fig. 8.4 Young's moduli of $TNTZ_{CR}$ and SPD $TNTZ_{HPT}$ at $N = 1$–60. N stands for rotation number (Reprinted with permission from Ref. [30]. Copyright 2013, Elsevier B. V)

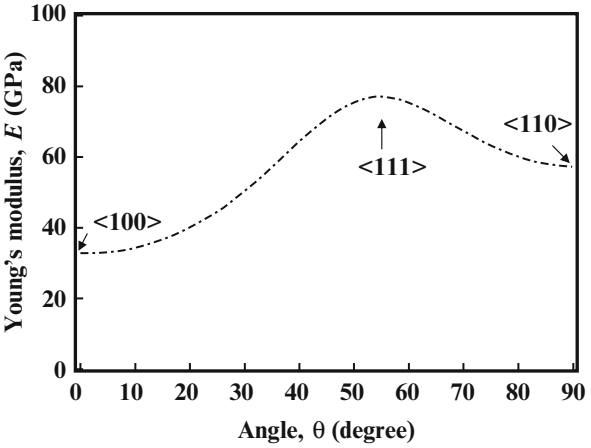

Fig. 8.5 Young's modulus of single-crystal Ti–29Nb–13Ta–4.6Zr in directions between [100] and [110] (Reprinted with permission from Ref. [31]. Copyright 2008, Elsevier B. V)

into the bone. Implant removal can result in undesirable results, such as palpable hardware, wound dehiscence, and/or exposure of the hardware [33, 34]. Any assimilation of the removable internal fixators with the bone, due to the precipitation of calcium phosphate, can cause refracture of the bone during the fixator-removal operation. In such cases, it is essential to prevent adhesion between the alloys and bone tissues. Thus, the precipitation of calcium phosphate must be inhibited.

Zirconium and titanium belong to the same group (i.e., same column in the periodic table), have the same crystal structure, and have unlimited solubility in each other [35]. Furthermore, zirconium is expected to be an effective element for solution strengthening and, with respect to toxicity, is no more harmful than titanium [36, 37]. Zirconium also has the ability to prevent the precipitation of

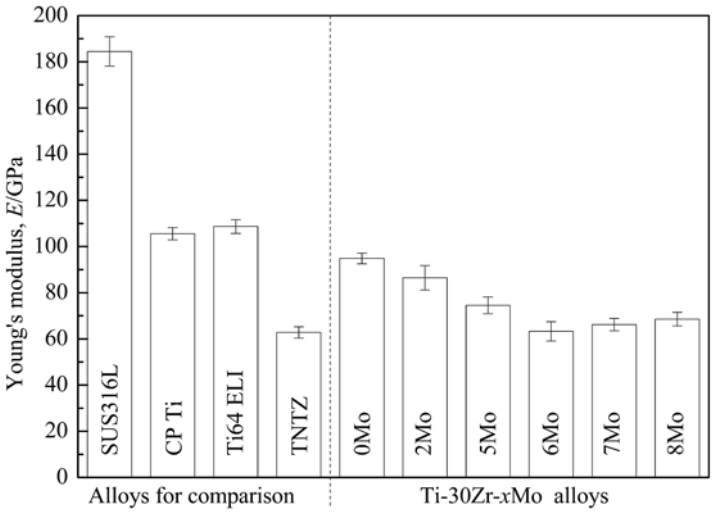

Fig. 8.6 Young's moduli of Ti–30Zr–*x*Mo ($x = 0$, 2, 5, 6, 7, and 8 wt.%) alloys subjected to solution treatment and SUS316L stainless steel (SUS316L), commercially pure titanium (CP Ti), Ti–6Al–4V ELI (Ti64 ELI), and TNTZ for comparison (Reprinted with permission from Ref. [12]. Copyright 2011, Elsevier B. V)

calcium phosphate [32, 38], the main component in bones [39], and this holds true for titanium alloys with zirconium contents exceeding 25 mass%. Moreover, the tensile strength of Ti–Zr alloys is fairly high, although the elongation to failure is reduced when the zirconium content exceeds 56 mass% [40]. Overall, binary Ti–Zr alloys with high zirconium contents exhibit a combination of high strength [40–43] and excellent biocompatibility [37]. On the basis of these findings, biomedical Ti–Zr-based alloys such as Ti–Zr–Nb [44], Ti–Zr–Nb–Ta [45], and Ti–Zr–Al–V [44] have been recently developed. Additionally, Ti–30Zr–Mo [12] has also been developed in titanium alloys optimized for use in removable implants.

The Young's moduli of Ti–30Zr–*x*Mo alloys subjected to solution treatment are compared to other biomedical materials in Fig. 8.6 [12]. The Young's moduli of Ti–30Zr–*x*Mo alloys are lower than those of the other alloys considered with the exception of TNTZ. The addition of Mo to Ti–30Zr reduces the Young's modulus, where a minimum value of around 60 GPa (a reduction of 34 % compared with Ti–30Zr) is achieved when 6Mo is added. TNTZ, Ti–30Zr–6Mo, and Ti–30Zr–7Mo exhibit the lowest Young's modulus values of all those compared in Fig. 8.6. Figure 8.7 [12] compares the elastic admissible strain against elongation to failure for a distribution of as-solutionized Ti–30Zr–*x*Mo alloys along with other biomedical materials. Typically in orthopedic applications, an ideal biomedical implant material is one which exhibits both a high strength and a low Young's modulus. The elastic admissible strain, defined as the strength-to-modulus ratio, is therefore a useful parameter for consideration in such applications, a higher value indicating that the material is more suitable [46]. From Fig. 8.7, it can be seen that Ti–30Zr–6Mo

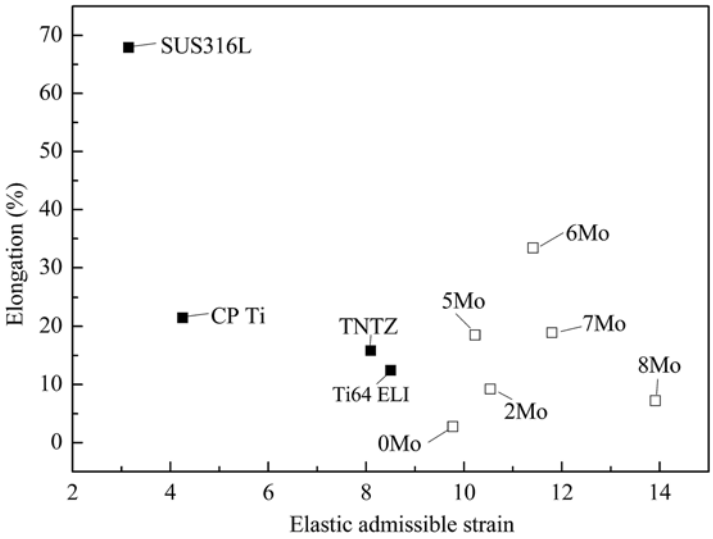

Fig. 8.7 A plot of elastic admissible strain versus elongation to fracture for a distribution of solutionized Ti–30Zr–*x*Mo (x=0, 2, 5, 6, 7, and 8 mass%) alloys and other biomedical materials (Reprinted with permission from Ref. [12]. Copyright 2011, Elsevier B. V)

and Ti–30Zr–7Mo exhibit a more attractive combination of higher elongation to failure and higher elastic admissible strain than those of the other Ti–30Zr–*x*Mo alloys as well as the other materials considered for comparison, including SUS316L stainless steel, commercially pure titanium (CP Ti), Ti–6Al–4V ELI, and TNTZ. In addition, both Ti–30Zr–6Mo and Ti–30Zr–7Mo exhibit a lower Young's modulus (almost three-fifths that of Ti–6Al–4V ELI), as shown in Fig. 8.6 [12]. These two alloys therefore show potential as candidates for use in biomedical applications.

Ti–30Zr–7Mo, on the basis of its low Young's modulus, high elastic admissible strain, large elongation, and high 0.2 % proof stress, was selected for cytocompatibility testing [12]. Figure 8.8 [12] shows the density of cells cultured in Ti–30Zr–7Mo after 86.4 ks (24 h), which is considerably greater than that observed for the other materials compared. The formation of sulfite and/or sulfide in SUS316L stainless steel is believed to be the reason for the relatively low cell density measured for this alloy when compared with CP Ti, Ti–6Al–4V ELI, and TNTZ, all of which garnered similar cell density values.

8.5 Titanium Alloys with a Self-Tunable Young's Modulus

For spinal fixation devices, which represent a specific type of orthopedic implant, a low Young's modulus is preferred for the formation of healthy bones [47]. However, during spinal fixation operations, surgeons are required to bend such devices in

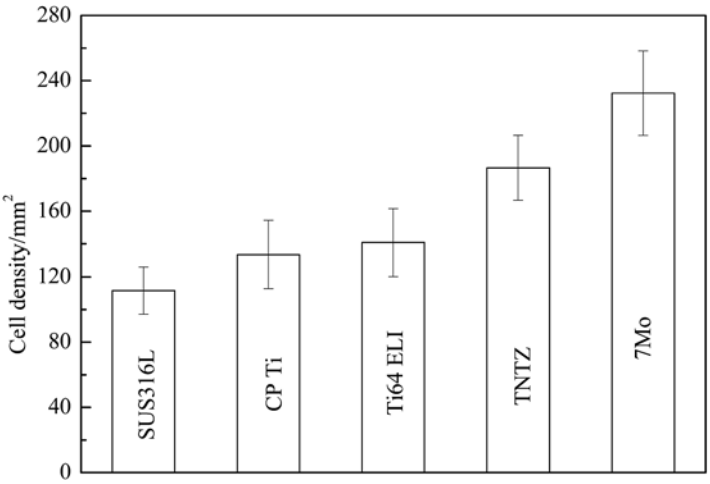

Fig. 8.8 A plot comparing the density of cells cultured in 24 h, during a cytocompatibility study, on samples of Ti–30Zr–7Mo and other biomedical materials (Reprinted with permission from Ref. [12]. Copyright 2011, Elsevier B. V)

order to reproduce the physiological curvature of the patient's spine [48]. This bending sometimes has to be performed within a limited space inside the patient's body. Therefore, a large springback is problematic for the formation of the desired shape of the devices. The degree of springback depends mainly on the strength and Young's modulus; a lower Young's modulus leads to a higher degree of springback. As a result, the Young's modulus of titanium alloys for spinal fixation devices must be sufficiently low to avoid the stress shielding effect, yet high enough to suppress springback [49]. New types of titanium alloys, in which the Young's moduli prior to deformation are low but increase during deformation (i.e., self-tuning Young's moduli), have therefore been proposed. Of these alloys, Ti–Cr was the first to be developed, followed later by Ti–17Mo [50], Ti–30Zr–5Cr [51], Ti–30Zr–7Mo [52], and Ti–30Zr–3Mo–3Cr [51]. At the same time, Ti–30Zr–5Cr [51] and Ti–30Zr–3Mo–3Cr [51] were also developed for use as removable titanium alloys.

The Young's moduli of a titanium alloy with a self-tunable Young's modulus (Ti–12Cr) and those for TNTZ subjected to solution treatment and cold rolling are shown in Fig. 8.9 [11]. Note that the Young's moduli of both Ti–12Cr and TNTZ subjected to solution treatment are similar (~62–64 GPa). During cold rolling, TNTZ does not exhibit a deformation-induced phase transformation, and therefore there is almost no change in its Young's modulus. On the other hand, an increase in Young's modulus due to cold rolling is observed in Ti–12Cr. The increase in Young's modulus is a result of the deformation-induced ω-phase transformation, which occurs during cold rolling in Ti–12Cr as confirmed using a transmission electron microscopy [11]. The Young's moduli of β-type titanium alloys are increased by the formation of the ω-phase [53], and this explains the increased Young's modulus

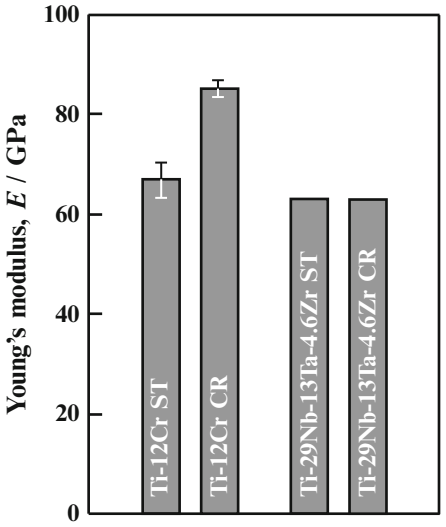

Fig. 8.9 Young's moduli of Ti–12Cr and TNTZ subjected to solution treatment (*ST*) and cold rolling (*CR*) (Reprinted with permission from Ref. [11]. Copyright 2011, Elsevier B. V)

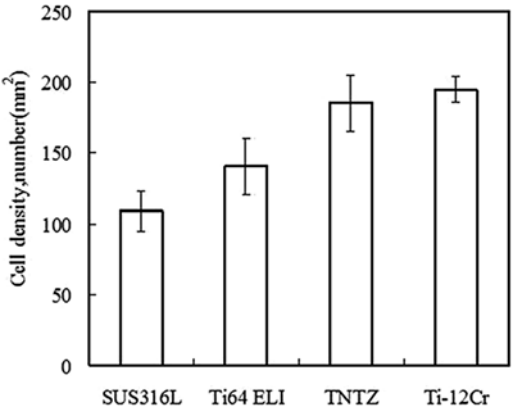

Fig. 8.10 Density of MC3T3-E1cells cultured in Ti–12Cr alloy subjected to solution treatment and SUS316L stainless steel (SUS316L), Ti–6Al–4V ELI (Ti64 ELI), and TNTZ considered for comparison for 86.4 ks (Reprinted with permission from Ref. [55]. Copyright 2012, Elsevier B. V)

observed in cold-rolled Ti–12Cr [11, 54]. Figure 8.10 [11] shows the density of cells cultured in Ti–12Cr for 86.4 ks (24 h) in comparison with other alloys. Ti–12Cr exhibited the highest cell density.

Decreasing the chromium content in Ti–(10–12)Cr alloys can reduce the β(bcc)-lattice stability, as chromium acts as a β-stabilizing element. This, in turn, increases the amount of the ω-phase, which is separated into the athermal ω-phase, formed during quenching, and the deformation-induced ω-phase, caused by cold rolling. This would seem to suggest that a lower chromium content is beneficial for enhancing the ω-phase transformation in Ti–(10–12)Cr alloys. It is important to point out that the suppression of the athermal ω-phase transformation is likely to result in an increase in the deformation-induced ω-phase transformation [55]. Therefore, suppressing the formation of the athermal ω-phase in low-Cr Ti–Cr

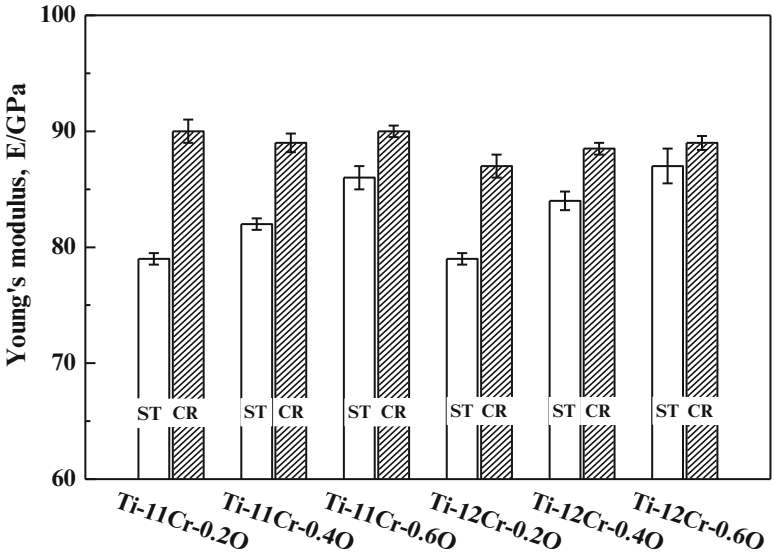

Fig. 8.11 Young's moduli of Ti–(11,12)Cr–(0.2, 0.4, 0.6)O alloys subjected to ST and CR (Reprinted with permission from Ref. [58]. Copyright 2014, Elsevier B. V)

alloys should achieve not only a low Young's modulus prior to deformation but also an increase in the deformation-induced ω-phase transformation after cold rolling, which would result in an increase in the Young's modulus.

The athermal ω-phase in titanium alloys can be suppressed by oxygen addition [56, 57]. As a consequence, the addition of oxygen to Ti–Cr alloys increases the Young's modulus of the alloy after deformation [58]. Figure 8.11 [58] shows the Young's moduli of Ti–(11,12)Cr–(0.2, 0.4, 0.6)O alloys subjected to solution treatment (ST) and cold rolling (CR). For the alloys with identical chromium contents, the Young's moduli increase with increasing oxygen content. This can be attributed to the solid solution-strengthening effect of oxygen as well as the aforementioned ω-phase transformation effect. Furthermore, the Young's moduli of Ti–11Cr–0.2O and Ti–12Cr–0.2O are almost identical, whereas Ti–12Cr–0.4O and Ti–12Cr–0.6O have slightly higher Young's moduli than those of Ti–11Cr–0.4O and Ti–11Cr–0.6O, respectively. The reasons for this have been reported as follows: For Ti–11Cr–0.2O and Ti–12Cr–0.2O, there is still a small amount of athermal ω-phase formed in the ST condition. Consequently, the Young's moduli of these alloys are influenced by the competing effects of the athermal ω-phase, which can be suppressed by increasing the chromium content to stabilize the β-lattice, and the solid solution-strengthening effect of chromium. Conversely, because almost no athermal ω-phase forms in the Ti–(11,12)Cr–(0.4, 0.6)O alloys, the solid solution-strengthening effect of chromium becomes the primary reason for the change in Young's modulus.

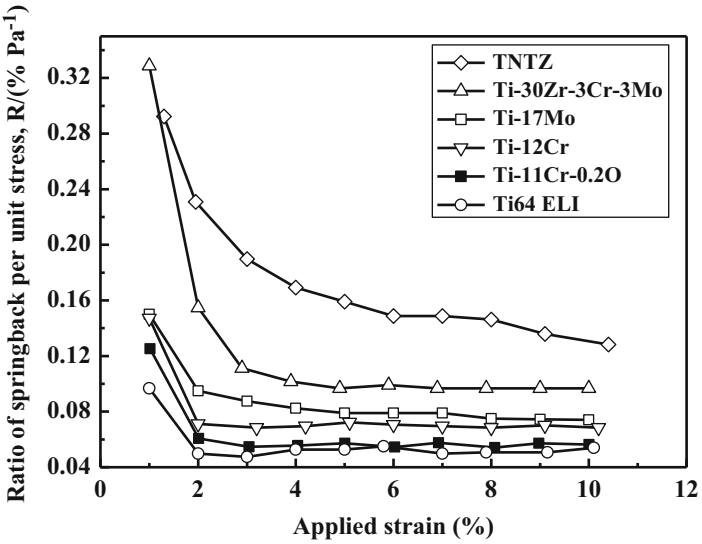

Fig. 8.12 Ratio of springback per unit stress (*R*) as a function of applied strain for Ti–11Cr–0.2O, TNTZ, Ti–30Zr–3Cr–3Mo, Ti–17Mo, Ti–12Cr, and Ti–6Al–4V ELI (Ti64 ELI) subjected to solution treatment (Reprinted with permission from Ref. [58]. Copyright 2014, Elsevier B. V)

The Young's modulus is always greater for the CR material compared to the ST material. Ti–11Cr–0.2O exhibits a Young's modulus of less than 80 GPa in the ST condition, which is much lower than that for SUS316L stainless steel, CP Ti, and Ti–6Al–4V ELI. Ti–11Cr–0.2O also exhibits a Young's modulus of more than 90 GPa in the CR condition. This change in Young's modulus, which is the greatest change in Young's modulus among all the materials examined, is desirable for satisfying the competing requirements of both surgeons and patients in spinal fixation applications. Figure 8.12 [58] depicts comparative profiles of the ratio of springback per unit stress as a function of the applied strain for TNTZ, Ti–30Zr–3Cr–3Mo, Ti–17Mo, Ti–12Cr, Ti–11Cr–0.2O, and Ti–6Al–4V ELI. These ratios all show a similar trend, with an initial significant decrease that then stabilizes with further increase in the applied strain. Ti–11Cr–0.2O reaches a low and stable ratio when the applied strain is greater than 2 %. It therefore exhibits a minimal ratio of springback per unit stress. The ratio for Ti–11Cr–0.2O is always much lower than that of TNTZ, and it is similar to that for Ti–6Al–4V ELI.

To satisfy the requirements for spinal fixation applications, chromium can be added to TNTZ, which results in a higher deformation-induced Young's modulus. Two newly designed alloys, TNTZ–8Ti–2Cr and TNTZ–16Ti–4Cr, possess a more stable β-phase than TNTZ, and their Young's moduli increase in going from the ST condition to the CR condition, where a higher Young's modulus value is exhibited by the alloy with the higher Cr content; see Fig. 8.13 [59]. These two alloys exhibit

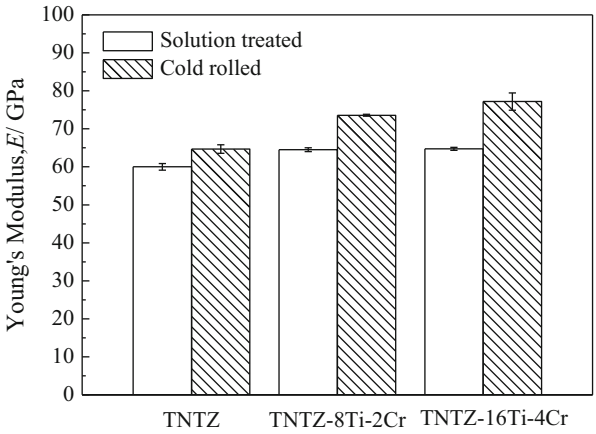

Fig. 8.13 Young's modulus of TNTZ subjected to solution treatment and cold rolling and Cr-added TNTZ subjected to solution treatment and cold rolling (Reprinted with permission from Ref. [59]. Copyright 2013, Elsevier B. V)

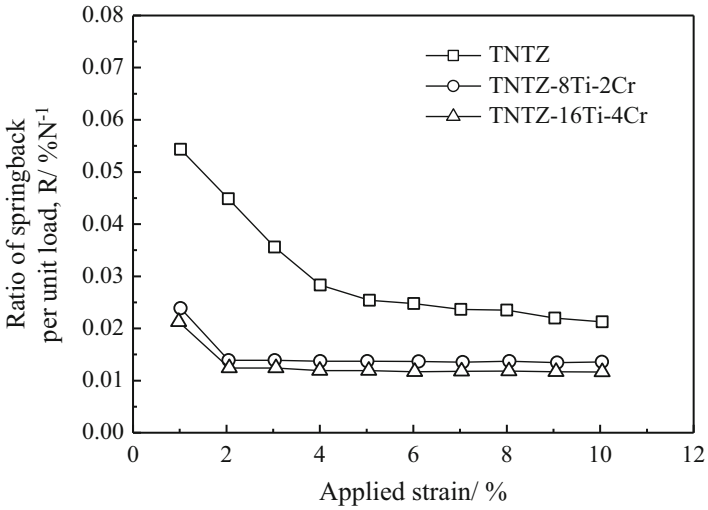

Fig. 8.14 Ratio of springback per unit load (R) as a function of applied strain for TNTZ and Cr-added TNTZ subjected to solution treatment (TNTZ–ST, TNTZ–8Ti–2Cr–ST, and TNTZ–16Ti–4Cr–ST) (Reprinted with permission from Ref. [59]. Copyright 2013, Elsevier B. V)

an increased Young's modulus after cold rolling, with TNTZ–16Ti–4Cr exhibiting the greatest increase (~20 %, from ~64 GPa after solution treatment to ~77 GPa after cold rolling). These Cr-modified TNTZ alloys also show significantly less springback than the original TNTZ as demonstrated from the results of tensile and bending loading–unloading tests shown in Fig. 8.14 [59].

8.6 Effectiveness of Low Young's Modulus for Preventing Stress Shielding

Animal studies on Japanese white rabbits have been conducted on TNTZ, SUS316L stainless steel, and Ti–6Al–4V ELI to investigate the effects of intramedullary rod implantation [60] and bone plate implantation [3]. Using three-point bend tests, the Young's moduli for the intramedullary rods of TNTZ, Ti–6Al–4V ELI, and SUS316L stainless steel were measured to be 58, 108, and 161 GPa, respectively. For the implantation of the intramedullary rods and bone plates, both the lowest bone atrophy and best bone remodeling were reported for the TNTZ. In the study on bone remodeling, utilizing bone plates of TNTZ, Ti–6Al–4V ELI, and SUS316L stainless steel implanted into fracture models made in the rabbit tibiae, the healing conditions were observed using X-ray photographs taken at regular intervals up to 48 weeks after implantation. Following this, both tibiae were extracted along with the bone plate, and the bone formation was externally observed. For all the materials, bone union was obtained at 4 weeks after implantation (4w), and the fracture line was barely discernible at 8 weeks after implantation (8w). Moreover, the trace of the experimental fracture was completely absent at 16–20 weeks after implantation (16 W and 20 W, respectively). However, bone atrophy (thinning of the cortical bone) was observed under the bone plate, with the time at which this occurred varying between the different materials. The X-ray images taken from 4 weeks after implantation to 18 weeks after implantation (18w) for each plate are shown in Fig. 8.15 [3]. In SUS316L stainless steel, the thinning of the cortical bone was first observed 7 weeks after implantation, and the cortical bone has almost disappeared at 12 weeks after implantation (12w), as shown in Fig. 8.15a. In Ti–6Al–4V ELI, the thinning was first observed 7 weeks after implantation and had almost disappeared at 14 weeks after implantation (14w), as shown in Fig. 8.15b. In TNTZ, the thinning was first observed 10 weeks after implantation and had almost disappeared at 18 weeks after implantation, as shown in Fig. 8.15c. Furthermore, an increase in the diameter of the tibia and in the double-wall structure in the intramedullary bone tissue was observed only in the case of the bone plate made of TNTZ, as shown in Fig. 8.16 [3]. In this figure, the inner wall bone structure represents the original cortical bone, i.e., the remaining old cortical bone, while the outer wall bone structure is the newly formed part. This bone remodeling is the direct result of using a bone plate with a low Young's modulus.

Guo et al. [61] also carried out a study to investigate the effect of Young's modulus on bone fracture healing by implanting intramedullary rods of a low Young's modulus β-type titanium alloy (Ti–24Nb–4Zr–7.9Sn (Ti2448) with a Young's modulus of 42 GPa) and Ti–6Al–4V ELI into fracture models made in rabbit tibiae. They reported the mean maximum pull-out force of an intramedullary rod made of Ti2448 to be higher than that of a rod made of Ti–6Al–4V ELI. This suggests that the lower Young's modulus assists new bone formation in the marrow cavity. They

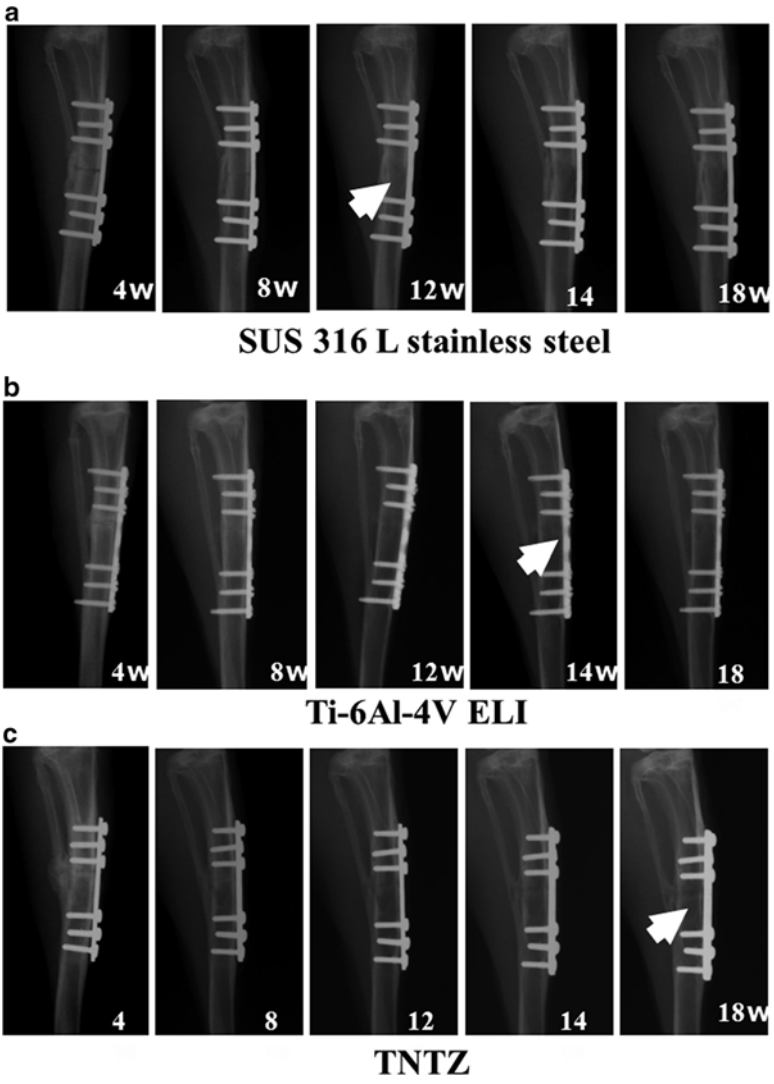

Fig. 8.15 X-ray photographs taken after implanting the bone plate into a fracture model made in the tibia of a rabbit: (**a**) SUS316L stainless steel, (**b**) Ti–6Al–4V ELI, and (**c**) TNTZ. The *bottom right*-hand corner of the image indicates the time in weeks after implantation in which the photograph was taken (Reprinted with permission from Ref. [3]. Copyright 2008, Springer International Publishing A. G)

also reported that the BMD (bone mineral density: mg (HyAp)/cm3) and BVP (bone volume fraction, the ratio between bone volume and total volume) were higher when an intramedullary rod of Ti2488 was implanted than when a Ti–6Al–4V ELI rod was used [61].

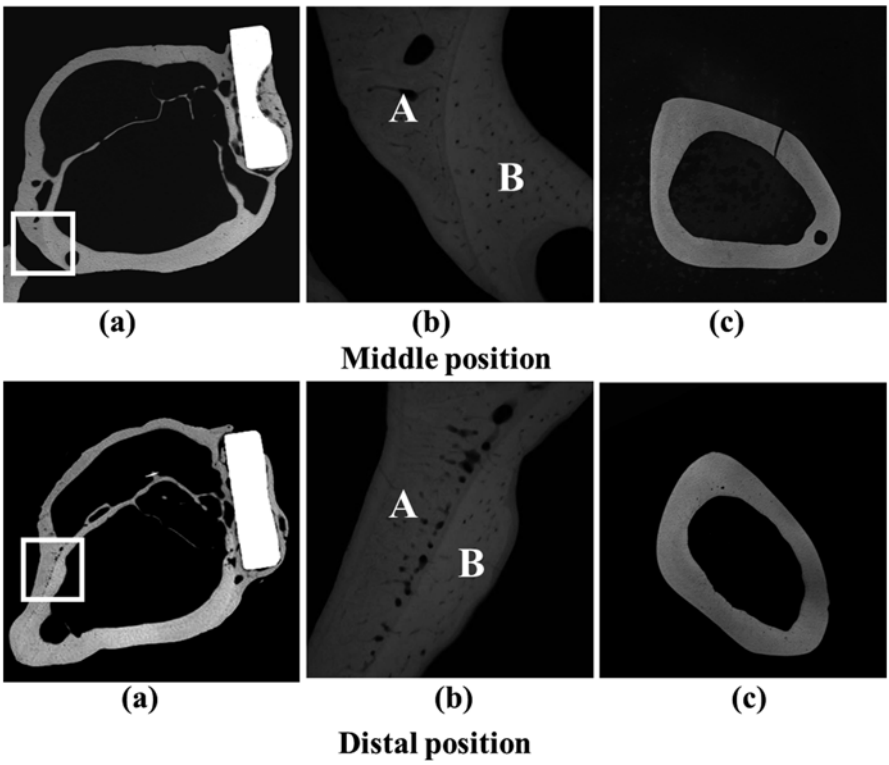

Fig. 8.16 Contact microradiograms (CMRs) of the cross sections of animal fracture models implanted (**a**) with and (**c**) without bone plates made of TNTZ at the middle position and distal positions at 48 weeks after implantation: (**a**) cross section of fracture model with implanted bone plate (*bright white*), (**b**) higher-magnification CMR images of regions highlighted in (**a**) where *A* represents new bone and *B* represents old bone (Reprinted with permission from Ref. [3]. Copyright 2008, Springer International Publishing A. G)

8.7 Enhancement of Mechanical Biocompatibility

For structural biomaterials used in implants that replace hard tissue, the Young's modulus needs to be controlled along with other factors, such as tensile strength, elongation to failure, fatigue life, fretting fatigue life, fracture toughness, wear properties, etc. These factors can be collectively referred to in a broad sense as mechanical biocompatibilities, and among these factors, fatigue strength is one of the most important from the viewpoint of an implant's endurance. In the case of β-type titanium alloys, the fatigue strength is generally poorer in the solution-treated condition, when the lowest Young's modulus is obtained.

The fatigue strength of β-type titanium alloys can, however, be improved by microstructural control (i.e., thermomechanical processing). With spinal rods, the

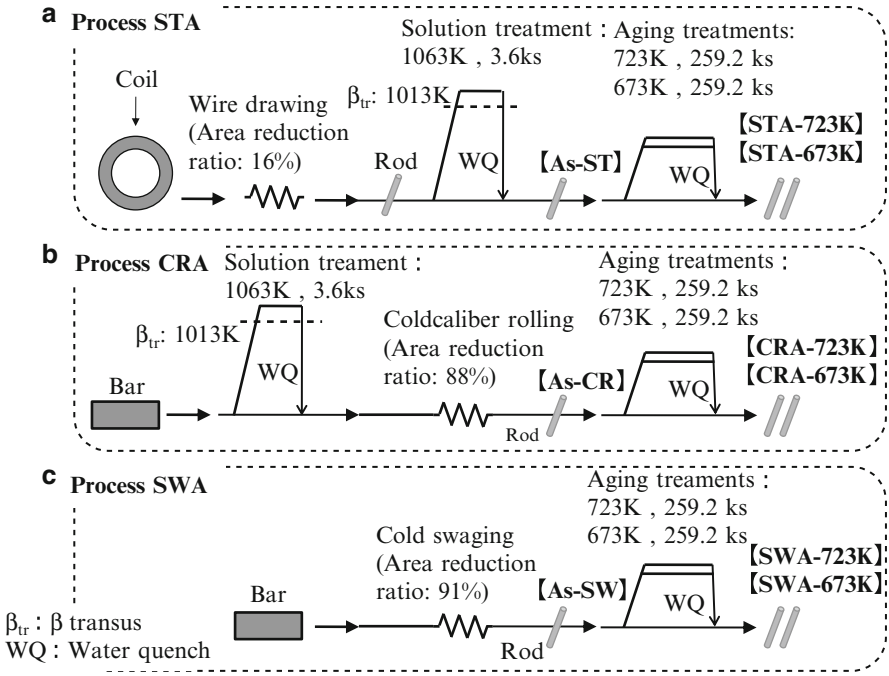

Fig. 8.17 Schematic drawings of thermomechanical treatments for TNTZ rods: (**a**) Process STA, (**b**) Process CRA, and (**c**) Process SWA (Reprinted with permission from Ref. [62]. Copyright 2013, Elsevier B. V)

fatigue strength is sometimes the primary driver; thereby the thermomechanical processing treatments are intentionally designed to improve the fatigue life of TNTZ (see Fig. 8.17 [62]). For each thermomechanical process depicted in Fig. 8.17, a different treatment is first applied prior to aging. In the first thermomechanical process (Process STA), the TNTZ bar is subjected to drawing to form a rod with an area reduction ratio of 15 %. This is then subjected to solution treatment in air for 3.6 ks at 1063 K, which is 50 K higher than the β-transus temperature, followed by water quenching (as-ST). The sample is then aged at either 673 K or 723 K for 259.2 ks in air followed by water quenching (ST-673 and ST-723, respectively).

For the second thermomechanical process (Process CRA), the TNTZ bar is subjected to cold caliber rolling to form a rod with an area reduction ratio of 88 % (as-CR) and then subjected to an aging treatment at 673 K or 723 K, followed by water quenching (CR-673 and CR-723, respectively).

For the final thermomechanical process (Process SWA), the TNTZ bar is subjected to cold swaging to form a rod with an area reduction ratio of 91 % (as-SW) and then subjected to an aging treatment at 673 K or 723 K, followed by water quenching (SW-673 and SW-723 K, respectively).

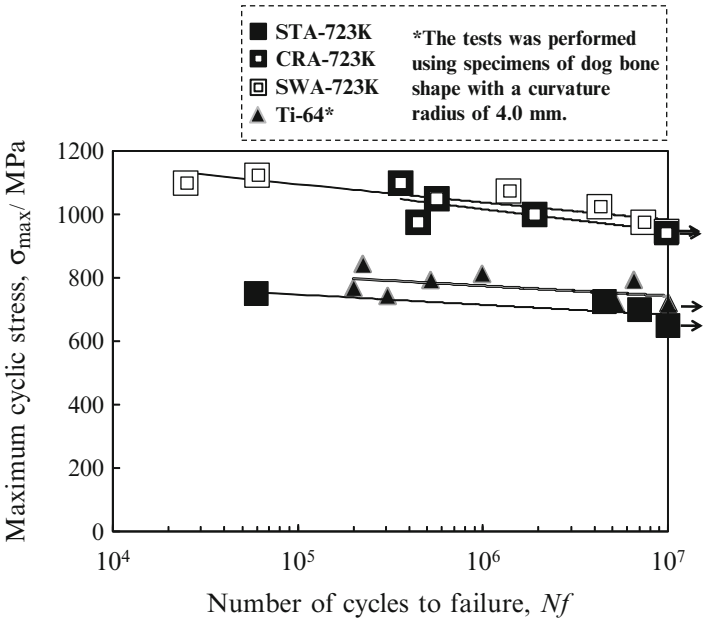

Fig. 8.18 S–N curves of TNTZ rod subjected to aging treatment at 723 K after solution treatment (STA-723 K), TNTZ rod subjected to aging treatment at 723 K after cold caliber rolling (CRA-723 K), and TNTZ rod subjected to aging treatment at 723 K after cold swaging (SWA-723 K) in comparison with that of Ti–6Al–4V ELI (Ti-64) (Reprinted with permission from Ref. [62]. Copyright 2012, Elsevier B. V)

The fatigue strength of TNTZ subjected to each thermomechanical process, where the aging temperature is 723 K, is shown in Fig. 8.18 [62] along with that of Ti–6Al–4V ELI. The fatigue limits of TNTZ after SWA-723 K, CRA-723 K, and STA-723 K are 950, 950, and 650 MPa, respectively, the fatigue limit of STA-723 being similar to that of Ti–6Al–4V ELI. The fatigue limits of TNTZ after SWA-723 and CRA-723 are significantly higher than that of Ti–6Al–4V ELI. Since the fatigue limit of TNTZ subjected to solution treatment is reported to be around 420 MPa [63], its fatigue strength can clearly be improved by thermomechanical treatments such as severe cold working and aging.

However, as shown in Fig. 8.19 [62], the Young's moduli of TNTZ rods subjected to each thermomechanical process increase when compared with as-ST, as-SW, or as-CR, though all the Young's moduli are lower than that of Ti–6Al–4V ELI. The Young's modulus therefore increases with aging treatment, the extent of which is dependent on the aging temperature. As previously mentioned, the precipitation of the ω-phase and α-phases increases the Young's moduli of β-type titanium alloys. The magnitude of the increase is determined by the type of phase which precipitates according to the following order: $\omega > \alpha > \beta$ [63, 64]. The Young's moduli of as-ST, as-SW, and as-CR are similar, as the strain and plasticity induced by cold working do not significantly affect the Young's modulus.

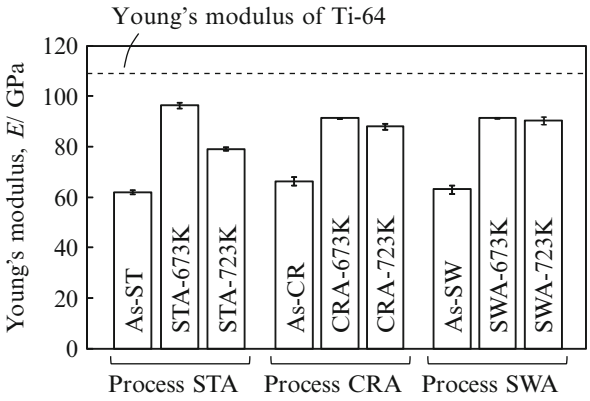

Fig. 8.19 Young's moduli of as-solutionized TNTZ rod (as-ST), TNTZ rods subjected to aging treatment at 673 K and 723 K after solution treatment (STA-673 K and STA-723 K, respectively), as-cold caliber-rolled TNTZ rod (as-CR), TNTZ rods subjected to aging treatment at 673 K and 723 K after cold caliber rolling (CRA-673 K and CRA-723 K, respectively), as-cold swaged TNTZ rod (as-SW), and TNTZ rods subjected to aging treatment at 673 K and 723 K after cold swaging (SWA-673 K and SWA-723 K, respectively) in comparison with that of Ti–6Al–4V ELI (Ti-64) (Reprinted with permission from Ref. [62]. Copyright 2012, Elsevier B. V)

8.8 Enhancement of Mechanical Biocompatibility While Maintaining a Low Young's Modulus

The static strength (i.e., tensile strength) of β-type titanium alloys, like TNTZ, can be improved through severe cold-working processes, such as severe cold rolling [65] and severe cold swaging [66], and/or SPD such as HPT [30, 67, 68]. Such processes have the potential to increase the tensile strength to levels similar to that or greater than that of Ti–6Al–4V ELI while still retaining adequate elongation to failure, as the high degree of plasticity introduced creates a great deal of work hardening. However, it is important to note that the dynamic strength (i.e., fatigue strength) is not improved by either severe cold working or SPD. Consequently, the most effective means of improving the fatigue strength of β-type titanium alloys is the introduction of a secondary phase, or secondary particles, into the β-phase matrix, either through aging or the direct addition of particles of hard materials such as ceramics.

ω-phase precipitation increases the strength and Young's modulus of β-type titanium alloys more than an equivalent amount of α-phase precipitation. However, the ω-phase precipitation also results in a decrease in the elongation to fracture of such alloys. A small amount of ω-phase precipitation is therefore expected to improve the fatigue strength of TNTZ while maintaining a low Young's modulus. A short-aging time at fairly low temperatures is effective in producing a small

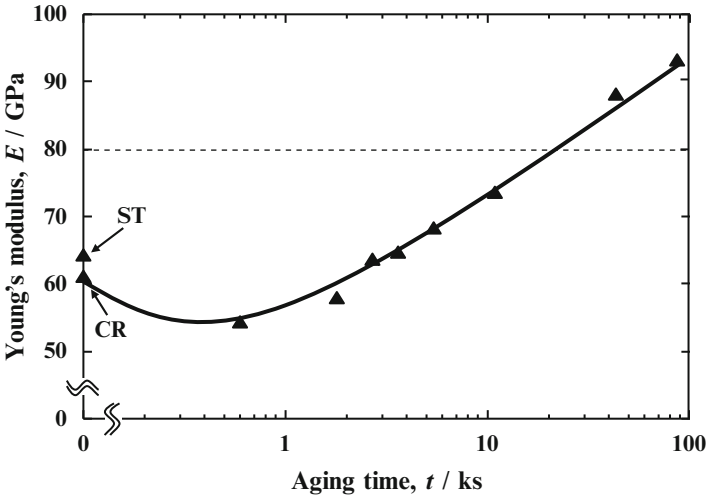

Fig. 8.20 Young's moduli of ST, CR, and AT samples as a function of aging time: ST, CR, and AT indicate TNTZ subjected to solution treatment, severe cold rolling, and aging treatment, respectively (Reprinted with permission from Ref. [69]. Copyright 2012, Springer International Publishing A. G)

amount of ω-phase precipitation. Figure 8.20 [30] shows the Young's moduli of TNTZ subjected to solution treatment (ST), severe cold rolling (CR), and aging after cold rolling at 573 K as a function of aging time (AT). With aging of up to approximately 10.8 ks, the Young's modulus is maintained at a value below 80 GPa. Figure 8.21 [69] shows the S–N curves for TNTZ subjected to ST, CR, and aging for 3.6 ks and 10.8 ks at 573 K. The fatigue strength of TNTZ can be improved by the aging treatment, while the Young's modulus is also maintained at less than 80 GPa. Transmission electron microscopy confirmed the presence of the ω-phase, therefore demonstrating that it is possible to effectively utilize the controlled precipitation of the ω-phase to improve the fatigue strength of TNTZ while also maintaining a low Young's modulus.

The addition of a small amount of ceramic particles into the matrix also improves the fatigue strength of β-type titanium alloys while still maintaining a low Young's modulus. This was confirmed by severe cold rolling of TNTZ containing TiB_2 or Y_2O_3. Figure 8.22 [70] shows the Young's modulus as a function of B or Y concentration from 0 to 1 mass%, and the Young's modulus was maintained around 60 GPa over this range.

Figure 8.23 [70] shows the S–N curves for TNTZ with 0.1 mass% and 0.2 mass% B or 0.2 mass% and 0.5 mass% Y subjected to cold rolling after solution treatment, along with comparative curves of TNTZ subjected to solution treatment or cold rolling after solution treatment. This demonstrates that the fatigue strength of TNTZ is indeed increased by the addition of either TiB_2 or Y_2O_3.

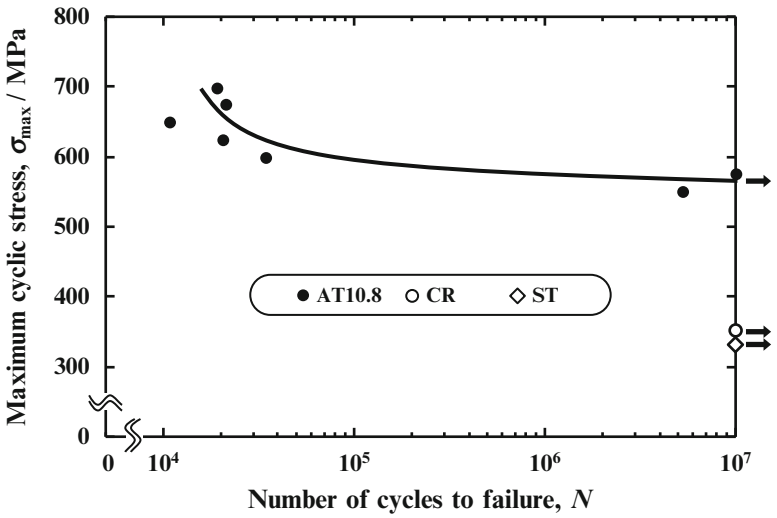

Fig. 8.21 Fatigue properties of TNTZ subjected to aging treatment at 573 K for 10.8 ks (AT10.8), solution treatment (*ST*), and severe cold rolling (*CR*) (Reprinted with permission from Ref. [69]. Copyright 2012, Springer International Publishing A. G)

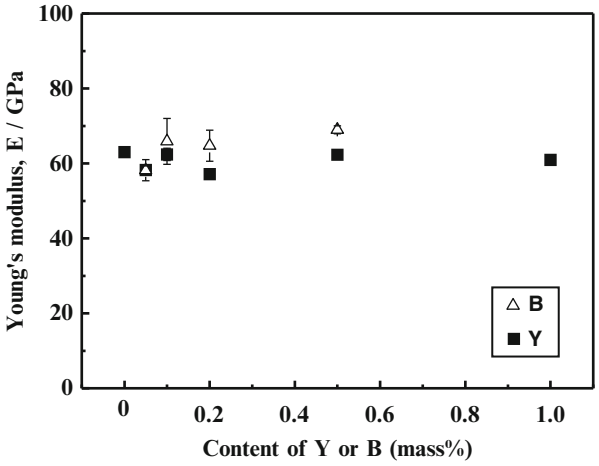

Fig. 8.22 Young's modulus as a function of Y or B concentration in TNTZ-B_{CR} or TNTZ-Y_{CR} (Reprinted with permission from Ref. [70]. Copyright 2011, John Wiley & Sons Ltd.)

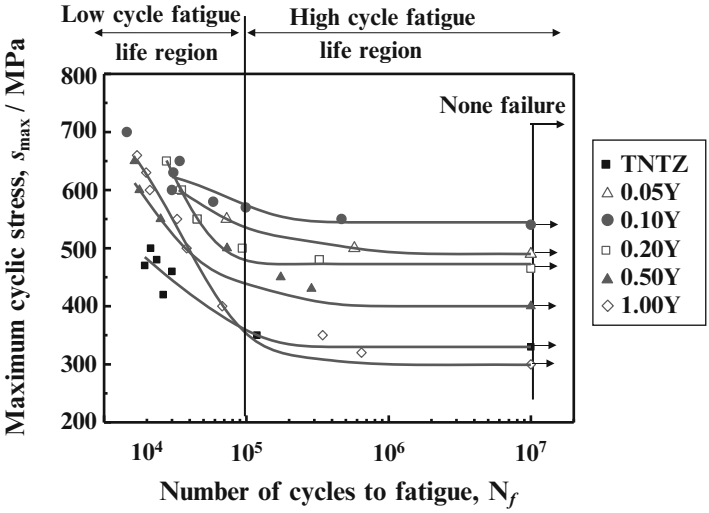

Fig. 8.23 S–N curves of cold-rolled TNTZ with different Y_2O_3 additions (Reprinted with permission from Ref. [70]. Copyright 2011, John Wiley & Sons Ltd.)

8.9 Super-Elastic and Shape-Memory Behavior

Many β-type titanium alloys exhibit super-elastic and shape-memory behavior. A number of shape-memory β-type titanium alloys have been developed for biomedical applications. The more commonly used super-elastic and shape-memory Ti–Ni alloys contain a large amount of Ni. This element represents a high risk from the point of view of metal allergies, although there are protection methods available to prevent the dissolution of Ni ions into the human body. Selected Ni-free super-elastic titanium and shape-memory alloys are listed in Table 8.2 [71], along with various Ni-free shape-memory alloys that generally also exhibit super-elasticity. These are all roughly divided into four groups: Ti–Nb system alloys [72–84], Ti–Mo system alloys [85–89], Ti–Ta system alloys [90], and Ti–Cr system alloys [91].

The addition of a small amount of oxygen (O) or nitrogen (N) enhances the super-elastic performance of Ni-free Ti-based alloys, as this lowers the starting temperature of the martensite transformation. The total elastic recovery strain, which is defined as the strain required for recovering to a value of 0 % when the load is released, is generally around 3 % for such alloys. Microstructural control, i.e., the texture formation caused by thermomechanical treatment, is also important for enhancing the super-elastic performance. For example, a total elastic recovery strain of around 6 % can be obtained for the Ti–Nb–Al system alloys simply by virtue of their texture [92]. Similarly, a total elastic recovery strain of around 6 % has also been reported in Ti–Nb–Zr, Ti–Nb–Zr–Ta, Ti–Nb–Zr–Ta–O, and Ti–Nb–Zr–Ta–N alloys [79]. The effects of other elements, such as Ta, Zr, Au, Pt, Al, Sn, O, Cu, Si, B, and N on the shape-memory and super-elastic behaviors of Ti–Nb, Ti–Nb–Al, and Ti–Zr–Nb, have also been investigated [93–99].

Table 8.2 Representative Ni-free shape-memory and super-elastic alloys

Alloy system	Super elastic and shape memory alloy
Ti-Nb system	Ti-Nb, Ti-Nb-O, Ti-Nb-Sn, Ti-Nb-Al, Ti-22Nb-(0.5-2.0)0 (at%), Ti-Nb-Zr, Ti-24Nb-2Zr (at%), Ti-Nb-Zr-Ta, Ti-Nb-Zr-Ta-O, Ti-Nb-Ta-Zr-N, Ti-Nb-Mo, Ti-22Nb-6Ta (at%), Ti-Nb-Au, Ti-Nb-Pl. Ti-Nb-Ta, Ti-Nb-Pd, Ti-24Nb-4Zr-8Sn (mass%)
Ti-Mo system	Ti-Mo-Ga, Ti-Mo-Ge, Ti-Mo-Sn, Ti-Mo-Ag, Ti-5Mo-(2-5)Ag (mol%), Ti-5Mo-(l-3)Sn (mol%), Ti-Sc-Mo
Ti-Ta system	Ti-50Ta (mass%), Ti-50Ta-4Sn (mass%), Ti-50Ta-10Zr (mass%)
Ti-Cr system	Ti-7Cr-(l.5, 3.0, 4.5)A1 (mass%)
	Alloy showing only super elasticity
	Ti_3(Ta + Nb + V) + (Zr, Hf) + O (at%), Ti-29Nb-13Ta-4.6Zr (TNTZ) (mass%), Ti-9.7Mo-4Nb-2V-3Al (mass%)

Reprinted with permission from Ref. [71]. Copyright 2012, Elsevier B. V

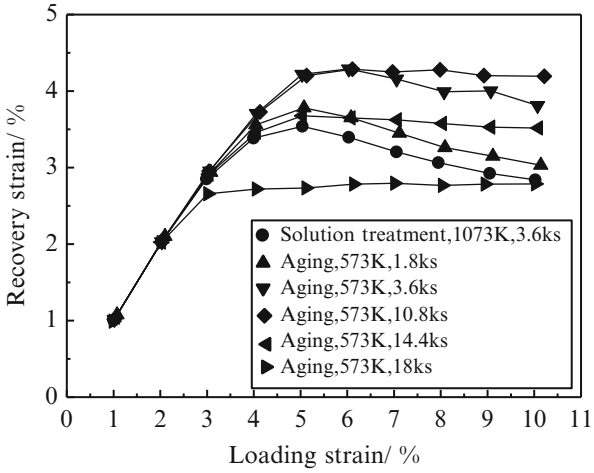

Fig. 8.24 Recovery strain of Ti–24Nb–2Zr measured during tensile loading and unloading tests where the applied strain was increased from 1 to 10 % by increments of 1 % (Reprinted with permission from Ref. [100]. Copyright 2011, Springer International Publishing A. G)

Both the shape-memory functionality and strength of Ni-free β-type titanium alloys can be improved through heat treatment. For example, in Ti–6Mo–8Al (mol%), an increase in strength and complete shape recovery can be achieved through low-temperature aging at 773 K, during which fine ω-phase precipitates form homogenously, followed by high-temperature aging at 1,023 K, during which the fine α-phase precipitates on the previously precipitated ω-phase, and further high-temperature aging at 1,123 K, during which the ω-phase disappears [100]. For Ti–24Nb–2Zr (at%) with a simple aging treatment at 573 K, the super-elastic performance first improves, but then deteriorates with extended aging time, as shown in Fig. 8.24 [100]. In this particular instance, a maximum super-elastic recovery of 4.3 % is obtained with an aging time of 10.8 ks.

The shape-memory and super-elastic behaviors in the aforementioned alloys result from a deformation-induced reversible martensite transformation, as in the

case of Ti–Ni. Those alloys that exhibit only super-elasticity are TNTZ [101], gum metal (Ti–25 mol% (Ta, Nb, V)+(Zr, Hf, O)) [16], and Ti–9.7Mo–4Nb–2V–3Al [102]. However, in the case of TNTZ, shape-memory behavior appears when the Nb content is slightly reduced. Until recently, the mechanisms behind the super-elastic behavior of TNTZ were unclear. Recent observations have related the super-elastic behavior of TNTZ to the reversible deformation-induced martensitic transformation [101]. The mechanisms of the super-elastic behavior of gum metal remain unclear.

8.10 Unique Behaviors of β-Type Titanium Alloys

Ti–Nb–Ta–Zr system alloys have been reported to exhibit Invar-like or Elinvar-like behaviors [103]. Figure 8.25 [104] shows the thermal expansion curves along with the rolling directions of cold-rolled TNTZ as a function of cold-rolling reduction ratios after solution treatment. When the cold-rolling reduction ratio is small, the thermal expansion rate is almost constant (Invar behavior) in the low-temperature range, while in the high-temperature range, the thermal expansion reaches a minimum value and then it increases with increasing temperature. When the cold-rolling reduction ratio is high, the thermal expansion ratio is negative in the low-temperature range. Consequently, when the cold-rolling reduction ratio is large, TNTZ exhibits a negative thermal expansion in the low-temperature region. However, the thermal expansion increases with increasing temperature after reaching its minimum value.

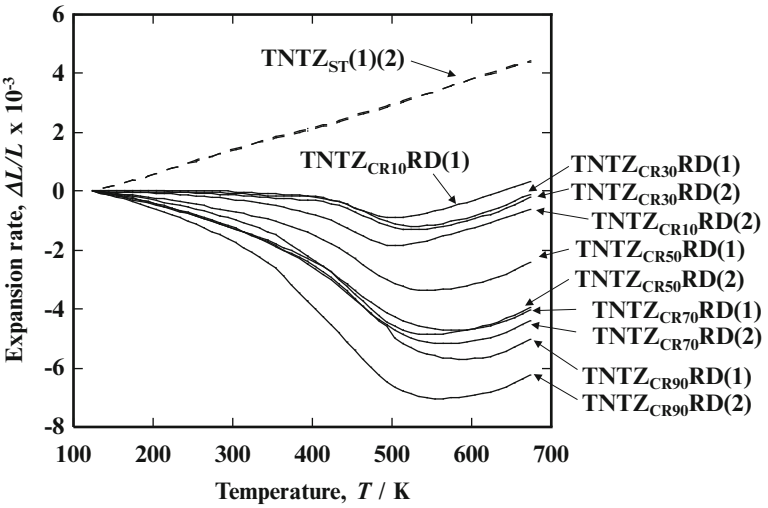

Fig. 8.25 Thermal expansion curves of TNTZ subjected to solution treatment ($TNTZ_{ST}$) and TNTZ subjected to ($TNTZ_{CR}$) cold rolling parallel the rolling direction (RD) at various working ratios ($TNTZ_{CR10\text{-}90}$) (Reprinted with permission from Ref. [104]. Copyright 2009, The Japan Institute of Metals and Materials)

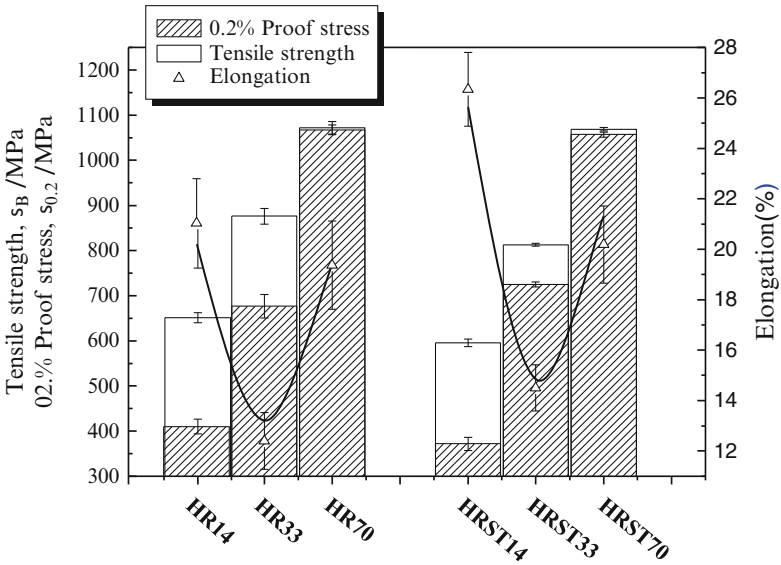

Fig. 8.26 Tensile properties: tensile strength, 0.2 % proof stress and elongation of TNTZ-0.14O, TNTZ-0.33O, and TNTZ-0.70O subjected to hot rolling (HR14, HR33, and HR70), and solution treatment at 1,003, 1,083, and 1,243 K for 3.6 ks after hot rolling (HRST14, HRST33, and HRST70) (Reprinted with permission from Ref. [105]. Copyright 2011, Elsevier B. V)

This anomalous behavior may be due to the reversibility of the thermally induced and deformation-induced martensite transformation. The mechanism can be considered as follows: First, the cold-rolled TNTZ exhibits an Invar behavior where the orthorhombic α" martensite undergoes a reverse transformation to the bcc β-phase during heating. Additionally, a strong {100}<110>β-rolling texture is formed by the cold rolling, resulting in the alignment of [010]α" parallel to the rolling direction. Since the length parallel to [010]α" is longer in the orthorhombic lattice than the original length in the bcc lattice, a negative thermal expansion results in TNTZ during heating.

Oxygen is generally regarded as an impurity for titanium alloys. The oxygen content is intentionally reduced as low as possible owing to its tendency to form an α-case, which can lead to brittle behavior. Nonetheless, an appropriate amount of homogeneously distributed oxygen can increase the strength of titanium alloys while still providing sufficient elongation to failure, though some decrease in elongation to failure is usually inevitable. However, the addition of a large amount of oxygen has been reported to unexpectedly increase both the strength and elongation to failure simultaneously in TNTZ. Figure 8.26 [105] shows the tensile strengths, 0.2 % proof stresses, and elongation-to-failure values of TNTZ, with oxygen contents ranging from 0.14 mass% through 0.70 mass%, subjected to hot rolling and solution treatment. Note that after hot rolling, these are referred to as HR14, HR33, HR70, HRST14, HRST33, and HRST70, respectively. With the increase in oxygen content, the tensile strength and 0.2 % proof stress of all the samples increased, but

their elongation to failure underwent an initial decrease, followed by an increase, which is opposite to the trend reported previously [106]. Both HR70 and HRST70 exhibit an attractive balance of elongation to failure and high strength with their respective maximum tensile strength and elongation-to-failure values of 1,100 MPa and 20 %, respectively. It is noted that these values are greater than that those for Ti–6Al–4V ELI.

8.11 Ti–Al–Nb Alloy System

Due to the previously mentioned research trend for the development of biomedical Ti alloys with low-rigidity β-type alloys composed of nontoxic and nonallergic elements with attractive mechanical properties, alloys based on the Ti–Al–Nb system, such as Ti–6Al–7Nb [107–119], Ti–7Al–51Nb [120–124], and Ti–10Al–47Nb [120–124], have been studied. The ambient-temperature tensile and fatigue strengths of the Ti–Al–Nb alloys compared favorably to those for Ti–6Al–4V, while their Young's modulus values were slightly lower than that for Ti–6Al–4V [121]. These Ti–Al–Nb alloys have been shown to have up to three times greater wear resistance [122], and they have also been shown to be nontoxic and biocompatible, where it is notable that Ti–Al–Nb alloy particles have been shown to be less toxic than Ti–Al–V particles [123].

The RT (room temperature) fatigue and tensile behavior of Ti–10Al–47Nb and Ti–7Al–51Nb alloys were compared to that for Ti–6Al–4V and other titanium alloys [121, 122]. The results indicated that the fatigue and tensile strength of the Ti–Al–Nb alloys were equivalent or superior to those for Ti–6Al–4V, and these alloys exhibited significantly greater fatigue strength than Ti–6Al–7Nb and other (α + β) titanium alloys (see Fig. 8.27 [121]). The greater Al content in the Ti–10Al–47Nb alloy was responsible for the low elongation to fracture (see Fig. 8.27b). The fatigue testing indicated that Ringer's solution (310 K) neither degraded nor improved the fatigue life of the Ti–Al–Nb alloys, and no significant differences were observed within the fracture surfaces for samples tested in Ringer's solution versus air.

The degree of biocompatibility and cytotoxicity of Ti–7Al–51Nb and Ti–10Al–47Nb alloys were examined and compared to that for CP Ti and Al_2O_3 [123]. In a mouse study, particle-treated calvaria underwent several tests to observe the deterioration of the bone, presence of osteoclasts, and T cells [123]. The various stains used were methylene blue/acid fuchsin, TRAcP, and immunohistochemistry. Overall, the Ti–Al–Nb alloys reacted favorably with mouse hard and soft tissue, forming a solid coherent interface without significant cell swelling. Particles of approximately 5–15 μm average diameter were placed on the calvaria and were harvested 6 weeks after implantation. No adverse reaction was found between the bone and the Ti–7Al–51Nb or Ti–10Al–47Nb alloy particles, where these particles were found to be well adhered to the bone (see Fig. 8.28 [123]). The Ti–Al–Nb alloy particles were also exposed to leukemia-affected macrophages for times ranging between 24 hours and 10 days. The macrophages either engulfed the particles or were unaf-

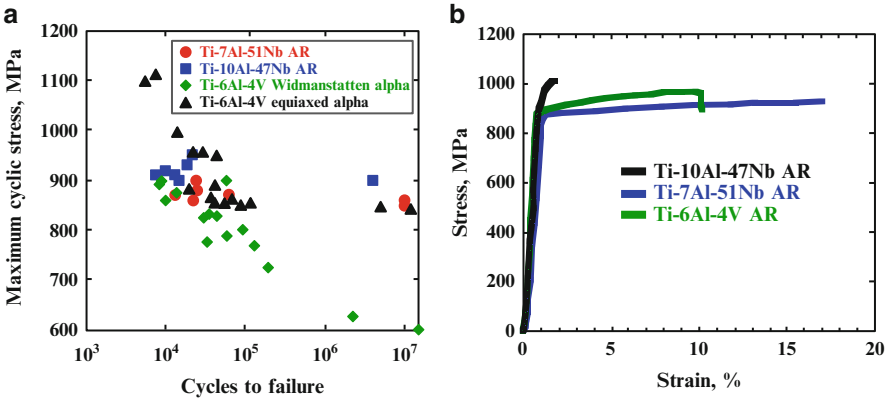

Fig. 8.27 Mechanical property comparisons of Ti–7Al–51Nb and Ti–10Al–47Nb with Ti–6Al–4V illustrating their comparable properties: (**a**) RT maximum cyclic stress versus cycles to failure where 10^7 cycles were considered run out and (**b**) RT stress versus strain behavior. *AR*: as rolled (Reprinted with permission from Ref. [121]. Copyright 2005, Elsevier B. V)

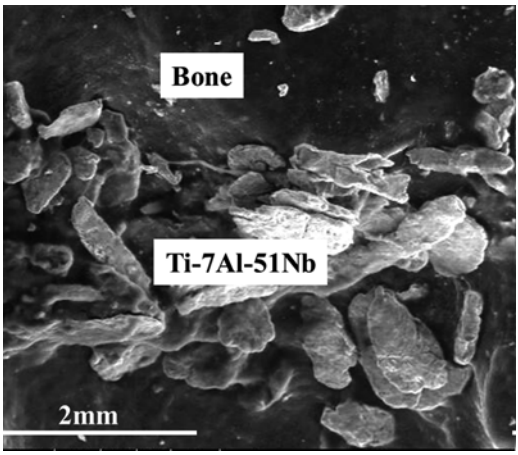

Fig. 8.28 Environmental SEM images of Ti–7Al–51Nb (mass%) [Ti–15Al–33Nb (at.%)] particles on mouse calvaria where no adverse reactions were noted with the cantilever or the soft tissue 6 weeks after attachment of the particles (Reprinted with permission from Ref. [123]. Copyright 2005, The Japan Institute of Metals)

fected by them (see Fig. 8.29 [123]) where LIVE/DEAD assay results found minimal cell death. This behavior is similar to that for the biocompatible CP Ti particles [125–128]. Other biocompatibility experiments involved measuring the resorption of mouse calvarial tissue in response to the Ti–Al–Nb alloy particles. For the particle-treated calvaria, Ti–7Al–51Nb exhibited a midline sagittal suture area comparable to that of untreated mice, and such experiments demonstrated that there is only a small difference in the biological response for this alloy and Ti–10Al–47Nb [123]. Both of these alloys were clearly superior to CP Ti and Al_2O_3 with respect to bone deterioration. More recent word has also indicated that Ti–7Al–51Nb and Ti–10Al–41Nb have statistically comparable cell adhesion characteristics to that of Ti–6Al–4V

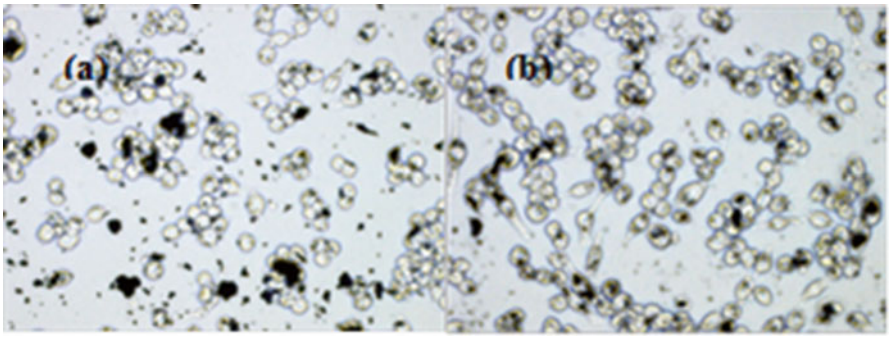

Fig. 8.29 Optical microscopy images of (**a**) Ti–7Al–51Nb and (**b**) Ti–10Al–47Nb particles either engulfed or adjacent to live leukemia-affected mice macrophages. No adverse reactions were exhibited comparable to that found for CP Ti particles. Cell diameter ~25 μm (Reprinted with permission from Ref. [123] Copyright 2005, The Japan Institute of Metals)

[124]. Overall, it is apparent that Ti–Al–Nb alloys have potential for biomedical implant applications. Due to its ductile behavior and lower Young's modulus, Ti–7Al–51Nb is preferred over Ti–10Al–47Nb.

8.12 Summary

A number of β-type titanium alloys with a low Young's modulus have been developed for biomedical applications; however, only a very small number of these have ever been put into practical applications. Greater numbers of such alloys will hopefully be put into practical applications in the future, as additional. Titanium alloys for biomedical applications are developed to provide advanced functionalities such as a high biological biocompatibility, through the use of nontoxic and allergy-free alloying elements; low Young's modulus for preventing bone atrophy; a self-tunable Young's modulus; ease of removability; and high mechanical biocompatibility, i.e., a high fatigue strength, high strength with ductility, high fracture toughness, high fretting fatigue strength, and high wear resistance. Other advanced bio-functionalities will undoubtedly be created in titanium alloys for future biomedical applications. However, in order to add substantially more advanced bio-functionalities, a greater integration with bioceramics, biopolymers, and tissue engineering is still required.

References

1. Yamamuro T (1989) Patterns of osteogenesis in relation to various biomaterials. J Jpn Soc Biomater 7:19–23
2. Niinomi M, Hattori T, Morikawa K et al (2002) Development of low rigidity β-type titanium alloy for biomedical applications. Mater Trans 43(12):2970–2977

3. Sumitomo N, Noritake K, Hattori T et al (2008) Experiment study on fracture fixation with low rigidity titanium alloy – plate fixation of tibia fracture model in rabbit. J Mater Sci Mater Med 19:1581–1586
4. Niinomi M, Nakai M, Hieda J (2012) Development of new metallic alloys for biomedical applications. Acta Biomater 8:3888–3903
5. Park JB, Lakes RS (1992) In: Biomaterials: an introduction. Plenum Press, New York
6. Brannon BP, Mild EE (1981) In: Luckey HA, Kubli F (eds) Ti alloys in surgical implants. ASTM Special Technical Publication, Philadelphia, pp 7–15
7. Dobbs HS, Scales JT (1981) In: Luckey HA, Kubli F (eds) Ti Alloys in Surgical Implants. ASTM Special Technical Publication, Philadelphia, pp 173–186
8. Froes FH (2004) How to market titanium: lower the cost. JOM 2:39
9. Froes FH, Friedrich H, Kiese J et al (2004) Titanium in the family automobile: the cost challenge. JOM 2:40–44
10. Niinomi M (2013) Titanium alloys with high biological and mechanical biocompatibility. J Jpn Soc Bone Morphometry 23(1):S59
11. Nakai M, Niinomi M, Zhao XF et al (2011) Self-adjustment of Young's modulus in biomedical titanium alloys during orthopedic operation. Mater Lett 65:688–690
12. Zhao XL, Niinomi M, Nakai M et al (2011) Development of high Zr-containing Ti-based alloys with low Young's modulus for use in removable implants. Mater Sci Eng C 31:1436–1444
13. Niinomi M, Hattori T, Kasuga T et al (2006) Titanium and its alloys. In: Encyclopedia of biomaterials and biomedical engineering. Marcel Dekker, New York, pp 1–8
14. Ahmed T, Long M, Silvestri J et al (1996) A new low modulus, biocompatible titanium alloy. In: Blenkinsop PA, Evans WJ, Flower HM (eds) Titanium '95 science and technology, vol II. Institute of Metals, London, pp 1760–1767
15. Kuroda D, Niinomi M, Morinaga M et al (1998) Design and mechanical properties of new beta type titanium alloys for implant materials. Mater Sci Eng A 243:244–249
16. Saito T, Furuta T, Hwang JH et al (2003) Multifunctional alloys obtained via a dislocation-free plastic deformation mechanism. Science 300:464–467
17. Kawahara H, Ochi S, Tanetani K et al (1963) Biological test of dental materials. Effect of pure metals upon the mouse subcutaneous fibroblast. Starin L cell in tissue culture. J Jpn Soc Dent Apparat Mater 4:65–75
18. Steinemann SG (1980) Corrosion of surgical implants-in vivo and in vitro tests. In: Winter GD, Leray JL, de Groot K (eds) Evaluation of biomaterials. Wiley, New York, pp 1–34
19. Uggowitzer PJ, Bähr WF, Speidel MO (1997) Metal injection molding of nickel-free stainless steels. Adv Powder Metal Part Mater 3:18.113–18.121
20. Hatanaka S, Ueda M, Ikeda M et al (2009) Isothermal aging behavior in Ti-10Cr-Al alloys for medical applications. Adv Mater Res 638–642:425–430
21. Ikeda M, Ueda M, Matsunaga R et al (2009) Isothermal aging behavior of beta titanium-manganese alloys. Mater Trans 50:2737–2743
22. Ikeda M, Ueda M, Kinoshita T et al (2012) Influence of Fe content of Ti-Mn-Fe alloys on phase constitution and heat treatment behavior. Mater Sci Forum 706–709:1893–1898
23. Ikeda M, Ueda M, Matsunaga R et al (2010) Phase constitution and heat treatment behavior of Ti-7mass%Mn-Al alloys. Mater Sci Forum 654–656:855–858
24. Ikeda M, Sugano D (2005) The effect of aluminum content on phase constitution and heat treatment behavior of Ti-Cr-Al alloys for healthcare applications. Mater Sci Eng C 25:377–381
25. Ashida S, Kyogak H, Hosoda H (2012) Fabrication of Ti-Sn-Cr shape memory alloy by PM and its properties. Mater Sci Forum 706–709:1943–1947
26. Murayama Y, Sasaki S (2009) Univ Res J Niigata Inst Technol 14:1–8
27. Kasan Y, Inamura T, Kanetaka H et al (2010) Phase constitution and mechanical properties of Ti-(Cr, Mn)-Sn biomedical alloys. Mater Sci Forum 654–656:2118–2121
28. Niinomi M (2010) Trends and present state of titanium alloys with body centered structure for biomedical applications. Bull Iron Steel Inst Jpn 15(11):661–670

29. Matsumoto H, Watanabe S, Hanada S (2006) Strengthening of low Young's modulus modulus beta Ti-Nb-Sn alloys by thermomechanical processing. In: Proceedings of the materials and processing for medical devices conference. ASM International, Materials Park, pp 9–14
30. Yilmazer H, Niinomi M, Nakai M et al (2013) Mechanical properties of a medical β-type titanium alloy with specific microstructural evolution through high pressure torsion. Mater Sci Eng C 33:2499–2507
31. Tane M, Akita S, Nakano T et al (2008) Peculiar elastic behavior of Ti-Nb-Ta-Zr single crystals. Acta Mater 56:2856–2863
32. Kobayashi E, Ando M, Tsutsumi Y et al (2007) Inhibition effect of zirconium coating on calcium phosphate precipitation of titanium to avoid assimilation with bone. Mater Trans 48:301–306
33. Kambouroglou GK, Axelrod TS (1998) Complications of the AO/ASIF titanium distal radius plate system (pi plate) in internal fixation of the distal radius: a brief report. J Hand Surg 23:737–741
34. Cook SD, Renz EA, Barrack RL et al (1985) Clinical and metallurgical analysis of retrieved internal-fixation devices. Clin Orthop Relat Res 194:236–247
35. Thibon I, Ansel D, Gloriant T (2009) Interdiffusion in beta-Ti-Zr binary alloys. J Alloy Compd 470:127–133
36. Albrektsson T, Hansson HA, Ivarsson B (1985) Interface analysis of titanium and zirconium bone implants. Biomaterials 6:97–101
37. Ikarashi Y, Toyoda K, Kobayashi E et al (2005) Improved biocompatibility of titanium-zirconium (Ti-Zr) alloy: tissue reaction and sensitization to Ti-Zr alloy compared with pure Ti and Zr in rat implantation study. Mater Trans 46:2260–2267
38. Tsutsumi Y, Nishimura D, Doi H et al (2009) Difference in surface reactions between titanium and zirconium in Hanks' solution to elucidate mechanism of calcium phosphate formation on titanium using XPS and cathodic polarization. Mater Sci Eng C 29:1702–1708
39. Hanawa T, Okuno O, Hamanaka H (1992) Compositional change in surface of Ti-Zr alloys in artificial bioliquid. J Jpn Inst Metals 56:1168–1173
40. Kobayashi E, Matsumoto S, Doi H et al (1995) Mechanical-properties of the binary titanium-zirconium alloys and their potential for biomedical materials. J Biomed Mater Res 29:943–950
41. Kobayashi E, Doi H, Yoneyama T et al (1995) Evaluation of mechanical properties of dental-cast Ti-Zr based alloys. J Jpn Dent Mater 14:321–328
42. Ho WF, Chen WK, Wu SC et al (2008) Structure, mechanical properties, and grindability of dental Ti-Zr alloys. J Mater Sci Mater Med 19:3179–3186
43. Imgram AG, Williams DN, Ogden HR (1962) Tensile properties of binary titanium-zirconium and titanium-hafnium alloys. J Less-Common Metal 4:217–225
44. Takahashi M, Kobayashi E, Doi H et al (2000) Phase stability and mechanical properties of biomedical β type titanium-zirconium based alloys containing niobium. J Jpn Inst Metals 64:1120–1126
45. Yang GJ, Zhang T (2005) Phase transformation and mechanical properties of the Ti50Zr30Nb10Ta10 alloy with low modulus and biocompatible. J Alloy Compd 392:291–294
46. Song Y, Xu D, Yang R et al (1999) Theoretical study of the effects of alloying elements on the strength and modulus of b-type bio-titanium alloys. Mater Sci Eng A 260:269–274
47. Narita K, Niinomi M, Nakai M et al (2008) Mechanical properties of implant rods made of low-modulus beta-type titanium alloy, Ti-29Nb-13Tta-4.6Zr, for spinal fixture. J Jpn Inst Metals 72:674–678
48. Steib JP, Dumas R, Skalli W (2004) Surgical correction of scoliosis by in situ contouring: a detorsion analysis. Spine 29:193–199
49. Nakai M (2010) Titanium alloys for spinal fixation devices. Materia Jpn 49:437–440
50. Zhao XF, Niinomi M, Nakai M (2012) Beta-type Ti-Mo alloys with changeable Young's modulus for spinal fixation applications. Acta Biomater 8:1990–1997

51. Zhao XL, Niinomi M, Nakai M et al (2011) Microstructures and mechanical properties of metastable Ti-30Zr-(Cr, Mo) alloys with changeable Young's modulus for spinal fixation applications. Acta Biomater 7:3230–3236
52. Zhao XL, Niinomi M, Nakai M (2011) Relationship between various deformation-induced products and mechanical properties in metastable Ti-30Zr-Mo alloys for biomedical applications. J Mech Behav Biomed Mater 4:2009–2016
53. Matsumoto H, Watanabe S, Masahashi N et al (2006) Composition dependence of Young's modulus in Ti-V, Ti-Nb, and Ti-V-Sn alloys. Metall Mater Trans A 37:3239–3249
54. Liu HH, Niinomi M, Nakai M et al (2014) Bending springback behavior related to deformation-induced phase transformations in Ti–12Cr and Ti–29Nb–13Ta–4.6Zr alloys for spinal fixation applications. JMBBM 34:66–74
55. Zhao XF, Niinomi M, Nakai M et al (2012) Optimization of Cr content of metastable β-type Ti-Cr alloys with changeable Young's modulus for spinal fixation applications. Acta Biomater 8:2392–2400
56. Williams JC, de Fontaine D, Paton NE (1973) The ω-phase as an example of an unusual shear transformation. Metall Trans 4:2701–2708
57. de Fontaine D, Paton NE, Williams JC (1971) The omega phase transformation in titanium alloys as an example of displacement controlled reactions. Acta Metall 19:1153–1162
58. Liu HH, Niinomi M, Nakai M et al (2014) Deformation-induced changeable Young's modulus with high strength in β-type Ti-Cr-O alloys for spinal fixture. J Mech Behav Biomed Mater 34:205–213
59. Li Q, Niinomi M, Hieda J et al (2013) Deformation-induced ω phase in modified Ti–29Nb–13Ta–4.6Zr alloy by Cr addition. Acta Biomater 9:8027–8035
60. Niinomi M, Hattori T, Niwa S (2004) Material characteristics and biocompatibility of low rigidity titanium alloys for biomedical applications. In: Yaszemski MJ, Trantolo DJ, Lewandrowski KU et al (eds) Biomaterials in orthopedics. Marcel Dekker, New York, pp 41–62
61. Guo Z, Fu J, Zhang YQ et al (2009) Early effect of Ti-24Nb-4Zr-7.9Sn intramedullary nails on fractured bone. Mater Sci Eng C 29:963–968
62. Narita K, Niinomi M, Nakai M et al (2012) Development of thermo-mechanical processing for fabricating highly durable β-type Ti-Nb-Ta-Zr rod for use in spinal fixation devices. J Mech Behav Biomed Mater 9:207–216
63. Akahori T, Niinomi M, Noda A et al (2006) Effect of aging treatment on mechanical properties of Ti-29Nb-13Ta-4.6Zr alloy for biomedical applications. J Jpn Inst Metals 70(4):295–303
64. Niinomi M (2003) Fatigue performance and cyto-toxicity of low rigidity titanium alloy, Ti-29Nb-13Ta-4.6Zr. Biomaterials 24(16):2673–2683
65. Akahori T, Niinomi M, Fukui H et al (2005) Improvement in fatigue characteristics of newly developed beta type titanium alloy for biomedical applications by thermo-mechanical treatments. Mater Sci Eng C 25(3):248–254
66. Niinomi M, Nakai M (2012) Mechanically bio-functional titanium alloys for substituting failed hard tissue. In: Flogen FK (ed) Composites, ceramics, nanomaterials & titanium processing, FLOGEN Star OUTREACH, Quebec, Canada, vol 7, 409–433
67. Niinomi M, Akahori T, Morikawa K et al (2005) Super elastic functional β titanium alloy with low Young's modulus for biomedical applications. J ASTM Int 2(6):473–488. Paper ID JA12818, ISSN:1546-962X, Published Online
68. Yilmazer H, Niinomi M, Akahori T et al (2012) Effects of severe plastic deformation and thermo-mechanical treatments on microstructures and mechanical properties of β-type titanium alloys for biomedical applications. Int J Microstruct Mater Prop (IJMMP) 7:168–188
69. Nakai M, Niinomi M, Oneda T (2012) Improvement in fatigue strength of biomedical β-type Ti–Nb–Ta–Zr alloy while maintaining low Young's modulus through optimizing ω-phase precipitation. Metall Mater Trans A 43(1):294–302
70. Niinomi M, Nakai M, Yonezawa S et al (2011) Effect of TiB_2 or Y_2O_3 Additions on mechanical biofunctionality of Ti-29Nb-13Ta-4.6Zr for biomedical applications. Ceram Trans 228:75–82

71. Niinomi M (2012) Shape memory, super elastic and low Young's modulus alloys. In: Ambrosioand L, Tanner E (eds) Biomaterials for spinal surgery. Woodhead Publishing, Philadelphia, pp 462–490
72. Kim HY, Ikehara Y, Kim JI et al (2006) Martensitic transformation shape memory effect and superelasticity of Ti-Nb-binary alloys. Acta Mater 54:2419–2429
73. Kim JI, Kim HY, Hosoda H et al (2005) Shape memory behavior of Ti-22Nb-(0.5-2.0)O(at%) biomedical alloys. Mater Trans 46:852–857
74. Takahashi E, Sakurai T, Watanabe S et al (2002) Effect of heat treatment and Sn content on superelasticity in biocompatible TiNbSn alloys. Mater Trans 43:2978–2983
75. Nitta K, Watanabe S, Masahashi N et al (2001) Ni-free Ti-Nb-Sn shape memory alloys. In: Niinomi M, Okabe T, Taleff E et al. (eds) Structural biomaterials for the 21st century TMS, Warrendale, pp 25–34
76. Hosoda H, Fukui Y, Inamura T et al (2003) Mechanical properties of Ti-base shape memory alloys. Mater Sci Forum 426–432:3121–3125
77. Inamura T, Hosoda H, Wakashima K et al (2005) Anisotropy and temperature dependence of Young's modulus in textured TiNbAl biomedical shape memory alloy. Mater Trans 46:1597–1603
78. Kim JI, Kim Y, Inamura T et al (2005) Shape memory characteristics of Ti-22Nb-(2-8) Zr(at%) biomedical alloys. Mater Sci Eng A 403:334–339
79. Kim HY, Hosoda H, Miyazaki S (2007) Development of super elastic Ti-Nb system alloys for biomedical applications. Collected abstracts of the 2007 spring meeting of the Japan institute of metals. JIM, Sendai, Japan, 91
80. Ohmatsu Y, Kim JI, Kim HY et al (2003) Shape memory characteristics of Ti-Nb-Mo alloys for biomedical applications. Collected abstracts of the 2003 spring meeting of the Japan institute of metals. JIM, Sendai, Japan, 144
81. Al-Zain Y, Kim HY, Hosoda H et al (2010) Shape memory properties of Ti-Nb-Mo biomedical alloys. Acta Mater 58:4212–4223
82. Kim HY, Sasaki T, Okutsu K et al (2006) Texture and shape memory behavior of Ti-22Nb-6Ta alloy. Acta Mater 54:423–433
83. Oshika N, Hashimoto S, Kim JI et al (2003) Shape memory characteristics of Ti-Nb-Au alloys for biomedical applications. Collected abstracts of the 2003 fall meeting of the Japan institute of metals. JIM, Sendai, Japan, 149
84. Ping D, Mitarai Y, Yin F (2005) Microstructure and shape memory behavior of a Ti-30Nb-3Pd alloy. Scr Mater 52:1287–1291
85. Hosoda H, Hosoda N, Miyazaki S (2001) Mechanical properties of Ti-Mo-Al biomedical shape memory alloys. Trans MRS-J 26:243–246
86. Kim HY, Ohmatsu Y, Kim JI et al (2004) Mechanical properties and shape memory behavior of Ti-Mo-Ga alloys. Mater Trans 45:1090–1095
87. Hosoda N, Yamamoto A, Hosoda H et al (2001) Mechanical properties of Ti-Mo-Ge shape memory alloys for biomedical applications. Collected abstracts of the 2001 fall meeting of the Japan Institute of Metals. JIM, Sendai, Japan, 401
88. Maeshima T, Nishida M (2004) Shape memory properties of biomedical Ti-Mo-Ag and Ti-Mo-Sn alloys. Mater Trans 45:1096–1100
89. Maeshima T, Nishida M (2004) Shape memory and mechanical properties of biomedical Ti-Sc-Mo alloys. Mater Trans 45:1101–1105
90. Ikeda M, Komatsu S, Nakamura Y (2004) Effects of Sn and Zr additions on phase constitution and aging behavior of Ti-50mass%Ta alloys quenched from β single phase region. Mater Trans 45:1106–1112
91. Ikeda M, Sugano D, Masuda S (2005) The influence of aluminum content on shape memory effect of Ti-7Cr-Al alloys fabricated using low grade sponge titanium. Mater Trans 46:1604–1609
92. Hosoda H, Miyazaki S (2004) Recent topics of shape memory materials and related technology. J Jpn Soc Mech Eng 107:509–515
93. Hanada S, Masahashi N, Jung TK et al (2014) Effect of swaging on Young's modulus of b Ti-33.6Nb-4Sn alloy. J Mech Behav Biomed Mater 32:310–320

94. Kim H, Hosoda H, Miyazaki S (2005) Beta-titanium shape memory alloys. J Jpn Inst Light Metal 55:613–617
95. Miyazaki S, Kim HY, Hosoda H (2006) Development and characterization of N-free Ti-base shape memory and superelastic alloys. Mater Sci Eng A 433–440:18–24
96. Masumoto K, Horiuchi Y, Inamura T et al (2006) Effects of Si addition on superelastic properties of Ti–Nb–Al biomedical shape memory alloys. Mater Sci Eng A 438–440:835–838
97. Tahara M, Kim HY, Inamura T et al (2009) Effect of nitrogen addition on superelasticity of Ti-Zr-Nb alloys. Mater Trans 50:2726–2730
98. Horiuchi Y, Inamura T, Kim HY et al (2007) Effect of boron concentration on martensitic transformation temperatures, stress for inducing martensite and slip stress of Ti-24mol%Nb-3mol%Al superelastic alloy. Mater Trans 48:407–413
99. Hosoda H, Taniguchi M, Inamura T et al (2010) Effect of aging on mechanical properties of Ti-Mo-Al biomedical shape memory alloy. Mater Sci Forum 654–656:2150–2153
100. Li Q, Niinomi M, Nakai M et al (2011) Improvements in the super-elasticity and change in deformation mode of β-type $TiNb_{24}Zr_2$ alloys caused by aging treatments. Metall Mater Trans A 42:2843–2849
101. Niinomi M, Akahori T, Nakai N (2008) In situ X-ray analysis of mechanism of nonlinear super elastic behavior of Ti-Nb-Ta-Zr system beta-type titanium alloy for biomedical applications. Mater Sci Eng C 28:406–413
102. Wu MH (2003) Assessment of a superelastic beta TiMo alloy for biomedical applications. In: Proceedings of ASM materials & processes for medical devices conference, 8–10 September, Anaheim, California, USA, pp 343–348
103. Obbard EG, Hao YL, Akahori T et al (2010) Mechanics of superplasticity in Ti-30Nb-(8-10) Ta-Zr alloy. Acta Mater 58:6790–6798
104. Nakai M, Niinomi M, Akahori T et al (2009) Anomalous thermal expansion of cold-rolled Ti-Nb-Ta-Zr alloy. Mater Trans 50:423–426
105. Geng F, Niinomi M, Nakai M (2011) Observation of yielding and strain hardening in a titanium alloy having high oxygen content. Mater Sci Eng A 528:5435–5445
106. Nakai M, Niinomi M, Akahori T et al (2009) Effect of oxygen content on microstructure and mechanical properties of biomedical Ti-29Nb-13Ta-4.6Zr alloy under solutionized and aged conditions. Mater Trans 50(2):2716–2720
107. Lopez MF, Jimenez JA, Gutierrez A (2003) Corrosion study of surface-modified vanadium-free titanium alloys. Electrochim Acta 48:1395–1401
108. Metikos-Hukovic M, Tkalcec E, Kwokal A et al (2003) An in vitro study of Ti and Ti-alloys coated with sol–gel derived hydroxyapatite coatings. Surf Coat Technol 165:40–50
109. Cai Z, Shafer T, Watanabe I et al (2003) Electrochemical characterization of cast titanium alloys. Biomaterials 24:213–218
110. Iijima D, Yoneyama T, Doi H et al (2003) Wear properties of Ti and Ti–6Al–7Nb castings for dental prostheses. Biomaterials 24:1519–1524
111. Khan MA, Williams RL, Williams DF (1999) The corrosion behavior of Ti–6Al–4V, Ti–6Al–7Nb and Ti–13Nb–13Zr in protein solutions. Biomaterials 20:631–637
112. Papakyriacou M, Mayer H, Pypen C et al (2000) Effects of surface treatments on high cycle corrosion fatigue of metallic implant materials. Int J Fatigue 22:873–888
113. Semlitsch MF, Weber H, Streicher RM et al (1992) Joint replacement components made of hot-forged and surface-treated Ti-6Al-7Nb alloy. Biomaterials 13(11):781–788
114. Watanabe I, Tanaka Y, Watanabe E et al (2004) Tensile properties and hardness of cast Fe-Pt magnetic alloys. J Prosthet Dent 92(3):278–282
115. Akahori T, Niinomi M, Fukunaga K et al (2000) Effects of microstructure on the short fatigue crack initiation and propagation characteristics of biomedical α/β titanium alloys. Metall Mater Trans A 31(8):1949–1958
116. Morant C, López MF, Gutiérrez A et al (2003) AFM and SEM characterization of non-toxic vanadium-free Ti alloys used as biomaterials. Appl Surf Sci 220(1–4):79–87
117. Khan MA, Williams RL, Williams DF (1999) Conjoint corrosion and wear in titanium alloys. Biomaterials 20(8):765–772

118. Watanabe K, Miyakawa O, Takada Y et al (2003) Casting behavior of titanium alloys in a centrifugal casting machine. Biomaterials 24(10):1737–1743
119. Metikos-Hukovic M, Kwokal A, Piljac J (2003) The influence of niobium and vanadium on passivity of titanium-based implants in physiological solution. Biomaterials 24(21):3765–3775
120. Boehlert CJ (2010) Ti, Al, and Nb alloys for biomedical applications. US Patent 7,682,47345, February 2010
121. Boehlert CJ, Cowen CJ, Jaeger CR et al (2005) Tensile and fatigue evaluation of Ti-15Al-33Nb(at.%) and Ti-21Al-29Nb(at.%) alloys for biomedical applications. Mater Sci Eng C 25:263–275
122. Boehlert CJ, Cowen CJ, Quast JP et al (2008) Fatigue and wear evaluation of Ti-Al-Nb alloys for biomedical applications. Mater Sci Eng C 28:323–330
123. Boehlert CJ, Rider KA, Flick LM (2005) Biocompatibility evaluation of Ti-15Al-33Nb(at.%) and Ti-21Al-29Nb(at.%). Mater Trans 46(7):1618–1626
124. Schlaud MA, Friederichs RJ, Baumann MJ et al (2010) Osteoblast attachment and growth on novel TiNbAl alloys. Red Cedar Undergrad Res J August (1):33–37
125. Childs LM, Goater JJ, O'Keefe RJ et al (2001) Efficacy of etanercept for wear debris-induced osteolysis. J Bone Miner Res 16:338–347
126. Wang JY, Wicklund BH, Gustilo RB et al (1996) Titanium, chromium, and cobalt ions modulate the release of bone associated cytokines by human monocytes/macrophages in vitro. Biomaterials 17:2233–2240
127. Blaine TA (1997) Modulation of the production of cytokines in titanium-stimulated human peripheral blood monocytes by pharmacological agents. The role of cAMP-mediated signaling mechanisms. J Bone Joint Surg Am 79:1519–1528
128. Lee SH (1997) Human monocyte/macrophage response to cobalt chromium corrosion products and titanium particles in patients with total joint replacements. J Orthop Res 15:40–44

Chapter 9
Zirconium Alloys for Orthopedic Applications

Naoyuki Nomura

Abstract Physical and chemical properties of zirconium (Zr) are introduced and the features and differences from titanium (Ti) are pointed out. Zr is principally applied to the nuclear power industry because of its low thermal neutron cross section. For medical applications, a Zr alloy (Zr-2.5Nb) is used in total knee and hip replacements because of its excellent wear resistance. The dense and adherent oxide layers are formed on the surface of Zr alloy and contribute to improving its wear resistance. Zr is also promising for suppressing artifacts in magnetic resonance images, because it shows lower magnetic susceptibility than that of SUS, Co-Cr alloy, and Ti. The magnetic susceptibilities of the Zr alloys are sensitive to their phase constitutions. Magnetic susceptibility in addition to mechanical properties could be controlled by changing the composition depending on the requirements for medical devices under magnetic resonance imaging (MRI).

Keywords Nuclear grades • Total knee replacement • Magnetic susceptibility • Magnetic resonance imaging (MRI) • Artifacts

9.1 Basic Properties

9.1.1 Physical and Chemical Properties

Zirconium (Zr) was discovered in 1789. When Klaproth analyzed the precious stone called jargon, he found it contained an element that he could not identify. Vauquelin had investigated the new compounds, called zirconia, by 1797. In 1824, Berzelius succeeded in isolating impure zirconium. In 1925, van Arkel and de Boer developed the iodide decomposition process for the purification of metals. Kroll developed the method to produce ductile Zr in 1947, which was expanded to large-scale commercial production later [1, 2].

N. Nomura (✉)
Department of Materials Processing, Graduate School of Engineering, Tohoku University, Aoba-yama 6-6-02, Aoba-ku, Sendai 980-8579, Japan
e-mail: nnomura@material.tohoku.ac.jp

M. Niinomi et al. (eds.), *Advances in Metallic Biomaterials*, Springer Series in Biomaterials Science and Engineering 3, DOI 10.1007/978-3-662-46836-4_9

The atomic number of Zr is 40, and the atomic weight is 91.22. The density of pure Zr is 6.52 g/cm^3. Zr has a hexagonal close-packed crystal structure (hcp; alpha phase) at room temperature and is stable up to 1,135 K. Allotropic transformation occurs at this temperature, and a body-centered cubic structure (bcc; beta phase) is stable above that temperature to a melting point of approximately 2,133 K. The lattice parameters of Zr are $a = 0.3233$ nm and $c = 0.5149$ nm at room temperature and $a = 0.361$ nm at 1,143 K [3]. The properties of Zr are generally similar to those of titanium (Ti), but the notably different properties are density, thermal neutron cross section, and magnetic susceptibility. The density of Zr is about 1.4 times higher than that of Ti (4.51 g/cm^3), and the specific strength is disadvantageous as compared with Ti. However, the thermal neutron cross section of Zr is one-thirtieth that of Ti; therefore, Zr has applications in the nuclear power industry. The magnetic susceptibility of Zr is almost half that of Ti, which is a promising property for medical applications. Details are given later.

Zr is one of the active metals and it easily reacts with oxygen to form dense and continuous zirconium oxide at the surface due to the high Pilling-Bedworth ratio. The black oxide layer forms in a steam at the temperature ranging from 533 to 673 K for the initial stage. With prolonging the reaction time, the oxide color turns ash gray, and the strong adhesion is lost at the interface between oxide and metal. Zr shows superior corrosion resistance in the nitric acid environment as compared with Ti and thus is widely utilized in the chemical industry [3].

9.1.2 Mechanical Properties

Highly pure Zr shows excellent deformability at room temperature because of dislocation slip as well as twining work as deformation modes, similar to Ti. However, the strength is insufficient and is improved by alloying. Tin (Sn) and oxygen (O) are added as alloying elements, which stabilize the α phase, i.e., the α stabilizer, and increase the allotropic temperature. On the other hand, iron, chromium, nickel, and niobium stabilize the β phase, i.e., the β stabilizer, decreasing the allotropic temperature. The amount of these elements to add can be adjusted to improve the strength and corrosion resistance.

Zr alloy grades are classified into industrial and nuclear grades. Table 9.1 lists the chemical compositions and tensile properties of industrial and nuclear grades of Zr alloys [2, 3]. The clear difference between the grades is the hafnium (Hf) content. Industrial grades permit Hf content of up to 4.5 %, but the content is restricted below 0.01 % for the nuclear grade because of the relatively higher thermal neutron cross section. The effects of Hf on the mechanical properties as well as corrosion resistance seem to be small; thus, the properties are quite similar between the two grades. For medical applications, the Zr-2.5Nb alloy (UNS R60901) is provided for surgical implant applications and is regulated in ASTM F2384-10 [4]. Various

Table 9.1 Compositions and tensile properties of industrial and nuclear grades of Zr alloys [2–4]

	(Mass%)			
Element	R60702	R60704	R60705	R60901
Zr + Hf, min	99.2	97.5	95.5	Balance
Hf, max	4.5	4.5	4.5	0.010
Fe + Cr	0.2, max	0.2–0.4	0.2, max	Fe:0.15, Cr:0.020
Sn	…	1.0–2.0	…	0.0050
H, max	0.005	0.005	0.005	0.0025
N, max	0.025	0.025	0.025	0.0080
C, max	0.05	0.05	0.05	0.027
Nb	…	…	2.0–3.0	2.40–2.80
O, max	0.16	0.18	0.18	0.13
Tensile properties	R60702	R60704	R60705	R60901
UTS, min (MPa)	379	413	552	450
Yield strength, min (MPa)	207	241	379	310
Elongation, min (%)	16	14	16	15

microstructures appear, depending on the annealing temperature and the cooling condition. For example, after cold rolling up to 20 % followed by stress-relief annealing at 673 K for 20 h, the network structure, consisting of the α phase surrounded by the β phase, is formed in the alloy [3].

9.2 Current Applications as Biomaterials

Typical use of Zr for biomedical applications is in total knee replacement (TKR) and total hip replacement (THR). The Zr-2.5 alloy is used for the femoral knee surface and the head of the hip joints, which was called Oxinium and developed by Smith and Nephew in 1997 for TKR and in 2002 for THR. Although the wear resistance of Zr is low because of its low hardness, thin zirconium oxides (ca. 5 μm) form when the Zr-2.5Nb alloy is heat-treated at approximately 773 K in air [5]. Relatively high compressive stress is generated in the oxide layer, and this contributes to the adherence to the base material [6]. Therefore, this alloy surface shows higher hardness and wear resistance as compared with Co-Cr and Ti alloys. During in vitro tests, the oxidized Zr femoral heads produced less polyethylene wear and fewer particles than did the Co-Cr heads [7]. The Zr alloy appears to have similar or superior bone response to the Co-Cr alloy when implanted in the rabbit tibia model [8]. On the other hand, the vulnerability of the oxidized Zr surface has been pointed out in vivo, in that deeper scratches were found as compared with the retrieved Co-Cr head [9, 10].

9.3 New Applications of Zr Alloys in Magnetic Resonance Image

Recently, new Zr alloys with low magnetic susceptibility have been studied extensively for the purpose of suppressing artifacts in magnetic resonance images, as Zr possesses lower magnetic susceptibility than stainless steels, Co-Cr, and Ti alloys that are currently used as metallic biomaterials. MRI has been widely used for medical diagnosis to acquire a cross-sectional view of the human body, especially in orthopedics and brain surgery. MRI can provide sectional images of anatomic regions in any arbitrary plane with excellent soft-tissue contrast resolution. On the other hand, MRI diagnostics are inhibited when metals are implanted in the body because of the heat generated by the implants, the displacement of the implant, and the generation of artifacts on the image. Imai et al. [11] investigated the relationship between artifacts and the magnetic susceptibility of metals. They showed that the artifact volume increased quantitatively with the increasing magnetic susceptibility, as shown in Fig. 9.1. To avoid the formation of artifacts, it could be a possible solution to substitute metals for ceramics and polymers with low magnetic susceptibility. However, metals are predominantly used in medical

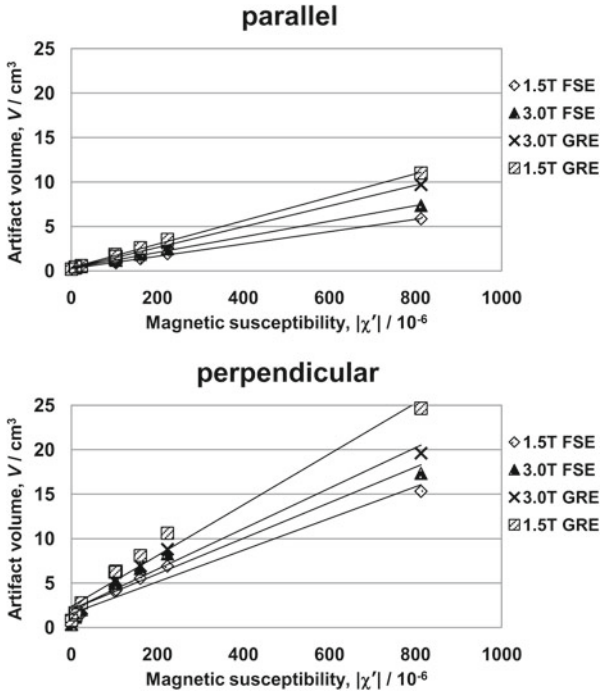

Fig. 9.1 Quantitative relationship between absolute magnetic susceptibility and the artifact volume (Reprinted from Ref. [11] with permission from Elsevier)

devices requiring strength, toughness, and other mechanical properties; in those areas, metals are superior to polymers and ceramics. Therefore, research on the development of alloys with low magnetic susceptibility needs to overcome the problem of artifacts.

Although Zr has an advantage of low magnetic susceptibility (1.36×10^{-6} g cm^{-3}) as compared to other metallic biomaterials, its strength is not sufficient for medical applications. Therefore, strengthening and lowering magnetic susceptibility should be achieved simultaneously. We used niobium (Nb) and molybdenum (Mo) as strengthening elements with low magnetic susceptibility and cytotoxicity [12, 13]. Several findings on the magnetic susceptibility and mechanical properties of Zr-Nb and Zr-Mo are discussed [14–17].

Figure 9.2 shows the compositional dependence of magnetic susceptibility of Zr-Mo alloys. The magnetic susceptibility of Zr-Mo suddenly decreases when the concentration of Mo increases from 0 to (0.5–1) mass% and then gradually decreases until 3 mass% Mo is reached. After showing the minimum value at 3 mass% Mo, the magnetic susceptibility abruptly increases when the concentration of Mo increases from 3 mass% to 7.5 mass% and then remained stable when the concentration of Mo increases from 10 to 15 mass% Mo. These results suggest that the magnetic susceptibility of Zr-Mo alloys shows a minimum value at a certain Mo content and does not monotonically decrease with Mo content in spite of the low

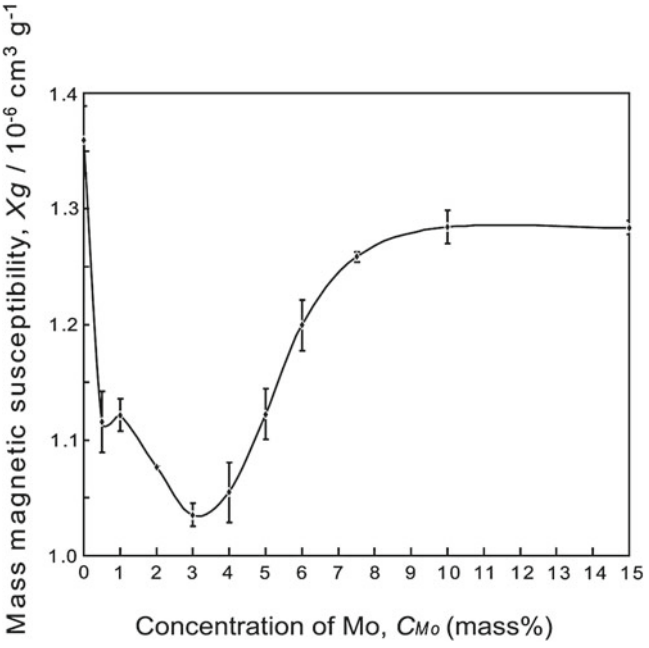

Fig. 9.2 Magnetic susceptibility of as-cast Zr-Mo alloys (Reprinted from Ref. [14], Copyright 2010, with permission from Elsevier)

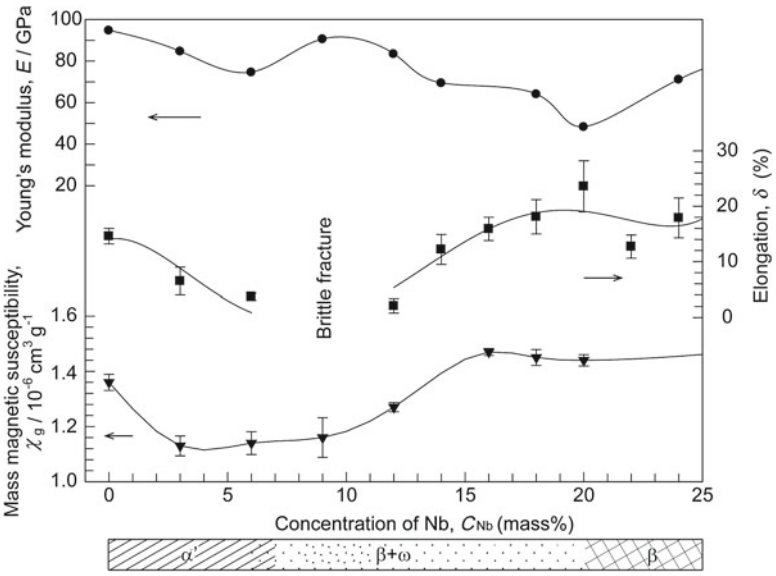

Fig. 9.3 Correlation between mechanical properties, magnetic susceptibilities, and phase constitutions in as-cast Zr-Nb alloys (Reprinted from Ref. [17] with permission from Elsevier)

magnetic susceptibility of Mo (7.3×10^{-7} g cm^{-3}) compared with Zr [14]. This behavior was also confirmed in the Zr-Nb alloy and was closely related to the phase constitution [16]. The magnetic susceptibility (χ) of the α′, β, and ω phases in Zr-based alloys was concluded as follows: $\chi\omega < \chi\alpha' < \chi\beta$.

Figure 9.3 shows the magnetic susceptibility and mechanical properties of Zr-Nb alloys [17]. The magnetic susceptibilities of Zr-Nb alloys are lower than those of Ti (2.74×10^{-6} g cm^{-3}) and Ti-6Al-4 V (3.17×10^{-6} g cm^{-3}). The formation of the ω phase contributed to the decrease of magnetic susceptibility, but limited elongation was obtained in Zr-(6–12)Nb alloys. Therefore, this composition range should be avoided, from the viewpoint of mechanical reliability and requirements for medical applications. The α′ phase-based Zr-Nb alloys are promising when low magnetic susceptibility and high Young's modulus are required (e.g., aneurysm clips). The β phase-based Zr-Nb alloys that contain a small amount of the ω phase are applicable when low magnetic susceptibility, low Young's modulus for avoiding stress-shielding effect [18], and large elongation are required (e.g., for hip prostheses, bone plates, and screws). Thus, magnetic susceptibility and mechanical properties can be tailored by changing the Nb or Mo content (i.e., the phase constitution) in Zr alloys so the alloys would be useful for medical devices under MRI.

9.4 Summary

In this chapter, basic properties of Zr are described, and the industrial and medical applications are introduced from the viewpoint of the specific features. Naval metallic medical devices that have notable wear resistance and low magnetic susceptibility can be developed using a Zr-based alloy. The cost reduction for processing Zr alloys also will be the key to expanding their usage in the medical field.

References

1. Miller GL (1953) Metallurgy of the rare metals-2, zirconium. Butterworth Scientific Publications, London, pp 1–10
2. Webster RT (1991) Zirconium and hafnium. In: ASM Handbook, vol 2, Properties and selection: nonferrous alloys and special-purpose materials section: specific metals and alloys. ASM International, Materials Park, DVD version
3. The Japan Society of Mechanical Engineers (1993) Zr alloy handbook. Nikkan Kogyo Shinbun, Tokyo, pp 1–129 (in Japanese)
4. ASTM F2384-10 (2010) Standard specification for wrought zirconium-2.5Niobium alloy for surgical implant applications (UNS R60901). American Society for Testing and Materials, Philadelphia
5. Hallab NJ, Jacobs JJ, Kats JL (2004) Orthopedic application. In: Ratner BD, Hoffman AS, Schoen FJ, Lemons JE (eds) Biomaterials science—an introduction to materials in medicine, 2nd edn. Elsevier Academic Press, San Diego, pp 537–538
6. Hobbs LN, Rosen VB, Mangin SP et al (2005) Oxidation microstructures and interfaces in the oxidized zirconium knee. Int J Appl Ceram Technol 2:221–246
7. Good V, Ries M, Barrack RL et al (2003) Reduced wear with oxidized zirconium femoral heads. J Bone Joint Surg Am 85-A(Suppl 4):105–110
8. Goodman SB, Davidson JA, Fornasier VL et al (1993) Histological response to cylinders of a low modulus titanium alloy (Ti-13Nb-13Zr) and a wear resistant zirconium alloy (Zr-2.5Nb) implanted in the rabbit tibia. J Appl Biomater 4:331–339
9. Rajpura A, Kendoff D, Board TN (2014) The current state of bearing surfaces in total hip replacement. Bone J Surg 96-B:147–156
10. McCalden RW, Charron KD, Davidson RD et al (2011) Damage of an oxinium femoral head and polyethylene liner following “routine” total hip replacement. J Bone Joint Surg (Br) 93-B:409–413
11. Imai H, Tanaka Y, Nomura N et al (2013) Three-dimensional quantification of susceptibility artifacts from various metals in magnetic resonance images. Acta Biomater 9:8433–8439
12. Lide DR (ed) (2006) CRC handbook of chemistry and physics, 87th edn. CRC Press, Boca Raton, pp 142–147
13. Yamamoto A, Homma R, Sumita M (1998) Cytotoxicity evaluation of 43 metal salts using murine fibroblasts and osteoblastic cells. J Biomed Mater Res 39:331–340
14. Suyalatu, Nomura N, Oya K et al (2010) Microstructure and mechanical properties of as-cast Zr-Mo alloys. Acta Biomater 6:1033–1038
15. Suyalatu, Kondo R, Tsutsumi Y et al (2011) Effects of phase constitution on magnetic susceptibility and mechanical properties of Zr-rich Zr-Mo alloys. Acta Biomater 7:4259–4266
16. Nomura N, Tanaka Y, Suyalatu et al (2009) Effects of phase constitution of Zr-Nb alloys on their magnetic susceptibilities. Mater Trans 50:2466–2472
17. Kondo R, Nomura N, Suyalatu et al (2011) Microstructure and mechanical properties of as-cast Zr-Nb alloys. Acta Biomater 7:4278–4284
18. O’Sullivian ME, Chao EY, Kelly PJ (1989) The effects of fixation on fracture-healing. J Bone Joint Surg 71:306–310

Chapter 10
The Use of Porous Tantalum for Reconstructing Bone Loss in Orthopedic Surgery

Nilesh Patil and Stuart B. Goodman

Abstract Porous tantalum, a novel biomaterial, was approved for use in orthopedic surgery by the Food and Drug Administration (FDA) in 1997. Several preclinical and experimental studies have demonstrated excellent biocompatibility with physical, mechanical, and tissue ingrowth properties conducive for enhanced osseointegration and superior structural integrity. Porous tantalum has high volumetric porosity (75–80 %). The modulus of elasticity of tantalum (3 Gpa) compares favorably to cancellous bone (1.2 GPa) or subchondral bone (2 GPa). Porous tantalum also has a high coefficient of friction with a high resistance to compression (50–80 Mpa) and rotational deformity (40–60 Mpa). Tantalum has been used in a wide array of clinical applications in orthopedics including primary and revision joint replacement, tumor reconstructive surgery, spine fusion, management of osteonecrosis of the femoral head, and foot and ankle surgery. Recent studies have demonstrated excellent clinical and radiographic outcomes, even in the presence of extensive bone loss in hip and knee reconstructive surgeries. Its use in spine surgeries and osteonecrosis of the hip has been associated with mixed clinical results. Further clinical studies are necessary to establish its role and refine its indications in specific orthopedic applications and determine whether the theoretical advantages of porous tantalum can provide long-term biological fixation and stability. This chapter presents a synopsis of the biomaterial properties and preclinical and clinical studies of porous tantalum in orthopedic surgery.

Keywords Porous tantalum • Hip replacement • Knee replacement • Spine fusion • Osteonecrosis • Bone ingrowth • Acetabular components • Tantalum augment

N. Patil, MD
Department of Orthopedics, Millinocket Regional Hospital,
165 Poplar St., Millinocket, ME 04462, USA

S.B. Goodman, MD (✉)
Department of Orthopaedic Surgery, Stanford Medical Center, Stanford University,
Outpatient Center, 450 Broadway St., M/C 6342, Redwood City, CA 94063, USA
e-mail: goodbone@stanford.edu

M. Niinomi et al. (eds.), *Advances in Metallic Biomaterials*, Springer Series
in Biomaterials Science and Engineering 3, DOI 10.1007/978-3-662-46836-4_10

10.1 Introduction

Orthopedic surgeons are often faced with the challenge of achieving biological fixation in the presence of significant bone loss and poorly vascularized tissue. During the last three decades, various biomaterials and porous surfaces have been used in orthopedic reconstructive surgery to achieve osseointegration of implants in such complex clinical scenarios. Conventional porous coatings using cobalt chrome alloy, titanium plasma spray, and diffusion-bonded titanium have demonstrated good clinical results in straightforward clinical scenarios. However, these constructs possess some inherent shortcomings such as higher modulus of elasticity relative to bone, relatively low volumetric porosity [ranging between 30 and 50 %], and suboptimal frictional characteristics [1–5].

Porous tantalum, a novel porous biomaterial, was developed to address these limitations. It was approved for use in orthopedic surgery by the Food and Drug Administration (FDA) in 1997. Porous tantalum was specifically designed to incorporate several important characteristics: increased volume of tissue ingrowth due to high porosity (75–85 %), comparable modulus of elasticity to cancellous bone, and favorable frictional properties [6–8]. Porous tantalum is commercially available under the trademark "Trabecular Metal" [TM, Zimmer, Warsaw, IN]. It can be used either as a bulk implant or as a surface coating. Tantalum implants have demonstrated excellent biocompatibility and properties suited for enhanced osseointegration and superior structural integrity. Due to superior biological characteristics, it has been used in a wide array of clinical applications in orthopedics including primary and revision joint replacement, tumor reconstructive surgery, spine fusion, and the management of avascular necrosis of femoral head. This material has revolutionized revision joint replacement surgeries and found wide acceptance among orthopedic surgeons around the world. The objective of this review is to present the biomaterial properties and clinical applications of porous tantalum in orthopedic surgery.

10.2 Porous Tantalum: Preparation and Properties

Porous tantalum is a transition metal consisting of repeating dodecahedrons with a physical appearance similar to cancellous bone. Porous tantalum is fabricated through pyrolysis (thermal conversion) of polyurethane foam. This foam transforms to a skeleton of low-density hyaloid carbon with a characteristic recurring fundamental structure that leads to a highly porous structure. Subsequently, deposition of the tantalum metal takes place on the carbon scaffold by a chemical vapor deposition-infiltration process. Orientation of the tantalum during deposition and the crystallographic process leads to creation of a surface with special texture similar to cancellous bone [6]. Typically, this process yields tantalum coating consisting of 99 mass% tantalum and 1 mass% vitreous carbon, ranging from 40 to 50 μm in thickness. The mean pore diameter is 547 ± 52 μm with volumetric porosity of 75–80 % [9].

The pore size is conducive for vascular ingrowth; the high interconnectivity between pores allows deep and extensive tissue penetration. The typical mean thickness of tantalum coating is 50 μm. The geometry also allows press molding of nonbiological materials such as polyethylene yielding a strong monoblock construct. Young's modulus of elasticity of tantalum (3 GPa) compares favorably to cancellous bone (1.2 GPa) or subchondral bone (2 GPa) [10]. Tantalum also has a high coefficient of friction [11]. These properties allow normal load transfer from the implant to the surrounding cancellous bone. It has high resistance to compression (50–80 MPa) and rotational deformity (40–60 MPa). Porous tantalum yields superior mechanical stability and higher resistance to compressive and rotational forces immediate post-implantation, which is critical for survivorship of weight-bearing implants, such as a hip prosthesis, in the presence of bone loss. Tantalum has demonstrated excellent biocompatibility without a surrounding inflammatory response [12]. It has excellent corrosion resistance derived from a natural passivating tantalum oxide layer, TaO_5 [13]. Porous tantalum offers favorable biological environment for growth and differentiation of osteoblasts. Recent studies have shown that the osseointegration potential of porous tantalum can be enhanced by the application of surface coatings (e.g., calcium phosphate) [14]. Pagnanis et al. evaluated the osseointegration potential of porous tantalum treated with thermal processing in an alkaline environment [15]. They noted that the new bone formation that occurs into such chemically altered tantalum retains the characteristics of normal bone, i.e., bone remodeling and haversian system formation. Furthermore, the osteoblasts derived from older women (>60 years) cultivated on porous tantalum grew relatively faster than osteoblasts from younger women (<45 years) cultivated on other substrates [titanium fiber mesh or tissue culture plastic]. Thus, porous tantalum is an appropriate substrate for osteoblast adherence, proliferation, and differentiation. The superior performance of porous tantalum could be explained by its microscopic texture and physicochemical properties. The cellular proliferation and adherence is enhanced by its higher surface roughness. It appears that these processes are mediated by specific integrins that attach to the tantalum surface. Moreover, higher surface energy due to its irregular microstructure and larger surface area secondary to high porosity offers a conducive environment for osteoblast adherence [16–18]. Tantalum is a highly malleable and ductile material. It can be manufactured as a surface coating or as bulk implants of various shapes and sizes which provides versatility to its applications in various reconstructive surgeries. Compared to bone grafts, it has more predictable mechanical properties and geometry which are retained after material implantation.

10.3 Bone and Fibrous Tissue Formation with Tantalum

Numerous preclinical and animal studies have demonstrated enhanced bone and fibrous tissue ingrowth potential of porous tantalum (Table 10.1). Bobyn et al. were one of the first investigators to analyze the biological processes at bone-porous

Table 10.1 Preclinical studies demonstrating bone ingrowth and fibrous ingrowth of porous tantalum

Author	Method	Results	Property of tantalum demonstrated
Bobyn et al.	Implantation of 22 acetabular porous tantalum components in 11 dogs	Thin section histology, high-resolution radiography, and backscattered scanning electron microscopy revealed that all 22 implants had stable bone-implant interfaces at the end of 6 months	Bone ingrowth
Hacking et al.	Eight dorsal subcutaneous tantalum implantation in two dogs evaluated at 4, 8, and 16 weeks	Analysis of retrieved specimens revealed fibrous tissue ingrowth and blood vessels in porous tantalum implants	Fibrous ingrowth
Rahbek et al.	Implantation of tantalum and glass bead-blasted titanium alloy into the knee joints of eight mongrel dogs in randomized paired design. Weekly polyethylene particle injection into the knees starting at three weeks postimplantation	Superior bone ingrowth and less polyethylene particle migration into porous tantalum compared with glass bead-blasted implants at 8 weeks	Resistance to migration of polyethylene particles
Reach et al.	Supraspinatus tendons from forty skeletally mature dogs were reattached to the greater tuberosity between two porous tantalum washers, and the reattachment evaluated postoperatively for strength, stiffness, and tendon function	Excellent biologic ingrowth of the tendon into porous tantalum was observed. Histomorphologic evaluation revealed Sharpey-like fibers inserting onto the surface of the porous tantalum washers	Direct healing potential of tendons to porous tantalum biomaterial

tantalum interface in preclinical studies [12]. They implanted porous tantalum cylinders into femoral cortical bone of skeletally mature dogs. The samples were examined histologically for osseointegration at 4, 16, and 52 weeks, respectively. They noted consistent new bone formation over considerable surface area at 4 weeks. The mechanical strength of fixation or shear strength was at least 18.5 Mpa at 4 weeks which is much higher compared to the shear strength observed with other conventional metallic porous materials (1.2–13 MPa) by the same investigator under a similar protocol. The bone penetration was even more dense and extensive at 16 and 52 weeks with the formation of haversian systems and bone remodeling.

The same team studied patterns of bone ingrowth into porous tantalum subjected to normal loading. They implanted acetabular monoblock tantalum components in a canine model and examined the bone-implant interface radiologically and histo-

logically after 6 months. Stable implant fixation and bone ingrowth were found in all cases. The depth of bone ingrowth varied from 0.2 to 2 mm, comparable to titanium fiber mesh [22, 23]. The bone ingrowth was intense and pronounced at the periphery of the implant due to uniform bone-implant contact. Interestingly, fibrous tissue formation was noted in pores devoid of bone. This phenomenon may serve as a barrier to wear debris and potentially avoid or minimize wear particle-induced osteolysis. Tantalum serves as a good substrate for growth and differentiation of fibroblasts as well. Hacking et al. evaluated eight dorsal subcutaneous tantalum implants in two dogs at 4, 8, and 16 weeks [19]. The retrieved specimens revealed reliable fibrous and vascular tissue ingrowth into the porous tantalum implants.

The bone ingrowth potential of porous tantalum can be enhanced with application of various surface coatings. Garbuz et al. compared bone formation into porous tantalum implants coated with calcium phosphate and alendronate with uncoated implants using an electron microscopy in eighteen rabbit femora [24]. They observed significantly enhanced bone ingrowth and filling of the bone-implant gap with the coated porous tantalum implants, thus illustrating that chemical surface treatment of porous tantalum may further improve its biological performance.

10.4 Bone Ingrowth in Retrieval Studies

There has been encouraging data from studies of retrieved tantalum implants (Table 10.2). D'Angelo et al. studied an acetabular porous tantalum component removed for recurrent hip dislocation 3 years after index surgery [25]. Bone

Table 10.2 Retrieval studies of porous tantalum following hip and knee reconstructive surgery

Author	Components removed	Indication for removal	Characteristics of bone ingrowth
D'Angelo F et al.	One acetabular component	Recurrent hip dislocation	95 % bone ingrowth
Hanzlik et al.	76 acetabular shells, five femoral stems, seven patellas, and 36 tibial trays	Infection [tibial trays], instability [acetabular], and loosening [two acetabular shells, one tibial tray]	Full depth penetration of bone into the porous tantalum layer for the acetabular shells and femoral stems
Sambaziotis et al.	One tibial component	Infection	Bone ingrowth present in the tibial posts (36.7 %) and 4.9 % into the tibial baseplate
Tanzer et al.	15 tantalum rods	Progression of osteonecrosis	Bone ingrowth in thirteen (87 %), extent of bone ingrowth was 1.9 %
Breer et al.	Four hip and three knee tantalum augments	Two fractures, two loosening, and three infections	No bone ingrowth 5/7, 2.6 mm bone ingrowth in 2/7 specimens

ingrowth was assessed with light microscopy, and a geometrical model was used to obtain quantitative evaluation of bone ingrowth. Their analysis revealed that more than 95 % of the voids on the implant were filled with bone. The histological findings were consistent with the radiological findings of complete osseointegration of the implant. In a recent multicenter study, Hanzlik et al. investigated the amount of bone ingrowth in retrieved porous tantalum components [26]. They analyzed bone volume fraction, extent of ingrowth, and maximum depth of ingrowth in 76 acetabular shells, 5 femoral stems, 7 patellas, and 36 tibial trays. They noted consistent full depth bone penetration into the porous tantalum layer in the acetabular shells and femoral stems. In another study, Sambaziotis et al. reported a histologic retrieval analysis of a porous tantalum tibial component in an infected total knee arthroplasty [27]. They observed bone ingrowth along tibial baseplate and the post, which was suggestive of viable bone tissue and healthy marrow, osteocytes, and lamella despite of the presence of infection. However, the bone ingrowth potential of porous tantalum may vary in different clinical scenarios. Tanzer et al. reported histopathologic retrieval analysis of failed porous tantalum rods used for treatment of hip osteonecrosis [28]. The retrieved implants were associated with little bone ingrowth and insufficient mechanical support of the subchondral bone. They suggested that the failures were probably multifactorial. They recommended close monitoring of implant design, surgical technique, and appropriate patient selection to avoid failures. Similarly, Breer et al. investigated the osseointegration pattern into porous tantalum augmentations harvested during re-revision after hip and knee replacement procedures [29]. They noted limited to no growth in 5/7 specimens. They attributed suboptimal bone ingrowth to poor direct implant to host bone contact secondary to the use of interposing cement or bone graft. Although porous tantalum has demonstrated excellent bone ingrowth potential, an adverse biological environment may influence the clinical performance of these implants.

10.5 Clinical Applications

10.5.1 Hip Reconstructive Surgery

The unique material properties of porous tantalum make it an ideal biomaterial for complex primary and revision total hip replacement (THR) especially in the presence of substantial bone loss and poor bone quality (Fig. 10.1). Porous tantalum has shown excellent fibrous tissue ingrowth throughout the porous structure in areas devoid of bone ingrowth in preclinical studies. This characteristic offers the potential to act as a mechanical barrier to access of fluid and particulate wear debris and implant by-products to the bone-implant interface to mitigate osteolysis. Currently, tantalum acetabular components are available in three versions for hip reconstructive surgeries – a monoblock acetabular component with direct compression molded polyethylene, a monoblock acetabular cup with peripheral screw fixation, and a modular acetabular component coated with porous tantalum framework. Several clinical studies have demonstrated good early clinical and

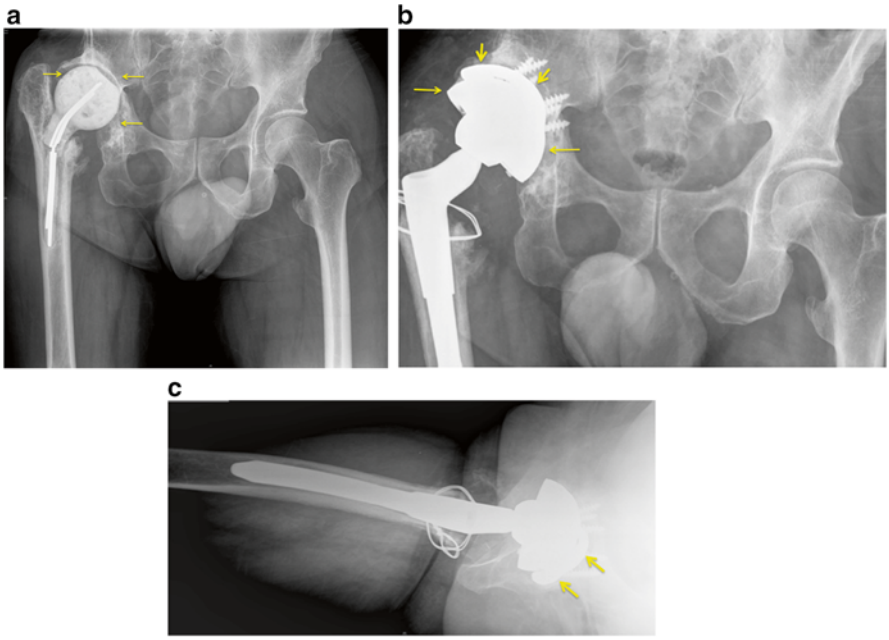

Fig. 10.1 Revision total hip replacement with severe acetabular bone loss. (**a**) anteroposterior radiograph of the pelvis showing an antibiotic-laden cement spacer and metal rods in the right hip and severe acetabular bone loss (*arrows*) compared to the contralateral left side. The original right hip replacement was excised due to infection, and a cement spacer was placed temporarily. (**b**) anteroposterior radiograph after revision total hip replacement of the case seen in (**a**). The tantalum acetabular shell (*thin arrows*) and screws are surmounted by a tantalum augment and screws (*short thick arrows*) to make up some of the lost acetabular bone and place the new cup in a more anatomical socket. (**c**) cross-table lateral view showing the hemispherical tantalum cup and surrounding tantalum augment (*arrows*)

radiographic with monoblock tantalum devices used for acetabular fixation (Table 10.3) [28–37]. Gruen et al. reported the outcome of tantalum monoblock components in 414 primary total hip replacements at an average follow-up of 3 years (2–5 years) [28]. There was no evidence of radiographic osteolysis or component loosening, and the average Harris hip score [HHS] was 90. Moen et al. reviewed 51 THRs using tantalum monoblock components [34]. The authors reported no evidence of osteolysis or loosening on computed tomography (CT) scan at an average follow-up of 10.3 years. In another recent study, Noiseux et al. reported clinical outcomes of tantalum acetabular components in a large group of patients (613) who underwent primary THR [36]. They noted excellent bone ingrowth with no failures related to component loosening at 2–10-year follow-up. However, the monoblock acetabular component has some theoretical disadvantages. The rough external surface of the implant may adhere to surrounding tissue and prevent complete seating of the component resulting in central radiolucency. Additionally monoblock components do not provide the option of isolated exchange of the bearing surface should polyethylene wear and osteolysis occur.

Table 10.3 Clinical results of porous tantalum in primary total hip replacement

Author	Number of hips	Average F/U	Clinical outcome [hip scores]	Complications	Reoperations
Gruen et al.	414	33 months	N/A	Six femoral and two acetabular intraoperative fractures, one traumatic cup loosening, six recurrent dislocations, and three infections	10
Komaraswamy et al.	112	32 months	Oxford hip score [average – 45]	Three periprosthetic femoral fractures, two DVT, and two trochanteric bursitis	3
Bargiotas et al.	102 [90 primary and 12 secondary] THRs	50 months	Harris hip score [94]	No cases of revision, osteolysis, or loosening	1
Macheris et al.	86	7.3 years	N/A	No cases of osteolysis or migration	Nil
Mullier et al.	40	46 months	65 % excellent Harris hip score [\90]	One dislocation, one radiographic cup migration without clinical failure	1
Lewis et al.	245	2–5 years	Harris hip score [improved from an average of 49–84]	Nine dislocations, two sepses, two acetabular fractures	Not documented
Noiseux et al.	613	2–10 years	N/A	Acetabular cup removal 6 [1.2 %], femoral and other revisions 19	25
Macheras et al.	27	10.2 years	Harris hip score 89.5	N/A	None

F/u follow-up, *N/A* data not available, *DVT* deep vein thrombosis

Porous tantalum components appear an attractive option in hip replacement procedures following radiation therapy. The pelvic bone often is comprised of islands of avascular bone interspersed within areas of viable vascularized bone postirradiation. The potentially superior biological and mechanical fixation due to rapid tissue ingrowth from viable host bone may lend itself to better clinical outcome compared to conventional porous coated acetabular components in these complex clinical situations. Rose et al. reported encouraging early clinical outcome in 12 THRs performed after radiation therapy for malignancy using porous tantalum acetabular components [38]. There were no clinical failures or radiographic loosening at an average follow-up of 31 months with average postoperative HHS of 88 points.

Acetabular revision procedures present challenging clinical scenarios with variable amount of bone loss ranging from small contained defects to extensive segmental defects or pelvic discontinuity. The clinical outcomes with reconstruction rings, cages, and bulk allografts used for reconstruction of large acetabular bone defects have been inconsistent and sometimes suboptimal [39–41]. Tantalum implants offer a wide array of options ranging from non-modular to modular acetabular components and augments of various sizes and shapes. The non-modular tantalum components offer the flexibility of placing the screws through the metal itself rather than through preexisting holes to obtain purchase in the best available bone stock. The tantalum augments have almost eliminated the use of bulk allograft which was associated with nonunion and graft collapse leading to compromised acetabular fixation. Historically, reconstruction cages and rings were used for management of extensive segmental acetabular defects and pelvic discontinuity with less than 50 % host bone contact [42]. These constructs do not provide biological fixation and are at risk for late loosening. Owing to enhanced biological and mechanical fixation, tantalum implants offer a good alternative reconstruction option in the presence of such a compromised biological and mechanical environment (Figs. 10.1 and 10.2) [43]. Several clinical studies have demonstrated consistently good clinical outcomes with tantalum implants in revision acetabular surgeries (Table 10.4) [44–52]. Recently, Del Gaizo et al. retrospectively reviewed 37 acetabular revisions at a mean follow-up of 60 months [47]. All patients had Paprosky type IIIa acetabular defects which were treated with porous tantalum acetabular components and augments. One patient developed aseptic loosening of the acetabular component requiring revision surgery. The majority of the patients with these reconstructions had good pain relief and reasonable function with low rates of loosening at midterm follow-up. Similar encouraging results were reported by Lachieweiz et al. in 39 revision acetabular reconstructions using tantalum implants at mean follow-up of 3.3 years [52]. They had 26 hips with Paprosky type III acetabular defects, 11 with type II, and two hips with type I defects. Only one patient developed mechanical failure at 6 months. Radiographic evaluation revealed that bone ingrowth and stable implants were present in all the other hips. They concluded that tantalum acetabular components provide stable fixation in difficult acetabular revision surgeries.

Pelvic discontinuity is characterized by separation of the superior and inferior hemi-pelvis due to either loss of bone or a fracture through the acetabular columns. Paprosky et al. described a surgical method to manage pelvic discontinuity with

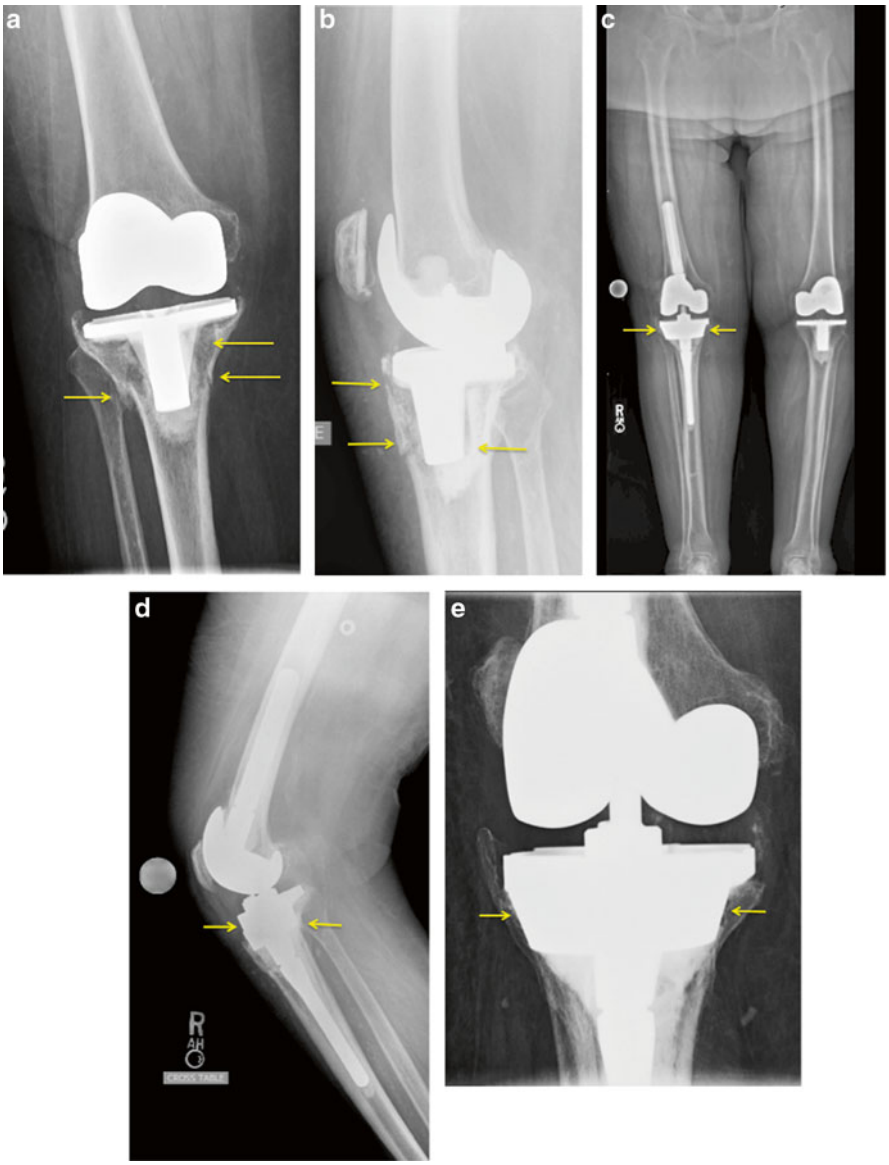

Fig. 10.2 Revision total knee replacement with severe tibial bone loss. Preoperative anteroposterior (**a**) and lateral (**b**) radiographs of the knee after cemented total knee replacement. There is loosening and marked bone loss around the tibial component with a fracture of the bone (*arrows*). Three-foot standing anteroposterior view (**c**), *lateral view* (**d**), and notch view showing the revision total knee replacement. The contralateral left knee is replaced with a conventional primary knee replacement. The right knee has been revised with stemmed more constrained components. The deficient tibial bone near the joint has a tantalum tibial cone (*arrows*) that replaces the lost metaphyseal cancellous bone in the area of the previous fracture

Table 10.4 Clinical results of porous tantalum in revision hip arthroplasty

Author	Number of revision hips	Follow-up	Complications	Clinical outcome
Unger et al.	60	42 months [14–68]	One revision for aseptic loosening, seven dislocations	Harris hip score 94.4
Mardones et al.	114	24 months	Four dislocations, six reoperations	97.3 % with complete incorporation with host bone
Paprosky et al.	12 [pelvic discontinuity]	2.1 years [1–3] years	One case of possible acetabular loosening secondary to screw breakage	Eleven patients had no or mild pain; one patient had moderate pain
Nehme et al.	16	31.9 months [24–39]	One revision for pelvic discontinuity, one dislocation, and one sciatic nerve palsy	Harris hip score [56–92] postoperatively
Boscainos et al.	14 [cup cage construct]	32 months [6–45]	Two dislocations, one thigh seroma	Oxford hip score 45 [33–53]
Del Gaizo et al.	37 [augments]	60 months [26–106]	One aseptic loosening, two fractures, three acute infections, and two recurrent dislocations	Harris hip scores 81.5 postoperatively
Davies et al.	46	50 months	One infection, two dislocations, and one arterial bleeding	Harris hip score 78.2
Lachiewicz et al.	37	39 months	One component loosening, three recurrent dislocations, two infections, and 1 fracture	Harris hip score 86
Sporer et al.	28	4.4 years	One aseptic loosening, one infection, one vascular injury, and one bowel injury	Merle d'Aubigné-Postel score was 6.6

tantalum implants [46]. They recommended the use of a tantalum augment to span the discontinuity and particulate bone graft to fill any residual cavities before placement of the acetabular component. They reported satisfactory clinical and radiographic outcome with this technique in 20 patients at a mean follow-up of 4.5 years [53]. One patient required revision for aseptic loosening of acetabular component. Implantation of tantalum acetabular components in revision surgery requires great care because of compromised bone stock. Springer et al. reported seven acetabular fractures following implantation of tantalum components during revision acetabular surgeries [54]. They attributed the fractures to potential weakening of the acetabular walls during reaming for revision procedures compounded further by physiological stresses of daily activities. They recommended conservative acetabular reaming and protected weight-bearing protocol to avoid this complication.

10.5.2 Knee Reconstructive Surgery

Porous tantalum is available as a monoblock tibial component with compression molded polyethylene for primary total knee replacement (TKR). Modular constructs of tantalum cones, wedges with the femoral and tibial components, have revolutionized revision knee reconstructive surgeries and have been widely used by surgeons for these complex clinical scenarios (Fig. 10.2). The monoblock tibial component is expected to produce less stress shielding and provide predictable bone ingrowth thus minimizing component loosening. Numerous recent clinical studies have demonstrated good to excellent results with porous tantalum components in primary total knee replacement (Table 10.5) [55–61]. In a recent study from the Finnish registry, Niemelanin et al. reported the 7-year survivorship of 1143 TKRs using monoblock tantalum tibial components [59]. They noted 100 % survivorship with revision for aseptic loosening of the tibial component and 97 % with revision for any reason as the respective endpoints, thus demonstrating excellent outcome in a large population-based study. In another study, Okeefe et al. reported clinical and radiographic findings in 101 TKRs performed with monoblock tibial components [56]. They observed 100 % survivorship of the tibial components with no evidence of osteolysis or change in periprosthetic bone density. Minoda et al. demonstrated favorable results of porous tantalum tibial components on bone mineral density of the proximal tibias in a matched cohort at 5-year follow-up [61]. In summary, monoblock tibial components have shown excellent midterm durability in primary TKR.

Revision total knee arthroplasty is often associated with bone deficiencies. Historically, the bone defects were managed with allograft, metal wedges, and augments. Porous tantalum components offer structural and mechanical support coupled with good ingrowth potential in revision knee replacements with varying amount of bone loss (Table 10.6) [62–65]. These components can be coupled with necessary stem extensions to provide optimal component alignment and fixation (Fig. 10.2). In a recent study, Lachiewicz et al. retrospectively reviewed the clinical

Table 10.5 Clinical outcome of monoblock tibial component in primary knee replacement

Author	Number of knees	Follow-up	Complications	Clinical outcome
Kamath et al.	100	Mean 5 years	Nil	Excellent Knee Society scores [KSS] in all patients
O'Keefe et al.	125	Mean 5.2 years	Nil	Knee Society score 87.1
Niemelainien et al.	1,143	Mean 7 years	Infections, instability	100 % survivorship with aseptic loosening
Unger et al.	95	Mean 4.5 years	One femoral revisions, two patella loosening, one patella fracture, and one patellar maltracking	Knee Society score 89

Table 10.6 Clinical results of tantalum implants in revision knee arthroplasty

Author	Tantalum component	Number of knees	Follow-up	Complications	Clinical outcome
Radney et al.	Ten tibial cones, two femoral cones	10	10.2 months [5–14]	One infection	Knee flexion 0–103° [average]
Schmitz et al.		44	37 months [32–48]	Two aseptic loosening	KSS mean 63
Lachiewicz et al.	24 tibial cones, nine femoral cones	27	3.3 years	One infection, one loosening, one fracture, and one wound problem	KSS mean 79
Howard et al.	All femoral cones	24	33 months	No cone-related complications	KSS mean 81
Meneghini et al.	All tibial cones	15	34 months	None	KSS mean 84

ROM range of motion, *avg* average

outcome in 33 revision knee procedures using 9 femoral and 24 tibial tantalum cones [64]. They observed radiographic evidence of osseointegration in all but one knee, and one knee was revised for component loosening. The mean Knee Society pain score improved from 40 points preoperatively to 79 points postoperatively. Howard et al. reported clinical outcome of 24 femoral cones used in revision knee arthroplasty at a mean follow-up of 33 months [65]. All femoral cones appeared well fixed radiographically, with no evidence of cone-related complications.

Porous tantalum can be used for patellar reconstruction in revision surgeries (Table 10.7) [67–70]. This involves cementing an all polyethylene patella into the tantalum metal base implanted into residual patellar bone stock. Additional fixation is achieved by suture attachment to soft tissue. In a recent study, Kamath et al.

Table 10.7 Clinical outcome of patellar reconstruction using tantalum implant in revision surgery

Author	Number of patellas	Follow-up	Complications	Clinical outcome
Ries et al.	18	1 year	Seven failures with soft tissue fixation, one infection	All [11] patellar components with bony fixation were stable and KSS was 87.2 in this group
Nasser et al.	11	32 months	One patellar fracture	ROM 0–104 [avg]
Nelson et al.	20	23 months	Three patellar fractures	ROM 108 [avg]
Kamath et al.	23	7.7 years	Four revision procedures	KSS mean 82.7

evaluated the midterm outcomes of porous tantalum patellar components [70]. The Knee Society scores for pain and function averaged 82.7 and 33.3, respectively, with survivorship of 83 % at an average follow-up of 7.7 years. Failures were associated with avascular residual bone and fixation of components to the extensor mechanism. The results of this study were consistent with a previous study in which the authors reported clinical outcome in 18 knees with patellar reconstruction utilizing tantalum implants for severe bone loss [67]. They noted very high failure rate when the tantalum implants were fixed to soft tissues, whereas stable fixation was retained in most of the cases when the components were fixed to at least 50 % residual host bone. Porous tantalum patellar components offer a good solution in these challenging revision situations; however, caution must be exercised in the liberal use of these implants due to failures associated with fixation to nonviable bone or soft tissues.

10.5.3 Limb Salvage Surgery

Tumor resection procedures and catastrophic joint replacement implant failures are often associated with extensive segmental bone loss. These procedures demand implantation of prostheses which can provide a biological and mechanical environment for soft tissue ingrowth to enable attachment of tendons and ligaments. The potential of porous tantalum for excellent vascularized soft tissue and fibrous ingrowth may aid in providing biological and mechanical fixation of ligaments and tendons directly to the implant. Porous tantalum can be incorporated mechanically or metallurgically in the form of sleeves, pads, or insets to help soft tissue attachment in limb salvage surgeries [71–73]. Khan et al. retrospectively reviewed 20 patients who underwent THRs using large tantalum shells following resection of periacetabular bone tumors [72]. The mean Harris hip scores improved from 32 preoperatively to 74 postoperatively at an average follow-up of 26 months. There were no cases of progressive radiolucent lines or component migration in their case series. Previously, Holt et al. reported seven patients managed with custom tantalum

implants following resection of skeletal sarcomas from the femur and proximal tibia [73]. They observed good clinical outcomes at a minimum follow-up of 6 years with reliable soft tissue ingrowth and osseointegration.

It is thought that in addition to its reconstructive potential in tumor surgery, tantalum may provide a medium for sustained delivery of local antineoplastic drugs. In an experimental study, Guo et al. analyzed the drug delivery capability of porous tantalum. Doxorubicin, an anticancer drug, was encapsulated into the multilayer copolymer membranes on porous tantalum implants [74]. They noted sustained delivery of doxorubicin from the functionalized tantalum implant for almost 1 month with inhibitory effects on the proliferation of the chondrosarcoma cell line SW1353. Thus, porous tantalum shows great promise for mechanical as well as biological solutions in limb salvage surgery following tumor resection. Additionally, its potential to offer reliable fixation and optimum clinical outcomes in compromised bone postirradiation makes it an attractive option in tumor surgery [75].

10.5.4 Spine Surgery

Anterior decompressive surgery of the cervical disk space and vertebral body often creates bone defects which require autologous bone graft to promote spinal fusion. Donor site morbidity, insufficient graft material, and additional surgical time have prompted the use of biomaterials to replace or supplement existing spinal reconstructive techniques. Several preclinical studies have demonstrated satisfactory results with the use of porous tantalum in spine surgery [76–78]. Zou et al. studied spine fusion in pigs with the use of porous tantalum cages filled with autologous bone graft supplemented with pedicle screws [76]. They noted reliable spine fusion with fewer amounts of bone graft and enhanced bone remodeling with porous tantalum cages compared to carbon fiber cages. There have been very few clinical studies comparing outcomes of anterior cervical decompression and fusion (ACDF) using traditional bone grafting techniques and porous tantalum cages. In a recent study, Fernández-Fairen et al. retrospectively compared the clinical results and cost effectiveness in 28 patients treated for single-level ACDF using an isolated porous tantalum implant without graft to 33 patients who underwent autograft and plating [77]. They suggested that porous tantalum as a stand-alone device is less costly and more effective than autograft and plate in ACDF procedures. However, in a prospective randomized multicenter study, Kasliwal et al. reported spine fusion failures with stand-alone porous tantalum device compared to traditional technique [78]. They also noted a risk of device fragmentation in patients with failures of spine fusion. Further clinical studies are necessary to support routine use of porous tantalum cages as a stand-alone device for ACDF procedures.

10.5.5 Osteonecrosis of the Hip

Osteonecrosis of the hip varies from a localized to a global lesion, which often progresses with time necessitating joint replacement if left untreated in early stages of the disease process. Various treatment strategies including core decompression, vascularized fibular grafting, or osteotomy have been recommended to halt the progression of disease. Free vascularized fibular grafting has been reported to provide satisfactory pain relief and functional improvement; however, this is a technically demanding procedure with a high complication rate. It has been speculated that porous tantalum may provide structural support and simultaneously promote bone ingrowth in the vicinity of the avascular femoral head. Few studies have reported favorable outcome with the use of porous tantalum rods and core decompression for early-stage osteonecrosis of the hip [79, 80]. Vielleitte et al. noted an overall survivorship of 68.1 % at 48 months with better survival (92 %) in patents without chronic systemic disease [79]. However, there have been concerns of poor bone ingrowth in the presence of avascular bone. Tanzer et al. performed histopathologic retrieval analysis on 17 clinically failed porous tantalum implants used in the treatment of stage II osteonecrosis of the hip [28]. They observed minimal bone ingrowth and insufficient mechanical support of the subchondral bone with failed implants. Thus, further research is necessary to refine the implant design, surgical technique, and patient selection to obtain consistently good clinical outcomes with this application of porous tantalum.

10.5.6 Foot and Ankle Surgery

Autograft is considered the gold standard to obtain bony fusion in foot and ankle arthrodesis procedures. However, its use is limited due to availability and donor site morbidity. It is proposed that tantalum may promote predictable bone ingrowth and provide structural support in complex foot and ankle reconstruction procedures. Frigg et al. retrospectively reviewed nine patients who underwent complex foot and ankle arthrodesis using a tantalum spacer. They noted clinical and radiological evidence of fusion in all arthrodesis after 2 years of follow-up [81]. These results were consistent with a recent retrospective review of 25 patients who had foot and ankle arthrodesis using porous tantalum implants [82]. A tantalum spacer appears to be a viable alternative to conventional autograft for foot and ankle arthrodesis procedures potentially avoiding donor site complications.

10.6 Future Trends

The midterm clinical results of porous tantalum in primary revision hip and knee reconstructive surgery have been encouraging. Several preclinical, clinical, and retrieval studies have shown that porous tantalum has physical, mechanical, and tissue ingrowth properties that support its use in complex hip and knee reconstructions.

The potential benefit of porous tantalum appears to be fully appreciated in the setting of substantial bone loss, where tantalum implants of various types provide stable fixation with good bone ingrowth potential. Recent clinical studies have also shown a potential advantage of tantalum devices in preventing stress shielding following implantation in knee replacement surgeries [61]. The use of tantalum implants has been extended to spine surgeries and osteonecrosis of hip with mixed results. Tantalum shows promise as a bone graft substitute in complex foot and ankle surgeries. Porous tantalum also holds potential as a drug delivery vehicle in tumor reconstructive surgery. Tantalum has been to shown to possess chondroprotective properties providing scaffold for cartilage growth, thus illustrating its potential for resurfacing of diseased joints [83]. However, it remains to be seen whether the theoretical advantages of porous tantalum can yield successful clinical outcome in other orthopedic applications besides hip and knee reconstructive surgery. Additionally, the high cost associated with fabrication of these implants remains a limiting factor in its widespread application. Long-term clinical studies are necessary to monitor the mechanical fixation and stability of tantalum implants in various orthopedic reconstructive surgeries.

References

1. Bobyn JD, Tanzer M, Miller JE (1996) Fundamental principles of biologic fixation. In: Morrey BF (ed) Reconstructive surgery of the joints. Churchill Livingstone, New York, pp 75–94
2. Galante J, Rostoker W, Lueck R, Ray RD (1971) Sintered fiber metal composites as a basis for attachment of implants to bone. J Bone Joint Surg Am 53A:101–114
3. Pilliar RM, Cameron HU, Macnab I (1975) Porous surface layered prosthetic devices. J Biomed Eng 10:126–131
4. Pilliar RM (1983) Powder metal-made orthopaedic implants with porous surface for fixation by tissue ingrowth. Clin Orthop 176:42–51
5. Stein T, Armand C, Bobyn JD, Krygier JJ, Miller J, Brooks CE (1991) Quantitative histological comparison of bone growth into titanium and cobalt-chromium porous coated canine implants. Orthop Trans 15:178
6. Cohen R (2003) A porous tantalum trabecular metal: basic science. Am J Orthop 31:216–217
7. Black J (1994) Biological performance of tantalum. Clin Mater 16:167–173
8. Kato H, Nakamura T, Nishiguchi S, Matsusue Y, Kobayashi M, Miyazaki T et al (2000) Bonding of alkali- and heat-treated tantalum implants to bone. J Biomed Mater Res 53:28–35
9. Zardiackas LD, Parsell DE, Dillon LD, Mitchell DW, Nunnery LA, Poggie R (2001) Structure, metallurgy, and mechanical properties of a porous tantalum foam. J Biomed Mater Res 58:180–187
10. Matsuno H, Yokoyama A, Watari F, Motohiro U, Kawasaki T (2001) Biocompatibility and osteogenesis of refractory metal implants, titanium, hafnium, niobium, tantalum and rhenium. Biomaterials 22:1253–1262
11. Zhang Y, Ahn PB, Fitzpatrick DC, Heiner AD, Poggie RA, Brown TD (1999) Interfacial frictional behavior: cancellous bone, cortical bone, and a novel porous tantalum biomaterial. J Musculoskelet Res 3:245–251
12. Bobyn JD, Toh KK, Hacking SA, Tanzer M, Krygier JJ (1999) Tissue response to porous tantalum acetabular cups: a canine model. J Arthroplasty 14:347–354
13. Bermudez MD, Carrion FJ, Martinez-Nicolas G, Lopez R (2005) Erosion–corrosion of stainless steels, titanium, tantalum and zirconium. Wear 258:693–700

14. Barrere F, van der Valk CM, Meijer G, Dalmeijer RA, deGroot K, Layrolle P (2003) Osteointegration of biomimetic apatite coating applied onto dense and porous metal implants in femurs of goats. J Biomed Mater Res B 67:655–665
15. Paganias CG, Tsakotos GA, Koutsostathis SD, Macheras GA (2012) Osseous integration in porous tantalum implants. Indian J Orthop 46(5):505–513
16. Findlay DM, Welldon K, Atkins GJ, Howie DW, Zannettino AC, Bobyn D (2004) The proliferation and phenotypic expression of human osteoblasts on tantalum metal. Biomaterials 25:2215–2227
17. Balla VK, Bodhak S, Bose S, Bandyopadhyay A (2010) Porous tantalum structures for bone implants: fabrication, mechanical and in vitro biological properties. Acta Biomater 6(8):3349–3359
18. Sagomonyants KB, Hakim-Zargar M, Jhaveri A, Aronow MS, Gronowicz G (2011) Porous tantalum stimulates the proliferation and osteogenesis of osteoblasts from elderly female patients. J Orthop Res 29(4):609–616
19. Hacking SA, Bobyn JD, Toh K, Tanzer M, Krygier JJ (2000) Fibrous tissue ingrowth and attachment to porous tantalum. J Biomed Mater Res 52:631–638
20. Rahbek O, Kold S, Zippor B, Overgaard S, Soballe K (2005) Particle migration and gap healing around trabecular metal implants. Int Orthop 29(6):368–374
21. Reach JS Jr, Dickey ID, Zobitz ME (2007) Direct tendon attachment and healing to porous tantalum: an experimental animal study. J Bone Joint Surg Am 89:1000–1009
22. Pidhorz LE, Urban RM, Jacobs JJ, Sumner DR, Galante JO (1993) A quantitative study of bone and soft tissues in cementless porous-coated acetabular components retrieved at autopsy. J Arthroplasty 8(2):213–225
23. Jasty M, Bragdon CR, Haire T Jr, Mulroy RD, Harris WH (1993) Comparison of bone ingrowth into cobalt chrome and titanium fiber mesh porous coated cementless canine acetabular components. J Biomed Mater Res 27:639–644
24. Garbuz DS, Hu Y, Kim WY (2008) Enhanced gap filling and osteoconduction associated with alendronate-calcium phosphate-coated porous tantalum. J Bone Joint Surg Am 90(5):1090–1100
25. D'Angelo F, Murena L, Campagnolo M, Zatti G, Cherubino P (2008) Analysis of bone ingrowth on a tantalum cup. Indian J Orthop 42(3):275–278
26. Hanzlik JA, Day JS, Acknowledged Contributors: Ingrowth Retrieval Study Group (2003) Bone ingrowth in well-fixed retrieved porous tantalum implants. J Arthroplasty 28(6):922–927
27. Sambaziotis C, Lovy AJ, Koller KE et al (2012) Histologic retrieval analysis of a porous tantalum metal implant in an infected primary total knee arthroplasty. J Arthroplasty 27(7):1413.e5–1413.e9
28. Gruen TA, Poggie RA, Lewallen DG, Hanssen AD, Lewis RJ, O'Keefe TJ et al (2005) Radiographic evaluation of a monoblock acetabular component: a multicenter study with 2- to 5-year results. J Arthroplasty 20:369–378; Tanzer M, Bobyn JD, Krygier JJ, Karabasz D (2008) Histopathologic retrieval analysis of clinically failed porous tantalum osteonecrosis implants. J Bone Joint Surg Am 90(6):1282–1289
29. Breer S, Hahn M, Kendoff D et al (2012) Histological ex vivo analysis of retrieved human tantalum augmentations. Int Orthop 36(11):2269–2274; Komarasamy B, Vadivelu R, Bruce A, Kershaw C, Davison J (2006) Clinical and radiological outcome following total hip arthroplasty with an uncemented trabecular metal monoblock acetabular cup. Acta Orthop Belg 72:320–325
30. Bargiotas K, Konstantinos M, Karachalios T, Hantes M, Varitimidis SE (2005) Total hip arthroplasty using trabecular metal acetabular component: middle term results. Paper presented at the 72nd annual meeting of the American Academy of Orthopaedic Surgeons, Washington, DC, February 23–26, 2005
31. Macheras GA, Papagelopoulos PJ, Kateros K, Kostakos AT, Baltas D, Karachalios TS (2006) Radiological evaluation of the metal-bone interface of a porous tantalum monoblock acetabular component. J Bone Joint Surg (Br) 88:304–309

32. Mulier M, Rys B, Moke L (2006) Hedrocel trabecular metal monoblock acetabular cups: midterm results. Acta Orthop Belg 72:326–331
33. Lewis RJ, O'Keefe TJ, Unger AS (2003) A monoblock trabecular metal acetabulum; two- to five-year results. Paper presented at annual meeting of the American Academy of Orthopaedic Surgeons, Dallas, TX, February 5–8, 2003
34. Moen TC, Ghate R, Salaz N, Ghodasra J, Stulberg SD (2011) A monoblock porous tantalum acetabular cup has no osteolysis on CT at 10 years. Clin Orthop Relat Res 469(2):382–386
35. Meneghini RM, Ford KS, McCollough CH, Hanssen AD, Lewallen DG (2010) Bone remodeling around porous metal cementless acetabular components. J Arthroplasty 25(5):741–747
36. Noiseux NO, Long WJ, Mabry TM, Hanssen AD, Lewallen DG (2013) Uncemented porous tantalum acetabular components: early follow-up and failures in 613 primary total hip arthroplasties. J Arthroplasty 29(3):617–620
37. Macheras GA, Kateros K, Koutsostathis SD et al (2010) The Trabecular Metal monoblock acetabular component in patients with high congenital hip dislocation: a prospective study. J Bone Joint Surg (Br) 92(5):624–628
38. Rose PS, Halasy M, Trousdale RT (2006) Preliminary results of tantalum acetabular components for THA after pelvic radiation. Clin Orthop Relat Res 453:195–198
39. Goodman S, Sastamoinen H, Shasha N, Gross A (2004) Complications of ilio-ischial reconstruction rings in revision total hip arthroplasty. J Arthroplasty 19:436–446
40. Joshi AB, Lee J, Christensen C (2002) Results for a custom acetabular component for acetabular deficiency. J Arthroplasty 17:643–648
41. Shinar AA, Harris WH (1997) Bulk structural autogenous grafts and allografts for reconstruction of the acetabulum in total hip arthroplasty. Sixteen-year average follow-up. J Bone Joint Surg Am 79:159–168
42. Gross AE, Goodman S (2004) The current role of structural grafts and cages in revision arthroplasty of the hip. Clin Orthop Relat Res 429:193–200
43. Garbuz DS (2004) Revision total hip: a novel modular cementless acetabular system for reconstruction of severe acetabular bone loss. Oper Tech Orthop 14:117–120
44. Unger AS, Lewis RJ, Gruen T (2005) Evaluation of a porous tantalum uncemented acetabular cup in revision total hip arthroplasty: clinical and radiological results of 60 hips. J Arthroplasty 20:1002–1009
45. Mardones RM, Talac R, Hanssen AD, Lewallen DG (2005) Use of a porous tantalum revision shell in revision total hip arthroplasty. Paper presented at the 72nd annual meeting of the American Academy of Orthopaedic Surgeons, Washington, DC, February 23–26, 2005
46. Paprosky WG, O'Rourke M, Sporer SM (2005) The treatment of acetabular bone defects with an associated pelvic discontinuity. Clin Orthop Relat Res 441:216–220
47. Del Gaizo DJ, Kancherla V, Sporer SM, Paprosky WG (2012) Tantalum augments for Paprosky IIIA defects remain stable at midterm follow-up. Clin Orthop Relat Res 470(2):395–401
48. Nehme A, Lewallen DG, Hanssen AD (2004) Modular porous metal augments for treatment of severe acetabular bone loss during revision hip arthroplasty. Clin Orthop 429:201–208
49. Boscaines PJ, Kellet CF, Maury AC et al (2007) Management of periacetabular bone loss in revision hip arthroplasty. Clin Orthop Relat Res 465:159–165
50. Malkani AL, Price MR, Crawford CH 3rd, Baker DL (2009) Acetabular component revision using a porous tantalum biomaterial: a case series. J Arthroplasty 24(7):1068–1073
51. Davies JH, Laflamme GY, Delisle J, Fernandes J (2011) Trabecular metal used for major bone loss in acetabular hip revision. J Arthroplasty 26(8):1245–1250
52. Lachiewicz PF, Soileau ES (2010) Tantalum components in difficult acetabular revisions. Clin Orthop Relat Res 468(2):454–458
53. Sporer SM, Bottros JJ, Hulst JB, Kancherla VK, Moric M, Paprosky WG (2012) Acetabular distraction: an alternative for severe defects with chronic pelvic discontinuity? Clin Orthop Relat Res 470(11):3156–3163
54. Springer BD, Berry DJ, Cabanela ME, Hanssen AD, Lewallen DG (2005) Early postoperative transverse pelvic fracture: a new complication related to revision arthroplasty with an uncemented cup. J Bone Joint Surg Am 87(12):2626–2631

55. Kamath AF, Lee GC, Sheth NP et al (2011) Prospective results of uncemented tantalum monoblock tibia in total knee arthroplasty: minimum 5-year follow-up in patients younger than 55 years. J Arthroplasty 26(8):1390–1395
56. O'Keefe TJ, Winter S, Lewallen DG, Robertson DD, Poggie RA (2010) Clinical and radiographic evaluation of a monoblock tibial component. J Arthroplasty 25(5):785–792
57. Fernandez-Fairen M, Hernández-Vaquero D, Murcia A, Torres A, Llopis R (2013) Trabecular metal in total knee arthroplasty associated with higher knee scores: a randomized controlled trial. Clin Orthop Relat Res 471(11):3543–3553
58. Hayakawa K, Date H, Tsujimura S, Nojiri S, Yamada H, Nakagawa K (2013) Mid-term results of total knee arthroplasty with a porous tantalum monoblock tibial component. Knee 21(1):199–203
59. Niemeläinen M, Skyttä ET, Remes V, Mäkelä K, Eskelinen A (2013) Total knee arthroplasty with an uncemented trabecular metal tibial component: a registry-based analysis. J Arthroplasty 29(1):57–60
60. Unger AS, Duggan JP (2011) Midterm results of a porous tantalum monoblock tibia component clinical and radiographic results of 108 knees. J Arthroplasty 26(6):855–860
61. Minoda Y, Kobayashi A, Ikebuchi M, Iwaki H, Inori F, Nakamura H (2013) Porous Tantalum tibial component prevents periprosthetic loss of bone mineral density after total knee arthroplasty for five years – a matched cohort study. J Arthroplasty 28(10):1760–1764
62. Radnay CS, Scuderi GR (2006) Management of bone loss: augments, cones, offset stems. Clin Orthop Relat Res 446:83–92
63. Schmitz HC, Klauser W, Citak M, Al-Khateeb H, Gehrke T, Kendoff D (2013) Three-year follow up utilizing tantalum cones in revision total knee arthroplasty. J Arthroplasty 28(9):1556–1560
64. Lachiewicz PF, Bolognesi MP, Henderson RA, Soileau ES, Vail TP (2012) Can tantalum cones provide fixation in complex revision knee arthroplasty? Clin Orthop Relat Res 470(1):199–204
65. Howard JL, Kudera J, Lewallen DG, Hanssen AD (2011) Early results of the use of tantalum femoral cones for revision total knee arthroplasty. J Bone Joint Surg Am 93(5):478–484
66. Meneghini RM, Lewallen DG, Hanssen AD (2009) Use of porous tantalum metaphyseal cones for severe tibial bone loss during revision total knee replacement. Surgical technique. J Bone Joint Surg Am 91(Suppl 2 Pt 1):131–138
67. Ries MD, Cabalo A, Bozic KJ, Anderson M (2006) Porous tantalum patellar augmentation: the importance of residual bone stock. Clin Orthop Relat Res 452:166–170
68. Nelson CL, Lonner JH, Lahiji A, Kim J, Lotke PA (2003) Use of trabecular metal patella for marked patella bone loss during revision total knee arthroplasty. J Arthroplasty 181(7 Suppl 1):37–41
69. Nasser S, Poggie RA (2004) Revision and salvage patellar arthroplasty using a porous tantalum implant. J Arthroplasty 19(5):562–572
70. Kamath AF, Gee AO, Nelson CL, Garino JP, Lotke PA, Lee GC (2012) Porous tantalum patellar components in revision total knee arthroplasty minimum 5-year follow-up. J Arthroplasty 27(1):82–87
71. Chalkin B, Minter J (2005) Limb salvage and abductor reattachment using a custom prosthesis with porous tantalum components. J Arthroplasty 20:127–130
72. Khan FA, Rose PS, Yanagisawa M, Lewallen DG, Sim FH (2012) Surgical technique: porous tantalum reconstruction for destructive non-primary periacetabular tumors. Clin Orthop Relat Res 470(2):594–601
73. Holt GE, Christie MJ, Schwartz HS (2009) Trabecular metal endoprosthetic limb salvage reconstruction of the lower limb. J Arthroplasty 24(7):1079–1085
74. Guo X, Chen M, Feng W (2011) Electrostatic self-assembly of multilayer copolymeric membranes on the surface of porous tantalum implants for sustained release of doxorubicin. Int J Nanomedicine 6:3057–3064
75. Joglekar SB, Rose PS, Lewallen DG, Sim FH (2012) Tantalum acetabular cups provide secure fixation in THA after pelvic irradiation at minimum 5-year follow-up. Clin Orthop Relat Res 470(2):594–601

76. Zou X, Li H, Teng X, Xue Q, Egund N, Lind M, Bünger C (2005) Pedicle screw fixation enhances anterior lumbar interbody fusion with porous tantalum cages: an experimental study in pigs. Spine 30(14):E392–E399
77. Fernández-Fairen M, Murcia A, Torres A, Hernández-Vaquero D, Menzie AM (2012) Is anterior cervical fusion with a porous tantalum implant a cost-effective method to treat cervical disc disease with radiculopathy? Spine 37(20):1734–1741
78. Kasliwal MK, Baskin DS, Traynelis VC (2013) Failure of porous tantalum cervical interbody fusion devices: two-year results from a prospective, randomized, multicenter clinical study. J Spinal Disord Tech 26(5):239–245
79. Veillette CJ, Mehdian H, Schemitsch EH, McKee MD (2006) Survivorship analysis and radiographic outcome following tantalum rod insertion for osteonecrosis of the femoral head. J Bone Joint Surg Am 88(Suppl 3):48–55
80. Zhang Y, Li L, Shi ZJ, Wang J, Li ZH (2013) Porous tantalum rod implant is an effective and safe choice for early-stage femoral head necrosis: a meta-analysis of clinical trials. Eur J Orthop Surg Traumatol 23(2):211–217
81. Frigg A, Dougall H, Boyd S, Nigg B (2010) Can porous tantalum be used to achieve ankle and subtalar arthrodesis? A pilot study. Clin Orthop Relat Res 468(1):209–216
82. Sagherian BH, Claridge RJ (2012) Porous tantalum as a structural graft in foot and ankle surgery. Foot Ankle Int 33(3):179–189
83. Gordon WJ, Conzemius MG, Birdsall E, Wannemuehler Y, Mallapragada S, Lewallen DG et al (2005) Chondroconductive potential of tantalum trabecular metal. J Biomed Mater Res B Appl Biomater 75:229–233

Chapter 11
Niobium Biomaterials

Barry O'Brien

Abstract Niobium is a particularly attractive metal for application as a biomaterial, due to the highly inert and unreactive nature of its surface. However, mechanical property limitations have restricted the use of the material in this field. This chapter initially reviews some of the fundamental aspects of niobium biocompatibility with a particular emphasis on surface technologies such as vapour deposition, sol-gel, anodizing and boronizing. Recent and ongoing activities aimed at improving bulk mechanical performance are also reviewed. These include approaches such as severe plastic deformation to refine grain structures and the development of new alloys. Where appropriate, data that demonstrates biocompatibility of these new niobium surfaces is also presented. Thus while niobium alloys have seen limited application to date, this chapter presents an overview showing the great potential for this material and the ongoing efforts in this regard.

Keywords Niobium alloy • Niobium oxide • Corrosion resistance • Ultrafine grain • Cardiovascular stent • Fatigue resistance

11.1 Introduction

Niobium offers great potential as an implantable metallic biomaterial due to its excellent corrosion resistance and associated biocompatibility. However, to date this potential has not been fully realized primarily because the mechanical properties of niobium, such as strength and fatigue resistance, do not meet the requirements of many device applications. By way of illustration, Table 11.1 shows the tensile properties of both pure Nb and Nb-1Zr in comparison with some traditional implant materials.

The potential for development of further higher-strength alloys is however also well demonstrated in Table 11.1 simply by comparing the superior tensile properties

B. O'Brien (✉)
Biomedical Engineering, School of Engineering and Informatics,
National University of Ireland Galway, Galway, Ireland
e-mail: barry.obrien@nuigalway.ie

M. Niinomi et al. (eds.), *Advances in Metallic Biomaterials*, Springer Series
in Biomaterials Science and Engineering 3, DOI 10.1007/978-3-662-46836-4_11

Table 11.1 Mechanical properties of selected metallic biomaterials including niobium

Material	Tensile strength (MPa)	0.2 % Yield strength (MPa)	Elongation (%)	Elastic modulus (GPa)	Reference
316L	595	275	60	193	[1]
Nb	195	105	25	103	[2]
Nb-1Zr	241	138	20	68.9	[3]
Ti	240–331	170–241	30	102.7	[3]
Ti-6Al-4V	900–993	830–924	14	113.8	[3]

of Nb-1Zr against pure Nb, in this instance the zirconium providing a precipitation strengthening and solid solution strengthening effect. Aside from pure Nb and Nb-1Zr, there are very few commercial niobium materials available; product forms, material specifications and availability of all niobium materials have primarily been influenced by the nuclear and aerospace industries where the corrosion resistance and high temperature performance of the material have been advantageous. A higher-strength Nb-10Hf-1Ti-0.5Zr (commercially known as Alloy C103) was also developed, specifically for the Apollo space program [4], but high costs and commercial restrictions on availability have seen limited access and application development for this material. Despite these challenges, an increasing awareness of the biocompatibility of niobium has seen several positive advances in recent years. This chapter reviews some of the fundamental studies that have increasingly demonstrated the biocompatibility aspects of niobium surfaces. In addition, some of the main developments aimed at improving specific features of mechanical performance are also described.

11.2 Biocompatibility of Niobium

It is widely recognized that the stability of the oxide layer on any metal surface is a good indicator of biocompatibility; in this regard, niobium very readily forms a stable and protective oxide layer. In this context, stability does not simply refer to the absence of corrosion, but also relates to the electrochemical properties of the surface and the nature of current flow between an implant surface and its environment. Early work by Zitter and Plenk [5] studied the relative merits of a number of metallic implant materials, including niobium, by measuring surface current densities under a range of in vitro test conditions. Niobium consistently demonstrated lower current densities than stainless steel, cobalt-chromium and gold, and the authors cite this behaviour as being fundamental to the biocompatibility of the material; the niobium had a performance comparable to pure titanium. This comparability between titanium and niobium has also been demonstrated in vivo by Johansson and Albrektsson [6] for an orthopaedic application. Screw-shaped components of both materials were implanted into the femur and tibia of rabbits. At 3-month follow-up, the removal torque for the niobium components was superior to

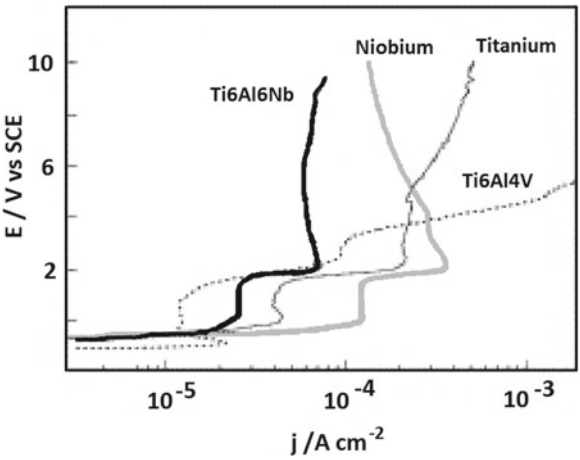

Fig. 11.1 Polarization diagrams for Ti-6Al-4V, Ti-6Al-6Nb, niobium and titanium rotating disc electrodes recorded in HBSS (pH 6.9, $T = 37$ °C) in the potential range −1.4 and 10 V (Reprinted with permission from Ref. [8]. Copyright 2003 by Elsevier)

the titanium components, indicating a good integration of the device within the surrounding bone tissue. While surface roughness was also acknowledged to be influencing this outcome, the histological studies did support the finding with similar levels of bone-to-metal contact observed for both materials. Matsuno et al. [7] have further demonstrated the biocompatibility of niobium in orthopaedic hard tissue environments, as well as in soft subcutaneous tissue. Small wire components, made from niobium, titanium and other refractory metals, were implanted into both the femur and abdominal subcutaneous tissue of Wistar rats. At 4 weeks, newly formed bone was demonstrated on histological sections – the level of osteogenesis on niobium was similar to the titanium. Elemental mapping techniques were also utilized, demonstrating that niobium had not diffused into the surrounding bone tissue. The outcomes of the soft tissue implants were also positive with the components being encapsulated within a thin layer of fibrous connective tissue at 4 weeks, with no inflammatory responses observed.

The electrochemical basis for the performance of niobium has also been demonstrated by Metikoš-Huković et al. [8] with niobium surfaces showing a high resistance to oxide film breakdown in physiological solutions, exhibiting passive behaviour up to 10 V, compared to Ti-6Al-4V which showed film breakdown at 4 V. This is illustrated in Fig. 11.1. Interestingly, this study also showed that the beneficial effects of niobium can be seen even when it is present only as an alloying addition within a material; Ti-6Al-6Nb performed superior to pure titanium and Ti-6Al-4V, and this has been attributed to a reduction in the amount of electronic defects in the oxide due to the presence of niobium. Consistent with these electrochemical findings, Rogers et al. [9] have also shown in vitro advantages of Ti-6Al-7Nb over Ti-6Al-4V. Clinically relevant orthopaedic wear debris was created from both metals, added to human monocyte cell cultures and tested for inflammatory mediators after 48 h. A higher inflammatory response was detected for the Ti-6Al-4V compared to the Ti-6Al-7Nb, and it is proposed that this could contribute to lower bone resorption for devices made from the niobium-containing

material. The superior performance of Ti-6Al-7Nb is attributed to the better corrosion resistance of this material.

In addition to the early in vivo and electrochemical work, the exceptional biocompatibility of pure niobium has also been demonstrated in vitro, by Eisenbarth et al. [10], using cell lines applicable to both orthopaedic and vascular applications. Niobium was compared to a number of metals, including pure titanium, using murine skull osteoblast-like cells and bovine aortic endothelial cells. Proliferation, mitochondrial activity, cell volume and morphology of both cell lines were assessed after 7 days in contact with the metal surfaces. Niobium performed better than titanium in terms of proliferation and mitochondrial activity, while both metals were similar in relation to cell volume and morphology changes.

11.3 Niobium-Based Coatings and Surface Modifications

11.3.1 Sol-Gel Deposition

With the increasing recognition of the excellent biocompatibility of niobium surfaces, and in particular niobium oxides, there have been a number of advances relating to deposition of niobium-based coatings onto substrates with more acceptable mechanical properties, i.e. stainless steel and titanium materials. Eisenbarth et al. [11] have used a sol-gel process to deposit a niobium oxide (Nb_2O_5) layer onto pure titanium surfaces. The sol was first created using a mixture of niobium(V) ethoxide precursor, a solvent and chelating agent. The substrates were then spin coated and dried, with multiple cycles used to build up the layer thickness to 100 nm. Following drying at 400 °C to remove organic residuals, the samples were given calcination heat treatments in the range 450–700 °C. Different temperatures and times provided oxides with structures ranging from amorphous to crystalline and with surface roughness values (Ra) from 7 to 40 nm, respectively. A range of cell tests were then performed, using murine skull osteoblast-like cells; these tests included cell migration, cell spreading and cell adhesion. Cells showed better migration and adhesion behaviour on the smoother surfaces, with cell spreading being optimum at intermediate roughness levels. This study also explored collagen synthesis by the cells; collagen I synthesis is an essential prerequisite for the bone remodelling process, with the subsequent mineralization of these collagen fibres leading to newly formed bone around an implant. Higher levels of collagen synthesis were observed on the intermediate and roughest surfaces compared to the smooth surface. While this work further demonstrates the potential for niobium surfaces, it also shows that in the case of such a sol-gel process, there is significant scope for tuning of the response.

The use of sol-gel technology to apply niobium oxide (Nb_2O_5) coatings to titanium has similarly been explored by Ochsenbein et al. [12], in a study that also assessed TiO_2, SiO_2 and combined TiO_2-SiO_2. The niobium oxide was created using a niobium(V) ethoxide precursor with acetylacetone as a solvent. The sol

was deposited onto the titanium substrate by spin coating; after drying, the deposit was heat treated at 450 °C. The Nb_2O_5 film produced was amorphous and porous in nature, with a thickness of 130 nm. No detectable process residues were identified in the coating; this will be a key aspect for such sol-gel technologies when considered from a quality assurance and regulatory approval perspective, i.e. being able to demonstrate that such chemical processes do not leave harmful residues. The osseointegration behaviour of these coatings was assessed using disc samples seeded with osteoblasts and incubated for up to 6 days. Proliferation, cell vitality, cell spreading and adhesion were all highly acceptable for the niobium oxide, though it was noted in this instance that higher levels of roughness on niobium oxide can reduce the level of proliferation and spreading. This again demonstrates the importance of being able to tune the biological response through coating design and process controls.

The ability to deposit niobium oxide coatings by sol-gel onto 316L stainless steel has been demonstrated by Nagarajan et al. [13], with the desire to create textured porous surfaces to enhance the formation of a bone-like apatite layer on implants. In this instance, niobium butoxide, ethanol and polyethylene glycol were used as the precursors. Following a dip coating and drying process, the samples were heat treated at 500 °C for 1 h. This study did not include biocompatibility evaluations, with FTIR used to confirm the presence of Nb_2O_5 and corrosion tests demonstrating that the deposit is providing a complete barrier between the physiological environment and the 316L substrate. This ability to completely seal the substrate from the environment will be another key issue for developing practical devices and applications from these technologies. Substrate ion release could impair the benefit being conferred by the niobium oxide and could also lead to issues with substrate corrosion and coating delamination.

11.3.2 Sputter Deposition and Ion Implantation

Coatings deposited by physical vapour deposition (PVD) techniques would invariably be expected to have higher density and lower porosity than those applied by chemical or electrochemical processes. Therefore, in the context of minimizing pathways between the physiological environment and the substrate metal (with lower biocompatibility than niobium), PVD techniques are also being explored for applying niobium oxide to metals such as stainless steel and titanium. Ramirez et al. [14] describe a magnetron sputtering technique for deposition of 200-nm niobium oxide coatings onto 316L stainless steel substrates. Oxygen was used as the reactive gas constituent in the argon plasma, with oxygen levels kept high enough to ensure Nb_2O_5 formation, rather than NbO or NbO_2; the oxides with lower oxygen contents were conductive and semiconducting and therefore potentially undesirable in terms of characteristics for corrosion resistance and biocompatibility. Coatings were verified to be amorphous, based on x-ray diffraction (XRD) data, while potentiodynamic polarization testing was used to assess the corrosion performance.

Oxide-coated samples showed improved corrosion resistance compared to 316L stainless steel, while it was also possible to identify how process conditions, including oxygen content, influenced corrosion resistance. (There is little data to support whether amorphous or crystalline niobium oxides are best from a biocompatibility perspective. In any event, other characteristics such as thickness, topography and porosity are all likely to change as structures shift from amorphous to crystalline, making isolation of crystallinity effects somewhat redundant. Work by Lai et al. [15], on magnetron-sputtered niobium oxides, has shown deposits to be amorphous below 2,010 nm and crystalline above this threshold.)

Further work by Ramirez et al. has taken these niobium oxide surfaces through to a range of in vitro biocompatibility evaluations, with a view to dental applications [16]. In this instance, the objective was to explore lower-cost dental implant materials and designs, i.e. to assess if niobium oxide-coated stainless steel components could compete with titanium. In addition, niobium nitride (NbN) coatings were also prepared – these nitride coatings would be expected to give high hardness and wear resistance [17] and may therefore also be candidates for dental applications. The niobium nitride coatings were also prepared by unbalanced magnetron sputtering, using nitrogen gas as the reactive constituent; deposits of 200 nm were again explored. The biocompatibility evaluations of both coatings were performed using cells derived from a human cementoblastoma. Cementoblasts promote formation of cementum around the teeth roots, which creates anchorage between the teeth and the alveolar bone. Cell adhesion, viability and proliferation were assessed after seeding of cells onto the test surfaces. The niobium nitride showed better adhesion than the niobium oxide, with the Ti-6Al-4V control being better than both. However, cell viability data showed that both coatings are not toxic for human cementoblast cells, while the proliferation data for both was comparable to that of the Ti-6Al-4V, with the niobium nitride slightly better than the niobium oxide. Overall, the investigators propose that both niobium-based coatings are likely to promote cementoblast differentiation and subsequent cementum formation. It is noted that the nitride coatings are crystalline while the oxide coatings are amorphous. Though as indicated earlier, there is not enough evidence to reliably identify if crystalline or amorphous surfaces would ideally be best; these various studies are showing positive outcomes for both, while factors such as inherent porosity, topography and mechanical integrity are likely to be much more significant in the overall performance. This is illustrated in the outcomes of a related study by Rojas and Rodil [18] where amorphous niobium oxide coatings were also created on 316L stainless steel using magnetron sputtering. In this instance, corrosion performance was impaired by coating delamination during immersion in NaCl test solutions. This is attributed to an open porous pathway through the coating, allowing the physiological solution to corrode the substrate, with corrosion product forcing delamination. Such reactions and performance would significantly disrupt overall biocompatibility. Thus even for PVD coatings, physical characteristics such as porosity and topography are likely to be more important in the overall biocompatibility context rather than the degree of crystallinity alone, and just like the sol-gel technology, process understanding and control are key to optimizing coating design.

The use of niobium nitride coatings has also been explored by Park et al. [19] for extending the lifetime of metal-on-polymer artificial joints, by application of the nitride to the metal component. Nitrogen ions were first implanted into the surface of the Co-Cr-Mo alloy to a depth of approx 60 nm using a plasma immersion ion implantation process. This created chromium nitrides (CrN and Cr_2N) which contributed to initial surface hardening of the Co-Cr-Mo. The plasma system was then used for deposition of a 600-nm niobium nitride film, using a niobium sputtering target and an argon-nitrogen gas mixture. Wear tests were performed using a pin-on-disc arrangement in distilled water; processed test samples were used as the disc and ultrahigh molecular weight polyethylene (UHMWPE) as the pin. The test data shows that the niobium nitride coating reduces wear of the UHMWPE significantly compared to untreated Co-Cr-Mo. Addition of the nitrogen ion implantation step before application of the coating gives further reductions in wear. Given the in vitro biocompatibility work reported by Ramirez et al. on niobium nitride and the mechanical performance reported here by Park et al., it will be interesting to see if this coating can be progressed next to in vivo preclinical evaluations.

Magnetron sputtering has also been used for deposition of niobium carbide coatings, with exploration of different carbon to niobium ratios [20]. The coatings were applied to Ti-6Al-4V substrates, with methane (CH_4) added to the argon as the source of carbon. The mass flow ratio of methane and argon was adjusted to control the carbon content. XPS evaluations showed that the carbon to niobium ratio values were in the range of 0.7–1.9, with nonstoichiometric NbC phases present. The coatings were primarily crystalline in nature, though at the highest C:Nb ratio (1.9), these crystalline structures coexisted with an amorphous carbon phase. Corrosion testing showed that while all coatings exhibited improved corrosion behaviour compared to Ti-6Al-4V, the composite structure with the amorphous carbon phase performed best; this structure also had the lowest porosity, again pointing to the importance of such physical characteristics. Biocompatibility was evaluated using osteoblasts (derived from a human osteosarcoma) for cell viability tests, after contact with the test surfaces for 5 days. There was no significant difference between the various niobium carbides and the Ti-6Al-4V, but the coating with the highest C:Nb ratio was showing the highest cell viability. While it is difficult to compare these carbide coatings directly with the oxides or nitrides, these initial results nevertheless show significant merit.

Coatings of pure niobium (not oxides, nitrides or carbides) have also been applied to 316L stainless steel using the same unbalanced magnetron sputtering techniques, and these have been evaluated for both corrosion performance and biocompatibility [21]. In this instance, cell culture evaluations have been performed using osteoblasts derived from human alveolar bone. Cell adhesion, viability, proliferation and morphology were assessed after seeding onto the niobium-coated samples and 316L stainless steel controls. The niobium-coated surfaces performed superior to the stainless steel in all evaluations. The morphology evaluation is more qualitative in nature but shows that the actin cytoskeleton organization occurs faster and more efficiently on the niobium compared to the stainless steel. The niobium promotes extension of the cell projections compared

to the stainless steel where the osteoblasts retained a more rounded appearance. While pure niobium surfaces are not likely to be as hard as oxides, nitrides or carbides, these pure metal surfaces still probably have some degree of niobium oxide present and in this condition will confer sufficient biocompatibility and hardness for some applications.

Implantation of niobium into the surface of nitinol (NiTi) has been explored by Zhao et al. [22] primarily to assess the impact it may have on corrosion performance of the NiTi. Samples of NiTi were first argon ion sputtered to clean the surface, and then the Nb ion implantation was performed using a metal vapour vacuum arc plasma source. Based on Auger electron spectroscopy (AES) and X-ray photoelectron spectroscopy (XPS) analysis, it is interpreted that a composite Nb_2O_5/TiO_2 film of approximately 30-nm thickness forms during the implantation process; nickel surface concentration is reduced. It is noted that the implantation process roughens the surface. Corrosion data, as determined by potentiodynamic polarization, show that the Nb-implanted NiTi has a higher breakdown potential (>1,000 mV) compared to the untreated NiTi (420 mV). In addition the Nb-NiTi exhibits lower corrosion current density as shown in Fig. 11.2. Overall, it would be expected that these improvements in corrosion performance should also lead to improved biocompatibility. In terms of the functional performance of the NiTi, further evaluations would also be needed to verify if the shape memory or superelastic response has been affected – at a scale relevant to practical medical devices. This is particularly important as this study showed that some softening and modulus reduction was observed beyond the depth of the implanted niobium ions.

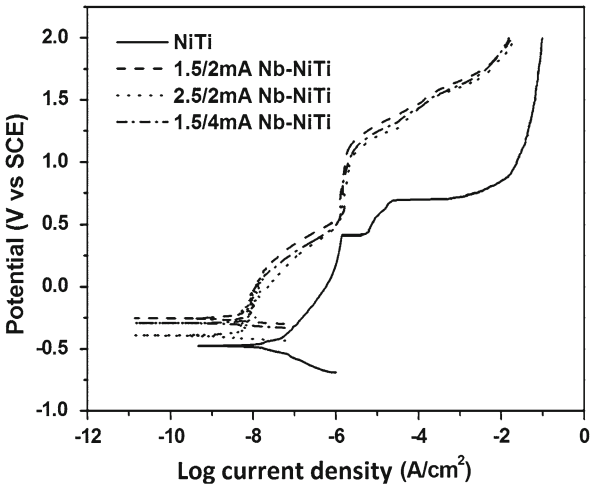

Fig. 11.2 Potentiodynamic anodic polarization curves for untreated NiTi and ion-implanted samples (Reprinted with permission from Ref. [22]. Copyright 2011 by Elsevier)

11.3.3 Alkali Treatment for Apatite Formation

The low elastic modulus of niobium makes it particularly attractive in terms of the potential for reducing stress shielding effects in large load-bearing implants. While the compatibility of pure niobium with bone formation and integration processes is already described, efforts to enhance this have also been explored through surface modifications that enhance the creation of bone-like apatite layers in the physiological environment. Goldley et al. [23] report on the formation of apatite structures on pure niobium in simulated body fluid (SBF), after pretreatment in alkaline solutions. Samples were soaked in NaOH solutions of different concentrations and at different temperatures for 24 h. A treatment using 0.5 M NaOH at 25 °C for 24 h produced well-adhered porous surface structures, with an average pore size of around 100 nm. Based on AES and EDS data, the investigators interpret this porous layer to be a sodium niobate hydrogel. After soaking the NaOH-treated samples in SBF for 6 days, a layer of spherical grains is observed to form. Calcium, phosphorus and oxygen are detected in this structure, indicating the layer to be calcium phosphate – the morphology is similar to calcium phosphate layers formed on titanium and titanium alloys. Below the calcium phosphate, an intermediate layer containing calcium, niobium and oxygen is observed, and this is deemed to be calcium niobate – comparable calcium titanate layers are reported for titanium surfaces. The calcium phosphate layer is identified to be amorphous, and in this regard it is similar to the initial calcium phosphate deposits that precipitate during the formation and maturing of natural bone apatite. It is therefore possible that such NaOH treatments could further enhance the suitability of niobium for orthopaedic implant applications.

Wang et al. [24] have explored a variation of the alkali treatment step. Pure niobium samples were immersed in 0.5 M NaOH and heated to 60 and 80 °C, in a sealed container, for 24 h. After washing, the samples were vacuum heat treated for 1 h at 600 °C. The treated surface exhibited a porous fibre-like structure with smaller diameters (50–100 nm) obtained at 80 °C than at 60 °C. This structure was identified to be crystalline sodium niobate ($NaNbO_3$). After immersion in SBF for 3 weeks at 37 °C, a dense globular-like film had deposited on the surface; the 80 °C treatment provided better coverage than the 60 °C treatment. Control surfaces, without alkali treatment, exhibited no apatite formation. While not described specifically in this study, it is likely that the 600 °C treatment should enhance adhesion of the apatite layer to the substrate. Similar treatments and approaches are already developed for titanium alloys [25], though much more work will be needed for niobium to understand adhesion and durability aspects in the context of in vivo device deformations and deformations/damage during implantation.

11.3.4 Anodic Oxidation of Niobium

Anodic oxidation has been explored for creating porous structures on a range of metals with the objective of increasing surface area, in applications such as sensors, catalysts and capacitors. In relation to medical devices, the approach is of interest to

create surfaces and reservoirs for attachment of drugs or biological structures, to promote tissue integration [26] and to potentially improve surface hardness (scratch resistance) and corrosion performance. As niobium also has application across a number of sectors, it is noted that much of the applicable research into anodic oxidation is coming from other industries and not just from the biomedical field; fundamentally, this research is still of high significance to medical device applications. Sieber et al. [27] describe a process for anodic oxidation of pure niobium in sulphuric acid (H_2SO_4), resulting in the formation of a highly ordered porous niobium oxide structure. The 1-M H_2SO_4 solution contained small quantities (0.5–2.0 wt%) of hydrofluoric acid (HF), and all anodization treatments were performed at room temperature. Samples were anodized at 20 V (relative to the mercury sulphate electrode) for different durations. Porous structures were obtained for a wide range of process conditions with, for example, pores of approximately 20–30 nm obtained at 20 V for 30 min with 0.5 % wt HF as illustrated in Fig. 11.3. Thickness typically increases with anodizing duration and also depends on HF concentration; values in the range of 100–500 nm were recorded. The films were confirmed to be Nb_2O_5.

Karlinsey [28] has also explored anodization of niobium, but in this instance using HF solutions (0.25–2.5 wt%), without H_2SO_4. A wide range of voltages, temperatures and durations were examined, with unusual conical-shaped niobium oxide structures formed under various conditions. The structures are relatively large with cone base diameters in the range 5–20 μm; though the growth process is such that sharp, well-defined tips with nanometre resolution are obtained. Higher voltages lead to a higher density of the conical structures on the surface. While no mechanical or in vitro testing is reported, such structures could also be interesting for modifying cell responses or for attaching of drugs or biologics – similar to the tubular porous structures already described.

An interesting anodization process from the electrical capacitors industry, which creates another unusual morphology, is described by Störmer et al. [29]. Using powder metal technologies, pure niobium powder is pressed and then vacuum sintered giving a porous, sponge-like structure. Samples were then anodized in a two-stage process, an initial galvanostatic step with constant current flow, followed by a potentiostatic step at 40 V. The process was carried out in a 1 mass% aqueous solution of phosphoric acid at 65 °C. After anodizing, samples were annealed at temperatures up to 320 °C. While this study naturally focuses on the electrical characteristics (and the annealing step in particular is a key aspect in that regard), the microstructure obtained could have biomedical applications; the sponge-like structure of niobium is surrounded by an amorphous layer of niobium oxide (Nb_2O_5). Thus from a cell and tissue integration perspective, it is potentially a biocompatible porous construct but with integrity and strength provided by the niobium substrate.

In a manner comparable with the sol-gel and sputtering techniques already described, the use of anodization to create niobium oxides on metallic substrates, other than niobium, has also been explored. This can be achieved by first applying a thin layer of niobium to the substrate as described by Mackey et al. [30] in the case of titanium dental implant screws. In this instance, a 5-μm coating of niobium was sputter deposited onto sand-blasted titanium screws. These components were then

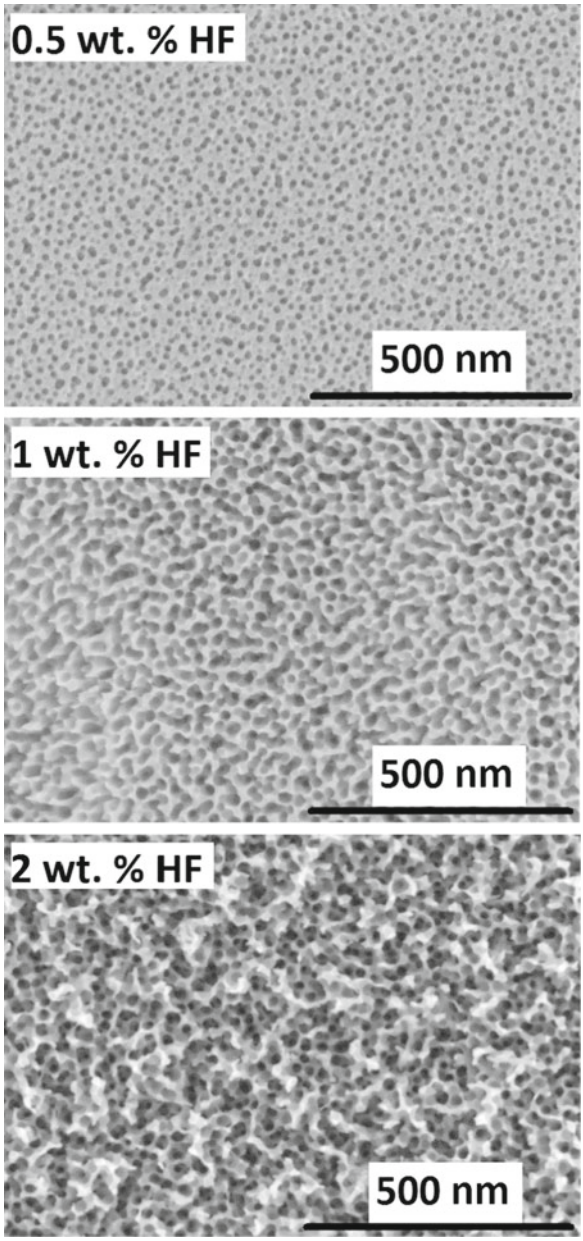

Fig. 11.3 SEM images of porous niobium oxide layers formed in 1 M H_2SO_4 with different concentrations of HF after 30-min polarization at 20 V (Reprinted with permission from Ref. [27]. Copyright 2004 by Elsevier)

anodized using the HF solution methods of Karlinsey (reviewed earlier). Careful process optimization was needed, balancing between promotion of niobium oxide growth and delamination of the niobium interlayer from the substrate; an anodizing duration of 1 h, with a 0.1 wt% HF solution, provided an optimum balance, resulting in a surface considered suitable for in vivo evaluations in the next phase of the work.

11.3.5 Boronizing of Niobium

Boronizing has been widely used for improving the hardness and wear resistance of many metallic materials; diffusion of boron atoms into the surface allows for the formation of hard boride phases. Usta [31] has investigated the process for pure niobium, with the aim of increasing surface hardness. The process was performed by surrounding the test samples in commercial boronizing powder (90 % SiC, 5 % B_4C and 5 % KBF_4) and soaking at 940 °C for durations of up to 8 h. The thickness of the boride layer formed was directly proportional to the soak duration, with the 8-h treatment resulting in a 22-μm boride layer. This layer consisted primarily of NbB_2 with a Vickers hardness (50 g) of 2,500 HV – this compares to a hardness of 110 HV for the niobium substrate itself. An intermediate layer also existed between the substrate and boride layer; this had a hardness of 670 HV with this increase in hardness being attributed to solid solution strengthening by the boron. These coatings have been evaluated for friction and wear performance in a subsequent study by Ribeiro et al. [32]. The tribological tests were carried out with a reciprocal pin-on-disc tribometer under dry conditions and also with simulated body fluid (SBF). The data shows a favourable outcome in SBF, with a coefficient of friction at 0.2 compared to 0.6 for the dry conditions. Less wear debris was also generated when tested with SBF. While this is a promising surface technology, with potential for orthopaedic wear-resistant applications, more work will be needed to evaluate this performance in comparison to requirements for specific targeted applications and to establish biocompatibility responses. A separate study by Dokumaci et al. [33] does however demonstrate that niobium boride surfaces have good oxidation and degradation resistance – this is at least a good starting position with regard to potential in vivo behaviour.

11.4 Strengthening of Niobium

The biocompatibility of niobium and niobium surfaces is now well demonstrated; however, as indicated, the mechanical performance of conventional niobium materials does not typically meet the expectations for implantable medical devices. Materials such as pure Nb and Nb-1Zr have relatively low yield strength and ultimate tensile strength, and this typically also translates to poor fatigue properties. Failure of a medical device is more likely to be due to fatigue than due to tensile yielding or overload. Papakyriacou et al. [34] report on the high-cycle fatigue behaviour of cold-worked pure niobium compared to tantalum, titanium and Ti-6Al-7Nb. Tests were performed in both ground and shot-peened surface conditions and in both ambient air and physiological saline; the niobium performed worse than the other materials in all surface and test configurations. For example, the mean endurance limit for shot-peened Ti-6Al-7Nb in saline was 560 ± 40 MPa, while for shot-peened pure Nb in saline, it was 230 ± 20 MPa. Ground surfaces

typically resulted in lower values than shot-peened surfaces. Further data from Papakryriacou et al. [35] describes how strengthening through cold work does not substantially improve the fatigue performance compared to annealed Nb – particularly for high numbers of cycles with small stress amplitudes. In this context, it is therefore also appropriate that efforts to improve the strength and fatigue of niobium materials generally involve either grain refinement or alloying. These approaches are now further reviewed.

11.4.1 Ultrafine Grain Niobium

The benefit of fine grain structures for improving yield strength of metallic materials is widely recognized. A substantial effort has therefore been invested in recent years towards the development of very fine-grained niobium materials, in order to bring them closer to the strength requirements for medical implant applications. The main approach explored is that of severe plastic deformation (SPD), which is essentially a metalworking process that imparts exceptionally high strains on the component, leading to high dislocation densities which ultimately provide a fine network of high-angle grain boundaries. There are several SPD processes, but the most widely established is equal-channel angular pressing (ECAP), also known as equal-channel angular extrusion (ECAE) [36].

A key aspect of the process is that no significant change in the shape or dimensions occurs for the structure being processed, i.e. bar, rod or plate, etc. The process involves use of a die in which the extrusion channel bends through an abrupt angle. The sample is machined to fit into this channel and is then pressed through the die as illustrated in Fig. 11.4. The sample has the same cross-sectional dimensions before and after pressing, allowing repeated pressing, but the material goes through a significant shear strain as it passes through the plane where the entrance and exit channels meet. The level of strain depends on the angle between the two channels. Different slip systems can be introduced by rotating the workpiece about the x-axis between passes. Different rotation sequences allow for the introduction of varying shearing patterns into the material and therefore provide control of homogeneity, shape and size of the final refined grain structure. These processing routes are given designations that are widely accepted norms within the industry [37]. A sample that is pressed without rotation is identified as route A, while route B_A involves rotating the sample by 90° in alternate directions between passes. Route B_C involves rotation by 90° in the same direction between passes, while in Route C the sample is rotated by 180° between passes. These processing routes are illustrated in Fig. 11.5.

Niendorf et al. have done extensive investigations into the development of ECAE processes for niobium materials including assessment of mechanical, corrosion and biocompatibility performance of the fine-grained materials produced. Initial process development utilized the commercially available Nb-1Zr alloy in its standard ‘coarse-grained’ condition, with a relatively low yield strength of 220 MPa [38]. Samples 25 mm × 25 mm × 175 mm were machined from a 50-mm-thick hot-rolled

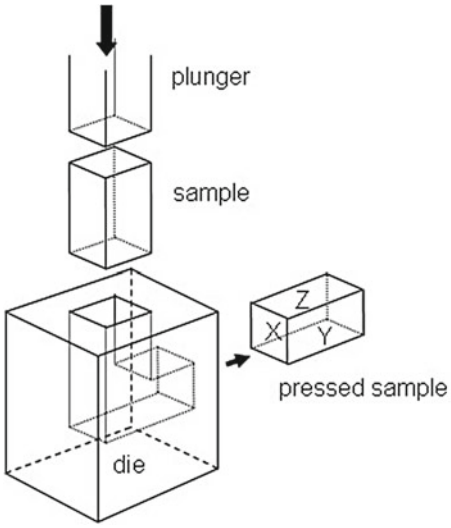

Fig. 11.4 The principle of ECAE processing (Reprinted with permission from Ref. [36]. Copyright 2007 by Elsevier)

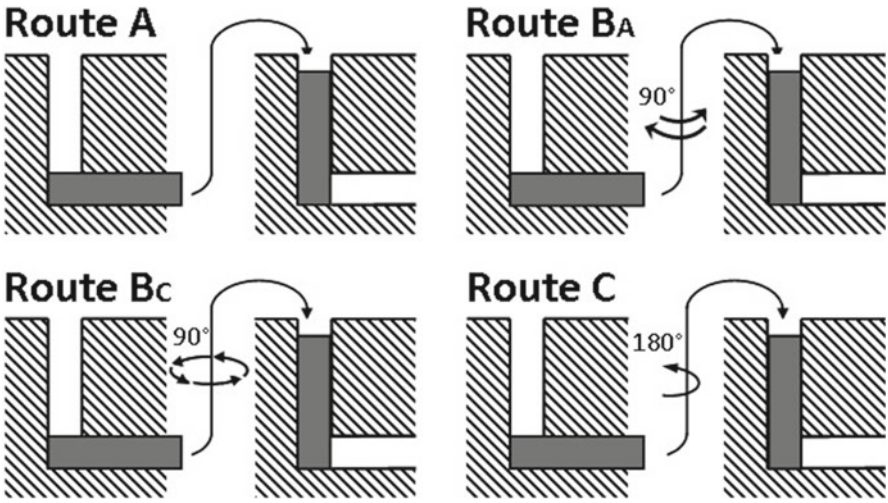

Fig. 11.5 The four basic processing routes of ECAE (Reprinted with permission from Ref. [37]. Copyright 2006 by Elsevier)

plate and then processed using an ECAE die with a 90° channel angle. The material was extruded using two of the ECAE routes, designated as $8B_C$ and 16E.

Route E is a combination of routes B_A and C that involves a rotation sequence of 180°/90°/180°; the prefix refers to the number of extrusion passes given to the material. Tensile data showed that the ECAE Nb-1Zr has over twice the strength of the unprocessed coarse-grained material. Importantly, this increase in strength is in

parallel with an increase in ductility; this is not always the case for many strengthening mechanisms, including ECAE processing of other materials. Microstructural investigations showed that the processed material has an equiaxed structure with grain sizes ranging between 250 and 500 nm. Conventional materials may have a grain size typically in the 5–100-μm range. These ultrafine-grained (UFG) Nb materials exhibited a high dislocation density within the grains and have a large proportion of high-angle grain boundaries compared to low-angle boundaries. A predominance of high-angle boundaries would be expected to provide a more stable microstructure (and mechanical performance) during cyclic plastic deformation, compared to low-angle boundaries where dislocation interaction could lead to boundary rearrangement. (It is also interesting to note that the classic Hall-Petch relationship between strength and grain size is demonstrated to be applicable to these ultrafine grain sizes, with a similar slope as for conventional niobium materials.) Low-cycle fatigue testing was also performed, describing significant advantages for UFG Nb over conventional UFG. Samples were also given a 1-h, 600 °C vacuum heat treatment before fatigue testing; this allowed some recovery, but no recrystallization, and produced a more stable structure with less damage accumulation and therefore a further improvement in fatigue life. In a related study of fatigue, Niendorf et al. [39] explored how creation of nanosized oxide particles, through heat treatment, could also enhance the performance of UFG niobium. Heat treating in air for 1 h, at nominally 600 °C, modifies the surface to a depth of approximately 80 μm; this layer develops a higher hardness due to the formation of zirconium oxide (ZrO_2) particles by an internal oxidation process. This phenomenon is not unique to UFG Nb-1Zr, but it is interesting to note that a finer precipitate (with a diameter of < 10 nm), with a higher hardening effect, is obtained for the UFG material compared to the precipitates (with a diameter of 50 nm) in the conventional coarse-grained Nb-1Zr. Strain-controlled fatigue testing of UFG material, with and without the oxidation treatment, demonstrated significantly longer fatigue life for the heat-treated samples, at strain amplitudes applicable to implantable device. It is proposed that the surface-hardened layer inhibits crack initiation, thereby prolonging the fatigue life.

The wear behaviour of this UFG Nb-Zr has also been assessed, particularly in relation to the added benefit of the internal oxidation step described [40]. Samples of Nb-2.3Zr were ECAE processed using the route E already described and then subjected to an internal oxidation treatment by heating in air at 560 °C for 6 h. In this instance, the coarse-grained unprocessed material had an average grain size of 25 μm, while the UFG material had an average diameter of 0.45 μm. Tensile data showed that the yield strength and ultimate tensile strength of the UFG material were approximately 60 % higher than the coarse-grained material, with only a very slight decrease in elongation to failure. The addition of the internal oxidation step caused a slight further increase in strength (contributed mainly by the strengthened surface layer) but with a drop in elongation to failure from 17 to 10 %. The hardened layer created by the oxidation is approximately 50 μm deep with a surface Vickers hardness of 830 HV (0.01 kgf) compared to a bulk hardness of approximately 200 HV (0.01 kgf). Wear tests were performed with a pin-on-disc tribometer arrangement; the niobium test samples were utilized as the pin with a sintered

alumina disc as the plate. The wear test results show that there is little difference between the (weight loss) performance of the conventional and UFG materials; strengthening by ECAE grain refinement therefore does not improve wear resistance. This is attributed to a continuous removal and reformation of the passivating layer due to the high affinity of freshly exposed niobium to oxygen. However, the wear resistance of the UFG was significantly improved after the internal oxidation treatment. This is a result of the adherent and hard 50-μm oxide layer that has been created. As compared to the dynamically reforming oxide layer of the untreated UFG material, this thick oxide layer is more adhered to the substrate and more durable – this eliminates the oxidative wear mechanism. At higher contact pressures (above 0.5 MPa), wear rates do increase notably on this internally oxidized material; however, total weight losses are still lower than nonoxidized samples. Overall, through a combined processing route of ECAE and internal oxidation, this work is very promising in terms of producing niobium alloys with high strength, good fatigue resistance and wear resistance.

As already eluded to in relation to cyclic plastic deformation stability, the microstructural stability of all UFG materials (not just niobium) is a critical question. The high dislocation density and the high proportion of nonequilibrium grain boundaries can drive recrystallization and grain growth processes at relatively low energy inputs. In this context, Rubitschek et al. [41] have challenged the stability of two ECAE UFG niobium alloys with both elevated temperature heat treatments and also high-temperature strain-controlled low-cycle fatigue tests. The Nb-1Zr and Nb-2.3Zr materials both reach approximately 600–700 °C before recrystallization commences, with significant grain growth demonstrated at 1,000 °C. This is shown in Fig. 11.6. The high-temperature fatigue data show the niobium materials to have a stable deformation response (at a constant strain amplitude of 5×10^{-3}) up to 600 °C. Above this temperature, cyclic softening with a rapid decrease in mean stresses occurs, leading to earlier failures. Overall, the study shows that the UFG materials have good microstructural stability up to significantly elevated temperatures and at high cyclic plastic deformations; these challenging conditions probably represent the most extreme cases of what the materials might be exposed to either during device manufacture or in vivo after implantation.

Specifically with orthopaedic or dental applications in mind, the impact behaviour of UFG niobium has also been investigated by Toker et al. [42]. The results generally show that the UFG material exhibits high toughness, though in certain orientations (relative to the extrusion direction), lower values were obtained. Grain boundary orientations are important in this regard; boundaries perpendicular to a crack path act as a barrier to propagation, deflecting the crack along the boundary, with a longer path than if it propagated directly through the boundary. This leads to higher energy absorption. While the lower values obtained in certain orientations are not deemed to be problematic, there is significant scope within the ECAE process for control and optimization of grain structures, once specific intended loading conditions are kept in mind – particularly considering the anisotropic nature of biological tissues and structures.

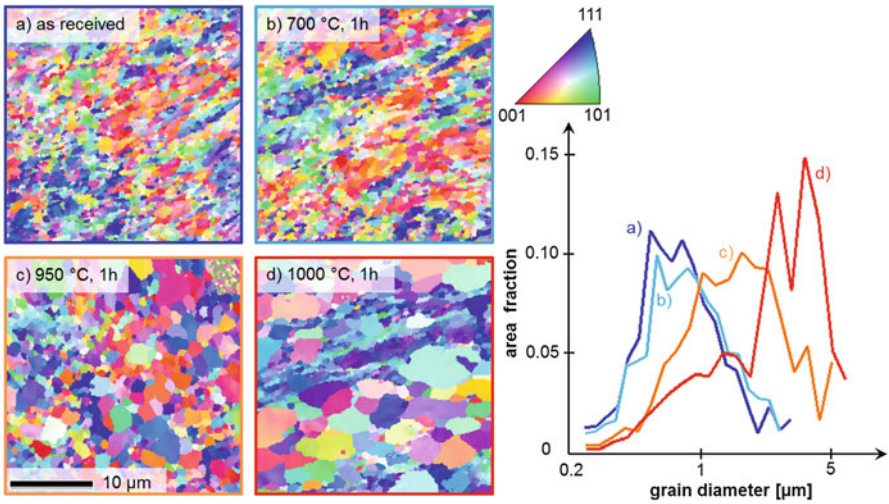

Fig. 11.6 Microstructural evolution upon static annealing of UFG Nb-2.3Zr alloy (**a**–**d**) and corresponding grain size distributions. Grain size remains unchanged up to 700 °C (**b**) as compared to the as-received condition (**a**). At 950 °C (**c**) and 1,000 °C (**d**), the structures are (partly) recrystallized, and average grain sizes are significantly increased (Reprinted with permission from Ref. [41]. Copyright 2012 by Elsevier)

Low-cycle fatigue of UFG niobium has been examined in some detail, primarily to address aspects relating to microstructural stability. Rubitschek et al. [43] have also recently studied the high-cycle fatigue behaviour in simulated body fluid (SBF). The ECAE-processed Nb-2.3Zr alloy was shown to have a yield strength of 667 MPa compared to 414 MPa for the standard coarse-grained condition. High-cycle fatigue testing of this material was performed in both laboratory air and SBF. Testing was done at 20 Hz with a load ratio of $R=-1$ and at stress amplitudes in the range 270–350 MPa. Results showed that the UFG niobium alloy had a mean fatigue limit of 291 MPa at 2×10^6 cycles and furthermore that testing in the SBF (Hanks' solution) did not influence this behaviour. No localized corrosion effects were observed. This fatigue performance for UFG niobium represents a modest improvement over the data for conventional material reported by Papakyriacou et al. [34]. Thus while this fatigue response is in an area that is potentially acceptable for medical device applications, it is still at the lower end of the spectrum that would be reported, for example, for biomedical titanium alloys [44]. The fatigue testing was complemented by surface electrochemical characterization and crack growth rate measurements. The electrochemical testing showed that the UFG Nb had highly stable surfaces with low corrosion current density and overall was comparable to both conventional Nb and to Ti-6Al-4V. The crack growth rate data showed that the UFG Nb generally compared favourably to Ti-6Al-4V, with the exception of corrosion fatigue effects tending to slightly increase growth rates in the threshold regime, at low test frequencies.

With a view to further enhancing high-cycle fatigue performance, Rubitschek et al. [45] have explored application of an improved internal oxidation step, aimed at improving oxide integrity and reducing embrittlement effects. Samples of Nb2.3Zr were put through the 8E ECAE process; this increased the yield strength from 415 MPa up to 675 MPa, with an elongation to failure of 17 %. Following extensive investigation, a two-stage heat treatment step was optimized. This consisted of an initial oxidation treatment (6 h at 620 °C), in a controlled partial pressure of oxygen (20 Pa). The second step is considered as a diffusion treatment, done in vacuum at 620–800 °C for 6–24 h. During the first-stage oxidation treatment, oxygen diffuses in from the surface causing an increase in hardness through formation of zirconium oxide particles and through interstitial hardening. The interstitial oxygen is considered to be the main cause of any surface embrittlement effects (and contributes to reduced ductility as described earlier). During the second-stage vacuum diffusion step, this interstitial oxygen diffuses further into the bulk, forming additional zirconium oxide particles. This leads to a reduced hardness and brittleness at the outer surface but provides increased strengthening further within the bulk, i.e. it gives a less-steep hardness profile with a better balance of strength and ductility. High-cycle fatigue testing has demonstrated the benefits of the various steps. For example, the mean endurance limit for the ECAEed material is approximately 290 MPa at 2×10^6 cycles; after the oxidation treatment, this is increased to approximately 400 MPa, though it is noted that data points for this condition are limited and more testing will be required. Furthermore, initial data is suggesting that additional increases in stress amplitude can be tolerated in samples that have also been subjected to the final diffusion treatment. Overall, this combination of ECAE and the dual-step oxidation process is very promising and has the potential to bring the fatigue performance of niobium firmly into the regime of other conventional biomedical metals.

11.4.2 Niobium Alloy Development

As indicated at the outset, there has not been substantial development or evolution of niobium materials, particularly when compared to other metallic biomaterials such as titanium. Pure niobium and Nb-1Zr are still two of the most widely used grades, even within the nuclear and aerospace industries. As general-purpose high-temperature and corrosion-resistant materials, these two grades perform satisfactory, and therefore there has been little driving force for extensive alloy development. Recognition of the excellent biocompatibility of niobium has however seen some increased interest from the medical device sector in the possibility of new alloys, with better strength and fatigue behaviour than Nb and Nb-1Zr.

As demonstrated by the earlier described work on UFG materials, even Nb-Zr alloys with a small increase in zirconium levels (to 2.3 wt%) already demonstrate some improvements. Within the Nb-Zr system itself, the zirconium contributes notable solid solution strengthening, but it also plays an important role in minimizing

oxygen embrittlement of the material [46]. Through the formation of zirconium oxide particles (which can also provide some precipitation strengthening), oxygen from the bulk material is consumed, reducing the amount of available interstitial solid solution oxygen. This reduces the matrix hardening and embrittlement associated with interstitial oxygen.

However, several other elements also have good solubility in niobium, therefore providing further opportunities for solid solution strengthening. An early study by Slining and Koss explored the strengthening effects of individual hafnium, tungsten and tantalum additions [47]. Alloys with up to 11.3 atomic weight % were prepared, in single crystal configuration, to allow fundamental studies of crystallographic shear stresses. The results showed that hafnium is the most potent strengthener, providing nearly twice the strengthening effect of tungsten at the same alloying levels; tantalum showed the lowest strengthening. The investigators propose that the relative differences in solid solution strengthening effect are at least partly due to differences in atomic size between the solvent and solute atoms, i.e. with the larger hafnium atoms providing the largest difference compared to the niobium matrix, thereby inducing larger elastic strain fields and better inhibiting dislocation movement. The potential for hafnium additions was ultimately commercialized through the development of Alloy C103 (Nb-10Hf-1Ti-0.5Zr). The yield strength of C103 is noted to be 310 MPa compared to 138 MPa for Nb-1Zr [3]. This alloy was developed as part of the Apollo space program in the USA and has also since been used in military aircraft [48]. As a consequence of these origins, published data on the material is not readily available and export restrictions in the USA have also inhibited application development in other jurisdictions. Thus from a practical perspective, this material has not been considered for biomedical applications, though fundamentally it is a very promising option and hopefully some independent (non-nuclear, nonmilitary) developments may take place in the area of Nb-Hf alloys, though it is noted that the high melting temperatures and sensitivity to oxygen content make processing of all of these refractory alloys somewhat difficult.

Alloy FS-85 is another niobium material with its origins in space nuclear programmes. This is a high-strength Nb-28Ta-10W-1Zr alloy with significant capacity for both solid solution strengthening and precipitation hardening. Leonard et al. [49] report a yield strength of 489 MPa and an elongation to failure of 18 % for this material in the annealed condition. Aging treatments result in precipitation of both intergranular and grain boundary precipitates – in addition to the zirconium oxide (ZrO_2) particles retained from the annealed structure. The composition of these particles is not precisely quantified, but they are identified as Zr(CON), i.e. they are a mixed composition incorporating some of the trace carbon, oxygen and nitrogen interstitials present in the alloy. The optimum aging conditions, particularly at non-elevated temperature, are not presented. In any event, this material is even less readily available than C103 and is not being commercially manufactured.

A variation of Nb-1Zr, with carbon additions, has also been explored sporadically for nuclear and high temperature applications. This alloy known as PWC-11, originally developed by Pratt & Whitney Aircraft Corp, has 0.1 % carbon added to form carbide precipitates for strengthening. It has never been fully commercially

exploited though continues to be investigated and characterized. While the carbon additions provide for enhanced creep strength, it is debatable if any lower temperature benefits exist. Dickerson and Gibeling report on a low-cycle fatigue study comparing the performance of Nb-1Zr and Nb-1Zr-0.1C at room and elevated temperatures [50]. While the presence of carbide particles was verified for the Nb-1Zr-0.1C alloy, there was very little difference in room temperature tensile behaviour, and ultimately there was also no difference in the fatigue behaviour of the two materials at room temperature. Thus it is difficult to envisage biomedical applications for this particular alloy – though it is recognized that more development of heat treatments may be possible to optimize the size and distribution of carbides. In a further evolution of carbide strengthening, Tan et al. report on additions of zirconium carbide (ZrC) to niobium, in concentrations from 10 at% to 60 at% of ZrC [51]. Microstructures are essentially two-phase composites, consisting of both niobium solid solution and carbides. While increasing ZrC content clearly increases strength at room temperature, there is also an associated drop in ductility and toughness. Ding and Jones similarly report on carbide strengthening of a Nb-Ti-Al-Cr-V alloy [52]; while significant strengthening can be obtained, the ductility at room temperature is likely to be too low for medical device applications. Thus while there are indeed numerous advances in relation to improving high temperature performance of niobium materials, these are not likely to be compatible with the requirements for implant applications.

It is interesting to note that despite these limited alloy options, the first significant clinical application of niobium has been the use of standard Nb-1Zr for cardiovascular devices. It is in the context of improved biocompatibility that Nb-1Zr was originally considered for cardiovascular stent application, i.e. by avoiding both nickel and molybdenum which are present in stainless steel. Thus while the yield strength of Nb-1Zr is substantially too low for orthopaedic applications, it is close to a usable range for cardiovascular stents and therefore merited clinical investigation in this instance. This initial clinical work, reported by Beier et al. [53], compared anodized Nb-1Zr stents against conventional stainless steel devices. While the Nb-1Zr devices performed satisfactorily, there was a trend to higher neointimal growth at 6-month follow-up. It was proposed that higher strength would indeed have been beneficial as it could have allowed for design of thinner struts on the Nb-1Zr devices, and this could have reduced neointimal growth.

At this point, it is worth highlighting some important differences in material requirements between orthopaedic applications and cardiovascular applications – specifically balloon-expandable stents. It is now well understood that matching the elastic modulus of orthopaedic implants as close as possible to the modulus of bone is a fundamental objective, with many β-Ti alloys being developed to achieve high strength but with low elastic modulus [54]. Conversely however, balloon-expandable stents need to have a relatively high elastic modulus combined with moderate plastic deformation capability. The high elastic modulus is required to minimize elastic recoil after the stent has been expanded out (by the balloon) against the vessel wall. Materials with low modulus will tend to allow the diameter of the stent to recoil/springback as the balloon is deflated and removed; this can lead to poor apposition

against the vessel wall with resultant poor clinical outcomes, such as thrombus formation and/or restenosis. This may also have been a factor in the performance of the Nb-1Zr stents, given the lower modulus of Nb-1Zr (102 GPa) compared to stainless steel (193 GPa).

The plastic deformation characteristics are also central to the design and performance of balloon-expandable stents. While high material strength is required in order to give high radial strength and compression resistance to the device, a low yield strength is desired for easier crimping of the stent onto the balloon catheter. This seemingly conflicting requirement is best addressed by use of materials with a high work hardening rate, i.e. materials with substantial increases in strength beyond yield, as the device undergoes plastic deformation out to the required final diameter. Thus the preferred materials are those with a significant difference between the yield strength and tensile strength as well as having extensive uniform plastic deformation before necking and fracture. Traditional 316L stainless steels, cobalt-chromium alloys and platinum-chromium have provided various balances of these requirements and are therefore used widely in the manufacture of balloon-expandable cardiovascular devices. However, these devices are not fully compatible with some of the newer imaging modalities, in particular magnetic resonance imaging (MRI) or more specifically when MRI is used to perform angiography (MRA) during stent follow-up examinations. The paramagnetic nature of these traditional materials causes a localized distortion of the magnetic fields which ultimately shows as an artefact on the image. This artefact can obscure the stent lumen and often extends beyond the boundary of the device into other regions [55]; this can impact on proper clinical interpretation of the image. Therefore, materials with low magnetic susceptibility are of interest in order to reduce the extent of this imaging artefact – niobium is positioned very well in this regard as illustrated by Table 11.2, which shows bulk magnetic susceptibility values for some typical implant materials.

In considering new stent materials for MRI compatibility, it is of course also desirable to target materials that are known to be highly inert and biocompatible. It is in this context that O'Brien et al. [57] report on the development of a new niobium alloy for MRI-compatible stent applications. This is one of the first reports of a new niobium alloy being developed with specific medical implant requirements in mind. The alloy selection and design rationale is presented in detail; niobium was an ideal candidate from the perspective of magnetic susceptibility and biocompatibility, but

Table 11.2 Magnetic susceptibility for selected metallic biomaterials including niobium [56]

Material	Magnetic susceptibility, χ
Titanium	182×10^{-6}
Niobium	237×10^{-6}
Tantalum	178×10^{-6}
Zirconium	109×10^{-6}
Nitinol	245×10^{-6}
Stainless steel	$3{,}520–6{,}700 \times 10^{-6}$

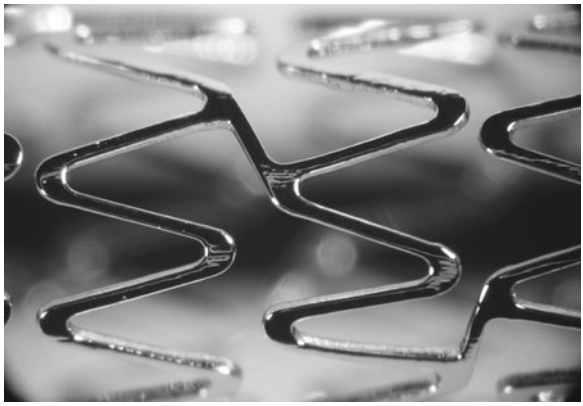

Fig. 11.7 Prototype Nb-Ta-W-Zr alloy coronary stent (Reprinted with permission from Ref. [57]. Copyright 2008 by Elsevier)

the elastic modulus and yield strength of pure Nb or Nb-1Zr were both considered to be too low. Niobium alloys with additions of tantalum, tungsten and zirconium were therefore explored – it was essential that all additions have low magnetic susceptibility. Tantalum was selected as the main addition in order to provide some level of solid solution strengthening, though more importantly to increase the X-ray attenuation of the alloy so that devices would have good visibility under X-ray fluoroscopy. Tungsten was selected as an addition to provide solid solution strengthening, and it was also expected to contribute to increasing elastic modulus. Zirconium was retained at the low levels observed in Nb-1Zr, serving primarily to reduce embrittlement from oxygen, through the formation of zirconium oxide particles, and also to provide strengthening. The resultant alloy developed was a Nb-28Ta-3.5W-1.3Zr composition; alloy prototyping, stent tubing manufacture and stent manufacture were all described. Conventional technologies of laser cutting, dross removal and electropolishing were all readily adapted for manufacture of stents. Figure 11.7 shows a typical stent structure made from the Nb-28Ta-3.5W-1.3Zr material. The new alloy has a yield strength of 339 MPa and an elastic modulus of 128 GPa, compared to 163 MPa and 102 GPa, respectively, for Nb-1Zr tubing. Mechanical testing of the stents made from this Nb-28Ta-3.5W-1.3Zr material showed them to be superior to Nb-1Zr; the new material provided for lower elastic recoil and higher compression strength. The elastic recoil values were in fact similar to those of stents made from Co-Cr alloy L605, demonstrating similarity to widely used commercial devices. Magnetic susceptibility testing also confirmed that the material retained the low susceptibility levels of all the constituents. In vitro evaluations of this material have also been reported, presenting corrosion behaviour, endothelial cell adhesion and image artefact during MR angiography [58]. Potentiodynamic polarization tests showed the Nb-28Ta-3.5W-1.3Zr alloy to be highly passive, exhibiting low current densities with no evidence of pitting. Extended duration immersion, in saline solutions, indicated that the level of metal ion release from the new alloy was exceptionally low and comparable to Co-Cr alloy L605. The nature of the surface oxide has not been precisely quantified, but XPS data pointed out that it was a mixed structure with both Nb_2O_5 and Ta_2O_5 present; tantalum oxide

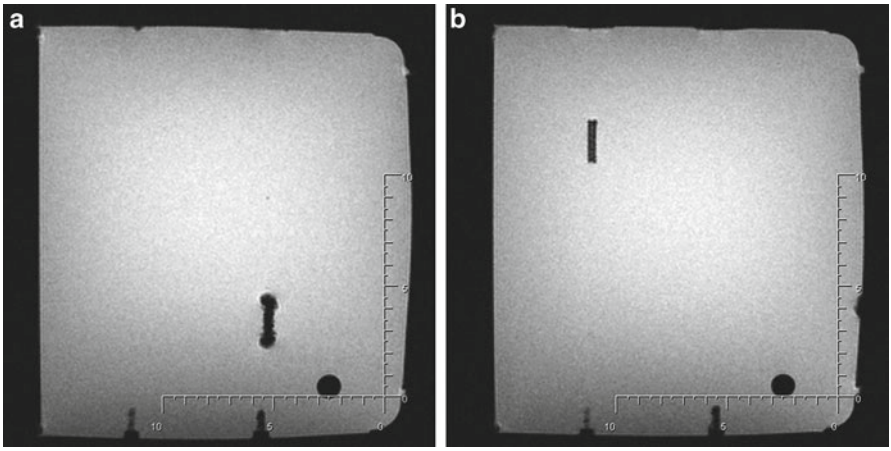

Fig. 11.8 MRI images (gradient echo) of a 3.0 × 17-mm coronary stent, made from (**a**) 316L stainless steel and (**b**) Nb-Ta-W-Zr alloy (Reprinted with permission from Ref. [58]. Copyright 2008 by Elsevier)

would also be expected to be highly biocompatible. In terms of endothelial cell adhesion and retention, the Nb-28Ta-3.5W-1.3Zr alloy performed similar to 316L stainless steel, which has long history of successful vascular use. While longer term in vivo studies will be needed to assess neointima proliferation and inflammatory response, this initial data is promising. In terms of MR imaging behaviour, the results showed that the new material has significantly reduced artefact compared to 316L control stents. In Nb-28Ta-3.5W-1.3Zr, the artefact was primarily retained within the outer dimensions of the stent, while for the 316L device, the artefact extended to several multiples of the stent diameter and also well beyond the stent length. This is illustrated in Fig. 11.8. Under certain imaging conditions, it is even possible to visualize into the lumen of the Nb-28Ta-3.5W-1.3Zr stent. Overall, development of this new alloy is a promising step towards cardiovascular devices with both improved biocompatibility and MRI compatibility but should also demonstrate the potential that exists for niobium alloys to be developed and tuned for other implant applications.

11.4.3 Niobium In Situ Composites

One of the more novel approaches to developing higher strength niobium alloys has been through the creation of duplex microstructures consisting of ductile niobium solid solution (Nb_{SS}) combined with stronger and stiffer intermetallic silicide compounds, such as Nb_5Si_3. Numerous such composites have been developed, with a variety of matrix alloying constituents and with silicon contents in the range

12–25 at%, giving a range of volume fractions for the matrix and intermetallic components [59]. By way of example, the work of Fujikura et al. described the development and characterization of ternary Nb-Mo-W solid solution alloys and quaternary Nb-Si-Mo-W silicide alloys [60]. A range of interesting microstructures were obtained, with strength generally increasing substantially as the volume fraction of silicide increased. Sha et al. [61] described similar effects for binary Nb-W and ternary Nb-W-Si alloys; a Nb-10W alloy showed the best room temperature toughness, but while a Nb-10W-10Si alloy showed the best high temperature strength, it had poor ductility at room temperature. The majority of these developments are of course focused on increasing high temperature strength, and therefore ductility at room temperature will always be too low for medical implant considerations. In addition, the corrosion mechanisms and failure modes of such constructs are also likely to be problematic from a medical device perspective. However, the concepts of metal-metal composites, rather than these metal-intermetallic composites, may be of interest to achieve a variety of balances of strength, stiffness and ductility for different device applications; powder metallurgy techniques may allow for unusual combinations of metal constituents that may not otherwise be possible by conventional ingot metallurgy.

11.5 Summary

Niobium surfaces develop a highly stable and inert oxide layer. This provides the basis for the excellent corrosion resistance and biocompatibility that is generally observed for the material. There are multiple in vitro studies, preclinical evaluations and even some clinical data that demonstrate this favourable response. However, this excellent surface performance has traditionally not been matched with bulk mechanical properties that are suitable for implant applications; typically yield strength and fatigue strength have been too low, and for some applications, elastic modulus is also lower than required.

There have however been extensive advances in recent years in terms of at least fully exploiting the biocompatible nature of niobium surfaces. Several technologies have been utilized for applying niobium or niobium oxides to the surfaces of less compatible materials, thereby giving combinations of attractive bulk mechanical properties with ideal surfaces for implantation. Physical vapour deposition (PVD) techniques and sol-gel methods have been used to apply these layers to metals such as 316L stainless steel, titanium and Ti-6Al-4V. Niobium nitride coatings have been explored for providing high wear resistance combined with biocompatibility, while niobium ion implantation has been examined for improving the corrosion resistance of NiTi.

Even though the natural surface of niobium is widely considered to be biocompatible, there have also been a number of developments aimed at further enhancing this surface layer for specific biological responses or mechanical behaviour. For example, alkali surface treatments have been shown to enhance apatite formation in

simulated body fluids, while a range of anodic oxidation techniques can provide control over the niobium oxide structure and porosity. Boronizing of niobium has been shown to improve wear resistance.

While strength and fatigue behaviour of traditional Nb and Nb-1Zr have not met the requirements for implant applications, there has however been a number of very significant developments and advances in this regard. Foremost amongst these has been the development of severe plastic deformation (SPD) process technologies that can provide ultrafine grains (UFG) to increase strength. Much work has been done with these techniques, utilizing conventional alloys, but achieving very promising combinations of increased strength and ductility. In addition, corrosion behaviour, fatigue testing and biocompatibility data are all indicating that niobium processed in this manner is now ready to be considered for device applications. Optimization of performance does also involve an additional heat treatment to provide an enhanced zirconium oxide surface strengthening; it remains to be seen if this combination of relatively specialized processes can be adapted economically into routine manufacture of medical implants.

In relation to alloy development, there has been a low level of activity from the nuclear and aerospace industries aimed at improving performance beyond Nb and Nb-1Zr. While some of these (such as C103, FS-85 and PWC-11) may have merit, limited availability has restricted consideration for medical device applications. This has however driven the development of new alloys specifically for implant application with significant progress already having been made on a Nb-Ta-W-Zr alloy designed for cardiovascular stents. It remains to be seen if this alloy will ultimately see clinical application; the investments needed in manufacturing systems, quality systems, preclinical trials, clinical trials and regulatory approvals are substantial for use of new materials in such critical applications.

To conclude, while niobium has not been widely used to date, there have been some significant advances in surface technologies, grain refinement and alloy development. While further work is needed in all of these areas, to bring them to clinical application, there is certainly a growing interest to achieve this objective.

References

1. Davies JR (1994) Stainless steel: ASM specialty handbook. ASM International, Ohio
2. Poncin P, Proft J (2003) Stent tubing – understanding the desired attributes. In: Shrivastave S (ed) Proceedings of the materials & processes for medical devices conference, Anaheim, CA, USA, 8–10 September 2003. ASM International, Ohio, pp 253–259
3. Davies JR (ed) (1990) Properties and selection: nonferrous alloys and special-purpose materials, vol 2, ASM handbook. ASM International, Ohio
4. El-Genk MS, Tournier JM (2005) A review of refractory metal alloys and mechanically alloyed-oxide dispersion strengthened steels for space nuclear power systems. J Nucl Mater 340:93–112
5. Zitter H, Plenk H (1987) The electrochemical behaviour of metallic implant materials as an indicator of their biocompatibility. J Biomed Mater Res 21:881–896

6. Johansson CB, Albrektsson T (1991) A removal torque and histomorphometric study of commercially pure niobium and titanium implants in rabbit bone. Clin Oral Implants Res 2:24–29
7. Matsuno H et al (2001) Biocompatibility and osteogenesis of refractory metal implants, titanium, hafnium, niobium, tantalum and rhenium. Biomaterials 22:1253–1262
8. Metikoš-Huković M et al (2003) The influence of niobium and vanadium on passivity of titanium-based implants in physiological solution. Biomaterials 24:3765–3775
9. Rogers SD et al (1997) In vitro human monocyte response to wear particles of titanium alloy containing vanadium or niobium. J Bone Joint Surg [Br] 79B:311–315
10. Eisenbarth E et al (2004) Biocompatibility of β-stabilizing elements of titanium alloys. Biomaterials 25:5705–5713
11. Eisenbarth E et al (2006) Nanostructured niobium oxide coatings influence osteoblast adhesion. J Biomed Mater Res 79A:166–175
12. Ochsenbein A et al (2008) Osteoblast responses to different oxide coatings produced by the sol-gel process on titanium substrates. Acta Biomater 4:1506–1517
13. Nagarajan S et al (2010) Synthesis and electrochemical characterization of porous niobium oxide coated 316LSS for orthopedic applications. Mater Chem Phys 119:363–366
14. Ramirez G et al (2010) Amorphous niobium oxide thin films. J Non Cryst Solids 365:2714–2721
15. Lai F et al (2006) Effect of thickness on the structure, morphology and optical properties of sputter deposited Nb2O5 films. Appl Surf Sci 253:1801–1805
16. Ramirez G et al (2011) Niobium based coatings for dental implants. Appl Surf Sci 257:2555–2559
17. Olaya JJ et al (2008) Comparative study of niobium nitride coatings deposited by unbalanced and balanced magnetron sputtering. Thin Solid Films 516:8319–8326
18. Rojas PN, Rodil SE (2012) Corrosion behaviour of amorphous niobium oxide coatings. Int J Electrochem Sci 7:1443–1458
19. Park WW et al (2012) Wear of UHMWPE against nitrogen-ion-implanted and NbN-coated Co-Cr-Mo alloy formed by plasma immersion ion implantation and deposition for artificial joints. Appl Surf Sci 258:8228–8233
20. Braic M et al (2011) Preparation and characterization of biocompatible Nb-C coatings. Thin Solid Films 519:4064–4068
21. Olivares-Navarrete R et al (2011) Biocompatibility of niobium coatings. Coatings 1:72–87
22. Zhao T et al (2011) Surface characteristics, nano-indentation and corrosion behavior of Nb implanted NiTi alloy. Surf Coat Technol 205:4404–4410
23. Godley R et al (2004) Bonelike apatite formation on niobium metal treated in aqueous NaOH. J Mater Sci Mater Med 15:1073–1077
24. Wang XJ et al (2008) In vitro bioactivity evaluation of titanium and niobium metals with different surface morphologies. Acta Biomater 4:1530–1535
25. Akahori T et al (2007) Bioactive ceramic surface modification of β-type Ti-Nb-Ta-Zr system alloy by alkali solution treatment. Mater Trans 48(3):293–300
26. Minagar S et al (2012) A review of the application of anodization for the fabrication of nanotubes on metal implant surfaces. Acta Biomater 8:2875–2888
27. Sieber I et al (2005) Formation of self-organized niobium porous oxide on niobium. Electrochem Commun 7:97–100
28. Karlinsey R (2005) Preparation of self-organized niobium oxide microstructures via potentiostatic anodization. Electrochem Commun 7:1190–1194
29. Störmer H et al (2009) Anodically formed oxide films on niobium: microstructural and electrical properties. J Eur Ceram Soc 29:1743–1753
30. Mackey AC et al (2012) Development of niobium oxide coatings on sand-blasted titanium alloy dental implants. Mater Sci Appl 3:301–305
31. Usta M (2005) The characterization of borided pure niobium. Surf Coat Technol 194:251–255

32. Ribeiro R et al (2006) Tribological characteristics of boronized niobium for biojoint applications. Vacuum 80:1341–1345
33. Dokumaci E et al (2013) Effect of boronizing on the oxidation of niobium. Int J Refract Met Hard Mater 41:276–281
34. Papakyriacou M et al (2000) Effects of surface treatments on high cycle corrosion fatigue of metallic implant materials. Int J Fatigue 22:873–886
35. Papakyriacou M et al (2002) Cyclic plastic deformation of tantalum and niobium at very high numbers of cycles. Mater Sci Eng A325:520–524
36. Langdon TG (2007) The principles of grain refinement in equal-channel angular pressing. Mater Sci Eng A462:3–11
37. Valiev RZ, Langdon TG (2006) Principles of equal-channel angular pressing as a processing tool for grain refinement. Prog Mater Sci 51:881–981
38. Niendorf T et al (2007) Microstructure-mechanical property relationships in ultrafine-grained NbZr. Acta Mater 55:6596–6605
39. Niendorf T et al (2008) Improvement of the fatigue performance of an ultrafine-grained Nb-Zr alloy by nano-sized precipitates formed by internal oxidation. Scr Mater 58:571–574
40. Purcek G (2011) Effect of internal oxidation on wear behavior of ultrafine-grained Nb-Zr. Acta Mater 59:7683–7694
41. Rubitschek F et al (2012) Microstructural stability of ultrafine-grained niobium-zirconium alloy at elevated temperatures. J Alloys Compd 517:61–68
42. Toker SM et al (2012) Anisotropy of ultrafine-grained alloys under impact loading: the case of biomedical niobium-zirconium. Scr Mater 66:435–438
43. Rubitschek F et al (2012) Corrosion fatigue behavior of a biocompatible ultrafine-grained niobium alloy in simulated body fluid. J Mech Behav Biomed Mater 5:181–192
44. Niinomi M (1998) Mechanical properties of biomedical titanium alloys. Mater Sci Eng A243:231–236
45. Rubitschek F et al (2013) Surface hardening of biocompatible ultrafine-grained niobium zirconium alloy by two-stage oxidation treatment. J Mater Sci 48:4549–4556
46. DiStefano JR, Chitwood LD (2001) Oxidation and its effects on the mechanical properties of Nb-1Zr. J Nucl Mater 295:42–48
47. Slining JR, Koss DA (1973) Solid solution strengthening of high purity niobium alloys. Metall Trans 4:1261–1264
48. Craig Wojcik C (1998) High-temperature niobium alloys. Adv Mater Process 12:27–30
49. Leonard KJ et al (2009) Nb-base FS-85 alloy as a candidate structural material for space reactor applications: effects of thermal aging. Metall Mater Trans 40A:838–855
50. Dickerson SL, Gibeling JC (2000) Low cycle fatigue of niobium-zirconium and niobium-zirconium-carbon alloys. Mater Sci Eng A278:121–134
51. Tan Y et al (2003) Effect of alloy composition on microstructure and high temperature properties of Nb-Zr-C ternary alloys. Mater Sci Eng A341:282–288
52. Ding R, Jones IP (2008) Mechanical properties and deformation behaviour of a niobium alloy with different carbon contents. Mater Sci Eng A497:301–308
53. Beier F et al (2006) First in-human randomized comparison of an anodized niobium stent versus a standard stainless steel stent. Clin Res Cardiol 95:455–460
54. Niinomi M (2008) Mechanical biocompatibilities of titanium alloys for biomedical applications. J Mech Behav Biomed Mater 1:30–42
55. Hug J et al (2000) Coronary arterial stents: safety and artifacts during MR imaging. Radiology 216:781–787
56. Schenck JF (1996) The role of magnetic susceptibility in magnetic resonance imaging: MRI magnetic compatibility of the first and second kinds. Med Phys 6:815–850
57. O'Brien B et al (2008) Development of a new niobium-based alloy for vascular stent applications. J Mech Behav Biomed Mater 1:303–312
58. O'Brien B et al (2008) Characterization of an NbTaWZr alloy designed for magnetic resonance angiography compatible stents. Biomaterials 29:4540–4545

59. Bewlay BP et al (2003) A review of very-high-temperature Nb-silicide-based composites. Metall Mater Trans 34A:2043–2052
60. Fujikura M et al (2004) Effect of alloy chemistry on the high temperature strengths and room temperature fracture toughness of advanced Nb-based alloys. Mater Trans 45(2):493–501
61. Sha J et al (2003) Toughness and strength characteristics of Nb-W-Si ternary alloys prepared by arc melting. Metall Mater Trans 34A:2861–2871

Part III
Reactions of Metals in Human Body

Chapter 12
Corrosion of Metallic Biomaterials

Burak Dikici, Ziya Esen, Ozgur Duygulu, and Serap Gungor

Abstract Metallic materials have been used as biomedical implants for various parts of the human body for many decades. The physiological environment (body fluid) is considered to be extremely corrosive to metallic surfaces; and corrosion is one of the major problems to the widespread use of the metals in the human body since the corrosion products can cause infections, local pain, swelling, and loosening of the implants. Recently, the most common corrosion-resistant metallic biomaterials are made of stainless steels and titanium and its alloys along with cobalt–chromium–molybdenum alloys. It is well known that protective surface films of the alloys play a key role in corrosion of the metallic implants. Key documents on the corrosion behavior of the metallic biomaterials in human body have been compiled under this chapter as a review.

Keywords Metallic biomaterials • Corrosion • Physical body fluid • Bioactive materials • Implant

12.1 Introduction

The main question is, "what is the most important property for a metallic biomaterial?" Clearly, the answer is *biocompatibility*. In addition, it is well known that corrosion is one of the major problems affecting the biocompatibility of orthopedic devices made of metals and alloys used as implants in the human body. Compared to other implants, metallic implants have excellent mechanical properties such as high elasticity, tensile strength, wear resistance, and machining.

B. Dikici (✉) • S. Gungor
Department of Mechanical Engineering, Yuzuncu Yil University, Van 65080, Turkey
e-mail: burakdikici@yyu.edu.tr

Z. Esen
Department of Materials Science and Engineering, Cankaya University,
Ankara 06810, Turkey

O. Duygulu
Materials Institute, TUBITAK Marmara Research Center, Gebze-Kocaeli 41470, Turkey

M. Niinomi et al. (eds.), *Advances in Metallic Biomaterials*, Springer Series
in Biomaterials Science and Engineering 3, DOI 10.1007/978-3-662-46836-4_12

Recently, stainless steels (SS), cobalt-chromium alloys (CoCr), and titanium (Ti) and its alloys are the most widely used metallic materials in order to extend biodevices' life in the human body [1, 2]. If the corrosion of a metallic implant occurs in the body, the flow of electrons in the metal leads to a flow of ions in the surrounding tissue, thereby disturbing the nerve cells. Potential difference formed between metal and body fluid is basically the driving force for corrosion process. However, any resistance in the solution or presence of oxide film on the metal surface decreases the corrosion rate. It is well known that the metallic biomaterials are physiologically inert and have high corrosion resistance due to the formation of a passive film on their surfaces. The passive and inert oxide layers are surrounded by the body environment; and due to biodegradability of metallic materials, adverse effects as inflammation, restenosis, and stress shielding caused by orthopedic implants are reduced [3]. Accordingly, due to the presence of passive surface films on most of the metallic implants such as stainless steel (SS), CoCr, and Ti-based alloys, the rate of attack of corrosion is very low, and thus, the metals are self-protected [4, 5]. Therefore, control of corrosion and/or keeping the corrosion rate is crucial to increase the success of the implant over a long period of time.

Artificial implants may induce several reactions in the biological microenvironment through the interaction of the biomaterial with body fluid, proteins, enzymes, and various cells which may induce toxicity and allergy and eventually implant failure. The biocompatibility of the metallic implant is one of the considerable concerns due to the corrosion during in vivo environment. The chemical composition (type and quantity of alloying elements, segregations, impurities), microstructure (grain size and orientation), and surface properties (coated and uncoated status) are classified as the material's variables, while the type and concentration of chemical ingredients (pH, chloride content, etc.), temperature, and pressure are medium properties that influence the corrosion behavior of the metallic biomaterials. In addition, the dominancy of the corrosion type depends on the working condition of the implant (static, dynamics loads) and the construction of the implant and thermomechanical history (dislocation density, amounts of thermal or residual stress, point defects, deformation ratio) [6, 7].

12.2 Common Corrosion Types of Metallic Biomaterials

Metallic biomaterials corrode in a variety of ways including general and localized corrosion types which are pertinent to the currently used alloys such as galvanic corrosion, pitting, crevice, intergranular, stress-corrosion cracking, corrosion fatigue, and tribocorrosion or fretting corrosion [2, 8].

Galvanic corrosion takes place in direct physical contact with a dissimilar metal within an electrolyte such as serum or body fluid, especially in acidic pH environment after any inflammation. It is well known that the contact of dissimilar materials is unavoidable in many surgical applications. For example, galvanic corrosion can occur if bone plate and bone screws are made of dissimilar metals or alloys [2]. In

these cases, the corrosion of the coupled implants is directly correlated to the relative surface area of the constituents that determines the galvanic corrosion response of the implant. Relatively smaller cathodic areas in the implant joints result in smaller galvanic currents. Less noble metal in the couple corrodes while galvanic corrosion is lower for more noble metals because of their passivation behavior [2, 9, 10]. However, dissimilar metals and alloys have different electrode potentials. Thus, some microgalvanic corrosion cells might occur in any case due to the different potentials of implant pairs and their microchemical constituents. For example, corrosion starts generally contacting points between implanted plate and bottom side of the screws.

Pitting corrosion is a form of localized corrosion caused by local dissolution of the protective oxide film and the formation of cavities/small holes in the implant [11]. This form of attack occurs more frequently in media containing chloride ions, which can be enhanced by the presence of proteins in the tissue fluid and serum. Electrochemical studies on the pitting corrosion have showed that characteristic pitting potentials exist. Stable pits form at potentials noble to the pitting potential. A stable pit to form follows a sudden increase in potential into the pitting range, where the current increases sharply from the passive current level. Whereas metastable pits can form at potentials far below the pitting potential, little or no pit propagation takes place as for stable pitting corrosion [12, 13]. Pitting occurs most often on the underside of implanted screwheads. The formation of pits is generally dangerous in load-bearing applications since they may induce other types of corrosion like stress-corrosion cracking (SCC), which leads to failure of stainless steel implant in service due to formation of crack at the root of pitting [2, 14]. The importance of pitting significantly depends on the nature of the surface layer or the film that has formed on the surface due to the interaction of the material with the environment.

Corrosion fatigue is the result of the combined action of an alternating or cycling stresses and a corrosive environment. If the metal is simultaneously exposed to a corrosive environment, the failure can take place at even lower loads and after shorter time. In general, corrosion fatigue resistance of the metallic implants is related to crack initiation and growth mechanisms. Inclusions, precipitated phases, micro-cracks, hidden imperfections, and surface damage act as fatigue starting points in the implant microstructure. The presence of corrosion pits in load-bearing surgical metals may also induce corrosion fatigue which is the fracture of implant due to the combined action of cyclic loading and electrochemical reactions [15]. Some researchers showed that the nitrogen implantation and heat treatments increase the corrosion fatigue of metallic implants, and large plates offer good resistance to corrosion fatigue than the small one [2, 16].

Fretting/tribocorrosion is a material degradation process due to the combined effect of corrosion and wear. This type of corrosion occurs when small relative movements or slight oscillations occur between the two opposing surfaces such as the bone plates and the screwheads of the prosthetic devices in body fluid. It is well accepted that the corrosion resistance of metallic implants is provided by a protective oxide film. However, fretting/tribocorrosion can drastically alter the normal corrosion behavior of the implant due to mechanical distortion of the passive film. Orthopedic implants, particularly hip and knee implants, exposed to the physiological

medium, suffer a lot due to fretting corrosion that leads to a reduction in the lifetime of such prosthesis. Due to fretting, a large amount of corrosion products are released into adjacent tissues or fretting may cause crack initiation and failure of the implant [17]. Fretting/tribocorrosion is an irreversible transformation of a material. Surface modification methods may improve the fretting/tribocorrosion resistance of biomaterials such as nitrogen ion implantation, plasma surface alloying, and high-intensity plasma ion nitriding [18–21].

Crevice corrosion is a type of localized corrosion and related to microstructure of the implant, which occurs preferentially in narrow crevices on the metal surface due to limited mass transfer. Examples of crevices are gaps and contact areas between counterparts, micro-cracks, and spaces filled with deposits. At these occluded areas, the concentration of aggressive chloride ions, decrease in pH value, and depletion of oxygen can rapidly lead to activation of the surface. The reduction of the pH and the increase in the concentration of Cl^- ions are two essential factors in the initiation and propagation of the crevice corrosion phenomenon [22]. This process could also take place in crevices, where the pH value becomes reduced due to the hydrolysis of dissolved and trapped metal cations [23].

12.3 Effect of Components and Physiological Environment on Corrosion of Metallic Biomaterials

The in vivo condition is an aggressive environment for implanted metals and alloys. The corrosion of metallic implants due to the body environment can affect the human life. Such interactions induce corrosion/ionization of the implanted devices. Artificial implants may induce several reactions in the biological environment through the interaction of the biomaterial with body fluid, proteins, enzymes, and various cells, which may induce toxicity and allergy and eventually implant failure. Biomedical implants require both biomedical safety and biomechanical compatibility. With regard to biomechanical compatibility, mechanical properties and corrosion resistance are expected not to degrade over prolonged use. Especially for metal implants, due to high corrosion resistance, low or negligible ion release is expected. The amount of released metal alters clearly depending on the nature and strength of the metal–oxide bond, structure, role of alloying element, composition, and thickness of protective oxide films. The formation of a passive film on surfaces of metallic biomaterials makes them physiologically inert and increases their corrosion resistance. The passive and inert oxide layers are surrounded by the body environment, and due to the biodegradability of metallic materials, adverse effects as inflammation, restenosis, and stress shielding caused by orthopedic implants are reduced [2, 3, 8, 24–26].

Various studies revealed that the 316 L stainless steel is not only nonresistant to corrosion but also causes pain due to the release of nickel ions [27]. Furthermore, due to the high content of nickel, which is around 12–15 %, 316 L stainless steel can

be toxic when nickel is released into the body. It has been proved that high levels of nickel ions in the body cause genotoxic and mutagenic activities, allergy, and cancer [28–31]. The ultimate rate of nickel release in the implants, which is made of nickel alloys, is calculated as 20 mg kg^{-1} day^{-1} [32]. As a consequence of the harmful effects of nickel ions released from the austenitic stainless steels, nickel-free steels have been developed (the HNS, the nickel-free high-nitrogen austenitic stainless steel), which are generally known as FeCrMnMoN system [33]. The addition of nitrogen has been notified to considerably increase the passive film stability and resistance toward localized corrosion such as pitting corrosion, crevice, intergranular, or stress-corrosion cracking [34, 35]. In addition, Sakamoto et al. [36] demonstrated that there is improvement in the crevice corrosion resistance of 25Cr16Ni3Mo2Cu austenitic steel with increasing levels of nitrogen. Another medical implant, components manufactured from Co-based alloys have been informed to release increased Co, Cr, and Ni concentrations in body fluids [37–40]. Considerably increased metal concentrations in body fluids of patients with CoCr alloy-on-metal-bearing hip implants have been enounced in a few articles [39, 41, 42]. Ardlin et al. [43] revealed the ion release of CoCrMo, CoCrFe, FeCoCr, Ti, TiZr, and AuAgPt alloys. The highest amount of ion released was observed for oxidized gold alloy and CoCrMo. As a result, the study revealed that the gold alloy forms a porous oxide layer, which decreases its corrosion resistance.

For long-term implantation, small quantities of metal release from Ti alloys can be acceptable. Zr, Nb, and Ta additions to Ti medical implants have demonstrated excellent compatibility in both hard and soft tissues and prevent metal release [44]. β-Type Ti alloys such as Ti13Zr13Nb, Ti12Mo6Zr2Fe, and Ti-15Mo have been developed for medical use [45–48]. Zr, Nb, Ta, and Pd are inserted to Ti alloy due to the resultant ZrO_2, Nb_2O_5, Ta_2O_5, and PdO, which improve the TiO_2 passive film that is formed on the Ti medical alloys [25]. For example, Ti15Zr4Nb4Ta alloy containing 0.2 % Pd indicates a much better immersion property than Ti6Al4V and Ti6Al7Nb alloys. The Ti15Zr4Nb4Ta alloy demonstrates excellent corrosion resistance under friction [49].

12.4 Standard Tests for Evaluation of Corrosion of Metallic Biomaterials in Physical Body Fluid

There are various standards for testing corrosion resistance of metallic materials under different conditions. One of them, ASTM International, known as the American Society for Testing and Materials (ASTM), is an international standards organization. The commonly used ASTM standards for testing different corrosion processes of metallic biomaterials are collected in Table 12.1 and their details can be reached from http://www.astm.org/.

In vitro corrosion studies on orthopedic biomaterials are carried out either in Hanks' solution or Ringer's solution whose constituents are given in Table 12.2,

Table 12.1 Standards for testing corrosion resistance of biomaterials [50, 51]

Standard	Specifications
ASTM F746	Standard Test Method for Pitting or Crevice Corrosion of Metallic Surgical Implant Materials
ASTM F897	Standard Test Method for Measuring Fretting Corrosion of Osteosynthesis Plates and Screws
ASTM F1089	Standard Test Method for Corrosion of Surgical Instruments
ASTM F1801	Standard Practice for Corrosion Fatigue Testing of Metallic Implant Materials
ASTM F2129	Standard Test Method for Conducting Cyclic Potentiodynamic Polarization Measurements to Determine the Corrosion Susceptibility of Small Implant Devices
ASTM G5	Standard Reference Test Method for Making Potentiodynamic Anodic Polarization Measurements
ASTM G31	Standard Guide for Laboratory Immersion Corrosion Testing of Metals
ASTM G48	Standard Test Methods for Pitting and Crevice Corrosion Resistance of Stainless Steels and Related Alloys by Use of Ferric Chloride Solution
ASTM G61	Standard Test Method for Conducting Cyclic Potentiodynamic Polarization Measurements for Localized Corrosion Susceptibility of Iron-, Nickel-, or Cobalt-Based Alloys
ASTM G71	Standard Guide for Conducting and Evaluating Galvanic Corrosion Tests in Electrolytes

Table 12.2 Compositions of Hanks' and Ringer's solutions [53]

Substance	Hank composition ($g \cdot L^{-1}$)	Ringer composition ($g \cdot L^{-1}$)
NaCl	8.00	8.69
KCl	0.40	0.30
$CaCl_2$	–	0.48
$NaHCO_3$	0.35	–
$NaH_2PO_4 \cdot H_2O$	0.25	–
$Na_2HPO_4 \cdot 2H_2O$	0.06	–
$CaCl_2 \cdot 2H_2O$	0.19	–
$MgCl_2$	0.19	–
$MgSO_4 \cdot 7H_2O$	0.06	–
Glucose	1.00	–
pH (~)	6.90	6.4

comparatively, whereas the corrosion resistance for dental materials is evaluated using synthetic saliva whose constituents are shown in Table 12.3 [52–54]. Furthermore, corrosion changes the chemical environment around the implant,

Table 12.3 Composition of different artificial saliva [54]

Components	Xialine 1 ($g \cdot L^{-1}$)	Xialine 2 ($g \cdot L^{-1}$)	Saliveze ($g \cdot L^{-1}$)
Xanthan gum	0.92	0.18	–
Sodium carboxymethylcellulose	–	–	10
Potassium chloride	1.2	1.2	0.62
Sodium chloride	0.85	0.85	0.87
Magnesium chloride	0.05	0.05	0.06
Calcium chloride	0.13	0.13	0.17
Dipotassium hydrogen orthophosphate	0.13	0.13	0.80
Potassium dihydrogen orthophosphate	–	–	0.30
Sodium fluoride	–	–	0.0044
Sorbitol	–	–	29.95
Methyl p-hydroxybenzoate	0.35	0.35	1.00
Spirit of lemon	–	–	5 ml

inducing an acidic pH after the inflammation of the implant and thus increasing the likelihood of corrosion.

The pH of normal blood and interstitial fluid is 7.35–7.45. Acidification increases metal ion release, especially below pH of 4. In this state, the Japanese Industrial Standards (JIS) [55] can be used for comparison of metallic biomaterials in the acidic simulating in vivo environment.

12.5 Corrosion of Stainless Steels

Stainless steels used in biomedical applications differ in microstructure and chemical composition, and they are classified mainly as martensitic, ferritic, and austenitic stainless steel with respect to their microstructures [7, 9, 14, 56]. On the other hand, according to chemical composition, martensitic and ferritic stainless steels are grouped as chromium and carbon alloys, while austenitic steels fall into chromium–nickel-type stainless steel group.

In medicine the austenitic stainless steels (AISI 316 L, ASTM F55, and F138) contain Cr (17–20 mass%), Ni (12–15 mass%), Mo (2–3 mass%), and small amounts of other elements. The letter "L" represents low carbon (<0.03 %) which is effective in lessening the intergranular corrosion. Cr is responsible for high passivation and it increases the resistance against localized breakdown of passivity. Likewise, Mo reduces the size and number of metastable pits [57]. Accordingly, 316 L stainless steels are desirable surgical implant materials as they additionally possess acceptable biocompatibility and suitable density for load-bearing applications [56]. Commonly used stainless steels in medical and surgical applications are presented in Table 12.4.

Table 12.4 Standards related to surgical stainless steel implants

Specification	Nominal contents
F 138-97	Wrought 18Cr–14Ni–2.5Mo, bar, and wire
F 139-96	Wrought 18Cr–14Ni–2.5Mo, sheet, and strip
F 745-95	18Cr–12.5Ni–2.5 Mo, cast, and solution annealed
F 899-95	Stainless steel billet, bar, and wire
F 1314-95	Wrought N strengthened, 22Cr–12.5Ni–5Mg–2.5Mo, bar, and wire
F 1586-95	Wrought N strengthened, 21Cr–10Ni–3Mg–2.5Mo, bar

Reprinted with the permission from Ref. [14]. Copyright (2004) Elsevier Science

Table 12.5 Nitrogen-containing nickel-free austenitic stainless steels (mass %)

Year	Chemical composition
1996	Fe-18Cr-18Mn-2Mo-0.9N
1996	Fe-15Cr-(10–15)Mn-4Mo-0.9N
1996	Fe-(15–18)Cr-(10–12)Mn-(3–6) Mo-0.9N
2000	Fe-17Cr-10Mn-3Mo-0.5N-0.2C
2001	Fe-(19–23)Cr-(21–24)Mn-(0.5–1.5) Mo-(0.85–1.1)N

Reprinted with the permission from Ref. [14]. Copyright (2004) Elsevier Science

Although the carbon content of traditional austenitic stainless steels like 316 and 317 L is below 0.03 % and Mo addition is around 2–3 %, they still do not fully meet the desired corrosion resistance in the case of a localized form of corrosion. In addition, austenitic stainless steels containing nickel cause a negative reaction when implanted into the body and may induce harmful effects due to the release of nickel ions [58–60], which can be toxic to the human body. Because of these, in recent years, nickel-free nitrogen-containing FeCrMnMoN stainless steels, Table 12.5, with non-ferromagnetic properties are considered as potential replacement for Ni-containing austenitic stainless steels [60–64].

Nitrogen has been reported to increase austenite and passive film stability and also the resistance to the localized form of corrosion [34, 35, 65]. In nickel-free austenitic stainless steels, as a nickel-substituting element, manganese is also used in addition to nitrogen [33]. Accordingly, nickel-free stainless steels with lower toxicity can solve the "nickel problem" in medical stainless steels and are developed as the next generation of metallic implants [14, 56].

High nitrogen content may cause precipitation of nitrides and degrade the corrosion resistance due to localized chromium depletion. Moreover, increased nitrogen content increases brittleness of the steel and ductile to brittle transition [56]. To avoid brittleness, usually nitrogen content is tried to be kept below 0.9 mass% for medical applications.

The passivity of stainless steels is enhanced by modifying the chemical composition and morphology of the oxide layer [66]. The oxide film formed on surgical steels is generally rich in Cr_2O_3 [67, 68]. In fact, the metal ion release from different grades of stainless steels depends on the Cr content of the film, which is responsible for passive film formation. It has been shown that with the increase in Cr/(Cr + Fe) ratio in passive film, the metal ion release from stainless steel into artificial lysosomal fluid decreases [69–71].

In general, the passivation process applied to stainless steels like thermal, electrochemical, and nitric acid treatment changes the composition of the oxide. Depending on the process, Cr-rich oxide [72, 73], Fe-rich oxide [74], and mixture of Fe and Cr oxide [75], Fe-Cr oxyhydroxide [76], or hydrated Cr-rich oxyhydroxide are obtained.

In addition to types of surface oxides, investigations have shown that thickness of the oxide layer plays a lesser role than the uniformity and structure of the oxide layer. Studies carried out on 316 L stainless steel have revealed that amorphous oxide film has higher corrosion resistance compared to the polycrystalline oxide layer [77]. The surface film crystalline defects act as active sites for corrosion. The absence of grain boundary, defects, and dislocations on amorphous oxide film provide the lowest current density and absence of breakdown potential, which minimizes the release of metallic ions [79, 80].

Chromium, molybdenum, nitrogen, and titanium in stainless steels are adjusted to improve corrosion resistance. For example, in a chloride-containing solution, the corrosion resistance of stainless steels is improved by the presence of Cr and Mo in the steel. Mo inhibits corrosion process by increasing the stability of passive film due to formation of protective molybdenum oxide film beneath the hydrated chromium-rich oxide film [2, 14]. The addition of titanium and nitrogen elements also improves the corrosion resistance of stainless steels. Corrosion studies conducted in Hanks' solution [15, 81] exhibited higher resistance for titanium-modified 316 L stainless steel compared to the commonly used 316 L, which was attributed to the enrichment of chromium and bound water in the form of OH^- ions at the outermost layer of the passive film. Likewise, addition of nitrogen increases resistance to pitting corrosion of stainless steels by dissolution of nitrogen at the pit site and subsequent formation of ammonium ions NH^{4+} and NO^{3-} in the metal/film interface which increases pH and thus slows down pit growth kinetics [82]. As well as the nature of the film, the presence of inclusions like MnS in stainless steel induces pitting corrosion since pits initiate on the inclusions.

12.6 Corrosion of Titanium and Its Alloys

Titanium and its alloys are frequently used in biomedical applications due to especially their good corrosion resistance, biocompatibility, greater specific strength, and much lower elastic modulus than the other metallic biomaterials. The

Table 12.6 Commonly used biomedical titanium alloys

Material	Standard	Alloy type
Commercially pure Ti (CP grades 1–4)	ASTM 1341	α
Ti-6Al-4V ELI (wrought)	ASTM F136	α + β
Ti-6Al-4V ELI (standard grade)	ASTM F1472	α + β
Ti-6Al-7Nb (wrought)	ASTM F1295	α + β
Ti-5Al-2.5Fe	–	α + β
Ti-13Nb-13Zr (wrought)	ASTM F1713	Metastable β
Ti-12Mo-6Zr-2Fe (TMZF)	ASTM F1813	β
Ti-35Nb-7Zr-5Ta (TNTZ)	–	β
Ti-29Nb-13Ta-4.6Zr	–	β
Ti-35Nb-5Ta-7Zr-0.4O (TNZTO)	–	β
Ti-15Mo-5Zr-3Al	–	β
Ti-Mo	ASTM F2066	β

Reprinted with the permission from Ref. [4]. Copyright (2009) Elsevier Science

applications of titanium and its alloys cover dental implants and parts for orthodontic surgery, joint replacement parts, bone fixation materials, housing device for the pacemakers and artificial heart valves, surgical instruments, and components in high-speed blood centrifuges [4, 83, 84]. Unlike many other types of materials, there is no general rule for corrosion resistance of titanium and its alloys such that they may corrode either very quickly or extremely slowly depending on the material properties and medium characteristics.

Table 12.6 summarizes the commonly used biomedical titanium and its alloys. Apart from the listed titanium alloys, the equiatomic intermetallic compound of TiNi which exhibits shape memory and superelastic properties is also used as biomaterial for fixation of bone fragments, anchoring of implants and dentures to the living tissues, and poisoning of tissues [85].

Titanium is known for its high corrosion resistance due to instant formation of an inert oxide layer on its surface. Titanium commonly consists of mainly TiO_2 in Ti alloys and corrosion resistance of the titanium results from this native titanium oxide [12, 67, 68, 86–90]. The film on titanium, which is typically 3–7 nm thick, consists of amorphous or crystalline anatase or rutile (TiO_2) with tetragonal structure. O to Ti concentration ratio varies gradually from 2 to 1, from the TiO_2 film to a much lower ratio in the bulk [85, 91–97].

The most stable form of titanium is the oxidation state IV (Ti^{4+}). However, when it reacts with water, hydrated titanium dioxide ($TiO_2 \cdot nH_2O$) is seen as the stable product other than $Ti(OH)_4$. Since these processes are pH and potential dependent, the pH and potential values of physiological systems should be considered to determine whether the passivation is achieved or not in vitro or in vivo. Pourbaix diagrams are useful in determining the passivity formation under various combinations of pH and potentials.

Although it is reported that the passive layers on Ti alloys are not different from that on pure Ti [98], some authors [99–102] state that the oxide layer in α- + β-alloys,

like Ti6Al4V or Ti6Al7Nb, contains oxides of the alloying elements. For example, relatively higher corrosion resistance of Ti6Al7Nb compared to Ti6Al4V alloy is attributed to the formation of Nb_2O_5, which is chemically more stable, less soluble, and more biocompatible compared to V_2O_5 formed on Ti6Al4V alloy [4]. The rate of ion transfer, stability of the oxide film against dissolution, and spontaneous regeneration in milliseconds even after damage determine the protectiveness of the passive film. The presence of defects, thickness, structure, and chemical composition of the film influence the ion transport. On the other hand, the nature and stability depend on medium conditions such as temperature and time of exposure, pH, and composition of the fluid surrounding the metal and redox reactions [7]. For example, TiO_2 is thermodynamically stable in the pH range between 2 and 12, and only complexing species, such as HF or H_2O_2, lead to substantial dissolution. Thus, the oxide film becomes thermodynamically unstable and dissolves if the interface potential is made negative or pH is made low, and this results in the dissolution of the oxide layer. Additionally, the corrosion resistance of the passive film is altered by the variation in the ionic or electrical conductivity of the film or by the structural changes in the film due to alloying elements. For example, by dissolution of vanadium oxide in Ti6Al4V alloy, vacancy generation and diffusion occur in the oxide layer [103]. However, Ti-Ta alloys exhibit relatively better corrosion resistance compared to Ti6Al4V by reducing the concentration of metal release as a result of strengthening the TiO_2 passive film with the aid of a more stable Ta_2O_5 passive film. Similarly, the surface film of Ti-based alloys is stabilized when Nb alloying element is used. The formation of highly stable Nb-rich oxide enhances corrosion resistance, and by the Nb addition, an improvement in the passivation property of the surface film is detected by decreasing the concentration of anion vacancies [104].

Titanium and its alloys show very high pitting potentials in chloride-containing solutions. Therefore, stable pitting corrosion is not a relevant failure mode for these materials in biomedical applications since the relevant potential region in the body is clearly <1 V. Nevertheless, metastable pitting corrosion has been observed for CP Ti and for the Ti6Al4V implant alloy in simulated physiological solutions [105]. Under certain conditions due to wear and fretting and/or due to biochemical factors, localized breakdown of passivity takes place. As a result of corrosion, ion release occurs if the destroyed oxide film remains unrepaired. The amount of metallic ions released during the period depends on the regeneration rate of the film. Spontaneous regeneration of the oxide layer in milliseconds even after damage makes titanium advantageous over the other metallic materials [106–108]. However, ions are detected in the tissue around a titanium implant [109–113] mainly due to continuous activation/repassivation which resulted from combined mechanical and chemical effects. Additionally, titanium ions may also be released from the separately implanted bone plate and screws due to biochemical factors like amino acids and proteins [111–115].

Under in vivo conditions, transient microscopic breakdown of the oxide layer was described to occur in Ti alloys [116, 117]. CP Ti exhibits lower current densities than TiAl6V4 and several β- and near-β-alloys [116]. Only the Ti-30Ta alloy (Ti30Ta) shows a value near that of CP Ti. Either way, there are reactions between

the surface and the surrounding liquid, which lead to a thickening of the oxide layer in vivo [94, 118]. These reactions result in a release of species containing Ti and/or, possibly, alloying elements, into the surrounding tissue and in the adsorption of oxygen-containing species from the biological liquids to the surface. The corrosion resistance of CP Ti, the α + β-alloy, TiAl6V4, and various β- and near-β-alloys could be improved by increasing the oxide thickness to around 100 nm, independent of the oxidation procedure [117, 119]. The release of alloying elements can lead to toxic, allergic, and idiosyncratic symptoms. For the Ti-based (TiAlV, TiAlNb, Ti15Zr4Nb4Ta) alloys, mostly Ti is released, but for TiAlV alloys, significant amounts of Al and a small amount of V could be detected. Since vanadium is toxic in the elemental state, new beta titanium alloys with nontoxic alloying elements like Ta, Nb, and Zr have been developed. Although the amounts of Ti and Al release are similar for both TiAlV and TiAlNb alloys, the quantity of Ti released from the TiZrNbTa alloy is much smaller than the quantity released from the TiAl–(V, Nb)-type alloys [7]. It is reported that the addition of Ta remarkably reduces the concentration of the metal release [44, 120–122]. Survival of released ions for a long time in the body fluid and the type of species combined to release metallic ions are important from a toxic point of view. The biomolecules do not contain titanium and comparatively large protein and enzyme molecules hardly react with titanium ions. Titanium oxide and salts are immediately formed as a result of reacting the titanium ions with water molecules and anion species. However, formation of complexes with organic ions such as amino acids survives in body fluids and has a high possibility of combining with biomolecules [123].

Nickel, at certain concentrations, leads to severe local tissue irritation, necrosis, and toxic reactions. However, in vivo and in vitro studies of NiTi implants show excellent biocompatibility [124–126]. There are few reports on release of Ni, but the amount of released nickel is not sufficient to induce such reactions [127]. Titanium alloys tend to repassivate faster than the stainless steel and other biomedical alloys; however, repassivation of titanium in vivo is slower than in vitro. The type of ions in the repassivated layer plays a deciding factor for corrosion resistance. The composition of the surface film changes with environment in which it is existing [128]. For example, after mechanical destruction, the regenerated surface oxide film on titanium in Hanks' solution was observed to contain calcium phosphate in the outer layer [128].

Apart from the regeneration after mechanical damage, the surface oxide of titanium is not always stable, and its composition changes through the incorporation of ions and molecules in vivo. Similar to passive film on stainless steel, titanium oxide film near the body fluid dissolves partially and reprecipitates. Calcium, phosphorus, and sulfur are incorporated in the film on titanium. As a result calcium phosphates are precipitated on titanium and its alloys in a simulated body fluid [95, 129–131]. Proteins are also incorporated into the reconstructed surface oxide in addition to calcium, phosphorus, and sulfur [132]. There are several methods like thermal, anodic oxidation and the sol–gel process which aim in thickening the oxide layer to get around 100 nm thickness, thereby optimizing the resistance against mechanical damage and corrosion [119, 133–136]. The methods change the chemical

composition along with the structure of the oxide layer. Although thermal oxidation induces predominantly TiO_2 in the rutile structure for pure titanium and titanium alloys, in certain β-alloys, mixed oxides of titanium are observed. On the other hand, in electrochemical methods depending on the anode potential and type of electrolyte solution, either amorphous or crystalline oxides are formed [119, 136]. Though titanium and its alloys are highly resistant to pitting corrosion under different in vivo conditions, they undergo corrosion in high-fluoride solutions in dental cleaning procedures [137].

12.7 Corrosion of Cobalt-Based Alloys

By the early 1930s, a cobalt–chromium (CoCr) alloy, called Vitallium, was introduced to dentistry as an alternative to gold alloys. CoCr alloys have been used as dental and orthopedic implant materials for fabrication of hip prostheses and internal fixation plates. The wear resistance of CoCr alloys is better than that of stainless steel and titanium (Ti) alloys and it has been shown that their corrosion resistance is better than that of stainless steel. The main disadvantage of CoCr alloys is their low ductility. The chromium enhances corrosion resistance as well as solid solution strengthening of the alloy. In orthopedics, CoCr–molybdenum (Mo) alloys are used for the head and stem of artificial joints, and CoCr–tungsten (W)–nickel (Ni) alloys (HS25) function as bone fixation wires. In dentistry, CoCrMo alloys, CoCrNi alloys, and CoCrNi–copper (Cu) alloys are applied for denture bases, and CoCr–iron (Fe)–Ni alloys are utilized for orthodontic wire.

The CoNiCrMo alloys are relatively new, now used for making the stems of prostheses for heavily loaded joints. The molybdenum is added to produce finer grains, which results in higher strengths after casting or forging. 5–7 wt% Mo in the alloy provides solid solution strengthening and good localized corrosion resistance. The alloy has an oxide layer on its surface, which forms a thin passive film that is enriched with chromium that gives very good corrosion resistance [138–141]. The CoNiCrMo alloy, originally called MP35N (Standard Pressed Steel Co.), contains approximately 35 mass% Co and Ni each. The alloy is highly corrosion resistant to seawater (containing chloride ions) under stress. The superior fatigue and ultimate tensile strength of the CoNiCrMo alloys make it suitable for the applications, which require long service life without fracture or stress fatigue. In the cardiovascular field, CoCr alloys are used for guide wires, while CoCrFeNi alloys, CoNiCrMo alloys (MP35N), and CoCrNiWFe alloys are used for stents. CoCr–tantalum (Ta)–Ni alloys and CoCrNiMoFe alloys are used for aneurysm clips [142]. Consequently, the alloys have become one of the three major biomedical metallic materials and the alloys have been used for many decades in dentistry and, relatively recently, in making artificial joints [143, 144].

Lin et al. [145] investigated the changes in surface oxides of the CoCrMo alloy by biological and cellular environments. Results show that increase in alloy surface oxides increases in vivo corrosion resistance of the alloy. Chromium oxides increase

the corrosion resistance of CoCrMo alloys in which heat and nitric acid passivation treatments enhanced alloy surface oxide thickness and raised the O and Cr contents to reduce corrosion [146, 147]. The biologically mediated modifications in surface oxides may affect corrosion of the implant devices [148–150].

The greater number of CoCrMo alloys possess good corrosion resistance and the corrosion resistance of alloys increases with Cr content, where Ni content has insignificant effect [151]. Hanawa et al. [128] characterized the surface oxide films on a CoCrMo alloy located in various environments to estimate their construction of the film in the human body. Results revealed that chromium and molybdenum were more widely distributed in the inner layer than in the outer layer of the oxide film. The result indicates that CoCrMo alloy releases cobalt. Hiromoto et al. [152] investigated the corrosion behavior and microstructure of low-Ni Co29Cr6.8Mo (mass%) alloys and a conventional Co29Cr6Mo1Ni alloy in saline solution, Hanks' solution, and cell culture medium. The current densities of the new low-Ni alloys are lower than those of the ASTM alloy, which demonstrate that the new low-Ni alloys can show as high corrosion resistance as that of the conventional ASTM alloy in the human body.

The hip resurfacing joint, which has "metal-on-metal" articulation between a metal cover on the femoral head and a metal-lined acetabular cup, is made of CoCrMo because of its corrosion and wear resistance. However, when implanted into the body, the metal-on-metal joint will experience tribocorrosion. Bellefontaine [153] suggested the heat treatment of the alloy could affect its resistance to tribocorrosion and the release of metal ions. After conducting anodic polarization curves in a range of different environments, the only consistent difference was seen in ringers and bovine serum solution acidified to pH 2. Double heat-treated samples were shown to be more susceptible to corrosion than the as-cast sample.

According to the carbon level, there are two types of CoCrMo alloys used for biomedical applications. However, both alloys have a balance of cobalt, which can be as low as 60 wt%. There is approximately 28 mass% chromium that forms a chromium-rich passive oxide film (Cr_2O_3) that spontaneously forms on the surface of the metal [20, 154, 155]. This gives good corrosion resistance by separating the metal from the air and aqueous environments [20, 21].

During the solidification process, carbides in the microstructure give strength and wear resistance by taking up Cr and Mo. Once CoCrMo alloys have undergone heat treatment, the carbides then remain richer in Cr and Mo. This then deprives the softer matrix of these important corrosion-resistant elements [156, 157]. Kauser et al. [158] demonstrated that double heat-treated samples had a higher corrosion rate than as-cast samples that was attributed to the Mo depletion as a result of the heat treatment. Codaro et al. [154] studied in vitro mechanism of corrosion in the case of CoCrMo alloys. Under the same experimental conditions, the corrosion resistance of CoCrMo alloy in 0.15 NaCl was higher than the cobalt and chromium.

CoCrMo alloy has been studied in inorganic solution and in serum to obtain an insight into the influence of serum on the corrosion reactions in the active state, the corrosion current, and the repassivation rate of the alloy. As a result, the serum

inhibits the hydrogen evolution reaction and generates a diffusion barrier that causes the anodic dissolution of the alloy to be under diffusion control. As a result, both in serum and inorganic buffer solutions, the corrosion current of CoCrMo alloy is higher at acidic pH than at neutral pH. One of the most important findings of the study is the corrosion current recorded in serum is significantly lower than that observed in inorganic solutions at both pHs [159].

Metikos-Hukovic [160] studied the corrosion resistance of both the cobalt and the Co30Cr6Mo alloy and the properties of the surface oxide layer in a simulated physiological solution (Hanks' solution) with a pH of 6.8. The results show that the surface layer does not adequately protect the metal against corrosion. Corrosion resistance of cobalt increases by increasing the anodic potential, but at higher anodic potentials, cobalt undergoes pitting corrosion caused by the presence of chloride and bicarbonate ions in the solution. Corrosion resistance of cobalt in the alloy is significantly increased due to the beneficial effect of chromium.

12.8 Corrosion of Coated Metallic Biomaterials

It can be concluded from the aforementioned results that corrosion and release of ions may provoke not only to mechanical failure of implant but also to local pain and swelling in the body. Thus, the implants need specific surface modification in order to minimize the adverse effects. There are many methods for coating of metallic based implant materials, such as plasma spray coating [161], sputter coating [162], electron deposition [163], sol–gel route [164, 165], electrolytic deposition [166, 167], electrophoretic deposition [168], and cold spray [169, 170].

The plasma spray technique was frequently used for the coating of metallic implants due to the process feasibility and the retention of the properties of source powder. However, extremely high temperature was used in the process. In view of the corrosion, it can vastly cause potentially serious problems in the complex implant coating such as internal cavities, porosity, unmelted or partially melted inclusions, and residual stress at the interface due to mismatch of thermal expansion coefficients of the coating and substrate, which result in the alterations of corrosion behavior of the implant [171, 172]. To overcome some disadvantages with the plasma-sprayed coatings, magnetron sputtering (ion beam) has been developed. Ion beam techniques such as ion implantation, ion beam-assisted deposition, and ion beam sputter deposition as a surface modification and coating technique have benefits such as excellent controllability, versatility, and possibility of low process temperature. A drawback of ion beam techniques is their line-of-sight character, and the effectiveness of corrosion protection strongly depends on the deposition process parameters [173, 174]. Electrochemical deposition, or electrodeposition for short, is increasingly being used for the preparation of thin films and coatings. Electrodeposition offers rigid control of film thickness, uniformity, and deposition rate and is especially attractive owing to its low equipment cost and starting materials. Nowadays, the sol–gel route appears as a very promising technique. It is a low-cost process and it is relatively

easy to control the deposition parameters. Another benefit of sol–gel process is to make coatings with properties depending on the required application [175, 176]. Electrophoretic deposition has significant speciation in the deposition of complex compounds and ceramic laminates. It revealed that electrophoretic phenomena have distinctive features for relatively large particles (several micrometers) and for particles on a submicron scale. Nevertheless, it is the need for a high-temperature heat treatment that has discouraged commercial use of this approach particularly for applications where long-term coating retention is required. Cathodic plasma electrolytic deposition (CPED), as a new surface modification method, has been developed to produce nanocrystalline graphite films, diamond-like carbon films, and ceramic coating on the surfaces of metal and its alloys [177].

The cold spray process provides attractive alternative coatings because of the easy formation of crystalline films at relatively low temperature, offering the possibility to tailor microstructures. The main advantages of cold spray coatings are strong bonding with substrate and no phase transformation retaining the original structure of feedstock [178–180]. Therefore, the process recently becomes more attractive to deposit highly reactive materials such as Ti and Mg and dissimilar materials. The deposition of stainless steel (SS) powder by cold spray process has great potential for application such as biomedical, high-temperature oxidation, and corrosion protection. Moreover, the cold spray process was found viable for the development of a new class of metallic biomaterials. The coating cold sprayed with mixing SS and Co powders showed lower corrosion rate than bulk SS material, which is considered for a new stent material [6, 170, 181].

Generally speaking, inclusions, second phase precipitations, grain boundaries, porosities, and cracks in the coating layer act as preferential sites for corrosion starting points [182]. It can be concluded from the literature that the most effective parameter on the corrosion susceptibilities of the coating implants is the intermetallic phases. These intermetallic phases frequently have solution potentials differing from that of the coating alloy in which they occur; localized galvanic cells may be formed between them and the coating alloy. Thus, these phases are cathodic to the coating and decrease resistance to corrosion in aqueous saline media. Also, corrosion susceptibilities of the coatings increase with increasing volume fraction of the inhomogeneity due to the increasing galvanic interactions.

Surface cracks for a coating have a detrimental effect since the integrity of surface cannot be sustained for long periods. The cracks that are generated in the coatings are the areas where the physiological environment (body fluid) is stagnating. Thus, these areas will act as anode and the environment of the cracks (crack-free region) will act as cathode. The interior crack pH will be decreased compared to the body pH and Cl^- ion concentration [22]. Consequently, it is proposed that the cracks are considered as weak regions in the coating structure. This may cause an increase in the solubility of the coating layer. As a result, the corrosion mechanism will occur which is the most detrimental where the corrosion extended in depth.

Most researches on coatings used for medical devices aim at increasing the corrosion resistance of metal implants. The corrosion resistance of the AISI 304 stainless steel increased after deposition of plasma-sprayed hydroxyapatite (HA + 20

wt% SiO_2) compared to uncoated, plasma-sprayed HA + 10 wt% SiO_2 and only HA coatings on AISI 304. Because, at the surface of HA + SiO_2 coating, the flattening ratio of spreading splats is more and number of unmelted particles of HA is less, that makes coating surface denser and less porous. It is known that the lesser the porosity is, the more corrosion resistance will be and all the coatings are crack-free after 24 h dipping in Ringer's solution for electrochemical corrosion testing [183]. Metikos-Hukovic et al. [184] showed that well-crystallized hydroxyapatite coatings obtained from sol–gel demonstrate a significant corrosion protection effect on the titanium substrate during long-term exposure to HBSS. In another study, Lavos-Valereto et al. [185] revealed the electrochemical behavior of Ti6Al7Nb alloy with and without plasma-sprayed hydroxyapatite coating in Hanks' solution and showed that the corrosion rate of coated samples is more than two times larger than that of uncoated ones.

These selected studies illustrate the number of variables involved in the implant failure and corrosion process. However, it is also important to see the effects of coating thickness on adhesion and corrosion that coated onto commonly used substrates via a fast and flexible dipping method. Aksakal et al. [164] studied the corrosion susceptibilities of Ti6Al4V and 316 L SS substrates coated with hydroxyapatite by sol–gel method. It was observed that the coating thickness was an effective parameter on both adhesion between the coating and material and corrosion resistance. It was shown that adhesion and corrosion resistance decreased with increasing coating thickness on both substrates. Dikici et al. [182] have investigated the effect of coating arc current on the corrosion behavior of NiTi coating on stainless steel. NiTi powder mixture was coated on the surface of austenitic AISI304 using a plasma-transferred arc (PTA) method. Results indicate that corrosion resistances of the coatings decrease with increasing arc current.

12.9 Corrosion of Degradable and Hybrid Metallic Biomaterials

Polymers are known to be degradable biomaterials for a while; however, to use metals as degradable biomaterials is a relatively new idea. For certain applications of implant materials such as bone fixation pine or screws and for cardiovascular stents, high mechanical properties are needed where metals are better candidates than biodegradable polymers [186] Moreover, biodegradable metals can be applied compared to traditional biodegradable materials such as polymers, ceramics, or bioactive glasses in load-bearing applications where a higher ultimate tensile strength and a modulus of elasticity that is closer to the bone are needed [187].

Interest to degradable metallic biomaterials research has been growing and a number of scientific journals and patents regarding them are increasing since 2000 [188]. Especially, metals which consist of trace elements that exist in the human body are promising candidates [187]. Magnesium alloys and iron-based alloys are the two classes of degradable metal [186].

Metals have been used as corrosion-resistant materials; however, using biodegradable metals breaks this paradigm [187]. Corrosion is known as a failure in metallurgical engineering. On the other hand, corrosion can be positive in the area of biodegradable metallic implants for magnesium and iron. These metals can degrade in the human body without toxic effects after finishing their job as implants. In addition, they can be applied as temporary implantable nanomedical devices such as sensors and actuators [189].

Biodegradable metallic stents (coronary stents), which have temporary function in the body, are one of the main application areas for degradable metals. Biodegradable metallic stents will provide a temporary opening for arterial vessel until the vessel remodels and will finally disappear. Biodegradable metallic stents have been tried for preclinical tests in humans since 2000. An ideal biodegradable stent has to compromise its degradation and mechanical integrity during implantation. Usually, degradation begins at a very slow rate in a total time of 6–12 months without causing an intolerable accumulation of degradation on the surface. A total time of 12–24 months is needed for total degradation. Therefore, not only the stent material but also the interaction with surrounding implantation sites is critical [188]

Iron-based biodegradable implants include pure Fe and Fe-Mn alloys. These alloys are mainly proposed for cardiovascular applications [186]. The first biodegradable iron-based metallic stent was pure iron (Fe > 99.8 %) and implanted in the descending aorta of New Zealand white rabbits in 2001. Iron can interconvert between Fe^{2+} and Fe^{3+} ions by accepting or donating electrons, which is useful for cytochromes, hemoglobin, myoglobin, and most enzymes. Iron has high mechanical properties. It has a high radial strength due to its high Young's modulus. This property is useful to achieve thinner struts. Iron's high ductility also helps the implantation process where the stent is heavily plastically deformed. There are several researches to increase the degradation rate of iron-based stents such as alloy development and thermomechanical processes, which were summarized elsewhere [189], compared to those of pure (Armco®) iron, which had already been tested in vivo and to 316 L SS which is the gold standard stent material.

Magnesium alloys are the second type of biodegradable metallic implants. They have low thrombogenicity and are known to be biocompatible. Magnesium as an element is an essential trace element and has a high systemic toxic level (7–10 millimoles/liter of serum). It is also a structural constituent of the tissue, an essential element in the living organism, and a noncarcinogenic element. On the other hand, pure magnesium degrades rapidly in body fluid where there is aggressive chloride environment. Accordingly, magnesium is alloyed with other elements such as aluminum, manganese, and rare earth elements to slow down the degradation process [189]. After invention of metallic magnesium by Sir Humphry Davy in 1808, biodegradable magnesium-based metal implants were first used in 1878 in the form of wires as ligature for bleeding vessels by the physician Edward C. Huse [190].

Magnesium alloys have also been investigated as bone implants as screws, plates, or other fixture devices. Magnesium powders have been investigated for vertebral fusion in spinal surgery of sheep, and open-porous magnesium alloy scaffolds were used as load-bearing biomaterials for tissue engineering [187]. Heublein and friends

[191] were the first to use magnesium alloys for cardiovascular stents. They used magnesium AE21 alloy where 50 % mass loss was expected during the first 6 months. However, the degradation occurred faster as the loss of mechanical integrity occurred only after 35–56 days after implantation. Four different new generations of biodegradable (AMS) stents were developed by the Biotronik company (Bulach, Switzerland). Di Mario et al. [192] reported the results of experimental results made from WE43 magnesium alloy. Peeters et al. [193] reported the results of the first clinical study of stent implantation in humans for the treatment of critical lower limb ischemia of 20 patients. It was observed that there were no symptoms of allergic or toxic reactions. Another and more recent study on the implantation of the same biodegradable magnesium stent in the lower limb artery of 60 patients demonstrated short-term life (less than 6 months). The first successful implantation of a biodegradable metal stent (Biotronik) in humans was performed by Zartner et al. [194] in the left pulmonary artery of a preterm baby with a congenital heart disease. Usually, biodegradable magnesium alloys have lower mechanical properties and faster degradation than iron-based biodegradable metal alloys.

12.10 Corrosion of Nanostructure Metallic Implants

Lately, there is an increasing interest on fine-grained materials due to their excellent mechanical and corrosion properties. Most of the investigations depend on understanding the corrosion behavior of the nanocrystalline materials in comparison to other materials. Bulk nanostructured materials or in our case metals (BNM) are pure metals, metallic alloys, intermetallics, and composites [195].

Severe plastic deformation (SPD) is a common technique for the fabrication of pure metals, metal alloys, and intermetallics with submicron grain structures. Some may have even nano-sized grains in which case the structure is called ultrafine grained (UFG). Severe plastic deformation processes have some size and geometry limitations due to their designs. Moreover, they are generally discontinuous processes where the production efficiency is low and labor costs are high. However, these disadvantages can be tolerable for implant applications. Therefore, SPD techniques are now moving from laboratories to commercial production of ultrafine-grained metals for metallic implant applications [195, 196]. The use of SPD-processed alloys as biomedical implant materials depended on Valiev et al. [197]. In order to prevent the side effect from the implant, high-strength pure Ti without any alloying elements was produced. When the coarse-grained (CG) and UFG materials were compared in microstructure perspective with osteogenetic cell reactions, in vitro and in vivo conditions of UFG have no detrimental effect. Also, Saldana and coauthors studied on UFG Zr, and they observed that biocompatibility of bio-inert alloys cannot be changed by the SPD application [198]. Thorpe et al. [199] have shown that ultrafine-grained and nanostructured materials may possess better corrosion properties than those of coarse-grained materials. On the other hand, it has been reported that the corrosion behavior of ultrafine-grained pure Cu is not considerably

different from that of coarse-grained pure Cu. Moreover, Rofagha et al. [200] have reported that the corrosion resistance of a nanostructured Ni–P alloy was lower than that of its coarse-grained one. Therefore, according to these reported results, the effect of ultrafine-graining and nanostructuring on corrosion resistance differs among metallic materials.

It was observed that the corrosion resistance of a nanocrystalline Ni–P alloy is lower than that of its CG counterpart. Also, it was examined that the corrosion behavior of UFG Cu processed by ECAE is not effected as coarse-grained (CG) polycrystalline Cu. Tafel tests showed that UFG copper produced by ECAE had lower corrosion current under natural corrosion conditions. It is speculated that the dilution of impurity content of grain boundaries is responsible for lower corrosion rate [201, 202].

The ECAPed (equal-channel angular pressing) UFG bulk pure copper with about 380 nm grains was tested by electrochemical methods in Hanks' solution. It was observed that it had a higher corrosion current density compared to conventional copper sample. During immersion, only CuO_2 was observed as corrosion product [203]. In a study of Branislav group with ECAPed UFG interstitial-free steel material, it was observed that the pitting potential in the 0.9 M NaOH alkaline medium with 5 % Cl^- rose as grain size dropped. It was stated that the protective passive layer in UFG material was more stable compared to conventional material [204]. UFG NbZr alloy was also studied by Rubitschek et al., and their results showed remarkable corrosion resistance [198].

Clearly, there is a strong connection between corrosion resistance and microstructural features of metallic materials, including grain diameter and states of grain boundary and secondary phases [205]. Therefore, these investigations clearly showed that the grain size of the metal plays an important role for developing the corrosion properties.

References

1. Williams DF (1998) Medical and dental materials, vol 14, Mater Sci Tech. VCH, Weinheim
2. Mudali KU, Sridhar TM, Raj B (2003) Corrosion of bio implants. Sadhana 28:601–637
3. Zhen Z, Xi T, Zheng Y (2013) A review on in vitro corrosion performance test of biodegradable metallic materials. Trans Nonferrous Metal Soc 23:2283–2293
4. Geetha M, Singh AK, Asokamania R, Gogia AK (2009) Ti based biomaterials, the ultimate choice for orthopaedic implants. Prog Mater Sci 54:397–425
5. Ratner BD, Hoffman AS, Schoen FJ, Lemons JE (2004) Biomaterials science: an introduction to materials in medicine. Elsevier/Academic, San Diego
6. Williams DF (1994) Titanium: epitome of biocompatibility or cause for concern. J Bone Joint Surg 76:348–349
7. Virtanen S, Milošev I, Gomez-Barren E, Trebše R, Salo J, Konttinen YT (2008) Special modes of corrosion under physiological and simulated physiological conditions. Acta Biomater 4:468–476
8. Okazaki Y, Gotoh E (2008) Metal release from stainless steel, Co–Cr–Mo–Ni–Fe and Ni–Ti alloys in vascular implants. Corros Sci 50:3429–3438

9. Bauer S, Schmuki P, Mark K, Park J (2013) Engineering biocompatible implant surfaces: part I: materials and surfaces. Prog Mater Sci 58:261–326
10. Mears DC (1975) The use of dissimilar metals in surgery. J Biomed Mater Res 9:133–148
11. Zsklarska-Smialowska Z (1986) Pitting corrosion of metals. National Association of Corrosion Engineers, Houston
12. Fraker AC (1987) Corrosion 13. ASM International, Ohio, USA
13. Virtanen S, Curty C (2004) Metastable and stable pitting corrosion of titanium in halide solutions. Corrosion 60:643–649
14. Sumita M, Hanawa T, Teoh SH (2004) Development of nitrogen-containing nickel-free austenitic stainless steels for metallic biomaterials—review. Mater Sci Eng C 24:753–760
15. Sivakumar M, Mudali KU, Rajeswari S (1994) Investigation of failures in stainless steel orthopaedic implant devices: fatigue failure due to improper fixation of a compression bone plate. J Mater Sci Lett 13:142–145
16. Yu J, Zhao ZJ, Li LX (1993) Corrosion fatigue resistances of surgical implant stainless steels and titanium alloy. Corros Sci 35:587–597
17. Syrett BC, Wing SS (1978) An electrochemical investigation of fretting corrosion of surgical implant materials. Corrosion 11:379–386
18. Lutz J, Mändl S (2010) Reduced tribocorrosion of CoCr alloys in simulated body fluid after nitrogen insertion. Surf Coat Technol 204:3043–3046
19. More NS, Diomidis N, Paul SN, Roy M, Mischler S (2011) Tribocorrosion behavior of β titanium alloys in physiological solutions containing synovial components. Mater Sci Eng C 31:400–408
20. Sinnett-Jones PE, Wharton JA, Wood RJK (2005) Micro-abrasion–corrosion of a CoCrMo alloy in simulated artificial hip joint environments. Wear 259:898–909
21. Yan Y, Neville A, Dowson D, Williams S (2006) Tribocorrosion in implants—assessing high carbon and low carbon Co–Cr–Mo alloys by in situ electrochemical measurements. Tribol Int 39:1509–1517
22. Reclaru L, Lerf R, Eschler PY, Blatter A, Meyer JM (2002) Pitting, crevice and galvanic corrosion of REX stainless-steel/CoCr orthopedic implant material. Biomaterials 23:3479–3485
23. Willert HG, Broba LG, Buchhorn GH, Jensen PH, Koster G, Lang I (1996) Crevice corrosion of cemented titanium alloy stems in total hip replacements. Clin Orthop Relat Res 333:51–75
24. Pholer OEM (2002) ASM Handbook 11. ASM International, Ohio, USA
25. Okazaki Y, Kyo K, Ito Y, Tateishi T (1997) Effect of friction on the corrosion resistance for implant alloys in physiological saline solution. J Jap Inst Met 38:344–352
26. Imam MA, Fraker AC, Brown SA, Lemons JE (1996) Medical applications of titanium and its alloys: the material and biological issues, ASTM STP 1272. American Society for Testing and Materials, Philadelphia, pp 3–16
27. Sumita M (1997) Present status and future trend of metallic materials used in orthopedics. Orthop Surg 48:927
28. Takazawa K, Miyagawa H, Hariya A (2003) Metal allergy to stainless steel wire after coronary artery bypass grafting. Jpn Soc Artif Organs 6:71
29. Vahter M, Berglund M, Akesson A, Liden C (2002) Metals and women's health. Environ Res 88:145
30. Staffolani N, Damiani F, Lilli C, Guerra M, Belcastro S, Locci P (1999) Ion release from orthodontic appliances. J Dent 27:449
31. Pulido M, Parrish A (2003) Metal-induced apoptosis: mechanisms. Mutat Res 533:227
32. Black J (1981) Biomedical engineering and instrumentation. Marcel Dekker, New York
33. Yang K, Ren Y (2010) Nickel-free austenitic stainless steels for medical applications. Sci Technol Adv Mater 11:13
34. Clayton CR (1986) Passivity mechanisms in stainless steels: Mo–N synergism. Report No. N00014-85-K-0437, New York

35. Mudali UK, Dayal RK, Gnanamoorthy JB, Rodriguez P (1996) High nitrogen steels. Relationship between pitting and intergranular corrosion of nitrogen-bearing austenitic stainless steels. Mater Trans 37:1568–1573
36. Sakamoto T, Abo H, Okazaki T, Ogawa T, Ogawa H, Zaizen T (1980) Alloys for the eighties. Climax Molybdenum Co., Greenwich
37. Hennig FF, Raithel HJ, Schaller KH (1992) Nickel-, chrom- and cobalt-concentrations in human tissue and body fluids of hip prosthesis patients. J Trace Elem Electrol Health Dis 6:239–243
38. Pazzaglia UE, Minoia C, Gualtieri G, Gualtieri I, Riccardi C, Ceciliani L (1986) Metal ions in body fluids after arthroplasty. Acta Orthop Scand 57:415–418
39. Sunderman FW Jr, Hopfer SM, Swift T, Rezuke WN, Ziebka L, Highman P, Edwards B, Folcik M, Gossling HR (1989) Cobalt, chromium, and nickel concentrations in body fluids of patients with porous-coated knee or hip prostheses. J Orthop Res 7:307–315
40. Jacobs JJ, Skipor AK, Patterson LM, Hallab NJ, Paprosky WG, Black J, Galante JO (1998) Metal release in patients who have had a primary total hip arthroplasty. A prospective, controlled, longitudinal study. J Bone Joint Surg 80-A:1447–1458
41. Schaffer AW, Pilger A, Engelhardt C, Zweymueller Z, Ruediger HW (1999) Increased blood cobalt and chromium after total hip replacement. Clin Toxicol 37:839–844
42. Bronder W, Bitzan P, Meisinger V, Kaider A, Gottsaune F, Kotz R (1997) Elevated serum cobalt with metal-on-metal articulating surfaces. J Bone Joint Surg 79-A:316–321
43. Ardlin BI, Dahl JE, Tibballs JE (2005) Static immersion and irritation tests of dental metal-ceramic alloys. Eur J Oral Sci 113:83–89
44. Steinemann SG, Revell P (1999) Materials for medical engineering, vol 2, Euromat'99. Wiley-VCH, Weinheim, pp 199–203
45. Zardiackas LD, Mitchell DW, Disegi JA, Lemons JE (1996) Medical applications of titanium and its alloys: the material and biological issues, ASTM STP 1272. American Society for Testing and Materials, Philadelphia
46. Wang KK, Gustavs LJ, Dumble JH, Lemon JE (1996) Medical applications of titanium and its alloys: the material and biological issues, ASTM STP 1272. American Society for Testing and Materials, Philadelphia
47. Mishra AK, Davidson JA, Poggie RA, Kovacs P, FitzGerald TJ, Lemons JE (1996) Medical applications of titanium and its alloys: the material and biological issues, ASTM STP 1272. American Society for Testing and Materials, Philadelphia, pp 96–113
48. Niinomi M (2008) Mechanical biocompatibilities of titanium alloys for biomedical applications. J Mech Behav Biomed Mater 1:30–42
49. Okazaki Y (2002) Effect of friction on anodic polarization properties of metallic. Biomaterials 23:2071–2077
50. Richard AC (2003) Laboratory corrosion testing of medical implants. ASM International, Newyark, Delaware, USA
51. Manivasagam G, Dhinasekaran D, Rajamanickam A (2010) Biomedical implants: corrosion and its prevention – a review. Recent Pat Corros Sci 2:40–54
52. Bundy KJ (1994) Corrosion and other electrochemical aspects of biomaterials. Crit Rev Biomed Eng 22:139–251
53. González JEG, Mirza-Rosca JC (1999) Study of the corrosion behavior of titanium and some of its alloys for biomedical and dental implant applications. J Electroanal Chem 471:109–115
54. Preetha A, Banerjee R (2005) Comparison of artificial saliva substitutes. Trend Biomater Artif Organs 18:178–186
55. JIS T 0302: Testing method for corrosion resistance of metallic biomaterials by anodic polarization measurement (2000) Japanese Industrial Standards, Japan
56. Talha M, Behera CK, Sinha OP (2013) A review on nickel-free nitrogen containing austenitic stainless steels for biomedical applications. Mater Sci Eng C 33:3563–3575
57. Ilevbare GO, Burstein GT (2001) The role of alloyed molybdenum in the inhibition of pitting corrosion in stainless steels. Corros Sci 43:485–513

58. Kanerva L, Forstrom L (2001) Allergic nickel and chromate hand dermatitis induced by orthopaedic metal implant. Contact Dermatitis 44:103–104
59. Torgerser S, Gilhuus-Moe OT, Gjerdet NR (1993) Immune response to nickel and some clinical observations after stainless steel miniplate osteosynthesis. Int J Oral Maxillofac Surg 22:246–250
60. Menzel J, Kirschner W, Stein G (1996) High nitrogen containing Ni-free austenitic steels for medical applications. ISIJ Int 36:893–900
61. Ren Y, Yang K, Zhang B (2005) In vitro study of platelet adhesion on medical nickel-free stainless steel surface. Mater Lett 59:1785–1789
62. Yamamoto A, Kohyama Y, Kuroda D, Hanawa T (2004) Cytotoxicity evaluation of Ni-free stainless steel manufactured by nitrogen adsorption treatment. Mater Sci Eng C 24:737–743
63. Montanaro L, Cervellati M, Campoccia D, Arciola CR (2006) Promising in vitro performances of a new nickel-free stainless steel. J Mater Sci Mater Med 17:267–275
64. Fini M, Aldini N, Torricelli P, Giavaresi G, Borsari V, Lenger H, Bernauer J, Giardino R, Chiesa R, Cigada A (2003) A new austenitic stainless steel with negligible nickel content: an in vitro and in vivo comparative investigation. Biomaterials 24:4929–4939
65. Newman RC, Lu YC, Bandy R, Clayton CR (1984) Proceedings of the ninth international congress on metallic corrosion, vol 4. National Research Council, Ottawa, p 394
66. World Health Organization (WHO), IARC Monographs on the evaluation of carcinogenic risks to humans, vol 74, Surgical implants and other foreign bodies. Lyon, p 65
67. Schultze JW, Lohrengel MM (2000) Stability, reactivity and breakdown of passive films. Problems of recent and future research. Electrochim Acta 45:2499–2513
68. Schmuki P (2002) From Bacon to barriers: a review on the passivity of metals and alloys. J Solid State Electrochem 6:145–164
69. Herting G, Odnevall Wallinder I, Leygraf C (2006) Factors that influence the release of metals from stainless steels exposed to physiological media. Corros Sci 48:2120–2132
70. Herting G, Odnevall Wallinder I, Leygraf C (2007) Metal release from various grades of stainless steel exposed to synthetic body fluids. Corros Sci 49:103–111
71. Herting G, Odnevall Wallinder I, Leygraf C (2008) Corrosion-induced release of chromium and iron from ferritic stainless steel grade AISI 430 in stimulated food contact. J Food Eng 87:291–300
72. Taveira LV, Frank G, Strunk HP, Dick LFP (2005) The influence of surface treatment in hot acid solution on corrosion resistance and oxide structure of stainless steels. Corros Sci 47:757–769
73. Kruger J (1989) The nature of the passive film on iron and ferrous alloys. Corros Sci 29:149–162
74. Shieu FS, Deng MJ, Lin SH (1998) Microstructure and corrosion resistance of a type 316 L stainless steel. Corros Sci 40:1267–1279
75. Scepanovic VM, MacDougall B, Graham MJ (1984) Nature of passive films on Fe–26Cr alloy. Corros Sci 24:479–490
76. Amonette JE, Rai D (1990) Identification of noncrystalline (Fe, Cr)(OH)3 by infrared spectroscopy. Clays Clay Miner 38:129–136
77. Chun-Che S, Chun-Ming S, Yea-Yang S, Lin Hui Julie S, Mau-Song C, Shing-Jong L (2004) Effect of surface oxide properties on corrosion resistance of 316 L stainless steel for biomedical applications. Corros Sci 46:427–444
78. DeLangis PA, Yen TF (1986) Electronic antihemocoagulation. Biomater Med Devices Artif Organs 14:195–225
79. Carroll WM (1990) The influence of temperature, applied potential, buffer and inhibitor addition on the passivation behaviour of a commercial grade 316 L steel in aqueous halide solutions. Corros Sci 30:643–655
80. Sato N (1990) An overview on the passivity of metals. Corros Sci 31:1–19
81. Sivakumar M, Mudali KU, Rajeswari S (1993) Pit-induced corrosion failures in stainless steel orthopaedic implant devices. Proc Twelfth Inter Corros Congress Houston (TX) 3B:1949–1956

82. Tanabe H, Mudali KU, Togashi K, Misawa T (1998) In situ pH measurements during localised corrosion of type 316LN stainless steel using scanning electrochemical microscopy. J Mater Sci Lett 17:551–553
83. Boehlert C, Niinomi M, Ikedu M (2005) Introduction. Mat Sci Eng C 25:247–252
84. Dowson D (1992) Friction and wear of medical implants and prosthetic devices. Friction, lubrication, and wear technology, ASM handbook, vol 18. ASM International, Ohio, USA, pp 1342–1360
85. Liua X, Chub PK, Ding C (2004) Surface modification of titanium, titanium alloys, and related materials for biomedical applications. Mater Sci Eng R 47:49–121
86. Leclerc MF (1987) ASM metals handbook 2. ASM International
87. Jacobs JJ, Gilbert JL, Urban RM (1990) Corrosion of metal orthopaedic implants. J Bone Joint Surg 80-A:268–282
88. Steinemann SG (1996) Metal implants and surface reactions. Injury 27:16–22
89. Knob LJ, Olson DL (1987) Corrosion. Metals Handbook 13:669
90. Kasemo B (2002) Biological surface science. Surf Sci 500:656–677
91. Ong JL, Lucas LC, Raikar GN, Connatser R, Gregory JC (1995) Spectroscopic characterization of passivated titanium in a physiologic solution. J Mater Sci Mater Med 6:113–119
92. Scharnweber D (1998) Metals as biomaterials. Wiley, Chichester
93. Bess E, Cavin R, Ma K, Ong JL (1999) Protein adsorption and osteoblast responses to heat-treated titanium surfaces. Implant Dent 8:126–132
94. Ellingsen JE (1991) A study on the mechanism of protein adsorption to TiO_2. Biomaterials 12:593–596
95. Hanawa T, Asami K, Asaoka KJ (1998) Repassivation of titanium and surface oxide film regeneration in simulated bioliquid. J Biomed Mater Res 40:530–538
96. Thull R (1978) Implantatwerkstoffe für die Endoprothetik. Fachverlag Schiele and Schön, Berlin, Germany
97. Kelly EJ (1982) Electrochemical behavior of titanium. Mod Aspect Electrochem 14:319–424
98. Schmidt M (1992) Spezifische Adsorption organischer Moleküle auf oxidiertem Titan: "Bioaktivität" auf molekularem Niveau. Osteologie 4:222–235
99. Schenk MK, Duschner H, Biehl V, Eisenbarth E, Breme J (2000) Influence of titanium–vanadium alloys on cell morphology: electron microscopy and ESCA studies. Surf Interface Anal 30:29–31
100. Mäusli PA, Bloch PR, Geret V, Steinemann SG (1986) Biological and biomechanical performance of biomaterials. Elsevier, Amsterdam, Netherlands
101. Mäusli PA, Simpson JP, Burri G, Steinemann SG (1988) Implant materials in biofunction advances in biomaterials. Elsevier, Amsterdam, Netherlands
102. Lausmaa J, Ask M, Rolander U, Kasemo B (1989) Preparation and analysis of Ti and alloyed Ti surfaces. Mater Res Soc Symp Proc 647–653
103. Aragon PJ, Hulbert SF (1972) Corrosion of Ti-6Al-4 V in simulated body fluids and bovine plasma. J Biomed Mater Res 6:155–164
104. Kobayashi E, Wang TJ, Doi H, Yoneyama T, Hamanaka H (1998) Mechanical properties and corrosion resistance of Ti-6Al-7Nb alloy dental castings. J Mater Sci Mater Med 9:567–574
105. Burstein GT, Liu C, Souto RM (2005) The effect of temperature on the nucleation of corrosion pits on titanium in Ringer's physiological solution. Biomaterials 26:245–256
106. Milošev I, Metikoš-Huković M, Strehblow HH (2000) Passive film on orthopaedic TiAlV alloy formed in physiological solution investigated by X-ray photoelectron spectroscopy. Biomaterials 21:2103–2113
107. Milošev I, Strehblow HH (2000) The behavior of stainless steels in physiological solution containing complexing agent studied by X- ray photoelectron spectroscopy. J Biomed Mater Res 52:404–412
108. Milošev I, Strehblow HH (2003) The composition of the surface passive film formed on CoCrMo alloy in simulated physiological solution. Electrochim Acta 48:2767–2774
109. Meachin G, Williams DF (1973) Change in non-osseous tissue adjacent to titanium implants. J Biomed Mater Res 7:555–572

110. Woodman JL, Jacobs JJ, Galante JO, Urban RM (1984) Metal ion release from titanium-based prosthetic segmental replacements of long bones in baboons: a long-term study. J Orthop Res 1:421–430
111. Ektessabi AM, Otsuka T, Tsuboi Y, Yokoyama K, Al-brektsson T, Sennerby L, Johansson C (1994) Application of micro beam PIXE to detection of titanium ion release from dental and orthopaedic implants. Int J PIXE 4:81–91
112. Ektessabi AM, Otsuka T, Tsuboi Y, Horino Y, Mokuno Y, Fujii K, Albrektson T, Sennerby L, Johansson C (1996) Preliminary experimental results on mapping of the elemental distribution of the organic tissues surrounding titanium-alloy implants. Nucl Instr Meth 109–110:278–283
113. Bianco PD, Ducheyne P, Cuckler JM (1996) Local accumulation of titanium released from a titanium implant in the absence of wear. J Biomed Mater Res 31:227–234
114. Merritt K, Brown SA (1988) Effect of proteins and pH on fretting corrosion and metal ion release. J Biomed Mater Res 22:111–120
115. Williams RL, Brown SA, Merritt K (1988) Electrochemical studies on the influence of proteins on the corrosion of implant alloys. Biomaterials 9:181–186
116. Semlitsch M, Staub F, Weber H (1986) Development of a vital, high strength titanium aluminum-niobium alloy for surgical implants. Proceedings of the 5th European conference on biomaterials, Paris, France, pp 69–74
117. Velten D, Biehl V, Aubertin E, Valeske B, Possart W, Breme J (2002) Preparation of TiO_2 layers on cp-Ti and Ti6Al4V by thermal and anodic oxidation and by sol–gel coating techniques and their characterization. Biomed Mater 59:18–28
118. Clark GCF, Williams DF (1982) The effects of proteins on metallic corrosion. J Biomed Mater Res 16:125–134
119. Velten D, Schenk-Meuser K, Biehl V, Duschner H, Breme J (2003) Characterization of thermal and anodic oxide layers on β- and on near-β-titanium alloys for biomedical application. Z Met 94:667–675
120. Okazaki Y, Ito A, Tateishi T, Ito Y (1994) Effect of alloying elements on of dental cast anodic polarization properties of titanium alloys in acid solutions. Mater Trans JIM 35:58–66
121. Okazaki Y (2001) A New Ti–15Zr–4Nb–4Ta alloy for medical applications. Curr Opinion Solid State Mater Sci 5:45–53
122. Niinomi M (2002) Recent metallic materials for biomedical applications. Metall Mater Trans A 33A:477–486
123. Gold JM, Schmidt M, Steinemann SG (1989) XPS study of amino acids adsorption to titanium surfaces. Helv Phys Act 62:246–249
124. Ryhanen J, Kallioinen M, Tuukkanen J, Junila J, Niemela E, Sandvik P et al (1998) In vivo biocompatibility evaluation of nickel-titanium shape memory metal alloy: muscle and perineural tissue responses and encapsule membrane thickness. J Biomed Mater Res 41:481–488
125. Assad M, Lemieux N, Rivard CH, Yahia LH (1999) Comparative in vitro biocompatibility of nickel-titanium, pure nickel, pure titanium, and stainless steel: genotoxicity and atomic absorption evaluation. Biomed Mater Eng 9:1–12
126. Putters JL, Kaulesar SDM, de Zeeuw GR, Bijma A, Besselink PA (1992) Comparative cell culture effects of shape memory metals (Nitinol), nickel and titanium: a biocompatibility estimation. Eur Surg Res 24:378–382
127. Kapanen A, Ryhanen J, Danilov A, Tuukkanen J (2001) Effect of nickel-titanium shape memory alloy on bone formation. Biomaterials 22:2475–2480
128. Hanawa T (2003) Reconstruction and regeneration of surface oxide film on metallic materials in biological environments. Corros Rev 21:161–181
129. Hanawa T, Ota M (1991) Calcium phosphate naturally formed on titanium in electrolyte solution. Biomaterials 12:767–774
130. Hanawa T (1991) Titanium and its oxide film; a substrate for formation of apatite. In: Davies JE (ed) The bone-biomaterial interface. University of Toronto Press, Toronto, Canada, pp 49–61

131. Hanawa T, Ota M (1992) Characterization of surface film formed on titanium in electrolyte using XPS. Appl Surf Sci 55:269–276
132. Murakami K, Ukai H, Hanawa T, Asaoka K (1997) Japanese Society for Biomaterials. Tokyo, Japan, 36
133. Hazan R, Brener R, Oron U (1993) Bone growth to metal implants is regulated by their surface chemical properties. Biomaterials 8:570–574
134. Ask M, Rolander U, Lausmaa J, Kasemo B (1990) Microstructure and morphology of surface oxide films on Ti-6Al-4VJ. Mater Res 5:1662–1667
135. Tummler HP (1986) Oberflächeneigenschaften von Titan und Tantal für Implantate. Dissertation, Friedrich-Alexander-Universität Erlangen-Nürnberg
136. Wälivaara B, Aronsson BJ, Rodahl M, Lausmaa J, Tengvall P (1994) Titanium with different oxides-in vitro studies of protein adsorption and contact activation. Biomaterials 15:827–834
137. Probster L, Dent M, Lin WL, Huttenmann H (1992) Effect of fluoride prophylactic agents on titanium surfaces. Int J Oral Max Impl 7:390–394
138. McMinn D, Daniel J (2006) History and modern concepts in surface replacement. Proc Inst Mech Eng H J Eng Med 220:239–251
139. McMinn R (2000) Hip Resurfacing (BHR) history, development and clinical results. Midland Medical Technologies, Birmingham
140. Contu F, Elsener B, Bohni H (2003) Electrochemical behavior of CoCrMo alloy in the active state in acidic and alkaline buffered solutions. J Electrochem Soc 150:419–424
141. Sun D, Wharton JA, Wood RJK, Ma L, Rainforth WM (2007) Microabrasion- corrosion of cast CoCrMo alloy in simulated body fluids. in 34th Leeds-Lyon Symposium on Tribology. Elsevier Science Ltd., Lyon
142. Nagai A, Tsutsumi Y, Suzuki Y, Katayama K, Hanawa T, Yamashita K (2012) Characterization of air-formed surface oxide film on a Co-Ni-Cr-Mo alloy (MP35N) and its change in Hanks' solution. Appl Surf Sci 258:5490–5498
143. Merchant RE, Wang I (1994) Physical and chemical aspects of biomaterials used in humans. In: Greco RS (ed) Implantation biology: the host response and biomedical devices. CRC Press, London, pp 13–38
144. Bates JF, Knapton AG (1977) Metals and alloys in dentistry. Inter Metals Rev 22:39–60
145. Lin H, Bumgardner JD (2004) Changes in the surface oxide composition of Co-Cr-Mo implant alloy by macrophage cells and their released reactive chemical species. Biomaterials 25:1233–1238
146. Strandman E, Landt H (1982) Oxidation resistance of dental chromium-cobalt alloys. Quintessence Dent Technol 6:67–74
147. Smith DC, Pilliar RM, Metson JB, McIntyre NS (1991) Dental implant materials. II. Preparative procedures and surface spectroscopic studies. J Biomed Mater Res 25:1069–1084
148. Pan J, Liao H, Leygraf C, Thierry D, Li J (1998) Variation of oxide films on titanium induced by osteoblast-like cell culture and the influence of an H_2O_2 pretreatment. J Biomed Mater Res 40:244–256
149. O'Brien B, Carroll WM, Kelly MJ (2002) Passivation of nitinol wire for vascular implants – a demonstration of the benefits. Biomaterials 23:1739–1748
150. Sawase T, Wennerberg A, Baba K, Tsuboi Y, Sennerby L, Johansson CB, Albrektsson T (2001) Application of oxygen ion implantation to titanium surfaces: effects on surface characteristics, corrosion resistance, and bone response. Clin Implant Dent Relat Res 3:221–229
151. Matkovic T, Matkovic P, Malina J (2004) Effects of Ni and Mo on the microstructure and some other properties of Co-Cr dental alloys. J Alloys Compd 366:293–297
152. Hiromotoa S, Onoderab E, Chibab A, Asamic K, Hanawa T (2005) Microstructure and corrosion behaviour in biological environments of the new forged low-Ni Co–Cr–Mo alloys. Biomaterials 26:4912–4923
153. Bellefontaine G (2010) The corrosion of CoCrMo alloys for biomedical applications. Master of Research, School of Metallurgy and Materials University of Birmingham, Birmingham

154. Codaro EN, Melnikov P, Ramires I, Guastaldi AC (2000) Corrosion behavior of a cobalt-chromium-molybdenum alloy. Russ J Electrochem 36:1117–1121
155. Yan Y, Neville A, Dowson D (2007) Tribo-corrosion properties of cobalt-based medical implant alloys in simulated biological environments. Wear 263:1105–1111
156. Cawley J, Metcalf JEP, Jones AH, Band TJ, Skupien DS (2003) A tribological study of cobalt chromium molybdenum alloys used in metal-on-metal resurfacing hip arthroplasty. 4th International Conference on Wear of Materials. Elsevier Science SA, Washington, DC
157. Kinbrum A, Unsworth A (2008) The wear of high-carbon metal-on-metal bearings after different heat treatments. Proc Inst Mech Eng H J Eng Med 222(H6):887–895
158. Kauser F (2007) Corrosion of CoCrMo alloys for biomedical applications'. Department of Metallurgy and Materials, School of Engineering, University of Birmingham, Birmingham, pp 4–285
159. Contu F, Elsener B, Bohni H (2005) Corrosion behaviour of CoCrMo implant alloy during fretting in bovine serum. Corros Sci 47:1863–1875
160. Metikos-Hukovic M, Babic R (2007) Passivation and corrosion behaviours of cobalt and cobalt–chromium–molybdenum alloy. Corros Sci 49:3570–3579
161. Cannillo V, Colmenares-Angulo J, Lusvarghi L, Pierli F (2009) In vitro characterisation of plasma-sprayed apatite/wollastonite glass-ceramic biocoatings on titanium alloys. J Eur Ceram Soc 29:1665–1667
162. Ong JL, Lucas LC, Lacefield WR, Rigney ED (1992) Structure, solubility and bond strength of thin calcium phosphate coatings produced by ion beam sputter deposition. Biomaterials 13:249–254
163. Schwartz M (1994) Deposition from aqueous solutions: an overview. In: Bunshah RF (ed) Handbook of deposition technologies for films and coatings: science, technology and applications, 2nd edn. Noyes Publications, Park Ridge, pp 506–617
164. Aksakal B, Gavgali M, Dikici B (2010) The effect of coating thickness on corrosion resistance of hydroxyapatite coated Ti6Al4V and 316L SS implants. J Mater Eng Perform 19:894–899
165. Sonmez S, Aksakal B, Dikici B (2012) Corrosion protection of AA6061-T4 alloy by sol&-gel derived micro and nano-scale hydroxyapatite (HA) coating. J Sol-Gel Sci Techn 63:510–518
166. Zhitomirsky I (2000) New developments in electrolytic deposition of ceramic films. Am Ceram Soc Bull 79:57–63
167. Zhitomirsky I (2002) Cathodic electrodeposition of ceramic and organoceramic materials: fundamental aspects. Adv Colloid Interfac 97:279–317
168. Sarkar P, Nicholson S (1996) Electrophoretic deposition (EPD): mechanisms, kinetics, and applications to ceramics. J Am Ceramic Soc 79:1987–2002
169. Spencer K, Zhang MX (2011) Optimisation of stainless steel cold spray coatings using mixed particle size distributions. Surf Coat Tech 205:5135–5140
170. Sova A, Grigoriev S, Okunkova A, Smurov I (2013) Cold spray deposition of 316 L stainless steel coatings on aluminium surface with following laser post-treatment. Surf Coat Tech 235:283–289
171. Campbell AA (2003) Bioceramics for implant coatings. Mater Today 6:26–30
172. Mohammadi Z, Ziaei-Moayyed AA, Mesgar SMA (2008) In vitro dissolution of plasma-sprayed hydroxyapatite coatings with different characteristics: experimental study and modeling. Biomed Mater 3:1–7
173. Ensinger W (2004) Ion beam sputter coating of three-dimensional objects: rings, cylinder, and tubes. Surf Coat Tech 177–178:264–270
174. Lensch O, Kraus T, Sundermann C, Enders B, Ensinger W (2002) Protection of cylinders by ion-beam sputter deposition: corrosion of carbon-coated aluminium tubes. Surf Coat 158–159:599–603
175. Liu D, Troczynskia T, Tseng WJ (2002) Aging effect on the phase evolution of water-based sol–gel hydroxyapatite. Biomaterials 23:1227–1236

176. Gross KA, Chai CS, Kannangara GK, Ben-Nissan B (1998) Thin hydroxyapatite coatings via sol–gel synthesis. J Mater Sci Mater Med 9:839–843
177. Liu P, Pan X, Yang W, Cai K, Chen Y (2012) Al_2O_3-ZrO_2 ceramic coating fabricated on WE43 magnesium alloy by cathodic plasma electrolytic deposition. Mater Lett 70:16–18
178. Seo D, Ogawa K, Sakaguchi K, Miyamoto N, Tsuzuki Y (2012) Parameter study influencing thermal conductivity of annealed pure copper coatings deposited by selective cold spray processes. Surf Coat Tech 206:2316–2324
179. Phani PS, Rao DS, Joshi SV, Sundararajan GJ (2007) Effect of process parameters and heat treatments on properties of cold sprayed copper coatings. J Therm Spray Techn 16:425–434
180. Cinca N, Rebled JM, Estrade S, Peiro F, Fernandez J, Guilemany JM (2013) Influence of the particle morphology on the Cold Gas Spray deposition behavior of titanium on aluminum light alloys. J Alloy Compd 554:89–96
181. Al-Mangoura B, Mongrain R, Irissou E, Yue S (2013) Improving the strength and corrosion resistance of 316 L stainless steel for biomedical applications using cold spray. Surf Coat Tech 216:297–307
182. Dikici B, Ozel S, Gavgali M, Somunkiran I (2012) The effect of arc current on the corrosion behaviour of coated NiTi alloy on AISI304 by plasma transferred arc process. Prot Met Phys Chem Surf 48:562–566
183. Singha G, Singh H, Sidhu BS (2013) In-Vitro corrosion investigations of plasma sprayed hydroxyapatite and hydroxyapatite-calcium phosphate coating on 316 L SS. Appl Surf Sci 284:81–818
184. Metikos-Hukovic M, Tkalcec E, Kwokal A, Piljac J (2003) An in vitro study Ti and Ti-alloys coated with sol–gel derived hydroxyapatite coating. Surf Coat Tech 165:40–50
185. Lavos-Valereto C, Costa I, Wolyne S (2002) The electrochemical behavior of Ti-6Al-7Nb alloy with and without plasma-sprayed hydroxyapatite coating in Hank's solution. J Biomed Mater Res 63:664–700
186. Hermawan H (2012) Biodegradable metals. SpringerBriefs in Materials. Chapter 2 Biodegradable metals: state of the art, Berlin, Germany
187. Witte F, Hort N, Vogt C, Cohen S, Kainer KU, Willumeit R, Feyerabend F (2008) Degradable biomaterials based on magnesium corrosion. Curr Opinion Solid State Mater Sci 12:63–72
188. Hermawan H, Dubé D, Mantovani D (2010) Review: developments in metallic biodegradable stents. Acta Biomater 6:1693–1697
189. Moravej M, Mantovani D (2011) Review biodegradable metals for cardiovascular stent application: interests and new opportunities. Int J Mol Sci 12:4250–4270
190. Witte F (2010) The history of biodegradable magnesium implants: a review. Acta Biomater 6:1680–1692
191. Heublein B, Rohde R, Kaese V, Niemeyer M, Hartung W, Haverich A (2003) Biocorrosion of magnesium alloys: a new principle in cardiovascular implant technology. Heart 89:651–656
192. Di Mario C, Griffiths H, Goktekin O, Peeters N, Verbist J, Bosiers M, Deloose K, Heublein B, Rohde R, Kasese V, Ilsley C, Erbel R (2004) Drug-eluting bioabsorbable magnesium stent. J Interv Cardiol 17:391–395
193. Peeters P, Bosiers M, Verbist J, Deloose K, Heublein B (2005) Preliminary results after application of absorbable metal stents in patients with critical limb ischemia. J Endovasc Ther 12:1–5
194. Zartner P, Cesnjevar R, Singer H, Weyand M (2005) First successful implantation of a biodegradable metal stent into the left pulmonary artery of a preterm baby. Catheter Cardiovasc Interv 66:590–594
195. Valiev RZ, Zehetbauer MJ, Estrin Y, Höppel HW, Ivanisenko Y, Hahn H, Wilde G, Roven HJ, Sauvage X, Langdon TG (2007) The innovation potential of bulk nanostructured materials. Adv Eng Mater 7:9
196. Yilmazer H, Niinomi M, Nakai M, Cho K, Hieda J, Todaka Y, Miyazaki T (2013) Mechanical properties of a medical β-type titanium alloy with specific microstructural evolution through high-pressure torsion. Mater Sci Eng C Mater Biol Appl 33:2499–2507

197. Valiev RZ, Estrin Y, Horita Z, Langdon TG (2006) Producing bulk ultrafine-grained materials by severe plastic deformation. JOM 58:33–39
198. Rubitschek FN, Karaman I, Maier HJ (2012) Corrosion fatigue behavior of a biocompatible ultrafine-grained niobium alloy in simulated body fluid. J Mech Behav Biomed 5:181–192
199. Thorpe SJ, Ramaswami B, Aust AT (1998) Corrosion and Auger studies of a nickel-base metal-metalloid. J Electrochem Soc 135:2162
200. Rofagha R, Erb U, Ostander D, Palumbo G, Aust KT (1993) The effects of grain size and phosphorous on the corrosion of nanocrystalline Ni–P alloys. Nanostruct Mater 2:12
201. Miyamoto H, Harada K, Mimaki T, Vinogradov A, Hashimoto S (2008) Corrosion of ultra-fine grained copper fabricated by equal-channel angular pressing. Corros Sci 50:1215–1220
202. Vinogradov A, Mimaki T, Hashimoto S, Valiev R (1999) On the corrosion behavior of ultra-fine grain copper. Scr Mater 41:319–326
203. Xu XX, Nie FL, Zhang JX, Zheng W, Zheng YF, Hu C, Yang G (2010) Corrosion and ion release behavior of ultra-fine grained bulk pure copper fabricated by ECAP in Hanks solution as potential biomaterial for contraception. Mater Lett 64:524–527
204. Hadzima B, Janecek M, Estrin Y, Kim HS (2007) Microstructure and corrosion properties of ultrafine-grained interstitial free steel. Mater Sci Eng A 462:243–247
205. Dikici B, Yilmazer H, Niinomi M, Nakai M, Ozdemir I, Gavgali M (2012) Effect of high-pressure torsion (HPT) processing on corrosion behavior of a new biomedical β-type titanium alloy. Corrosion-2012, Physico Chemical Mechanics of Materials, Special Issue No: 9, 95–100, 4–6 June, Lviv/Ukraine

Chapter 13
Pathological Analysis of Metal Allergy to Metallic Materials

Mitsuko Kawano, Yuri Takeda, and Kouetsu Ogasawara

Abstract Metal allergy is thought to be caused by the release of ions from metallic materials. Extensive use of metal in jewelry, coins, surgical instruments, and dental restorations may be responsible for recent increases in allergy incidence. Metal allergic disease is categorized as a delayed-type hypersensitivity, which is developed more than 24 h after exposure to the causal metal. The hallmark of delayed-type hypersensitivity is the recruitment of lymphocytes and inflammatory cells, including T cells and granulocytes, to the site of allergic inflammation. During the development of metal allergy, T cells are known to play a role, and since metal ions are thought to function as haptens, T cell-mediated responses likely contribute to allergic disease. While the involvement of pathogenic T cells in the development of metal allergy has not been explored using animal models, studies utilizing human patient samples have been conducted. T cell clones, both $CD4^+$ and $CD8^+$, have been established from peripheral blood mononuclear cells of patients with metal allergy, and their responsiveness to the causal metal has been analyzed. It was found that metal ions induced proliferation of these T cells in vitro and some of the T cell clones produced IFN-γ or IL-4 after metal stimulation, while others produced both T helper 1- and 2-type cytokines. However, the subset of pathogenic T cells involved in the development of metal allergy and their cytokine profiles remain controversial. Recently, a novel animal model that reproduces human metal allergy has been established. Here we show the pathogenesis of metal allergy in the view of immunological responses using this animal model.

Keywords Delayed-type hypersensitivity • Contact hypersensitivity • Pathogenic T cell • Hapten • Adjuvant antigen presentation

M. Kawano • Y. Takeda • K. Ogasawara (✉)
Department of Immunobiology, Institute of Development, Aging and Cancer, Tohoku University, 4-1 Seiryo-machi, Aoba-ku, Sendai, Miyagi 980-8575, Japan
e-mail: ogasawara@idac.tohoku.ac.jp

M. Niinomi et al. (eds.), *Advances in Metallic Biomaterials*, Springer Series in Biomaterials Science and Engineering 3, DOI 10.1007/978-3-662-46836-4_13

13.1 Categorization of Metal Allergy

The word “allergy” was first used by von Pirquet to denote both host-protective and potentially host-injurious immune responses [1]. In a similar manner, the word “hypersensitivity” was first used to describe the status of a mammalian organism after exposure to an infectious agent. The mammal is then “hypersensitive” to this agent and, therefore, able to deal with it effectively upon second exposure. Over the past century, however, these two terms have acquired the connotation of deleterious responses [2]. It is in the context of this deleterious connotation that Gell and Coombs developed their widely accepted classification of hypersensitivity reactions into four types (types I–IV) [3].

The type I hypersensitivity reaction has the most clear-cut immunopathological correlation and is driven predominantly by IgE bound to mast cells. Upon engagement of the cytophilic IgE with its appropriate antigen, mast cell degranulation occurs as well as the subsequent release of histamine, leukotrienes, and other mediators resulting in the classic symptoms of allergic airway disease. Type II hypersensitivity reactions are characterized by antigen-antibody interactions resulting in the local production of anaphylatoxin, the recruitment of polymorphonuclear leukocytes, and subsequent tissue injury due to the release of hydrolytic neutrophil enzymes after their autolysis. Type III hypersensitivity reactions arise when antibody reactions occur in the blood resulting in the formation of antigen-antibody complexes, which are deposited in the glomerular and/or pulmonary basement membranes. This reaction has a host-protective response and is perhaps ideal for elimination of circulating viral particles. Gell and Coombs conceived of several tissue-specific autoimmune disorders as falling into the Type IV hypersensitivity reactions, which are also known as delayed-type hypersensitivity. Delayed-type hypersensitivity is a T cell-mediated inflammatory reaction occurring at the site of allergen challenge in sensitized individuals [4]. It is characterized by redness and the formation of papules and vesicles followed by scaling and dry skin [5]. Elicitation of sensitized individuals with the same allergen leads to the apparition of delayed-type hypersensitivity in 24–96 h [2, 6].

Metal allergy is categorized as a Type IV hypersensitivity reaction, and metals are the most common contact sensitizers in children and adults [7, 8]. In sensitized patients, allergic contact dermatitis occurs 24–96 h after contact with the same metal with the initial localization being the site of contact. In addition, the edge of the lesion may be well defined. During the acute phase, allergic contact dermatitis to metals consists of erythema and edema followed by the appearance of papules, numerous vesicles, and oozing followed by crusting. In the chronic phase, the skin becomes lichenified, fissured, and pigmented, but new episodes of blistering, oozing, and crusting can occur with further exposure to the metal [6].

13.2 Background of Metal Allergy

Allergic contact dermatitis is caused by environmental exposure to external agents that trigger an inflammatory reaction in the skin. The precise incidence and prevalence of contact sensitization are not well known in the pediatric population. However, it is estimated that 28 % of adults have allergic contact dermatitis [9, 10]. Metals are the most common contact sensitizers in children and adults, and environment and lifestyle play an important role in the development of this sensitization. Nickel, cobalt, and chromium are metals with uses in fields ranging from the military, to health care, aerospace, and the transportation industries as well as having household and architectural uses [9]. Furthermore, several European studies have reinforced the role of detergents in triggering dermatitis, particularly hand eczema in individuals sensitized to metals, as they may contain nickel, cobalt, and chromium [11].

Nickel, a silver-colored metal, was first identified in 1751 by Baron Axel Fredrik Cronstedt [12]. In the 19th century, after the discovery of the method for its extraction, it was broadly employed in large quantities due to its attractive qualities such as resistance to corrosion, durability, and the fact that it binds easily to many other metals [13]. The first report of allergic contact dermatitis caused by nickel appeared late in 1880. The disease was described by Blaschko as "galvanizing eczema," a skin disease seen in the hands and forearms of miners and workers in nickel industries [14]. Furthermore, traces of nickel have been found in natural foods including vegetables, nuts, cereals, potatoes, cocoa, and fish. The level of nickel in food is determined by components of the soil where the food is grown, the fungicides used, and by the equipment used in harvesting. Thus, this level may vary considerably between regions. It is also found in water and cooking utensils and can be released from stainless steel when the pH of boiling water is acidic [11].

Cobalt is a hard, silver-gray metal usually found associated with nickel. It was discovered by George Brandt in 1730s [9]. Used in the production of metal alloys and pigments (cobalt blue and cobalt green), sensitization to cobalt occurs mainly because of its presence in objects that also contain chromium and nickel, and thus, it is often associated with allergy to other metals. In many cases, sensitization may occur through the use of cosmetics as they often contain cobalt [9, 11].

Chromium was discovered in 1797 by Louis Nicolas Vauquelin [9], and it is the fourth most commonly found substance in the earth's crust. In contrast to other metals, chromium allergy has been reported to be stable or declining [15]. Chromium is mainly used in metallurgy to increase corrosion resistance and give a glossy finish, in alloys such as stainless steel, in plating processes (depositing a protective layer of chrome on objects), in paints, as well as in leather tanning and wood preservation. Detergents and cosmetics may also contain chromium. Historically, the most important cause of allergy to chromium has been occupational exposure to cement. In children, the most common source is leather, and chromium sensitivity is the leading cause of shoe contact dermatitis [7].

Palladium and gold are typically used in dental restorations and jewelry [16]. Additionally, gold has also been used for coronary stents and rheumatic therapy [17], while occupational palladium exposure may occur in the electronics and chemical industries.

Biomedical devices are typically made from metals known to be hypoallergenic and, as a result, rarely produce localized or systemic reactions [9]. Stainless steel, vitallium, and titanium are alloys used in orthopedic prostheses. These metals are resistant to corrosion by physiological fluids and can be left in the body indefinitely. Vitallium alloy is composed of cobalt, chromium, and molybdenum. Stainless steel is composed of iron, chromium, nickel, molybdenum, and, sometimes, small amounts of other metals. During the production of stainless steel, crystal network is formed between metals making them adhere firmly to one another and reducing the likelihood of sensitization [9].

Repeated and/or prolonged skin contact with metal ions is considered to induce development of metal allergy. Before metal ions can elicit a cutaneous immune response, they must gain access to the viable epidermis. Thus, they should have certain physicochemical characteristics necessary for passage across the stratum corneum, as it is an effective barrier to many chemicals [18]. Exogenous (e.g., dose, size, counter ions, polarity, valence, and pH) and endogenous (e.g., age of the skin, anatomical site, oxidation, and reduction) factors are important and should also be accounted for when investigating metal absorption [16, 19].

Contact allergens are either inherently protein reactive or can be metabolized in the skin to protein-reactive species. Metal ions are haptens and, as such, are of insufficient size to provoke an immune response on their own. Thus, they must form stable conjugates with proteins once inside the skin in order to produce such a response [20]. However, it was recently shown that some contact allergens, for example, nickel, may interact directly with the human major histocompatibility complex (MHC) in a peptide-independent manner [21].

At the mechanistic level, two distinct phases are present, a sensitization phase and an elicitation phase (Fig. 13.1). The sensitization phase usually develops over a few days to several weeks and includes the immunological events following primary skin contact with the metal. This phase is complete when antigen-specific T cells have been developed and the individual is sensitized. The elicitation phase usually develops within 1–2 days but may take place as early as 2 h after exposure. Activation of antigen-specific T cells results in dermatitis at the site of allergen skin contact, and the reaction usually resolves within days to weeks. At the clinical level, the sensitization phase is referred to as contact sensitization or contact allergy, whereas the elicitation phase is referred to as allergic contact dermatitis. Metal allergy is considered to be a chronic and potentially lifelong condition [22]. Risk factors for metal allergy include the inherent sensitizing potential of an allergen, elevated allergen concentration, high frequency of exposure, occlusion, long exposure time, the presence of penetration-enhancing factors, and an altered skin barrier function [16, 23–25].

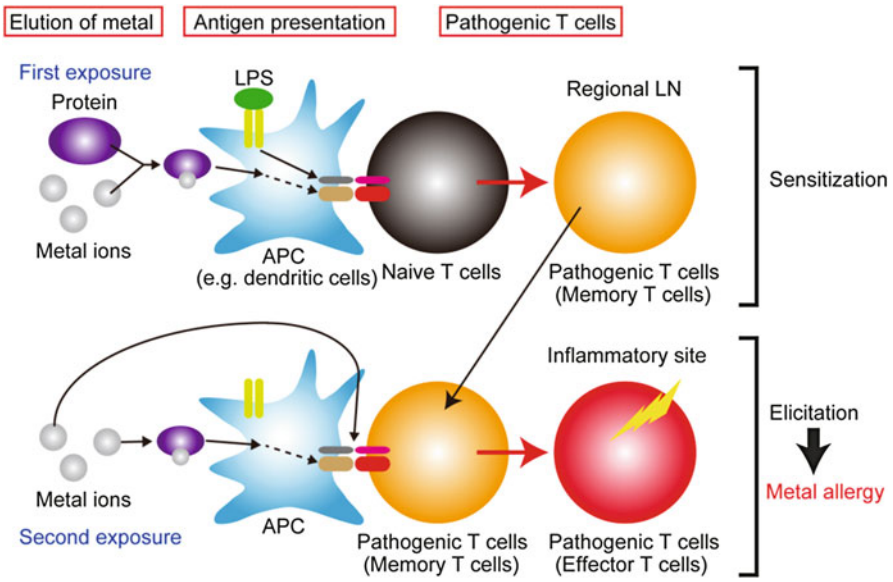

Fig. 13.1 Explanation of the sensitization and elicitation phases of metal allergy. At first exposure, metal ions are eluted from metal devises. Eluted metal ions interact with proteins and are captured by antigen-presenting cells (*APC*). Captured complexes of metal ions and proteins are digested into antigen peptides and then are presented by major histocompatibility complexes (*MHC*) to naïve T cells. For T cell activation, innate immune stimulation is required simultaneously with antigen presentation, for example, stimulation by lipopolysaccharide (*LPS*). Antigen-presented T cells become pathogenic T cells (memory T cells) and migrate into regional lymph nodes (*LN*). Upon secondary exposure, metal ions with protein were captured by APC or metal ions are coordinated to immune synapse directly. Memory T cells are activated and migrated into the inflammatory site

The key event in the initiation of allergic contact dermatitis is the sensitization of hapten-specific naïve $CD4^+$ and $CD8^+$ T cells, which then become activated, proliferate, and differentiate into effector T cells. Since metal ions are also considered haptens, the same mechanism likely underlies metal allergy. This sensitizing reaction occurs in the regional lymph node via lymphatic flow [26–28]. Antigen presentation in the lymph node by migratory dendritic cells is absolutely essential for the generation of responses to peripheral antigens [27–30]. Therefore, antigen-presenting cells (e.g., dendritic cells) presented antigen, and naïve T cells are activated. Activated T cells which work as pathogenic T cells induce inflammation. Upon secondary exposure, pathogenic T cells expand, which induces to development of allergy.

13.3 Pathology in Patients with Metal Allergy

Metal allergy is developed dependent on various factors. Among these, elution of metal is a key factor. It was reported that sweat, through the action of its salts, promotes the elution of metal and, thus, explains the worsening of dermatitis in the summer [9, 11].

The sensitization phase starts when metals, as haptens, penetrate the skin. They are captured and conveyed by antigen-presenting cells on MHC class I or II molecules to the regional lymph nodes, where they induce hapten-specific $CD8^+$ or $CD4^+$ T cells, respectively (Fig. 13.2). The sensitization phase lasts 1–2 weeks in humans. In the elicitation phase, the presence of even one antigen-specific T lymphocyte at the site of antigen reintroduction in the skin triggers an antigen-specific immunologic response to clear the antigen, with inflammation and tissue destruction manifested by allergic contact dermatitis symptoms such as erythema, edema, and even blisters. The elicitation phase takes 24–96 h in humans [6, 31, 32]. The inflammatory reaction persists over several days and progressively decreases due to physiologic downregulation mechanisms [32].

Most studies of systemic allergic contact dermatitis caused by metals have focused on nickel-induced allergy; however, a number of other metals have been implicated including cobalt, chromium, mercury, palladium, and gold.

Patch tests against various metals showed that prevalence of nickel allergy is the highest [15]. Furthermore, approximately 30–40 % of people sensitive to nickel develop hand eczema, which appears to be further aggravated by the presence of cobalt [33]. Systemic nickel allergy is often seen in children and is usually symmetrical and related to the first contact site. Nickel is a frequent component of a variety of products including costume jewelry, coins, belt buckles, and keys. Thus, dermatitis caused by nickel typically presents as a rash on the earlobes or wrists resulting from contact with costume jewelry.

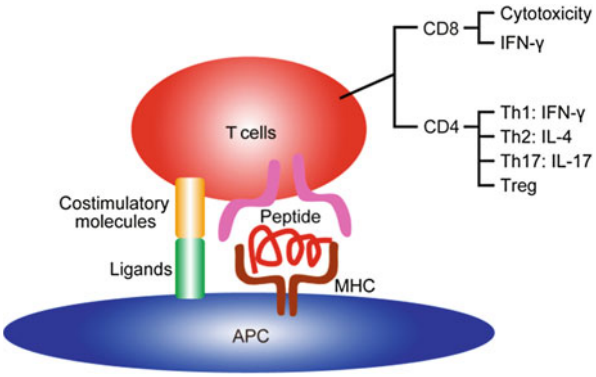

Fig. 13.2 Illustration of antigen presentation. Antigen peptide is presented by the MHC to $CD4^+$ or $CD8^+$ T cells. Simultaneous signals through costimulatory molecules are required for T cell activation

Some patients with nickel allergy experience oral elicitation symptoms due to a diet high in nickel content. Therefore, to reduce nickel exposure, a low-nickel diet is utilized resulting in improvement in approximately half of nickel allergy patients [34, 35]. Recent studies have indicated that children also have manifestations of nickel and cobalt sensitivity that improved on a diet with a low content of these metals [36].

Cobalt sensitivity is often associated with nickel sensitivity. In fact, a positive patch test to cobalt without concomitant nickel allergy is unusual. For some cobalt-sensitive persons, it is possible to reactivate previous dermatitis after oral cobalt challenge. Six of nine cobalt-sensitive patients reacted to oral challenge with 1 mg cobalt in a placebo-controlled design with most of the patients exhibiting vesicular hand eczema. Additional clinical features associated with systemic cobalt dermatitis include stomatitis and widespread dermatitis. Stuckert and Nedorost have made suggestions for a low-cobalt diet [31, 37–39].

Hypersensitivity to chromium was reported in 9 of 29 allergic patients who underwent coronary stent implantation. Coronary stents used in the United States since 1997 have been constructed using 316 L stainless steel, cobalt-chromium alloy, or platinum-chromium alloy platforms. In varying amounts, all such stents contain nickel (10–35 %), chromium as chromate (18–20 %), and, aside from the Multi-link Vision stent, molybdenum (2.7–9.7 %). Conceptually, any stent component may have the propensity to induce immune-mediated thrombosis or restenosis in hypersensitive individuals [40]. Chromate-induced systemic contact hypersensitivity is primarily exacerbated by skin contact with hexavalent and trivalent chromium compounds [41]; however, the ingestion of the allergen in the dichromate form has also been reported to cause exacerbations [42]. Systemic contact dermatitis in chromate-sensitive patients has been linked to recurrent and vesicular hand eczema [43, 44]. Metal allergy has also been associated with device failures following the insertion of intracoronary stents, hip and knee prostheses, and other implants, although this complication is very rare [45]. The majority of total joint prostheses are now made of cobalt-chromium alloys with a nickel content of less than 1 % [46]. The occurrence of systemic contact dermatitis is particularly uncommon following total knee arthroplasty because there is a polyethylene insert between the femoral and tibial components and no metal-on-metal contact exists [42].

Palladium is a precious, silvery-white metal discovered by William Hyde Wollaston in 1803 that belongs to the platinum group of metals (palladium, platinum, rhodium, ruthenium, iridium, and osmium). Patients with dermatitis are mainly exposed to palladium through jewelry and dental appliances, but palladium is also found in electronics, aircraft spark plugs, surgical instruments, and an automotive emission control catalyst [47]. Although palladium allergy is nearly always seen together with nickel allergy, this is not fully understood [48, 49]. The incidence of patients sensitized to palladium has increased in recent years as palladium is more frequently been used in dental restorations [47, 48]. However, compared to nickel, little is known about the pathology of this allergic disease. Hence, palladium allergy has been a subject of debate for decades. The use of palladium-silver alloys has increased significantly since their introduction in 1973, and they now comprise

a substantial part of the noble metal ceramic alloy sales in the United States [50]. It has been debated whether the use of nickel in jewelry has or will be replaced by the use of palladium following the EU Nickel Directive [51, 52].

Gold is a very stable metal, and while sensitization to it does occur, there are few examples of classical allergic contact dermatitis at cutaneous sites of contact with high-carat gold. Lichenoid eruptions on the gingiva and buccal mucosa at sites of contact with gold fillings are the most common clinical manifestation of gold contact stomatitis. Controlled elicitation experiments have shown that the injection of gold salts in gold-sensitized persons can cause systemic dermatitis similar to the eruptions seen in mercury-sensitive persons [53, 54]. Furthermore, there is a statistical correlation between gold allergy and the presence of dental gold or gold-plated stents for coronary arteries as well as for the risk of restenosis [35].

Historically, treatment of metal allergy has focused on the reduction of local inflammation for which steroids and/or anti-inflammatory medicines are used. While treatment with steroids is known to have some effect on metal allergy, the molecular mechanisms underlying the onset of metal allergy have not been defined. Using peripheral blood cells obtained from patients, several studies have shown that T cells are involved in the development of metal allergy [55–57]. In addition, since metal ions are believed to function as haptens, T cell-mediated responses are expected in metal allergy [58, 59]. In fact, metal ions induce proliferation of human T cells in vitro, and limited TCRs (T cell receptors) from 1×10^{18} TCRs were found in human T cells from patients of metal allergy [56, 60, 61]. However, the role of pathogenic T cells in the development of metal allergy has not been explored in detail because suitable animal models had not previously been available. Therefore, to investigate the molecular mechanisms of metal allergy, establishment of animal models is an essential first step.

13.4 Development of Animal Models of Metal Allergy

Although there previously existed no adequate animal models of metal allergy, there are several mouse models of contact hypersensitivity using chemical haptens. Allergic contact dermatitis is one of the most common skin diseases, affecting 15–20 % of the general population worldwide [62], and murine contact hypersensitivity is one of the most frequently used animal models of allergic contact dermatitis. During the last decade, new subsets of immune cells, such as regulatory T cells (Tregs) and $CD4^+$ T helper 17 (Th17) cells, have been identified from studies in murine contact hypersensitivity models. Based on these results, it has been determined that similar responses also exist in humans [63].

Most of the chemicals that induce contact hypersensitivity are small compounds called haptens, which typically have a molecular mass of <500. Haptens require interactions with proteins to elicit adaptive immune responses [64, 65]. In addition,

because haptens, including metal ions, are composed of molecules small enough to penetrate the dermis across the tight junctions, cutaneous dendritic cells may encounter haptens directly [63].

Full activation of dendritic cells is essential for the establishment of sensitization by haptens; however, the molecular mechanisms underlying dendritic cell activation by haptens remain unknown. Martin et al. have intensively investigated the involvement of the innate immunity system in hapten-induced dendritic cell activation [66]. Innate immunity is activated through pattern recognition receptors, such as membrane-associated toll-like receptors (TLRs) and cytosolic nucleotide-binding oligomerization domain (NOD)-like receptors. Among TLRs, TLR2 and TLR4 have a critical role in dendritic cell maturation in murine contact hypersensitivity reactions.

Nickel is one of the most frequent causes of contact dermatitis in humans, although it rarely occurs in mice. It has been reported that coadministration of adjuvant, such as complete Freund's adjuvant or lipopolysaccharide, efficiently induced nickel allergy in mice suggesting an important role of TLR signaling in efficient sensitization with nickel. Schmidt et al. reported that nickel ions induced an inflammatory response by directly activating human TLR4. Furthermore, this activation required distinct sequence motifs that are present in human, but not mouse, TLR4. Thus, only TLR4-deficient mice expressing transgenic human TLR4 developed contact hypersensitivity to nickel, whereas animals expressing mouse TLR4 failed to generate contact hypersensitivity [67]. Therefore, TLR4 is important for induction of nickel allergy in both mice and humans.

Because induction of nickel allergy requires two components, the metal ion and TLR ligands, it is not surprising that symptoms of metal allergy most often present in the skin or oral cavity where resident flora exist. Thus, we attempted to establish an animal model for palladium allergy, which is known to be caused by dental restorations. Mice were sensitized with a mixed solution of palladium and lipopolysaccharides from one of the resident flora, *Escherichia coli*. After ten days, these mice were elicited with palladium solution injected into ear auricles under anesthesia. Ear thickness was measured before the elicitation and at 24, 48, and 72 h after elicitation, and ears were found to be swollen and infiltrated by $CD3^+$ T cells similar to pathogenesis of human metal allergy (Fig. 13.3) [68]. Metal allergy was also induced on the footpad in mouse model. For these studies, mice were sensitized twice followed by three separate applications for elicitation of nickel allergy [69] as well as palladium allergy [70]. We observed that footpad swelling continued up to 10 days and then returned to basal levels 14 days after the last elicitation. Furthermore, the epidermis was thickened and large numbers of $CD3^+$ T cell infiltrates were present in the inflamed skin epidermis as early as 7 days after elicitation. Thickening of epidermis and infiltration of T cells in palladium allergy were similar to that seen with nickel allergy [69, 70]. Together these findings show that we have established mouse models that accurately represent the pathology of human metal allergy.

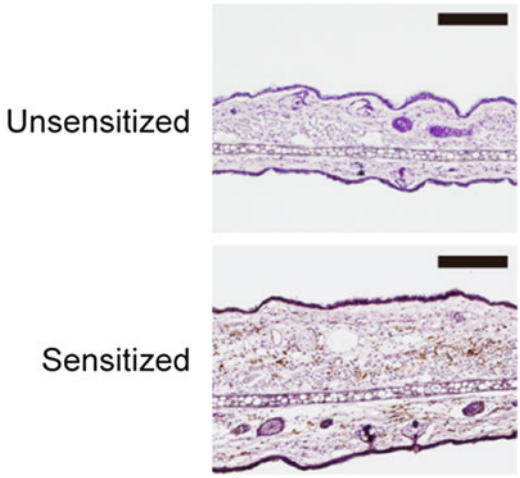

Fig. 13.3 Pathogenic T cells are present in a mouse model of metal allergy. Immunohistochemical analysis of the ear auricles at 24 h after elicitation with palladium in palladium plus LPS-sensitized wild type mice. As controls, unsensitized and palladium challenged mice were assessed. Ear sections were stained by anti-CD3ε mAb and visualized by DAB (*brown*). The sections were counterstained with hematoxylin (*blue*). The scale bars indicate 100 μm

13.5 Analysis of Pathogenic T Cells During Metal Allergy

Although metal allergy has long been known to be T cell dependent and metal ions are known to function as haptens, the involvement of pathogenic T cells in the development of metal allergy has not yet been explored using animal models. To identify the pathogenic T cells responsible for the onset of metal allergy, we utilized an adoptive transfer approach. In brief, we selectively isolated regional lymph node cells from mice in which allergic inflammation was elicited by palladium administration and then transferred these cells into naïve nude mice until more than 90 % of recipient mice exhibited allergic inflammation (Fig. 13.4). Analysis of these cells indicated that pathogenic T cells were responsible for the development of metal allergy.

When pathogenic T cells were enriched using sequential adoptive transfer, the allergic inflammation rate also increased. Although the period of ear swelling was not prolonged, the intensity was increased by sequential rounds of adoptive transfer [68]. Because we found that pathogenic T cells infiltrated into inflammatory lesions of nude mice that had received T cells derived from mice with metal allergic disease, we further investigated whether $CD4^+$ or $CD8^+$ T cells were preferentially involved in Pd allergy. To this end, we depleted $CD4^+$ or $CD8^+$ T cells from 8th transferred nude mice by administration of anti-CD4 or anti-CD8 mAbs in vivo. Although ear swelling was observed in mice depleted of $CD4^+$ T cells as well as mice administered rat IgG, ear swelling was significantly inhibited in mice depleted of $CD8^+$ T cells alone or of both $CD8^+$ and $CD4^+$ T cells [68]. To confirm the role of

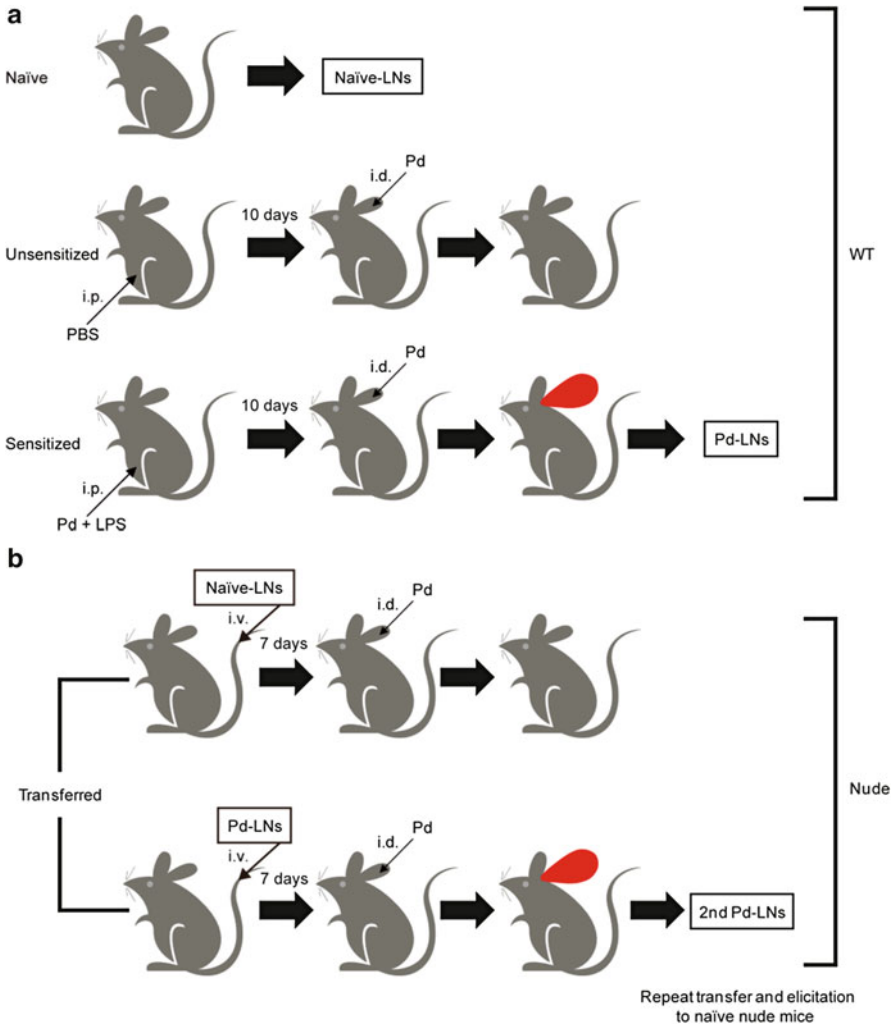

Fig. 13.4 Schematic view of metal allergy induction. (**a**) Metal allergy was elicited in WT mice by sensitization with intraperitoneal injection (*i.p.*) of palladium plus lipopolysaccharides (*LPS*) and subsequent elicitation with palladium. (**b**) Regional lymph node cells were isolated from ear-swollen mice (Pd-LNs) or naïve mice (naïve-LNs) and adoptively transferred to naïve nude mice. The transferred nude mice were elicited and ear-swollen mice were selected, and then Pd-LNs were isolated from this secondary transfer and further transferred to naïve nude mice

$CD8^+$ T cells in metal allergy, we induced metal allergy in MHC class I-deficient mice and MHC class II-deficient mice that lack $CD8^+$ T cells and $CD4^+$ T cells, respectively. We did not observe significant ear swelling in MHC class I-deficient mice, whereas MHC class II-deficient mice exhibited an inflammatory response to metal administration. These results indicate that, similar to that seen with other

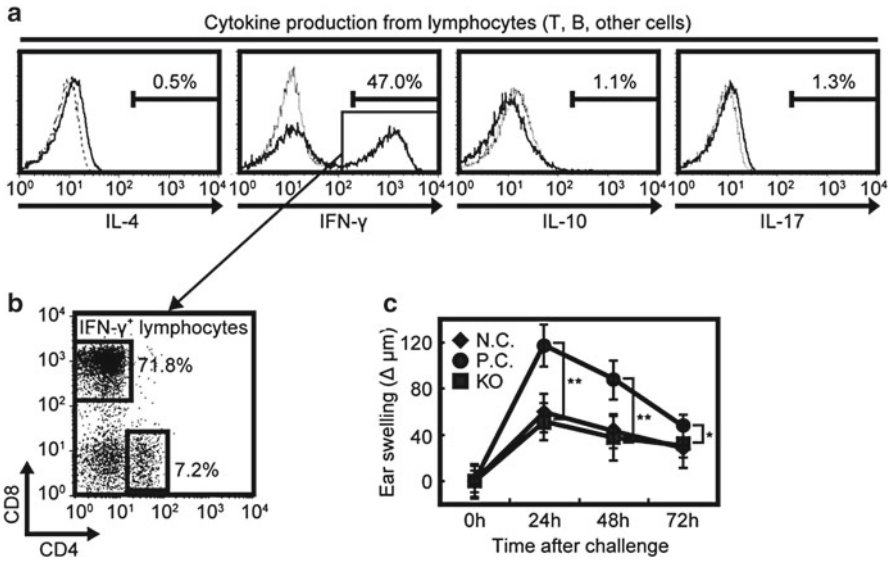

Fig. 13.5 IFN-γ from CD8⁺ T cells contributes to the development of metal allergy. (**a**) Fifteen hours after elicitation with palladium, cells from regional lymph nodes from the 8th mouse transfer were isolated and analyzed for cytokine production (IL-4, IFN-γ, IL-10, and IL-17). Data presented were obtained from total lymphocytes. (**b**) IFN-γ + T cell subset analysis. Cells were prepared and stained with anti-CD4, anti-CD8, and anti-IFN-γ mAbs then analyzed by flow cytometry. Percentages of T cell subsets in IFN-γ positive lymphocytes are indicated. (**c**) Palladium allergy was induced in IFN-γ-deficient mice. As experimental controls, wild type mice ($n = 5$) were sensitized by intraperitoneal injection with 2.5 μmol palladium and 2.5 μg lipopolysaccharides (LPS) (P.C.) or with PBS (unsensitized, N.C.). Ear thickness was measured before elicitation and at the indicated time points after elicitation. Data represent means ± SD of 10 ear samples. Asterisks (* or **) indicate statistical significance ($0.01 < {}^{*}P < 0.05$ or ${}^{**}P < 0.01$, respectively) between sensitized deficient (KO) mice and sensitized WT mice

strong experimental haptens, MHC class I-restricted CD8⁺ T cells are required for the onset of palladium allergy [71].

CD8⁺ T cells preferentially accumulated in the draining lymph nodes of sequentially transferred recipient mice [68]. Because cytokines have also been reported to play important roles in metal allergy [55, 58, 59], we examined production of IL-4, IFN-γ, IL-10, or IL-17 from lymphocytes of sequentially transferred nude mice (Fig. 13.5a). We found that pathogenic T cells preferentially secrete IFN-γ as an effector molecule at 15 h after elicitation of metal allergy [68]. To determine which T cell subset contributes to IFN-γ production, we analyzed the ratio of CD4⁺ T versus CD8⁺ T cells in IFN-γ positive lymphocytes and found that more than 70 % of IFN-γ⁺ cells were CD8⁺ T cells (Fig. 13.5b). Because IFN-γ is the main cytokine produced by CD8⁺ T cells responding to metal allergy, we evaluated allergic inflammation in mice deficient for IFN-γ and found no response when metal allergy was induced (Fig. 13.5c).

For optimal activation, T cells must be stimulated both through their TCRs and a costimulatory receptor. CD28, inducible costimulator (ICOS), and cytolytic T lymphocyte-associated antigen (CTLA)-4 are all involved in the delayed-type hypersensitivity reaction [72–75]. In addition, NKG2D is a costimulatory receptor expressed on NK cells, $CD8^+$ T cells, NKT cells, and γδ T cells [76–78]. Furthermore, NKG2D is expressed on activated/memory mouse $CD8^+$ T cells but not on naïve mouse $CD8^+$ T cells and $CD4^+$ T cells. However, costimulatory and effector molecule expression on pathogenic T cells during metal allergy has not previously been examined. Therefore, given that $CD8^+$ T cells are crucial for the development of palladium allergy, we hypothesized that NKG2D on $CD8^+$ T cells may be important for the pathogenesis of palladium allergy. Indeed, $CD8^+$ T cells of 8th transferred mice express NKG2D on their surface, indicating that the NKG2D molecule is upregulated on $CD8^+$ T cells during enrichment by sequential adoptive transfer. We also measured whether $NKG2D^+$ $CD8^+$ T cells produce IFN-γ in response to induction of palladium allergy and found that approximately 82 % of the $NKG2D^+$ $CD8^+$ T cells produced IFN-γ. To investigate whether a neutralizing anti-NKG2D mAb might be useful as a therapeutic reagent for Pd allergy, we performed an anti-NKG2D mAb administration study. To this end, blocking of NKG2D significantly ameliorated Pd-induced ear swelling in 8th transferred nude mice [68]. Together, these results indicate that $NKG2D^+$ $CD8^+$ T cells function as pathogenic T cells that produce IFN-γ in response to Pd allergy in vivo, and thus, NKG2D is a promising target for the treatment of metal allergy.

Limited TCR repertoires are known to be utilized in human metal allergy [21, 79]. To investigate whether pathogenic T cells in our mouse models also use limited TCR repertoires, we comprehensively examined the TCR repertoires in these mice. We found an increased representation of the TCR repertoires TCR AV18-1 and TCR BV8-2 at the sites of inflammation during palladium allergy. Furthermore, the expression of AV18-1 and BV8-2 increased gradually in the footpads over the 7 days post-elicitation. Sequencing analyses showed that identical TCR clonotypes bearing AV18-1 were obtained from the footpads of different mice, while diverse TCR clonotypes with BV8-2 were obtained from the footpads of all mice. These results indicated that T cells bearing AV18-1 and BV8-2 are responsible for metal allergy. Furthermore, certain T cells bearing AV18-1 and BV8-2 were expanded and continuously present for >1 week in the inflamed skin [70].

In the case of the nickel allergy mouse footpad model, we found that TCR VA14-1 and VB8-2 were most frequently utilized. Interestingly, VA14-1 and VB8-2 have been reported to be the TCR of invariant NKT (iNKT) cells, which produce IFN-γ, suggesting that iNKT cells are major pathogenic T cells involved in the murine nickel allergy [69].

In conclusion, we demonstrate that enrichment of mouse pathogenic T cells by sequential adoptive transfer affects the frequency and severity of development of metal allergic symptoms. Further, limited TCR repertoires are utilized in the development of metal allergy and IFN-γ is produced by these T cells. These results suggest that information of metal-specific TCR repertoires is useful for diagnosis of metal allergic patients.

Description of Technical Terms

Delayed-type Hypersensitivity: often called type IV hypersensitivity as the reaction takes 24 to 48 h to develop. Unlike the other types of hypersensitivity, it is not antibody mediated but rather is a cell-mediated response.

Allergic Contact Dermatitis: a form of contact dermatitis that is the manifestation of an allergic response caused by contact with a substance, the other type being irritant contact dermatitis. Allergic contact dermatitis is accepted to be the most prevalent form of immunotoxicity found in humans. The underlying immunology centers on the interaction of immunoregulatory cytokines and discrete subpopulations of T lymphocytes.

Contact Hypersensitivity: a murine model of allergic contact dermatitis, which is a form of delayed-type hypersensitivity, a classic T cell-mediated, clinically important phenomenon.

References

1. Bendiner E (1981) Baron von Pirquet: the aristocrat who discovered and defined allergy. Hosp Pract (Off Ed) 16:137, 141, 144 passim
2. Rajan TV (2003) The Gell-Coombs classification of hypersensitivity reactions: a re-interpretation. Trends Immunol 24:376–379
3. Gell PGH, Coombs RRA (1963) The classification of allergic reactions underlying disease. In: Coombs RRA, Gells PGH (eds) Clinical aspects of immunology. Blackwell, Oxford
4. Saint-Mezard P, Rosieres A, Krasteva M, Berard F, Dubois B et al (2004) Allergic contact dermatitis. Eur J Dermatol 14:284–295
5. Krasteva M, Kehren J, Sayag M, Ducluzeau MT, Dupuis M et al (1999) Contact dermatitis II. Clinical aspects and diagnosis. Eur J Dermatol 9:144–159
6. Nosbaum A, Vocanson M, Rozieres A, Hennino A, Nicolas JF (2009) Allergic and irritant contact dermatitis. Eur J Dermatol 19:325–332
7. Mortz CG, Andersen KE (1999) Allergic contact dermatitis in children and adolescents. Contact Dermatitis 41:121–130
8. Onder M, Adisen E (2008) Patch test results in a Turkish paediatric population. Contact Dermatitis 58:63–65
9. Brandão MH, Gontijo B (2012) Contact sensitivity to metals (chromium, cobalt and nickel) in childhood. An Bras Dermatol 87:269–276
10. Schäfer T, Böhler E, Ruhdorfer S, Weigl L, Wessner D et al (2001) Epidemiology of contact allergy in adults. Allergy 56:1192–1196
11. Rietschel RL, Fowler JFJ (2008) Metals. BC Decker Inc., Hamilton
12. Ostendrop P (2001) Nickel: hidden in plain sight. Dartmouth.edu [Internet].
13. Kornik R, Zug KA (2008) Nickel. Dermatitis 19:3–8
14. Thyssen JP, Johansen JD, Menné T (2007) Contact allergy epidemics and their controls. Contact Dermatitis 56:185–195
15. Vozmediano JM, Hita JCA (2005) Allergic contact dermatitis in children. J Eur Acad Dermatol Venerol 19(1):42–46
16. Thyssen JP, Menné T (2010) Metal allergy – a review on exposures, penetration, genetics, prevalence, and clinical implications. Chem Res Toxicol 23:309–318
17. Ekqvist S, Svedman C, Möller H, Kehler M, Pripp CM et al (2007) High frequency of contact allergy to gold in patients with endovascular coronary stents. Br J Dermatol 157:730–738

18. Hostynek JJ (2003) Factors determining percutaneous metal absorption. Food Chem Toxicol 41:327–345
19. Larese F, Gianpietro A, Venier M, Maina G, Renzi N (2007) In vitro percutaneous absorption of metal compounds. Toxicol Lett 170:49–56
20. Cavani A, De Pità O, Girolomoni G (2007) New aspects of the molecular basis of contact allergy. Curr Opin Allergy Clin Immunol 7:404–408
21. Gamerdinger K, Moulon C, Karp DR, Van Bergen J, Koning F et al (2003) A new type of metal recognition by human T cells: contact residues for peptide-independent bridging of T cell receptor and major histocompatibility complex by nickel. J Exp Med 197:1345–1353
22. Nielsen NH, Linneberg A, Menné T, Madsen F, Frølund L et al (2001) Persistence of contact allergy among Danish adults: an 8-year follow-up study. Contact Dermatitis 45:350–353
23. Andersen KE, Johansen JD, Bruze M, Frosch PJ, Goossens A et al (2001) The time-dose-response relationship for elicitation of contact dermatitis in isoeugenol allergic individuals. Toxicol Appl Pharmacol 170:166–171
24. Hextall JM, Alagaratnam NJ, Glendinning AK, Holloway DB, Blaikie L et al (2002) Dose-time relationships for elicitation of contact allergy to para-phenylenediamine. Contact Dermatitis 47:96–99
25. Agner T, Johansen JD, Overgaard L, Vølund A, Basketter D et al (2002) Combined effects of irritants and allergens. Synergistic effects of nickel and sodium lauryl sulfate in nickel-sensitized individuals. Contact Dermatitis 47:21–26
26. Kaplan DH, Igyártó BZ, Gaspari AA (2012) Early immune events in the induction of allergic contact dermatitis. Nat Rev Immunol 12:114–124
27. Förster R, Schubel A, Breitfeld D, Kremmer E, Renner-Müller I et al (1999) CCR7 coordinates the primary immune response by establishing functional microenvironments in secondary lymphoid organs. Cell 99:23–33
28. Itano AA, McSorley SJ, Reinhardt RL, Ehst BD, Ingulli E et al (2003) Distinct dendritic cell populations sequentially present antigen to CD4 T cells and stimulate different aspects of cell-mediated immunity. Immunity 19:47–57
29. Allenspach EJ, Lemos MP, Porrett PM, Turka LA, Laufer TM (2008) Migratory and lymphoid-resident dendritic cells cooperate to efficiently prime naive CD4 T cells. Immunity 29:795–806
30. Ohl L, Mohaupt M, Czeloth N, Hintzen G, Kiafard Z et al (2004) CCR7 governs skin dendritic cell migration under inflammatory and steady-state conditions. Immunity 21:279–288
31. Balato A, Balato N, Di Costanzo L, Ayala F (2011) Contact sensitization in the elderly. Clin Dermatol 29:24–30
32. Saint-Mezard P, Krasteva M, Chavagnac C, Bosset S, Akiba H et al (2003) Afferent and efferent phases of allergic contact dermatitis (ACD) can be induced after a single skin contact with haptens: evidence using a mouse model of primary ACD. J Invest Dermatol 120:641–647
33. Lidén C, Norberg K (2005) Nickel on the Swedish market. Follow-up after implementation of the Nickel Directive. Contact Dermatitis 52:29–35
34. Kaaber K, Veien NK, Tjell JC (1978) Low nickel diet in the treatment of patients with chronic nickel dermatitis. Br J Dermatol 98:197–201
35. Veien NK (2011) Systemic contact dermatitis. Int J Dermatol 50:1445–1456
36. Hsu JW, Matiz C, Jacob SE (2011) Nickel allergy: localized, id, and systemic manifestations in children. Pediatr Dermatol 28:276–280
37. Veien NK, Hattel T, Laurberg G (1995) Placebo-controlled oral challenge with cobalt in patients with positive patch tests to cobalt. Contact Dermatitis 33:54–55
38. Asano Y, Makino T, Norisugi O, Shimizu T (2009) Occupational cobalt induced systemic contact dermatitis. Eur J Dermatol 19:166–167
39. Stuckert J, Nedorost S (2008) Low-cobalt diet for dyshidrotic eczema patients. Contact Dermatitis 59:361–365
40. Romero-Brufau S, Best PJ, Holmes DR, Mathew V, Davis MD et al (2012) Outcomes after coronary stent implantation in patients with metal allergy. Circ Cardiovasc Interv 5:220–226

41. Hansen MB, Johansen JD, Menné T (2003) Chromium allergy: significance of both Cr(III) and Cr(VI). Contact Dermatitis 49:206–212
42. Yoshihisa Y, Shimizu T (2012) Metal allergy and systemic contact dermatitis: an overview. Dermatol Res Pract 2012:749561
43. Kaaber K, Veien NK (1977) The significance of chromate ingestion in patients allergic to chromate. Acta Derm Venereol 57:321–323
44. Veien NK, Hattel T, Laurberg G (1994) Chromate-allergic patients challenged orally with potassium dichromate. Contact Dermatitis 31:137–139
45. Gao X, He RX, Yan SG, Wu LD (2011) Dermatitis associated with chromium following total knee arthroplasty. J Arthroplasty 26:665.e613–666
46. Merad M, Manz MG, Karsunky H, Wagers A, Peters W et al (2002) Langerhans cells renew in the skin throughout life under steady-state conditions. Nat Immunol 3:1135–1141
47. Faurschou A, Menné T, Johansen JD, Thyssen JP (2011) Metal allergen of the 21st century – a review on exposure, epidemiology and clinical manifestations of palladium allergy. Contact Dermatitis 64:185–195
48. Larese Filon F, Uderzo D, Bagnato E (2003) Sensitization to palladium chloride: a 10-year evaluation. Am J Contact Dermat 14:78–81
49. Hindsén M, Spirén A, Bruze M (2005) Cross-reactivity between nickel and palladium demonstrated by systemic administration of nickel. Contact Dermatitis 53:2–8
50. Goodacre CJ (1989) Palladium-silver alloys: a review of the literature. J Prosthet Dent 62:34–37
51. Rebandel P, Rudzki E (1990) Allergy to palladium. Contact Dermatitis 23:121–122
52. Hackel H, Miller K, Elsner P, Burg G (1991) Unusual combined sensitization to palladium and other metals. Contact Dermatitis 24:131–132
53. Möller H, Ohlsson K, Linder C, Björkner B, Bruze M (1999) The flare-up reactions after systemic provocation in contact allergy to nickel and gold. Contact Dermatitis 40:200–204
54. Möller H, Björkner B, Bruze M, Lundqvist K, Wollmer P (1999) Laser Doppler perfusion imaging for the documentation of flare-up in contact allergy to gold. Contact Dermatitis 41:131–135
55. Summer B, Paul C, Mazoochian F, Rau C, Thomsen M et al (2010) Nickel (Ni) allergic patients with complications to Ni containing joint replacement show preferential IL-17 type reactivity to Ni. Contact Dermatitis 63:15–22
56. Hashizume H, Seo N, Ito T, Takigawa M, Yagi H (2008) Promiscuous interaction between gold-specific T cells and APCs in gold allergy. J Immunol 181:8096–8102
57. de Vos G, Abotaga S, Liao Z, Jerschow E, Rosenstreich D (2007) Selective effect of mercury on Th2-type cytokine production in humans. Immunopharmacol Immunotoxicol 29:537–548
58. Pennino D, Eyerich K, Scarponi C, Carbone T, Eyerich S et al (2010) IL-17 amplifies human contact hypersensitivity by licensing hapten nonspecific Th1 cells to kill autologous keratinocytes. J Immunol 184:4880–4888
59. Minang JT, Areström I, Troye-Blomberg M, Lundeberg L, Ahlborg N (2006) Nickel, cobalt, chromium, palladium and gold induce a mixed Th1- and Th2-type cytokine response in vitro in subjects with contact allergy to the respective metals. Clin Exp Immunol 146:417–426
60. Budinger L, Neuser N, Totzke U, Merk HF, Hertl M (2001) Preferential usage of TCR-Vbeta17 by peripheral and cutaneous T cells in nickel-induced contact dermatitis. J Immunol 167:6038–6044
61. Silvennoinen-Kassinen S, Karvonen J, Ikaheimo I (1998) Restricted and individual usage of T-cell receptor beta-gene variables in nickel-induced CD4+ and CD8+ cells. Scand J Immunol 48:99–102
62. Peiser M, Tralau T, Heidler J, Api AM, Arts JH et al (2012) Allergic contact dermatitis: epidemiology, molecular mechanisms, in vitro methods and regulatory aspects. Current knowledge assembled at an international workshop at BfR, Germany. Cell Mol Life Sci 69:763–781

63. Honda T, Egawa G, Grabbe S, Kabashima K (2013) Update of immune events in the murine contact hypersensitivity model: toward the understanding of allergic contact dermatitis. J Invest Dermatol 133:303–315
64. Lepoittevin JP, Karlberg AT (1994) Interactions of allergenic hydroperoxides with proteins: a radical mechanism? Chem Res Toxicol 7:130–133
65. Lepoittevin JP (2006) Metabolism versus chemical transformation or pro-versus prehaptens? Contact Dermatitis 54:73–74
66. Martin SF, Esser PR, Weber FC, Jakob T, Freudenberg MA et al (2011) Mechanisms of chemical-induced innate immunity in allergic contact dermatitis. Allergy 66:1152–1163
67. Schmidt M, Raghavan B, Müller V, Vogl T, Fejer G et al (2010) Crucial role for human Toll-like receptor 4 in the development of contact allergy to nickel. Nat Immunol 11:814–819
68. Kawano M, Nakayama M, Aoshima Y, Nakamura K, Ono M et al (2014) NKG2D$^+$ IFN-gamma$^+$ CD8$^+$ T cells are responsible for palladium allergy. PLoS One 9(2):e86810
69. Eguchi T, Kumagai K, Kobayashi H, Shigematsu H, Kitaura K et al (2013) Accumulation of invariant NKT cells into inflamed skin in a novel murine model of nickel allergy. Cell Immunol 284:163–171
70. Kobayashi H, Kumagai K, Eguchi T, Shigematsu H, Kitaura K et al (2013) Characterization of T cell receptors of Th1 cells infiltrating inflamed skin of a novel murine model of palladium-induced metal allergy. PLoS One 8:e76385
71. Bour H, Peyron E, Gaucherand M, Garrigue JL, Desvignes C et al (1995) Major histocompatibility complex class I-restricted CD8+ T cells and class II-restricted CD4+ T cells, respectively, mediate and regulate contact sensitivity to dinitrofluorobenzene. Eur J Immunol 25:3006–3010
72. Wong SC, Tan AH, Lam KP (2009) Functional hierarchy and relative contribution of the CD28/B7 and ICOS/B7-H2 costimulatory pathways to T cell-mediated delayed-type hypersensitivity. Cell Immunol 256:64–71
73. Warnecke G, Chapman SJ, Bushell A, Hernandez-Fuentes M, Wood KJ (2007) Dependency of the trans vivo delayed type hypersensitivity response on the action of regulatory T cells: implications for monitoring transplant tolerance. Transplantation 84:392–399
74. Friedmann-Morvinski D, Bendavid A, Waks T, Schindler D, Eshhar Z (2005) Redirected primary T cells harboring a chimeric receptor require costimulation for their antigen-specific activation. Blood 105:3087–3093
75. Hazlett LD, McClellan S, Barrett R, Rudner X (2001) B7/CD28 costimulation is critical in susceptibility to Pseudomonas aeruginosa corneal infection: a comparative study using monoclonal antibody blockade and CD28-deficient mice. J Immunol 166:1292–1299
76. Cerwenka A, Lanier LL (2001) Ligands for natural killer cell receptors: redundancy or specificity. Immunol Rev 181:158–169
77. Diefenbach A, Tomasello E, Lucas M, Jamieson AM, Hsia JK et al (2002) Selective associations with signaling proteins determine stimulatory versus costimulatory activity of NKG2D. Nat Immunol 3:1142–1149
78. Wu J, Song Y, Bakker AB, Bauer S, Spies T et al (1999) An activating immunoreceptor complex formed by NKG2D and DAP10. Science 285:730–732
79. Thierse HJ, Gamerdinger K, Junkes C, Guerreiro N, Weltzien HU (2005) T cell receptor (TCR) interaction with haptens: metal ions as non-classical haptens. Toxicology 209:101–107

Chapter 14
Cytotoxicity of Metallic Biomaterials

Akiko Obata and Toshihiro Kasuga

Abstract The increasing use of orthopedic and dental implants, such as joints and roots, has stimulated interest and concern regarding the chronic, long-term effects of metallic biomaterials used. This chapter focuses on cytotoxicity of metallic implants, particles, and ions. Metallic biomaterials may corrode and wear after being implanted in the body, which induces cytotoxicity and inflammatory. In addition, metallic particles and ions may be released through wear or abrasion. Therefore, it is important to understand the effects of metallic materials, including particles and ions, on surrounding cells and tissues. Reactions of fibroblasts and osteoblastic cells to metallic biomaterials have already been investigated by many researchers. Intensity of the cytotoxicity has been reported to depend on the kinds of metallic elements. Some metallic ions alter osteoblastic cell behavior and stimulate the cell functions, such as proliferation, differentiation, and mineralization, while for several ions, there is an appropriate amount for upregulation of such cell functions.

Keywords Metallic implants • Metallic particles and ions • Cytotoxicity • Cell adhesion • Cell viability • Biocompatibility • Bioactivity

14.1 Introduction

Many different types of metal and alloys are now available in the market to be used for bone and tooth reconstruction. In the past several decades, there has been an increase in the use of orthopedic and dental implants, which has raised questions about the potential cytotoxicity of such materials. In vivo corrosion of these implant materials is a major potential disadvantage of the implants.

A number of investigations have demonstrated that metal ions can be released from metallic implants as the results of corrosion [1, 2]. The metal ions can be localized in blood, serum, urine, and other organs, as well as bone tissue adjacent to implants [3].

A. Obata (✉) • T. Kasuga
Graduate School of Engineering, Nagoya Institute of Technology,
Gokiso-cho, Showa-ku, Nagoya 466-8555, Japan
e-mail: obata.akiko@nitech.ac.jp; kasuga.toshihiro@nitech.ac.jp

M. Niinomi et al. (eds.), *Advances in Metallic Biomaterials*, Springer Series
in Biomaterials Science and Engineering 3, DOI 10.1007/978-3-662-46836-4_14

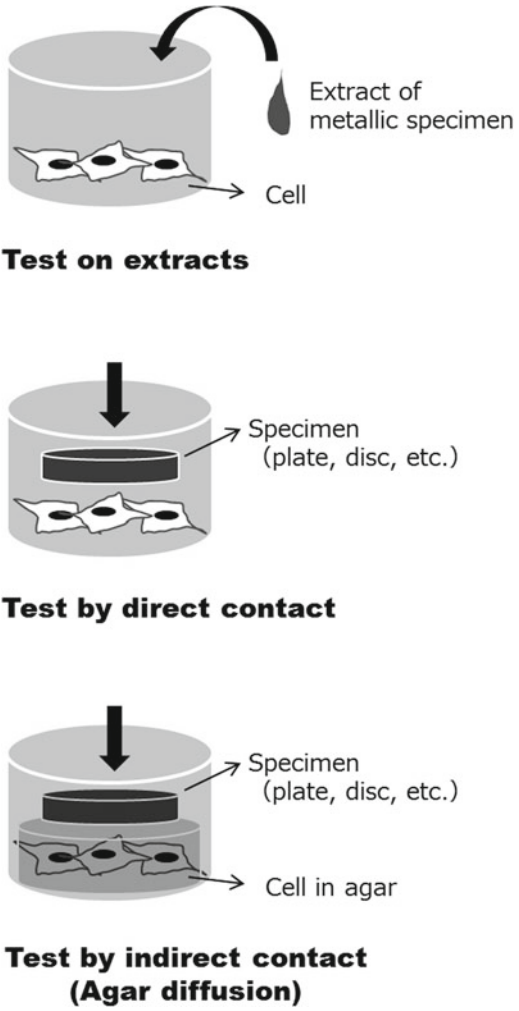

Fig. 14.1 Cytotoxicity test methods. Agar diffusion method is one of the methods of "test by indirect contact"

Thus, cytotoxicity of metallic implants themselves, metal ions, and extracts of the implants has been studied for many years. In vitro cytotoxicity tests are generally designed by the International Organization for Standardization (ISO) to evaluate the acute cytotoxicity of a material. In many recent reports, the cytotoxicity tests for metallic biomaterials have been carried out following ISO 10993-5 "Biological evaluation of medical devices – Part 5: Tests for in vitro cytotoxicity." Test procedures mentioned in ISO 10993-5 were "test on extracts," "test by direct contact," and "test by indirect contact" which includes agar diffusion and filter diffusion (Fig. 14.1).

Most metallic biomaterials are alloys which consist of several kinds of metallic elements. Although their cytotoxicity has been investigated by using the materials themselves, it was difficult to clarify from the obtained results which metallic element had cytotoxicity on cells and responsible to adverse reactions to natural

tissues. To solve these problems, metal salts or solutions of metal cations have been used for the in vitro cytotoxicity tests [4]. Such studies have revealed that the cytotoxicity and cell reactions depend on the concentration of metal ions.

The biomedical use of inorganic nanoparticles has enjoyed an increasing interest over the past decade. The nanoparticles enable noninvasive and long-term imaging of the whole body, potential treatment of cancer as currently being studied in clinical trials for magnetite and fold particles, or shedding of light on the complex cellular environment [5]. Rivera Gil et al. mentioned that several properties of nanoparticles have been demonstrated to change the in vitro (and partly also in vivo) toxicity of nanoparticles as compared to the bulk state, and the properties are (1) a higher surface-to-volume ratio and thus an enhanced contact area with their surroundings than bulk materials of the same mass do, (2) their retention in many cells and organs to a larger extent than larger particles, and (3) their crucial role in determining response based on the nanoparticle shape [6]. Thus, the state of metallic materials used for cytotoxicity tests, such as bulk, ion, and nanoparticles, plays an important role in their cytotoxicity and cell reactions.

Naturally, the choice of cytotoxicity test model, such as cell and tissue types, is critical to a more thorough understanding of the safety of metallic implants. This must depend on application fields in which the metallic implants are used, such as orthopedic or dental field. Various types of cells (e.g., osteoblasts, fibroblasts) have been used for in vitro tests. In addition, several types of assay have been applied to the tests: cells are cultured on metallic implant surface directly or in extracts of the implants, in media containing metal ions, etc. Most types of adherent cells are influenced by surface properties of the substrates used, such as roughness, hydrophilicity, chemical component, etc., in their reactions. We need to pay attention to not only the type of metallic materials used but also the culture conditions to understand cytotoxicity of the materials by in vitro tests.

The assessment of cytotoxicity of metallic implants has been complicated due to a great variety in sample shapes (including ions), physicochemical parameters of samples, type of cells used, type of assay used, etc. It would be difficult to compare results based on varying methods and sample types. In addition, in vitro tests focus on specific interactions between metallic samples (including ions) and cells. Extrapolation to in vivo is not straightforward. Comprehensive investigation must be required to thoroughly understand cytotoxicity of metallic implants.

Many cases, in which human beings or experimental animals have adverse reactions to metallic implants, are reported. However, positive reactions by metallic implants have enjoyed an increasing interest recently. Effects of metallic materials on specific cellular functions have been focused to identify the material biocompatible to bone or tooth rather than to evaluate general cytotoxicity. Characteristic reactions of several metal ions with cells have been found via in vitro tests, for example, upregulation of proliferation and mineralization of osteogenic cells by several metal ions was reported.

This chapter provides a comprehensive update of the cytotoxicity of metallic materials (implants themselves, ions, and particles), differences in cell reactions to metallic materials depending on cell type, and positive cell reactions to metallic materials.

14.2 Metallic Samples for Cytotoxicity Test

14.2.1 Plates and Disks

Direct method of cytotoxicity tests using plates, disks, and commercialized devices of metallic materials has been applied in order to assess the cell response to such material surfaces (Table 14.1). Generally, cells are seeded on sample surfaces or cultured with samples in the same well and then examined in their adhesion, viability, and proliferation. Cell functions are influenced by not only the type of metallic component but also several surface properties, such as hydrophilicity, roughness, etc. Therefore, to take account of such properties is important when we compare the cytotoxicity of several materials.

Retamoso et al. reported the cell culture test for ten kinds of orthodontic devices including metallic, polycarbonate, monocrystalline ceramic, and polycrystalline ceramic samples using mouse fibroblasts (NIH/3T3) [7]. The cells were cultured in a well containing specimen. After 24 h of culturing, the cytotoxicity was evaluated by MTT assay, which is based on the ability of the mitochondrial enzyme succinate dehydrogenase to convert the yellow water-soluble tetrazolium salt into formazan crystals in metabolically active cells. Three types of commercialized nickel-free samples, including two types of 100 % of Ti and one alloy (Ti–Cr–Mo–Fe), were found to have better biocompatibility than the others. The alloy sample showed some toxic effects compared with the titanium one. This might be due to effects of molybdenum released from the sample, referring the past literatures. The release of ions from the tested samples, however, was not evaluated in this report. Nickel-free and steels with reduced nickel content have been tried in orthodontic use. There are biocompatibility concerns from the use of nickel alloys in the human oral cavity for

Table 14.1 Reports on cytotoxicity of metal bulks

Metallic material	Specimen	Cell type	Assay	Ref.
Ti	–	Mouse fibroblast (NIH/3T3)	MTT	[7]
Ti–Cr–Mo–Fe				
Stainless steel				
Ag–Sn–Co–Hg				
Au alloy	Cast disk	Mouse fibroblast (NCTC clone 929)	Agar overlay	[8]
Unalloyed Cu			Millipore filter	
Unalloyed Ag				
Cr–Co alloy			MTT	
Au–Pt–Pd–Ag	Block	Human fibroblast	BrdU immunocytochemistry	[9]
Au–Pt–Pd–Ag–Cu–In–Ir				
Au–Pt–Pd–Ag–In–Ru–Zn				
Au–Pt–Pd–Ag–Sn–In–Ga				
Au–Pt–Pd–Ag–Cu–In				
Au–Pt–Pd–Ag–Cu				

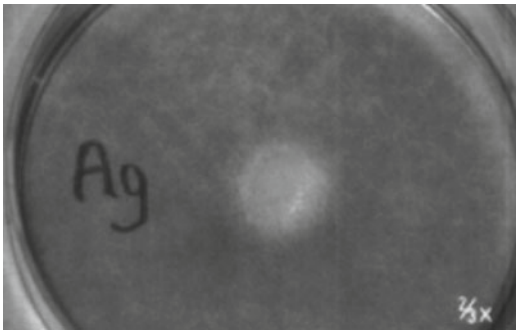

Fig. 14.2 Cytotoxicity of unalloyed Ag assessed by agar overlay test and presented as unstained area in cell monolayer (Reprinted from Ref. [8], Copyright 2000, with permission from Elsevier)

extended periods of time, while nickel has been incorporated into the alloys to decrease corrosion. In this report, austenitic stainless steel (17–20 mass % Cr, 8–10.5 mass % Ni, 65–69 mass % Fe) was used as a negative control (showing a low toxicity). The titanium and its alloy had significant lower cell viability than the negative control and cellular control (no sample).

The viability of mouse fibroblast contacting several types of dental metallic materials (Au alloys, unalloyed Cu or Ag, Cr–Co alloy, etc.) intended for fixed and removable prostheses was reported by Sjögren et al. [8]. The materials were placed on an agar surface where the cells were seeded and then incubated for 24 h. After the culturing, unstained area in cell monolayer by neutral red was evaluated, as damaged or dead cells appear decolorized in comparison to healthy control cells (Fig. 14.2). In their report, Millipore filter and MTT tests (in direct method) were also applied for the cytotoxicity test of the samples. From the results of all tests, the authors concluded that the cytotoxicity was related to the alloy composition and treatment. The alloys releasing Cu and Zn had lower cell compatibility in comparison with the others. Especially, the adverse effects of released Cu depended on its amount. Surface treatment for the materials influenced the cytotoxicity; sandblasting and polishing reduced both cytotoxicity and release of metal ions from the test specimens.

The influence of six types of dental alloys (Au–Pt–Pd–Ag, Au–Pt–Pd–Ag–Cu–In–Ir, Au–Pt–Pd–Ag–In–Ru–Zn, Au–Pt–Pd–Ag–Sn–In–Ga, Au–Pt–Pd–Ag–Cu–In, and Au–Pt–Pd–Ag–Cu) on the proliferation and fibronectin arrangement in human fibroblasts was reported by Grill et al. [9]. The cells were cultured in a dish in which the alloy block was placed. The cytotoxicity was evaluated by calculating the percentage of cells in the S-phase and observing fibronectin organization. The authors concluded that the alloy with the highest Au content had the most biocompatibility among the samples tested, and this agreed with the results reported by other literatures. The reason why Au content in alloy was effective for high cell compatibility was unclear. The authors also mentioned that a correlation exists between fibronectin organization and cell proliferation, and the observation of the fibronectin arrangement could be a farther useful tool in evaluating the biocompatibility of biomaterials. Some reports suggested such correlation [10]; each type of fibronectin organization is strictly related to cell proliferation; fibronectin organized in focal adhesions

enhances cell entry into the S-phase and therefore stimulates the growth cycle; different morphological and functional features of fibroblasts can influence cell proliferation.

14.2.2 Particles

Several types of nanoparticles and microparticles have been investigated in their cell compatibility by in vitro tests (Table 14.2). Nanoparticles have been investigated for the application in the invasive and long-term imaging of the whole body, cancer treatment, etc. Therefore, cells are exposed to a wide array of nanoparticles. Understanding the interaction between nanoparticles and cell must be necessary.

Iron oxide and gold nanoparticles are one of the frequently used inorganic nanoparticles. As iron oxide is a ferromagnetic material, its nanoparticles are useful for many kinds of biomedical applications, such as magnetic resonance imaging (MRI), mediators in magnetic cancer hyperthermia, and magnetically enhanced and targeted drug or gene delivery. Therefore, small particles are preferably employed.

The diameter of the iron oxide core is smaller than the superparamagnetic limit. Although iron oxide nanoparticles have been regarded to be degraded and released, resulting in the normal iron metabolism, there are concerns that its small size pose an additional hazard. Gold nanomaterials have enjoyed an increasing interest in biomedical field such as drug or gene delivery, cancer treatment, and biological imaging, as they have unique optical features, such as localized surface plasmon resonance. Although bulk gold has been expected not to have toxicity, its nanoparticles have been suggested to induce toxicity by penetrating the nuclear compartment and binding to DNA.

"Nanofactor" itself appears to cause several adverse effects on cells [5]. Nanoparticles reach places where larger particles cannot enter, such as the nucleus; nanoparticles internalized into cells [11, 12] and passed across a cellular barrier (Fig. 14.3) [13], and ultrafine particles (<100 nm) were transferred to the brain [14]. Their high surface area is available for interaction with cellular components. They suggested several factors which are expected to relate the cytotoxicity of nanoparticles: (1) the generation of reactive oxygen species, (2) the cell morphology and cytoskeleton defects, (3) the intracellular signaling pathways and genotoxicity, (4) the intracellular nanoparticle degradability, (5) the interaction with biological molecules, etc. Thus, the cytotoxicity of metallic nanoparticles is influenced by not only the type of metal component but also these nanofactors of the materials.

Reactive oxygen species have been expected to be of major importance in the toxicological prolife of nanoparticles. They are generated by cultured cells upon exposure to nanoparticles. Their generation has been controlled by coating nanoparticles with various materials, such as dextran, citrate, etc. The intercellular volume of nanoparticles influences cellular morphology or the structure of the cellular cytoskeleton network. In the case of iron oxide nanoparticles, their intracellular localization is related to the disruption of the cell cytoskeleton network [11]. The coating

Table 14.2 Reports on cytotoxicity of metal particles

Metallic material	Specimen	Cell type	Assay	Ref.
Iron oxide	Nanoparticle (around 13 nm)	Primary human fibroblast (h-TERT BJ1)	MTT	[11]
Iron oxide	Nanoparticle (40–45 nm)	Primary human fibroblast (h-TERT BJ1)	MTT	[12]
Iron oxide	Nanoparticle (60 nm)	Professional phagocyte	XTT	[15, 16]
Cu	Microparticle (1–147 μm)	Human osteoblast-like cell (MG-63)	Neutral red	[17]
Al				
Ti				
Zr				
V				
Nb				
Ta				
Cr				
Mo				
W				
Mn				
Fe				
Co				
Ni				
Cd	Microparticle (0.1–150 μm)	Human erythrocyte	Hemolysis measurement	[18]
Cr				
Co				
Fe				
Mo				
Ni				
Ta				
Ti				
Zn				
Co–Cr alloy				
Au–Cu–Ag–Pd–others	Sphere (9.1 mm)	Mouse fibroblast (L929)	Neutral red	[19]
Ag–Pd–Cu–others				
Ti–others				
Co–Cr–Mo–others				
Ni–Cr–others				

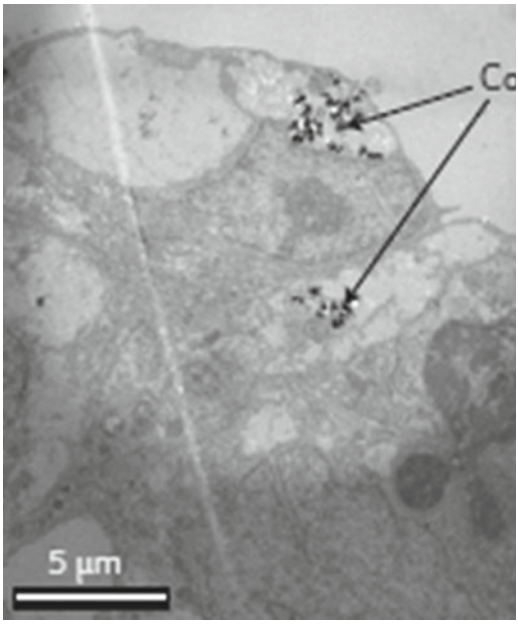

Fig. 14.3 TEM image of a nanoparticle-treated BeWo cell (human trophoblast choriocarcinoma-derived cell line) barrier showing aggregates of CoCr nanoparticles (NP) internalized in the upper layers of the barrier (Reprinted by permission from Macmillan Publishers Ltd: Ref. [13], copyright 2009)

is effective for controlling the adverse effects, because the effects have been found to depend on the concentration of generated reactive oxygen species and the particles penetrating into the cells (Fig. 14.4) [11].

Nanoparticles influence intracellular signaling pathways [13]. This is suggested to be carried out via the high levels of reactive oxygen species, change in the level of protein or gene expression, altered activation status of proteins, and influenced gene expression [5]. The nanoparticle degradation inside of the cells has been reported to play a significant role for the cell reactions [15, 16]. The local pH at the nanoparticle surface increases or decreases compared with the physiological condition through the degradation of the particles. Subsequently, free metal ions are released from the particles. The nanoparticle degradation inside of the cells has been reported to induce adverse effects on cell functions, such as apoptosis and inhibition of differentiation. On the other hand, different cell reactions are observed when gold nanoparticles are induced into cells. Gold nanoparticles possess high stability; therefore, the degradation hardly happens inside of the cells. Most of the cytotoxicity of gold nanoparticles has been regarded to be due to the particle size and the coating. Thus, the adverse effects on cells by the nanoparticle degradation depend on the kinds of metal component of the nanoparticles.

Microparticles are produced by the wear on metallic implant surfaces implanted in the body and have been recognized as one of the major factors responsible for loosening implants. Two materials placed together under load develop electrorepulsive and atomic binding interactions in the area of contact. These reactions are disrupted, when the surfaces slide across each other. Thus, wear debris

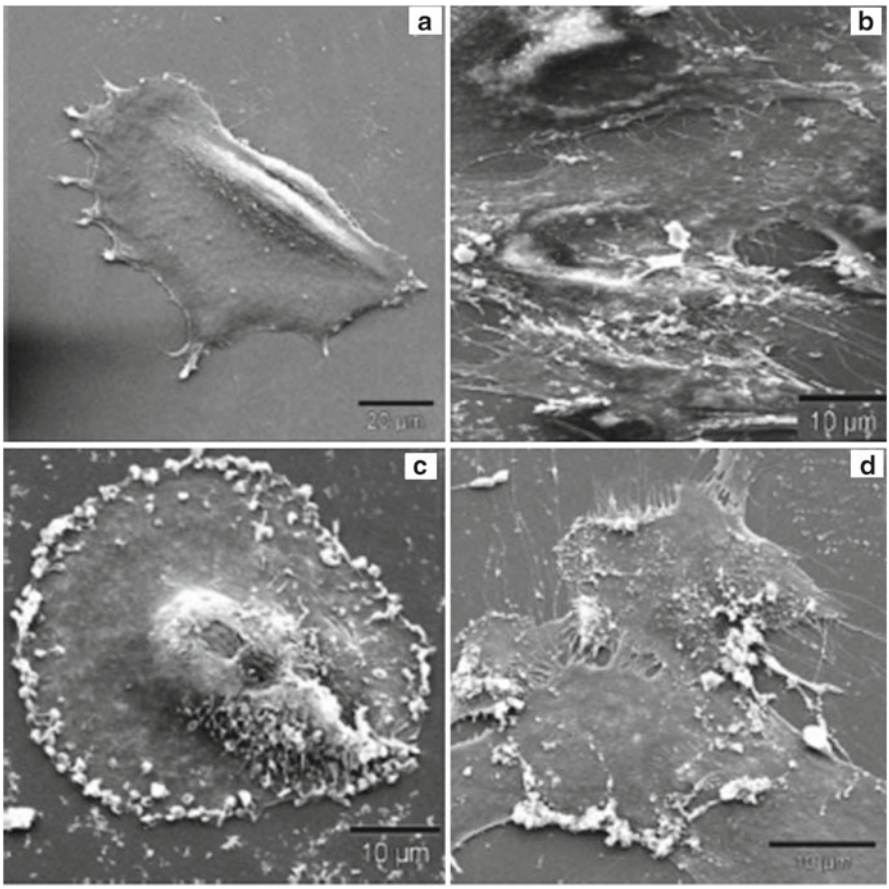

Fig. 14.4 SEM pictures of human fibroblasts incubated with magnetic nanoparticles: (**a**) control cells, (**b**) plain-uncoated particles, (**c**) lactoferrin-coated, and (**d**) ceruloplasmin-coated nanoparticles. The picture shows that lactoferrin- and ceruloplasmin-coated nanoparticles adhere to the cell surface, whereas plain-uncoated particles were found to be phagocytosed by the cells (Reprinted from Ref. [11], Copyright 2004, with permission from Elsevier)

(particles of the implant material) are produced and may attach to the counter face, remain between the two surfaces, or disperse into the system of the host.

The cytotoxicity of metal particles (Cu, Al, Si, Ti, Zr, V, Nb, Ta, Cr, Mo, W, Mn, Fe, Co, and Ni) with several micrometers in size was reported by Sakai et al. [17]. They cultured human osteoblast-like cell (MG-63) with the particles and also in the culture medium containing extract of each particle. The cytotoxicity was assessed by evaluating the viability with neutral red assay after 3 and 6 days of culturing. Nb and Zr showed no inhibition of the cell viability in any conditions where the amount of particles in the medium changed, while other metal materials inhibited the viability depending on the dose of particles. Mn particles showed the most severe inhibi-

tion. The extracts of Al, Ti, Zr, Nb, Ta, Cr, and Fe had no adverse effects on the cell viability, while the viability was decreased by the metal particles in the case of direct culturing. This result suggested that there was a direct interaction between the particle surface and cellular membranes, which influenced the cell viability.

Rae et al. revealed effects of the direct interaction on the hemolytic properties [18]. Erythrocytes were incubated in a buffer solution containing metal particles (Cd, Cr, Co, Fe, Mo, Ni, Ta, Ti, Zn, and Co–Cr alloy), and the hemolysis was measured. Cd, Ta, Ti, and Zn possessed a mild hemolysis, while Co, Ni, and Co–Cr alloy had a severe hemolysis. The others appeared to cause some hemolysis which was intermediate to the above groups. The authors also did similar tests for soluble nickel and cobalt chlorides, respectively, to clarify if soluble metallic product of the Co, Ni, and Co–Cr alloy related to the hemolysis. Results demonstrated no measurable hemolysis by these metal ions. Therefore, the direct interaction between particle surfaces and erythrocyte surfaces was suggested to be responsible for the observed hemolysis. Thus, cell activities are affected by such direct interaction rather than metal ions released, when metal samples have low cytotoxicity. We, however, need to pay attention to the size of particles tested. As determined in this section, nanoparticles internalized into cells, whereas microparticles did not. A route to adverse effects on cell viability is different between the two types of particles. The particle size must relate to the development of the direct interaction.

Takeda et al. reported that wear debris of some alloys, rather than the extract from them, were responsible for adverse effects on fibroblasts [19]. They did culture tests using L929 mouse fibroblast cells for three different culture media conditioned by metal particles (Au–Cu–Ag–Pd–others, Ag–Pd–Cu–others, Ti–others, Co–Cr–Mo–others, and Ni–Cr–others), (1) medium containing extracts of metal particles prepared with static condition, (2) medium after mixing with metal particles (dynamic system), and (3) medium after the treatment in the dynamic system followed by filtration with 0.22 μm membrane filter. After 3 days of culturing the cells in the three different types of medium, the cytotoxicity was determined by evaluating the cell viability with neutral red assay. No adverse effects of the metal particles tested on the cell viability were observed in the results of culture tests using medium 1. However, the cell viability in media 2 and 3 varied with the metal type. Figure 14.5 shows possible interactions with the cell response. In the case of Au-based alloy, the viability in the medium 2 was lower than that in the medium 3. Wear debris of the alloy were generated by the action of mechanical forces in the medium 2 and influenced the viability via a direct interaction between debris surfaces and cells. The authors suggested based on these results that even if metallic biomaterials are not toxic due to excellent corrosion resistance, cytotoxic effects can occur when wear debris is produced. Co-based alloy possessed a severe deterioration of the cell viability in both cases of media 2 and 3. Although the alloy tested had good corrosion resistance, Co or Cr ions dissolved from the alloy affected the cell viability. The ion dissolution was suggested to increase due to a break of the protective surface layer (passivation layer) of the alloy through the mixing. Ni-based alloy also had a severe deterioration of the cell viability in both cases of media 2 and 3. This was due to Ni dissolution.

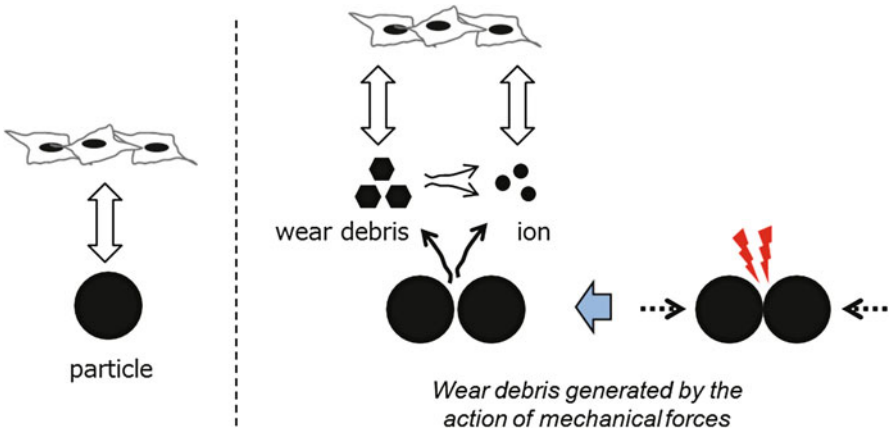

Fig. 14.5 Schematic image of possible interactions between metal specimen and cells

14.2.3 Ions

Extracts of metallic biomaterials (a solution containing ions released from the materials) have been applied for cytotoxicity tests (Table 14.3). This is because metal ions have been reported to be released from some biomaterials in vivo and may be associated with local inflammation or other adverse reactions. The international standards complied as ISO 10993 recommend in vitro cellular toxicity testing on established cell lines and using the extracts. In the case of alloys, several ions are simultaneously released from them.

To investigate in the effects of single metal ion on cell functions, culture media containing single ion which are prepared using metal salts, such as metal chlorides, are also applied for the cytotoxicity tests (Table 14.4).

Mockers et al. carried out the cytotoxicity test for 28 new and 9 used biomaterials (stainless steel, gold-plated steel, pure Ti, Ni–Ti, Ti–Mo, and silver-based soldering alloy) which were commercially used as brackets, molar bands, and archwires [20]. Polycarbonates and ceramic materials were also tested. The extracts of each material were prepared by incubating the materials in a culture medium for 3 or 14 days. For the cytotoxicity test, L929 cells were incubated for 24 h using the pure culture medium, and then the medium was replaced by the extracts. The cell activity was assessed by MTT assay after an additional incubation of 24 h. The tested materials were noncytotoxic, while only one sample (silver-based soldering alloy) possessed toxicity. When comparing the results of cytotoxicity of 3- and 14-day extracts, 6 materials out of 37 showed a statistically different cytotoxicity after the 3- and 14-day release period and three cases of increased cell viability and three cases of decreased cell viability after the 14-day release period. Although no data of ion concentration of the extract was shown in the report, the concentration might be different between 3- and 14-day release period. The authors recommended using

Table 14.3 Reports on cytotoxicity of metal extracts

Metallic material	Specimen	Cell type	Assay	Ref.
Stainless steel	Extract	Mouse fibroblast (L929)	MTT	[20]
Au-plated steel				
Ti				
Ni–Ti alloy				
Ti–Mo alloy				
Ag-based soldering alloy				
Au–Pt alloy	Extract	Human gingival fibroblast	MTT	[21]
Co–Cr alloy				
Ni–Cr alloy				
4 types of Ti alloys	Extract	Human gingival fibroblast and mouse osteoblast (MC3T3-E1)	Impedance-based real-time cell analyzer	[22]
316 stainless steel containing alloy				

Table 14.4 Reports on cytotoxicity of metal ions

Metallic material	Specimen	Cell type	Assay	Ref.
Ag	Ag_2SO_4	Mouse fibroblast (L929)	Trypan blue	[23]
Al	$AlCl_3$			
Be	$BeCl_2$			
Cr	$CrCl_3$			
Cu	CuCl			
Fe	$FeCl_3$			
Mo	MoC_{l5}			
Ni	$NiCl_2$			
Pd	$PdCl_2$			
Zn	$ZnCl_2$			
Al	Pure metal	Mouse fibroblast (L929)	Borenfreund's assay	[25]
Co				
Cr				
Cu				
Fe				
Mn				
Mo				
Ni				
Ti				
V				

(continued)

Table 14.4 (continued)

Metallic material	Specimen	Cell type	Assay	Ref.
Ag	Ag_2SO_4	Mouse fibroblast (Balb/c 3T3, L929) Human fibroblast (Wl-38) Rat osteoblast (ROS 17/2.8)	SDH activity	[29]
Al	$AlCl_3$			
Au	$HAuCl_4 \cdot 3H_2O$			
Be	$BeSO_4 \cdot 4H_2O$			
Cd	$CdCl_2$			
Co	$CoCl_2 \cdot 6H_2O$			
Cr	$CrCl_3 \cdot 6H_2O$			
Cu	$CuCl_2 \cdot 2H_2O$			
Ga	$Ga(NO_3)_3$			
Ni	$NiCl_2 \cdot 6H_2O$			
Pd	$PdCl_2$			
Ti	$TiCl_4$			
V	VCl_3			
Zn	$ZnCl_2 \cdot 6H_2O$			
Ag	Ag_2SO_4	Mouse fibroblast (Balb/c 3T3,)	SDH activity DNA synthesis Protein synthesis Total protein	[30]
Au	$HAuCl_4 \cdot 3H_2O$			
Cd	$CdCl_2$			
Cu	$CoCl_2$			
Ga	$Ga(NO_3)_3$			
In	$InCl_3$			
Ni	$NiCl_2 \cdot 6H_2O$			
Pd	$PdCl_2$			
Zn	$ZnCl_2$			
Ag	Ag_2SO_4	Mouse fibroblast (L929) Human gingival fibroblast Human tissue mast cell	DNA synthesis Histamine release	[32]
Au	$HAuCl_4 \cdot 4H_2O$			
Co	$CoCl_2$			
Cr	$CrCl_2$			
Cu	$CuCl_2$			
Ga	$GaCl_3$			
In	$InCl_3$			
Mo	$MoCl_5$			
Ni	$NiCl_2$			
Pd	$PdCl_2$			
Pt	$PtCl_4$			
Sn	$SnCl_2$			
Zn	$ZnCl_2$			
Ag	AgCl	Primary human osteoblast Primary rat osteoblast	MTT ALP activity	[33]
Al	$AlCl_3$			
Cr+3	$CrCl_3$			
Cr+6	$CrCl_2O_4$			
Ni	$NiCl_2$			
V	$VOCl_3$			

(continued)

Table 14.4 (continued)

Metallic material	Specimen	Cell type	Assay	Ref.
Ag	Ag_2SO_4	Primary human endometrial epithelial cells	MTT	[35]
Cu	$CuCl_2$			
Zn	$ZnCl_2$			
Al	$AlCl_3$	Rat osteoblast (ROS 17/2.8)	DNA synthesis SDH activity ALP activity Von Kossa Gene expression	[3]
Co	$CoCl_2 \cdot 6H_2O$			
Cr	$CrCl_3 \cdot 6H_2O$			
Ni	$NiCl_2 \cdot H_2O$			
Ti	$TiCl_4$			
V	VCl_3			
43 types	43 metal salts	Mouse fibroblast (L929) Mouse osteoblast-like cell (MC3T3-E1)	Colony formation	[4]

longer release times to reproduce clinically relevant release times, and the ion release time must be sufficient to measure the cytotoxicity, but the norm ISO 10993 does not set any precise time.

Imirzalioglu et al. reported the effects of different proportions of recast alloy on the elemental release and the human gingival fibroblast's cytotoxicity of alloys (Au–Pt, Co–Cr, and Ni–Cr) [21]. Many dental laboratories combine previously cast metal with new alloy for financial reasons. Thus, it is important to evaluate the effects of repeated casting of alloys on cytotoxicity. The authors prepared extracts by incubating each alloy in a culture medium for 24 h and cultured the cells with the extracts for 72 h. The cell activity was assessed by MTT assay. The MTT activity decreased with the increase in the amount of recast alloy addition in the results of all tested alloys. Especially, the activity of Ni–Cr alloy drastically decreased. This might be related to the amount of Ni released from recast alloy; Ni release increased with recast alloy addition. The effect of repeated casting of alloy was found to depend on the alloy composition.

Cell culture tests for five kinds of orthodontic mini-implants (four types of Ti alloys and one type of 316 stainless steel containing alloy) using human gingival fibroblasts and mouse osteoblasts (MC3T3-E1 cells) were reported by Malkoç et al. [22]. They prepared the extracts of each material by incubating in a culture medium for 3 days and assessed the cell activity by the impedance-based real-time cell analyzer for 190 h. Results showed that the material containing 316 stainless steel had the worse effects on the viability of MC3T3-E1 cells. In the case of Ti alloy materials, although two materials showed no significant adverse effects on MC3T3-E1 cells, the other two materials showed significant decrease in their viability after 190 h of incubation. These Ti alloys, however, possessed no adverse effect on the

fibroblast viability. There were differences in the cytotoxicity among the four Ti alloys even though they had the similar chemical component. The authors mentioned that the cytotoxicity depends on several factors, including composition, surface, and size of the particles. They also mentioned that different chemical compositions or handling procedures might influence results of the cytotoxicity test, because there were differences in cell responses to the same alloys between the present study and other reports.

The cytotoxicity of metal ions released from different prosthodontic materials (Ag, Pd, Cu, Zn, Al, K, Ni, Cr, Mo, Be, and Fe) was reported by Elshahawy et al. [23]. They prepared a culture medium containing single metal ion using metal salts. The ion concentration ranges were set to be similar to the concentrations of ions found to be released from four different fixed prosthodontic materials (Type IV gold alloy, Ni–Cr alloy, stainless steel alloy, and CAD–CAM ceramic material) in NaCl and lactic acid solutions [24]. That is, the ion concentration in the tested culture medium was different among the metal elements. L929 cells were used for the cytotoxicity test, and their viability was assessed by means of trypan blue exclusion assay after 1-week culturing. The rank order of cytotoxicity of the metal ions was Zn > Cu > Ni > Be and Ag > Fe > Cr > Mo > Al > Pd > K. The authors mentioned that there was a little difference of rankings between the present study and other reports, and this can be related to the difference in the amount of used metal salt solution. Ni, Zn, Cu, and Be were the highly released elements and the most cytotoxic elements.

The L929 cell viability in the extracts containing metal ions released from pure metals (Cu, Al, Ti, V, Cr, Mo, Mn, Fe, Co, and Ni) was reported by Takeda et al. [25]. Each metal powder or granule was incubated in a culture medium for 24 h and diluted using a pure medium to set the optimum metal ion concentrations. L929 cells were cultured in the prepared extract for 6 days, and their viability was assessed by Borenfreund's assay. The rank order of cytotoxicity was Cr > V > Co > Fe > Mn > Cu > Ni > Mo. No Al and Ti ions were released from each pure metal; therefore, no cytotoxicity of these two ions was found. The order was compared with that reported by previous reports, and the authors mentioned that Cr response observed in the present study was completely different from that. This was suggested to be due to the difference in valence of Cr tested. Cr+6 has been reported to be more toxic than Cr+3 [26]. In addition, it has been reported that Cr+6 is released from 316 LVM stainless steel (surgical grade), and both of Cr+3 and Cr+6 are released from 316 L stainless steel; Co–Cr–Mo alloy in a solution contains 10 % of serum [27, 28]. Thus, the authors suggested that Cr+6 might be released from the tested material, resulting in its severe toxicity. Ionic states of released metal ions can be regarded to be one of the important factors for the expression of adverse effects on cell functions.

Wataha et al. have investigated in the effects of metal ions on the functions of several types of fibroblasts and osteoblasts and published a lot of research papers. They reported the responses of four cell lines, mouse fibroblast (Balb/c 3T3 and L929), human fibroblast (WI-38), and rat osteoblast (ROS 17/2.8) to 14 metal ions (Ag, Al, Au, Be, Cd, Co, Cr, Cu, Ga, Ni, Pd, Ti, V, Zn) [29]. The cells were cultured

Table 14.5 Comparison of ranks of toxicity of metal ions by different cell lines

Cell line	Most toxic						Least toxic			
Balb/c 3T3 Cd	V	Ag	Zn	Au	Co	Pd	Cu	Be	Ti	
ROS 17/2.8	Cd	Ag	V	Zn	Au	Cu	Ti	Co	Pd	Be
L929	Cd	Ag	Zn	V	Au	Cu	Co	Pd	Ti	Be

Note: Only elements which caused 50 % toxicity were included. The Wi-38 cell line was omitted because most metal ions did not cause 50 % toxicity in the concentration range used
Reproduced from Ref. [29], Copyright 1994, with permission from Elsevier

in a culture medium in which the sterile distilled water containing metal ion source, e.g., Ag_2SO_4, were added. To evaluate the cytotoxicity, cell metabolic activity was assessed by succinic dehydrogenase (SDH) activity, which is a measure of the mitochondrial activity of the cells. The ion concentration required to cause a 25 or 50 % depression in SDH activity was estimated. Cr, Al, Ga, and Ni ions did not cause 50 % depression for all of the cell lines in the tested concentration ranges. Although WI-38 cell line was omitted because most metal ions did not cause 50 % depression, the rank order of toxicity (50 % depression) of metal ions was similar for the other three cells (Table 14.5). For example, the order for L929 cell line was Cd > Ag > Zn > V > Au > Cu > Co > Pd > Ti > Be. Cd and Ag ions were the most toxic, Be ion was the least toxic. Zn, Au, or Cu ion toxicity was between the two groups. The Balb/c 3T3 cell line exhibited the most sensitive for the metal ions, and the WI-38 cell line did the least sensitive. The authors mentioned that the cell lines responded differently to most metal ions and the passage number of the cells affected the cytotoxic response. They also reported the correlation between the effects of nine metal ions (Ag, Au, Cd, Cu, Ga, In, Ni, Pd, and Zn) on cellular metabolism and the uptake of the ions [30]. The rate of uptake of the metal ions correlated most closely with depression of SDH activity or protein synthesis of Balb/c 3T3 cell line. The authors also reported about synergistic and antagonistic effects of six metal ions (Ag, Cd, Cu, Ga, Ni, and Zn) on the cellular metabolism of Balb/c 3T3 [31]. They measured MTT-f production of the cells cultured in the media containing two different metal ions, e.g., Ag–Cu and Ag–Ni, and found that the interactive effects depended on the element. For example, Ag–Cu combination possessed no synergistic effect, while Ag–Ni showed it (Table 14.6). The authors mentioned that further study would be needed to support this finding but also suggested that the interactive effects of two metal ions would depend both upon the cytotoxic character of each ion and interplay among the ions.

Schedle et al. also investigated the effects of 13 metal ions (Ag, Pt, Co, In, Ga, Au, Cu, Ni, Zn, Pd, Mo, Sn, and Cr) on the functions of L929, human gingival fibroblasts, and human tissue mast cells [32]. They prepared the culture medium containing each ion by using metal salts, e.g., Ag_2SO_4. The ion concentration required to cause 50 % depression in ^{3}H-thymidine incorporation (indicative of DNA synthesis) into the cells was measured after 72-h culturing. The authors mentioned that a similar rank order of toxicity of the metal ions was observed for L929 and human gingival fibroblasts. For example, the rank for L929 was Ag > Pt > Co > In > Ga > Au > Cu > Ni > Zn > Pd > Mo > Sn > Cr.

Table 14.6 Summary of synergistic and antagonistic effects of several binary cation systems, 24-h duration of exposure

Cations	Synergism	Antagonism
Ag–Cu	No	Yes
Ag–Ni	Yes	Yes
Ag–Zn	No	Yes
Cu–Cd	Yes	No
Cu–Ni	Yes	No
Cu–Zn	Yes	No
Ga–Ni	Yes	Yes

Reproduced from Ref. [31] by permission of John Wiley & Sons Ltd

Cytotoxicity test for 43 metal salts using L929 and mouse osteoblast-like cell (MC3T3-E1) was reported by Yamamoto et al. [4]. They used the colony formation method to assess the concentration required to cause 50 % of depression in the cell functions after 8 days of culturing in the medium conditioned with each salt. Most of the highly toxic metal salts were reported to be salts of soft (Lewis) acids such as Cd, Ag, Hg, Tl, and Ga. The correlation of metal salts' cytotoxicity between L929 and MC3T3-E1 was examined by plotting the concentration (50 % depression) of each metal salt for MC3T3-E1 against the concentration for L929, and its coefficient was found to be 0.82. Thus, the cytotoxicity of the metal salts tested was similar between the two kinds of cells.

14.3 Cytotoxicity

14.3.1 Osteogenic Cells

Metals and alloys have been mainly applied for the use in bone and tooth tissue reconstruction. Different cells expose to the metallic materials implanted in the body. Therefore, various cell lines, such as osteogenic cells and fibroblasts, have been used for the cytotoxicity tests for the materials. It is, however, general that cells of different origins have different cellular responses to implanted materials. Comprehensive investigation must be required to thoroughly understand cytotoxicity of metallic implants using several types of cells.

Several types of osteoblasts and osteoblast-like cell lines and primary cells have been used for the tests and evaluated in their viability and bone-specific gene expression to assess biocompatibility of the metallic materials. The biocompatibility between the materials and osteoblasts is one of the important factors for the applications as implant devices, since new bone tissue is generated by osteoblasts in the surroundings of the devices and fixes the devices in natural bone. Osteoblasts generate new bone tissue through their proliferation, differentiation, and mineralization. Thus, the activity of osteoblasts tested is assessed by estimating not only their via-

bility but also alkaline phosphatase (ALP) activity and expressions of bone matrix proteins, such as osteopontin and osteocalcin. To the author's knowledge, the cytotoxicity of metal materials for osteoblasts has been assessed using the extracts, metal ions, and particles, not metal plates or disks.

Sun et al. reported effects of six metal ions (Al, Co, Cr, Ni, Ti, and V) on the metabolism and differentiation of rat osteoblast-like cell line (ROS 17/2.8) [3]. They cultured the osteoblast-like cells in the medium containing metal ions which was prepared by using metal salts. DNA synthesis, SDH activity, ALP activity, calcification, and gene expression (ALP, osteocalcin, and osteopontin) were evaluated after 7 days of culturing in pure medium followed by 3 days of culturing in the prepared medium. The rank order of cytotoxicity determined by the SDH activity was V > Ti, Co > Ni > Cr + 3, and Al. The authors mentioned that there is a common agreement about the order of V, Co, Ni, and Al in comparison with other reports on the effects of metal ions on different cell lines (fibroblasts). Al showed little adverse effects on the viability but had very strong effects on the gene expression. In addition, Al and Cr significantly inhibited ALP gene expression, while the ALP activity in the cells was not suppressed (Table 14.7). The other ions also possessed unique effects on the cell activities.

MTT assay and ALP activity test were used for the cytotoxicity test using primary human osteoblasts and primary rat osteoblasts for five metal ions (Al, Ni, Cr, V, and Ag) by Zhou et al. [33]. ALP activity was employed in the present report

Table 14.7 Effects of six metal ions on ROS 17/2.8 cell metabolism and gene expression

		Cell activity (%)[b]			Osteogenic gene expression[c]		
Ion conc. (μmol/L)[a]		DNA synth.	SDH activity	ALP activity	ALP	OCN	OPN
Al^{+3}	195	122[d]	92[d]	91[d]	+	+	++
	3120	52	82	85	–	±	++
Co^{+2}	13	57	64	65	++++	++++	+++/++
	104	12	55	46	+	++	+++/++
Cr^{+3}	120	103	97	126	++++	++	+++/++
	1920	55	106	106	+	–	–
Ni^{+2}	76	13	88	66	++++	+	+++
	304	10	48	22	–	–	–
Ti^{+4}	26	37	117	92	++	+++	++
	104	11	42	53	++	++	++
V^{+3}	5	36	90	88	++	+++	++
	20	20	42	57	++++	++++	+++
Control		100	100	100	++++	++++	++++

Reproduced from Ref. [3] by permission of John Wiley & Sons Ltd

[a]The low concentration had low cytotoxicity, and the high concentration had high cytotoxicity as determined by SDH activity

[b]Percentage of control (without addition of metal ions)

[c]Determined by comparing the visual band density of sample with control sample (without addition of metal ions)

[d]The error for the mean is about 15 %

because it is a more sensitive index of toxicity than MTT assay. The rank order of cytotoxicity determined by the ALP activity in human and rat osteoblasts was similar: Cr + 6 > V > Ni > Cr + 3 > Ag > Al.

The cytotoxicity of metal particles and ions (Cu, Al, Si, Ti, Zr, V, Nb, Ta, Cr, Mo, W, Mn, Fe, Co, and Ni) was investigated using human osteoblast-like cell (MG-63) [17]. The cell viability was examined using neutral red assay after culturing the cells in the culture media containing metal particles or ions for 3 or 6 days. The rank order of cytotoxicity was different between the particles and ions. The orders of the particles and ions were Mn > V > Co ≅ Ni > W > Cu > Si > Mo, Fe > Al, Ti, Nb, Cr, Zr, Ta and V > Co > Ni > W ≅ C ≅ Si > Mn > Mo > Al, Ti, Zr, Nb, Ta, Cr, Fe, respectively.

Wataha et al. reported the effects of 14 metal ions on the SDH activity of ROS 17/2.8 cells [29]. The rank order of cytotoxicity, which was determined by the ion concentration required to cause 50 % depression of the activity, was Cd > Ag > V > Zn > Au > Cu > Ti > Co > Pd > Be. Cr, Al, Ga, and Ni did not cause 50 % depression of the activity in the tested concentration ranges. There were differences in the cell sensitivity to metal ions among four types of cells tested (ROS 17/2.8 and three types of fibroblasts).

From these reports, we can find an agreement about the rank of Al, Cr + 3 (low toxicity), Ni (middle toxicity), V, and Co (high toxicity). However, a disagreement about the rank was also found for several ions. This might be due to differences in cell type used and assay used to assess the cytotoxicity. In addition, passage number of cell line used influenced the cell response to metal ions [29].

14.3.2 Fibroblasts

Fibroblasts are the most popular cell in research filed of cytotoxicity of biomaterials, including metallic materials. Mouse fibroblast cell lines (e.g., L929, Balb/c 3T3, and NIH 3T3) and several types of human fibroblasts have been used in previous reports. Especially, gingival fibroblasts have been used for the cytotoxicity test for dental materials. The cytotoxicity of metallic devices themselves, the extract and metal ions for fibroblasts, has been reported by many researchers. It is quite difficult to simply compare the results (cytotoxicity level) among the reports, because there are a lot of differences in culture test conditions, sample treatments, cell types, etc.

In case of the reports on the cytotoxicity of metallic devices themselves, most of the samples tested were alloys and have been commercialized. Sjögren et al. carried out the cytotoxicity test for prostheses using mouse fibroblasts. They used disk-shaped specimens which were prepared by casting manufactured metallic materials. Surface treatment for the specimens tested was found to influence their cytotoxicity. Sandblasting and polishing reduced both cytotoxicity and release of metal ions from the specimens [8]. This means that the cytotoxicity of metallic specimens shaped originally by researchers relates to their surface conditions. We must pay attention to the surface conditions of test specimens, especially when the specimens can release metal ions affecting cell functions.

Elshahawy et al. also reported the cytotoxicity of prostheses for L929 cells [23]. They prepared the test specimens by the conventional lost-wax technique followed by polishing and measured the amount of metal ions released from the specimens in 0.9 % NaCl and 1 % lactic acid solution which resembles the natural human saliva in composition [24]. The release amount was different between the two solutions and significantly higher in the lactic acid solution than the NaCl solution in cases of several metal ions, such as Ni from Ni–Cr alloy and Zn and Cu from gold alloy. The cytotoxicity test of metal ions which has been found to release from the specimens in both solutions was carried out in the range of the measured ion amounts. The rank order of cytotoxicity of the metal ions was Zn > Cu > Ni > Be and Ag > Fe > Cr > Mo > Al > Pd > K. The cytotoxicity likely depended on the released amount rather than metal type. Thus, their work focused on the effects of the metal ions on the cell viability, regarding the ion amount actually released from metallic devices in the body.

On the other hand, Takeda et al., Wataha et al., and Schedle et al. reported the dependence of cytotoxicity for L929 cells on metal type [25, 30, 32]. They prepared a culture medium containing single metal ion in a certain concentration range and estimated the concentration required to cause 50 % depression of the cell viability. Takeda et al. prepared the ion containing medium using pure metal granule or powders, while Wataha et al. and Schedle et al. prepared it using metal salts. In the report by Takeda et al., the rank order of cytotoxicity was Cr > V > Co > Fe > Mn > Cu > Ni >>Mo. No Al and Ti ions were released from each pure metal; therefore, no cytotoxicity of these two ions was found. The rank for L929 cells reported by Schedle et al. was Ag > Pt > Co > In > Ga > Au > Cu > Ni > Zn > Pd > Mo > Sn > Cr. In the case of the report by Wataha et al., there were no information of the rank order, but figures demonstrated the effects of metal ions on the SDH activity, DNA synthesis, protein synthesis, and total protein (Fig. 14.6). The rank determined by reading the SDH activity level (after 12 h of exposure) in the figures was Au > Zn > Ga > Ag ≅ Cu > Ni > Pd ≅ Cd. From these reports, although there were disagreements about the rank of several ions, Cu and Ni likely possessed middle toxicity in any cases. The disagreements might be due to differences in valence, assay, and duration of culture (exposure to metal ion) used for the cytotoxicity test. For example, Cr+6 has been reported to be more toxic than Cr +3 (hamster fibroblasts and human epithelial-like cells were used for the test) [26]. The ion concentration required to cause 50 % of depression varied with the duration of culture (exposure) and related to the assay used for determining the concentration, e.g., SDH activity and ^{3}H-thymidine incorporation [31].

14.3.3 Others

Metal and alloys have been applied for not only orthopedic and dental implants but also implants for other tissues, such as cardiovascular and intrauterine implants. It should be important to use a relevant cell type with regard to the present in vivo conditions for the cytotoxicity test.

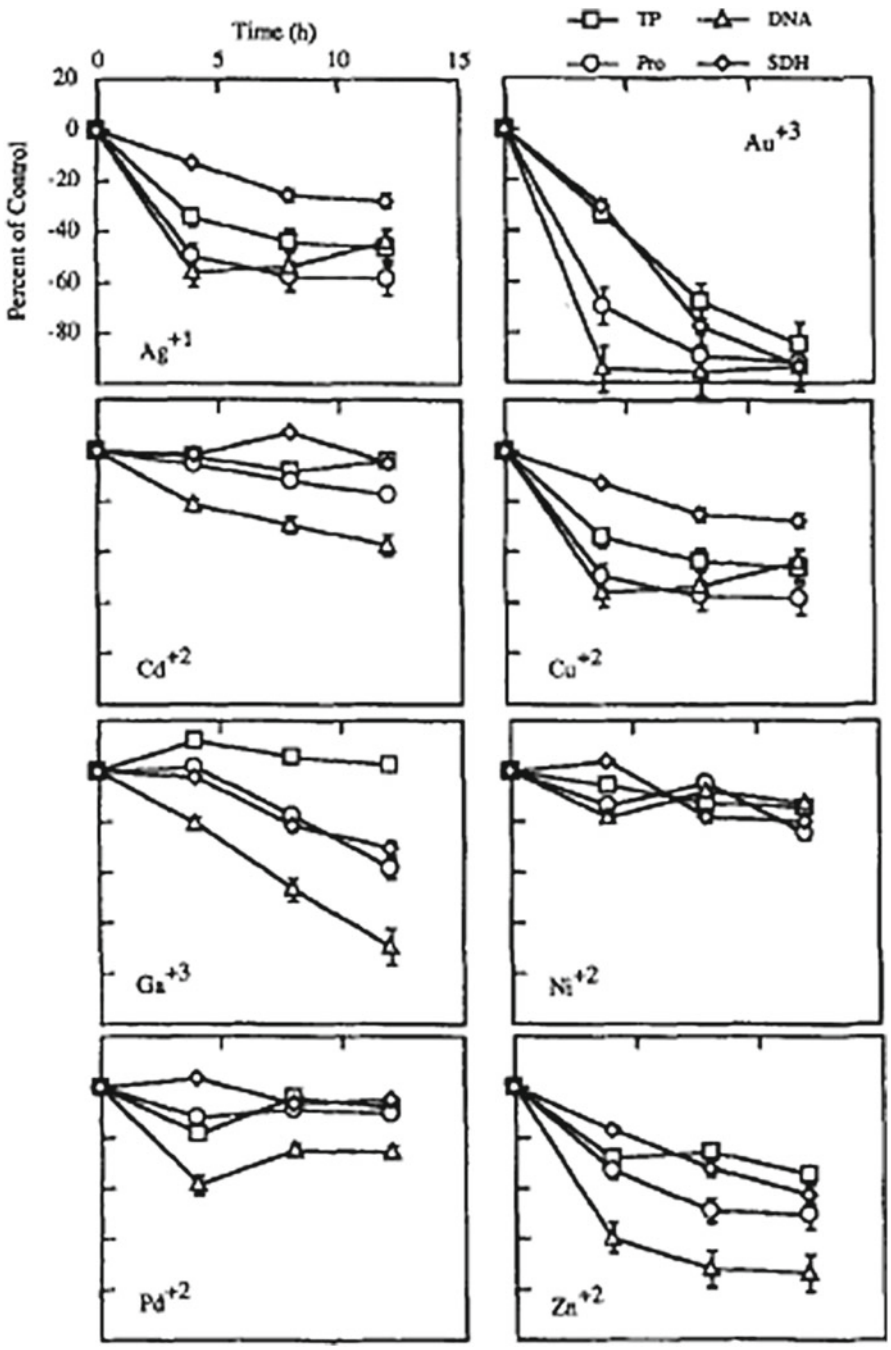

Fig. 14.6 The effects of metal ions on DNA synthesis (DNA), protein synthesis (Pro), succinic dehydrogenase (SDH) activity, and total protein (TP) over 12 h of exposure. Cellular functions are expressed as a percentage of a control group to which no metal ions were added. Error bars represent three standard errors of the mean at $P = .05$. Cell functions were inhibited at different rates, but the order of the decrease was generally similar among metals (Reproduced from Ref. [30] by permission of John Wiley & Sons Ltd)

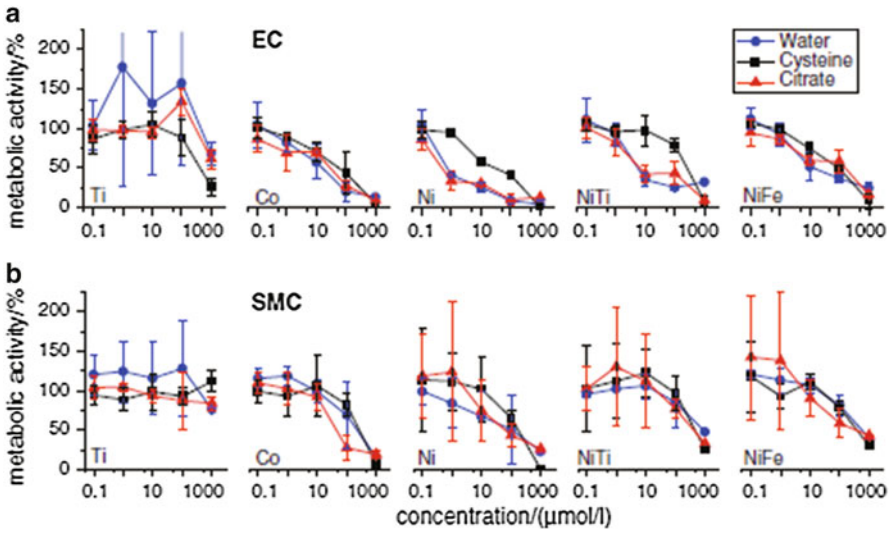

Fig. 14.7 Metabolic activity of human endothelial cells (EC) (**a**) and smooth muscle cells (SMC) (**b**) after 72 ± 2 h of incubation with different concentrations of Ti, Co, Ni, Ni–Ti, and Ni–Fe nanoparticles generated in water, citrate, or cysteine solution (Reprinted from Ref. [34], with kind permission from Springer Science + Business Media)

Ni–Ti and Co–Cr alloys have been used for cardiovascular implants. The alloy nanoparticles might be unintentionally generated via failure, wear, or abrasion and released into the surrounding tissues. Hahn et al. reported the cytotoxicity of metallic nanoparticles (Ni–Ti, Ni, Ti, Ni–Fe, and Co) for human primary endothelial and smooth muscle cells [34]. The cells were exposed to the culture medium containing the nanoparticle colloids in the concentration range of 0.1–1,000 μM for 72 h. Three different solvents, water, citrate, and cysteine, were used for preparing nanoparticle colloids. The concentration required to cause 20 % depression of the cell metabolic activity was measured, and the rank order of the cytotoxicity for endothelial cells determined by the concentration was Ni, Co > Ni–Fe, and Ni–Ti > Ti. The endothelial cells were more sensitive to the nanoparticles than the smooth muscle cells (Fig. 14.7).

Cu-intrauterine device (Cu-IUD) has been widely used, but there are concerns that the Cu-IUD causes unfavorable side reactions, such as irregular and heavy bleeding and pain. Wu et al. assessed the cytotoxicity of three metal ions (Cu, Zn, and Ag) for primary human endometrial epithelial cells [35]. Zn and Ag are known for essential trace element required for cell growth and broad-spectrum antibiotic activity, respectively. Thus, the authors expected that future IUDs will be endowed with more corresponding functions, such as trace element supplementation, long-acting antibiotic activity, irregular bleeding prevention, and biocompatibility improvement with supplement of Zn and Ag to Cu-IUD. The cytotoxicity of the cells was assessed after 1, 2, and 3 days of exposure to the culture medium contain-

ing each metal ion prepared with metal salts. The rank order of cytotoxicity determined by the ion concentration required to cause 50 % depression was Ag > Cu > Zn. The cytotoxicity of only Cu increased with the increase in duration of exposure.

Schedle et al. reported the response of human tissue mast cells to 13 different metal ions (Ag, Pt, Co, In, Ga, Au, Cu, Ni, Zn, Pd, Mo, Sn, and Cr) [32]. They prepared the culture medium containing single metal ion by using metal salts and exposed the cells to various concentrations of metal ions for 30 min. The cytotoxicity for the mast cells was assessed by measuring secretion of the proinflammatory mediator histamine, because the cells usually release vasoactive mediator substances (histamine) in response to specific cell activation. Ag and Au (lesser extent than Ag) induced histamine secretion from the cells, whereas the other ions showed no effect. In the present report, they also evaluated the cytotoxicity for L929 cells and human gingival fibroblasts and revealed that not only Ag but also other several ions showed adverse effects on the viability. Thus, the response of the mast cells to the metal ions can be regarded to be considerably different from that to the fibroblasts.

14.4 Positive Cell Reactions

In most cases, in vitro cytotoxicity test for metal and alloys has been carried out to clarify if the materials possess adverse effects on cell, since many cases have been reported in which human beings or experimental animals have adverse reactions to metallic implants. On the other hand, positive reactions of cells on metal ions have been reported by many researchers recently. For example, the upregulation of osteoblast activity by ionic dissolution products released from bioactive glasses and glass ceramics has enjoyed an increasing interest in bioceramics research field [36]. Most of bioactive glasses and glass ceramics dissolve in the body and release ions. Specific effects of the released ions (Si, Ca, P, Zn, Mg, Sr, Cu, etc.) on osteoblasts are expected to be one of the important factors for achieving bioactivity of these materials. Biological response in vivo and in vitro to these ions relates to ion type. For example, Zn was reported to show anti-inflammatory effect and stimulates bone formation, and Cu was reported to promote synergistic stimulating effects on angiogenesis. Zhou et al. evaluated the ALP activity of primary human osteoblasts and primary rat osteoblast cells after culturing in the culture medium containing metal ions to assess the cytotoxicity [33]. They revealed that Al is biphasic in cytotoxicity; the ion enhanced the cell proliferation at low ion concentration (<10 μM), while its cytotoxicity increased when the concentration was over 1,000 μM. The exact mechanism of interaction between these ions and cells is not fully understood, which has prompted considerable research work. However, such upregulation of cell activity by these ions is expected to be useful for developing new biomaterials having better biocompatibility and bioactivity in vivo and in vitro.

14.5 Summary

This chapter focused on cytotoxicity of metallic materials including ions, since the increasing use of orthopedic and dental implants has stimulated interest and concern regarding the chronic, long-term effects of metallic biomaterials used. A comprehensive analysis of the available literature on the cytotoxicity of metal and alloys has been presented. Since most data was derived from stand-alone studies, there are still disagreements about the cytotoxicity, including the ion amount required to cause severe depression in cell activity, of several metal ions. Standardization of culture conditions, cell types, assay for evaluating the cytotoxicity, duration of exposure to metal, etc. and large-scale comparative studies could be a first step in increasing our understanding in this field. The cytotoxicity of metallic devices themselves is one of the considerable factors for assessment of safety of the devices. Especially, in the case of nanoparticles of metallic materials, "nano"-factor itself may appear to cause several adverse effects on cells. In addition, microparticles are unexpectedly produced by wear on metallic implant surfaces and influence cell functions. Therefore, we need to pay attention to size and shape of metallic materials as well. Many devices have been already tested, following the procedure recommended by ISO. On the other hand, as discussed in the present chapter, cell response considerably relates to the metal type. It would be important to identify the specific role of single metal ion for understanding fully molecular mechanisms and chemical pathways dictating the interaction between metallic materials and cells.

References

1. Dobbs HS, Minski MJ (1980) Metal ion release after total hip replacement. Biomaterials 1:193–198
2. Solar RJ, Pollack SR, Korostoff E (1979) In vitro corrosion testing of titanium surgical implant alloys: an approach to understanding titanium release from implants. J Biomed Mater Res 13:217–250
3. Sun ZL, Wataha JC, Hanks CT (1997) Effects of metal ions on osteoblast-like cell metabolism and differentiation. J Biomed Mater Res 34:29–37
4. Yamamoto A, Honma R, Sumita M (1998) Cytotoxicity evaluation of 43 metal salts using murine fibroblasts and osteoblastic cells. J Biomed Mater Res 39:331–340
5. Soenen SJ, Rivera-Gil P, Montenegro JM, Parak WJ, De Smedt SC, Braeckmans K (2011) Cellular toxicity of inorganic nanoparticles: common aspects and guidelines for improved nanotoxicity evaluation. Nano Today 6:446–465
6. Rivera GP, Oberdörster G, Elder A, Puntes V, Parak WJ (2010) Correlating physico-chemical with toxicological properties of nanoparticles: the present and the future. ACS Nano 4:5527–5531
7. Retamoso LB, Luz TB, Marinowic DR, Machado DC, De Menezes LM, Freitas MPM, Oshima HMS (2012) Cytotoxicity of esthetic, metallic, and nickel-free orthodontic brackets: cellular behavior and viability. Am J Orthod Dentofac Orthop 142:70–74
8. Sjögren G, Sletten G, Dahl JE (2000) Cytotoxicity of dental alloys, metals, and ceramics assessed by Millipore filter, agar overlay, and MTT tests. J Prosthet Dent 84:229–236

9. Grill V, Sandrucci MA, Basa M, Di Lenarda R, Dorigo E, Narducci P, Martelli AM, Delbello G, Bareggi R (1997) The influence of dental metal alloys on cell proliferation and fibronectin arrangement in human fibroblast cultures. Arch Oral Biol 42:641–647
10. Couchman JR, Rees DA, Green MR, Smith CG (1982) Fibronectin has a dual role in locomotion and anchorage of primary chick fibroblasts and can promote entry into the division cycle. J Cell Biol 93:402–410
11. Gupta AK, Curtis ASG (2004) Lactoferrin and ceruloplasmin derivatized superparamagnetic iron oxide nanoparticles for targeting cell surface receptors. Biomaterials 25:3029–3040
12. Gupta AK, Gupta M (2005) Cytotoxicity suppression and cellular uptake enhancement of surface modified magnetic nanoparticles. Biomaterials 26:1565–1573
13. Bhabra G, Sood A, Fisher B, Cartwright L, Saunders M, Evans WH, Surprenant A, Lopez-Castejon G, Mann S, Davis SA and others (2009) Nanoparticles can cause DNA damage across a cellular barrier. Nat Nanotechnol 4:876–883
14. Oberdörster G, Sharp Z, Atudorei V, Elder A, Gelein R, Kreyling W, Cox C (2004) Translocation of inhaled ultrafine particles to the brain. Inhal Toxicol 16:437–445
15. Lunov O, Syrovets T, Röcker C, Tron K, Ulrich NG, Rasche V, Mailänder V, Landfester K, Simmet T (2010) Lysosomal degradation of the carboxydextran shell of coated superparamagnetic iron oxide nanoparticles and the fate of professional phagocytes. Biomaterials 31:9015–9022
16. Lunov O, Syrovets T, Büchele B, Jiang X, Röcker C, Tron K, Nienhaus GU, Walther P, Mailänder V, Landfester K and others (2010) The effect of carboxydextran-coated superparamagnetic iron oxide nanoparticles on c-Jun N-terminal kinase-mediated apoptosis in human macrophages. Biomaterials 31:5063–5071
17. Sakai T, Takeda S, Nakamura M (2002) The effects of particulate metals on cell viability of osteoblast-like cells *in vitro*. Dent Mater J 21:133–146
18. Rae T (1978) The haemolytic action of particulate metals (Cd, Cr, Co, Fe, Mo, Ni, Ta, Ti, Zn, Co-Cr alloy). J Pathol 125:81–89
19. Takeda S, Akiyama M, Sakane K, Sakai T, Nakamura M (2000) Effects of metal combinations on cytotoxicity evaluation using a dynamic extraction method. Dent Mater J 19:373–380
20. Mockers O, Deroze D, Camps J (2002) Cytotoxicity of orthodontic bands, brackets and archwires in vitro. Dent Mater 18:311–317
21. Imirzalioglu P, Alaaddinoglu E, Yilmaz Z, Oduncuoglu B, Yilmaz B, Rosenstiel S (2012) Influence of recasting different types of dental alloys on gingival fibroblast cytotoxicity. J Prosthet Dent 107:24–33
22. Malkoç S, Öztürk F, Öreki B, Bozkurt BS, Hakki SS (2012) Real-time cell analysis of the cytotoxicity of orthodontic mini-implants on human gingival fibroblasts and mouse osteoblasts. Am J Orthod Dentofac Orthop 141:419–426
23. Elshahawy WM, Watanabe I, Kramer P (2009) In vitro cytotoxicity evaluation of elemental ions released from different prosthodontic materials. Dent Mater 25:1551–1555
24. Elshahawy W, Watanabe I, Koike M (2009) Elemental ion release from four different fixed prosthodontic materials. Dent Mater 25:976–981
25. Takeda S, Kakiuchi H, Doi H, Nakamura M (1989) Cytotoxicity of pure metals. Jpn J Dent Mater 8:648–652
26. Levis AG, Bianchi V, Tamino G, Pegoraro B (1978) Cytotoxic effects of hexavalent and trivalent chromium on mammalian cells in vitro. Br J Cancer 37:386–396
27. Merritt K, Wortman RS, Millard M, Brown SA (1983) XPS analysis of 316 LVM corroded in serum and saline. Artif Cells Blood Substit Biotechnol 11:115–124
28. Brown SA, Farnsworth LJ, Merritt K, Crowe TD (1988) In vitro and in vivo metal ion release. J Biomed Mater Res 22:321–338
29. Wataha JC, Hanks CT, Sun Z (1994) Effect of cell line on in vitro metal ion cytotoxicity. Dent Mater 10:156–161
30. Wataha JC, Hanks CT, Craig RG (1994) In vitro effects of metal ions on cellular metabolism and the correlation between these effects and the uptake of the ions. J Biomed Mater Res 28:427–433

31. Wataha JC, Hanks CT, Craig RG (1992) In vitro synergistic, antagonistic, and duration of exposure effects of metal cations on eukaryotic cells. J Biomed Mater Res 26:1297–1309
32. Schedle A, Samorapoompichit P, Rausch-Fan XH, Franz A, Füreder W, Sperr WR, Sperr W, Ellinger A, Slavicek R, Boltz-Nitulescu G (1995) Response of L-929 fibroblasts, human gingival fibroblasts, and human tissue mast cells to various metal cations. J Dent Res 74:1513–1520
33. Zhou Z, Liu X, Liu Q, Liu L (2009) Evaluation of the potential cytotoxicity of metals associated with implanted biomaterials (I). Prep Biochem Biotechnol 39:81–91
34. Hahn A, Fuhlrott J, Loos A, Barcikowski S (2012) Cytotoxicity and ion release of alloy nanoparticles. J Nanoparticle Res 14:686
35. Wu J, Wang L, He J, Zhu C (2012) In vitro cytotoxicity of Cu 2+, Zn 2+, Ag + and their mixtures on primary human endometrial epithelial cells. Contraception 85:509–518
36. Hoppe A, Güldal NS, Boccaccini AR (2011) A review of the biological response to ionic dissolution products from bioactive glasses and glass-ceramics. Biomaterials 32:2757–2774